FLEXIBLE BIOSENSORS AND INTELLIGENT MEDICAL DEVICES IN HEALTH AND DISEASE

EDITED BY: Zhiwei Luo, Xiaoguang Zhou, Jian Yang and Jie Deng
PUBLISHED IN: Frontiers in Bioengineering and Biotechnology

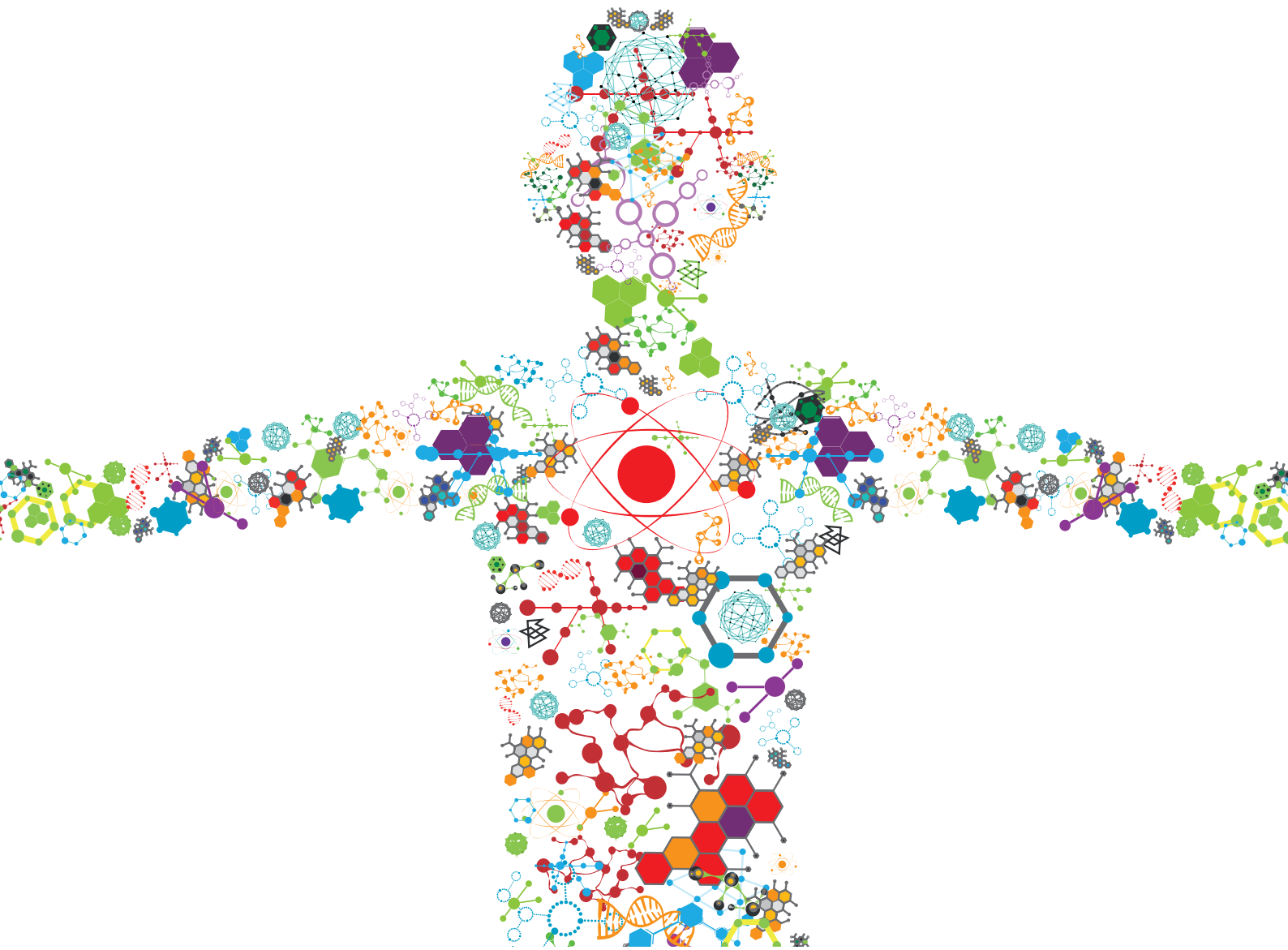

frontiers Research Topics

ISSN 1664-8714
ISBN 978-2-88976-445-7
DOI 10.3389/978-2-88976-445-7

About Frontiers

Frontiers is more than just an open-access publisher of scholarly articles: it is a pioneering approach to the world of academia, radically improving the way scholarly research is managed. The grand vision of Frontiers is a world where all people have an equal opportunity to seek, share and generate knowledge. Frontiers provides immediate and permanent online open access to all its publications, but this alone is not enough to realize our grand goals.

Frontiers Journal Series

The Frontiers Journal Series is a multi-tier and interdisciplinary set of open-access, online journals, promising a paradigm shift from the current review, selection and dissemination processes in academic publishing. All Frontiers journals are driven by researchers for researchers; therefore, they constitute a service to the scholarly community. At the same time, the Frontiers Journal Series operates on a revolutionary invention, the tiered publishing system, initially addressing specific communities of scholars, and gradually climbing up to broader public understanding, thus serving the interests of the lay society, too.

Dedication to Quality

Each Frontiers article is a landmark of the highest quality, thanks to genuinely collaborative interactions between authors and review editors, who include some of the world's best academicians. Research must be certified by peers before entering a stream of knowledge that may eventually reach the public - and shape society; therefore, Frontiers only applies the most rigorous and unbiased reviews.
Frontiers revolutionizes research publishing by freely delivering the most outstanding research, evaluated with no bias from both the academic and social point of view. By applying the most advanced information technologies, Frontiers is catapulting scholarly publishing into a new generation.

What are Frontiers Research Topics?

Frontiers Research Topics are very popular trademarks of the Frontiers Journals Series: they are collections of at least ten articles, all centered on a particular subject. With their unique mix of varied contributions from Original Research to Review Articles, Frontiers Research Topics unify the most influential researchers, the latest key findings and historical advances in a hot research area! Find out more on how to host your own Frontiers Research Topic or contribute to one as an author by contacting the Frontiers Editorial Office: frontiersin.org/about/contact

FLEXIBLE BIOSENSORS AND INTELLIGENT MEDICAL DEVICES IN HEALTH AND DISEASE

Topic Editors:
Zhiwei Luo, Kobe University, Japan
Xiaoguang Zhou, Beijing University of Posts and Telecommunications (BUPT), China
Jian Yang, Wuyi University, China
Jie Deng, Rush University, United States

Citation: Luo, Z., Zhou, X., Yang, J., Deng, J., eds. (2022). Flexible Biosensors and Intelligent Medical Devices in Health and Disease. Lausanne: Frontiers Media SA. doi: 10.3389/978-2-88976-445-7

Table of Contents

frontiers | Frontiers in Bioengineering and Biotechnology

EDITORIAL
published: 02 June 2022
doi: 10.3389/fbioe.2022.849617

Editorial: Flexible Biosensors and Intelligent Medical Devices in Health and Disease

*Jian Yang**

Faculty of Intelligent Manufacturing, Wuyi University, Jiangmen, China

Keywords: flexible biosensors, medical devices, machine learning, artificial intelligence, health care

Editorial on the Research Topic

Flexible Biosensors and Intelligent Medical Devices in Health and Disease

Recent advances have been made in biosensors and medical devices for diagnosis and health monitoring of various diseases. Flexible biosensors accelerate the development of wearable biomedical technologies and intelligent medical devices help doctors or patients to understand clinical characteristics and biomedical data. This Research Topic focuses on both the hardware and software of intelligent biomedical devices, including flexible or wearable biosensors, machine learning algorithms, and artificial intelligence-based technologies in health and disease. Flexible or wearable biosensors provide a new efficient way to monitor and obtain medical data, on the other hand, artificial intelligence shows its effectiveness in massive medical data mining and clinical diagnosis. With the recent development of flexible electronics and artificial intelligence, both innovative machine learning algorithms and high-performance data processing, and intelligent medical devices are applied to meet the need of personalized medicine and patient healthcare in various areas.

In this collection, a wearable ear device system was proposed by Lian et al. to address facial emotion recognition disorders with a deep-learning based multi-model physiological signal recognition algorithm. Multiple data from sensors such as heart rate, triaxial acceleration, skin electricity, body temperature, and facial images were analyzed and proved the effectiveness of this system for patients with potential nervous system diseases. As for post-surgical patients, especially those with upper extremity lymphedema, a portable monitoring and auxiliary treatment device was presented by Yanmin et al. to help them better rehabilitate. The pressure sensing layer embedded in the device can constantly measure and compare the change of arm circumference in different parts of the upper limb, which can provide the patients with early detection and effective control. Gori et al. exhaustively reviewed the biomedical and tissue engineering strategies to control foreign body reactions to invasive neural electrodes in recent years. From molecular mechanism and cellular components of foreign body reactions to design and geometry of the electrodes, they mentioned the development of innovative and advanced functional biomaterials including MEMS polymer materials and hydrogels and the interface-microenvironment interaction affected by anti-inflammatory or anti-fibrotic drugs, intraneural interfaces, or neuroprostheses that are beneficial for amputees to restore their sensorimotor limb function. The authors also indicated that next-generation intraneural electrodes produced by current microfluidic, microscale, and nanoscale technologies deserved further investigation. Flexible or wearable biosensors have promoted these advances in disease diagnosis and the healthcare of various patients.

On the other side, it is a burden for doctors or patients to treat and analyze huge medical data, especially image data. Computational intelligent algorithms such as machine learning, deep learning, and transfer learning have been applied to medical imaging classification, showing predictable advantages in massive data treatment and clinical diagnosis. For instance, Li et al. compared eight

OPEN ACCESS

Edited and reviewed by:
Manolo Garabini,
University of Pisa, Italy

***Correspondence:**
Jian Yang
yyyjian@gmail.com

Specialty section:
This article was submitted to Bionics and Biomimetics, a section of the journal Frontiers in Bioengineering and Biotechnology

Received: *06 January 2022*
Accepted: *14 April 2022*
Published: *02 June 2022*

Citation:
Yang J (2022) Editorial: Flexible Biosensors and Intelligent Medical Devices in Health and Disease. Front. Bioeng. Biotechnol. 10:849617. doi: 10.3389/fbioe.2022.849617

classical supervised machine learning methods, two deep learning models, and one transfer learning model with more than 1,000 radiological samples. The results showed that transfer learning is most effective in the classification of colorectal cancer lymph node metastasis with a better accuracy; they did not need to train the model and it could be applied to a smaller medical image dataset. As for childhood cataract patients, Lin et al. developed an intelligent system based on machine learning models and the features of optical coherence tomography images, 200 eye data of 132 patients in 8 years were collected and analyzed, demonstrating that the best corrected visual acuity of childhood cataract patients in 3 and 5 years can be predicted with a small error. Similarly, Huang et al. combined different machine learning algorithms with the radiomics features of multiparameter MRI and clinicopathological characteristics to predict the tumor shrinkage pattern of breast cancer patients prior to neoadjuvant chemotherapy. A total of 4,198 features in segmented MRI sequences and a set of clinicopathological data including age, menstrual state, biomarkers, and receptors for each patient were treated and analyzed. The multilayer perception neural network achieved a higher area under the curve and better accuracy, it established a feasibility for early diagnosis and prediction of breast cancer. Because of the increasing incidence rate of breast cancer, Dou et al. investigated kernel function selection and combined a genetic algorithm, particle swarm optimization, and simulated annealing with support vector machine algorithm. The optimization algorithm could significantly improve the diagnosis efficiency of their medical institution.

Magnetic resonance images play an important role in clinical disease diagnosis and physiological mechanism. However, the automatic segmentation of the left ventricle wall in the four-chamber view of MRI is still a challenge. Zhang et al. proposed a dense recurrent neural network algorithm to accurately achieve left ventricle wall segmentation in a four-chamber view of MRI sequences, this method provided compensation for the first long short-term memory cells and made the hidden information in the cells more visible, with better cardiac state estimation. Similarly, Duan et al. proposed a multi-branch feature fusion network to achieve the real-time segmentation of liver lesion images for colonoscopy, which can detect rectal polyps with high accuracy and read-time performance. Deng et al. designed medical ultrasound remote control software which can use mobile devices to remotely control ultrasound devices in the same local area network, Yanbo et al. utilized a fuzzy neural network control system model to improve the removal efficiency of toxic and refractory organic water in waste water.

Therefore, it is clearly seen that artificial intelligence-based technologies have been widely studied in various areas of disease diagnosis, which are especially helpful for computer-aided diagnosis. This topic showed recent advances in *Flexible Biosensors and Intelligent Medical Devices in Health and Disease*.

AUTHOR CONTRIBUTIONS

The author confirms being the sole contributor of this work and has approved it for publication.

ACKNOWLEDGMENTS

We especially thank the editors, Dr. Zhiwei Luo, Dr. Xiaoguang Zhou, JY, Dr. Jie Deng for organizing the topic and reviewing the articles, as well as the technical support from Frontiers.

Conflict of Interest: The author declares that the research was conducted in the absence of any commercial or financial relationships that could be construed as a potential conflict of interest.

frontiers in Bioengineering and Biotechnology

ORIGINAL RESEARCH
published: 14 January 2021
doi: 10.3389/fbioe.2020.620257

Different Machine Learning and Deep Learning Methods for the Classification of Colorectal Cancer Lymph Node Metastasis Images

Jin Li[1], *Peng Wang*[1], *Yang Zhou*[1,2], *Hong Liang*[1] *and Kuan Luan*[1]*

[1] College of Intelligent System Science and Engineering, Harbin Engineering University, Harbin, China, [2] Department of Radiology, Harbin Medical University Cancer Hospital, Harbin, China

The classification of colorectal cancer (CRC) lymph node metastasis (LNM) is a vital clinical issue related to recurrence and design of treatment plans. However, it remains unclear which method is effective in automatically classifying CRC LNM. Hence, this study compared the performance of existing classification methods, i.e., machine learning, deep learning, and deep transfer learning, to identify the most effective method. A total of 3,364 samples (1,646 positive and 1,718 negative) from Harbin Medical University Cancer Hospital were collected. All patches were manually segmented by experienced radiologists, and the image size was based on the lesion to be intercepted. Two classes of global features and one class of local features were extracted from the patches. These features were used in eight machine learning algorithms, while the other models used raw data. Experiment results showed that deep transfer learning was the most effective method with an accuracy of 0.7583 and an area under the curve of 0.7941. Furthermore, to improve the interpretability of the results from the deep learning and deep transfer learning models, the classification heat-map features were used, which displayed the region of feature extraction by superposing with raw data. The research findings are expected to promote the use of effective methods in CRC LNM detection and hence facilitate the design of proper treatment plans.

Keywords: colorectal cancer, lymph node, classification, transfer learning, deep learning

OPEN ACCESS

Edited by:
Zhiwei Luo,
Kobe University, Japan

Reviewed by:
Chengzhen Xu,
Huaibei Normal University, China
Yanjun Wei,
University of Texas MD Anderson Cancer Center, United States

***Correspondence:**
Kuan Luan
luankuan@aliyun.com;
luankuan@hrbeu.edu.cn

Specialty section:
This article was submitted to Bionics and Biomimetics, a section of the journal Frontiers in Bioengineering and Biotechnology

Received: *22 October 2020*
Accepted: *14 December 2020*
Published: *14 January 2021*

Citation:
Li J, Wang P, Zhou Y, Liang H and Luan K (2021) Different Machine Learning and Deep Learning Methods for the Classification of Colorectal Cancer Lymph Node Metastasis Images. Front. Bioeng. Biotechnol. 8:620257. doi: 10.3389/fbioe.2020.620257

INTRODUCTION

Colorectal cancer (CRC) has a higher recurrence rate than all other cancers (Bray et al., 2018). CRC lymph node metastasis (LNM) is the root cause of CRC recurrence (Ding et al., 2019; Yang and Liu, 2020). CRC patients with LNM have a 5-year survival rate ranging from 50 to 68%, but those without LNM have a higher rate up to 95% (Ishihara et al., 2017; Zhou et al., 2017). Treatment of CRC is also influenced by the presence of LNM. The conventional treatment plan involves endoscopic resection, and surgical resection accompanied by LN dissection is necessary for patients with LNM (Nasu et al., 2013). Hence, it is important to determine the presence of CRC LNM, and to this end, an automatic classification method for CRC LNM should be explored to give a second objective opinion and then assist the radiologist in providing a correct report.

As computer technologies advance in these years, medical imaging classification methods have seen wider adoption. Many new methods based on machine learning (Al-Absi et al., 2012), deep learning (Sun et al., 2016), or deep transfer learning (Pratap and Kokil, 2019), have gradually been applied to medical imaging classification. These methods can provide additional preoperative information to aid radiologists in making proper treatment plans (Carneiro et al., 2017; Lu et al., 2017).

There are many types of machine learning algorithms that can be applied to medical imaging classification, such as support vector machine (SVM) (Burges, 1998), decision trees (DT) (Quinlan, 1986), and naïve Bayes (NB) (Friedman et al., 1997). Vibha et al. (2006) used DT to classify mammograms and obtained a classification accuracy of almost 90%. Inthajak et al. (2011) presented a k-nearest neighbor (KNN) algorithm to categorize medical images. Ahmad et al. (2016) used NB classification to categorize each chest X-ray image to either normal with infection or with fluid in capture features. García-Floriano et al. (2019) proposed a machine learning model based on SVM. This model could classify age-related macular degeneration in fundus images and achieved a higher classification accuracy than many well-regarded state-of-the-art methods. Luo et al. (2018) used SVM to classify human stomach cancer in optical coherence tomography images and obtained a higher classification accuracy than human detection. Although these methods outperformed human radiologists in terms of classification accuracy, they are subject to problems in feature extraction. The features that are often manually extracted fall short of objectivity and will affect the algorithms' performance and hence the classification accuracy. Thus, a method that could learn underlying data features is needed.

Deep learning (Lecun et al., 2015) has achieved stunning success in image classification in the ImageNet Large Scale Visual Recognition Challenge (Krizhevsky et al., 2017) in 2012. There are several landmark studies (Ma et al., 2017; Golatkar et al., 2018) that have promoted the development of deep learning algorithms. Compared to machine learning, deep learning has a vital advantage, i.e., the ability to automatically learn the potential features of data by utilizing the convolution neural network (CNN). A CNN could automatically learn potential features from raw data layer by layer with little or no hands-on intervention. Now, CNNs have already become a study focus, especially in medical imaging (Litjens et al., 2017; Shen et al., 2017). For instance, Song et al. (2017) used a CNN for lung nodule classification on computed tomography (CT). Liu and An (2017) built a classification model for detection of prostate cancer based on deep learning. Despite the good performance of deep learning methods in image classification, however, there are two problems that undermine their wider adoption – the need for massive number of data and high-performance computing devices, like graphic processing units (GPUs). As deep learning needs a large number of data to train and fit the CNN parameters, GPUs are preferred than other equipment to process the images faster, but it incurs a high training cost. Thus, reducing the training cost is the key to solving the problem.

Transfer learning, introduced by Pan and Yang (2010), uses the existing knowledge learned from one environment to solve similar problems in different environments. Pan and Yang (2010) summarized the classification process as well as the pros and cons of transfer learning methods. Transfer learning methods have a lower training cost than their deep learning counterparts as the former does not require as many data as the latter needs for training. In transfer learning, a model pretrained on another large dataset, such as ImageNet, is employed to complete a task through fine-tuning[1] or other methods (Long et al., 2013, 2017; Tzeng et al., 2014), so it has a lower cost than deep learning. Because of these advantages, transfer learning is widely used in medical imaging. Vesal et al. (2018) used two pre-trained models to classify breast cancer histology images and obtained an accuracy of 97.50 and 91.25%. da Nobrega et al. (2018) used a deep transfer learning model (Tan et al., 2018) to classify lung nodules in CT lung images. Dornaika et al. (2019) used transfer learning to estimate age through facial images, and the experiments were carried out on three public databases.

In previous studies, comparisons were made to find the most effective method for specific diseases. Wang L. et al. (2017) used four methods with eight classification schemes to classify ophthalmic images and found that local binary pattern with SVM and wavelet transformation with SVM had the best classification performance, with an accuracy of 87%. Wang H. et al. (2017) used five methods, including random forest, SVM, adaptive boosting, back-propagation artificial neural network (ANN), and CNN to classify mediastinal LNM of non-small cell lung cancer. Lee et al. (2019) used eight deep learning algorithms to differentiate benign and malignant tumors from cervical metastatic LN of thyroid cancer based on preoperative CT images, trying to identify the most suitable model. However, to the authors' knowledge, there are few methods used for CRC LNM classification based on machine learning, deep learning, or deep transfer learning. Furthermore, no previous studies have compared these three methods. Therefore, which method is the most effective one for CRC LNM classification is unclear.

According to the literature, the use of machine learning, deep learning, or transfer learning in medical imaging is rapidly developing and evolving. Using computational approaches to provide additional preoperative information can help doctors design proper treatment plans (Carneiro et al., 2017; Lu et al., 2017). Several papers have been published on CRC (Simjanoska et al., 2013; Ciompi et al., 2017; Nakaya et al., 2017; Bychkov et al., 2018), but few studies have explored the performance of machine learning, deep learning, and transfer learning in CRC LNM classification, and which method has the best performance is yet to be determined, which motivated us to conduct this research. To identify the most effective method for CRC LNM classification, the following approaches were taken in this study.

First, eight machine learning, two deep learning, and one transfer learning classification methods were used to classify CRC LNM images.

Next, the classification results were compared to evaluate the performance of different methods and identify the one with the best classification performance.

[1]Transfer learning and Fine-Tuning. Available online at: https://ru.coursera.org/lecture/machine-learning-duke/transfer-learning-and-fine-tuning-OdURo

Finally, a classification heat-map was used to improve the interpretability of the classification method for CRC LNM.

MATERIALS AND METHODS

Data

Data used in the present study were collected from Harbin Medical University Cancer Hospital. There were 3,364 samples in the dataset, among which 1,646 were positive and 1,718 were negative. The standard of all samples was an LN of a diameter >3 mm. All patients underwent 3.0T magnetic resonance imaging (MRI) before surgery using Philips Achieva, with a 16-channel torso array coil. MRI sagittal T2WI scan sequence was performed with the following parameters: TR/TE 3000/100 ms, the number of signal frequency (NSA) 2, and the layer thickness 4.0 mm, and layer spacing 0.4 mm. The position of the rectal lesions was determined by the sagittal position, which was perpendicular to the intestinal canal lesions, with a transverse T2WI scan: TR/TE 3,824/110 ms, NSA 0–3, layer thickness 3.5 mm, and interval 0.2 mm. According to the sagittal lesion position, patients with parallel pathological changes received coronal T2WI scans: TR/TE 3,824/110 ms, NSA 3, and layer spacing 0.2 mm. Then, the objective LN in the sagittal, transverse, and coronal images were located. All images used in this study were marked as CRC LNs and classified as negative or positive by experienced radiologists. All patches were manually segmented by experienced radiologists, and the image size was based on the lesion to be intercepted. **Figure 1** presents the CRC LN.

Methods

In this study, intensity features were extracted by a gray-level histogram (GLH) (Otsu, 1979), and the textural features were extracted by the gray-level co-occurrence matrix (GLCM) (Haralick et al., 1973). These two features are global features. Furthermore, the scale-invariant feature transform (SIFT) (Lowe, 1999, 2004) operator was used for local features. These methods were implemented in Python.

Eight classical supervised machine learning methods, including AdaBoost (AB) (Freund and Schapire, 1997), DT (Quinlan, 1986), KNN (Cover and Hart, 1967), logistic regression (LR) (Cucchiara, 2012), NB (Friedman et al., 1997), SVM (Burges, 1998), stochastic gradient descent (SGD) (Ratnayake et al., 2014), and multilayer perceptron (MLP), two deep learning models [LeNet (Lecun et al., 1998) and AlexNet (Krizhevsky et al., 2017)], and one transfer learning model (AlexNet pre-trained model) were studied for CRC LNM classification. The results of these methods were compared.

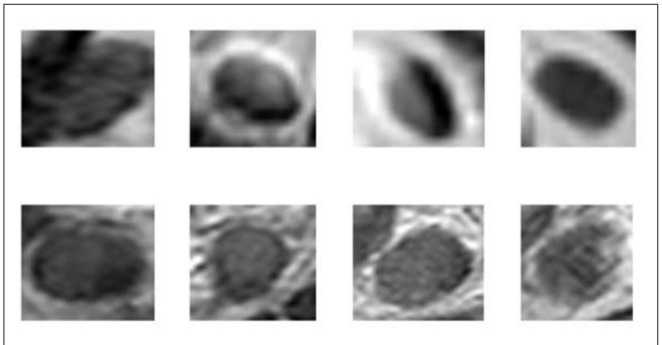

FIGURE 1 | Sample CRC LN images (top row, negative; bottom row, positive).

A detailed introduction to classical machine learning methods was presented in Marsland (2009). Classical machine learning methods were implemented using Python and the sckit-learn package. The optimal parameters of each method were searched via grid search in the parameter space and determined based on the four folds of training samples (Wang H. et al., 2017). AB used 100 decision stumps as weak learners, the learning rate was 0.1, and the maximum split number was equal to 1. DT used sckit-learn package default parameters. The KNN used 10 points of nearest neighbors. LR was a linear classification model, for which the parameters of the norm were l2, the optimization algorithm was selected as linear, and iteration was 100. The NB classifier selected Gaussian NB from the sckit-learn package. SVM used a radial basis function as the kernel function, the kernel coefficient was 1e-3, and the penalty parameter was 1.0. SGD employed hinge as the loss function and l2 as a penalty, and the iteration was 100. MLP, a form of ANN, was trained with a back-propagation algorithm (Rumelhart et al., 1985). In this method, two hidden layers with 32 and 16 neurons for the first and second layers were used. Epochs were 200, and the learning rate was 1e-3.

Deep learning methods were implemented by Python and Keras library for Python. LeNet and AlexNet's structures were based on Lecun et al. (1998) and Krizhevsky et al. (2017). A relu activation function was used in the convolution layer, and a sigmoid function in the full connection layer. The optimization function was SGD (Bottou, 2010). The loss function was binary_crossentropy. The learning rate was 1e-3, and epochs were 200. To avoid overfitting, L2 normalization (Van Laarhoven, 2017) and dropout regularization (Srivastava et al., 2014) were utilized. The methods were running on GPUs (NVIDIA Company GTX 1080ti).

Transfer learning and deep learning share something in common in parameter settings, but are different in training: deep learning starts from scratch, whereas transfer learning uses a pre-trained model. Because the pre-trained model was not trained by ImageNet, it did not need to initialize parameters. As stated in Yosinski et al. (2014), the first three layers were frozen because the layers that extracted the features were general. The other parameters were fine-tuned. In the implementation process, the structure must follow AlexNet then load AlexNet model weight. The fully connected layer activation function was changed to sigmoid. The optimization function was SGD. The loss function was binary_crossentropy, and the learning rate was 1e-4, and epochs were 200. In this study, methods used to avoid overfitting were L2 normalization and dropout regularization. The dropout was set to 0.5. Finally, transfer learning retrained on GPU was like deep learning.

The explanation of the internal relationship between the input data and label prediction has always been a vital issue (Lipton, 2018) in the CNN-based classification tasks. In this study, a classification heat-map was used to improve the interpretability

of the model (Lee et al., 2019). This experiment contained three steps. First, the model was used to display the last convolutional layer feature-map. Then, the feature-map was converted into a heat-map. Last, raw data and heat-map were superimposed into a new image.

RESULTS

Classification Performance

In this study, three kinds of features were employed in eight machine learning methods, respectively. **Table 1** displays the performance indicators of all methods for CRC LNM classification, including accuracy (ACC), area under the curve (AUC), sensitivity, specificity, positive predictive value (PPV), and negative predictive value (NPV). Based on the ACC and AUC values, the optimal features set of each machine learning method for CRC LNM classification was defined. As shown in **Figures 2**, **3**, LR achieved the best performance using the GLH and GLCM features sets. NB obtained the highest ACC and AUC values for the SIFT features set. Deep learning and transfer learning had significantly better performance than machine learning methods in CRC LNM classification. Although deep learning and transfer learning did not use global and local features sets, the ACC and AUC values of these two methods were still better than machine learning methods (**Table 1**). Hence, transfer learning was identified as the best method for CRC LNM classification in this study.

Lesion Classification Heat-Map

Although CNN has enabled unprecedented breakthroughs in computer vision tasks, interpretability remains unclear (Lipton, 2018). Therefore, to present a classification heat-map (Lee et al., 2019), the interpretability of the CNN model was improved. The classification heat-map identified discriminative regions (Selvaraju et al., 2017). As shown in **Figure 4**, the last convolution layer features heat-map was superimposed on the original MRI so that the location of the actual LN could be compared to the region highlighted by the model (Lee et al., 2019). Red regions represent class information, whereas the others correspond to class evidence.

DISCUSSION

First, as shown by the comparison of machine learning results, one method could yield different results if the selected features differed, and different methods would have different results

TABLE 1 | Performance results of all methods for CRC LNM.

	ACC	AUC	Sensitivity	Specificity	PPV	NPV
AB+GLH	0.6369	0.6357	0.6753	0.6431	0.6910	0.5805
AB+GLCM	0.6458	0.6449	0.6431	0.6491	0.6880	0.6018
AB+SIFT	0.6280	0.6270	0.6267	0.6295	0.6706	0.5836
DT+GLH	0.4598	0.4588	0.4728	0.4441	0.5073	0.4103
DT+GLCM	0.4866	0.4859	0.4972	0.4745	0.5190	0.4529
DT+SIFT	0.4955	0.4950	0.5057	0.4844	0.5190	0.4711
KNN+GLH	0.5967	0.5900	0.5650	0.7458	0.7125	0.2675
KNN+GLCM	0.5818	0.5752	0.5562	0.7	0.7051	0.2553
KNN+SIFT	0.6280	0.6222	0.5886	0.7687	0.7009	0.3435
LR+GLH	0.6429	0.6416	0.6359	0.6519	0.7026	0.5805
LR+GLCM	0.6815	0.6802	0.6684	0.6990	0.7464	0.6140
LR+SIFT	0.6250	0.6242	0.6253	0.6246	0.6618	0.5866
MLP+GLH	0.5402	0.5395	0.5472	0.5321	0.5743	0.5046
MLP+GLCM	0.5759	0.5748	0.5780	0.5733	0.6268	0.5228
MLP+SIFT	0.5744	0.5738	0.5803	0.5678	0.6006	0.5471
NB+GLH	0.6354	0.6331	0.6184	0.6628	0.7464	0.5198
NB+GLCM	0.6637	0.6623	0.6527	0.6782	0.7289	0.5957
NB+SIFT	0.6518	0.6500	0.6373	0.6727	0.7376	0.5623
SGD+GLH	0.6101	0.6089	0.6181	0.6128	0.6742	0.5532
SGD+GLCM	0.5372	0.5375	0.5488	0.5262	0.5248	0.5502
SGD+SIFT	0.5833	0.5838	0.5981	0.5698	0.5598	0.6079
SVM+GLH	0.4896	0.4924	0.5000	0.4836	0.3586	0.6261
SVM+GLCM	0.5208	0.5247	0.5500	0.5076	0.3382	0.7112
SVM+SIFT	0.5327	0.5359	0.5617	0.5172	0.3848	0.6869
LeNet	0.6577	0.7305	0.6535	0.6535	0.6535	0.6535
AlexNet	0.6716	0.7696	0.6708	0.6711	0.6714	0.6706
AlexNet pre-trained model	0.7583	0.7941	0.8004	0.7997	0.7992	0.8009

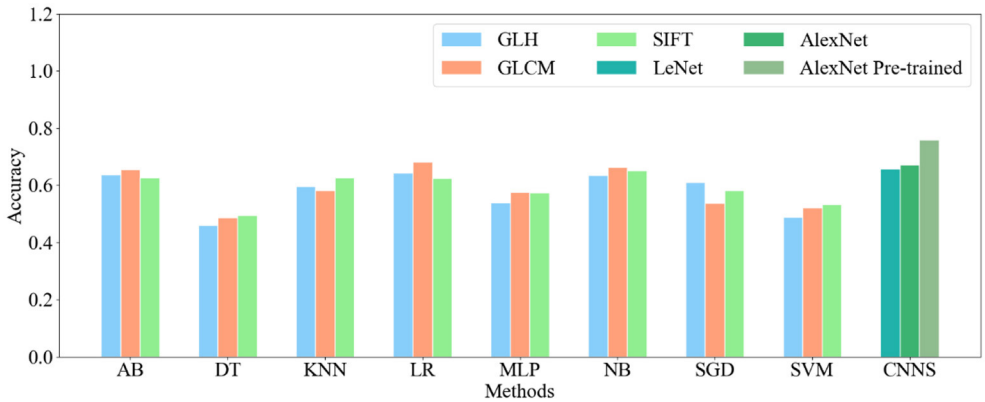

FIGURE 2 | Accuracy of all classification methods.

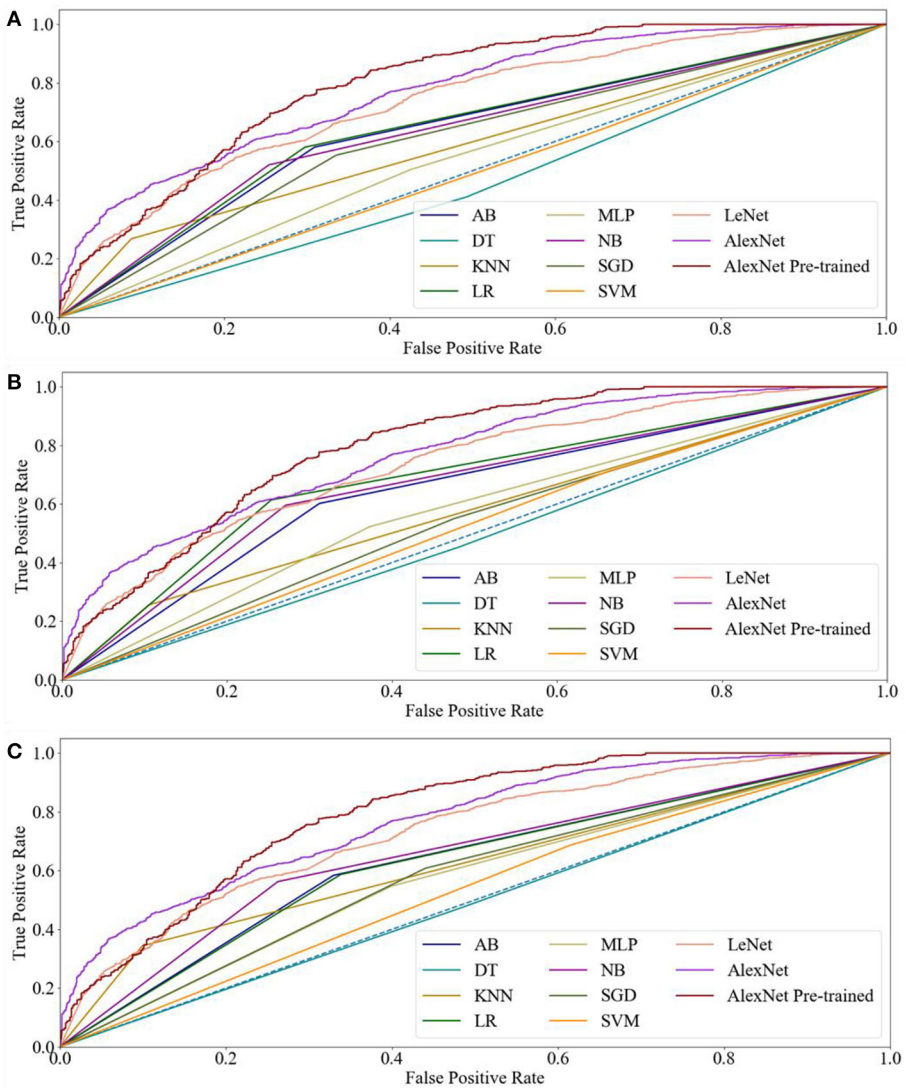

FIGURE 3 | Receiver operating characteristic curves of all methods for CRC LNM: **(A)** ML with GLH and CNN, **(B)** ML with GLCM and CNN, and **(C)** ML with SIFT and CNN.

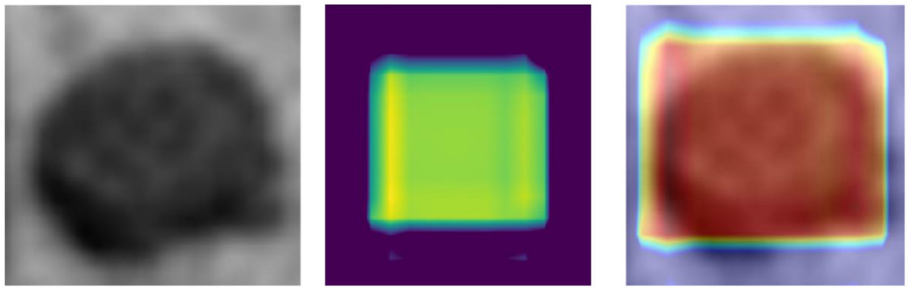

FIGURE 4 | CRC LN classification heat-map (left – original image; middle – feature heat-map; right – superimposed image).

even if the same features were selected. In **Table 1**, when each feature set was used as an input, AB, LR, and NB were better than the other machine learning methods in terms of both ACC and AUC. AB is an ensemble of DT from the view of methodology. AB utilizes multiple weak classifiers which could learn more information from the input and develop into a strong classifier when combined. Hence, AB could become a better classification method based on these weak classifiers. As a linear classification method, LR gives each input feature a weight factor which will have impact on the classification result. Based on the LR methodology, gradient descent iterates were used to find the right factors. Then, predicted values were obtained, and a sigmoid function was used for final classification. NB, with the Bayesian theorem as its foundation, is considered one of the simplest yet most powerful classification methods. A NB classifier calculates the posterior probability of input features as per the prior probability, and the input features must be independent of each other. Other machine learning methods, such as SVM and DT, performed worse. For instance, SVM is based on the kernel function which implicitly maps features into a higher-dimensional feature space and measures the distance between the feature points. Hence, the choice of the kernel function is vital. DT is based on a tree structure, which contains nodes and a directed edge. In general, there is a root node, some internal nodes and leaf nodes in a DT. The leaf nodes are decision results, and other nodes represent the features. Therefore, the higher the feature purity is, the better the classification result is.

In this study, the comparison results revealed that all other methods employed outperformed the classical machine learning methods for CRC LNM classification. LeNet and AlexNet are deep learning methods, and the AlexNet pre-trained model is a transfer learning model. In deep learning, a CNN is used to extract features from raw data layer by layer. Comparison of LeNet and AlexNet showed that the latter had better performance than the former. The reason is the structure: a deep structure performs better than a shallow one (Bottou et al., 2007; Montufar et al., 2014). The number of parameters also played a part (Tang, 2015): there are more CNN layers in AlexNet which also has more extracted features than LeNet (Lecun et al., 1998; Simonyan and Zisserman, 2014). Hence, even though the same classification function was employed, AlexNet achieves a better result. Although the problem of parameters was considered, more parameters meant more data to fit. Therefore, AlexNet needs more data, and is more likely to result in overfitting than LeNet. Overfitting hinders medical imaging analysis, and it is often difficult to collect enough medical images, like CRC LN images. In this study, the AlexNet pre-trained model solved the problem of shortage of medical data. As the AlexNet pre-trained model was trained by ImageNet, it did not need extra data for training from scratch. Hence, the pre-trained model parameters could be directly used to train new data with the help of some processing techniques, such as freezing and fine-tuning parameters. As low-level features are general, the parameters of these features could be frozen, and other parameters could be fine-tuned. In transfer learning, the learning rate is often set smaller than that for training from scratch. If the learning rate is set high, the model's parameters would be updated quickly and affect the original weight information (Wang, 2018).

As shown in **Figure 4**, the visualization experiment could show the model focus region of the input image. The classification heat-map represents evidence of the CNN model-based classification and could assist in clinical decision-making by directly identifying the region of interest (Lee et al., 2019).

Feature extraction has direct impacts on the performance of the classification method. **Figure 5** shows the original data and the features extracted by all methods. SIFT are features extracted based on the interest points of the local appearance of the original data. The more the points are, the more the features are. However, there are few points on the CRC LN lesion, whereas some points are on the edge. There is little classification information. The GLCM includes multiple-type features. Entropy and angular second moment features are listed in **Figure 5**. It is not easy to distinguish the region of the lesion. GLH represents the relationship between the occurrence frequency of each gray-level pixel and the gray level. Gray-level pixels could be observed. The central area of the CRC LN lesion is more than the edge area. Nevertheless, GLH does not reflect the features of the central area. The features of the AlexNet pre-trained model are from low to high levels. The features of the first two convolutional layers display the overall contour of the lesion, and others represent the semantic features of a high level. This is helpful for classification. Hence, the features extracted by the pre-trained CNN were better than those extracted by the other methods for CRC LNM classification.

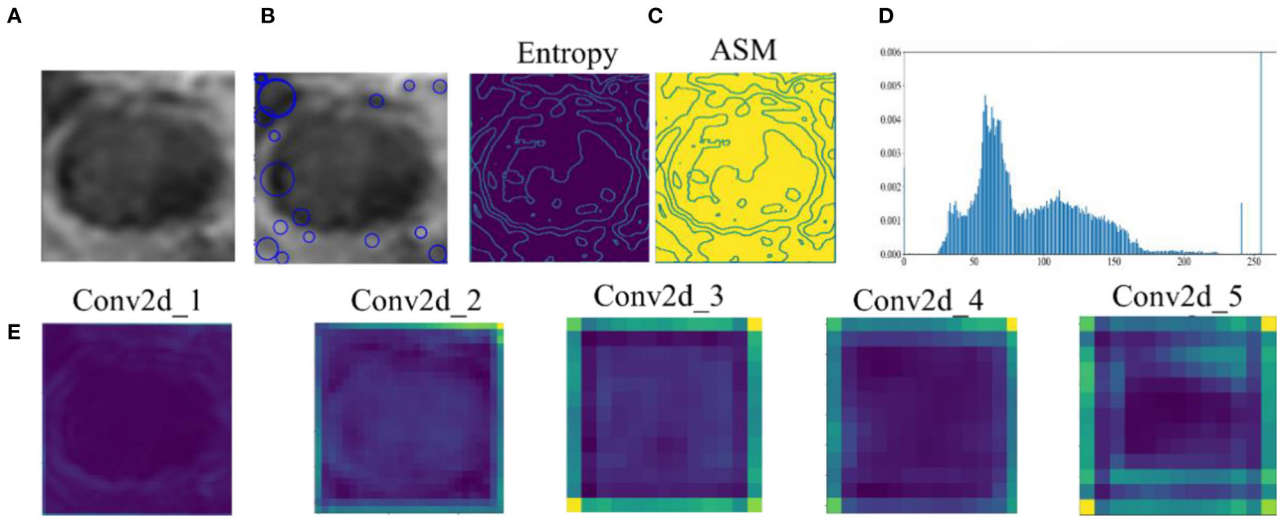

FIGURE 5 | Comparison of original data and features: **(A)** original data, **(B)** SIFT feature, **(C)** GLCM feature, **(D)** GLH feature, and **(E)** features by AlexNet pre-trained model extracted from convolutional layers 1–5.

Based on the experiment's results, the observations are as follows: (1) The traditional feature extraction methods are not effective in CRC LNM classification. (2) The pre-trained model of deep learning has strong transferability. Deep transfer learning applied to a small medical image dataset is better than traditional methods, and it does not need to train the model from scratch. (3) The weights of the pre-trained model realize better initialization of the parameters.

CONCLUSION

In conclusion, this study showed that deep transfer learning is better than deep learning and machine learning mainly because the pre-trained CNN extracts features are more discriminative than those extracted by a CNN and artificially-extracted features. Deep transfer learning has been a popular method for image classification in recent years, and it was proved to be the best classification method among all the methods selected in this study. It could extract underlying features from raw data, does not need to select features or use raw data as input, and is less prone to user bias. A pipeline of transfer learning will be established in future studies, and the optimal deep transfer learning model for CRC LNM classification will be found.

DATA AVAILABILITY STATEMENT

The original contributions presented in the study are included in the article/supplementary materials, further inquiries can be directed to the corresponding author.

AUTHOR CONTRIBUTIONS

All authors listed have made a substantial, direct and intellectual contribution to the work, and approved it for publication.

FUNDING

The project was partially supported by the National Natural Science Foundation of China (Grant Nos. 61773134 and 61803117), the Fundamental Research Funds for the Central Universities (Grant No. HEUCFG201824), and the National Key Scientific Instrument and Equipment Development Projects of China (Grant No. 2012YQ04014010).

REFERENCES

Ahmad, W. S. H. M. W., Zaki, W. M. D. W., Fauzi, M. F. A., and Tan, W. H. (2016). "Classification of infection and fluid regions in chest x-ray images," in *2016 International Conference on Digital Image Computing: Techniques and Applications (DICTA)* (Gold Coast, QLD: IEEE), 1–5.

Al-Absi, H. R. H., Samir, B. B., Shaban, K. B., et al. (2012). "Computer aided diagnosis system based on machine learning techniques for lung cancer," in *2012 international conference on computer & information science (ICCIS)*, Vol. 1 (Kuala Lumpeu: IEEE), 295–300.

Bottou, L. (2010). "Large-scale machine learning with stochastic gradient descent," in *Proceedings of COMPSTAT'2010* (Physica-Verlag, HD), 177–186.

Bottou, L., Chapelle, O., Decoste, D., Weston, J. (2007). "Scaling learning algorithms toward AI," in *Large-Scale Kernel Machines* (MIT Press). p. 321–359.

Bray, F. I., Ferlay, J., Soerjomataram, I., Siegel, R. L., Torre, L. A., and Jemal, A. (2018). Global cancer statistics 2018: GLOBOCAN estimates of incidence and mortality worldwide for 36 cancers in 185 countries. *CA Cancer J. Clin.* 68, 394–424. doi: 10.3322/caac.21492

Burges, C. J. C. (1998). A tutorial on support vector machines for pattern recognition. *Data Min. Knowl. Discov.* 2, 121–167. doi: 10.1023/A:1009715923555

Bychkov, D., Linder, N., Turkki, R., Nordling, S., Kovanen, P. E., Verrill, C., et al. (2018). Deep learning based tissue analysis predicts outcome in colorectal cancer. *Sci. Rep.* 8:3395. doi: 10.1038/s41598-018-21758-3

Carneiro, G., Zheng, Y., Xing, F., and Yang, L. (2017). "Review of deep learning methods in mammography, cardiovascular, and microscopy image analysis," in *Deep Learning and Convolutional Neural Networks for Medical Image Computing* (Cham: Springer), 11–32.

Ciompi, F., Geessink, O., Bejnordi, B. E., de Souza, G. S., Baidoshvili, A., Litjens, G., et al. (2017). "The importance of stain normalization in colorectal tissue classification with convolutional networks," in *2017 IEEE 14th International Symposium on Biomedical Imaging (ISBI 2017)* (Melbourne, VIC: IEEE), 160–163.

Cover, T. M., and Hart, P. E. (1967). Nearest neighbor pattern classification. *IEEE Trans. Inform. Theory* 13, 21–27. doi: 10.1109/TIT.1967.1053964

Cucchiara, A. (2012). Applied logistic regression. *Technometrics* 34, 358–359. doi: 10.2307/1270048

da Nóbrega, R. V. M., Peixoto, S. A., da Silva, S. P. P., and Filho, P. P. R. (2018). "Lung nodule classification via deep transfer learning in CT lung images," in *2018 IEEE 31st International Symposium on Computer-Based Medical Systems (CBMS)* (Karlstad: IEEE), 244–249.

Ding, L., Liu, G. W., Zhao, B. C., Zhou, Y. P., Li, S., Zhang, Z. D., et al. (2019). Artificial intelligence system of faster region-based convolutional neural network surpassing senior radiologists in evaluation of metastatic lymph nodes of rectal cancer. *Chin. Med. J.* 132, 379–387. doi: 10.1097/CM9.0000000000000095

Dornaika, F., Argandacarreras, I., and Belver, C. (2019). Age estimation in facial images through transfer learning. *Mach. Vis. Appl.* 30, 177–187. doi: 10.1007/s00138-018-0976-1

Freund, Y., and Schapire, R. E. (1997). A decision-theoretic generalization of on-line learning and an application to boosting. *Conf. Learn. Theory* 55, 119–139. doi: 10.1006/jcss.1997.1504

Friedman, N., Geiger, D., and Goldszmidt, M. (1997). Bayesian network classifiers. *Mach. Learn.* 29, 131–163. doi: 10.1023/A:1007465528199

García-Floriano, A., Ferreira-Santiago, Á., Camacho-Nieto, O., Yáñez-Márquez, C. (2019). A machine learning approach to medical image classification: Detecting age-related macular degeneration in fundus images. *Comp. Electr. Eng.* 75, 218–229. doi: 10.1016/j.compeleceng.2017.11.008

Golatkar, A., Anand, D., and Sethi, A. (2018). "Classification of breast cancer histology using deep learning," in *International Conference Image Analysis and Recognition*. (Póvoa de Varzim; Cham: Springer), 837–844.

Haralick, R. M., Shanmugam, K. S., and Dinstein, I. (1973). Textural features for image classification. *Syst. Man Cybernet.* 3, 610–621. doi: 10.1109/TSMC.1973.4309314

Inthajak, K., Duanggate, C., Uyyanonvara, B., Makhanov, S. S., and Barman, S. (2011). "Medical image blob detection with feature stability and KNN classification," in *2011 Eighth International Joint Conference on Computer Science and Software Engineering (JCSSE)* (Nakhon Pathom: IEEE), 128–131.

Ishihara, S., Kawai, K., Tanaka, T., Kiyomatsu, T., Hata, K., Nozawa, H., et al. (2017). Oncological outcomes of lateral pelvic lymph node metastasis in rectal cancer treated with preoperative chemoradiotherapy. *Dis. Colon Rectum*. 60, 469–476. doi: 10.1097/DCR.0000000000000752

Krizhevsky, A., Sutskever, I., and Hinton, G. E. (2017). Imagenet classification with deep convolutional neural networks. *Commun. ACM* 60, 84–90. doi: 10.1145/3065386

Lecun, Y., Bengio, Y., and Hinton, G. (2015). Deep learning. *Nature* 521:436. doi: 10.1038/nature14539

Lecun, Y., Bottou, L., Bengio, Y., and Haffner, P. (1998). Gradient-based learning applied to document recognition. *Proc. IEEE.* 86, 2278–2324. doi: 10.1109/5.726791

Lee, J., Ha, E. J., and Kim, J. H. (2019). Application of deep learning to the diagnosis of cervical lymph node metastasis from thyroid cancer with CT. *Eur. Radiol.* 29, 5452–5457. doi: 10.1007/s00330-019-06098-8

Lipton, Z. C. (2018). The mythos of model interpretability. *ACM Queue* 16:30. doi: 10.1145/3236386.3241340

Litjens, G., Kooi, T., Bejnordi, B. E., Setio, A. A. A., Ciompi, F., Ghafoorian, M., et al. (2017). A survey on deep learning in medical image analysis. *Med. Image Anal.* 42, 60–88. doi: 10.1016/j.media.2017.07.005

Liu, Y., and An, X. (2017). "A classification model for the prostate cancer based on deep learning," in *2017 10th International Congress on Image and Signal Processing, BioMedical Engineering and Informatics (CISP-BMEI)*, (Shanghai: IEEE), 1–6.

Long, M., Wang, J., Ding, G., Sun, J., and Yu, P. S. (2013). "Transfer feature learning with joint distribution adaptation," in *Proceedings of the IEEE International Conference on Computer Vision*, (Sydney, NSW), 2200–2207. doi: 10.1109/ICCV.2013.274

Long, M., Zhu, H., Wang, J., and Jordan, M. I. (2017). "Deep transfer learning with joint adaptation networks," in *International Conference on Machine Learning* (Sydney, NSW: PMLR), 2208–2217.

Lowe, D. G. (1999). Object recognition from local scale-invariant features. *Int. Conf. Comput. Vis.* 2, 1150–1157. doi: 10.1109/ICCV.1999.790410

Lowe, D. G. (2004). Distinctive image features from scale-invariant keypoints. *Int. J. Comput. Vis.* 60, 91–110. doi: 10.1023/B:VISI.0000029664.99615.94

Lu, L., Zheng, Y., Carneiro, G., and Yang, L. (2017). "Deep learning and convolutional neural networks for medical image computing," in *Advances in Computer Vision and Pattern Recognition* (Cham: Springer International Publishing). doi: 10.1007/978-3-319-42999-1

Luo, S., Yingwei, F., Liu, H., An, X., Xie, H., Li, P., et al. (2018). "SVM based automatic classification of human stomach cancer with optical coherence tomography images," in *Conference on Lasers and Electro-Optics* (San Jose, CA). doi: 10.1364/CLEO_AT.2018.JTu2A.99

Ma, L., Lu, G., Wang, D., et al. (2017). "Deep learning based classification for head and neck cancer detection with hyperspectral imaging in an animal model," in *Medical Imaging 2017: Biomedical Applications in Molecular, Structural, and Functional Imaging* (Orlando, FL: International Society for Optics and Photonics), 101372G.

Marsland, S. (2009). *Machine Learning: An Algorithmic Perspective*. New York, NY: Chapman and Hall/CRC.

Montufar, G. F., Pascanu, R., Cho, K., and Bengio, Y. (2014). On the number of linear regions of deep neural networks. *Adv. Neural Inf. Proc. Syst.* 27, 2924–2932. Available online at: https://arxiv.org/abs/1402.1869v2

Nakaya, D., Endo, S., Satori, S., Yoshida, T., Saegusa, M., Ito, T., et al. (2017). Machine learning classification of colorectal cancer using hyperspectral images. *J. Colo. Assoc. Jpn.* 41,99–101. Available online at: https://www.jstage.jst.go.jp/article/jcsaj/41/3+/41_99/_article/-char/en

Nasu, T., Oku, Y., Takifuji, K., Hotta, T., Yokoyama, S., Matsuda, K., et al. (2013). Predicting lymph node metastasis in early colorectal cancer using the CITED1 expression. *J. Surg. Res.* 185, 136–142. doi: 10.1016/j.jss.2013.05.041

Otsu, N. (1979). A tlreshold selection method from gray-level histograms. *IEEE Trans. Syst. Man Cybernet.* 9, 62–66. doi: 10.1109/TSMC.1979.4310076

Pan, S. J., and Yang, Q. (2010). A survey on transfer learning. *IEEE Trans. Knowl. Data Eng.* 22, 1345–1359. doi: 10.1109/TKDE.2009.191

Pratap, T., and Kokil, P. (2019). Computer-aided diagnosis of cataract using deep transfer learning. *Biomed. Signal Process. Control.* 53:101533. doi: 10.1016/j.bspc.2019.04.010

Quinlan, J. R. (1986). Induction of decision trees. *Mach. Learn.* 1, 81–106. doi: 10.1007/BF00116251

Ratnayake, R. M. V. S., Perera, K. G. U., Wickramanayaka, G. S. K., Gunasekara, C. S., and Samarawickrama, K. C. J. K. (2014). Application of stochastic gradient descent algorithm in evaluating the performance contribution of employees. *IOSR J. Bus. Manage.* 16, 77–80. doi: 10.9790/487X-16637780

Rumelhart, D. E., Hinton, G. E., and Williams, R. J. (1985). "Learning Internal Representations by Error Propagation," in *Parallel Distributed Processing: Explorations in the Microstructure of Cognition: Foundations*, MIT Press, 1987, p. 318–362.

Selvaraju, R. R., Cogswell, M., Das, A., Vedantam, R., Parikh, D., and Batra, D. (2017). "Grad-CAM: visual explanations from deep networks via gradient-based localization," in *International Conference on Computer Vision* (Venice), 618–626.

Shen, D., Wu, G., and Suk, H. I. (2017). Deep learning in medical image analysis. *Annu. Rev. Biomed. Eng.* 19, 221–248. doi: 10.1146/annurev-bioeng-071516-044442

Simjanoska, M., Bogdanova, A. M., and Popeska, Z. (2013). "Bayesian multiclass classification of gene expression colorectal cancer stages," in *International Conference on ICT Innovations* (Heidelberg: Springer), 177–186.

Simonyan, K., and Zisserman, A. (2014). Very deep convolutional networks for large-scale image recognition. *arXiv [preprint]*. arXiv:1409.1556.

Song, Q., Zhao, L., Luo, X., and Dou, X. (2017). Using deep learning for classification of lung nodules on computed tomography images. *J. Healthc. Eng.* 2017:831470. doi: 10.1155/2017/8314740

Srivastava, N., Hinton, G., Krizhevsky, A., Sutskever, I., and Salakhutdinov, R. (2014). Dropout: a simple way to prevent neural networks from overfitting. *J. Mach. Learn. Res.* 15, 1929–1958.

Sun, W., Zheng, B., and Wei, Q. (2016). Computer aided lung cancer diagnosis with deep learning algorithms. *Med. Imaging Comput. Aided Diagn.* 9785:97850z. doi: 10.1117/12.2216307

Tan, C., Sun, F., Kong, T., Zhang, W., Yang, C., and Liu, C. (2018). "A survey on deep transfer learning," in *International Conference on Artificial Neural Networks*. Eds V. Kurková, Y. Manolopoulos, B. Hammer, L. Iliadis and I. Maglogiannis (Cham: Springer), 270–279. doi: 10.1007/978-3-030-01424-7_27

Tang, X. Y. X. H. (2015). The influence of the amount of parameters in different layers on the performance of deep learning models. *Comput. Sci. Appl.* 5, 445–453. doi: 10.12677/CSA.2015.512056

Tzeng, E., Hoffman, J., Zhang, N., Saenko, K., and Darrell, T. (2014). Deep domain confusion: maximizing for domain invariance. *arXiv [preprint]*. arXiv:1412.3474.

Van Laarhoven, T. (2017). L2 regularization versus batch and weight normalization. *arXiv [preprint]*. arXiv:1706.05350.

Vesal, S., Ravikumar, N., Davari, A., Ellmann, S., and Maier, A. (2018). Classification of breast cancer histology images using transfer learning. *arXiv* 1802.09424v1. doi: 10.1007/978-3-319-93000-8_92

Vibha, L., Harshavardhan, G. M., Pranaw, K., Deepa Shenoy, P., Venugopal, K. R., and Patnaik, L. M. (2006). "Classification of mammograms using decision trees," in *2006 10th International Database Engineering and Applications Symposium (IDEAS'06)* (Delhi: IEEE), 263–266. doi: 10.1109/IDEAS.2006.14

Wang, H., Zhou, Z., Li, Y., Chen, Z., Lu, P., Wang, W., et al. (2017). Comparison of machine learning methods for classifying mediastinal lymph node metastasis of non-small cell lung cancer from 18 F-FDG PET/CT images. *EJNMMI Res.* 7:11. doi: 10.1186/s13550-017-0260-9

Wang, J., et al. (2018). *Transfer Learning Tutorial*. Available online at: https://github.com/jindongwang/transferlearning-tutorial

Wang, L., Zhang, K., Liu, X., Long, E., Jiang, J., An, Y., et al. (2017). Comparative analysis of image classification methods for automatic diagnosis of ophthalmic images. *Sci. Rep.* 7:41545. doi: 10.1038/srep41545

Yang, Z., and Liu, Z. (2020). The efficacy of 18F-FDG PET/CT-based diagnostic model in the diagnosis of colorectal cancer regional lymph node metastasis. *Saudi J. Biol. Sci.* 27, 805–811. doi: 10.1016/j.sjbs.2019.12.017

Yosinski, J., Clune, J., Bengio, Y.,and Lipson, H. (2014). "How transferable are features in deep neural networks?," in *Advances in Neural Information Processing Systems*, 3320–3328.

Zhou, L., Wang, J. Z., Wang, J. T., Wu, Y. J., Chen, H., Wang, W. B., et al. (2017). Correlation analysis of MR/CT on colorectal cancer lymph node metastasis characteristics and prognosis. *Eur. Rev. Med. Pharmacol. Sci.* 21, 1219–1225.

Conflict of Interest: The authors declare that the research was conducted in the absence of any commercial or financial relationships that could be construed as a potential conflict of interest.

frontiers in Bioengineering and Biotechnology

ORIGINAL RESEARCH
published: 11 February 2021
doi: 10.3389/fbioe.2020.620237

Design and Implementation of Medical Ultrasound Remote Control Software Based on Sensor Design

Shuhao Deng[1], *Quan Jiang*[1], *Yingchun Zhang*[2], *Xin Lu*[1], *Xiurong Shi*[1] *and Yuan Zhang*[1,3]*

[1] Department of Ultrasound, Pudong New Area Peoples' Hospital Affiliated to Shanghai University of Medicine & Health Sciences, Shanghai, China, [2] Second Affiliated Hospital of Soochow University, Suzhou, China, [3] Shanghai Pudong New Area Public Interest Hospital, Pudong, China

With the development of medical technology, medical ultrasound technology is widely used in the diagnosis of human diseases. It has become an indispensable diagnostic method in modern clinical medicine by detecting the internal physiology or tissue structure of the human body by ultrasound and then discovering diseases. Based on this, this paper designs a medical ultrasonic remote control software based on sensor design. The system software communicates with the stimulator through the Bluetooth port of the mobile phone and can send the parameter information input by the mobile phone to the field-programmable gate array of the stimulator for compilation. The upper computer control interface with a remote communication function is written by Lab VIEW software. A socket is used to establish inter-network process connection, and medical ultrasonic equipment simulates hardware key input according to the received control instructions so as to achieve the purpose of remote control. Experiments show that, compared with other systems, the infrared human body temperature measurement system with the functions of environmental temperature compensation and distance compensation can effectively reduce the influence of environmental temperature, distance, and other factors and has the advantages of non-contact, low power consumption, fast response speed, high sensitivity, and high accuracy, which is suitable for rapid and accurate human body temperature measurement in crowded places with large traffic.

Keywords: sensor, medical ultrasound, remote control, screen sharing, computer control

OPEN ACCESS

Edited by:
Zhiwei Luo,
Kobe University, Japan

Reviewed by:
Jihong Shen,
Yangpu Hospital, Tongji University, China
Lianfang Gu,
Shanghai First People's Hospital, China

***Correspondence:**
Yuan Zhang
doct1167@126.com

Specialty section:
This article was submitted to Bionics and Biomimetics, a section of the journal Frontiers in Bioengineering and Biotechnology

Received: *22 October 2020*
Accepted: *30 November 2020*
Published: *11 February 2021*

Citation:
Deng S, Jiang Q, Zhang Y, Lu X, Shi X and Zhang Y (2021) Design and Implementation of Medical Ultrasound Remote Control Software Based on Sensor Design. Front. Bioeng. Biotechnol. 8:620237. doi: 10.3389/fbioe.2020.620237

INTRODUCTION

At present, power ultrasound is widely used in machinery, electronics, electrical appliances, metallurgy, chemical industry, medicine, energy, materials, textiles, agriculture, environmental protection, and many other important fields (Xiaobin et al., 2017). Under this social background, mobile medicine, and telemedicine have gained wide application prospects. In the field of medical ultrasound, all kinds of ultrasonic examination equipment have the characteristics of large volume and inconvenient transportation, which makes clinicians only operate in front of ultrasonic equipment when performing an ultrasonic examination on patients, and has certain limitations (Yao et al., 2018; Wang et al., 2019). With the improvement of people's quality and quality of life, people pay more and more attention to their own health, hoping that potential diseases can be diagnosed and treated in advance. Using one of the most commonly used mobile terminals in life

can meet the needs of doctors not only to control ultrasonic equipment but also to view real-time images displayed on the screen and manage remote files.

An ultrasonic sensor is developed by using the characteristics of ultrasonic (Li et al., 2017). In the past, ultrasonic detection mainly used manual detection, that is, according to the experience of professional inspectors, moving the detection probe to detect the object, so human factors have a great influence on the accuracy of detection. Moreover, this method has low detection efficiency, high cost, easy to cause false detection, and missed detection and is not suitable for remote automatic detection. In this paper, the network architecture of the ultrasonic remote application is designed to realize the remote control of the ultrasonic vibration system. By connecting the Internet with the server or controlling the ultrasonic diagnosis system through Bluetooth, the client interface is used to access the examinee's file and understand the examinee's information. The Ethernet communication between the multi-axis motion controller and the upper computer is realized by using User Datagram Protocol, and the remote automatic control of ultrasonic probe motion is realized, which improves the efficiency of ultrasonic detection and has important application value.

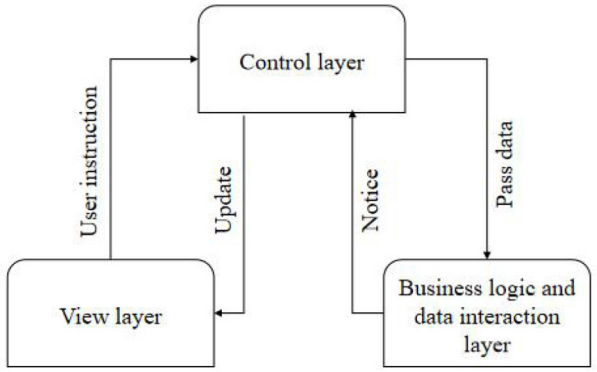

FIGURE 1 | Interaction between layers of Model–View–Controller pattern.

RELATED WORK

In China, ultrasonic diagnosis technology began in the 1960s. In recent years, technology has made rapid progress, and medical ultrasonic technology has also made great progress. Thanks to the rapid progress of human beings in expanding outer space in the middle of the last century, telemedicine has attracted more and more attention from medical practitioners. Hospitals, research institutions, and institutions of higher learning in Germany, Britain, Spain, Sweden, and the Netherlands have jointly put forward a plan called MobiHealth, which automatically collects the physiological parameters of patients by measuring and sensing equipment and uses wireless communication technology to transmit the obtained parameters to the monitoring center, so as to achieve the purpose of sharing medical resources and better rescuing patients. Burnik et al. (2019) developed the Otelo (Mobile Tele-Echo Geography Using an Ultra-Light Robot) system. This system is a mobile mechanical remote ultrasonic control system based on 4G point-to-point communication. The system uses the H.263 coded ultrasound image stream. It is verified that the image information can be transmitted in real-time in a 4G network environment. In recent years, to balance the distribution of medical resources, the state has promulgated targeted policies and invested a lot of money to establish service nodes in some central areas of provinces and promote the development of local telemedicine networks.

DESIGN SCHEME

System Architecture

This system needs two people to complete all the work: an ultrasonic imaging expert at the far end and an operator at the near end. Operators do not need much professional knowledge of ultrasonic imaging and only need to know the basic use of the instrument (Wei, 2018). This is because good software architecture can greatly reduce the cost of software development, improve the efficiency of software, and prolong the life cycle of software. As shown in **Figure 1**, it is the interactive relationship among all layers of the Model–View–Controller (MVC) pattern. The Controller is the bridge between View and Model, which ensures the synchronization between View and Model. After the Controller accepts the instruction from View and gives it to Model for logical processing, Model informs the Controller to update View according to the processing result (Yingjuan et al., 2017; Wang and Liying, 2018). The ultrasonic transducer chips at the transmitting end and the receiving end are packaged in a cylindrical shell. To ensure higher receiving efficiency at the receiving end, the centers of the transmitting surface and the receiving surface should be kept in a horizontal plane as far as possible. The upper computer sends a data request to the server (lower computer) as a client. When returning data, the upper computer reads the data returned by the lower computer as a server.

The whole system consists of client, ultrasonic equipment, and server program on the equipment. Each control cabinet contains 24 ultrasonic vibration systems, and each ultrasonic vibration system includes a numerical control ultrasonic generator and a 2-kW vibrator. The core of the monitoring terminal is the development board based on an ARM9 processor, which can be connected with the sensor modules for collecting physiological parameters such as blood pressure, respiration, blood oxygen, body temperature, and electrocardiogram (ECG). The main module of the monitoring center is the upper computer application software system on the computer, which can receive the measurement signals transmitted by the monitoring terminal and complete the functions of displaying, storing, and analyzing the measurement data. The system can be assembled by installing the corresponding software on the client and server computers (Chen et al., 2019). However, the system may not normally work at this time, so it is necessary to test the connectivity of the network and choose the way to establish the connection according to the network conditions.

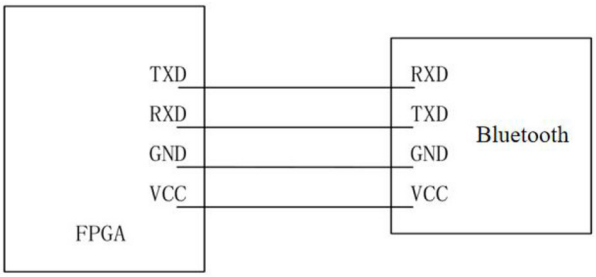

FIGURE 2 | Communication diagram between FPGA and Bluetooth module.

Design of Front-End Parameter Control and Display Module

In this module, the used probe needs to be automatically identified; the interface displays the probe information (probe name and picture) and the corresponding diagnosis type information and monitors whether the probe changes at any time and operates when the probe changes. The remote control module is the core of this system, which realizes that the remote computer can observe the real-time ultrasound images on the screen of the near-end computer through the remote desktop technology and can send control commands through the operation interface of the near-end computer. If the liquid level is lower than the detection surface of the sensor, the liquid density on the ultrasonic propagation path will decrease, the received signal energy will be attenuated, and the reflected waveform will decrease rapidly in amplitude with the decrease of the liquid level (Liangsheng and Chenglong, 2017). Because MVC is not suitable for small applications, strictly separating the view, controller, and model will make the code structure very complicated, and it is not easy to carry out subsequent development. Therefore, only separating the view layer from the data layer will not only make the classes displayed on the interface simpler but also make the code structure clearer.

The Bluetooth serial port module of the stimulator is located on the field-programmable gate array (FPGA) control board. The Bluetooth model used is HC-05, which is a high-performance Bluetooth serial port module and can be used for pairing with various intelligent terminals such as computers, Bluetooth hosts, and mobile phones with Bluetooth function. The baud rate range of this module is wide, ranging from 4,800 to 1,382,400 bits/s. The wiring mode of the communication circuit between the Bluetooth module and FPGA is shown in **Figure 2**, in which TX is the signal sending end, RX is the signal receiving end, GND is the ground, and the power supply VCC is 3.3 V.

When selecting a diagnosis type, it is necessary to read the control parameters corresponding to the diagnosis type (Ruoyu et al., 2020). These control parameters are divided into front-end parameters and desired state configuration parameters. The front-end parameters are downloaded to the front-end to obtain different echo data for changing the image display quality. This sub-module also adopts the MVC mode, and the software structure level is shown in **Figure 3**.

A mechanical actuator is installed on the stepping motor to fix the ultrasonic probe, and a limit switch is installed on

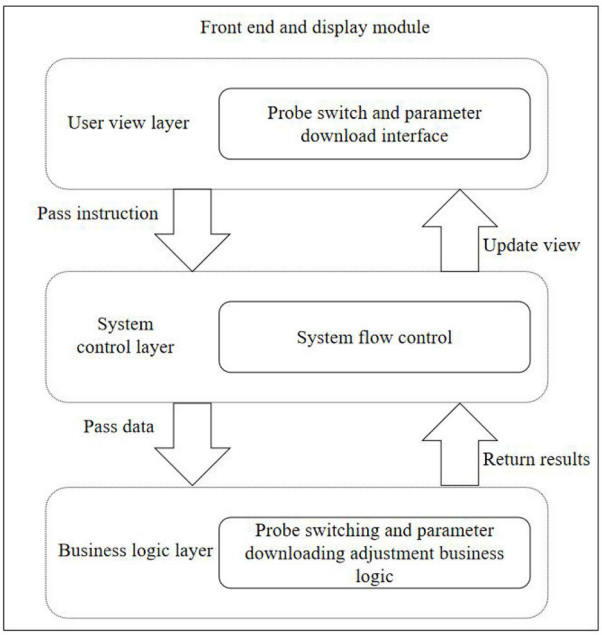

FIGURE 3 | Front-end and display module hierarchy.

the mechanical actuator to control the motion range of the motor. Bluetooth communication is widely used as a wireless communication method with strong anti-interference ability, low cost, and low power consumption. During the measurement, the arterial blood flow is blocked by the cuff, and the pressure sensor is used to detect the oscillation wave of the gas in the cuff during the gradual deflation process (Shuli, 2018; Yanxia and Helin, 2020). The function of the remote controller is realized by establishing a Socket connection and simulating key input, that is, medical ultrasonic equipment and mobile terminal equipment are placed in the same local area network (LAN), and the internet protocol (IP) address of medical ultrasonic equipment is an input to establish a corresponding connection with a mobile terminal. Each ultrasonic generator shall have an automatic frequency searching function without a manual setting. At the same time, the system should ensure that the amplitude of each ultrasonic vibration system is constant and adapt to the change of workload.

Software Design of Data Transmission Module

In this paper, the monitoring terminal of telemedicine system separately designed the storage function to realize the storage of five physiological parameters and related values, including heart rate value, blood oxygen value, pulse rate value, respiration value, blood pressure value (systolic pressure, diastolic pressure, and average pressure), and body temperature value in turn. Under this requirement, it is necessary to design an ultrasonic image remote sharing module, which can clearly display the ultrasonic images and related parameters on the ultrasonic equipment to the client of the mobile equipment. The data collected from the ultrasonic generator are forwarded to the touch screen and operator station by multicast communication. In addition,

the instructions from the touch screen or operator station are received in a point-to-point manner, and the ultrasonic generator is controlled by the Modbus protocol. The function of control system software is designed on Linux operating platform, and the remote communication between the upper computer and motion controller is realized by the user datagram protocol (Hongping et al., 2017).

The data transmission module of the monitoring terminal is divided into two parts: the data sending module and the data receiving module. **Figure 4** is the program flow chart of the transmission module.

The ultrasonic transducer chips at the transmitting end and the receiving end are packaged in a cylindrical shell. To ensure higher receiving efficiency at the receiving end, the centers of the transmitting surface and the receiving surface should be kept on a horizontal plane as far as possible. The transport layer is located in the fourth layer of the seven-layer network model. The upper three layers process data and provide interfaces for users to operate conveniently, whereas the lower three layers transmit data, and the transport layer is located in the middle for isolation, encapsulating the communication interface of the lower layer and hiding the contents. It is mainly responsible for receiving the data transmitted from the user view layer and handing it over to the corresponding business logic class for processing. In this module, the system control layer is composed of Android Manifest.xml, monitoring events, and Activity jumps (Hongli et al., 2019).

The sensor module should communicate with the main controller in the system to receive commands such as start-up detection and resolution setting and send alarm signals to the host. Due to the limitation of the PICl2F675 pin and the requirement of long-distance data exchange, parallel data transmission cannot be realized. After the connection is established, the ARM processor encapsulates the collected physiological data according to the data protocol and sends a data transmission request to the upper computer monitoring software. After receiving the response, it sends a data packet to the upper computer monitoring software. At this time, the upper computer monitoring software analyzes the data packet and displays the data and waveform of physiological parameters. The data management module mainly realizes importing, viewing, and deleting various files stored in the database, displays them in the file list according to the time sequence of the year, month, and day of the files, views all the files on a certain date, queries the files according to keywords, and displays the contents of the searched files.

Ultrasonic Transmitting and Receiving Circuit

The block diagram of the ultrasonic transmission circuit is shown in **Figure 5**. The DC stabilized power supply provides energy for the ultrasonic transducer. According to the characteristics of this transducer, it only needs about tens of volts, which can generally be selected within the safe voltage. The current limiting resistance in the circuit is $\sim$1 kΩ/3 W, which is used to limit the ultrasonic energy (Zhenping and Qianhe, 2020). Adjust each limit switch to the edge of the workpiece to be measured so that the moving range of the probe is the range of the workpiece. Because the stimulator converts the rectangular pulse drive into sine wave output through the matching circuit, the ultrasonic intensity control can be realized by changing the driving duty ratio in the ultrasonic cycle. This can not only save the hardware cost but also improve data throughput. The data processing module analyzes and processes the data transmitted from the communication module. The function of the motion control module is to realize interpolation and other control algorithms and control operations.

Extracellular recording signals are electric field change signals generated by the superposition of various transmembrane currents of local neurons. According to the different sizes of signal acquisition electrodes, extracellular recorded signals can reflect the activated state of neurons in different volume ranges in real-time and thus reflect the state of neural circuits stimulated and regulated in real-time.

The generation of brain stimulation signals needs some specific parameters to control, and different stimulation signals need different parameters. The motion control module can control the whole system's motion process according to the detection rules, including setting relative origin, running, resetting, exiting, and other related operations. There is a need to establish and manage channels between network nodes. By means of error control and flow control, the network channel with various interferences becomes more reliable, and the data packets transmitted from the upper layer are converted into bitstreams and sent to the physical layer (Xiaodan et al., 2019). Under the action of capacitor charging and discharging, a negative high voltage pulse wave with the same resonant frequency as the ultrasonic wafer is formed and applied to both ends of the transducer, thereby emitting ultrasonic waves. The inductor in that output circuit is used for eliminating stray capacitance of the cable and capacitive reactance of the ultrasonic transducer. The sensor does not need DC, and the inductor also acts as a bypass.

The microcontroller PIC12F675 generates a pulse with a frequency of approximately 500 kHz, which is output through the I port and supply to the waveform transformation and driving circuit. The pulse frequency here should be consistent with the resonant frequency of the piezoelectric wafer. When bubbles are mixed in the liquid, the amplitude of the detected pulse signal decreases, and the output of the comparator is "low"; otherwise, it is "high." When the whole liquid level is lower than the mounting plane of the sensor, the output is always "low," so the sensor can also be used for liquid level monitoring. Any application can easily establish its own SQLite private database according to needs, and by default, other applications cannot directly access the private data file. In the inter-network communication, the high-level protocols of the two processes must be the same, and the situation that one side uses transmission control protocol (TCP) and the other side uses user datagram protocol for data transmission cannot occur.

Signal Detection and Processing

In the process of using medical equipment, it is generally required to set the monitoring sensitivity according to the actual situation of patients. If the design is too high, it will alarm frequently and fail to work normally, whereas if it is too low, it may lead to malignant accidents. When carrying out ultrasonic testing,

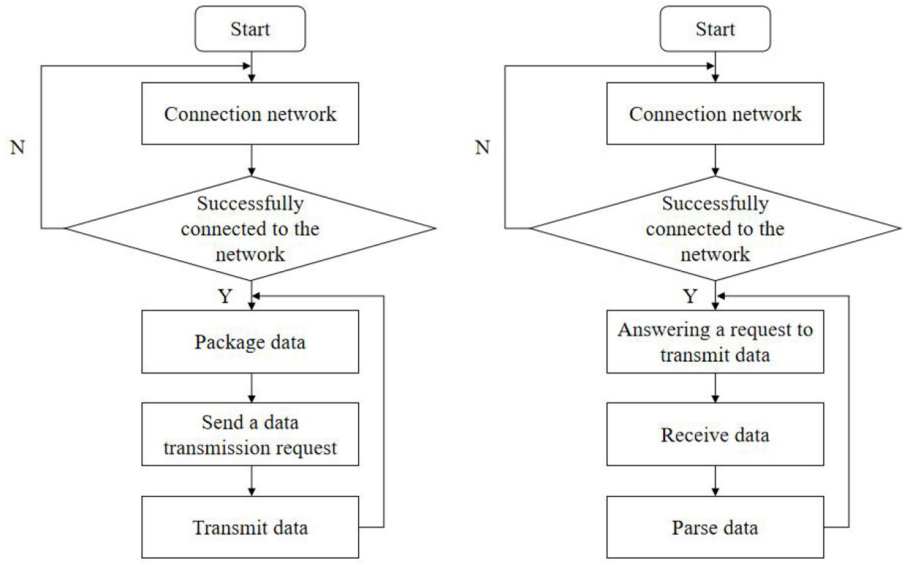

FIGURE 4 | Flow chart of data transmission module.

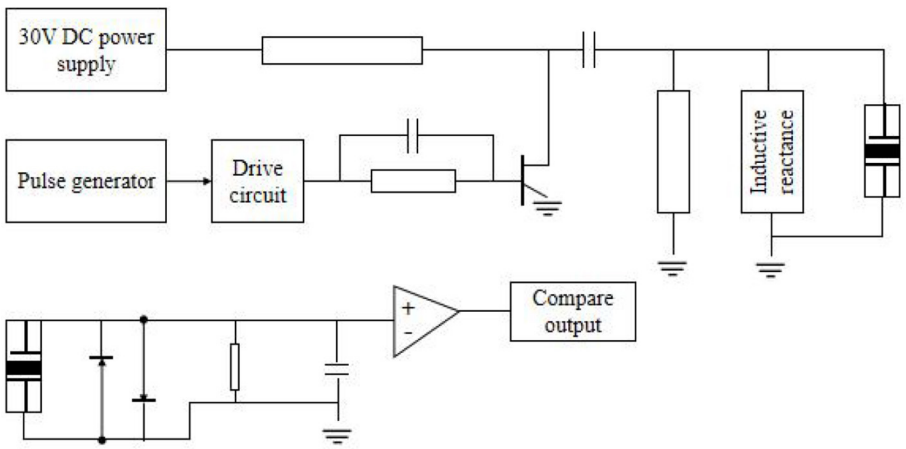

FIGURE 5 | Ultrasonic generator and receiver circuit.

the controller should not only make the probe move according to the specified movement track by controlling the operation of the motor but also return the position information of the probe so that the position information can establish a one-to-one correspondence with the ultrasonic digital signals collected by the ultrasonic data acquisition system. The bit-type of the button switch on the touch screen can be converted into the float type required by the serial port server so that the serial port server can receive the correct operation instruction and forward it to the ultrasonic generator; after compression, it is packaged by using relevant protocols, and the header information is added and sent to the mobile device. After unpacking and decoding, the mobile device can display the image information of the ultrasonic device display screen. The static pressure signal corresponding to the point with the largest increasing amplitude is systolic pressure, and the static pressure signal corresponding to the point with the largest decreasing amplitude is the diastolic pressure. Then, the average blood pressure value is calculated by two data of systolic pressure and average pressure.

When the liquid flows normally and no air bubbles are mixed in, the amplitude of the ultrasonic pulse signal detected by the receiving end is large enough, and the pulse signal consistent with the ultrasonic resonance frequency can be obtained by the comparator. Therefore, if the client continuously obtains the screen display information of the server, it needs to adopt a polling mechanism. The corresponding layout file is New patient_edit.xml, which mainly completes the operation of creating new patient information. There are two intents that can

jump in. One is when creating a new case, there are no data in the extras part of the intent, and the other is when clicking a piece of information, the intent will carry the data obtained by extras from the database. When there are bubbles passing through the cross-section of the sensor, even when the liquid level is lower than the detection surface of the sensor, the converted value will be greatly reduced. After comparison and digital filtering, an alarm will be generated. By setting the comparison value and the sampling time of A/D conversion, the sensitivity of the alarm can be changed, thus realizing the recognition of bubbles of different sizes.

IMPLEMENTATION OF MEDICAL ULTRASOUND REMOTE CONTROL SOFTWARE

Implementation of the Measurement Module

In the design of the measurement module, the drawing of primitive is the premise of realizing other more complex functions (Jianqun et al., 2018). To improve the various functions of the software, it is necessary to constantly increase the drawing of various primitives. The medical ultrasound equipment is the server, and the mobile equipment used by users to log in is the client. After the connection between the monitoring terminal and the monitoring software of the upper computer is completed, the five physiological parameters of blood pressure, blood oxygen, electrocardiogram, respiration, and body temperature are collected to debug the collection and transmission functions of each module software. When a device has a communication failure, the serial server will have a communication timeout and try to connect several times, which leads to the high CPU occupancy rate, thus reducing the computing and communication capabilities and affecting normal communication. Because the clock frequency of FPGA is 50 MHz, the single pulse of the stimulation waveform is converted according to the clock frequency, and then according to the adjustment range of various parameters, the binary conversion formula and the corresponding number of bits of parameters can be obtained as shown in **Table 1**.

In addition, four data bits representing the working state and mode are required, which are output switch, mode selection, continuous or pulse stimulation selection, and single or repeated stimulation selection.

ON_OFF (output switch: output off = 0 output on = 1,);
F_mode (Mode selection: stimulation = 0 positioning = 1,);
S_mode (selection of continuous or pulse stimulation: continuous = 0, pulse = 1,)
T_mode (single or repeated stimulation selection: repeat = 0 single = 1,).

Singleton pattern belongs to the creation pattern of objects, which is the simplest design pattern. GOF defines a singleton pattern as follows: ensure that a class can only have one instance object and give a global access point to access the object (Wenchao et al., 2019). The unified modeling language class diagram of the singleton pattern is shown in **Figure 6**.

TABLE 1 | Parameter conversion.

Parameter	Parameter range	Transformation relation	Digit
Ft	100 KHz−2 MHz	A = 500/Ft*10	6
PRF	10 Hz−2 KHz	B = 1,000*cpp/Ft*30	22
cpp	0–3,000	C = 110/PRF*8	17
np	0–2,000	D = 110/PRF*8*np	28
SD	0.05–1.5 s	E = 103*SD*6	23
I	0.2–24 W/cm^2	F = (I + 2.5)/23/7*A	6
Interval	0..3–15 s	G = 103*interval*6	31

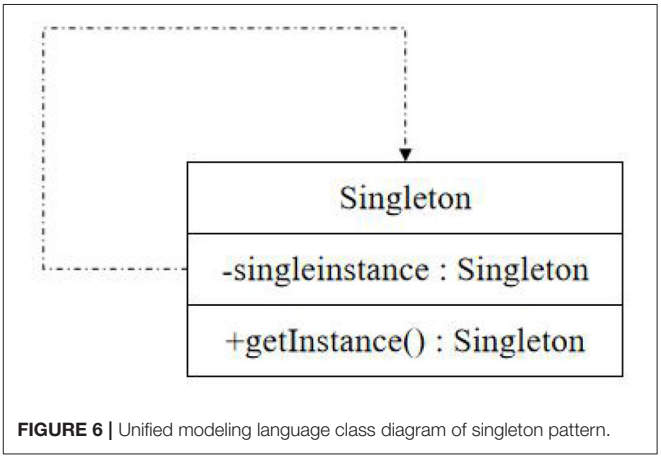

FIGURE 6 | Unified modeling language class diagram of singleton pattern.

File import can be divided into two types: saved echo data and file path: saved echo data are frames of echo data during real-time detection, and a single frame of an echo data file, whose basic parameters, echo defects and echo data, can be directly saved in the database. In addition to creating its own unique instance, the singleton class should also provide a class method with public access rights to access the instance so that it can be accessed in other classes. The file path is when its external line changes; it is difficult to have enough attenuation in the whole speech band because the balance degree of the opposite end changes in different degrees. The measured results show that the opposite end attenuation of the hybrid coil can sometimes be as low as 10 dB at some frequency points. However, the maximum attenuation of the far-end signal after passing through the line is allowed to be 43 dB. Therefore, the echo caused by the end-to-end leakage of the hybrid coil may be 30–40 dB stronger than that of the far-end signal.

Ultrasound equipment will search and match in the database according to the requested username and password. If the authentication is successful, the directory information bound by the user is returned, and the mobile device displays according to the returned directory information. ECG can reflect the activity changes of bioelectricity produced by the human heart in each cardiac cycle. In the debugging of the ECG module, the electrodes of ECG leads are attached to the left and right upper limbs and the left and right lower limbs to measure ECG parameters. By observing the transmission situation, the test shows that within 20 m^2 around the stimulator, the data transmission is stable, and

the Bluetooth connection is effective, which greatly increases the range of activities of the control system.

Implementation of Network Communication

After realizing the function of monitoring terminal software, it is necessary to realize the data transmission between the monitoring software of the upper computer of the monitoring terminal box through the network. First, search the database to see if the root directory is set. If so, get all the file names in the directory by the list () method and store them in a string group. Then, check the file information, remove the file information that is not a folder, and save only the folder information in the string group. Call helper.get Users () to get qualified information items, then store them in the form of Array List, and add them to Simple Adapter, the object of a simple adapter. Finally, call set Adapter () method to display the found patient information items on the interface. Save it to the database in the form of a binary bitstream. The remote communication module, motion control module, and data processing module of the upper computer Lab VIEW software cooperate with each other to form the upper computer software of the ultrasonic testing multi-axis motion control system.

In this design, the socket socket mechanism is used for network programming to realize data transmission between the monitoring terminal and upper computer monitoring software (Jiatao, 2019). The software is divided into a server part and a client part. The socket socket programming model is shown in **Figure 7**. In the telemedicine system, the monitoring terminal as the client initiates the communication connection request actively, and the monitoring center as the server is responsible for responding to various connection requests, thus realizing the data communication function between the monitoring terminal and the monitoring center.

Client process and server process use TCP/IP protocol for data communication. First, the client initiates a connection establishment request to the server, and then, the server accepts the client's connection request. Patients and medical staff can log in to the account on the mobile device client to obtain the file directory information on the ultrasonic device and preview, download, print, and other operations, which greatly facilitates doctors and patients to use medical records. When a communication failure occurs between a certain device and the serial server, the system automatically extends the communication cycle of the failed device and then restores the communication cycle to the normal value after a certain communication is normal. The Ethernet communication protocol between the multi-axis motion controller and the upper computer Lab VIEW is defined to realize the remote communication between the lower computer and the upper computer. Add the string group to the adapter, and add special strings to the adapter, so that the user can click this option to return to the higher level directory, and bind the adapter with List View, so that List View can display these string information.

The client–server model describes the relationship between services and serviced processes, in which the client is the service requester, and the server is the service provider. Client/server (C/S) mode has strong interactivity, good real-time and flexibility, and strong data manipulation and transaction processing capabilities. The specificity and closeness of the adopted protocol make the whole C/S mode system relatively safe, so this system adopts TCP/IP protocol and is based on C/S operation mode. This way implies the inequality of hardware resources between client/server and the asymmetry of communication. In actual measurement and control, multiple photoelectric measurement and control devices measure at different stations at the same time, and the data processing center coordinates and monitors multiple measurement stations (Zhuo, 2019), that is, the structure of one client to multiple servers (the client is the data processing center). Clinicians and patients need to register their own accounts and set their own usernames, login passwords, and corresponding directory files before applying the remote file management module.

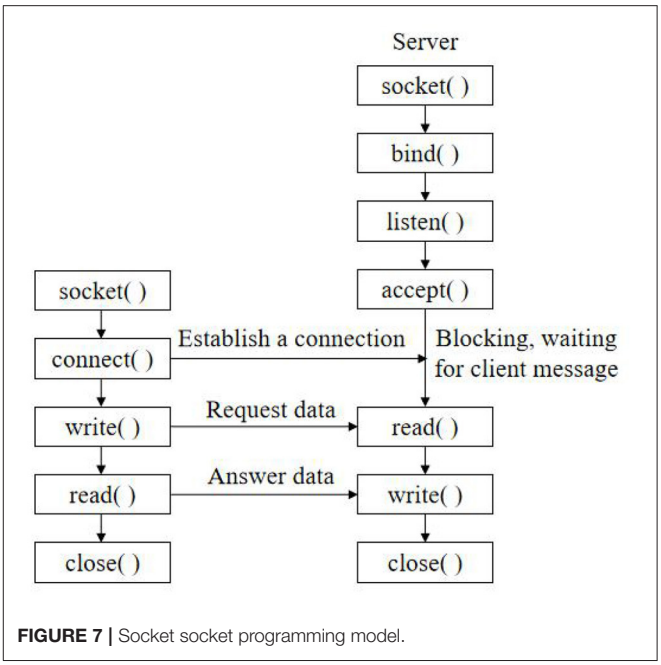

FIGURE 7 | Socket socket programming model.

Implementation of Screen Sharing Function

Due to the limitation of system level, the traditional method of obtaining screen information can only obtain screen data by calling frame buffer through JNI, which is the main reason for the poor quality of screen sharing. If you want to delete, just let the patient information item to be deleted get the focus first and then click Delete Medical Record Item. If you want to re-edit the existing information, you only need to click the corresponding patient information item to enter the editing interface, save it after modification, and then return to the patient information management interface. After the client request comes, accept the connection request through the accept () function and return a new socket corresponding to this connection. Use the returned socket to communicate data with the client and perform read and write operations. After data transmission, the socket waits for another request from the client. Therefore, the CPU of the system

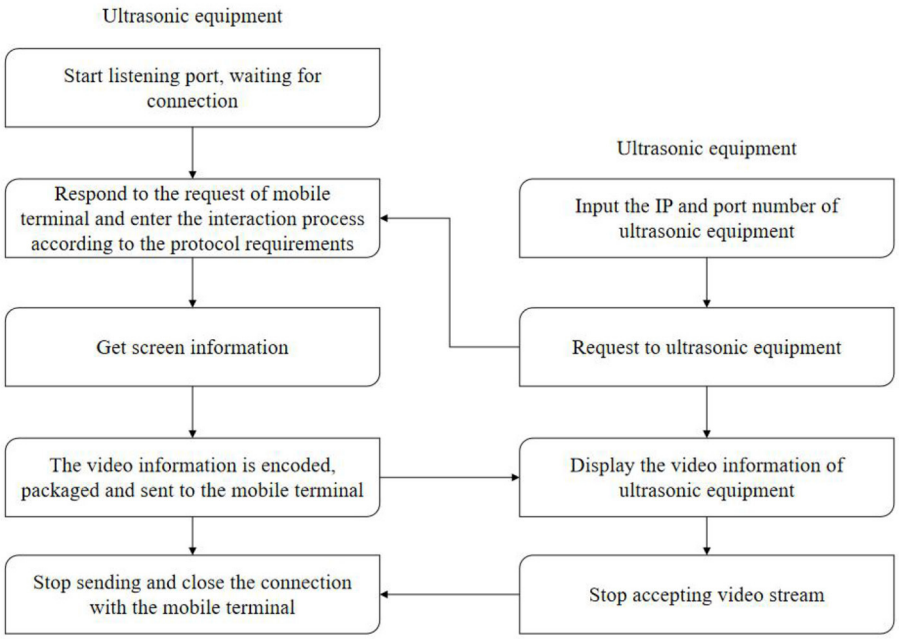

FIGURE 8 | Screen sharing implementation flowchart.

is maintained at a low level, and the communication with other devices will not be affected after a single communication failure.

In terms of transmission mode, the conventional unicast protocol is mainly used for point-to-point transmission, and multicast protocol is used for transmission in this subject. The flowchart of screen sharing is shown in **Figure 8**.

There may be different types of files in the memory card. If you open it for viewing, you need to start the corresponding activity. You can first get the path and file name of the file and determine a uniform resource identifier. H.264 encoded video stream can adapt to bandwidth and can generate video stream suitable for network transmission according to needs (Yanping et al., 2018); The FPGA controls the A/D conversion circuit to convert the ultrasonic echo signal and stores the data in the dual-port random-access memory. After the storage is completed, it sends a signal to ARM, and ARM receives the acquisition completion signal and sends the data to the upper computer through Ethernet. Reset is to return the probe to the absolute zero position. Origin setting can set the current arbitrary scene as the relative origin, as the starting point of the new movement and as the relative zero point of the probe position coordinates. After the connection is successful, the program enters the cycle of sending and receiving data until the connection is closed. If the reception is successful, the data will be processed accordingly; if it is unsuccessful, the close () function will be called to close the current connection.

After the medical ultrasound equipment software is started, the screen real-time sharing service is started, and the response port is monitored. When a mobile device is connected, a request will be sent to the corresponding port of the medical ultrasound equipment, and the medical ultrasound equipment will respond to the request of the mobile device and start to acquire screen information. For the sake of holding the medical ultrasound device, the operation should be done on the touch screen as much as possible. Click a frame of image lightly, and the image display area will be displayed accordingly. The body temperature of the human body is measured by the upper computer monitoring software to verify the monitoring performance of the upper computer monitoring software on body temperature. The data can be stored in an Excel file, the data file of each test can be opened and called, the relevant information can be read, and the test image can be generated by combining with image processing software. According to the video streaming protocol and the compression protocol, the obtained video information is displayed on the screen of the mobile device.

CONCLUSION

In this paper, the application programs of mobile devices and medical ultrasound devices are developed based on sensor design so that users can use mobile devices to remotely control medical ultrasound devices in the same LAN, view shared screens, and manage file systems and other remote operations. According to the communication protocol between monitoring software and host computer monitoring software, the development platform of host computer monitoring software is built, and the design and implementation of host computer software are completed. The network communication between the monitoring terminal and the monitoring software of the upper computer is realized by socket programming under TCP/IP. The upper computer software of ultrasonic testing multi-axis motion control system based on Ethernet is written by Lab VIEW, which realizes the processing of ultrasonic testing control signals by the upper computer and the automation of ultrasonic testing remote

control. It realizes not only the local automatic control of the ultrasonic vibration system but also the remote control of the operator station, which greatly improves the automation level of the ultrasonic system.

This design has basically achieved the expected design effect, but there are still some deficiencies in system stability, practicability, scalability, and network communication, which need to be improved and perfected continuously. In the next step, we can expand the use range of telemedicine from LAN to wide area network so that the coverage of LAN is no longer the main limitation.

DATA AVAILABILITY STATEMENT

The original contributions presented in the study are included in the article/supplementary material, further inquiries can be directed to the corresponding author/s.

AUTHOR CONTRIBUTIONS

QJ and YZ participated in the design and coordination of experimental work, and acquisition of data. YZ carried out the study design, the analysis and interpretation of data, and drafted the manuscript. All authors read and approved the final manuscript.

FUNDING

This paper is supported by the Pudong New Area Health and Family Planning Commission Subject Leader Course Project (Grant No. PWRd 2017-06, Pudong New Area Science and Technology Development (Grant No. PKJ2018-Y11) and Youth project of Shanghai Pudong New Area Municipal Health Burean (PW2018B-04).

REFERENCES

Burnik, U., Dobravec, S., and Meza, M. (2019). Design of a secure remote management module for a software-operated medical device. *Biomed. Tech.* 64, 67–80. doi: 10.1515/bmt-2017-0005

Chen, Z., Fangsheng, P., and Zeyong, T. (2019). Research on motion control system of multi-axis manipulator for ultrasonic testing. *Indust. Control Comp.* 32, 1–2.

Hongli, B., Yuwen, L., and Jianlin, C. (2019). Development of ultrasonic nondestructive testing software for thick-walled composite pressure vessels. *Instrum. Equip.* 7, 193–201. doi: 10.12677/IaE.2019.73026

Hongping, S., Ni, Z., and Rui, H. (2017). Software design and development based on interactive digital automatic breast volume ultrasound teaching resource platform. *J. Clin. Ultrasound Med.* 19, 851–853. doi: 10.3969/j.issn.1008-6978.2017.12.023

Jianqun, F., Jiahui, H., and Xiying, P. (2018). Design and implementation of ultrasound diagnosis reference system based on knowledge point tree structure. *Chin. Med. Equip.* 15, 137–139. doi: 10.3969/J.ISSN.1672-8270.2018.11.036

Jiatao, X. (2019). Design of an intelligent ultrasonic ranging system. *Electron. World* 577, 158–159. doi: 10.19353/j.cnki.dzsj.2019.19.083

Li, S., Xiao, L., Deng, H., Shi, X., and Cao, Q. (2017). Remote controlled drug release from multi-functional Fe3O4/GO/Chitosan microspheres fabricated by an electrospray method. *Colloids Surf. B Biointerfaces* 151, 354–362. doi: 10.1016/j.colsurfb.2016.12.029

Liangsheng, H., and Chenglong, L. (2017). Design of remote ultrasonic signal generating system based on Kinetis60 and AD9951. *Test Sci. Instrum.* 8, 396–404. doi: 10.3969/j.issn.1674-8042.2017.04.013

Ruoyu, L., Junrui, F., and Xiangshuai, D. (2020). Design of airport UAV bird repellent system based on vision. *Chin N Commun.* 22, 104–105.

Shuli, M. (2018). Design of ultrasonic inspection and control system for machine tools under the control of single-chip microcomputer. *Shandong Indust Technol.* 271:64.

Wang, Y., and Liying, W. (2018). Design of remote control device for gestural TV based on DSP. *Inform. Record. Mater.* 19, 72–74.

Wang, Z. Y., Wang, J., Chen, Y. Q., Jia, M. H., Zhang, G. Y., Tang, Q. J., et al. (2019). Design of EPICS and web-based remote control software of near-infrared sky brightness monitor in Antarctica. *IEEE Trans. Nucl. Sci.* 66, 1998–2004. doi: 10.1109/TNS.2019.2924474

Wei, L. (2018). Design of remote control system. *J. Dezhou Univ.* 34, 74–76.

Wenchao, L., Juan, Y., and Huibin, Y. (2019). Design of ultrasonic testing system for nuclear power bolts based on labVIEW. *Chem. Indust. Automat. Instrum.* 46, 278–281.

Xiaobin, K., Wang, K., and Qing, Y. (2017). Study of medical diagnostic digital subtraction angiography and design of remote control device. *Chin. Med. Equip.* 32:44–47.e.56. doi: 10.3969/j.issn.1674-1633.2017.12.010

Xiaodan, W., Shuncai, Y., and Fei, D. (2019). Software design and implementation of ultrasonic motor data acquisition system. *Mod. Electron. Technol.* 42, 113–116.e121.

Yanping, Y., Haitao, W., and Kai, Z. (2018). Software design of ultrasonic phased array inspection imaging system. *Nondestruct. Test.* 40, 1–49. doi: 10.11973/wsjc201811001

Yanxia, D., and Helin, X. (2020). Design of the control system of ultrasonic mites removal instrument based on frequency conversion speed regulation. *Electro. Compon. Inform. Technol.* 4, 114–115.

Yao, W., Bao, Y., and Chen, Y. (2018). Formation of microcapsules by ultrasound stimulation for use in remote-controlled drug-eluting stents. *Med. Eng. Phys.* 56, 42–47. doi: 10.1016/j.medengphy.2018.04.001

Yingjuan, Z., Zheng, Z., and Yongliang, W. (2017). Design and implementation of the control system of the ultrasonic stimulator based on android. *Software* 11, 142–146. doi: 10.3969/j.issn.1003-6970.2017.11.028

Zhenping, Y., and Qianhe, Y. (2020). The design of intelligent liquid level control system based on ultrasonic. *Electro. Des. Eng.* 28, 76–80.

Zhuo, M. (2019). Design of ultrasonic blind guide system based on HC-SR04. *Electron. Des. Eng.* 27, 136–139.

Conflict of Interest: The authors declare that the research was conducted in the absence of any commercial or financial relationships that could be construed as a potential conflict of interest.

frontiers in Bioengineering and Biotechnology

ORIGINAL RESEARCH
published: 05 March 2021
doi: 10.3389/fbioe.2021.646479

Longtime Vision Function Prediction in Childhood Cataract Patients Based on Optical Coherence Tomography Images

Yifan Xiang[1†], Jingjing Chen[1†], Fabao Xu[1†], Zhuoling Lin[1], Jun Xiao[1], Zhenzhe Lin[1] and and Haotian Lin[1,2]**

[1] State Key Laboratory of Ophthalmology, Zhongshan Ophthalmic Center, Sun Yat-sen University, Guangzhou, China, [2] Center of Precision Medicine, Sun Yat-sen University, Guangzhou, China

OPEN ACCESS

Edited by:
Jian Yang,
Wuyi University, China

Reviewed by:
Xin Liu,
University of California, San Diego, United States
Ivan S. Babichuk,
Wuyi University, China

***Correspondence:**
Haotian Lin
linht5@mail.sysu.edu.cn;
haot.lin@hotmail.com
Zhenzhe Lin
of0727@163.com

[†] These authors have contributed equally to this work

Specialty section:
This article was submitted to Bionics and Biomimetics, a section of the journal Frontiers in Bioengineering and Biotechnology

Received: 27 December 2020
Accepted: 08 February 2021
Published: 05 March 2021

Citation:
Xiang Y, Chen J, Xu F, Lin Z, Xiao J, Lin Z and Lin H (2021) Longtime Vision Function Prediction in Childhood Cataract Patients Based on Optical Coherence Tomography Images. Front. Bioeng. Biotechnol. 9:646479. doi: 10.3389/fbioe.2021.646479

The results of visual prediction reflect the tendency and speed of visual development during a future period, based on which ophthalmologists and guardians can know the potential visual prognosis in advance, decide on an intervention plan, and contribute to visual development. In our study, we developed an intelligent system based on the features of optical coherence tomography images for long-term prediction of best corrected visual acuity (BCVA) 3 and 5 years in advance. Two hundred eyes of 132 patients were included. Six machine learning algorithms were applied. In the BCVA predictions, small errors within two lines of the visual chart were achieved. The mean absolute errors (MAEs) between the prediction results and ground truth were 0.1482–0.2117 logMAR for 3-year predictions and 0.1198–0.1845 logMAR for 5-year predictions; the root mean square errors (RMSEs) were 0.1916–0.2942 logMAR for 3-year predictions and 0.1692–0.2537 logMAR for 5-year predictions. This is the first study to predict post-therapeutic BCVAs in young children. This work establishes a reliable method to predict prognosis 5 years in advance. The application of our research contributes to the design of visual intervention plans and visual prognosis.

Keywords: machine learning, optical coherence tomography, childhood cataract, visual prediction, intelligent system

INTRODUCTION

Normal visual development and visual acuity (VA) are important for young children and are the basis of infantile brain development (Stjerna et al., 2015; Danka Mohammed and Khalil, 2020) and ability development (Wu et al., 2019; Havstam Johansson et al., 2020). Consequently, the results of visual prediction are meaningful by reflecting the tendency and speed of visual development during a future period. Exact VA prediction is beneficial for young children, especially children with ophthalmopathy, based on which ophthalmologists and guardians can determine the potential visual prognosis in advance, decide on an intervention plan, and contribute to visual development. However, the nature of ocular growth and myopia drift in young children may disrupt exact visual prediction and affect result accuracy. To date, no children-applicable technology for VA prediction

has been reported. Existing research (Rohm et al., 2018) has focused on short-term visual prediction for adults within a year.

Fundus imaging, especially optical coherence tomography (OCT), is recognized as a key factor for visual prediction (Guo et al., 2017; Esaka et al., 2019; Park et al., 2020). OCT images have been applied to predict prognostic visual function in age-related macular degeneration (AMD) (Rohm et al., 2018) and have achieved excellent performance in visual prediction. In our study, based on clinical data, features of OCT images, and follow-up results of children with childhood cataract (CC), we developed a machine learning system for long-term visual prediction of best corrected visual acuity (BCVA) 3 and 5 years in advance. This system can help ophthalmologists and guardians monitor patients' visual development (Long et al., 2017) and adopt necessary visual intervention (Sniatecki et al., 2015; Wang and Xiao, 2015) in time, thereby contributing to the visual prognosis of young children.

MATERIALS AND METHODS

A prospective study was conducted at the Zhongshan Ophthalmic Center (ZOC), Guangdong, China, from June 2011 to February 2019. The data were collected from a national project for CC treatment and research: the CC Program of the Chinese Ministry of Health (CCPMOH). This study followed the tenets of the Declaration of Helsinki and was approved by the Institutional Review Board of the ZOC at Sun Yat-sen University (IRB-ZOC-SYSU).

Clinical and Imaging Data

Two hundred eyes of 132 patients from the ZOC were included in the study. The inclusion criteria were as follows: (1) diagnosed with CC at the ZOC, (2) had surgical treatment, (3) had a horizontal OCT B scan with a scan quality index of good, (4) had a clear axis after treatment, and (5) had follow-up BCVA exams at 3 or 5 years after the OCT B scan. The exclusion criteria were as follows: (1) diagnosed with another ophthalmic disease or (2) diagnosed with a neurological or mental disease. The collected clinical data included sex, laterality, surgical age, surgical type, age at OCT B scan, follow-up BCVA results, and other examination and prognostic information.

Measured features of OCT images were extracted from the Optovue software. The retinal thickness of nine parts, namely the macular area and its eight surrounding regions (inner and outer sides of nasal, temporal, superior, and inferior regions to macula, see **Figure 1C**), was recorded. Furthermore, the thickness of the retinal nerve fiber layer (RNFL) was labeled manually based on the OCT images. The thickness of the RNFL was divided into four grades. A label of 1 indicated the complete existence of RNFL, 2 indicated the existence of most of RNFL with a thickness more than half of the normal one, 3 indicated the intermittent existence of RNFL with a thickness less than half of the normal one, and 4 indicated the complete absence of RNFL. The label work was finished by three retinal ophthalmologists and confirmed by a retinal professor.

Model Training and Evaluation

The research procedure is shown in **Figure 1**. To predict the BCVA of CC patients 3 and 5 years in advance, we tried six machine learning models, namely random forest, ExtraTrees, gradient boosting decision tree (GBDT), ridge regression, lasso regression, and ElasticNet. The age at OCT B scan, the label of RNFL thickness, and the retinal thickness of nine parts obtained from OCT were applied as training features.

For the prediction tasks, we used five-fold cross-validation. The proportion of the training set and the test set were 80 and 20%, respectively. To quantitatively evaluate the prediction performance, we applied two evaluation metrics, mean absolute error (MAE) and root mean square error (RMSE). The MAE is calculated as the average value of the absolute error of the prediction results, which directly reflects the deviation of the predicted values from the actual values. The formula for MAE is as follows:

$$\mathrm{MAE} = \frac{1}{N}\sum_{i=1}^{N}\left|\tilde{y}_i - y_i\right|$$

The RMSE is the square root of mean square error (MSE). The MSE is calculated as the average value of the square of the error of the prediction results. The RMSE is more interpretable considering its unit consistency with the original variables. The formula for RMSE is as follows:

$$\mathrm{RMSE} = \sqrt{\frac{1}{N}\sum_{i=1}^{N}\left(\tilde{y}_i - y_i\right)^2}$$

In the above two formulas, N is the number of predictions per fold, y_i is the ground truth, and $\tilde{y}_i$ is the predicted value.

RESULTS

The training data included 200 eyes of 132 patients (46 females and 86 males), containing 197 eyes of 131 patients for 3-year prediction training and 172 eyes of 114 patients for 5-year prediction training (**Table 1**). The average surgical age was nearly 47 months, and the average age at OCT B scan was close to 55 months. The average endpoint BCVAs were 0.45 and 0.33 logMAR, respectively, in the two prediction groups.

For the prediction evaluation, most of the models achieved excellent performance of errors within two lines (0.2 logMAR) of the VA chart in both 3- and 5-year predictions (**Table 2**). The random forest and GBDT models achieved the best 3-year prediction, and the ExtraTrees and GBDT models achieved the best 5-year prediction. In the 3-year prediction test, the MAEs ranged from 0.1482 to 0.2117, and the RMSEs ranged from 0.1916 to 0.2942. In the 5-year prediction test, the MAEs ranged from 0.1198 to 0.1845, and the RMSEs ranged from 0.1692 to 0.2537. For the same model, the prediction errors of 5-year tasks were always lower than those of 3-year tasks.

Figure 2 shows the weights of features for 3- and 5-year BCVA predictions in the random forest model. The thickness of RNFL plays a key role in BCVA prediction with a weight of nearly 0.8. The age at OCT B scan is the second most important factor with

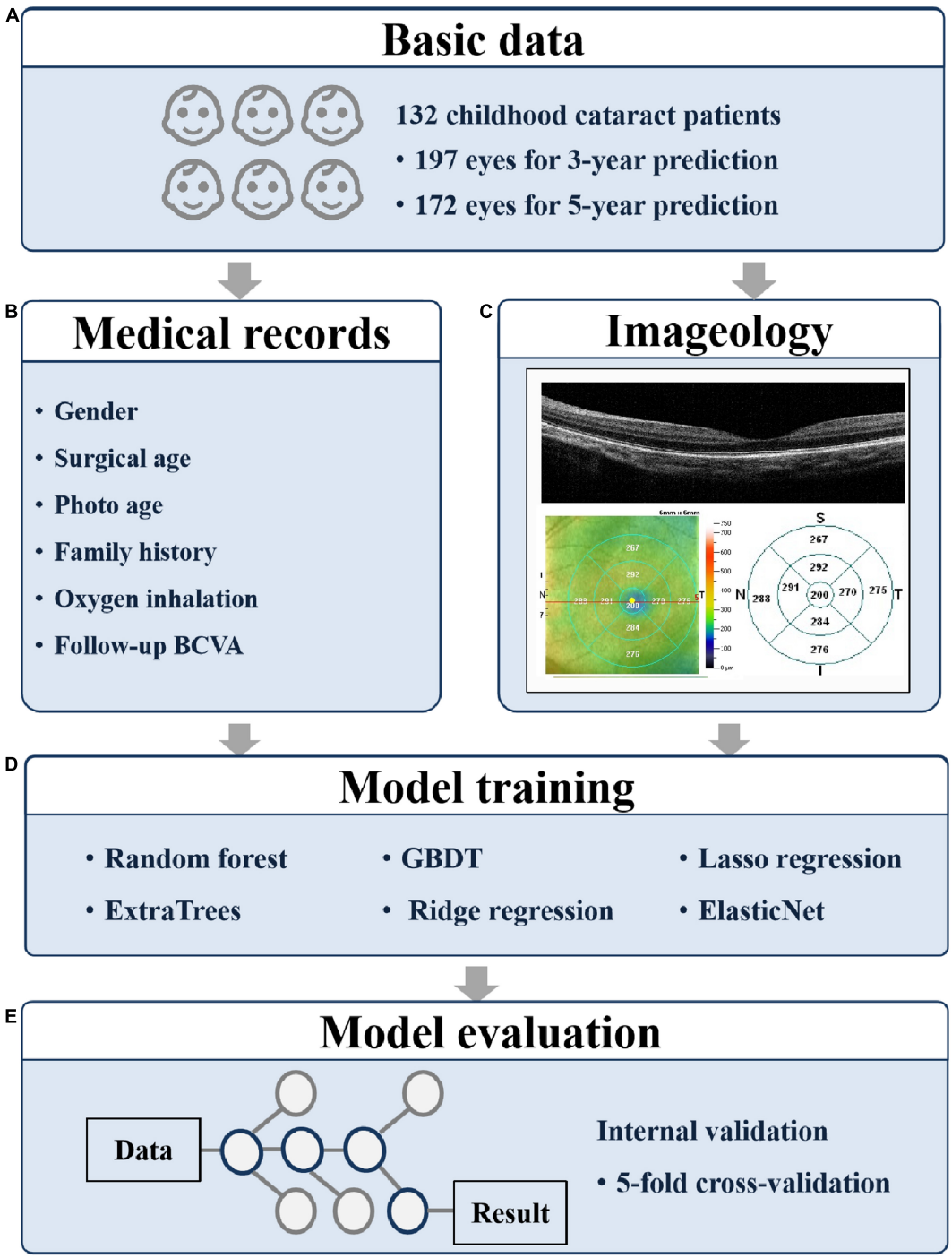

FIGURE 1 | Overall study pipeline. The work flow of developing machine learning models for predicting 3- and 5-year BCVA based on medical records and fundus images. **(A)** The participant numbers; **(B)** the collected medical records; **(C)** the collected fundus images; **(D)** the applied models; and **(E)** the evaluation method. BCVA, best corrected visual acuity; GBDT, gradient boosting decision tree.

a weight of very nearly 0.1. The retinal thickness of the macula is the most important of the retinal thickness of the nine regions at and near the macula. In the 5-year prediction, the weight of the thickness of RNFL is higher than that of the 3-year prediction. The results of other models are similar to those of the random forest model. The thickness of RNFL remains most important in all the models.

Figure 3 shows both the ground-truth and prediction values of each test example in 3- and 5-year predictions, respectively, based on the random forest model. The examples were ordered

TABLE 1 | Characteristics of patients regarding the 3- and 5-year predictions.

Characteristic	3-Year prediction	5-Year prediction
Eyes	197	172
Patients	131	114
Male	85 (64.8%)	76 (66.6%)
Surgical age (months)	46.74 ± 34.17	46.70 ± 34.75
Photo age (months)	55.40 ± 34.12	54.63 ± 34.83
Endpoint BCVA (logMAR)	0.45 ± 0.49	0.33 ± 0.42

BCVA, best corrected visual acuity.

based on the ground-truth BCVA in **Figures 3A,B**. When the true BCVAs were lower than 0.2 logMAR, the prediction values were always higher than the true results. As the true BCVAs increased, the prediction values fluctuated around the true results. In **Figures 3C,D**, the examples were ordered based on the age at OCT B scan, and the prediction values mainly fluctuated around the true results.

DISCUSSION

This is the first study to predict the post-therapeutic long-term BCVA of CC children based on OCT images through artificial intelligence (AI), and it demonstrated that the long-term visual function of children can be accurately predicted based on imageology using machine learning.

The post-therapeutic visual function of children with ocular diseases is one of the most important factors (Mndeme et al., 2020) focused on by doctors and guardians, as visual prognosis plays a key role in intelligence development (Li et al., 2017), school attendance (Negretti et al., 2015), and quality of life. However, there has been limited research contributing to the visual prediction of children with ophthalmopathy, with most published studies paying attention to the short-term visual prediction of adults within a year (Rohm et al., 2018). Our study addresses both limitations by demonstrating children-applicable prediction and long-term prediction of VA based on imageology. The machine learning models can predict 3- and 5-year BCVAs in advance with a small error within two lines of the visual chart. Based on the results predicted by our model, ophthalmologists and guardians can provide necessary assistance and individually targeted intervention (Sniatecki et al., 2015) to help children obtain better visual outcomes (Pinto et al., 2015) and quality of life, which may be of significant importance to childhood brain development.

Our research achieves precise prediction of long-term BCVA based only on features of OCT images and age, which makes it more accessible and stable than other methods. Most CC patients will take a fundus photo or undergo an OCT B scan to check fundus function after cataract surgery, and our model can be conveniently applied. The reported research (Rohm et al., 2018) applied 165 features to achieve a 6-month prediction, including 41 features from clinical records and 124 features from OCT images. Compared with previous research, our models are simpler and more convenient for general application.

The feature weights shown in **Figure 2** specify that the thickness of the RNFL is closely related to long-term visual development after therapy. In the longer prediction, its importance increases. The RNFL lacks the ability to regenerate (Cen et al., 2018; Wu et al., 2020). If the OCT image indicates that the RNFL has atrophied (balducci et al., 2017) at the baseline examination, the visual function would not improve much in the post-therapeutic follow-up. On the other hand, if the OCT image indicates that the RNFL is complete at baseline, CC patients may achieve remarkable visual improvement after surgery with proper intervention. Above all, the thickness of RNFL is a dominant and stable indicator in post-therapeutic BCVA prediction.

Random forest (Breiman, 2001), ExtraTrees (Geurts et al., 2006), and GBDT (Schwenk and Bengio, 1998) all belong to ensemble learning (Kadiyala and Kumar, 2018), in which random forest and ExtraTrees apply the bagging method

TABLE 2 | Prediction errors in 3- and 5-year BCVA predictions.

Model	3-Year prediction		5-Year prediction	
Validation set	**MAE**	**RMSE**	**MAE**	**RMSE**
Random forest	0.2121 ± 0.0153	0.2841 ± 0.0230	0.1685 ± 0.0011	0.2414 ± 0.0019
ExtraTrees	0.2252 ± 0.0009	0.3044 ± 0.0012	0.1558 ± 0.0012	0.2250 ± 0.0015
GBDT	0.2234 ± 0.0024	0.3172 ± 0.0034	0.1807 ± 0.0023	0.2564 ± 0.0026
Ridge regression	0.2253 ± 0.0203	0.2994 ± 0.0322	0.1709 ± 0.0207	0.2566 ± 0.0430
Lasso regression	0.2362 ± 0.0179	0.3073 ± 0.0249	0.1743 ± 0.0139	0.2425 ± 0.0261
ElasticNet	0.2154 ± 0.0176	0.2973 ± 0.0191	0.1719 ± 0.0172	0.2478 ± 0.0308
Test set	MAE	RMSE	MAE	RMSE
Random forest	0.1515 ± 0.0025	0.1916 ± 0.0040	0.1315 ± 0.0031	0.1752 ± 0.0045
ExtraTrees	0.1676 ± 0.0024	0.2108 ± 0.0022	0.1334 ± 0.0019	0.1692 ± 0.0022
GBDT	0.1482 ± 0.0065	0.2024 ± 0.0048	0.1198 ± 0.0040	0.1734 ± 0.0034
Ridge regression	0.2117 ± 0.0401	0.2942 ± 0.0716	0.1475 ± 0.0430	0.2135 ± 0.0664
Lasso regression	0.2046 ± 0.0374	0.2909 ± 0.0768	0.1845 ± 0.0669	0.2537 ± 0.1172
ElasticNet	0.2089 ± 0.0517	0.2937 ± 0.0971	0.1778 ± 0.0345	0.2487 ± 0.0604

BCVA, best corrected visual acuity; GBDT, gradient boosting decision tree; MAE, mean absolute error; RMSE, root mean square error.

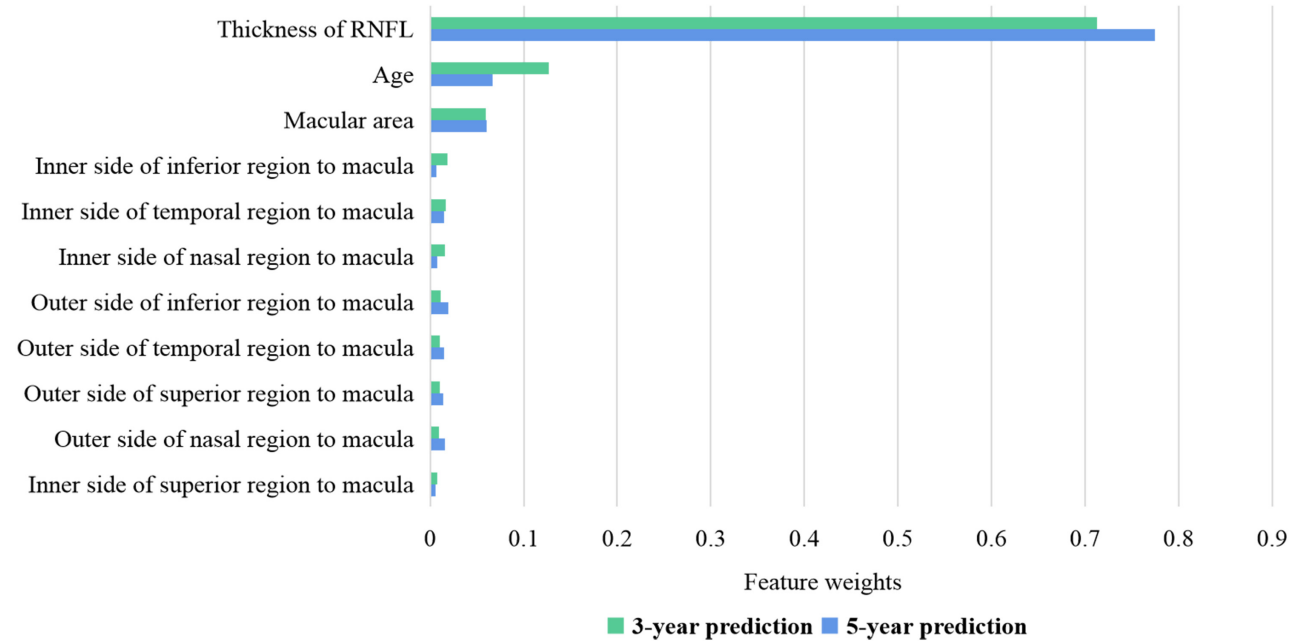

FIGURE 2 | Feature weights of random forest for 3- and 5-year BCVA predictions. The thickness of RNFL has a weight of nearly 0.7–0.8. The age at OCT B scan has a weight of nearly 0.1. The retinal thickness of the macula is the most important of the retinal thickness of the nine regions at and near the macula. BCVA, best corrected visual acuity; RNFL, retinal nerve fiber layer.

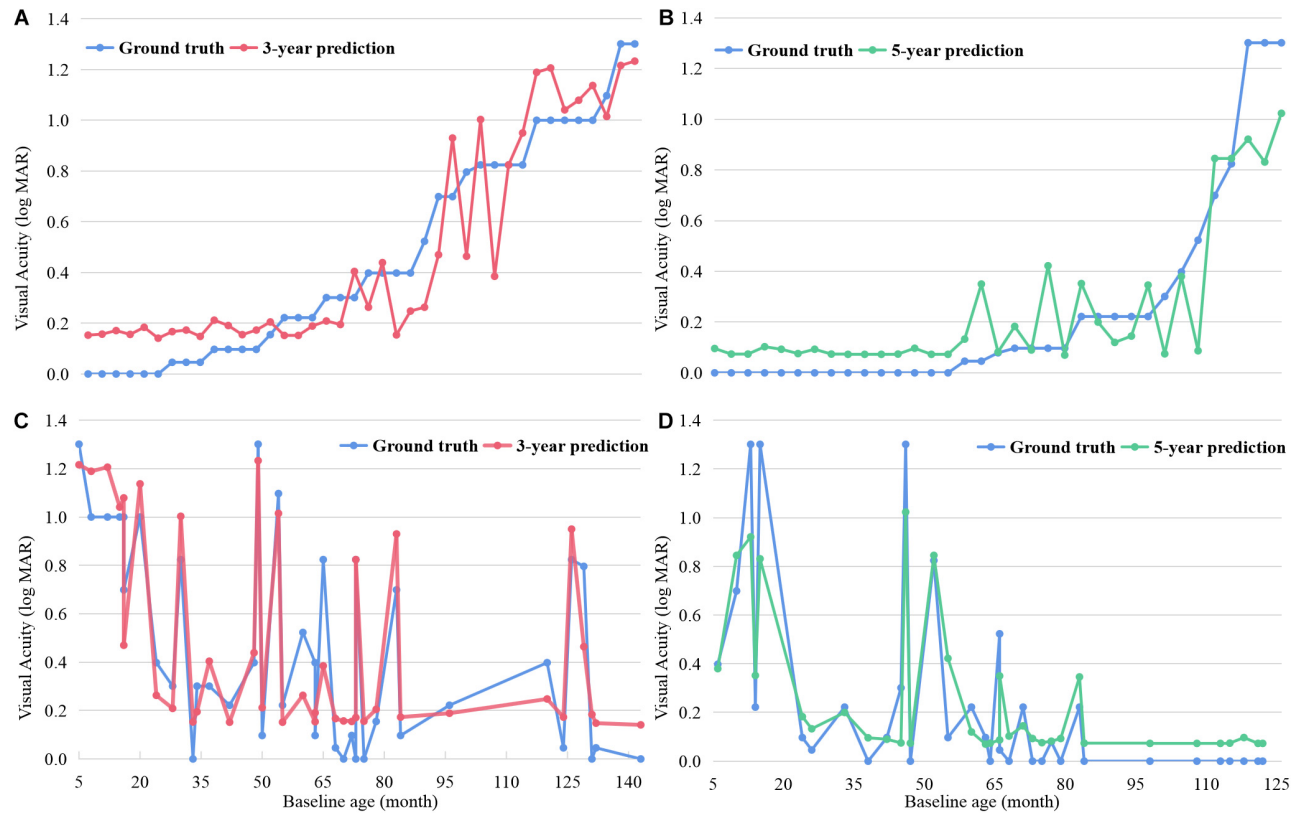

FIGURE 3 | The ground-truth and prediction values of each test example in 3- and 5-year BCVA predictions based on random forest. The examples were ordered based on the ground-truth BCVA in **(A,B)** and ordered based on the age undergoing OCT B scan in **(C,D)**. BCVA, best corrected visual acuity.

(Kristína et al., 2006) and GBDT uses the boosting method. Each predicted function was parallel in the bagging model and serial in the boosting model. Bagging always behaves better in preventing overfitting in small sample learning. The models of ridge regression, lasso regression, and ElasticNet (Ogutu et al., 2012) tend to apply the least squares method to predict values, which behaves better in data with multicollinearity and does not exactly fit the weights of each dimension of our data without multicollinearity.

LIMITATION

The limitations of our research should be considered. Larger samples of CC patients are necessary to increase the dataset and to improve the prediction stability. Additionally, a longer follow-up period contributes to extending the predicted time span. Besides, data for external validation are warranted to test the prediction model in real-world settings.

DATA AVAILABILITY STATEMENT

The data is available from the corresponding author upon reasonable request.

ETHICS STATEMENT

The studies involving human participants were reviewed and approved by the institutional review board of the ZOC at Sun Yat-sen University (IRB-ZOC-SYSU). Written informed consent to participate in this study was provided by the participants' legal guardian/next of kin.

AUTHOR CONTRIBUTIONS

YX, JC, and HL conceived and designed the experiments. JC and ZuL collected the data. YX and FX labeled the data. ZeL and JX performed the experiments and analyzed the data. YX wrote the manuscript. JC, FX, and HL revised it. All authors read and approved the final manuscript.

FUNDING

This study was funded by the National Key R&D Program of China (2018YFC0116500), the National Natural Science Foundation of China (81770967 and 81822010), and the Science and Technology Planning Projects of Guangdong Province (2019B030316012). The sponsors of the study played no role in the study protocol design, data collection, analysis, or interpretation, manuscript preparation, or the decision to submit the manuscript for publication.

ACKNOWLEDGMENTS

The authors are grateful to all the participants and CC patients for supporting our study.

REFERENCES

Balducci, N., Ciardella, A., Gattegna, R., Zhou, Q., Cascavilla, M. L., La Morgia, C., et al. (2017). Optical coherence tomography angiography of the peripapillary retina and opti nerve head in dominant optic atrophy. *Mitochondrion* 36, 60–65. doi: 10.1016/j.mito.2017.03.002

Breiman, L. (2001). Random forests. *Mach. Learn.* 45, 5–32.

Cen, L. P., Ng, T. K., Liang, J. J., Zhuang, X., Yao, X., Yam, G. H., et al. (2018). Human periodontal ligament-derived stem cells promote retinal ganglion cell survival and axon regeneration after optic nerve injury. *Stem Cells* 36, 844–855. doi: 10.1002/stem.2812

Danka Mohammed, C. P., and Khalil, R. (2020). Postnatal development of visual cortical function in the mammalian brain. *Front. Syst. Neurosci.* 14:29. doi: 10.3389/fnsys.2020.00029

Esaka, Y., Kojima, T., Dogru, M., Hasegawa, A., Tamaoki, A., Uno, Y., et al. (2019). Prediction of best-corrected visual acuity with swept-source optical coherence tomography parameters in keratoconus. *Cornea* 38, 1154–1160. doi: 10.1097/ICO.0000000000002043

Geurts, P., Ernst, D., and Wehenkel, L. (2006). Extremely randomized trees. *Mach. Learn.* 63, 3–42.

Guo, Z., Kwon, Y. H., Lee, K., Wang, K., Wahle, A., Alward, W., et al. (2017). Optical coherence tomography analysis based prediction of humphrey 24-2 visual field thresholds in patients with glaucoma. *Invest. Ophthalmol. Vis. Sci.* 58, 3975–3985. doi: 10.1167/iovs.17-21832

Havstam Johansson, L., Škiljić, D., Falk Erhag, H., Ahlner, F., Pernheim, C., Rydberg Sterner, T., et al. (2020). Vision-related quality of life and visual function in a 70-year-old Swedish population. *Acta Ophthalmol.* 98, 521–529. doi: 10.1111/aos.14341

Kadiyala, A., and Kumar, A. (2018). Applications of python to evaluate the performance of bagging methods. *Environ. Prog. Sustain. Energy* 37, 1555–1559.

Kristína, M., František, B., and Peter, B. (2006). A bagging method using decision trees in the role of base classifiers. *Acta Polytech. Hung.* 3, 121–132.

Li, Q., Song, M., Xu, J., Qin, W., Yu, C., and Jiang, T. (2017). Cortical thickness development of human primary visual cortex related to the age of blindness onset. *Brain Imaging Behav.* 11, 1029–1036. doi: 10.1007/s11682-016-9576-8

Long, E., Zhang, X., Liu, Z., Wu, X., Tan, X., Lin, D., et al. (2017). Dynamic response to initial stage blindness in visual system development. *Clin. Sci.* 131, 1515–1527. doi: 10.1042/CS20170234

Mndeme, F. G., Mmbaga, B. T., Msina, M., Mwende, J., Vaitha, S. J., Kim, M. J., et al. (2020). Presentation, surgery and 1-year outcomes of childhood cataract surgery in Tanzania. *Br. J. Ophthalmol.* 105, 334–340. doi: 10.1136/bjophthalmol-2020-316042

Negretti, G. S., Ayoub, T., Ahmed, S., Deb, R., Majumder, U., Jewel, J., et al. (2015). Cataract surgery outcomes in bangladeshi children. *Ophthalmology* 122, 882–887. doi: 10.1016/j.ophtha.2015.01.013

Ogutu, J. O., Schulz-Streeck, T., and Piepho, H. P. (2012). Genomic selection using regularized linear regression models: ridge regression, lasso, elastic net and their extensions. *BMC Proc.* 6:S10. doi: 10.1186/1753-6561-6-S2-S10

Park, K., Kim, J., Kim, S., and Shin, J. (2020). Prediction of visual field from swept-source optical coherence tomography using deep learning algorithms. *Graefes Arch. Clin. Exp. Ophthalmol.* 258, 2489–2499. doi: 10.1007/s00417-020-04909-z

Pinto, J. G., Jones, D. G., Williams, C. K., and Murphy, K. M. (2015). Characterizing synaptic protein development in human visual cortex enables alignment of synaptic age with rat visual cortex. *Front. Neural Circuits* 9:3. doi: 10.3389/fncir.2015.00003

Rohm, M., Tresp, V., Müller, M., Kern, C., Manakov, I., Weiss, M., et al. (2018). Predicting visual acuity by using machine learning in patients treated for neovascular age-related macular degeneration. *Ophthalmology* 125, 1028–1036. doi: 10.1016/j.ophtha.2017.12.034

Schwenk, H., and Bengio, Y. (1998). "Training methods for adaptive boosting of neural networks," in *Advances in Neural Information Processing Systems*, eds M. Jordan I, M. J. Kearns, and S. A. Solla (Cambridge, MA: The MIT Press).

Sniatecki, J. J., Styles, C., Boyle, N., and Sanders, R. (2015). Cataract surgery: factors influencing decision to treat and implications for training (south-east Scotland 2008-2014). *Clin. Ophthalmol.* 9, 1821–1827. doi: 10.2147/OPTH.S92803

Stjerna, S., Sairanen, V., Gröhn, R., Andersson, S., Metsäranta, M., Lano, A., et al. (2015). Visual fixation in human newborns correlates with extensive white matter networks and predicts long-term neurocognitive development. *J. Neurosci.* 35, 4824–4829. doi: 10.1523/JNEUROSCI.5162-14.2015

Wang, M., and Xiao, W. (2015). Congenital cataract: progress in surgical treatment and postoperative recovery of visual function. *Eye Sci.* 30, 38–47.

Wu, N., Kong, X., Gao, J., and Sun, X. (2019). Vision-related quality of life in glaucoma patients and its correlations with psychological disturbances and visual function indices. *J. Glaucoma.* 28, 207–215. doi: 10.1097/IJG.0000000000001178

Wu, Y., Zhan, Z., Quan, Y., Yang, Y., Chen, X., Liu, L., et al. (2020). SP1-mediated upregulation of LINGO-1 promotes degeneration of retinal ganglion cells in optic nerve injury. *CNS Neurosci. Ther.* 26, 1010–1020. doi: 10.1111/cns.13426

Conflict of Interest: The authors declare that the research was conducted in the absence of any commercial or financial relationships that could be construed as a potential conflict of interest.

frontiers in Bioengineering and Biotechnology

ORIGINAL RESEARCH
published: 01 April 2021
doi: 10.3389/fbioe.2021.656716

Study on the Design and Optimization of a Portable Monitoring and Auxiliary Treatment Device for Upper Extremity Lymphedema–Focus on the Rehabilitation Function of the Device

Xue Yanmin[1], Zhang Xuyang[1], Yan Wen[1], Yu Suihuai[2] and Li Sinan[3]*

[1] Department of Industrial Design, Xi'an University of Technology, Xi'an, China, [2] Industrial Design Institute, Northwestern Polytechnical University, Xi'an, China, [3] School of Life Sciences and Technology, Xi'an Jiaotong University, Xi'an, China

OPEN ACCESS

Edited by:
Xiaoguang Zhou, Beijing University of Posts and Telecommunications (BUPT), China

Reviewed by:
Zhaohua Zhu, China University of Mining and Technology, China
Guo Lei, University of Electronic Science and Technology of China, China

***Correspondence:**
Xue Yanmin
xueym@xaut.edu.cn

Specialty section:
This article was submitted to Bionics and Biomimetics, a section of the journal Frontiers in Bioengineering and Biotechnology

Received: *21 January 2021*
Accepted: *22 February 2021*
Published: *01 April 2021*

Citation:
Yanmin X, Xuyang Z, Wen Y, Suihuai Y and Sinan L (2021) Study on the Design and Optimization of a Portable Monitoring and Auxiliary Treatment Device for Upper Extremity Lymphedema–Focus on the Rehabilitation Function of the Device. Front. Bioeng. Biotechnol. 9:656716. doi: 10.3389/fbioe.2021.656716

Female patients suffer from the risk of upper limb lymphedema after breast cancer removal surgery. At present, the detection and the adjuvant treatment of this disease are not convenient enough, leading to delay of the disease and increase in the burden of patients. This paper presents a portable monitoring and treatment device for upper extremity lymphedema, enabling patients to monitor the symptoms of upper limb lymphedema and auxiliary rehabilitation. This design utilizes the arm circumference measurement and contrast method to realize symptom monitoring. The device realizes auxiliary rehabilitation using the regional pressure method to imitate traditional manual lymphatic drainage technology. According to the MRI images of volunteers' upper limbs, the upper arm and forearm's finite element models are reconstructed in ANSYS. The static simulation experiment is completed. The working mode and parameter design of each rehabilitation module of the device are obtained. The experimental results show that the integrated design principle of monitoring and treatment proposed in this paper has good feasibility, has auxiliary rehabilitation effect, and meets the principle of human comfort. The device can help patients find lymphedema in time and implement auxiliary treatment, which can effectively avoid the further deterioration of lymphedema.

Keywords: upper limb lymphedema recovered, static analysis, wearable design, massage pressure simulation, rehabilitation function of the device

INTRODUCTION

Breast cancer is the leading cancer disease in women. After breast cancer surgery, 15–30% of patients (Chen et al., 2017) in rehabilitation have secondary lymphedema. The cause of the disease was that the lymph nodes draining the patient's site were also removed at the same time of tumor resection. Therefore, the drainage lymphatic vessel was cut off, which led to the obstruction of lymph reflux in the distal tissue, leading to lymphedema of the upper limbs.

Once lymphedema occurs, edema fluid rich in macromolecules remains in the human body's soft tissue. The human body's soft tissue will gradually become hard fibrous tissue with fat deposition and proliferation. The patient's limbs will gradually enlarge and thicken. At the same time, these will cause tissue inflammation. Each infection will aggravate edema, thus forming a vicious cycle. Lymphedema is a chronic disease with slow progress and cannot be completely cured, but if the treatment is timely and there is proper nursing, lymphedema can be obviously relieved.

At present, there is no effective monitoring method for early occult lymphedema. For clinical dominant lymphedema, the following technical methods are generally used for evaluation and measurement: (1) direct measurement of limb circumference or volume, including limb circumference measurement, water substitution method, higher-precision professional equipment Perometer (Shaitelman et al., 2015), etc., (2) bioelectrical impedance analysis equipment is used to indirectly evaluate the degree of swelling by analyzing the body fluid composition of lymphedematous limbs (Kilbreath et al., 2017), and (3)

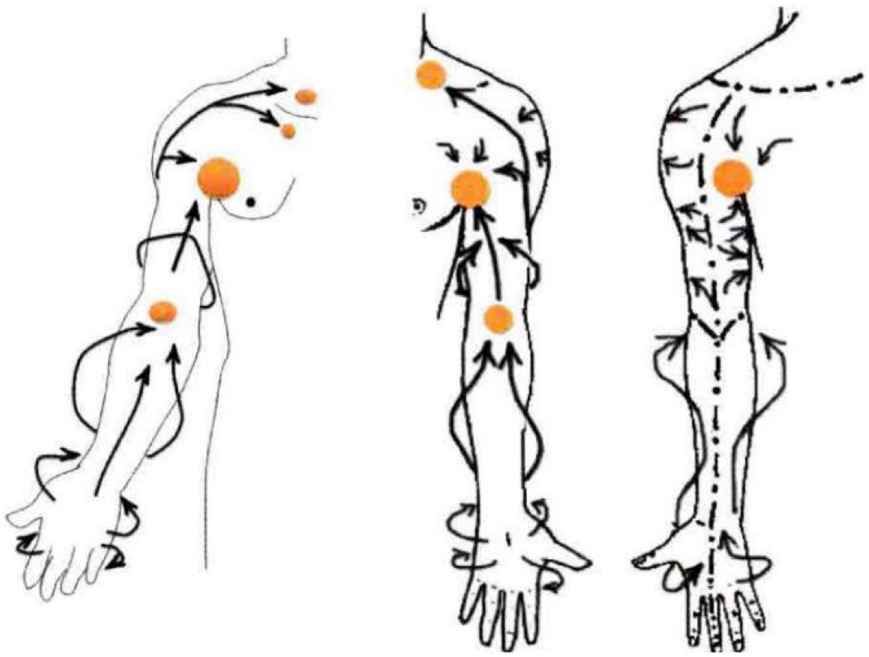

FIGURE 1 | Upper extremity lymph node distribution and manual lymphatic drainage (Ningfei, 2014).

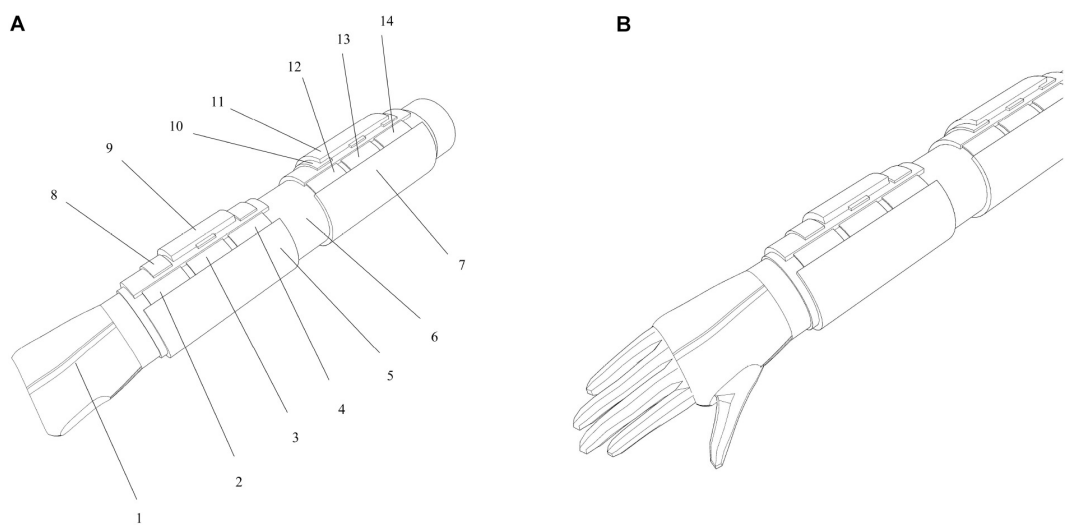

FIGURE 2 | Device diagram: **(A)** schematic diagram of the device structure and **(B)** device wearing diagram.

imaging auxiliary examination of lymphedema, including isotope lymphography (Yoon et al., 2020), near-infrared fluorescence imaging (Kraft et al., 2018), and MRI (Lim et al., 2016). At present, the treatment strategy of lymphedema after breast cancer surgery is still in the exploratory stage, and there is no consensus on the treatment of lymphedema. As far as the conservative treatment of upper limb edema is concerned, there are strength training, pressure-assisted therapy, intermittent air wave pressure pump, far-infrared thermotherapy, medication, and so on. These monitoring equipment and auxiliary treatment equipment are set in special nursing institutions or hospitals; patients need to be checked and treated at regular intervals. Patients often miss the best treatment time because they cannot get checked and treated on time for various reasons, resulting in deterioration of the condition. Therefore, it is urgent to develop a wearable monitoring and auxiliary treatment device for lymphedema after breast cancer surgery.

For patients with upper extremity lymphedema, this study can shorten the detection time and increase the convenience of rehabilitation treatment. Compared with the existing clinical diagnosis and rehabilitation treatment technology, this study provides a new and innovative convenient monitoring integrated method and can be used with the existing clinical technology, which will greatly increase the recovery rate of upper limb lymphedema and reduce the delay of rehabilitation treatment due to time. At present, this research belongs to the forefront in China, which will greatly enrich the research field of lymphedema. The device will reduce the pain of patients with lymphedema, achieve the purpose of early detection and treatment, and effectively control the patient's condition. According to the needs of patients with upper limb lymphedema, this paper designs a portable monitoring and treatment integrated device for upper limb lymphedema and carries out static finite element simulation of human upper limb through ANSYS software, which further optimizes the design of the device, improves the rehabilitation treatment effect of the device, and effectively avoids the further deterioration of patients with lymphedema. Further improvement and application of the device will further improve the living conditions of patients with upper extremity lymphedema and further improve the development of human health.

PRINCIPLE OF DEVICE DESIGN

In this study, female patients with grade 0 lymphedema after breast cancer surgery (patients with mild or who might have tissue damage) were selected as design users. It can be found that the users lack a device for basic monitoring and auxiliary treatment at home. According to the needs of users, a portable monitoring and auxiliary treatment device for upper limb lymphedema is proposed, which belongs to wearable medical equipment.

Monitoring and Treatment Principle of Lymphedema of the Upper Limbs

For the portable lymphedema monitoring method, the arm circumference measurement comparison method (Hayes et al., 2008; Czerniec et al., 2010) is more convenient and simple. This method is suitable for household monitoring products because of its low development cost. The arm circumference of the patient was measured regularly every time to detect whether upper limb edema occurred. If upper limb edema is detected, the device will automatically perform the auxiliary treatment function.

For portable lymphedema rehabilitation methods, the mainstream method is pressure-assisted therapy (Sierla et al., 2018). Because of the gradient pressure difference between the distal end and the proximal end of the limb, pressure will be generated on the lymphatic vessels or blood vessels in the arm. Through uniform pressure bandaging of the whole upper limb, filling, and emptying of lymph and blood can

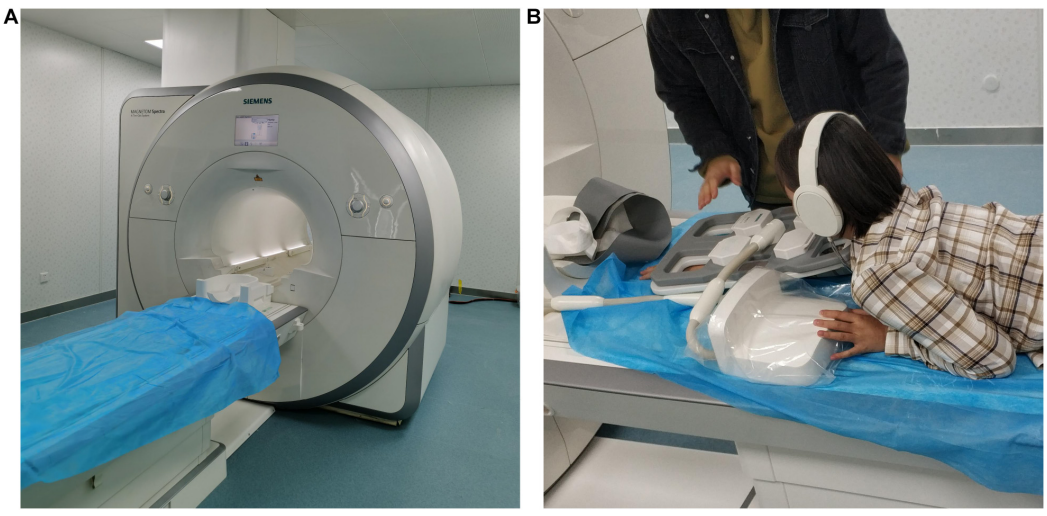

FIGURE 3 | Schematic diagram of human upper limb information collection: **(A)** Siemens MAGNETOM spectra and **(B)** scanned images of a female volunteer.

be accelerated, and lymph reflux can be reduced. At present, various elastic bandages are widely used in the market. Another professional mainstream rehabilitation method is manual lymphatic drainage, with the full name of lymphedema manual drainage comprehensive detumescence treatment (Keilani et al., 2020), also known as complete decongestion therapy. At present, this kind of conservative treatment is widely used in the world and has the best rehabilitation effect. Manual lymphatic drainage technology is used to increase or promote the reflux of lymph and interstitial fluid. The implementation method follows the anatomical and physiological pathway of the lymphatic system, which is a professional massage technique. According to **Figure 1**, in the implementation of the method, the following requirements are essential: massage pressure should be moderate, weak force has no effect, and strong force will lead to lymphatic spasm (Ningfei, 2014; Iannello and Biller, 2020). The speed of force application should be moderate, which is conducive to the smooth change of pressure between tissues in the arm. Each time lasted for 1 to 2 s, and each action was repeated five to seven times. The massage direction should be based on the direction of lymphatic reflux, from the distal end to the proximal end. The massage mode is circular push forward rotary extrusion. The portable monitoring and auxiliary treatment device for upper extremity lymphedema

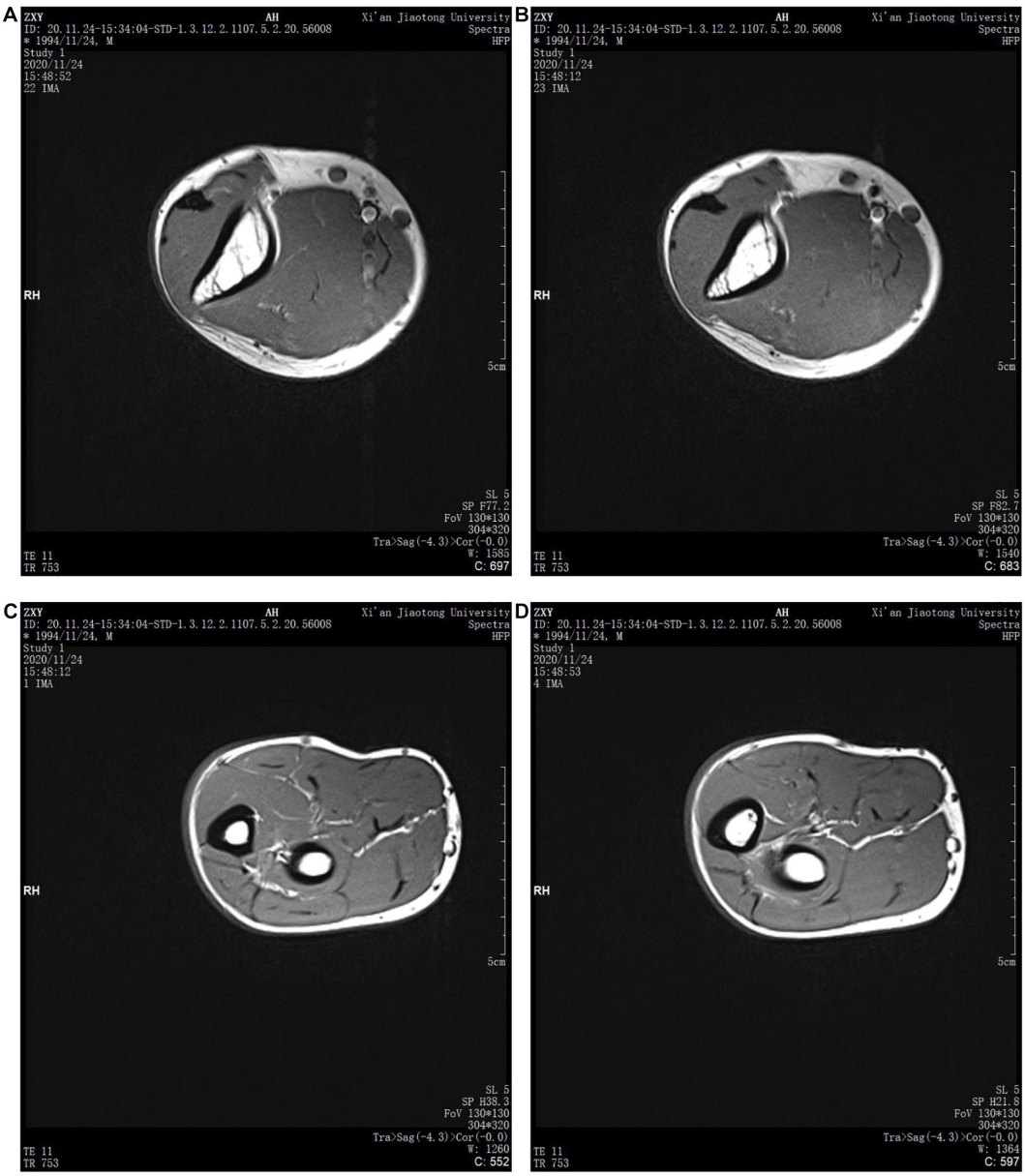

FIGURE 4 | MRI images of human upper limbs: **(A)** upper arm scan **Figure 1**, **(B)** upper arm scan **Figure 2**, **(C)** forearm scan **Figure 1**, and **(D)** forearm scan **Figure 2**.

will adopt and combine the above-mentioned detection and rehabilitation methods.

Principle of Conceptual Design

As shown in **Figure 2**, the device is based on the use of the pressure-sensing module and the tightening-diastolic module. The device can solve three pain points of users at the same time: how to wear, how to monitor, and how to perform auxiliary treatment. The device is roughly divided into three layers: inner elastic fabric layer (rehabilitation layer: including pressure-assisted therapy), pressure-sensing embedded layer (rehabilitation layer: including manual lymphatic drainage treatment), and external fastening layer (thin rubber, hard cloth, etc.).

The detailed structure of each module is as follows: (1) positioning glove, (2) forearm low-ductility massage belt C,

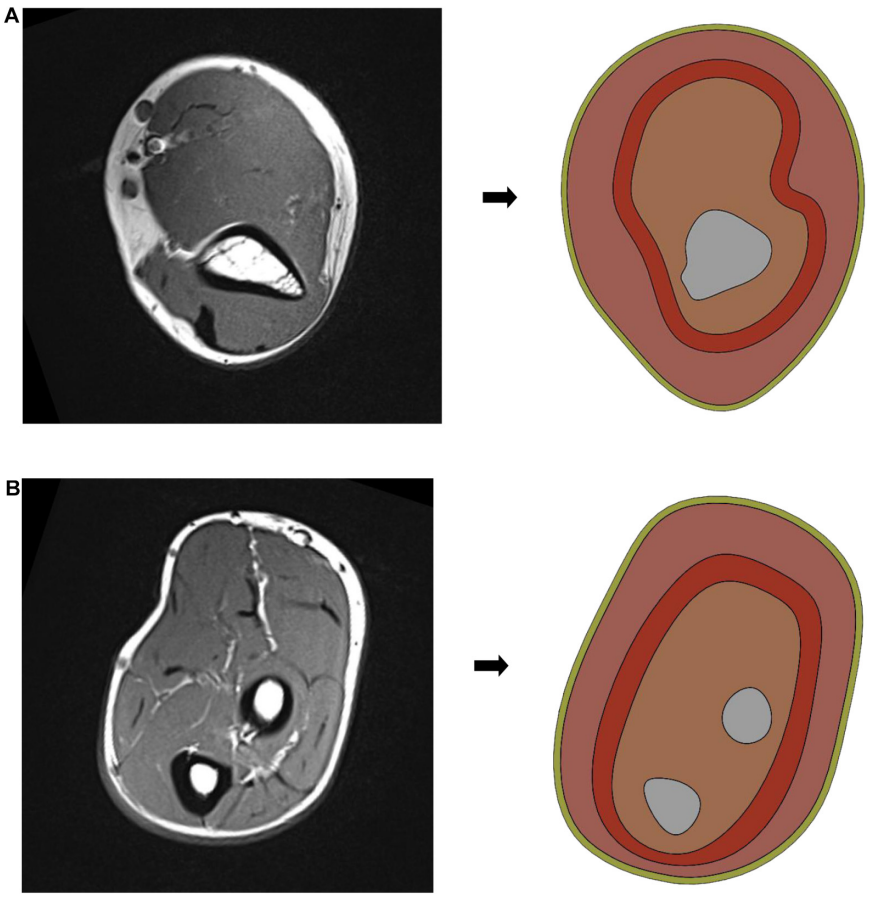

FIGURE 5 | Simplified model of human upper limb: **(A)** simplified schematic of upper arm middle model and **(B)** simplified schematic of forearm middle model.

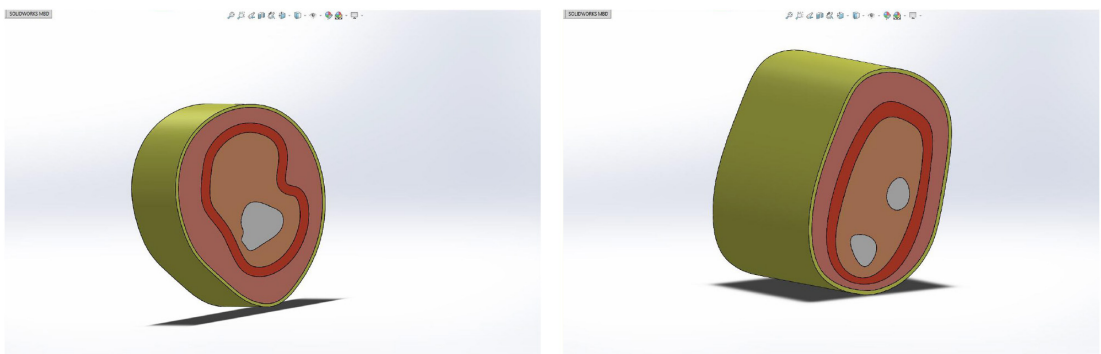

FIGURE 6 | Reconstructed model of upper limb.

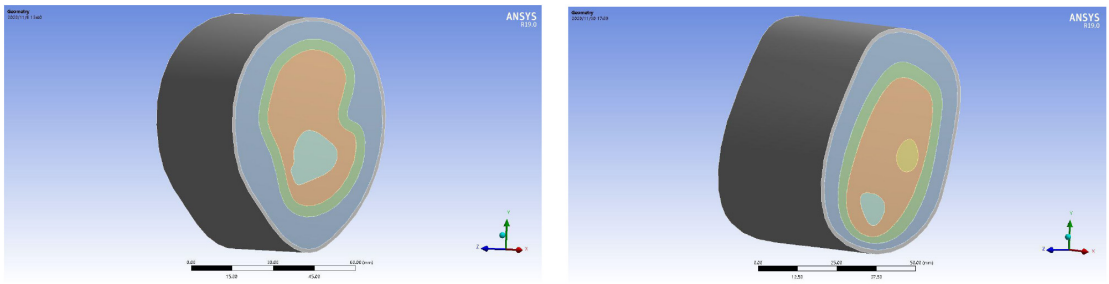

FIGURE 7 | Reconstructed model of upper limb import.

(3) forearm low-ductility massage belt B, (4) forearm low-ductility massage belt A, (5) forearm rehabilitation module, (6) elastic fabric, (7) upper arm rehabilitation module, (8) forearm monitoring module, (9) forearm signal processing module, (10) upper arm monitoring module, (11) upper arm signal processing module, (12) upper arm low-ductility massage belt C, (13) upper arm low-ductility massage belt B, and (14) upper arm low-ductility massage belt A.

The principle of the scheme can solve the problem of inconvenient wearing by one user, monitoring the lymphedema function of the user's upper limbs, and auxiliary treatment of lymphedema of the upper limbs. Patients can use this device according to their needs after breast cancer surgery.

The principle of the monitoring method is the arm circumference measurement comparison method in portable monitoring and auxiliary treatment device for upper extremity lymphedema. The principle of the device is that the arm circumference measurement module is set in different parts of the upper limb. The user measures the circumference of the same part of his arm every time and compares it with previous data to determine whether the arm circumference changes so as to judge whether the upper limb has lymphedema. Positioning gloves can be used to help in device wear positioning. The principle of rehabilitation is to simulate manual lymphatic drainage treatment and pressure-assisted treatment by mechanical massage. There are two rehabilitation modules in the device that are wrapped in the forearm and the upper arm of the upper limb, which are, respectively, the forearm rehabilitation module and the upper arm rehabilitation module. Each rehabilitation module is provided with three low-ductility massage belts with a width of 50 mm. In the upper arm from top to bottom are the upper arm low-ductility massage belt A, the upper arm low-ductility massage belt B, and the upper arm low-ductility massage belt C. In the forearm from top to bottom are the forearm low-ductility massage belt A, the forearm low-ductility massage belt B, and the forearm low-ductility massage belt C. Each massage belt can apply a fixed output pressure load to each part of upper limb through motor driving or air compression to simulate manual lymphatic drainage.

The subjects of this paper were women aged 20–30 years old with healthy upper limb. The inclusion criteria were breast cancer patients who might have slight upper limb lymphedema after partial mastectomy. The exclusion criteria were other physical defects of the upper limb, such as abnormal growth of lymphatic vessels, partial resection of the upper limb, etc. The middle part of the upper arm and the middle part of the forearm are taken as the rehabilitation reference parts. The simulation of the upper arm low-ductility massage belt B and the forearm low-ductility massage belt B is carried out to improve the parameter design and optimization of the total rehabilitation module of the device. As an excellent finite element analysis software, ANSYS has been more and more used in biological simulation experiments (Nowak et al., 2019; Aubert et al., 2020; Kumar et al., 2020). According to the biological structure of human upper limb, a 3D reconstruction of an upper limb model was carried out, and the simulation results were output by ANSYS software. According to the simulation results, the appropriate force should be applied to the device and how much pressure and energy should be provided by the power module of the device. It provides suggestions for the following detailed design of the device.

RESEARCH ON DEVICE SIMULATION EXPERIMENT BASED ON ANSYS

Construction of Finite Element Model of Human Upper Limb

There are many ways to build the finite element model of biology. Some researchers (Chaojie, 2017) use an MRI scanned image as the original scanning data to simplify and reconstruct the model. In this paper, the scanned image of Siemens MAGNETOM

TABLE 1 | Material properties of upper limb tissue.

Structure	Material type	Density (kg/m^3)	Elastic modulus (MPa)	Poisson's ratio
Skin (Hong, 2012)	Elastic	1,000	5.45	0.42
Inner and outer soft tissue (Lulu et al., 2010)	Elastic	1,060	1.5	0.35
Lymph and blood (Lingpeng et al., 2015)	Elastic	1,025	50	0.45
Bone (Hassan and El-Sheemy, 2004; Vanaclocha et al., 2019)	Elastic	1,800	2,084	0.3

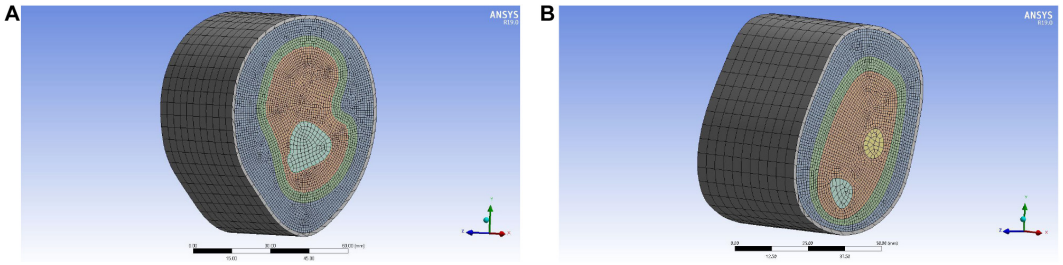

FIGURE 8 | Mesh generation of the reconstruction model of upper limb: **(A)** upper arm model and **(B)** forearm model.

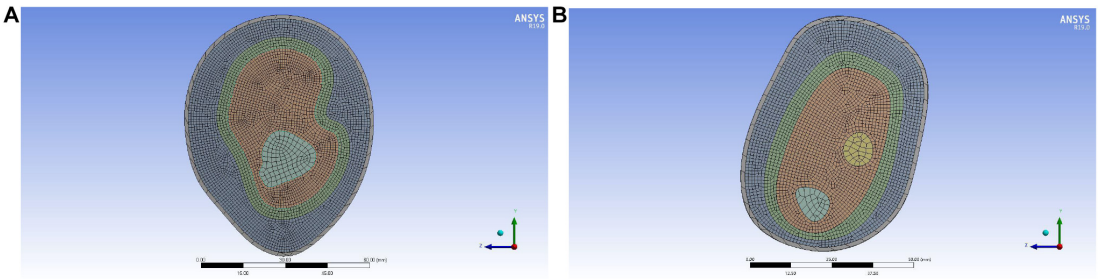

FIGURE 9 | Cross-section of the reconstruction model of upper limb meshing: **(A)** upper arm model and **(B)** forearm model.

Spectra Magnetic Resonance Imaging System is used as the template to scan the active human upper limb. The middle of the upper arm and the middle of the forearm are used as reference images to simplify and reconstruct the original scanned image. The volunteer for upper limb information collection was a 24 years old urban woman, 165 cm in height and 115 kg in weight. The scanning process is shown in **Figure 3**.

Biologically, the cross-sectional structure of the human upper limb is composed of skin, subcutaneous fat, muscle, inner fat, blood, lymph, tissue fluid, and bone. As shown in **Figure 4**, there are specific gravity differences between the structures of the upper arm and the forearm. In order to obtain accurate experimental data, the upper arm and the forearm should be separated for finite element model reconstruction and simulation experiment.

The human upper arm model was constructed based on the upper limb data of female patients with grade 0 lymphedema (patients with mild or who might have tissue damage). In order to build the finite element model, it is necessary to reasonably stratify the tissues and simplify them according to their similarities and differences, as shown in **Figure 5**.

In this paper, the structure of the human upper limb is simplified into five parts, which are as follows: bone layer, inner soft tissue layer, lymph and blood layer, outer soft tissue layer, and skin layer. The images of the bone layer were layered obviously and were constructed according to MRI scanned images. Lymph and blood are distributed in the soft tissue layer. Muscle, inner fat, and subcutaneous fat are regarded as soft tissue layer, and they are divided into inner soft tissue layer and outer soft tissue layer by dividing the lymphatic and blood layer. Because the biological structures of lymph and blood are similar due to their physical characteristics, in order to simplify the model, the lymph and blood vessels were divided into a layer with an average width of 4 mm, distributed between the inner and outer soft tissue layers. According to previous research results (Yanning et al., 2008; Jinping and Lianbin, 2020), the width of the skin layer is set at 1.3 mm, and the circumference of the upper arm and forearm is set at 260 and 230 mm, respectively. As shown in **Figure 6**, in SOLIDWORKS.2016, solid construction of each layer was carried out. The tensile thickness of the middle cross-section of each part of the upper limb model was 50 mm, and it was assembled and saved as X _ T file.

TABLE 2 | Unit number and node number in each layer of the upper arm model.

Structure	Node size (mm)	Number of nodes	Unit number
Skin layer	5	1,368	2,990
Outer soft tissue layer	1	343,387	80,631
Lymph and blood layer	1	3,960	550
Inner soft tissue layer	1	169,906	35,598
Bone layer	2	464,199	106,692

TABLE 3 | Unit number and node number in each layer of the forearm model.

Structure	Node size (mm)	Number of nodes	Unit number
Skin layer	5	3,410	495
Outer soft tissue layer	1	282,046	62,883
Lymph and blood layer	1	156,301	33,048
Inner soft tissue layer	1	272,544	63,546
Bone layer	2	7,647	1,536

Mechanical Properties of the Upper Limbs

In this paper, static structural module of ANSYS Workbench 19.0 is used for static simulation, and the 3D model built by SOLIDWORKS.2016 in the previous step is imported, as shown in **Figure 7**. According to the material properties of biological tissues in the relevant literature (Hassan and El-Sheemy, 2004; Lulu et al., 2010; Hong, 2012; Lingpeng et al., 2015; Vanaclocha et al., 2019), the material of each layer of the 3D reconstruction model was reset, as shown in **Table 1**.

Mesh Generation of the Reconstruction Model

In order to get an accurate simulation effect, it is necessary to mesh each layer structure and refine the important parts. The skin layer, as the unimportant part, is set as 5 mm, the outer soft tissue layer, lymph and blood layer, and inner soft tissue layer as

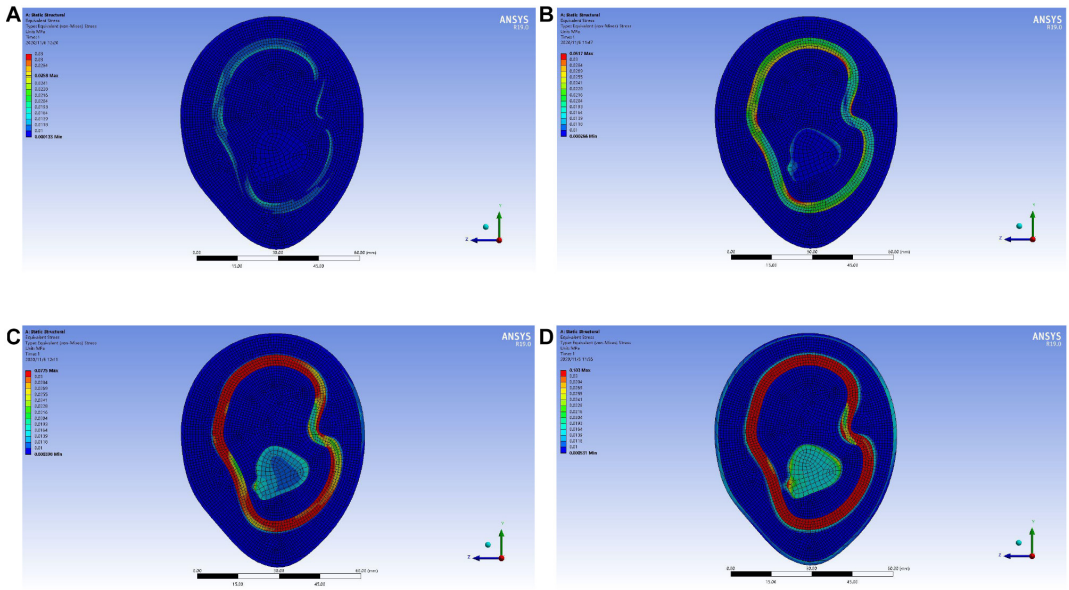

FIGURE 10 | Rainbow diagram of pressure distribution in the lymph and blood layers of the upper arm model under different external pressure loads: **(A)** 002 MPa external pressure, **(B)** 0.004 MPa external pressure, **(C)** 0.006 MPa external pressure, and **(D)** 0.008 MPa external pressure.

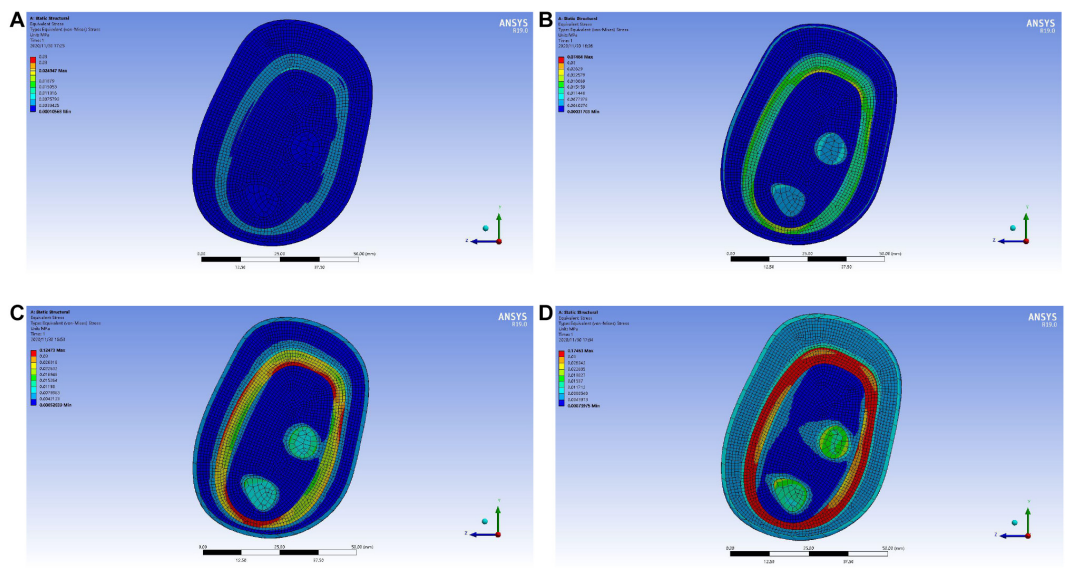

FIGURE 11 | Rainbow diagram of pressure distribution in the lymph and blood layers of the forearm model under different external pressure loads: **(A)** 001 MPa external pressure, **(B)** 0.003 MPa external pressure, **(C)** 0.005 MPa external pressure, and **(D)** 0.007 MPa external pressure.

important parts had a node size of 1 mm, and the bone layer is 2 mm. The mesh generation of the 3D reconstruction model is shown in **Figure 8**, and the cross-section of the 3D reconstruction model is shown in **Figure 9**.

According to the node size divided, the number of elements and nodes of different structural layers in the upper arm model are obtained, as shown in **Table 2**. According to the node size divided, the number of elements and nodes of different structural layers in the forearm model are obtained, as shown in **Table 3**.

Boundary Condition Setting

The simulation experiment should be similar to the actual massage effect of the device. The boundary conditions are defined as follows: The internal load pressure is applied to the outer surface of the skin layer, and the bone layer is set as fixed. Different pressure was applied to the surface of the skin layer, and the pressure direction was around the skin layer and pointed to the center.

Solution and Analysis of the Simulation Experiment

In order to promote the reflux of intralymphatic fluid, the pressure in lymphatic vessels should be increased appropriately. The lymphatic research of Olscewski's team (Olsewski and Engeset, 1980) showed that the pressure of the lymphatic terminal in supine position was 37 mmHg, while standing it was 44 mmHg, and the pressure in the lymphatic vessels was 13.5 mmHg in resting state. In obstructive lymphedema, the pressure in the dilated lymphatics was 0 or slightly higher in supine position, 50–60 mmHg in standing position, and 200–230 mmHg, or even higher, in muscle contraction. According to literature (Avraham et al., 2010), for female patients with grade 0 lymphedema (patients with mild or who might have tissue damage), in order to achieve the rehabilitation effect, the maximum load of the lymphatic tissue layer should be about 0.03 MPa (1 mmHg = 133 Pa), and the overflowing lymph will be squeezed back into the lymphatic vessels.

In the upper arm model experiment, after the continuous test of ANSYS simulation experiment, as shown in **Figure 10**, the skin layer is continuously applied with a progressive external load. When the loading pressure is 0.002 to 0.008 MPa, the pressure load of the lymph and the blood layer is basically stable within 0.03 MPa. In the pressure rainbow diagram, the red part indicates that the pressure in this area exceeds 0.03 MPa. In the forearm model experiment, after the continuous test of ANSYS simulation experiment, as shown in **Figure 11**, the skin layer is continuously applied with a progressive external load. When the loading pressure is 0.001 to 0.007 MPa, the pressure load of the lymph and the blood layer is basically stable within 0.03 MPa. In the pressure rainbow diagram, the red part indicates that the pressure in this area exceeds 0.03 MPa.

In order to locate the accurate range of external load pressure, the "米-shaped" line mark is used for point selection and positioning, as shown in **Figure 12**. The center point of the reconstructed model is taken as the origin of the "米-shaped" line. Eight rays from the origin intersect with the midline of the lymph and the blood layers, respectively, and eight intersections are obtained. The eight points were marked clockwise as points D1, D2, D3, D4, D5, D6, D7, and D8. Each point can be selected to obtain the pressure load at this point. In the pressure load diagram of each fixed point, when the values of four random points among the eight points are greater than 0.03 MPa, these indicate that the load of the lymph and the blood layer is too large, indicating that the external load force exerted by the skin layer is too large.

As shown in **Figure 13**, the distribution range of the external force and the pressure of the upper arm model is further refined. When the upper arm model is applied with 0.002 MPa external force pressure, 0.003 MPa external force pressure, 0.004 MPa external force pressure, 0.005 MPa external force pressure, and 0.006 MPa external force pressure, the selected point pressure diagram of eight punctuation points is displayed. As shown in **Figure 14**, the distribution range of the external force and the pressure of the forearm model are further refined. When the

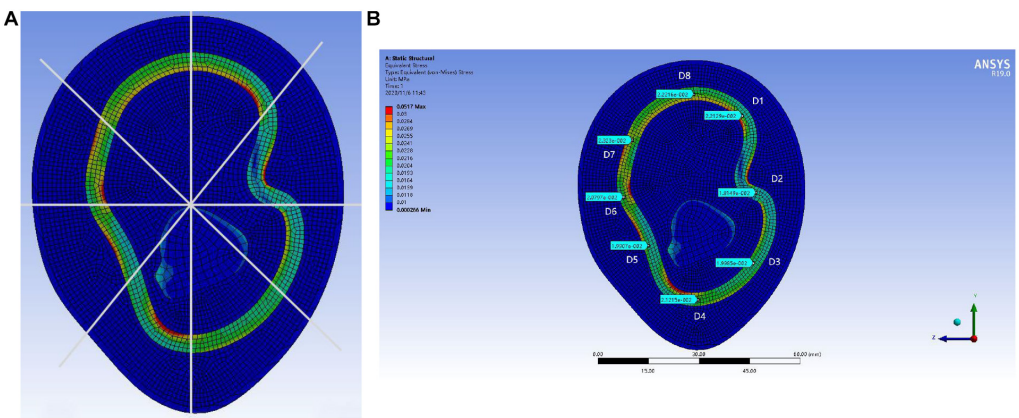

FIGURE 12 | Display of point selection and positioning method of "米-shaped" line mark: **(A)** "米-shaped" line mark and **(B)** 0.004 MPa external pressure value of "米-shaped" line mark pressure.

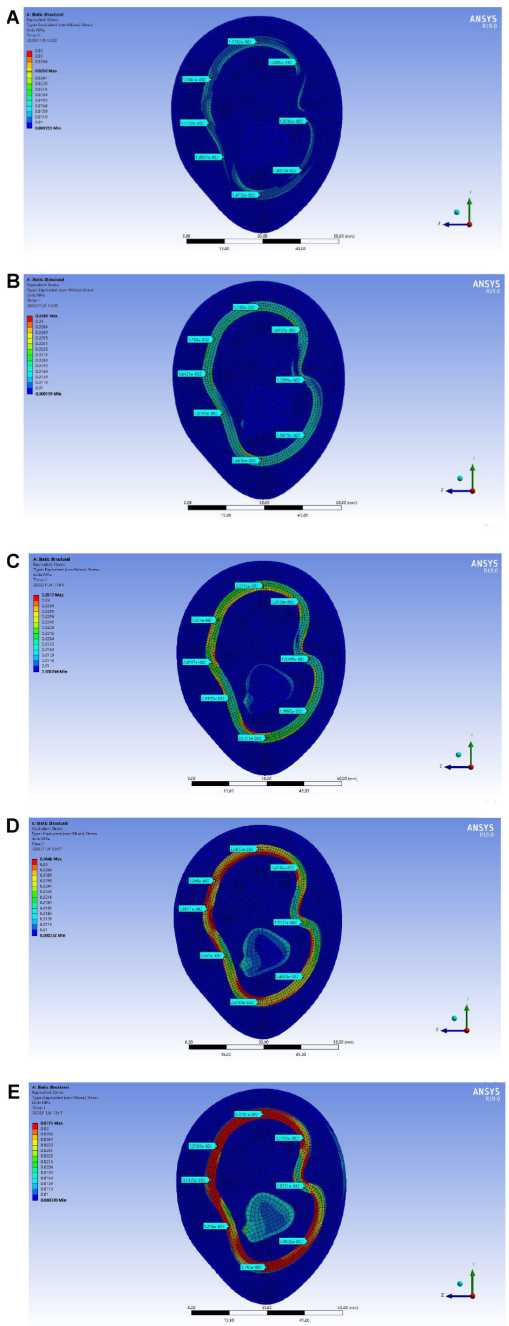

FIGURE 13 | Point selection picture of the lymph and blood layers of the upper arm model with different external pressure loads: **(A)** 002 MPa external pressure, **(B)** 0.003 MPa external pressure, **(C)** 0.004 MPa external pressure, **(D)** 0.005 MPa external pressure, and **(E)** 0.006 MPa external pressure.

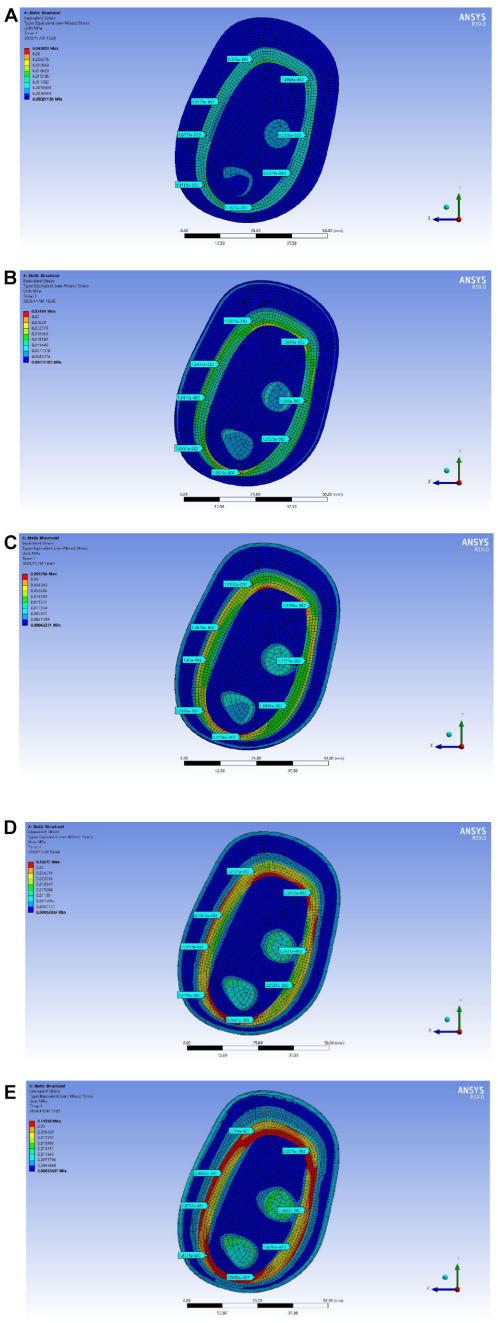

FIGURE 14 | Point selection picture of the lymph and blood layers of the forearm model with different external pressure loads: **(A)** 002 MPa external pressure, **(B)** 0.003 MPa external pressure, **(C)** 0.004 MPa external pressure, **(D)** 0.005 MPa external pressure, and **(E)** 0.006 MPa external pressure.

forearm model is applied with 0.002 MPa external force pressure, 0.003 MPa external force pressure, 0.004 MPa external force pressure, 0.005 MPa external force pressure, and 0.006 MPa external force pressure, the selected point pressure diagram of eight punctuation points is displayed. The eight point pressure tables of the lymph and the blood layers of the upper arm model with different external force pressures are obtained, as shown in **Table 4**. The eight point pressure tables of the lymph and the blood layers of the forearm model with different external force pressures are obtained, as shown in **Table 5**.

The data obtained by ANSYS software are sorted out and analyzed. In the upper arm model and the forearm model, when

TABLE 4 | Eight-point-specific pressure table of lymph and blood layers of the upper arm model with different external force pressure values.

Applied external force load pressure	Pressure of eight punctuation points in lymph and blood layers (MPa)
0.002 MPa external pressure	D1: 0.012006, D2: 0.010282, D3: 0.010022, D4: 0.010736,D5: 0.010857, D6:0.011158, D7: 0.011842, D8: 0.011192
0.003 MPa external pressure	D1: 0.016937, D2: 0.012508, D3: 0.015015, D4: 0.016636,D5: 0.016749, D6: 0.016421, D7: 0.017680, D8: 0.017090
0.004 MPa external pressure	D1: 0.022129, D2: 0.018149, D3: 0.019985, D4: 0.021215,D5: 0.019907, D6: 0.020797, D7: 0.023230, D8: 0.022216
0.005 MPa external pressure	D1: 0.024236, D2: 0.017331, D3: 0.024878, D4: 0.025795,D5: 0.023630, D6: 0.028651, D7: 0.029460, D8: 0.026672
0.006 MPa external pressure	D1: 0.031751, D2: 0.020721, D3: 0.029826, D4: 0.031530,D5: 0.030160, D6: 0.033325, D7: 0.035509, D8: 0.033751

TABLE 5 | Eight-point-specific pressure table of lymph and blood layers of the forearm model with different external force pressure values.

Applied external force load pressure	Pressure of eight punctuation points in lymph and blood layers (MPa)
0.002 MPa external pressure	D1: 0.010069, D2: 0.009233, D3: 0.008162, D4: 0.011672,D5: 0.009917, D6: 0.009678, D7: 0.009818, D8: 0.009378
0.003 MPa external pressure	D1: 0.013695, D2: 0.013680, D3: 0.012525, D4: 0.019515,D5: 0.014657, D6: 0.014517, D7: 0.014832, D8: 0.013393
0.004 MPa external pressure	D1: 0.019196, D2: 0.017577, D3: 0.015895, D4: 0.025154D5: 0.020066, D6: 0.019100, D7: 0.019635, D8: 0.017832
0.005 MPa external pressure	D1: 0.023423, D2: 0.022601, D3: 0.020397, D4: 0.029481D5: 0.024755, D6: 0.023875, D7: 0.024041, D8: 0.022321
0.006 MPa external pressure	D1: 0.028075, D2: 0.026861, D3: 0.024651, D4: 0.035986D5: 0.030325, D6: 0.028782, D7: 0.029061, D8: 0.027190

the external load pressure of the skin layer is 0.002–0.006 MPa, the pressure range of the internal lymphatic and blood layer is within 0.03 MPa. The experimental results are refined again, and the parameters are optimized according to the design principle of the device.

SIMULATION PARAMETER ANALYSIS AND DESIGN OPTIMIZATION

Analysis of the Simulation Parameters

In order to verify that the eight punctuation points measured in each picture have a reference value, the 10 groups of data obtained are sorted and analyzed. Shown in formula (1) is the variance formula that was used:

$$S^2 = \frac{\sum_{i=1}^{n}(x_i - x)^2}{n} \tag{1}$$

Shown in formula (2) is the standard deviation calculation formula:

$$S = \sqrt{\frac{\sum_{i=1}^{n}(x_i - \bar{x})^2}{n-1}} \tag{2}$$

The average pressure load and error range of each group of data were analyzed.

As shown in **Table 6**, it can be found that, under the same external pressure of the upper limb, the average pressure of the lymph and the blood layer of the upper arm model is slightly higher than that of the forearm. This is because, in human upper limbs, the arm circumference of the upper arm is generally larger than that of the forearm, and the pressure area of the upper arm is larger. According to the formula $F = P \cdot S$, there is greater force on the upper arm. According to the variance and standard deviation data in **Table 6**, we can see that there are still some errors in this experiment, but in 10 groups of data, the errors of nine groups of data are within reasonable range, so the experiment has a certain reference value.

Optimization Design of the Device Parameters

Through the ANSYS simulation experiment, in the rehabilitation module of the portable upper limb lymphedema monitoring and auxiliary treatment integrated device, aiming at female patients with grade 0 lymphedema (patients with mild or who might have tissue damage), the optimization design scheme of the device rehabilitation module parameters is obtained.

The working mode of the upper arm low-ductility massage belt B in the upper arm rehabilitation module will be set to three pressure ranges: weak grade, 0.003 MPa; medium grade, 0.004 MPa; and strong grade, 0.005 MPa. In order to form a pressure gradient, the pressure at the distal end of the upper limb should be greater than that at the proximal end. The working mode of the forearm low-ductility massage belt B in the forearm rehabilitation module will also be set to the pressure range of the three gears: weak grade, 0.0035 MPa; medium grade, 0.0045 MPa; and strong grade, 0.0055 MPa. The application range of the low-ductility massage belt of the rehabilitation module is 260 mm in length and 50 mm in width. The range of applied force can be obtained.

According to these data, the device parameters in each rehabilitation module are set in detail. In order to achieve the recovery effect of pressure reflux of lymph, it is necessary to adjust the pressure intensity to form a pressure gradient. The working mode values of each low-ductility massage belt of the upper arm rehabilitation module and the forearm rehabilitation module in **Table 7** are obtained. The pressure time is set to automatically adjust the frequency, and the pressure time is gradually increased to 1, 2, and 3 s. The starting time of the different grade pressures of each rehabilitation module was not carried out at the same time, and there was a small sequence time. This starts with a low-stretch massage band at the far end of the upper extremity. This will form a better rehabilitation effect; the device will achieve better auxiliary treatment effect.

Compared with this device, the traditional detection methods, such as measuring with a tape measure, need the help of others every time and cannot guarantee an accurate measurement of the same marked point of the upper limb; measuring with

TABLE 6 | Eight-point-specific pressure table of lymph and blood layers of the upper limb model with different external force pressure values.

Applied external force load pressure	Mean pressure (MPa)	Variance (S^2: × 10^{-6})	Standard deviation (S)
0.002 MPa external pressure of upper arm	0.0110	0.4225	0.00065
0.002 MPa external pressure of forearm	0.0097	84.456	0.00919
0.003 MPa external pressure of upper arm	0.0161	2.3716	0.00154
0.003 MPa external pressure of forearm	0.0146	3.9601	0.00199
0.004 MPa external pressure of upper arm	0.0210	2.2801	0.00151
0.004 MPa external pressure of forearm	0.0193	6.4516	0.00254
0.005 MPa external pressure of upper arm	0.0251	12.2500	0.00350
0.005 MPa external pressure of forearm	0.0239	6.0516	0.00246
0.006 MPa external pressure of upper arm	0.0308	17.7241	0.00421
0.006 MPa external pressure of forearm	0.0289	9.7344	0.00312

TABLE 7 | Set value of working mode of the massage belt in each rehabilitation module.

Rehabilitation module	Massage belt	Weak (MPa)	Medium (MPa)	Strong (MPa)
Upper arm rehabilitation module	Upper arm low stretch massage belt A	0.0028	0.0038	0.0048
	Upper arm low stretch massage belt B	0.0030	0.0040	0.0050
	Upper arm low stretch massage belt C	0.0032	0.0042	0.0052
Forearm rehabilitation module	Forearm low stretch massage belt A	0.0033	0.0043	0.0053
	Forearm low stretch massage belt B	0.0035	0.0045	0.0055
	Forearm low stretch massage belt C	0.0037	0.0047	0.0057

a measuring cylinder with water displacement method, the measurement error of the patient's upper limb is great, and the front and rear measurement is cumbersome and inaccurate than using professional equipment, such as Perometer, isotope lymphography, near-infrared fluorescence imaging, etc., Every time the cost is more; each test costs 1,000–3,000 yuan, which ordinary patients cannot afford. For the function of adjuvant therapy, many treatment equipment are time-consuming and expensive; non-surgical treatment methods need long-term and timely treatment, such as strength training, skin care, lymphatic massage, etc., which cost 300–1,000 yuan each time; surgical treatment costs 20,000–50,000 yuan each time, which is particularly expensive, and the patients feel uncomfortable. This device uses arm circumference measurement method, the test results are more accurate and cheap, and the cost of the device is controlled within 2,000 yuan. The auxiliary treatment module can also simulate manual lymphatic drainage, which can replace the traditional rehabilitation treatment method and be used directly at home.

There are some limitations in this paper. We only take the middle part of the upper arm and the middle part of the forearm as the research model, and other parts of the experiment are regarded under the same experimental conditions, but there are still some errors. This device is still in the early stage of development, and there is no good rehabilitation verification effect for different disease stages of upper limb lymphedema. In the future, it will further refine the construction of upper limb finite element model and simulation experiment, further improve the accuracy of experimental data, and provide a more significant auxiliary treatment device for patients with upper limb lymphedema. In this paper, only one female volunteer was scanned, and data were collected. In future research, the database of the upper limb will be enriched and data will be collected and analyzed.

CONCLUSION

In this paper, the demand status of female patients with lymphedema of the upper limb after breast cancer surgery was analyzed. Combined with wearable design and detection and rehabilitation of lymphedema, a portable monitoring and auxiliary treatment device for upper limb lymphedema was designed. In order to optimize the parameters of the rehabilitation module of the device, ANSYS software was used for static finite element simulation. By simplifying the biological model of the upper arm and the biological model of the forearm, a 3D reconstruction of the model, reasonable layering and simulation experiments are carried out. After a detailed analysis of the simulation results, the specific parameters of the refining device are obtained according to the simulation results. At the same time, setting the pressure range and working time of the device can further improve its rehabilitation effect. The design of this scheme can solve the problem such that patients with upper extremity lymphedema can complete the process of edema monitoring and adjuvant treatment at home, achieving the purpose of early detection and early treatment and effectively controlling the patient's condition. This paper makes up for the research content of female patients with upper limb lymphedema after breast cancer surgery and provides a design scheme and optimization method for other researchers.

DATA AVAILABILITY STATEMENT

The original contributions presented in the study are included in the article/supplementary material, further inquiries can be directed to the corresponding author/s.

ETHICS STATEMENT

Ethical review and approval was not required for the study on human participants in accordance with the local legislation and institutional requirements. The patients/participants provided their written informed consent to participate in this study. Written informed consent was obtained from the individual(s) for the publication of any potentially identifiable images or data included in this article.

AUTHOR CONTRIBUTIONS

XY contributed to the methodology and project administration of the study. ZX wrote the original draft of the manuscript and contributed to the product conceptualization and formal analysis. YW contributed to the software and review of the study. YS provided supervision and resources of the study. LS provided experimental equipment and organized the data curation. All authors contributed to the article and approved the submitted version.

FUNDING

This study was supported by the Ministry of Education of Humanities and Social Science of China (grant no. 17YJAZH100) and the Social Science Foundation of Shaanxi Province (grant no. 2020J040).

REFERENCES

Aubert, K., Germaneau, A., Rochette, M., Rigoard, P., and Vendeuvre, T. (2020). The interest of FE simulation for the reduction of tibial plateau fracture using balloon inflation. *Comput. Methods Biomech. Biomed. Eng.* 22, 418–420. doi: 10.1080/10255842.2020.1714966

Avraham, T., Daluvoy, S. V., Kueberuwa, E., Kasten, J. L., and Mehrara, B. J. (2010). Anatomical and surgical concepts in lymphatic regeneration. *Breast J.* 16, 639–646. doi: 10.1111/j.1524-4741.2010.00978.x

Chaojie, W. (2017). *Analysis of Mechanical Properties of Soft Tissue of Human Arm in Vivo*. Ph.D. thesis, Harbin Institute of Technology, Harbin.

Chen, W. L., Wu, C.-C., and Kan, C. D. (2017). Using medical-device wearable to improve hemodialysis patient's live and access the holistic health. *Mater. Sci. Eng.* 209:012105. doi: 10.1088/1757-899X/209/1/012105

Czerniec, S. A., Ward, L. C., Refshauge, K. M., Beith, J., Lee, M. J., York, S., et al. (2010). Assessment of breast cancer-related arm lymphedema — comparison of physical measurement methods and self-report. *Cancer Investig.* 28, 54–62. doi: 10.3109/07357900902918494

Hassan, H. T., and El-Sheemy, M. (2004). Adult bone-marrow stem cells and their potential in medicine. *J. R. Soc. Med.* 97, 465–471. doi: 10.1177/0141076809701003

Hayes, S., Janda, M., Cornish, B., Battistutta, D., and Newman, B. (2008). Lymphedema secondary to breast cancer: how choice of measure influences diagnosis, prevalence, and identifiable risk factors. *Lymphology* 41, 18–28.

Hong, L. (2012). *Research on Pressure Comfort of Elastic Sports Vest*. Ph.D. thesis, Jiangnan University, Wuxi.

Iannello, C., and Biller, M. K. (2020). Management of edema using simple manual lymphatic drainage techniques for hand and upper extremity patients. *J. Hand Ther.* 33, 616–619. doi: 10.1016/j.jht.2018.09.013

Jinping, B., and Lianbin, Z. (2020). Body circumference of Chinese han nationality. *J. Anthropol.* 39, 152–158.

Keilani, M., Hasenoehrl, T., Palma, S., and Crevenna, R. (2020). Resistance exercise and breast cancer related lymphedema – a systematic review update. *Disabil. Rehabil.* 42, 26–35. doi: 10.1080/09638288.2018.1514663

Kilbreath, S. L., Dylke, E. C., and Ward, L. C. (2017). Bioimpedance spectroscopy does have a valid and evidence-based role in detection and monitoring of lymphoedema. *Surg. Oncol.* 115, 221–222. doi: 10.1002/jso.24498

Kraft, J. C., Treuting, P. M., and Ho, R. J. Y. (2018). Indocyanine green nanoparticles undergo selective lymphatic uptake, distribution and retention and enable detailed mapping of lymph vessels, nodes and abnormalities. *J. Drug Target.* 26, 494–504. doi: 10.1080/1061186X.2018.1433681

Kumar, N., AbdulKhader, S. M., Pai, R., Khan, S. H., and Kyriacou, P. A. (2020). Fluid structure interaction study of stenosed carotid artery considering the effects of blood pressure. *Int. J. Eng. Sci.* 154:103341. doi: 10.1016/j.ijengsci.2020.103341

Lim, C., Hwang, B., Park, H. W., Lee, D. H., Park, J. E., Kim, S. K., et al. (2016). Optimal pressure for measuring objective lymphedema with postoperative ultrasonography in patients with breast cancer. *Comput. Assist. Surg.* 21, 102–110. doi: 10.1080/24699322.2016.1240310

Lingpeng, R., Wei, W., Rixian, D., and Changchun, L. (2015). Study on semi parametric design optimization of comfortable earphone. *J. Audiol. Speech Pathol.* 23, 646–650.

Lulu, Y., Qimei, L., and Hongbing, L. (2010). Establishment of three dimensional finite element model of facial soft tissue. *Sci. Technol. Eng.* 10, 2844–2847, 2860.

Ningfei, L. (2014). *Diagnosis and Treatment of Lymphedema*. Beijing: Science Press, 1.

Nowak, M., Melka, B., Rojczyk, M., Gracka, M., Nowak, A. J., Golda, A., et al. (2019). The protocol for using elastic wall model in modeling blood flow within human artery. *Eur. J. Mechan. B Fluids* 77, 273–280. doi: 10.1016/j.euromechflu.2019.03.009

Olsewski, W. L., and Engeset, A. (1980). Intrinsic contractility of prenodal lymph vessels and lymph flow in human leg. *Am. J. Physiol.* 239:H775. doi: 10.1152/ajpheart.1980.239.6.H775

Shaitelman, S. F., Cromwell, K. D., Rasmussen, J. C., Stout, N. L., Armer, J. M., Lasinski, B. B., et al. (2015). Recent progress in the treatment and prevention of cancer-related lymphedema. *CA Cancer J. Clin.* 65, 55–81. doi: 10.3322/caac.21253

Sierla, R., Dylke, E. S., and Kilbreath, S. (2018). A systematic review of the outcomes used to assess upper body lymphedema. *Cancer Investig.* 36, 458–473. doi: 10.1080/07357907.2018.1517362

Vanaclocha, V., Vanaclocha-Saiz, A., Rivera-Paz, M., Atienza-Vicente, C., Ortiz-Criado, J. M., Belloch, V., et al. (2019). S1 pedicle subtraction osteotomy in sagittal balance correction. A feasibility study on human cadaveric specimens. *World Neurosurg.* 123, 85–102. doi: 10.1016/j.wneu.2018.11.052

Yanning, L., Zhixian, L., Yuehua, L., Shihai, C., Youkun, L., Xuejing, L., et al. (2008). Measurement of skin thickness in normal adults by high frequency ultrasound. *Chin. Med. Imaging Technol.* 24, 1622–1624.

Yoon, J. A., Shin, M. J., Shin, Y. B., Kim, K., Park, H., Kang, T., et al. (2020). Correlation of ICG lymphography and lymphoscintigraphy severity stage in secondary upper limb lymphedema. *J. Plastic Reconstruct. Aesth. Surg.* 73, 1982–1988. doi: 10.1016/j.bjps.2020.08.055

Conflict of Interest: The authors declare that the research was conducted in the absence of any commercial or financial relationships that could be construed as a potential conflict of interest.

frontiers in Bioengineering and Biotechnology

REVIEW
published: 25 May 2021
doi: 10.3389/fbioe.2021.659033

Biomedical and Tissue Engineering Strategies to Control Foreign Body Reaction to Invasive Neural Electrodes

Manuele Gori[1,2], Gianluca Vadalà[1], Sara Maria Giannitelli[3], Vincenzo Denaro[1] and Giovanni Di Pino[4]*

[1] Laboratory for Regenerative Orthopaedics, Department of Orthopaedic Surgery and Traumatology, Università Campus Bio-Medico di Roma, Rome, Italy, [2] Institute of Biochemistry and Cell Biology (IBBC) - National Research Council (CNR), Rome, Italy, [3] Laboratory of Tissue Engineering, Department of Engineering, Università Campus Bio-Medico di Roma, Rome, Italy, [4] NeXT: Neurophysiology and Neuroengineering of Human-Technology Interaction Research Unit, Università Campus Bio-Medico di Roma, Rome, Italy

OPEN ACCESS

Edited by:
Sandro Mussa-Ivaldi, Northwestern University, United States

Reviewed by:
Xin Liu, University of California, San Diego, United States
Senentxu Lanceros-Mendez, Basque Center for Materials, Applications and Nanostructures, Spain

***Correspondence:**
Manuele Gori
m.gori@unicampus.it

Specialty section:
This article was submitted to Bionics and Biomimetics, a section of the journal Frontiers in Bioengineering and Biotechnology

Received: *26 January 2021*
Accepted: *27 April 2021*
Published: *25 May 2021*

Citation:
Gori M, Vadalà G, Giannitelli SM, Denaro V and Di Pino G (2021) Biomedical and Tissue Engineering Strategies to Control Foreign Body Reaction to Invasive Neural Electrodes. Front. Bioeng. Biotechnol. 9:659033. doi: 10.3389/fbioe.2021.659033

Neural-interfaced prostheses aim to restore sensorimotor limb functions in amputees. They rely on bidirectional neural interfaces, which represent the communication bridge between nervous system and neuroprosthetic device by controlling its movements and evoking sensory feedback. Compared to extraneural electrodes (i.e., epineural and perineural implants), intraneural electrodes, implanted within peripheral nerves, have higher selectivity and specificity of neural signal recording and nerve stimulation. However, being implanted in the nerve, their main limitation is represented by the significant inflammatory response that the body mounts around the probe, known as Foreign Body Reaction (FBR), which may hinder their rapid clinical translation. Furthermore, the mechanical mismatch between the consistency of the device and the surrounding neural tissue may contribute to exacerbate the inflammatory state. The FBR is a non-specific reaction of the host immune system to a foreign material. It is characterized by an early inflammatory phase eventually leading to the formation of a fibrotic capsule around intraneural interfaces, which increases the electrical impedance over time and reduces the chronic interface biocompatibility and functionality. Thus, the future in the reduction and control of the FBR relies on innovative biomedical strategies for the fabrication of next-generation neural interfaces, such as the development of more suitable designs of the device with smaller size, appropriate stiffness and novel conductive and biomimetic coatings for improving their long-term stability and performance. Here, we present and critically discuss the latest biomedical approaches from material chemistry and tissue engineering for controlling and mitigating the FBR in chronic neural implants.

Keywords: neural electrodes, foreign body reaction, coatings, biomaterials, hydrogel, tissue engineering, microfluidics, nanofabrication techniques

INTRODUCTION

Since scientists started to invasively study the function of the central nervous system (CNS) and peripheral nervous system (PNS), single electrodes, and later on electrode arrays, have been implanted to record neuronal activity and to stimulate single or groups of neurons to artificially induce their activation, in light of decoding their functions.

Once study protocols moved from acute tests to chronic implantations and the safety of implants performed in primates suggested the possibility to move to studies in humans, a further possible application of invasive neural electrodes, beside that to investigate neuronal functions, became concrete. Electrodes started to be employed to decode subject motor intention and, bypassing neural or osteo-muscular lesions, to artificially interface the nervous system to the external environment.

When this happened, neural interfaces -often named brain to computer or to machine interfaces- and the field of neuroprosthetics were born. Depending on the site and the subject receiving the implant, electrodes can also be interfaced with sensory area and fibers and, by relaying afferent streams of information, convey artificial sensory feedback.

Insofar, some applications for stimulating neural electrodes, particularly deep brain stimulation (DBS) and cochlear implants, have gained the maturity to be commonly applied in clinical practice. Other applications targeting a more spatially-selective information exchange, such as cortical or peripheral nerve implants, are very-promising, yet still in a developmental phase. Their not-complete maturity is mostly due to the lack of long-lasting stability of their performance over time, mainly because of the reaction that the body mounts around them. This factor hampers to a less extent cochlear electrodes, because they do not penetrate the neural structures, and DBS, because these electrodes do not need to achieve the level of stimulation selectivity needed by information exchange. The long-term functionality and longevity of cochlear implants and deep brain stimulators have already been widely demonstrated (Deuschl et al., 2006; Woeppel et al., 2017).

Contrarily, the use of invasive multichannel electrodes, implanted within stump peripheral nerves to control cybernetic hand prostheses, is an application field of neural interfaces where electrodes should achieve an intimate contact with neural fibers required to reach a reliable information transmission, and where implantable solutions seem to favor exchange selectivity.

Since peripheral nerves contain both motor and sensory fibers, peripheral nerve electrodes can achieve proper bidirectional communication through the use of a single device by stimulating afferent axons (Xavier and Jaume, 2014).

Regained sensory feedback from hand prosthesis has the potential to improve motor control (Valle et al., 2018; Zollo et al., 2019), discrimination abilities (Raspopovic et al., 2014), and to reverse aberrant brain plasticity triggered by the amputation (Rossini et al., 2010; Di Pino et al., 2012, 2014; Ferreri et al., 2014; Serino et al., 2017).

Unfortunately, the standard control systems of prosthetic limbs rely on surface electromyogram, which is mainly limited by problems of high latency, as well as low specificity and robustness in long-term implants (Anderson and Weir, 2019). Although some of the current peripheral nerve interfaces can shorten latency and provide single axon specificity, their performances tend to degrade with time due to the biological response of the organism to the electrode, which is triggered by the damage provoked by the implant procedure itself (Anderson and Weir, 2019). The body tends to insulate and exclude the foreign material from the surrounding microenvironment, leading to scar tissue growth around the device that is made of a fibrous capsule.

In the conductive surface, the dielectric constant, dissipation factor and dielectric loss factor rise with the increase of the capsule thickness. The increase of the electrical impedance is proportional to the development of the fibrotic tissue, which determines difficulties to distinguish the signal from background noise (Szostak et al., 2017) and, eventually, the drop of stimulation and registration capacities (Guadarrama-Santana and Garcia-Valenzuela, 2007; Jayamani et al., 2014).

The immune-mediated response responsible for the capsule growth is known as Foreign Body Reaction (FBR). FBR reduction over time is probably the main challenge for future neural electrode applications in neuroprosthetics to extend the reliability of the interface (Lotti et al., 2017).

The aim of this review is to analyze the latest tissue engineering strategies and biomedical approaches for controlling and evading FBR around implantable interfaces.

Although the FBR process can occur in any living tissue implanted with foreign material, such as molecularly engineered surfaces and medical devices (Anderson et al., 1999; Luttikhuizen et al., 2006), we will restrict our field of investigation and focus the review toward intraneural electrode applications to interface robotic prosthetic limbs.

We analyze factors supposed to be the main causes of acute and chronic neural tissue reactions, such as scarce biocompatibility, excessive size, poor flexibility, reduced electrical properties, low compliance, mechanical mismatch and micromotion.

Finally, we examine the shortcomings of current electrode-producing technologies and discuss possible cutting-edge solutions for the development of promising alternatives to the present intraneural interfaces. Strategies and technologies analyzed in light of the specific application we pursue could be potentially tailored to any electrode inserted in the CNS or PNS, and interfaced with different artificial devices.

MOLECULAR MECHANISMS AND CELLULAR COMPONENTS OF THE FBR

In a living tissue or a nerve, any implantation of foreign material, including advanced biomaterials that surround an invasive electrode, triggers an unbalanced biological reaction (i.e., characterized by scarce wound healing and chronic inflammatory state) of the non-specific immune system, known as FBR, which is the natural protection mechanism of the host to the foreign body (Anderson et al., 1999; Luttikhuizen et al., 2006). This complex host reaction (**Figure 1**) consists in a sequential and orderly cascade of molecular events that involves adhesive blood and

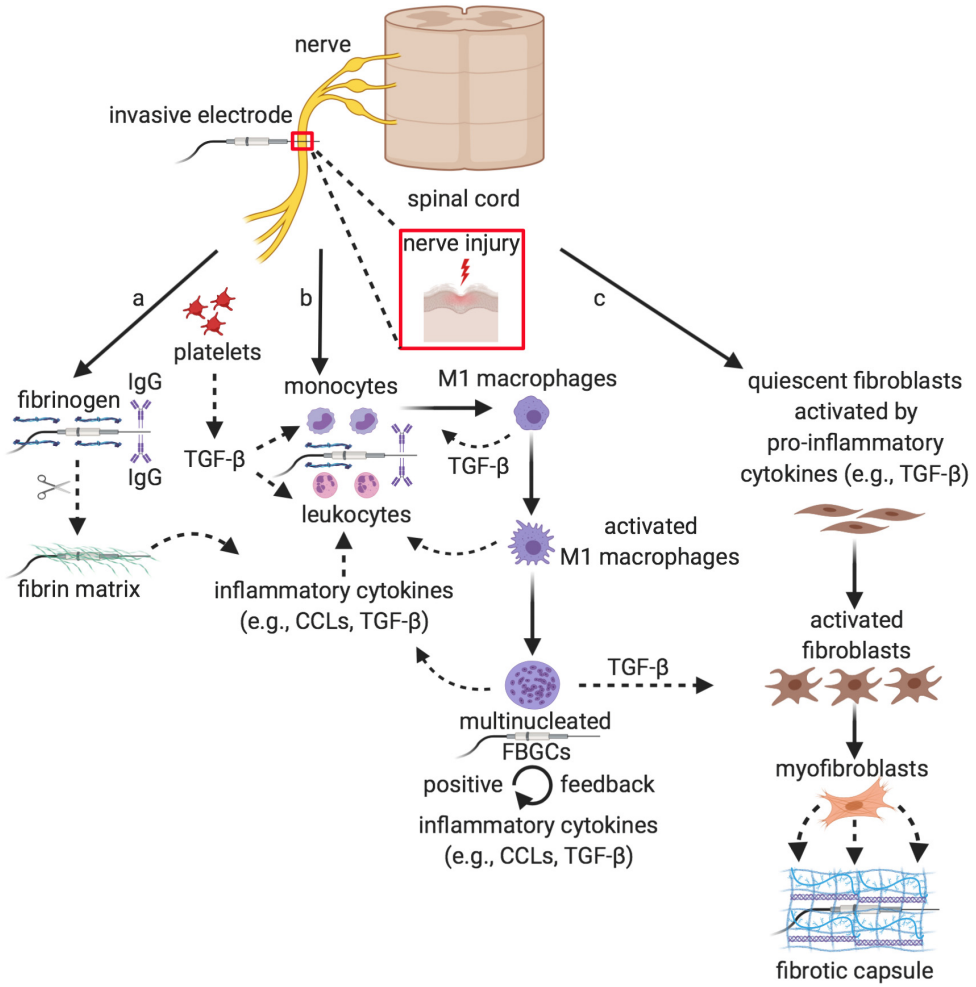

FIGURE 1 | Onset, progression and resolution of the Foreign Body Reaction. Sequence of cellular events of the non-specific immune response elicited by the biomaterial surrounding the invasive electrode implanted into the nervous tissue, which is perceived as a nerve injury: (a) onset, similarly to the wound healing, the adsorption of blood and plasma proteins [in particular, fibrinogen and antibodies (IgG), which will be recognized by the white blood cells of the immune system, and the complement system providing specific binding sites and chemoattractants for circulating leukocytes and monocytes] to the surface of the implant leads to the second step of the process, (b) the progression of the FBR, during which leukocyte and monocyte extravasation that is due to the influence of various chemokines, such as TGF-β, promotes their attraction and adhesion to the electrode surface. Recruited monocytes differentiate into activated M1 macrophages that fuse together into multinucleated FBGCs, which carry out multiple functions including: the increase of the inflammatory response both through a positive feedback mechanism (mainly *via* additional TGF-β production) and through the recruitment of further monocytes and macrophages, the digestion of the electrode surface while promoting the recruitment of the fibroblasts and their activation to myofibroblasts in the last step of the process, (c) the resolution of the FBR, during which the myofibroblasts secrete the different ECM components around the implant that are responsible for the formation of the fibrotic capsule, which ultimately isolates the electrode from the surrounding tissue. IgG, immunoglobulin G; CCLs, CC chemokines; TGF-β, transforming growth factor β; FBGCs, foreign body giant cells. Created with BioRender.com.

plasma proteins, tissue and infiltrated inflammatory cells, and inflammatory cytokines.

The first step (onset), which is similar to wound healing, upon foreign body implantation is the adsorption of blood and plasma proteins, such as fibrinogen, fibronectin, albumin and antibodies to the implant surface (Andrade and Hlady, 1987; Jenney and Anderson, 2000). The type of the proteins adsorbed and the progression of the FBR depend on the surface shape, chemistry composition and charge (Tang and Eaton, 1993; Hunt et al., 1996; Thull, 2002). In the second step (progression), the adsorbed protein layer and its composition in turn promote monocyte and leukocyte extravasation, attraction and adhesion to the surface, along with the activation of the coagulation cascade (Richardson et al., 1976; Smiley et al., 2001; Szaba and Smiley, 2002).

Fibrinogen is hydrolyzed to fibrin that creates a sort of matrix able to attract circulating leukocytes and local macrophages around the implanted surface under the chemoattractive influence of different chemokines (Tang et al., 1998; Smiley et al., 2001; Tao and Kobzik, 2002; Lishko et al., 2004). At the onset of the FBR and during its progression, circulating platelets first and macrophages then secrete transforming growth factor β (TGF-β). This pivotal cytokine serves as chemoattractant

and activator of monocytes, besides being responsible for the continuum of the inflammation and its exacerbation until fibrosis (DiPietro et al., 1998; Crowe et al., 2000). Leukocytes express and secrete a series of other inflammatory cytokines, such as CCL2, CCL3, CCL5, which are the principal players involved in the recruitment of blood-borne monocytes and local macrophages in the foreign body microenvironment (DiPietro et al., 1998; Hancock et al., 2000; Ono et al., 2003; Armstrong et al., 2004). Afterward, extravasated monocytes differentiate to macrophages that, once activated under the stimulation of activated T cells, fuse together to form multinucleated foreign body giant cells (FBGCs). FBGCs start releasing further inflammatory cytokines, thus boosting the inflammatory response through a mechanism of positive feedback, giving rise to a chronic inflammation (Anderson, 2000; Kyriakides et al., 2004). This cell recruitment from the bloodstream is allowed by vasodilatation and increase of vessels permeability, which is induced by the platelet release of the angiogenic cytokine vascular endothelial growth factor (VEGF) (Banks et al., 1998; Ferrara et al., 2003). The biological activity of the FBGCs represents a hallmark of the FBR, as it is aimed to protect implanted tissue against the foreign body, mediating its surface damage and digestion through the release of various proteases and acids (Kyriakides et al., 2004). In the last step of the process (resolution), macrophages play a key role *via* the production of TGF-β. This multifunctional cytokine has a paramount importance as it will stimulate the fibroblast-mediated extracellular matrix (ECM) production, while reducing at the same time inflammation (Bellingan, 1996; Ashcroft, 1999). Thus, the role of the recruited macrophages is to promote further monocyte and macrophage recruitment and to stimulate the growth and differentiation of quiescent fibroblasts to myofibroblasts. Myofibroblasts are eventually responsible for the massive production and secretion of ECM components, including collagen I, collagen III, fibronectin and proteoglycans that give rise to the dense fibrotic capsule around the implanted electrode (Luttikhuizen et al., 2006; Anderson et al., 2008; Ward, 2008). In the very final stage of the process, the capsule becomes impermeable to the non-specific immune system and to many chemicals, including some therapeutic inhibitors of inflammation, and responsible for the augmentation of the electric impedance and progressive isolation of the implanted device, impairing its long-term functionality (Anderson et al., 1999, 2008; Luttikhuizen et al., 2006).

INTRANEURAL VS. EXTRANEURAL ELECTRODES IN FBR

To interface with a peripheral nerve invasive intraneural and extraneural electrodes can be employed. Among intraneural electrodes, the most used are Multielectrode arrays (MEAs), Longitudinal Intra-Fascicular Electrodes (LIFEs) and Transverse Intrafascicular Multichannel Electrode (TIME) (Yoshida and Stein, 1999; Branner et al., 2004; Badia et al., 2011; Yildiz et al., 2020). The extraneural electrodes developed to interface with peripheral nerve are cuff electrodes (Navarro et al., 2001; Ortiz-Catalan et al., 2013) and Flat Interface Nerve Electrodes (FINEs) (Tyler and Durand, 2002; Freeberg et al., 2020).

Intraneural electrodes should offer a better signal-to-noise ratio during neural recording and the reduced current intensity necessary to reach the appropriate nerve stimulation (Navarro et al., 2005). Nonetheless, being implanted within the nerve, these interfaces are traumatic for the surrounding tissue triggering an early inflammatory response caused by the injury of the vascularized connective tissue. Indeed, as the electrode proximity to the nerve increases, a higher selectivity of neural recording of the signal and stimulation can be obtained. However, the formation of the fibrotic capsule around the interface reduces recording and stimulation long-term stability compared to extraneural electrodes (Rossini et al., 2010; Badia et al., 2011, 2016; Lotti et al., 2017).

The chronically implanted devices stimulate the aforementioned multistep cascade of foreign body response, ending in scar tissue formation and electrode encapsulation, and thus in the need of increased currents (i.e., power consumption) to maintain appropriate nerve stimulation due to a progressive increase of the electrical impedance. The most frequently used metals for the fabrication of neural electrodes are gold, tungsten, platinum (Pt) and Platinum-Iridium (Pt-Ir) alloy, with Pt being considered the preferred choice for long-term neuroprosthetic applications due to its electrochemical stability, safety, resistance to corrosion and limited reactivity within a tissue environment (Brummer et al., 1983; Geddes and Roeder, 2003; Merrill et al., 2005; Polikov et al., 2005). However, the stiffness of Pt has a traumatic impact on the surrounding soft neural tissue (Green et al., 2012), causing a shear stress that over time induces an inflammatory reaction, which can be further stimulated by the tissue movements and electrode micromotion (Rousche et al., 2001; Leach et al., 2010). In addition, another weakness of Pt and other metallic electrodes is due to their fabrication, which is usually performed with smooth surfaces that do not allow complete nervous tissue adhesion and integration. As a result, immune cells may invade the remaining space between device surface and target nerve in the implanted area, fostering the FBR (Aregueta-Robles et al., 2014). Therefore, the strength of the implant-tissue integration is influenced by the presence of FBGCs and monocytes/macrophages (Fink et al., 2008). On the other hand, manufacturing excessively rough surfaces may risk increasing the local strain and producing friction forces, thereby causing tissue damage. It is also known that rougher surfaces are able to alter cell adhesion, growth, activation and behavior (Fink et al., 2008; Gamboa et al., 2013; Hulander et al., 2013) including macrophage fusion (Chen et al., 2010), although these effects depend on the different cell types as well as on the materials used and their fabrication methods. Consequently, the right compromise should be sought between the optimal flatness, smoothness and suitable roughness that meet the texture of the nerve tissue, thus avoiding local insults and hazardous damages that could trigger inflammation and a deranged wound healing process. Because of these intrinsic limitations in metallic electrode efficiency, the continuous search for valid alternatives and chemical modifications to material

composition is encouraged. For example, electrodes can be coated with conductive and soft polymers, like a core of flexible and insulating polyimide with metallic tracks of Pt or Pt-Ir, as detailed below. Such a strategy can be adopted for mitigating the stiffness disparity between device and host tissue and for relieving the biological rejection of the nerve tissue (Geddes and Roeder, 2003; Merrill et al., 2005; Polikov et al., 2005).

So far, diverse strategies are being pursued (**Figure 2**) to create minimally invasive neural implants that may address the FBR issue and guarantee their long-term use, which can be summarized as follows: (i) working on the design and geometry of the device (such as surface roughness, electrode shape, size, and flexibility); (ii) working on the chemical composition of the coating material to develop novel organic and synthetic polymer substrates that can be tolerated much better by the host tissue. Finally, another important approach consists in (iii) working on the interaction between interface and microenvironment for controlling the local delivery of therapeutic molecules (e.g., anti-inflammatory and anti-fibrotic drugs) making use of functionalized biomimetic and biodegradable coatings.

Working on the Design and Geometry of the Electrode

The shape and topography of medical-grade polymers implanted in animal models profoundly influences the FBR at the implant surface, with the broadly accepted experimental outcome that circular and smooth surfaces, in intramuscular and percutaneous implants, minimally affect the aggressive behavior of macrophages (Matlaga et al., 1976; Salthouse, 1984). The use of flexible implants of multifunctional polymeric fibers (Canales et al., 2015), and microfabrication of the electrode shape with a new flexible sinusoidal design and a 3D spheroid tip that reduce local strain and tissue damage caused by micromotion (Sohal et al., 2014) may represent alternative strategies to gain some mechanical benefits, without remarkably modifying the size of neural implants, and improve their *in vivo* longevity and recording performances. The importance to focus on the coating stiffness and geometric configuration (i.e., size effect), to reduce the mechanical mismatch between chronic implanted electrodes and neural tissue, has been highlighted by a recent work of Spencer et al. (2017). They investigated the ability of soft polyethylene glycol dimethacrylate (PEG-DMA) hydrogel coatings, compared to hard implants of identical diameter, to reduce chronic glial scar formation on the surface of neural probes in rodent brains, by lowering the local strain and diameter (from 400 to 150 μm) of the coating. The authors suggest that a similar technique could be adapted to coat more complex geometries through a dip coating, or spray coating method, including electrodes made of various materials, such as metal, silicone and polymer implants, by slightly changing the chemistry.

The strategy of coating neural electrodes with hydrogels of PEG and PEG-based copolymers, leveraging their high versatility, low-fouling and bioinert properties, has long been used with moderate success in many studies (as reported with various examples in the subsection "other advanced biomedical materials") (Wichterle and Lím, 1960; Rao et al., 2011; Gutowski et al., 2015; Heo et al., 2016), although some limitations that were somehow addressed combining PEG with other polymers. However, PEG shows high susceptibility to oxidative damage *in vivo*, it may activate severe immune response, and its functionalization is usually troublesome, thereby limiting its application for neural interfaces that require long-term stability (Ostuni et al., 2001; Ward et al., 2002; Knop et al., 2010). Likewise, poly(2-hydroxyethyl methacrylate) (PHEMA), which is, together with PEG, the most widely used coating material for implantable devices (Campioni et al., 1998; Ratner, 2002) is susceptible to non-specific protein adsorption, and eventually to fibrotic encapsulation (Zhang et al., 2017), thereby raising the same problems faced with PEG for the extended stability over time and for restraining an immune reaction. Instead, hydrogels made of zwitterionic polymers, such as poly(carboxybetaines), poly(sulfobetaines), and poly(phosphobetaines) (Chen et al., 2005; Jiang and Cao, 2010; Sin et al., 2014a,b) are biocompatible and highly hydrated materials, showing anti-inflammatory and ultralow-fouling characteristics *in vivo*, which hold great potential to reduce FBR a way better than PEG hydrogels (Jiang and Cao, 2010; Zhang et al., 2013; Wu et al., 2018), as further discussed below in the hydrogel section.

In the last decades, many endeavors have been made in different biomedical and clinical frameworks, merging microengineering and material chemistry skills with molecular biology knowledge, to modify the physicochemical features of implanted interfaces and tuning their structural and surface features with the aim to control the FBR and increase their neurocompatibility. For example, it was initially proposed the use of the focused ion beam technology as high precision machining technique to create and modify the surface morphology of the interface material, up to nanometric scale, by controlling the ion milling of the substrate or its coating in three dimensions, and thereby modulating *in vitro* the neural cell adhesion (Raffa et al., 2007). Afterward, other promising solutions developed for patterning the design and morphology of the surface are briefly summarized as follows: the generation of combinatorial libraries of cationic polymer coatings in mice (Ma et al., 2011); the intramuscular implantation, in rat spinotrapezius muscles, of biodegradable poly(l-lactide-co-d/l-lactide) (PLA), as membranes and uncoated electro-spun fiber meshes with a positively charged plasma-polymer coating, to alter material morphology (Lucke et al., 2018). Finally, the development of a method to control surface porosity of poly(2-hydroxyethyl methacrylate-co-methacrylic acid) (pHEMA-co-MAA) hydrogels, consisting in the fabrication of parallel channels interconnected to a micrometer-sized spherical pore network (Madden et al., 2010). These surface-modified scaffolds were able to increase neovascularization and reduce the inflammation and tissue scarring. This last work represents another smart approach to control channel size and spacing of a functionalizable surface, which can be achieved by varying the dimensions of the microsphere templates. With regard to changing the geometry of the electrode material, the anionic polysaccharide, alginate, is a naturally-derived polymer able to form biocompatible hydrogels, with the addition of divalent cations, to encapsulate

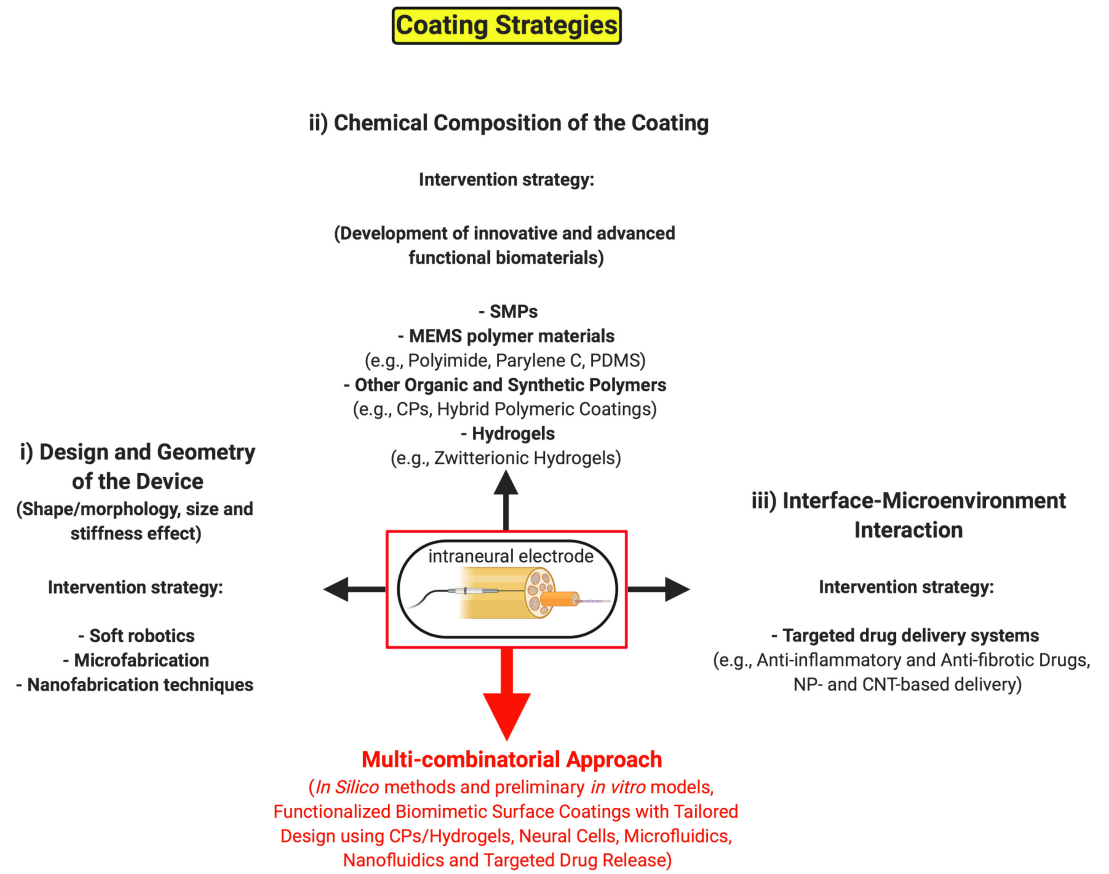

FIGURE 2 | Possible coating strategies of invasive neural implants to minimize the long-term FBR. Schematic representation of the main tissue engineering strategies for coating intraneural electrodes against the FBR: (i) the long-term stability and performance of invasive interfaces can be enhanced through the manipulation of the electrode shape, size, geometry, flexibility and surface roughness to create minimally invasive neural implants by leveraging on micro- and nano-manufacturing methods. (ii) An alternative intervention strategy consists in the development of novel chemical coatings, making use of advanced functional biomaterials, as biocompatible surfaces. (iii) Lastly, the functionalization of the coating with therapeutic drugs and, accordingly, innovative drug-delivery systems may help better integrate and tolerate the invasive device by the host nervous tissue. All of the above intervention strategies could be hopefully integrated into a unique multi-combinatorial approach (red arrow) in the next future. SMPs, shape memory polymers; MEMS, micro-electro-mechanical systems; PDMS, poly(dimethylsiloxane); CPs, conductive polymers; NP, nanoparticle; CNT, carbon nanotube. Created with BioRender.com.

cells and materials for biomedical applications (Lee and Mooney, 2012; Veiseh et al., 2015; Vegas et al., 2016; Bochenek et al., 2018). Semi-permeable alginate spheres have been developed since long time as a common tissue engineering strategy to isolate implanted biological material from the effect of the local immune cells, thus reducing the FBR *in vivo* (Chang, 1964; Lim and Sun, 1980; Veiseh et al., 2015). Significantly, in one of these works, the authors showed for the first time the importance of the size and spherical geometry not only for the SLG20 alginate hydrogel encapsulation of pancreatic islets, but also for stainless steel, glass and polystyrene spheres on the fibrotic response in immunocompetent and fibrosis-prone rodent and non-human primate models (Veiseh et al., 2015). They tested different sizes and time windows, including a chronic time-point (i.e., 6 months), for transplanted grafts encapsulated with the SLG20 alginate capsules and found the 1.5 mm-sized spheres as the ideal geometry to protect grafted cells and surfaces from macrophage activation and fibrosis compared to smaller spheres. In conclusion, they demonstrated that size (1.5 mm in diameter or greater) and spherical shape, rather than stiffness, of alginate hydrogels as well as ceramic, metal and plastic surfaces represent critical features for obtaining prolonged biocompatibility and for resisting to fibrosis rejection. So, this biomaterial design strategy is potentially applicable to intraneural interfaces although, at present, such dimensions are not always achievable for all the intraneural electrodes. Instead, the strategy proposed by Rubehn and Stieglitz (2010) consists in a novel 3D design of a spiked ultraflexible neural (SUN) interface that integrates spiked structures for intrafascicular nerve recording from the PNS with an ultraflexible substrate, thereby enabling a unique conformal interface to the target nerve. The advantage is represented by the features of the material used, which is an insulating polyimide substrate that does not cause excessive inflammation. Hitherto, this new sensor model has been used only in acute animal experiments, whereas for chronic implantations important challenges still remain to be

faced such as, among others, the FBR with fibrotic scar tissue that could displace the electrode from its original position and thus jeopardize the quality of the neural signal (Rubehn and Stieglitz, 2010; Wang J. et al., 2018).

Overall, it seems very important to modify the electrode surface with more smooth and circular shape, without major changes in size, to reduce both the local strain of the material and the mechanical mismatch between the device and the host tissue. The consequences of altering the surface topography, in particular the effect of the roughness, are still debated and quite complex to understand (Fink et al., 2008). In fact, topography-induced changes seem to affect macrophage behavior (e.g., cell adhesion, fusion and cytokine secretion *in vitro*) in the FBR to diverse polymer surfaces (Chen et al., 2010). Furthermore, the continuous search for novel 3D surface design of the device, with coatings at high flexibility, which can be able to adapt to the microenvironment, shaping themselves to the nervous tissue would represent a plus for improving more and more the implant integration. To this aim, 3D bioprinting of hydrogels and thin-film deposition technologies of biocompatible and soft polymers will facilitate the task.

MODIFICATIONS OF THE INTRANEURAL ELECTRODES BY INTEGRATING SOFT ROBOTICS, MICROFABRICATION OF MICROFLUIDIC SYSTEMS AND CARBON NANOTUBES

In the research field of neural electrodes and probes continuous efforts are being made in search of smaller and more flexible devices to reduce the trauma caused by their insertion and, in turn, the biological tissue response (chronic inflammation and fibrosis), leveraging on micro- and nano-fabrication techniques. Recently, an innovative soft robotics approach has been devised to mitigate the FBR by controlling fluid flow and shear stress perceived by the host cells (Dolan, 2019). In a rat model, the authors implanted subcutaneously a milliscale dynamic soft reservoir (DSR), surrounded by an actuatable polyurethane membrane, and modulated the biomechanics of the biotic-abiotic interface *via* tunable pressure. After 14 days, an important reduction in the number of αSMA+ myofibroblasts and in fibrotic encapsulation of the implantable device was observed through histological and immunohistochemical analysis. Furthermore, as an example of a proof-of-concept study using a porous and permeable actuating membrane, they were also able to regulate therapeutic delivery of epinephrine, used as a model pharmacological agent, to test its functional effect in the adjacent tissue. Hence, the presented DSR may have the potential to be integrated into intraneural electrodes for an extended period to modulate the inflammatory and fibrotic response, making it a promising tool also for future neural applications. In fact, the design of the platform can be easily modified and tailored to be integrated into diverse types of implantable devices through its incorporation into a thin matrix that can be part of an intraneural electrode. In the past decades, flexible polymer-based microelectrodes have been developed also for neural prosthetic devices (e.g., testing different device size, shape, surface smoothness and structural stiffness) taking advantage of microfluidic and micromachining techniques (Szarowski et al., 2003; Lee et al., 2004; Polikov et al., 2005). Despite these microelectrodes provide multiple and high-quality stimulation and recording sites, the lack of long-term stability has been reported due to the neural tissue reaction and scar formation following extended microelectrodes implantation (Lee et al., 2004). To overcome this limitation, scientists sought to integrate microfluidic channels into flexible microelectrodes combining different techniques for achieving controlled delivery of anti-inflammatory and anti-fibrotic drugs through the microchannels, as further reviewed in Section "Interface-Microenvironment Interaction." However, micromachining of the electrode polymer through a lamination technique (Metz et al., 2004), micromolding and thermal bonding of the polymer (Ziegler et al., 2006), combined electrochemical deposition of conductive polymer and drugs on the electrode (Wadhwa et al., 2006), turned out to be complex and expensive for a large-scale use. Hence, novel microelectrodes, combining thin-film fabrication with poly(dimethylsiloxane) (PDMS) molding and a more rapid, easy, and cost-effective bonding technique, enabled long-term drug release for a more stable recording performance (Gao et al., 2013). A new hybrid cuff electrode that integrates microelectrodes, for recording and stimulation, embedded within microfluidic channels for drug delivery is an example of flexible thin-film polymer device fabricated *via* surface micromachining techniques on a temporary silicon wafer carrier (Elyahoodayan et al., 2020). The electrode was designed and developed to improve fascicular selectivity and sensitivity in rat sciatic nerves following minimal handling during surgical implantation. Its main advantage is represented by the combined possibility to acutely stimulate, record and deliver lysing drugs, to remove connective tissue (i.e., epineurium layer) that separates electrodes from nerve fibers, and neurotrophic factors that promote axonal sprouting from the exposed fibers. Nevertheless, the authors stated that future studies will be necessary for functional testing in prolonged implant conditions to check for chronic electrophysiological recording as well as nerve health and interface stability after collagenase delivery to verify possible levels of axonal inflammation and fibrosis. Regarding novel and advanced production methods of microelectrodes, a great deal of interest has recently emerged in the additive manufacturing techniques, a versatile and powerful tool to overcome various shortcomings of conventional lithography techniques. Additive manufacturing of microelectrode arrays or microneedle arrays provides a novel, quick and low-cost method to fabricate custom-shaped electrochemical devices, by rapid prototyping, for a wide range of applications (Yang et al., 2016; Morrison et al., 2019; Soltanzadeh et al., 2020). For example, the manufacturing method performed by an aerosol jet technology, for the fabrication of the microelectrode arrays used in a biosensor platform for electrochemical measurements, was based on the use of a silver nanoparticle (NP) ink and a UV-curable polymer (Yang et al., 2016). Instead, in another

work, compared to microfabricated microneedle arrays, 3D-printed arrays, made of an amorphous polymer of acrylonitrile-butadiene-styrene, showed almost identical geometric properties and equivalent performance with high frequency biosignals (such as in electromyogram recordings), whereas for recording low frequency signals they turned out to be not suitable (Soltanzadeh et al., 2020). However, in these works, only preliminary and short-term tests were run to measure their functionality (e.g., electrical stimulation in mouse brain, signal recording ability and impedance characteristics) either in human subjects in a non-invasive manner (Soltanzadeh et al., 2020), or in mice (Morrison et al., 2019) and as electrochemical laboratory biosensors (Yang et al., 2016), thus requiring further and deeper *in vivo* investigation to establish the real advantages and drawbacks of 3D-printed microelectrodes and the biocompatibility of the materials used before their clinical application.

To date, microelectrode technologies present important limitations mainly due to the stiffness mismatch between metals or micromachined silicon, used for electrode microfabrication, and surrounding tissue, particularly soft brain tissue (Winslow and Tresco, 2010). Thus, the mismatch results in fibrotic encapsulation of the microelectrode in chronic implants (Polikov et al., 2005). Furthermore, the problem of controlling possible micromotion of the interface that can change its position in the tissue may also gradually increase the inflammatory reaction (Gilletti and Muthuswamy, 2006). Similar issues can occur with chronic implants of microfabricated peripheral nerve devices. Thus, another group developed a novel fluidic microdrive technology to implant and microactuate ultraflexible electrodes, with a parylene-coated core of carbon nanotube (CNT) fibers, in animal models that could find useful applications also in peripheral nerves (Vitale et al., 2018). Indeed, following fluidic implantation into the nervous tissue, the authors were able to perform electrophysiological recordings, enhancing the stability of the device without the need of increasing the stiffness and thickness of the microdevices, and thus preventing also the onset of inflammatory responses. Fluidic microdrives were fabricated in PDMS by conventional replica molding technique and the microelectrodes insertion was obtained *via* viscous drag force due to the finely controlled liquid flow in the microfluidic channel, limiting tissue damage at a negligible extent. Such brilliant strategy could be further implemented for peripheral nerve electrodes, envisioning exciting opportunities for their chronic implants. Wireless and flexible film-based ion-selective electrodes (ISEs) have also been recently developed as miniaturized systems for performing highly sensitive and non-invasive measurements (Lim et al., 2020). These sensor systems, made of carbon–polymer composite transducers integrated onto a flexible circuit, enable ions detection in body fluids with high accuracy and selectivity and for prolonged lifetime, showing great potential for their application also in health studies and clinical systems. Another recent approach to drastically reduce the risk of alteration of the performance of the transducer material used for sensors and electrodes, was the development and characterization of solid contact ion-selective electrodes using novel composite material (Kałuża et al., 2019). The formulation of the present nanocomposite was based on multi-walled carbon nanotubes (MWCNTs) and poly(3-octylthiophene-2,5-diyl) (POT), with the immobilization of the polymer on the carbon nanostructures, preventing its spontaneous and unwanted partition to the membrane phase. The obtained sensors were characterized with good performance, high conductivity as well as high stability of potential readings over time. Nevertheless, although the remarkable electrical and physical properties of CNTs that can be exploited for enhancing the functionality of metallic electrodes (Aregueta-Robles et al., 2014), the main concern for their long-term use *in vivo* remains related to their cytotoxicity and to the risk of causing intracellular damages. Indeed, because of their elevated stiffness and reduced size (Krishnan et al., 1998), CNTs can easily penetrate cellular membranes (Kagan et al., 2006; Gilmour et al., 2013) and damage nuclei and cytoplasmic organelles. Additionally, they are known to be cytotoxic at high concentrations in different cell types (Bottini et al., 2006; Tian et al., 2006). In spite of such significant risks, which need to be carefully evaluated before clinical applications, nanoscale features of CNTs enable their escape from the immune system surveillance, thereby providing an undoubtedly appealing resource for the future development of innovative intraneural electrodes. A summary of the intervention strategies based on the design and geometry of the electrode with representative examples is reported in **Table 1**.

Developing Innovative and Advanced Functional Biomaterials

Recently, other research groups worked on the development of more suitable materials that can be tolerated by the neural tissue, leveraging on material chemistry, micro- and nano-fabrication techniques (Fekete and Pongrácz, 2017). Many different polymers turned out to be possible substrates of neural interfaces due to their proper flexibility, stability, insulation properties and biocompatibility (Svennersten et al., 2011; Ordonez, 2012; Ware et al., 2013; Nguyen et al., 2014; Arreaga-Salas et al., 2015; Boddupalli et al., 2016). Noteworthy, among these are: shape memory polymers (SMPs) [such as polyurethanes, polylactides, polystyrenes, poly(cyclooctene), thiol-enes and poly(vinyl acetate)]; the widely used micro-electro-mechanical systems (MEMS) polymer materials, namely polyimide, parylene C, PDMS and SU-8 (an epoxy-based photoresist suitable for microelectronic applications). In the soft neural tissue, the use of new smart SMPs is gradually overcoming the one of more stiff materials, as the former seem to drastically reduce the inflammatory response in the surrounding tissue becoming compliant after implantation (Ware et al., 2013; Nguyen et al., 2014; Minev et al., 2015). Likewise, in the PNS the use of flexible polymer materials seems to eliminate the mechanical mismatch of compliance between the implanted electrode and the biological tissue (Blakney et al., 2012; Nguyen et al., 2014).

MEMS POLYMER MATERIALS

Polyimide

It is a highly resistant and biocompatible polymer, made by imide monomers, among the most widely used substrates

TABLE 1 | Intervention strategies based on the design and geometry of the electrode.

(i) Design and geometry		
Features	**Examples**	**References**
Size effect	PEG-DMA hydrogel coatings and deep and spray coating method	Spencer et al., 2017
	PEG-based coatings	Reviewed in Knop et al. (2010) Wichterle and Lím, 1960; Rao et al., 2011; Gutowski et al., 2015; Heo et al., 2016; Lee et al., 2017
	PHEMA-based coatings	Reviewed in Ratner (2002) Campioni et al., 1998; Jhaveri et al., 2009; Zhang et al., 2017
Surface morphology	FIB technology as machining technique to modify surface morphology	Raffa et al., 2007
Shape	Flexible implants of multifunctional polymeric fibers	Canales et al., 2015
Design and topography	Physical properties, surface micro-/nano-topography and surface chemistry modifications	Reviewed in Ware et al. (2013) Anderson et al., 1999; Thull, 2002; Fink et al., 2008; Chen et al., 2010; Gamboa et al., 2013; Hulander et al., 2013
	3D design of spiked ultraflexible substrates	Rubehn and Stieglitz, 2010; Wang M. et al., 2018
	Neural probe with sinusoidal design and a 3D spheroid tip	Sohal et al., 2014
	Microgeometry and implant thickness effect	Ward et al., 2002
Material morphology	Cationic polymer coatings and PLA and electro-spun fiber meshes with plasma-polymer coating	Ma et al., 2011; Lucke et al., 2018
Surface porosity	Channel size control through (pHEMA-co-MAA) hydrogels	Madden et al., 2010
	PU-based porous implants	Ward et al., 2002
Size and spherical geometry	Alginate spheres/capsules	Veiseh et al., 2015
Intervention strategy		
Soft robotics	Control over fluid flow and shear stress through milliscale dynamic soft reservoir with actuatable membrane	Dolan, 2019
Microfabrication	Micro-machined neural prosthetic devices: flexible polymer-based microelectrodes with different shape, size and geometry	Reviewed in Szarowski et al. (2003); Lee et al. (2004), Metz et al. (2004); Polikov et al. (2005), Spataro et al. (2005); Ziegler et al. (2006), Winslow and Tresco (2010); Blau et al. (2011), Gerwig et al. (2012); Gao et al. (2013), Minev et al. (2015); Qi et al. (2017), Vitale et al. (2018); Kozai (2018), Fallahi et al. (2019), and Kumar et al. (2020) Elyahoodayan et al., 2020
	Encapsulation technologies of flexible microelectrodes	Reviewed in Ahn et al. (2019)
	Electrically-responsive flexible microfibers	Chen et al., 2017
	Microfabrication of a neural probe with sinusoidal design and a 3D spheroid tip	Sohal et al., 2014
	Wireless, flexible, film-based carbon-polymer composite microelectrode system	Lim et al., 2020
	Additive manufacturing of microelectrode arrays and microneedle arrays	Yang et al., 2016; Morrison et al., 2019; Soltanzadeh et al., 2020
Nanofabrication	CNTs	Reviewed in Aregueta-Robles et al. (2014) Castagnola et al., 2016
	Parylene-coated flexible CNTf microelectrodes	Vitale et al., 2018
	Conducting-polymer carbon nanotubes	Abidian et al., 2010; Gerwig et al., 2012; Alba et al., 2015; Mandal et al., 2015; Samba et al., 2015; Du et al., 2018; Altun et al., 2019; Kałuża et al., 2019; Zheng et al., 2019
	PPy nanowires	Reviewed in Qi et al. (2017)
	PPy nanoparticles	Hosseini-Nassab et al., 2017
	SWCNT-PPy/PEGDA composite hydrogels	Xiao et al., 2012
	PPy/CNT films	Luo et al., 2011
	Graphene oxide nanocomposite films of PPy	Weaver et al., 2014
	PLGA nanoparticles embedded in alginate hydrogels	Kim and Martin, 2006
	Nanoparticle-coated nanoelectrodes	Bazard et al., 2017
	Nanoscale biomimetic surfaces	Reviewed in Von Der Mark et al. (2010)

PEG, polyethylene glycol; DMA, dimethacrylate; PHEMA, poly(2-hydroxyethyl methacrylate); FIB, focused ion beam; PLA, poly(l-lactide-co-d/l-lactide); pHEMA-co-MAA, poly(2-hydroxyethyl methacrylate-co-methacrylic acid); PU, polyurethane; CNTs, carbon nanotubes; CNTf, carbon nanotube fiber; PPy, polypyrrole; SWCNT-PPy/PEGDA, single-walled carbon nanotubes-polypyrrole/poly(ethylene glycol) diacrylate; PLGA, poly(lactic-co-glycolic acid). References: except were specifically indicated as 'Reviewed in,' all others are research articles.

for the fabrication of the core of novel neural electrodes with metallic tracks, such as Pt and gold, often coated with different biomaterials for counteracting and delaying the onset of the FBR (Oddo et al., 2016; Delgado-Martínez et al., 2017; Wurth et al., 2017; de la Oliva et al., 2018c). Indeed, among the possible neuroprosthetic applications of this polymer, the group of Navarro X. developed a novel double-aisle electrode to regenerate separated nerve fascicles, made of a double-side thin-film of polyimide (Delgado-Martínez et al., 2017). Although such interface allowed regeneration of nerve branches, it caused FBR in chronic implants. The reaction was indeed similar to that obtained previously with other chronically implanted polyimide intrafascicular electrodes and non-obstructive regenerative electrodes (Lago et al., 2007; Garde et al., 2009), thus affecting the quality of neural signal over time. This common limitation when using polyimide electrodes might be overcome through the functionalization of the polyimide core with advanced biomimicry ultra-low fouling organic or synthetic coatings that can be much more tolerated by the implanted tissue. Toward this direction, diverse efforts have been made to reduce the inflammatory response and electrode encapsulation through new biomimetic solutions. One of these involved the coating with bioresorbable layers of molten saccharose for intracortical insertion in rat models (Hassler et al., 2016). Another option was a superhydrophobic coating from a natural Xanthosoma sagittifolium leaf nanocasted on an electroactive polyimide surface (Chang et al., 2013). A different nanotechnological approach was attempted using hybrid conductive material: an indium tin oxide substrate associated to a nanostructured polyimide film deposited on a glass surface, using a new and simple nanopatterning technique (Rombaut et al., 2019). Very recently, a flexible and transparent polyimide-based electrode was fabricated with a trilayer-stacked geometry that exploits the properties of a high-quality ultrathin film of graphene. This solution showed enhanced power and current efficiencies, with properties comparable to indium tin oxide-based diodes, increased flexibility and long-term stability in different devices (Lee et al., 2019). Finally, another strategy to increase the long-term reliability, while maintaining high flexibility, of a polyimide-based neural interface in free-moving rats, was the one adopted by a research group from China, through a MEMS fabrication approach (Ji et al., 2018). This group developed an innovative optogenetics tool consisting in a polyimide-based hybrid (opto-electric) flexible device that integrates 16 micro-LEDs and 16 IrOx-modified microelectrode arrays. Such device allowed simultaneous, high-resolution optical stimulation and electrical recording of cortical areas. Using this tool, they observed little reduction in the electrical or optical performance for 3 months. Although the fabrication process was quite complex, the device revealed itself to be a promising neural interface for further neuroscience applications, expandable also to larger animals (e.g., non-human primates) and possibly to human patients. However, in order to evade the issue of non-specific protein and cell absorption on the polyimide surface, several groups tried to devise valid alternatives to polyimide substrates, using either diverse MEMS polymers or newly emerged biomedical materials, as shown below.

Parylene C

Parylene C is a variety of high flexible and chemically inert poly(p-xylylene) polymer commonly used as biocompatible coating and substrate material of electrodes for soft neural implants (Fekete and Pongrácz, 2017). In a recent work, the authors tested parylene C as a substrate material for peripheral nerve interfaces both *in vitro* and *in vivo* (de la Oliva et al., 2018a). In this study, longitudinal devices made of parylene C and polyimide were implanted in the rat sciatic nerve for up to 8 months and the induced FBRs were compared one another. In spite of the advantage to produce parylene C-based thinner substrates than polyimide ones, with no harmful effect on nerve function, long-term stability of such electrodes could be affected by a thicker tissue capsule than polyimide devices. Indeed, the authors observed much more fibroblasts surrounding the former device, thus making parylene C not suitable for chronic implantations (Lecomte et al., 2017; Mueller et al., 2017; de la Oliva et al., 2018a). However, the diverse pattern of FBR around parylene C vs. polyimide, due to their different chemical structures, deserves further investigation before parylene C drops out of other possible invasive neural applications. For example, in another study the authors microfabricated and tested *in vivo* up to 24 months, even though in the rabbit brain, a sinusoidal probe electrode made of a tungsten titanium alloy (WTi) core encased in flexible layers of parylene C with novel design features (Sohal et al., 2014). Interestingly, over the chronic experimental period of the study the electrode performances and neuronal integration were better than other conventional electrodes used for recording of neuronal activity in humans, showing low levels of gliosis. Another interesting attempt to improve the long-term stability *in vivo* of an intrafascicular neural interface (i.e., a flexible microelectrode array with a recording system), was made through a mechanically enhanced flexible interconnection cable using a combination of parylene C and polyimide (Kang et al., 2019). The former provided chemical and electrochemical stability while the latter improved the mechanical strength and handling, with no damage reported, during the implantation procedure of the whole neural interfacing device in canine sciatic nerves. However, before clinical translation, these promising results need more investigation to test their reproducibility in chronic implants of peripheral nerves in larger animal models. Despite the many benefits of parylene C as conformational coating, such as its chemical inertness, there are also significant disadvantages that can limit its wider application compared to the liquid epoxy or silicon coatings. Notably, a better performance and a more controlled deposition process of the latter that are, moreover, much more cost-effective in their production-run make them a preferable choice for researchers. Furthermore, the chemical vapor deposition process required to apply parylene C onto a surface, especially a conductive-metal one, is not only time-consuming but also costly in the attempt to increase its metal adhesion through different methods.

Poly(Dimethylsiloxane) (PDMS)

This silicon-based organic polymer is the elective material for microfabrication of microfluidic devices including

microelectrodes, with tissue-like elastic modulus, easily compliant to neural tissue. These flexible electrodes are usually realized through the process of replica molding, from a master obtained by soft photolithography with a SU-8 photoresist (Qin et al., 2010). Alternatively, they can be fabricated *via* simple and cost-effective photolithography-free methods, such as laser micromachining and master molding of PDMS. Such versatile processes give rise to planar metal electrodes with microfluidic channel geometries (Chatzimichail et al., 2018), and stable neural interfaces (Gao et al., 2013; Minev et al., 2015).

Poly(dimethylsiloxane) micromachining is not only cheap, and easy to realize with high parallelization, but also suitable for the fabrication of long-term neural implants that are able to produce lower inflammatory response than polyimide-based electrodes (Minev et al., 2015). Flexibility and elasticity of PDMS are clearly advantageous features for the fabrication of neural electrodes, as well as in promoting neuronal maturation (Teixeira et al., 2009; Yang and Suo, 2018). Notwithstanding, because of PDMS hydrophobicity, achieving its stable adhesion to hydrated surfaces and materials, such as hydrogels, can be problematic (Yang and Suo, 2018). Furthermore, the proper stability and adhesion between different layers of elastic polymers in implantable electronic devices, such as stretchable electrodes, is difficult to achieve. Actually, under the pressure of muscle contraction and of the strain imposed by the micromotion between nerve tissue and the implant, the electrode can crack. This issue can eventually jeopardize the device functionality. Therefore, alternative solutions have been pursued using all-polymer and metal-free microelectrode arrays with a mixture of various stretchable polymers and *via* replica molding with PDMS (Blau et al., 2011; Guo et al., 2014; Qi et al., 2017), although with mixed fortunes, as described in the next section.

OTHER ADVANCED BIOMEDICAL MATERIALS

From the close collaboration between the bioengineering field and the biomedical research area in the development of novel biomaterials for chronic neural applications, diverse strategies are being pursued to decrease the FBR in the next-generation neural interfaces. Some of them are based on the use of organic and synthetic polymeric coatings, including conductive polymers (CPs). Among organic coatings, CPs have been recently investigated with the aim to improve the long-term performance of neural electrodes as they can increase their effective surface, thereby decreasing the impedance, and enhance the electrical properties of neural interfaces, thus seeming the most promising materials (Wilks et al., 2011; Charkhkar et al., 2016). In particular, Poly (3,4-ethylenedioxythiophene) PEDOT, and some of its modified and hybrid versions, have been shown to be safe and reliable candidates in neuroprosthetic applications, being stable and able to improve neural adhesion, electrochemical impedance and dramatically reduce electrical noise and host tissue response (Abidian et al., 2010; Green et al., 2013; Ferlauto et al., 2018; Ganji et al., 2018). Moreover, PEDOT can be easily doped and bio-functionalized with anti-inflammatory drugs, such as dexamethasone (Alba et al., 2015; Boehler et al., 2017; Kleber et al., 2019). It can also be conjugated with other biocompatible and bioinert materials, such as PDMS thin films, CNTs, tetrafluoroborate (TFB), poly(styrenesulfonate), alginate and nafion to guarantee electrochemical stability both *in vivo* and *in vitro* (Blau et al., 2011; Alba et al., 2015; Charkhkar et al., 2016; Ferlauto et al., 2018; Carli et al., 2019). To date, PEDOT functionality has already been demonstrated *in vitro* in terms of improvement of neurite outgrowth bioactivity, and stability of neural micro-stimulation (Green et al., 2009; Mandal et al., 2015). Nonetheless, the long-term performance and integrity *in vivo* of such coatings for chronic recordings have yet to be verified, despite some interesting data collected from short-term epicortical and epidural recordings (Blau et al., 2011). However, these aspects start to be evaluated with promising long-term results, such as for the chronic intracortical neural recordings with high stability and activity in rat motor cortex and mice visual cortex, which deserve further investigation (Charkhkar et al., 2016; Ferlauto et al., 2018; Carli et al., 2019). Another important example was provided by a research team that developed a metal-free electrode array of polypyrrole/polycaprolactone-block-polytetrahydrofuran-block-polycaprolactone (PCTC) sandwiched in between films of PDMS. This group compared the *in vivo* performance of such all-polymer interface with a Pt electrode of the same area in a rat (Guo et al., 2014). They demonstrated a lower impedance of the metal-free device, along with excellent electrical stimulation performances in a stimulated rat hind-limb muscle following squeezing of the sciatic nerve and higher charge injection capacity compared to the Pt electrode, as well as to other PEDOT-coated metal electrodes. Future work from the same group will be necessary to improve and characterize the device physical integrity and mechanical performance in long-term *in vivo* assays also in peripheral nerves.

Two of the most widely used synthetic polymers for coating electrodes are poly (ethylene glycol) PEG (Drury and Mooney, 2003; Gutowski et al., 2015) and PHEMA (Jhaveri et al., 2009; Mario Cheong et al., 2014), as they can form hydrogels with low- or non-fouling characteristics *in vivo*, thus enhancing tissue response around implanted electrodes. However, their long-term use is limited by oxidative mechanisms that partially compromised non-specific protein absorption and device performance. Therefore, recent hybrid solutions have been proposed to overcome some of the issues related to their prolonged stability and sensitivity *in vivo*, such as hybrid thin film photopatternable polymers, combining the properties of PEDOT with the long-term (over 10 days) moisture stability of PEG (Zhu et al., 2017). Another successful test was the integration between PEDOT-poly(styrene sulfonate) (PSS)-CNT nanocomposites and biocompatible PHEMA hydrogels (Castagnola et al., 2016), for potential acute and chronic flexible and high sensitivity electronic applications in rat brains. Thus, the PHEMA hydrogel was able to guarantee the electrochemical performance of the device and improve the quality of intracortical recording until 28 days after the implant, along with the advantage of reducing the mechanical mismatch between neural tissue and device preventing the nanomaterial detachment. Instead, other

researchers produced a polydopamine-based coating, resistant to protein adsorption, also for potential applications in intraneural electrodes (Kwon et al., 2016). They developed a polydopamine melanin (PDM) film in the nanometer-scale, a synthetic analog of the two naturally-occurring chemicals dopamine and eumelanin holding unique ionic and electronic properties (Ambrico et al., 2013, 2014; Wünsche et al., 2013), which could be harnessed to increase neural electrodes performance by improving their *in vivo* biocompatibility, while reducing their interfacial impedance. However, further studies will be needed to verify the potentiality of such PDM films. Another group biofunctionalized roughened Pt black (BPt) peripheral nerve cuff electrodes for chronic implantation in animal models using two coatings of PEG or nafion, with the latter showing low interfacial impedance, together with good stability and reduced fibrotic capsule, thus justifying deeper investigation also for possible clinical applications (Lee et al., 2017). A different research team developed a novel CP for neural electrodes made of a soft wire conductive matrix, which showed optimal mechanical (suitable flexibility) and electrochemical properties, as well as excellent biocompatibility after 1 month implantation in a rat sciatic nerve (Zheng et al., 2019). The conducting core of the electrode was based on silicone/poly(3,4-ethylenedioxythiophene)-polyethylene glycol (PEDOT-PEG) elastomer encapsulating 3D CNTs, and it was shown to be more compliant to soft nerve tissue than traditional polyimide implants in terms of FBR. Finally, another CP frequently used as electromechanically active coating for biosensors, implantable gold electrodes (Yamato et al., 1995; Cui et al., 2003; Green et al., 2008), fiber scaffolds capable of dynamic mechanical actuation (Gelmi et al., 2016) and microelectrode arrays (Qi et al., 2017; Du et al., 2018), is the polypyrrole (PPy). However, it has often shown limited performances and chronic recording failure over extended periods of time *in vivo*, also due to chronic inflammation and fibrotic encapsulation (Yamato et al., 1995; Cui et al., 2003; McConnell et al., 2009). In a recent work, a research group tried to improve the performance of biosensing interfaces based on copolymerization of benzenamine-2,5-di(thienyl)pyrrole (SNS-An) with 3,4-ethylenedioxythiophene (EDOT) (Altun et al., 2019). The so-developed copolymer films showed increased biosensing efficiency after the incorporation of CNTs and fullerene, albeit evidence of the effect of such copolymerization on their performance *in vivo* is still missing. Conversely, others observed high conductivity and good performances in their *in vivo* recordings of rat electrocorticographic signals, and in the stimulation of the sciatic nerve of the animals through the use of stretchable polymeric microelectrode arrays. These arrays were composed of PPy electrodes anchored to an underlying PDMS film using PPy nanowires. Moreover, these flexible devices showed high stretchability with no cracking, high resistance up to 100% strain and good electrode-substrate adhesion (Qi et al., 2017). To sum up, composite PEDOT-PEG or PEDOT-PHEMA solutions would seem to offer a suitable compromise between long-term mechanical and bio-stability as well as high electrical performance ensuring, at the same time, very good biocompatibility, if were not for the current limit of the few available *in vivo* results against FBR.

HYDROGELS

The use of highly hydrated and ultralow-fouling polymeric hydrogels outperforms other coating materials in terms of biocompatibility although the existing issue of the low electrical properties of some chemical hydrogel compositions. This drawback could be solved by including in hydrogels some of the conductive components examined above, such as CPs and CNTs (Green et al., 2012; Xiao et al., 2012). Another alternative solution could be the use of zwitterionic hydrogels with ionic conductive capacity as well as biomimetic and anti-inflammatory features, which can also resist the FBR for longer time-scale than other synthetic HEMA hydrogels (Zhang et al., 2013; Diao et al., 2019). For instance, in one of these most recent papers, it was demonstrated that highly stretchable, tough and flexible PVA/P(AM-co-SBMA) zwitterionic hydrogels possess high intrinsic ionic conductivity due to the zwitterionic counterions, and could therefore fulfill flexible electrical device applications (Diao et al., 2019). Further examples are represented by the synthesis of ultralow-fouling zwitterionic hydrogels and non-leaching polymeric sulfobetaine (polySB) coatings for subcutaneous implantation of medical devices in animal models up to 2—3 months (Smith et al., 2012; Zhang et al., 2013; Yesilyurt et al., 2017). Another recent paper showed the synthesis and *in vitro* validation of poly(carboxybetaine) zwitterionic hydrogel coating, with a Young's modulus in the range of the neural tissue, of a polyimide-based device to minimize the fibroblast and macrophage adhesion (Trel'Ová et al., 2019). Similarly, a previous carboxybetaine methacrylate zwitterionic hydrogel synthesized *via* photopolymerization, rather than thermal polymerization, with a more reactive and functionalizable crosslinker showed superior stability at diverse pH values and improved mechanical properties than many other photopolymerized hydrogels (Carr et al., 2011). Finally, in their work some researchers developed a well-controllable electrochemically-mediated surface-initiated atom transfer radical polymerization (e-siATRP) method to fabricate a superlow protein absorption zwitterionic hydrogel coating that was based on poly(sulfobetaine methacrylate) (pSBMA) (Hu et al., 2015). The main advantage of the present method is represented by the usage of the commercially available SBMA and its very easy and controllable synthesis process, which can be also applied to implantable neural electrodes with optimal biocompatibility and antifouling capacity as proven by *in vitro* tests (Hu et al., 2015).

Besides, another frequently encountered issue related to such systems is the delamination of the hydrogel from the electrode surface, and thus the establishment of adequate patterning methods for binding it to the substrate. In a recent work, microsystem engineers and chemists addressed these problems by developing a new hybrid conductive system made from the combination between the synthetic hydrogel P(DMAA-co-5%MABP-co-2,5%SSNa) and the conducting polymer PEDOT, which can be covalently attached to the electrode surface and patterned using a photolithographic process *via* UV irradiation. In such a way, the authors created an interpenetrating network, suitable for coating neural microelectrodes, showing excellent electrochemical stability and no toxicity *in vitro* (Kleber et al.,

2017). Conductive hydrogel coatings can ameliorate the electrical properties and performances of conventional metal electrodes, with lower energy demand to interface with and control target nerve activity. To achieve a suitable response from a distant stimulated nerve, the application of higher currents is necessary with possible adverse reactions, such as the corrosion of the uncoated metallic electrode and its failure over time. Hence, due to their high efficiency and electrochemical stability, conductive hydrogels can provide stable and long-term activity also when applied to stainless steel (SS) electrode arrays in peripheral nerves as showed in this work (Staples et al., 2018). The researchers fabricated planar electrode arrays by electrodepositing a thin layer of PEDOT/pTS onto the SS electrode and then coating it with a 20 wt% poly(vinylalcohol)-methacrylate-taurine (PVA-taurine) hydrogel. In their *in vitro* tests the conductive hydrogel coating improved electrochemical properties and device stability over 42 days regardless of the underlying metallic substrate of the electrode. Nonetheless, the authors used non-penetrating cuff-electrodes and only for *in vitro* analysis, thereby the benefit of such hydrogel coating against FBR over chronic invasive implant periods *in vivo* will be the focus of their future work. Accordingly, their principal task will be the demonstration of low scar tissue development due to the reduced hydrogel stiffness and to its natural anti-fouling properties.

Modulation of the FBR for intraneural interfaces can also be achieved taking inspiration from recent works in animal models of type-I diabetes (Vegas et al., 2016; Bochenek et al., 2018). In these *in vivo* studies the authors performed encapsulation of human pancreatic β-cells with chemically modified alginate formulations [i.e., triazole-thiomorpholine dioxide (TMTD) alginate, Z2-Y12 and Z1-Y15 immune-modulating alginate derivatives] to long-term protect cells from the chronic response of the immune system, without the need for broad immunosuppression. In particular, these different hydrogel formulations increased the immunoprotection of cells in immune competent mice and non-human primate models, successfully reducing FBR and preventing from pericapsular fibrotic overgrowth. Similar strategies with alginate hydrogels could therefore be translated into clinical practice to encapsulate intraneural electrodes, and exploited to overcome the challenge of foreign body rejection from the host immune system. Overall, despite the many advantages provided by conductive hydrogel coatings in terms of high electrochemical performance of the device, especially when using zwitterionic formulations, augmented quality of signal recording, reduction of the mechanical mismatch along with ultralow-fouling properties, their long-term stability and functionality *in vivo* still represent main limitations that need to be solved in the next future. In fact, because of their soft texture, highly hydrated jelly structure and low mechanical strength, hydrogels can be slowly degraded or damaged already during the implantation surgery, thus impairing their permanence and performance within neural tissue. However, to the best of our knowledge, at present they are by far the most promising biomimetic coatings in this context.

A summary of the intervention strategies based on the development of advanced functional biomaterials with representative examples is reported in **Table 2**.

Interface–Microenvironment Interaction

The aqueous characteristic of synthetic and organic hydrogel coatings, such as PEG-based and zwitterionic-based formulations, and their synthesis methods could be harnessed for therapeutic purposes. In order to modulate locally the immune response of the host tissue, various hydrogel formulations could represent a means to encapsulate or covalently incorporate growth factors, therapeutic anti-inflammatory and anti-fibrotic medications as well as small-molecule drugs (Jhaveri et al., 2009; Mario Cheong et al., 2014; Gutowski et al., 2015; Doloff et al., 2017). To this aim, a considerable list of potential therapeutic drugs could be loaded during polymer fabrication into biodegradable CPs, polymeric coatings and hydrogels (Lotti et al., 2017; Zeglio et al., 2019), and many others could be tested as good candidates for contrasting FBR. In the following sections we will take into account some of the most promising lead compounds and novel drug delivery strategies to further improve the biological response to the electrodes in chronically implanted nerve tissues.

DEXAMETHASONE

One of the most frequently anti-inflammatory agents loaded into electrode coatings for chronic applications is the corticosteroid drug dexamethasone and its phosphate derivative (Spataro et al., 2005; Kim and Martin, 2006; Mercanzini et al., 2010; Alba et al., 2015). Interestingly, in two FBR models in the rat sciatic nerve, one with longitudinal parylene C intraneural implants, and the other with longitudinal polyimide-based implants, the beneficial effects of dexamethasone were clearly demonstrated (de la Oliva et al., 2018b). In fact, in this work only subcutaneous administration of dexamethasone up to 8 weeks, compared to other anti-inflammatory drugs (i.e., ibuprofen, maraviroc, and clodronate liposomes), was able to reduce the inflammatory reaction as well as matrix deposition around the electrodes in a comparable manner. In another model of FBR, developed by the same group, using TIME interfaces implanted in the rat sciatic nerve, the long-term functionality (i.e., 3 months) of the electrodes was maintained by systemic administration of dexamethasone. The drug was indeed able to reduce the loss of functioning contacts of the TIMEs that stimulated the target nerves and evoked a muscle response while reducing the inflammatory cell infiltration during the first month, which is the critical time-frame for FBR development (de la Oliva et al., 2019). Since dexamethasone showed similar beneficial effects in different devices and substrates, it may represent an ideal drug treatment to extend the implant functionality over time in peripheral nerves. Accordingly, the use of dexamethasone could be combined with tissue engineering strategies, such as substrate functionalization with biodegradable hydrogels and porous CPs, for its controlled local release in order to specifically target its activity around the implant, while reducing potential side effects caused by its systemic toxicity at too high doses. In relation to this approach, one of the first *in vitro* attempts to control the release of dexamethasone from a conducting polymer coating of PPy on Au electrode

TABLE 2 | Intervention strategies based on the development of advanced functional biomaterials.

(ii) Advanced functional biomaterials		
Intervention strategy	**Examples**	**References**
Novel flexible and biocompatible polymers	Extended overview	Reviewed in Ordonez (2012); Ware et al. (2013), Boddupalli et al. (2016), and Fekete and Pongrácz (2017)
	Polypyrrole microactuators	Svennersten et al., 2011
	Hydrogel core of bacterial cellulose and conductive polymer shell layer of PEDOT	Chen et al., 2017
	PEG-RGD hydrogels	Blakney et al., 2012
SMPs	Extended overview	Reviewed in Ware et al. (2013)
	Bioinspired cellulose nanocomposites	Nguyen et al., 2014
	Thiol-ene based softening substrates	Arreaga-Salas et al., 2015
Micro-electro-mechanical systems (MEMS) polymer materials	Polyimide	Reviewed in Kozai (2018) Lago et al., 2007; Garde et al., 2009; Mercanzini et al., 2010; Chang et al., 2013; Hassler et al., 2016; Oddo et al., 2016; Boehler et al., 2017; Delgado-Martínez et al., 2017; Wurth et al., 2017; de la Oliva et al., 2018b,c; Ji et al., 2018; Kang et al., 2019; Lee et al., 2019; Rombaut et al., 2019
	Parylene C	Reviewed in Fekete and Pongrácz (2017) Ziegler et al., 2006; Sohal et al., 2014; Xie et al., 2014; Lecomte et al., 2017; Mueller et al., 2017; de la Oliva et al., 2018a,b; Vitale et al., 2018; Kang et al., 2019
	PDMS	Blau et al., 2011; Gao et al., 2013; Guo et al., 2014; Minev et al., 2015; Chatzimichail et al., 2018; Kumar et al., 2020
CP coatings	Extended overview	Reviewed in Aregueta-Robles et al. (2014) and Balint et al. (2014)
Hydrogels	Alginate hydrogels	Reviewed in Lee and Mooney (2012)
	PEG-containing hydrogels	Spencer et al., 2017; Zhang et al., 2017
	PEG-maleimide hydrogel coatings	Gutowski et al., 2015
	Poly(SB) hydrogels	Smith et al., 2012
	PEDOT:PSS/alginate conductive hydrogels	Ferlauto et al., 2018
	Conducting PEDOT/PDMAAp hydrogels	Kleber et al., 2017, 2019
	PHEMA hydrogels	Jhaveri et al., 2009; Castagnola et al., 2016; Zhang et al., 2017
	Conducting hydrogels with biomolecules	Reviewed in Aregueta-Robles et al. (2014) and Lotti et al. (2017) Green et al., 2012; Mario Cheong et al., 2014; Chen et al., 2017; Staples et al., 2018
	SWNT-PPy/PEGDA composite hydrogels	Xiao et al., 2012
	Chemically-modified alginate microspheres	Vegas et al., 2016; Bochenek et al., 2018
Zwitterionic hydrogels	Phosphorylcholine polymer	Yesilyurt et al., 2017
	PVA/P(AM-co-SBMA) polyelectrolyte	Diao et al., 2019
	Poly(carboxybetaine) and pCBMA	Jiang and Cao, 2010; Carr et al., 2011; Zhang et al., 2013; Trel'Ová et al., 2019
	Phosphorylcholine self-assembled monolayers	Chen et al., 2005
	Poly(sulfobetaine) and pSBMA	Reviewed in Sin et al. (2014a) Jiang and Cao, 2010; Sin et al., 2014b; Hu et al., 2015; Wu et al., 2018
	Zwitterionic hydrogels with bioactive materials	Reviewed in Von Der Mark et al. (2010)

SMPs, shape memory polymers; RGD, Arg-Gly-Asp motif; MEMs, micro-electro-mechanical systems; PDMS, poly(dimethylsiloxane); CPs, conductive polymers; PEG, polyethylene glycol; Poly(SB), polymeric sulfobetaine; PEDOT:PSS, poly(3,4-ethylenedioxythiophene):Polystyrene sulfonate; PEDOT/PDMAAp, poly(3,4-ethylenedioxythiophene)/poly(dimethylacrylamide-co-4-methacryloyloxy benzophenone-co-4-styrenesulfonate; PHEMA: poly(2-hydroxyethyl methacrylate); SWNT-PPy/PEGDA, single-walled carbon nanotubes-polypyrrole/poly(ethylene glycol) diacrylate; PVA/P(AM-co-SBMA), polyvinyl alcohol/acrylamide and sulfobetaine methacrylate copolymer; pCBMA, poly(carboxybetaine methacrylate); pSBMA, poly(sulfobetaine methacrylate). References: except were specifically indicated as 'Reviewed in,' all others are research articles.

sites was done through an electrochemically-controlled release of dexamethasone phosphate as a dopant (Wadhwa et al., 2006). The authors elicited an anti-inflammatory response in murine glial cells, although they experienced a low adhesion of the coating to the electrode, turning out to be unable to sustain an extended drug-delivery time. Instead, MWCNT and dexamethasone-doped electropolymerized PEDOT coatings have shown promise to improve chronic neural electrode performance. Indeed, despite the impedance increase, coated electrodes successfully recorded neural activity throughout the implantation period (Alba et al., 2015), and showed excellent stability and no signs of inflammation, in response to electrical stimulation, over 45 days in rat brain. Similarly, another team filled MWCNTs with a solution of dexamethasone phosphate

and then sealed the open ends of the nanotubes with a film of PPy, *via* electropolymerization, as electrode coating for an on-demand drug release strategy (Luo et al., 2011). The researchers detected an effective anti-inflammatory activity *in vitro*, and the smaller the size of the nanotubes the higher the drug release. Furthermore, such PPy coating significantly decreased the electrode impedance. However, despite some preliminary evidence of the dexamethasone success, there are still a few reliable data *in vivo* and some considerable kinks to work out before long-term use of the drug as a resolutive anti-inflammatory treatment for clinical applications in humans. For instance, an important issue, not only related to dexamethasone but to any other loaded chemicals, is that of the drug exhaustion around the implant microenvironment.

ANTI-FIBROTIC DRUGS

It has recently been found another molecular target underpinning the development of the FBR. Actually, targeting colony stimulating factor-1 receptor (CSF1R), which is upregulated on the macrophage surface after implantation of different biomaterials, including biocompatible hydrogels, may represent a smart strategy to hamper fibrosis and capsule formation (Doloff et al., 2017). Such therapeutic approach may indeed avoid to directly targeting macrophages or applying massive immunosuppression with possible harmful side effects to the whole organism.

Another potential target protein is the connective tissue growth factor (CTGF), a key player underlying the progression of the fibrotic reaction driven by TGF-β, which is quickly induced by TGF-β in different contexts of fibrotic disease as a specific downstream effector of its activity (Leask et al., 2002). To date, the *in vivo* silencing of target genes involved also in chronic disease such as fibrosis, including CTGF, can be achieved through various therapeutic strategies, either *via* local or by means of systemic administration of viral and non-viral vectors. One of the most promising strategy is represented by the gene therapy through the selective gene knock-down mediated by the small interfering RNAs (siRNAs) or the microRNAs (miRNAs) (Lam et al., 2015; Salazar-Montes et al., 2015; Omar et al., 2016). These therapeutic molecules are short non-coding RNAs with a great potential for different clinical applications (Gori et al., 2015; Lam et al., 2015). However, in order to increase the silencing efficiency of siRNAs and miRNAs the search for the most suitable carrier in terms of low toxicity and immunogenicity to target cells remains an open challenge. In such a scenario, NP-based delivery of siRNAs might represent an ideal solution by improving not only the safety of this potential therapy, but also its effectiveness (Surendran et al., 2017; Yu et al., 2020). The main advantages of NPs are their tunable size, shape and surface features along with their adjustable biological properties (Miele et al., 2012). Among the various material formulations tested, including gold, silica, porous silicon, CNT and diverse polymers, magnetic iron oxide NPs seem to be the most interesting for gene therapy due to their reduced toxicity, easy surface modification and high versatility in a wide range of biomedical applications (Wu et al., 2008; Xiao et al., 2014; Saeed et al., 2018). In this regard, a research group has recently investigated *in vitro* the anti-fibrotic activity of polyethyleneimine (PEI)-functionalized magnetic iron oxide NP-mediated delivery of siRNAs against CTGF (Yu et al., 2020). The siRNA-loaded NPs showed low cytotoxicity and high transfection efficiency, along with significant CTGF silencing performance, reducing collagen production and deposition in the hepatic stellate cell line LX-2. Thus, taking the cue from this study one could envision the use of invasive electrodes with nanoparticle-embedded coatings, such as hydrogels, to regulate the controlled delivery of siRNAs or miRNAs for the specific silencing of CTGF, or other mediators of inflammation and fibrosis.

FURTHER TISSUE ENGINEERING STRATEGIES FOR TARGETED DRUG RELEASE

Ideally, drug loading within the coating of an implantable neural device with tunable physicochemical characteristics, can help avoid adverse side effects associated to systemic administration thanks to the controlled local delivery of the appropriate amount of the drug and for the desired time-window. In the last decades, a considerable number of brilliant approaches have been attempted in order to dope, absorb and incorporate in the interface coating the desired drug to accomplish a safe, effective, controlled and long-term pharmacological release as the aforementioned examples with dexamethasone. Drug loading into the coating can be realized through a self-assembly procedure, by means of electrostatic interactions, using a charged drug as dopant agent or hydrophobic interactions, *via* physical entrapment, as well as covalent bonding using degradable peptides or cleavable molecular linkers (Balint et al., 2014; Zeglio et al., 2019). The miniaturization of biomedical devices through the use of microfluidics is a novel opportunity for tuning the properties of flexible and stretchable biomaterials in many smart applications, from biology to medicine and tissue engineering, including drug delivery purposes (Fallahi et al., 2019). Also, novel technologies for long-term encapsulation using new arising materials have recently emerged with promising results. These include: thin-films of inorganic coatings of Al_2O_3 (alumina), SiO_2 (silica), SiC (carborundum) and diamond; in addition, several organic coatings have been used, which are made of – among others - parylene C, polyimide, liquid crystal polymer (LCP), SU-8 and silicone elastomer for implantable microfabricated medical devices. Both chemical solutions, organic and inorganic, leverage on the miniaturization of the implants thanks to the material flexibility and scalability (Ahn et al., 2019). Although the extended suitability - over several decades – of these materials for the encapsulation of biomedical devices has been largely demonstrated in the literature, they have not yet been approved for chronic implantation in patients (Ahn et al., 2019). However, for the prospective chronic encapsulation of microfabricated implants, these novel materials could overcome the performances of conventional macroscale ceramics- or metal-based packaging technologies that offer scarce adaptability to the microfabrication processes; these emerging materials possess indeed largely

tunable physicochemical properties and higher biocompatibility as well as reliability for clinical applications in order to control the FBR. Nevertheless, much efforts need to be done for their complete processing and engineering, in particular a multi-combinational approach with the association of various organic and inorganic materials will be advisable in the next future for developing an optimal deposition process and studying their barrier characteristics (Ahn et al., 2019). In a representative example of such approach, the authors compared the long-term behavior of Utah electrode array-based neural interfaces, encapsulated in a bilayer of Al_2O_3 and parylene C, vs. the same electrodes with parylene C-only encapsulation (Xie et al., 2014). They observed higher performance stability (i.e., stable power-up frequencies and constant radio-frequency signal strength) and thus increased lifetime of the bilayer encapsulated devices compared with the parylene-only devices. Moreover, the former represented a more reliable encapsulation method for the functionality of chronically implanted neural interfaces.

As regards the investigation of ideal biomaterials for controlled drug delivery, in an *in vitro* analysis three different types of carefully designed pHEMA hydrogel coatings were applied to microfabricated neuroprosthetic devices, through specific hydrogel casting methods, with incorporation of lysine and NaCl to increase both storage capacity and local pharmacological delivery rate in the brain (Jhaveri et al., 2009). Although promising in terms of favorable neural cell response upon Nerve Growth Factor (NGF) delivery, their study needs to be refined for extended *in vivo* applications. In fact, the mechanical properties of these coatings need to be improved to mimic more closely those of peripheral nervous tissue in order to avoid delamination following their insertion in the body; also, more detailed studies should be planned for determining specific local drug delivery and degradation time *in vivo* besides the NGF tested herein. In another interesting *in vitro* investigation on new smart multifunctional biomaterials, electrically-responsive core-shell hybrid microfibers, coated with PEDOT by chemical polymerization, were used for the controlled release of the anti-inflammatory diclofenac sodium salt (Chen et al., 2017). The microfibers were fabricated through a combination of co-axial wet spinning of a hydrogel core of bacterial cellulose, using a microfluidic device, and a dip-coating method of the hydrogel with a conductive polymer shell layer of PEDOT. The developed hybrid microfibers showed very high biocompatibility, electroactivity and allowed the researchers to control the diclofenac release *via* external electrical stimulation in a rat neural cell line. Instead, a remarkable intervention strategy at relevant time scales for chronic clinical applications was the one proposed by Boehler et al. (2017). They microfabricated flexible layers of polyimide on a Pt-IrOx electrode with subsequent coating of PEDOT to harness its conductive properties and drug delivery capacity, for sustained (12 weeks) dexamethasone delivery in implanted rat brains. The drug was incorporated during the polymerization step of PEDOT and released in a controlled manner for attenuating the FBR over the 12-week period that is way beyond the initial healing phase of 6 weeks. Instead, an engineered PEG-maleimide hydrogel coating for neural electrodes was developed to actively control the local release of an anti-inflammatory molecule (IL-1Ra) *in vivo* (Gutowski et al., 2015). They tuned the physiochemical properties of the hydrogel by developing a stimulus-responsive degradable portion for on-demand release of the anti-inflammatory agent in rat brain tissue. Indeed, by taking advantage of the high expression of matrix metalloproteinases (MMPs) in the inflamed rat brain, the authors functionalized the hydrogel coating with MMP-degradable crosslinking peptides that were able to release IL-1Ra at the brain-implant interface in response to inflammation. Altogether, they observed only a moderate reduction of inflammatory markers, although neuronal survival around the electrodes was higher than uncoated controls. However, further improvements are necessary to verify the efficacy of this strategy also in peripheral nerves and for chronic implants, such as a reduced adhesion to the coating of other cell types besides glial and neuronal cells. Importantly, since no evident differences were detected in the recruitment and activation of inflammatory cells involved in scar formation between coated and uncoated implants, it will be of utmost importance to work more on this aspect. Another interesting avenue leverages the properties of conducting and conjugated polymer-based devices to create a drug-eluting electrode. The device can be loaded with the drug of choice and the release is electronically triggered by electrostatic interactions and/or electrical stimulation. In one of these studies, the drug of interest was entrapped in an electropolymerized PEDOT:PSS film by means of a gentle supercritical carbon dioxide ($scCO_2$) treatment and then gradually released *in vitro via* electrical stimulation, retaining an elevated activity while maintaining normal electrochemical properties of the polymer surface (Löffler et al., 2016). Such $scCO_2$-based method could represent a smart approach for loading anionic and cationic drugs in any conductive bio-coating, which can be adjusted depending on the purpose. A different strategy that exploited the mixed conductivity of PEDOT:PSS is the one based on implantable ion pumps (Isaksson et al., 2007). Such technological platform can be potentially utilized not only for targeted ion delivery, but also for larger biomolecules, such as glutamate, aspartate and y-aminobutyric acid (GABA) (Simon et al., 2009), which can be particularly useful for the treatment of CNS disorders. For example, a clinically relevant *in vivo* application of an ion pump for controlled GABA delivery was carried out in rat models of peripheral nerve injury (Jonsson et al., 2015). In this study, a specific design of the outlets of the implantable organic electronic delivery device was developed for local GABA release along the spinal cord. It showed the ability to mitigate neuropathic pain with no side effects.

A recent advancement of this technology for *in vivo* applications, was the development of a microfluidic ion pump with high drug-delivery ability (Uguz et al., 2017). The major advantage of this novel configuration was represented by the reduced distance for the electrophoretic transport of the drug, requiring a low voltage for its delivery, and by the fact that the microfluidic channels were connected to an almost inexhaustible drug reservoir. A similar microfluidic ion device with PEDOT:PSS-based recording electrodes was fabricated for releasing GABA in a specific brain region of an epilepsy

mouse model (Proctor et al., 2018). The device, composed by a neural probe incorporating a microfluidic ion pump and neural electrodes for recording neural activity, allowed the inhibitory neurotransmitter to be selectively delivered to the seizure source for its control and termination. Accordingly, these ion pump devices may represent very interesting spatially and temporally controlled electrophoretic drug delivery systems. These implanted platforms may hold tremendous potential for on-demand therapeutic drug delivery also when combined to intraneural electrodes. The authors speculate that their device could be useful also in chronic drug delivery settings for reducing the FBR after additional technological developments, especially related to the drug reservoir reloading and the improvement of their long-term biostability.

Other investigators generated graphene oxide (GO) nanocomposite films, deposited inside a conducting PPy scaffold, to enhance the dexamethasone phosphate-loading capacity of the graphene component, by means of physical adsorption, and to elicit its electrically controlled delivery (Weaver et al., 2014). *In vitro* tests carried out in primary rat astrocytes showed the possibility to finely control and adjust the drug-release time and dosage, depending on the need, by varying the ultrasonication time required to prepare the graphene oxide nanosheets. Thereby, modulating the ultrasonication treatment one can influence the film morphology, drug load and release profile in a versatile manner. However, many of these smart tissue engineering strategies have failed to reach patients' bed because of a series of drawbacks. Among them, it is worth considering the frequent lack of a suitably charged dopant molecule and the poor drug loading performance with low and unsatisfactory concentration, particularly when using conjugated and conductive polymeric films. Besides, additional hurdles to be addressed include film instability and drug leakage. In particular, the undesired leakage of the drug from the polymeric coating may indeed occur when the loaded molecule is too small compared to the pore size of the releasing hydrogel (Zeglio et al., 2019). As for the limitation of poor drug loading performance, mostly for delivering large molecule therapeutics, it can be addressed through the use of NPs made of conductive polymers (such as PPy) (Hosseini-Nassab et al., 2017). Thanks to their higher surface area than conventional conductive thin films, the electroresponsive PPy NPs enabled a controlled and efficient release of surface-loaded bioactive insulin, triggered by electrical stimuli on a coated Pt electrode, also in *in vivo* tests of therapeutic delivery in mouse models. The authors speculate that such drug-loaded NPs may be enclosed into a semi-permeable hydrogel coating that allows only drug molecules to pass through. In conclusion, this strategy could be potentially envisioned also for peripheral neural interfaces. Such implantable drug delivery system could improve spatially and temporally controlled drug release by simply varying the ratio of the quantity of NPs to the concentration of the desired drug, while maintaining its bioactivity.

Lastly, alternative and smart methods for interfering with the interaction between device surface and tissue microenvironment, thereby evading the host immune response, could be represented by: (a) modifications of biomaterial surface with adhesive peptides (e.g., RGD cell adhesion ligand on PEG surfaces) to partially attenuate inflammatory reaction and capsule formation (Lynn et al., 2011); (b) functionalization of PEG-coated surfaces with synthetic human-based "self" peptides (e.g., the immunomodulatory membrane proteins CD47 and CD200) to inhibit macrophage-mediated clearance of the surface and prolong its *in vivo* survival (Rodriguez et al., 2013; Kim et al., 2014).

A summary of the intervention strategies based on the control of the interface-microenvironment interaction with representative examples is reported in **Table 3**.

FINAL REMARKS AND FUTURE DIRECTIONS

To date, the design of resolutive solutions to modulate the FBR, based on the exhaustive comprehension of its molecular mechanisms, represents a major challenge for a suitable and long-lasting implantation of intraneural devices.

Modern neuroprostheses may employ electrodes produced with microtechnology that, however, do not go below the size of some tens of micrometers. Various techniques of micromachining and micromolding of flexible and conductive polymer coatings may allow scientists to fine tuning the features of the electrodes to the characteristics of the host tissue, thus creating more stable devices over time. Furthermore, the integration of microfluidic ion pumps and channels into neural probes can be harnessed for extended drug delivery in the implanted tissue, so to dramatically reduce the FBR and to be much better tolerated than plain implants.

Indeed, microfluidics and, most of all, nanofluidics, although promising are still quite unexplored in neuroprosthetics, and deserve further investigation.

Strategies based on microfluidic, microscale and nanoscale technologies provide scalability. They can lead from the long-term and stable neurotransmission simultaneously to many tissue points, to an enhancement of spatial selectivity stimulation, through implantable microelectrode arrays and microscale actuators (Kozai, 2018; Kumar et al., 2020). Even more so because conventional electrodes and recording systems are bulky and unsuitable for single cell resolution. By micro- and nano-engineering the surface properties of the implant, one can obtain a better control of therapeutic drug release from artificial nanopores, NPs made of conductive polymers and other nanostructured materials. Compared to traditional bulk materials, this latter mechanism can take advantage of the higher surface area of loaded NPs, their variable degradation rate depending on the biomaterial used, and the adjustable selectivity and permeability of hydrogel coatings to drug molecules. Biofunctionalization of NPs with antigen-recognized antibodies may further ameliorate targeting efficiency by increasing the drug concentration within a specific tissue (Cai and Xu, 2011).

For example, bioinspired cellulose nanocomposites have higher versatility and functionality than rigid silicone implants, due to their switchable stiffness characteristics, reducing neuroinflammation in chronic implants (Nguyen et al., 2014).

TABLE 3 | Intervention strategies based on the control of the interface-microenvironment interaction.

(iii) Interface-microenvironment interaction		
Intervention strategy	**Examples**	**References**
Targeted drug delivery systems	Extended overview	Reviewed in Cai and Xu (2011)
Anti-inflammatory drugs	Dexamethasone	Reviewed in Lotti et al. (2017) and Zeglio et al. (2019) Spataro et al., 2005; Kim and Martin, 2006; Wadhwa et al., 2006; Mercanzini et al., 2010; Luo et al., 2011; Weaver et al., 2014; Alba et al., 2015; Boehler et al., 2017; de la Oliva et al., 2018b, 2019; Kleber et al., 2019
	IL-1Ra	Gutowski et al., 2015)
	Ibuprofen	de la Oliva et al., 2018b
x	Clodronate liposomes	de la Oliva et al., 2018b
	Diclofenac	Reviewed in Zeglio et al. (2019) Chen et al., 2017
	RGD cell adhesion ligands on glass and PEG surfaces	Reviewed in Zeglio et al. (2019) Anderson et al., 1999; Lynn et al., 2011; Blakney et al., 2012
	Functionalization of PEG surfaces with human self-peptides	Reviewed in Lotti et al. (2017) Kim et al., 2014
Anti-fibrotic drugs	Extended overview	Reviewed in Lotti et al. (2017)
	Targeted silencing of CTGF via siRNAs-, miRNAs- and nanoparticle-based silencing	Reviewed in Leask et al. (2002); Wu et al. (2008), Miele et al. (2012); Gori et al. (2015), Salazar-Montes et al. (2015); Omar et al. (2016), Surendran et al. (2017), and Saeed et al. (2018) Xiao et al., 2014; Yu et al., 2020
	CSF1R inhibition	Doloff et al., 2017
Tissue engineering strategies for targeted drug release	Extended overview	Reviewed in Ratner (2002); Drury and Mooney (2003), Knop et al. (2010); Balint et al. (2014), Gori et al. (2015); Lam et al. (2015), Salazar-Montes et al. (2015), and Zeglio et al. (2019)
	Human self-peptides	Rodriguez et al., 2013
	Conductive polymer films	Wadhwa et al., 2006; Mario Cheong et al., 2014; Löffler et al., 2016
	Electrically-responsive microfibers	Chen et al., 2017
	Milliscale dynamic soft reservoir (DSR)	Dolan, 2019
	Embedded microfluidic channels	Metz et al., 2004; Retterer et al., 2004; Ziegler et al., 2006; Gao et al., 2013; Takehara et al., 2014; Minev et al., 2015; Elyahoodayan et al., 2020
	Hydrogel coating (e.g., pHEMA, PEG-maleimide, PVA-heparin)	Jhaveri et al., 2009; Mario Cheong et al., 2014; Gutowski et al., 2015
	CNTs nanoreserviors	Luo et al., 2011
	Electronic ion pumps	Isaksson et al., 2007; Simon et al., 2009; Jonsson et al., 2015; Uguz et al., 2017; Proctor et al., 2018
	Microencapsulation	Campioni et al., 1998
	Nanoparticle-based delivery	Reviewed in Wu et al. (2008); Cai and Xu (2011), Miele et al. (2012); Surendran et al. (2017), and Saeed et al. (2018) Kim and Martin, 2006; Xiao et al., 2014; Hosseini-Nassab et al., 2017; Yu et al., 2020
	Electrically controlled drug delivery from graphene oxide nanocomposite film of PPy	Weaver et al., 2014

IL-1Ra, interleukin-1 receptor antagonist; RGD, Arg-Gly-Asp motif; PEG, polyethylene glycol; CTGF, connective tissue growth factor; siRNAs, small interfering RNAs; miRNAs, microRNAs; CSF1R, colony stimulating factor-1 receptor; DSR, dynamic soft reservoir; pHEMA, poly(2-hydroxyethyl methacrylate); PVA, polyvinyl alcohol; CNTs, carbon nanotubes; PPy, polypyrrole. References: except were specifically indicated as 'Reviewed in,' all others are research articles.

Indeed, these mechanically adaptive nanomaterials although initially rigid become compliant after intracortical implantation in rats. They have been proven to lower neuroinflammatory response at chronic time-points, with no neuronal loss, limited scarring, reduced blood-brain barrier damage as well as decreased accumulation of activated microglia and macrophages at the implant-tissue interface. Upon insertion in the brain, when exposed to physiological conditions, the nanocomposites exhibited a massive reduction in tensile storage modulus and, in turn, the induced tissue strain was dramatically lowered (Nguyen et al., 2014).

Moreover, nanofiber-formed nanogels and self-assembly nanoscaffold hydrogels are broadly adopted for targeted and controlled drug delivery. For instance, some antibody-drug conjugate payloads can be maintained in a target area by side chains, chemical moieties and interactions with the nanogel, thus prolonging their protective effect (Cai and Xu, 2011).

Taking into consideration all of the above reviewed biomedical strategies, ultraflexible nanosized devices, coated with biocompatible and mechanically dynamic materials, may represent an optimal solution. Owing to their advantageous features of stiffness/compliance in a neural context, such

devices seem to be able to significantly attenuate the intraneural invasiveness, tissue strain, micromotion stress and, in turn, the chronic inflammatory response of the tissue.

It is worth noting, though, that there still remain several technical snags that must be overcome in the manufacturing of suitable nanofluidic components over the next decade. Because of its novelty, expertise in nanofluidics is not as robust as the one in microfluidics and it lacks standardized procedures for the fabrication of neural nanodevices. So, manufacturing accuracy of neural nanointerfaces still depends a lot on the ability of the single producer.

However, current fabrication technologies of advanced neural electrodes that combine the employment of new CPs with complex micro- and nano-structured configurations, such as fluidic microdrives, are based on rapidly growing micro- and nano-electronics expertise. These novel methodologies permit the development and use of flexible and small-sized devices with more targeted stimulation by applying low voltages in a safe manner. Therefore, they allow researchers to obtain very good neural signals while reducing the implant invasiveness and its mechanical deformation (Gerwig et al., 2012; Lorach et al., 2015; Samba et al., 2015; Bazard et al., 2017; Qi et al., 2017; Vitale et al., 2018). Furthermore, to match the mechanical texture of the neural tissue, especially of the brain, conductive and ultraflexible nanomaterials, such as CNTs, ultrathin films of graphene and nanowires have been explored. Such highly flexible and compliant electrodes can thus bend and adapt to the movements of the host tissue only in a slightly invasive and detrimental manner. Nevertheless, various methods for the implantation into the neural tissue of these nanofabricated devices require temporary stiffening factors that sometimes tend to augment the electrode size and stiffness, thereby increasing also tissue damage, cell death and eventually giving rise to a severe and unwanted inflammatory response (Vitale et al., 2018).

Hitherto, the majority of these studies that investigate alternative strategies against the FBR have been carried out either on the CNS or using other cell types *in* vitro, such as cardiac cells. Hence, many efforts have yet to be done to achieve suitable solutions also in peripheral nerves. Despite these hurdles, we believe that the challenge of ensuring a high-resolution release of bioactive chemicals against the FBR by minimally invasive neural interfaces while, at the same time, precisely controlling neurostimulation will need nanofluidics to be fully accomplished. Indeed, the smaller the size of the invasive electrode with an associated lower stiffness, the better the response of the neural tissue and the more selective and tailored will be the control over the device functionality. Among the main advantages for the use of nanoelectrodes, there is undoubtedly the enhanced mass transport, favored by the reduced dimensions, which determines an increased flow of Faradaic currents (Kotov et al., 2009). Another plus is represented by the increased spatial resolution of neural stimulation compared to microelectrodes (Fattahi et al., 2014), and the possibility to miniaturize several parallel nanoelectrodes within the same device, so to be used for simultaneous multiplexed measurements (Wang M. et al., 2018). Indeed, a more accurate control of the structural features of neural interfaces at subcellular level, with improved electrical properties, is preferable for neural recordings *in vivo*, while limiting detrimental side effects.

However, the chronic use of such invasive, although soft and small-sized electrodes, for neuroprosthetic applications will require biochemical functionalization of the surface with biocompatible coatings. These could be bioactive moieties (e.g., specific chemical signals from peptide epitopes) incorporated within conductive polymers, leveraging their tunable physicochemical properties that provide a wide versatility of intervention. A detailed investigation on how the nanotopography modifications and the chemical reactive potential of the surface can reduce plasma protein adsorption and immune cell adhesion will help control the inflammatory response. In addition, the controlled and continuous release of neurotrophic factors and the targeted delivery of therapeutic drugs to further improve the biological response to the implant and avoid the FBR will be of paramount importance. Accordingly, tailoring zwitterionic hydrogels to incorporate bioactive materials, such as ECM-derived organic components (e.g., RGD motifs that mediate the cell-fibronectin attachment) or neural cells will be pivotal (Von Der Mark et al., 2010). In this regard, it could be envisioned as particularly appealing a cell-based co-therapy, with the integration of autologous neural cells or patient-specific induced pluripotent stem cell (iPSC)-derived neural cells into the interface coating so to escape their recognition by the host immune system, hampering the consequent inflammatory cascade (Xu et al., 2013; Amin et al., 2016). Together with these solutions, loading the hydrogel with selected chemicals and drugs either linked to the surface or encapsulated into novel NPs seem the best routes to take (Aregueta-Robles et al., 2014; Lotti et al., 2017). Also, diffusion-mediated delivery systems based on micro-optical fluidic devices and microfluidic channels integrated into neural interfaces may represent another valid intervention strategy for a controlled release of therapeutics in chronic implants (Retterer et al., 2004; Takehara et al., 2014). These newly developed microfluidic devices have been characterized only *in vitro* and *in vivo*, though in mouse brain and in chronically implanted intracortical probes in rats, but they have been proven to be effective in controlling and hindering reactive responses in neural cells and brain tissue.

How limiting the leakage and the exhaustion of the drug payload in the microenvironment around the electrode site? This question still remains an open issue that the implementation of surface micromachining for the synthesis of NPs as ideal drug carriers, and microfluidic technologies could likely solve in the next years. For instance, integration and modification of the electrode surface through MEMS devices, microactuators and DSRs with permeable actuating membranes, may at least help control the pharmacological release and limit the drug leakage.

It is well known that biomaterials or tissue-engineered constructs can strongly influence the interactions between a foreign body and the host immune system. Therefore, the deposition technology of the most appropriate coating on the invasive electrode and its modification with biomimetic surfaces targeted to support tissue-specific cell functions will pave the way to the definitive solution for mitigating the FBR and for advancing the long-term use of neural-interfaced prostheses.

It follows that, before *in vivo* testing, the choice of the best biomimetic coating to be used will rely on preliminary results gained from complex *in vitro* co-culture systems, as Lab-on-a-Chip devices. The latter should indeed be developed so as to recapitulate more closely all biological aspects of the intricate tissue damage, vascular injury and inflammatory cascade associated with electrode implantation. Thus, leveraging on complex microfluidic and, hopefully, nanofluidic co-culture platforms for mimicking both nervous tissue microenvironment, with patient-specific cell types, and the implant-induced FBR, one could preliminarily analyze the tissue response to a certain biomaterial coating in a physiologically relevant manner (Sharifi et al., 2019). Such opportunity raises the need for a strict collaboration between medical sciences and bioengineering. The former are necessary for having a detailed knowledge on specific mechanisms and timing of adsorption of the host proteins and cells on the implant surface; bioengineering expertise and technologies are instead essential to reproduce and simulate the entire environment, behavior and physiological responses of the nervous tissue to biomaterials. Additional work will be required to identify exactly and control the biological mechanisms of the wound healing process, and shed light on the causal connections between mechanical, chemical, immunological and inflammatory events underlying the acute and chronic peripheral nerve response. Notably, the important role played by the blood-nerve barrier must be better investigated, whose stability can be compromised by the traumatic event of the device insertion (Stubbs, 2020).

A further technical enrichment for increasing *a priori* our knowledge on the mechanisms underlying the development of the FBR for a more effective electrode engineering, comes from the use of *in silico* methods. In this respect, a very illuminating example showed a data-driven approach based on polynomial functions to simulate and investigate the development of scar tissue outgrowth around an implanted neural device over time (Sergi et al., 2020). Such computer-based approach could be combined with micro/nanofabrication and biochemical functionalization techniques for having a more representative prediction of the possible fibrous capsule consistency before collecting experimental data, thereby helping scientists in the choice of the most suitable surface coating against the development of the FBR (Di Pino et al., 2010). Overall, addressing these interesting challenges will require a close interaction between neuroengineering and biology on multiple levels for producing and, once inserted, stabilizing cutting-edge neural interfaces, and thus responding to the requests of the clinical therapy.

AUTHOR CONTRIBUTIONS

MG conceived the idea, wrote the manuscript, and prepared figures and tables. GV supervised and revised the manuscript. SG contributed to wrote the manuscript and prepared the tables. VD supervised the manuscript preparation. GD contributed to wrote, supervised, revised, and critically discussed the manuscript. All authors contributed to the article and approved the submitted version.

FUNDING

Funding for the open access publication fees was provided in the framework of the joint projects: WiFi Myo-Hand "Sistema impiantabile ottimizzato per l'interfacciamento con il sistema nervoso periferico e il controllo della protesi di arto superiore" and "RGM5: (re)-Give me five, exploring new frontiers in prosthetic surgery" between Università Campus Bio-Medico di Roma (UCBM) and Istituto Nazionale per l'Assicurazione contro gli Infortuni sul Lavoro (INAIL).

ACKNOWLEDGMENTS

The authors acknowledge the financial support from Istituto Nazionale per l'Assicurazione contro gli Infortuni sul Lavoro (INAIL). MG dedicates this review article to Agnese for her loving commitment to our kids and the resilience shown during the harsh lockdown due to the COVID-19 pandemic.

REFERENCES

Abidian, M. R., Corey, J. M., Kipke, D. R., and Martin, D. C. (2010). Conducting-polymer nanotubes improve electrical properties, mechanical adhesion, neural attachment and neurite outgrowth of neural electrodes. *Small* 6, 421–429. doi: 10.1002/smll.200901868

Ahn, S. H., Jeong, J., and Kim, S. J. (2019). Emerging encapsulation technologies for long-term reliability of microfabricated implantable devices. *Micromachines* 10:508. doi: 10.3390/mi10080508

Alba, N. A., Du, Z. J., Catt, K. A., Kozai, T. D. Y., and Cui, X. T. (2015). In vivo electrochemical analysis of a PEDOT/MWCNT neural electrode coating. *Biosensors* 5, 618–646. doi: 10.3390/bios5040618

Altun, A., Apetrei, R. M., and Camurlu, P. (2019). The effect of copolymerization and carbon nanoelements on the performance of poly(2,5-di(thienyl)pyrrole) biosensors. *Mater. Sci. Eng. C* 105:110069. doi: 10.1016/j.msec.2019.110069

Ambrico, M., Ambrico, P. F., Cardone, A., Cicco, S. R., Palumbo, F., Ligonzo, T., et al. (2014). Melanin-like polymer layered on a nanotextured silicon surface for a hybrid biomimetic interface. *J. Mater. Chem. C* 2, 573–582. doi: 10.1039/c3tc31327a

Ambrico, M., Ambrico, P. F., Cardone, A., Della Vecchia, N. F., Ligonzo, T., Cicco, S. R., et al. (2013). Engineering polydopamine films with tailored behaviour for next-generation eumelanin-related hybrid devices. *J. Mater. Chem. C* 1, 1018–1028. doi: 10.1039/c2tc00480a

Amin, H., Maccione, A., Marinaro, F., Zordan, S., Nieus, T., and Berdondini, L. (2016). Electrical responses and spontaneous activity of human iPS-derived neuronal networks characterized for 3-month culture with 4096-electrode arrays. *Front. Neurosci.* 10:121. doi: 10.3389/fnins.2016.00121

Anderson, H. E., and Weir, R. F. (2019). On the development of optical peripheral nerve interfaces. *Neural Regen. Res.* 14, 425–436. doi: 10.4103/1673-5374.245461

Anderson, J. M. (2000). Multinucleated giant cells. *Curr. Opin. Hematol.* 7, 40–47. doi: 10.1097/00062752-200001000-00008

Anderson, J. M., Defife, K., Mcnally, A., Collier, T., and Jenney, C. (1999). Monocyte, macrophage and foreign body giant cell interactions with

molecularly engineered surfaces. *J. Mater. Sci. Mater. Med.* 10, 579–588. doi: 10.1023/a:1008976531592

Anderson, J. M., Rodriguez, A., and Chang, D. T. (2008). Foreign body reaction to biomaterials. *Semin. Immunol.* 20, 86–100. doi: 10.1016/j.smim.2007.11.004

Andrade, J. D., and Hlady, V. (1987). Plasma protein adsorption: the big twelve. *Ann. N. Y. Acad. Sci.* 516, 158–172. doi: 10.1111/j.1749-6632.1987.tb33038.x

Aregueta-Robles, U. A., Woolley, A. J., Poole-Warren, L. A., Lovell, N. H., and Green, R. A. (2014). Organic electrode coatings for next-generation neural interfaces. *Front. Neuroeng.* 7:15. doi: 10.3389/fneng.2014.00015

Armstrong, D. A., Major, J. A., Chudyk, A., and Hamilton, T. A. (2004). Neutrophil chemoattractant genes KC and MIP-2 are expressed in different cell populations at sites of surgical injury. *J. Leukoc. Biol.* 75, 641–648. doi: 10.1189/jlb.0803370

Arreaga-Salas, D. E., Avendaño-Bolívar, A., Simon, D., Reit, R., Garcia-Sandoval, A., Rennaker, R. L., et al. (2015). Integration of high-charge-injection-capacity electrodes onto polymer softening neural interfaces. *ACS Appl. Mater. Interf.* 7, 26614–26623. doi: 10.1021/acsami.5b08139

Ashcroft, G. S. (1999). Bidirectional regulation of macrophage function by TGF-β. *Microb. Infect.* 1, 1275–1282. doi: 10.1016/S1286-4579(99)00257-9

Badia, J., Boretius, T., Andreu, D., Azevedo-Coste, C., Stieglitz, T., and Navarro, X. (2011). Comparative analysis of transverse intrafascicular multichannel, longitudinal intrafascicular and multipolar cuff electrodes for the selective stimulation of nerve fascicles. *J. Neural Eng.* 8:36023. doi: 10.1088/1741-2560/8/3/036023

Badia, J., Raspopovic, S., Carpaneto, J., Micera, S., and Navarro, X. (2016). Spatial and functional selectivity of peripheral nerve signal recording with the transversal intrafascicular multichannel electrode (TIME). *IEEE Trans. Neural Syst. Rehabil. Eng.* 24, 20–27. doi: 10.1109/TNSRE.2015.2440768

Balint, R., Cassidy, N. J., and Cartmell, S. H. (2014). Conductive polymers: towards a smart biomaterial for tissue engineering. *Acta Biomater.* 10, 2341–2353. doi: 10.1016/j.actbio.2014.02.015

Banks, R. E., Forbes, M. A., Kinsey, S. E., Stanley, A., Ingham, E., Walters, C., et al. (1998). Release of the angiogenic cytokine vascular endothelial growth factor (VEGF) from platelets: significance for VEGF measurements and cancer biology. *Br. J. Cancer* 77, 956–964. doi: 10.1038/bjc.1998.158

Bazard, P., Frisina, R. D., Walton, J. P., and Bhethanabotla, V. R. (2017). Nanoparticle-based plasmonic transduction for modulation of electrically excitable cells. *Sci. Rep.* 7:7803. doi: 10.1038/s41598-017-08141-4

Bellingan, G. J. (1996). In vivo fate of the inflammatory macrophage during the resolution of inflammation: inflammatory macrophages do not die locally, but emigrate to the draining lymph nodes. *J. Immunol.* 157, 2577–2585.

Blakney, A. K., Swartzlander, M. D., and Bryant, S. J. (2012). Student award winner in the undergraduate category for the society of biomaterials 9th World Biomaterials Congress, Chengdu, China, June 1-5, 2012: the effects of substrate stiffness on the in vitro activation of macrophages and in vivo host response to poly(ethylene glycol)-based hydrogels. *J. Biomed. Mater. Res. Part A* 100 A, 1375–1386. doi: 10.1002/jbm.a.34104

Blau, A., Murr, A., Wolff, S., Sernagor, E., Medini, P., Iurilli, G., et al. (2011). Flexible, all-polymer microelectrode arrays for the capture of cardiac and neuronal signals. *Biomaterials* 32, 1778–1786. doi: 10.1016/j.biomaterials.2010.11.014

Bochenek, M. A., Veiseh, O., Vegas, A. J., McGarrigle, J. J., Qi, M., Marchese, E., et al. (2018). Alginate encapsulation as long-term immune protection of allogeneic pancreatic islet cells transplanted into the omental bursa of macaques. *Nat. Biomed. Eng.* 2, 810–821. doi: 10.1038/s41551-018-0275-1

Boddupalli, A., Zhu, L., and Bratlie, K. M. (2016). Methods for implant acceptance and wound healing: material selection and implant location modulate macrophage and fibroblast phenotypes. *Adv. Healthc. Mater.* 5, 2575–2594. doi: 10.1002/adhm.201600532

Boehler, C., Kleber, C., Martini, N., Xie, Y., Dryg, I., Stieglitz, T., et al. (2017). Actively controlled release of Dexamethasone from neural microelectrodes in a chronic in vivo study. *Biomaterials* 129, 176–187. doi: 10.1016/j.biomaterials.2017.03.019

Bottini, M., Bruckner, S., Nika, K., Bottini, N., Bellucci, S., Magrini, A., et al. (2006). Multi-walled carbon nanotubes induce T lymphocyte apoptosis. *Toxicol. Lett.* 160, 121–126. doi: 10.1016/j.toxlet.2005.06.020

Branner, A., Stein, R. B., Fernandez, E., Aoyagi, Y., and Normann, R. A. (2004). Long-term stimulation and recording with a penetrating microelectrode array in cat sciatic nerve. *IEEE Trans. Biomed. Eng.* 51, 146–157. doi: 10.1109/TBME.2003.820321

Brummer, S. B., Robblee, L. S., and Hambrecht, F. T. (1983). Criteria for selecting electrodes for electrical stimulation: theoretical and practical considerations. *Ann. N. Y. Acad. Sci.* 405, 159–171. doi: 10.1111/j.1749-6632.1983.tb31628.x

Cai, X. J., and Xu, Y. Y. (2011). Nanomaterials in controlled drug release. *Cytotechnology* 63, 319–323. doi: 10.1007/s10616-011-9366-5

Campioni, E. G., Nobrega, J. N., and Sefton, M. V. (1998). HEMA/MMMA microcapsule implants in hemiparkinsonian rat brain: biocompatibility assessment using [3H]PK11195 as a marker for gliosis. *Biomaterials* 19, 829–837. doi: 10.1016/S0142-9612(97)00241-X

Canales, A., Jia, X., Froriep, U. P., Koppes, R. A., Tringides, C. M., Selvidge, J., et al. (2015). Multifunctional fibers for simultaneous optical, electrical and chemical interrogation of neural circuits in vivo. *Nat. Biotechnol.* 33, 277–284. doi: 10.1038/nbt.3093

Carli, S., Bianchi, M., Zucchini, E., Di Lauro, M., Prato, M., Murgia, M., et al. (2019). Electrodeposited PEDOT:Nafion composite for neural recording and stimulation. *Adv. Healthc. Mater.* 8:e1900765. doi 10.1002/adhm.201900765

Carr, L. R., Zhou, Y., Krause, J. E., Xue, H., and Jiang, S. (2011). Uniform zwitterionic polymer hydrogels with a nonfouling and functionalizable crosslinker using photopolymerization. *Biomaterials* 32, 6893–6899. doi: 10.1016/j.biomaterials.2011.06.006

Castagnola, E., Maggiolini, E., Ceseracciu, L., Ciarpella, F., Zucchini, E., De Faveri, S., et al. (2016). pHEMA encapsulated PEDOT-PSS-CNT microsphere microelectrodes for recording single unit activity in the brain. *Front. Neurosci.* 10:151. doi: 10.3389/fnins.2016.00151

Chang, K. C., Lu, H. I., Peng, C. W., Lai, M. C., Hsu, S. C., Hsu, M. H., et al. (2013). Nanocasting technique to prepare lotus-leaf-like superhydrophobic electroactive polyimide as advanced anticorrosive coatings. *ACS Appl. Mater. Interf.* 5, 1460–1467. doi: 10.1021/am3029377

Chang, T. M. S. (1964). Semipermeable microcapsules. *Science* 146, 524–525. doi: 10.1126/science.146.3643.524

Charkhkar, H., Knaack, G. L., Mchail, D. G., Mandal, H. S., Peixoto, N., Rubinson, J. F., et al. (2016). Chronic intracortical neural recordings using microelectrode arrays coated with PEDOT-TFB. *Acta Biomater.* 32, 57–67. doi: 10.1016/j.actbio.2015.12.022

Chatzimichail, S., Supramaniam, P., Ces, O., and Salehi-Reyhani, A. (2018). Micropatterning of planar metal electrodes by vacuum filling microfluidic channel geometries. *Sci. Rep.* 8:14380. doi: 10.1038/s41598-018-32706-6

Chen, C., Chen, X., Zhang, H., Zhang, Q., Wang, L., Li, C., et al. (2017). Electrically-responsive core-shell hybrid microfibers for controlled drug release and cell culture. *Acta Biomater.* 55, 434–442. doi: 10.1016/j.actbio.2017.04.005

Chen, S., Jones, J. A., Xu, Y., Low, H. Y., Anderson, J. M., and Leong, K. W. (2010). Characterization of topographical effects on macrophage behavior in a foreign body response model. *Biomaterials* 31, 3479–3491. doi: 10.1016/j.biomaterials.2010.01.074

Chen, S., Zheng, J., Li, L., and Jiang, S. (2005). Strong resistance of phosphorylcholine self-assembled monolayers to protein adsorption: insights into nonfouling properties of zwitterionic materials. *J. Am. Chem. Soc.* 127, 14473–14478. doi: 10.1021/ja054169u

Crowe, M. J., Doetschman, T., and Greenhalgh, D. G. (2000). Delayed wound healing in immunodeficient TGF-β1 knockout mice. *J. Invest. Dermatol.* 115, 3–11. doi: 10.1046/j.1523-1747.2000.00010.x

Cui, X., Wiler, J., Dzaman, M., Altschuler, R. A., and Martin, D. C. (2003). In vivo studies of polypyrrole/peptide coated neural probes. *Biomaterials* 24, 777–787. doi: 10.1016/S0142-9612(02)00415-5

de la Oliva, N., Del Valle, J., Delgado-Martinez, I., Mueller, M., Stieglitz, T., and Navarro, X. (2019). Long-term functionality of transversal intraneural electrodes is improved by dexamethasone treatment. *IEEE Trans. Neural Syst. Rehabil. Eng.* 27, 457–464. doi: 10.1109/TNSRE.2019.2897256

de la Oliva, N., Mueller, M., Stieglitz, T., Navarro, X., and Del Valle, J. (2018a). On the use of Parylene C polymer as substrate for peripheral nerve electrodes. *Sci. Rep.* 8:5965. doi: 10.1038/s41598-018-24502-z

de la Oliva, N., Navarro, X., and del Valle, J. (2018b). Dexamethasone reduces the foreign body reaction to intraneural electrode implants in the peripheral nerve of the rat. *Anat. Rec.* 301, 1722–1733. doi: 10.1002/ar.23920

de la Oliva, N., Navarro, X., and del Valle, J. (2018c). Time course study of long-term biocompatibility and foreign body reaction to intraneural polyimide-based implants. *J. Biomed. Mater. Res. Part A* 106, 746–757. doi: 10.1002/jbm.a.36274

Delgado-Martínez, I., Righi, M., Santos, D., Cutrone, A., Bossi, S., D'Amico, S., et al. (2017). Fascicular nerve stimulation and recording using a novel double-aisle regenerative electrode. *J. Neural Eng.* 14:aa6bac. doi: 10.1088/1741-2552/aa6bac

Deuschl, G., Schade-Brittinger, C., Krack, P., Volkmann, J., Schäfer, H., Bötzel, K., et al. (2006). A randomized trial of deep-brain stimulation for Parkinson's disease. *N. Engl. J. Med.* 355, 896–908. doi: 10.1056/nejmoa060281

Di Pino, G., Denaro, L., Vadalà, G., Marinozzi, A., Tombini, M., Ferreri, F., et al. (2014). Invasive neural interfaces: the perspective of the surgeon. *J. Surg. Res.* 188, 77–87. doi: 10.1016/j.jss.2013.12.014

Di Pino, G., Formica, D., Lonini, L., Accoto, D., Benvenuto, A., Micera, S., et al. (2010). ODEs model of foreign body reaction around peripheral nerve implanted electrode. *Annu. Int. Conf. IEEE Eng. Med. Biol. Soc.* 2010, 1543–1546. doi: 10.1109/IEMBS.2010.5626825

Di Pino, G., Porcaro, C., Tombini, M., Assenza, G., Pellegrino, G., Tecchio, F., et al. (2012). A neurally-interfaced hand prosthesis tuned inter-hemispheric communication. *Restor. Neurol. Neurosci.* 30, 407–418. doi: 10.3233/RNN-2012-120224

Diao, W., Wu, L., Ma, X., Zhuang, Z., Li, S., Bu, X., et al. (2019). Highly stretchable, ionic conductive and self-recoverable zwitterionic polyelectrolyte-based hydrogels by introducing multiple supramolecular sacrificial bonds in double network. *J. Appl. Polym. Sci.* 136:47783. doi 10.1002/app.47783

DiPietro, L. A., Burdick, M., Low, Q. E., Kunkel, S. L., and Strieter, R. M. (1998). Mip-1α as a critical macrophage chemoattractant in murine wound repair. *J. Clin. Invest.* 101, 1693–1698. doi: 10.1172/JCI1020

Dolan, A. (2019). Title an actuatable soft reservoir modulates host foreign body response Publication Information. *Sci. Robot.* 4:eaax7043. doi: 10.1126/scirobotics.aax7043

Doloff, J. C., Veiseh, O., Vegas, A. J., Tam, H. H., Farah, S., Ma, M., et al. (2017). Colony stimulating factor-1 receptor is a central component of the foreign body response to biomaterial implants in rodents and non-human primates. *Nat. Mater.* 16, 671–680. doi: 10.1038/nmat4866

Drury, J. L., and Mooney, D. J. (2003). Hydrogels for tissue engineering: scaffold design variables and applications. *Biomaterials* 24, 4337–4351. doi: 10.1016/S0142-9612(03)00340-5

Du, Z. J., Bi, G. Q., and Cui, X. T. (2018). Electrically controlled neurochemical release from dual-layer conducting polymer films for precise modulation of neural network activity in rat barrel cortex. *Adv. Funct. Mater.* 28:1703988. doi: 10.1002/adfm.201703988

Elyahoodayan, S., Larson, C., Cobo, A. M., Meng, E., and Song, D. (2020). Acute in vivo testing of a polymer cuff electrode with integrated microfluidic channels for stimulation, recording, and drug delivery on rat sciatic nerve. *J. Neurosci. Methods* 336:108634. doi: 10.1016/j.jneumeth.2020.108634

Fallahi, H., Zhang, J., Phan, H. P., and Nguyen, N. T. (2019). Flexible microfluidics: fundamentals, recent developments, and applications. *Micromachines* 10:830. doi: 10.3390/mi10120830

Fattahi, P., Yang, G., Kim, G., and Abidian, M. R. (2014). A review of organic and inorganic biomaterials for neural interfaces. *Adv. Mater.* 26, 1846–1885. doi: 10.1002/adma.201304496

Fekete, Z., and Pongrácz, A. (2017). Multifunctional soft implants to monitor and control neural activity in the central and peripheral nervous system: a review. *Sens. Actuat. B Chem.* 243, 1214–1223. doi: 10.1016/j.snb.2016.12.096

Ferlauto, L., D'Angelo, A. N., Vagni, P., Leccardi, M. J. I. A., Mor, F. M., Cuttaz, E. A., et al. (2018). Development and characterization of PEDOT:PSS/alginate soft microelectrodes for application in neuroprosthetics. *Front. Neurosci.* 12:648. doi: 10.3389/fnins.2018.00648

Ferrara, N., Gerber, H. P., and LeCouter, J. (2003). The biology of VEGF and its receptors. *Nat. Med.* 9, 669–676. doi: 10.1038/nm0603-669

Ferreri, F., Ponzo, D., Vollero, L., Guerra, A., Di Pino, G., Petrichella, S., et al. (2014). Does an intraneural interface short-term implant for robotic hand control modulate sensorimotor cortical integration? An EEG-TMS co-registration study on a human amputee. *Restor. Neurol. Neurosci.* 32, 281–292. doi: 10.3233/RNN-130347

Fink, J., Fuhrmann, R., Scharnweber, T., and Franke, R. P. (2008). Stimulation of monocytes and macrophages: possible influence of surface roughness. *Clin. Hemorheol. Microcirc.* 39, 205–212. doi: 10.3233/ch-2008-1090

Freeberg, M. J., Pinault, G. C. J., Tyler, D. J., Triolo, R. J., and Ansari, R. (2020). Chronic nerve health following implantation of femoral nerve cuff electrodes. *J. Neuroeng. Rehabil.* 17:95. doi: 10.1186/s12984-020-00720-3

Gamboa, J. R., Mohandes, S., Tran, P. L., Slepian, M. J., and Yoon, J. Y. (2013). Linear fibroblast alignment on sinusoidal wave micropatterns. *Colloids Surf. B Biointerf.* 104, 318–325. doi: 10.1016/j.colsurfb.2012.11.035

Ganji, M., Hossain, L., Tanaka, A., Thunemann, M., Halgren, E., Gilja, V., et al. (2018). Monolithic and scalable au nanorod substrates improve PEDOT-metal adhesion and stability in neural electrodes. *Adv. Healthc. Mater.* 7:923. doi: 10.1002/adhm.201800923

Gao, K., Li, G., Liao, L., Cheng, J., Zhao, J., and Xu, Y. (2013). Fabrication of flexible microelectrode arrays integrated with microfluidic channels for stable neural interfaces. *Sens. Actuat. A Phys.* 197, 9–14. doi: 10.1016/j.sna.2013.04.005

Garde, K., Keefer, E., Botterman, B., Galvan, P., and Romero-Ortega, M. I. (2009). Early interfaced neural activity from chronic amputated nerves. *Front. Neuroeng.* 2:5. doi: 10.3389/neuro.16.005.2009

Geddes, L. A., and Roeder, R. (2003). Criteria for the selection of materials for implanted electrodes. *Ann. Biomed. Eng.* 31, 879–890. doi: 10.1114/1.1581292

Gelmi, A., Cieslar-Pobuda, A., de Muinck, E., Los, M., Rafat, M., and Jager, E. W. H. (2016). Direct mechanical stimulation of stem cells: a beating electromechanically active scaffold for cardiac tissue engineering. *Adv. Healthc. Mater.* 5, 1471–1480. doi: 10.1002/adhm.201600307

Gerwig, R., Fuchsberger, K., Schroeppel, B., Link, G. S., Heusel, G., Kraushaar, U., et al. (2012). PEDOT-CNT composite microelectrodes for recording and electrostimulation applications: fabrication, morphology, and electrical properties. *Front. Neuroeng.* 5:8. doi: 10.3389/fneng.2012.00008

Gilletti, A., and Muthuswamy, J. (2006). Brain micromotion around implants in the rodent somatosensory cortex. *J. Neural Eng.* 3, 189–195. doi: 10.1088/1741-2560/3/3/001

Gilmour, A. D., Green, R. A., and Thomson, C. E. (2013). A low-maintenance, primary cell culture model for the assessment of carbon nanotube toxicity. *Toxicol. Environ. Chem.* 95, 1129–1144. doi: 10.1080/02772248.2013.844429

Gori, M., Trombetta, M., Santini, D., and Rainer, A. (2015). Tissue engineering and microRNAs: future perspectives in regenerative medicine. *Expert Opin. Biol. Ther.* 15, 1601–1622. doi: 10.1517/14712598.2015.1071349

Green, R. A., Hassarati, R. T., Goding, J. A., Baek, S., Lovell, N. H., Martens, P. J., et al. (2012). Conductive hydrogels: mechanically robust hybrids for use as biomaterials. *Macromol. Biosci.* 12, 494–501. doi: 10.1002/mabi.201100490

Green, R. A., Lovell, N. H., and Poole-Warren, L. A. (2009). Cell attachment functionality of bioactive conducting polymers for neural interfaces. *Biomaterials* 30, 3637–3644. doi: 10.1016/j.biomaterials.2009.03.043

Green, R. A., Lovell, N. H., Wallace, G. G., and Poole-Warren, L. A. (2008). Conducting polymers for neural interfaces: challenges in developing an effective long-term implant. *Biomaterials* 29, 3393–3399. doi: 10.1016/j.biomaterials.2008.04.047

Green, R. A., Matteucci, P. B., Hassarati, R. T., Giraud, B., Dodds, C. W., Chen, S., et al. (2013). Performance of conducting polymer electrodes for stimulating neuroprosthetics. *J. Neural Eng.* 10:016009. doi: 10.1088/1741-2560/10/1/016009

Guadarrama-Santana, A., and Garcia-Valenzuela, A. (2007). Determination of thickness and dielectric constant of coatings from capacitance measurements. *IEEE Instrum. Measur. Mag.* 10, 26–31. doi: 10.1109/MIM.2007.4343564

Guo, L., Ma, M., Zhang, N., Langer, R., and Anderson, D. G. (2014). Stretchable polymeric multielectrode array for conformal neural interfacing. *Adv. Mater.* 26, 1427–1433. doi: 10.1002/adma.201304140

Gutowski, S. M., Shoemaker, J. T., Templeman, K. L., Wei, Y., Latour, R. A., Bellamkonda, R. V., et al. (2015). Protease-degradable PEG-maleimide coating with on-demand release of IL-1Ra to improve tissue response to neural electrodes. *Biomaterials* 44, 55–70. doi: 10.1016/j.biomaterials.2014.12.009

Hancock, W. W., Gao, W., Faia, K. L., and Csizmadia, V. (2000). Chemokines and their receptors in allograft rejection. *Curr. Opin. Immunol.* 12, 511–516. doi: 10.1016/S0952-7915(00)00130-8

Hassler, C., Guy, J., Nietzschmann, M., Plachta, D. T. T., Staiger, J. F., and Stieglitz, T. (2016). Intracortical polyimide electrodes with a bioresorbable coating. *Biomed. Microdev.* 18:81. doi: 10.1007/s10544-016-0106-7

Heo, D. N., Song, S. J., Kim, H. J., Lee, Y. J., Ko, W. K., Lee, S. J., et al. (2016). Multifunctional hydrogel coatings on the surface of neural cuff electrode for improving electrode-nerve tissue interfaces. *Acta Biomater.* 39, 25–33. doi: 10.1016/j.actbio.2016.05.009

Hosseini-Nassab, N., Samanta, D., Abdolazimi, Y., Annes, J. P., and Zare, R. N. (2017). Electrically controlled release of insulin using polypyrrole nanoparticles. *Nanoscale* 9, 143–149. doi: 10.1039/c6nr08288b

Hu, Y., Yang, G., Liang, B., Fang, L., Ma, G., Zhu, Q., et al. (2015). The fabrication of superlow protein absorption zwitterionic coating by electrochemically mediated atom transfer radical polymerization and its application. *Acta Biomater.* 13, 142–149. doi: 10.1016/j.actbio.2014.11.023

Hulander, M., Lundgren, A., Faxälv, L., Lindahl, T. L., Palmquist, A., Berglin, M., et al. (2013). Gradients in surface nanotopography used to study platelet adhesion and activation. *Colloids Surf. B Biointerf.* 110, 261–269. doi: 10.1016/j.colsurfb.2013.04.010

Hunt, J. A., Flanagan, B. F., McLaughlin, P. J., Strickland, I., and Williams, D. F. (1996). Effect of biomaterial surface charge on the inflammatory response: evaluation of cellular infiltration and TNFα production. *J. Biomed. Mater. Res.* 31, 139–144. doi: 10.1002/(sici)1097-4636(199605)31:1<139::aid-jbm15>3.0.co;2-i

Isaksson, J., Kjäll, P., Nilsson, D., Robinson, N., Berggren, M., and Richter-Dahlfors, A. (2007). Electronic control of Ca2+ signalling in neuronal cells using an organic electronic ion pump. *Nat. Mater.* 6, 673–679. doi: 10.1038/nmat1963

Jayamani, E., Hamdan, S., Rahman, R., and Bakri, M. K. B. (2014). Comparative Study of dielectric properties of hybrid natural fiber composites. *Proc. Eng.* 97, 536–544. doi: 10.1016/j.proeng.2014.12.280

Jenney, C. R., and Anderson, J. M. (2000). Adsorbed serum proteins responsible for surface dependent human macrophage behavior. *J. Biomed. Mater. Res.* 49, 435–447. doi: 10.1002/(sici)1097-4636(20000315)49:4<435::aid-jbm2>3.0.co;2-y

Jhaveri, S. J., Hynd, M. R., Dowell-Mesfin, N., Turner, J. N., Shain, W., and Ober, C. K. (2009). Release of nerve growth factor from HEMA hydrogel-coated substrates and its effect on the differentiation of neural cells. *Biomacromolecules* 10, 174–183. doi: 10.1021/bm801101e

Ji, B., Guo, Z., Wang, M., Yang, B., Wang, X., Li, W., et al. (2018). Flexible polyimide-based hybrid opto-electric neural interface with 16 channels of micro-LEDs and electrodes. *Microsyst. Nanoeng.* 4:27. doi: 10.1038/s41378-018-0027-0

Jiang, S., and Cao, Z. (2010). Ultralow-fouling, functionalizable, and hydrolyzable zwitterionic materials and their derivatives for biological applications. *Adv. Mater.* 22, 920–932. doi: 10.1002/adma.200901407

Jonsson, A., Song, Z., Nilsson, D., Meyerson, B. A., Simon, D. T., Linderoth, B., et al. (2015). Therapy using implanted organic bioelectronics. *Sci. Adv.* 1:e1500039. doi: 10.1126/sciadv.1500039

Kagan, V. E., Tyurina, Y. Y., Tyurin, V. A., Konduru, N. V., Potapovich, A. I., Osipov, A. N., et al. (2006). Direct and indirect effects of single walled carbon nanotubes on RAW 264.7 macrophages: role of iron. *Toxicol. Lett.* 165, 88–100. doi: 10.1016/j.toxlet.2006.02.001

Kałuża, D., Jaworska, E., Mazur, M., Maksymiuk, K., and Michalska, A. (2019). Multiwalled Carbon Nanotubes-Poly(3-octylthiophene-2,5-diyl) nanocomposite transducer for ion-selective electrodes: raman spectroscopy insight into the transducer/Membrane interface. *Anal. Chem.* 91, 9010–9017. doi: 10.1021/acs.analchem.9b01286

Kang, Y. N., Chou, N., Jang, J. W., Byun, D., Kang, H., Moon, D. J., et al. (2019). An intrafascicular neural interface with enhanced interconnection for recording of peripheral nerve signals. *IEEE Trans. Neural Syst. Rehabil. Eng.* 27, 1312–1319. doi: 10.1109/TNSRE.2019.2917916

Kim, D. H., and Martin, D. C. (2006). Sustained release of dexamethasone from hydrophilic matrices using PLGA nanoparticles for neural drug delivery. *Biomaterials* 27, 3031–3037. doi: 10.1016/j.biomaterials.2005.12.021

Kim, Y. K., Que, R., Wang, S. W., and Liu, W. F. (2014). Modification of biomaterials with a self-protein inhibits the macrophage response. *Adv. Healthc. Mater.* 3, 989–994. doi: 10.1002/adhm.201300532

Kleber, C., Bruns, M., Lienkamp, K., Rühe, J., and Asplund, M. (2017). An interpenetrating, microstructurable and covalently attached conducting polymer hydrogel for neural interfaces. *Acta Biomater.* 58, 365–375. doi: 10.1016/j.actbio.2017.05.056

Kleber, C., Lienkamp, K., Rühe, J., and Asplund, M. (2019). electrochemically controlled drug release from a conducting polymer hydrogel (PDMAAp/PEDOT) for local therapy and bioelectronics. *Adv. Healthc. Mater.* 8:1801488. doi: 10.1002/adhm.201801488

Knop, K., Hoogenboom, R., Fischer, D., and Schubert, U. S. (2010). Poly(ethylene glycol) in drug delivery: pros and cons as well as potential alternatives. *Angew. Chemie Int. Edn.* 49, 6288–6308. doi: 10.1002/anie.200902672

Kotov, N. A., Winter, J. O., Clements, I. P., Jan, E., Timko, B. P., Campidelli, S., et al. (2009). Nanomaterials for neural interfaces. *Adv. Mater.* 21, 3970–4004. doi: 10.1002/adma.200801984

Kozai, T. D. Y. (2018). The history and horizons of microscale neural interfaces. *Micromachines* 9:445. doi: 10.3390/mi9090445

Krishnan, A., Dujardin, E., and Ebbesen, T. (1998). Young's modulus of single-walled nanotubes. *Phys. Rev. B Condens. Matter Mater. Phys.* 58, 14013–14019. doi: 10.1103/PhysRevB.58.14013

Kumar, S. S., Baker, M. S., Okandan, M., and Muthuswamy, J. (2020). Engineering microscale systems for fully autonomous intracellular neural interfaces. *Microsyst. Nanoeng.* 6:1. doi: 10.1038/s41378-019-0121-y

Kwon, I. S., Kim, Y. J., Klosterman, L., Forssell, M., Fedder, G. K., and Bettinger, C. J. (2016). In vitro electrochemical characterization of polydopamine melanin as a tissue stimulating electrode material. *J. Mater. Chem. B* 4, 3031–3036. doi: 10.1039/c5tb02618k

Kyriakides, T. R., Foster, M. J., Keeney, G. E., Tsai, A., Giachelli, C. M., Clark-Lewis, I., et al. (2004). The CC chemokine ligand, CCL2/MCP1, participates in macrophage fusion and foreign body giant cell formation. *Am. J. Pathol.* 165, 2157–2166. doi: 10.1016/S0002-9440(10)63265-8

Lago, N., Yoshida, K., Koch, K. P., and Navarro, X. (2007). Assessment of biocompatibility of chronically implanted polyimide and platinum intrafascicular electrodes. *IEEE Trans. Biomed. Eng.* 54, 281–290. doi: 10.1109/TBME.2006.886617

Lam, J. K. W., Chow, M. Y. T., Zhang, Y., and Leung, S. W. S. (2015). siRNA versus miRNA as therapeutics for gene silencing. *Mol. Ther. Nucleic Acids* 4:e252. doi: 10.1038/mtna.2015.23

Leach, J. B., Achyuta, A. K. H., and Murthy, S. K. (2010). Bridging the divide between neuroprosthetic design, tissue engineering and neurobiology. *Front. Neuroeng.* 2:18. doi: 10.3389/neuro.16.018.2009

Leask, A., Holmes, A., and Abraham, D. J. (2002). Connective tissue growth factor: a new and important player in the pathogenesis of fibrosis. *Curr. Rheumatol. Rep.* 4, 136–142. doi: 10.1007/s11926-002-0009-x

Lecomte, A., Degache, A., Descamps, E., Dahan, L., and Bergaud, C. (2017). In vitro and in vivo biostability assessment of chronically-implanted Parylene C neural sensors. *Sens. Actuat. B Chem.* 251, 1001–1008. doi: 10.1016/j.snb.2017.05.057

Lee, D. H., Yun, H. D., Jung, E. D., Chu, J. H., Nam, Y. S., Song, S., et al. (2019). Ultrathin Graphene Intercalation in PEDOT:PSS/colorless polyimide-based transparent electrodes for enhancement of optoelectronic performance and operational stability of organic devices. *ACS Appl. Mater. Interf.* 11, 21069–21077. doi: 10.1021/acsami.9b04118

Lee, K. K., He, J., Singh, A., Massia, S., Ehteshami, G., Kim, B., et al. (2004). Polyimide-based intracortical neural implant with improved structural stiffness. *J. Micromech. Microeng.* 14, 32–37. doi: 10.1088/0960-1317/14/1/305

Lee, K. Y., and Mooney, D. J. (2012). Alginate: properties and biomedical applications. *Prog. Polym. Sci.* 37, 106–126. doi: 10.1016/j.progpolymsci.2011.06.003

Lee, Y. J., Kim, H. J., Kang, J. Y., Do, S. H., and Lee, S. H. (2017). Biofunctionalization of nerve interface via biocompatible polymer-roughened pt black on cuff electrode for chronic recording. *Adv. Healthc. Mater.* 6:1601022. doi: 10.1002/adhm.201601022

Lim, F., and Sun, A. M. (1980). Microencapsulated islets as bioartificial endocrine pancreas. *Science* 210, 908–910. doi: 10.1126/science.6776628

Lim, H. R., Kim, Y. S., Kwon, S., Mahmood, M., Kwon, Y. T., Lee, Y., et al. (2020). Wireless, flexible, ion-selective electrode system for selective and repeatable detection of sodium. *Sensors* 20, 1–11. doi: 10.3390/s20113297

Lishko, V. K., Podolnikova, N. P., Yakubenko, V. P., Yakovlev, S., Medved, L., Yadav, S. P., et al. (2004). Multiple binding sites in fibrinogen for integrin αMβ2 (Mac-1). *J. Biol. Chem.* 279, 44897–44906. doi: 10.1074/jbc.M408012200

Löffler, S., Seyock, S., Nybom, R., Jacobson, G. B., and Richter-Dahlfors, A. (2016). Electrochemically triggered release of acetylcholine from scCO2 impregnated conductive polymer films evokes intracellular Ca2 + signaling in neurotypic

SH-SY5Y cells. *J. Control. Release* 243, 283–290. doi: 10.1016/j.jconrel.2016.10.020

Lorach, H., Goetz, G., Smith, R., Lei, X., Mandel, Y., Kamins, T., et al. (2015). Photovoltaic restoration of sight with high visual acuity. *Nat. Med.* 21, 476–482. doi: 10.1038/nm.3851

Lotti, F., Ranieri, F., Vadalà, G., Zollo, L., and Di Pino, G. (2017). Invasive intraneural interfaces: foreign body reaction issues. *Front. Neurosci.* 11:497. doi: 10.3389/fnins.2017.00497

Lucke, S., Walschus, U., Hoene, A., Schnabelrauch, M., Nebe, J. B., Finke, B., et al. (2018). The in vivo inflammatory and foreign body giant cell response against different poly(l-lactide-co-d/l-lactide) implants is primarily determined by material morphology rather than surface chemistry. *J. Biomed. Mater. Res. Part A* 106, 2726–2734. doi: 10.1002/jbm.a.36500

Luo, X., Matranga, C., Tan, S., Alba, N., and Cui, X. T. (2011). Carbon nanotube nanoreservior for controlled release of anti-inflammatory dexamethasone. *Biomaterials* 32, 6316–6323. doi: 10.1016/j.biomaterials.2011.05.020

Luttikhuizen, D. T., Harmsen, M. C., and Van Luyn, M. J. A. (2006). Cellular and molecular dynamics in the foreign body reaction. *Tissue Eng.* 12, 1955–1970. doi: 10.1089/ten.2006.12.1955

Lynn, A. D., Blakney, A. K., Kyriakides, T. R., and Bryant, S. J. (2011). Temporal progression of the host response to implanted poly(ethylene glycol)-based hydrogels. *J. Biomed. Mater. Res. Part A* 96, 621–631. doi: 10.1002/jbm.a.33015

Ma, M., Liu, W. F., Hill, P. S., Bratlie, K. M., Siegwart, D. J., Chin, J., et al. (2011). Development of cationic polymer coatings to regulate foreign-body responses. *Adv. Mater.* 23, H189–H194. doi: 10.1002/adma.201100513

Madden, L. R., Mortisen, D. J., Sussman, E. M., Dupras, S. K., Fugate, J. A., Cuy, J. L., et al. (2010). Proangiogenic scaffolds as functional templates for cardiac tissue engineering. *Proc. Natl. Acad. Sci. U. S. A.* 107, 15211–15216. doi: 10.1073/pnas.1006442107

Mandal, H. S., Kastee, J. S., McHail, D. G., Rubinson, J. F., Pancrazio, J. J., and Dumas, T. C. (2015). Improved Poly(3,4-Ethylenedioxythiophene) (PEDOT) for neural stimulation. *Neuromodulation* 18, 657–663. doi: 10.1111/ner.12285

Mario Cheong, G. L., Lim, K. S., Jakubowicz, A., Martens, P. J., Poole-Warren, L. A., and Green, R. A. (2014). Conductive hydrogels with tailored bioactivity for implantable electrode coatings. *Acta Biomater.* 10, 1216–1226. doi: 10.1016/j.actbio.2013.12.032

Matlaga, B. F., Yasenchak, L. P., and Salthouse, T. N. (1976). Tissue response to implanted polymers: the significance of sample shape. *J. Biomed. Mater. Res.* 10, 391–397. doi: 10.1002/jbm.820100308

McConnell, G. C., Rees, H. D., Levey, A. I., Gutekunst, C. A., Gross, R. E., and Bellamkonda, R. V. (2009). Implanted neural electrodes cause chronic, local inflammation that is correlated with local neurodegeneration. *J. Neural Eng.* 6, 056003. doi: 10.1088/1741-2560/6/5/056003

Mercanzini, A., Reddy, S. T., Velluto, D., Colin, P., Maillard, A., Bensadoun, J. C., et al. (2010). Controlled release nanoparticle-embedded coatings reduce the tissue reaction to neuroprostheses. *J. Control. Release* 145, 196–202. doi: 10.1016/j.jconrel.2010.04.025

Merrill, D. R., Bikson, M., and Jefferys, J. G. R. (2005). Electrical stimulation of excitable tissue: design of efficacious and safe protocols. *J. Neurosci. Methods* 141, 171–198. doi: 10.1016/j.jneumeth.2004.10.020

Metz, S., Bertsch, A., Bertrand, D., and Renaud, P. (2004). Flexible polyimide probes with microelectrodes and embedded microfluidic channels for simultaneous drug delivery and multi-channel monitoring of bioelectric activity. *Biosens. Bioelectron.* 19, 1309–1318. doi: 10.1016/j.bios.2003.11.021

Miele, E., Spinelli, G. P., Miele, E., Fabrizio, E., Di Ferretti, E., Tomao, S., et al. (2012). Nanoparticle-based delivery of small interfering RNA: challenges for cancer therapy. *Int. J. Nanomed.* 7, 3637–3657. doi: 10.2147/IJN.S23696

Minev, I. R., Musienko, P., Hirsch, A., Barraud, Q., Wenger, N., Moraud, E. M., et al. (2015). Electronic dura mater for long-term multimodal neural interfaces. *Science* 347, 159–163. doi: 10.1126/science.1260318

Morrison, T. J., Sefton, E., Marquez-Chin, M., Popovic, M. R., Morshead, C. M., and Naguib, H. E. (2019). A 3D printed device for low cost neural stimulation in mice. *Front. Neurosci.* 13:784. doi: 10.3389/fnins.2019.00784

Mueller, M., De La Oliva, N., Del Valle, J., Delgado-Martinez, I., Navarro, X., and Stieglitz, T. (2017). Rapid prototyping of flexible intrafascicular electrode arrays by picosecond laser structuring. *J. Neural Eng.* 14:066016. doi: 10.1088/1741-2552/aa7eea

Navarro, X., Krueger, T. B., Lago, N., Micera, S., Stieglitz, T., and Dario, P. (2005). A critical review of interfaces with the peripheral nervous system for the control of neuroprostheses and hybrid bionic systems. *J. Peripher. Nerv. Syst.* 10, 229–258. doi: 10.1111/j.1085-9489.2005.10303.x

Navarro, X., Valderrama, E., Stieglitz, T., and Schüttler, M. (2001). Selective fascicular stimulation of the rat sciatic nerve with multipolar polyimide cuff electrodes. *Restor. Neurol. Neurosci.* 18, 9–21.

Nguyen, J. K., Park, D. J., Skousen, J. L., Hess-Dunning, A. E., Tyler, D. J., Rowan, S. J., et al. (2014). Mechanically-compliant intracortical implants reduce the neuroinflammatory response. *J. Neural Eng.* 11:056014. doi: 10.1088/1741-2560/11/5/056014

Oddo, C. M., Raspopovic, S., Artoni, F., Mazzoni, A., Spigler, G., Petrini, F., et al. (2016). Intraneural stimulation elicits discrimination of textural features by artificial fingertip in intact and amputee humans. *eLife* 5:e09148. doi: 10.7554/eLife.09148

Omar, R., Yang, J., Liu, H., Davies, N. M., and Gong, Y. (2016). Hepatic stellate cells in liver fibrosis and sirna-based therapy. *Rev. Physiol. Biochem. Pharmacol.* 172, 1–37. doi: 10.1007/112_2016_6

Ono, S. J., Nakamura, T., Miyazaki, D., Ohbayashi, M., Dawson, M., and Toda, M. (2003). Chemokines: roles in leukocyte development, trafficking, and effector function. *J. Allergy Clin. Immunol.* 111, 1185–1199. doi: 10.1067/mai.2003.1594

Ordonez, J. (2012). Thin films and microelectrode arrays for neuroprosthetics - ProQuest. *MRS Bull. Suppl. Mater. Neural Interf.* 37, 590–598. doi: 10.1557/mrs.2012.117

Ortiz-Catalan, M., Marin-Millan, J., Delbeke, J., Håkansson, B., and Brånemark, R. (2013). Effect on signal-to-noise ratio of splitting the continuous contacts of cuff electrodes into smaller recording areas. *J. Neuroeng. Rehabil.* 10:22. doi: 10.1186/1743-0003-10-22

Ostuni, E., Chapman, R. G., Holmlin, R. E., Takayama, S., and Whitesides, G. M. (2001). A survey of structure-property relationships of surfaces that resist the adsorption of protein. *Langmuir* 17, 5605–5620. doi: 10.1021/la010384m

Polikov, V. S., Tresco, P. A., and Reichert, W. M. (2005). Response of brain tissue to chronically implanted neural electrodes. *J. Neurosci. Methods* 148, 1–18. doi: 10.1016/j.jneumeth.2005.08.015

Proctor, C. M., Slézia, A., Kaszas, A., Ghestem, A., del Agua, I., Pappa, A. M., et al. (2018). Electrophoretic drug delivery for seizure control. *Sci. Adv.* 4:aau1291. doi: 10.1126/sciadv.aau1291

Qi, D., Liu, Z., Liu, Y., Jiang, Y., Leow, W. R., Pal, M., et al. (2017). Highly stretchable, compliant, polymeric microelectrode arrays for in vivo electrophysiological interfacing. *Adv. Mater.* 29:1702800. doi: 10.1002/adma.201702800

Qin, D., Xia, Y., and Whitesides, G. M. (2010). Soft lithography for micro- and nanoscale patterning. *Nat. Protoc.* 5, 491–502. doi: 10.1038/nprot.2009.234

Raffa, V., Pensabene, V., Menciassi, A., and Dario, P. (2007). Design criteria of neuron/electrode interface. The focused ion beam technology as an analytical method to investigate the effect of electrode surface morphology on neurocompatibility. *Biomed. Microdev.* 9, 371–383. doi: 10.1007/s10544-006-9042-2

Rao, S. S., Han, N., and Winter, J. O. (2011). Polylysine-modified PEG-based hydrogels to enhance the neuro-electrode interface. *J. Biomater. Sci. Polym. Edn.* 22, 611–625. doi: 10.1163/092050610X488241

Raspopovic, S., Capogrosso, M., Petrini, F. M., Bonizzato, M., Rigosa, J., Di Pino, G., et al. (2014). Bioengineering: restoring natural sensory feedback in real-time bidirectional hand prostheses. *Sci. Transl. Med.* 6:222ra19. doi: 10.1126/scitranslmed.3006820

Ratner, B. D. (2002). Reducing capsular thickness and enhancing angiogenesis around implant drug release systems. *J. Control. Release* 78, 211–218. doi: 10.1016/S0168-3659(01)00502-8

Retterer, S. T., Smith, K. L., Bjornsson, C. S., Neeves, K. B., Spence, A. J. H., Turner, J. N., et al. (2004). Model neural prostheses with integrated microfluidics: a potential intervention strategy for controlling reactive cell and tissue responses. *IEEE Trans. Biomed. Eng.* 51, 2063–2073. doi 10.1109/TBME.2004.834288

Richardson, D. L., Pepper, D. S., and Kay, A. B. (1976). Chemotaxis for human monocytes by fibrinogen-derived peptides. *Br. J. Haematol.* 32, 507–514. doi: 10.1111/j.1365-2141.1976.tb00953.x

Rodriguez, P. L., Harada, T., Christian, D. A., Pantano, D. A., Tsai, R. K., and Discher, D. E. (2013). Minimal "self" peptides that inhibit phagocytic clearance

and enhance delivery of nanoparticles. *Science* 339, 971–975. doi: 10.1126/science.1229568

Rombaut, J., Fernandez, M., Mazumder, P., and Pruneri, V. (2019). Nanostructured hybrid-material transparent surface with antireflection properties and a facile fabrication process. *ACS Omega* 4, 19840–19846. doi: 10.1021/acsomega.9b02775

Rossini, P. M., Micera, S., Benvenuto, A., Carpaneto, J., Cavallo, G., Citi, L., et al. (2010). Double nerve intraneural interface implant on a human amputee for robotic hand control. *Clin. Neurophysiol.* 121, 777–783. doi: 10.1016/j.clinph.2010.01.001

Rousche, P. J., Pellinen, D. S., Pivin, D. P., Williams, J. C., Vetter, R. J., and Kipke, D. R. (2001). Flexible polyimide-based intracortical electrode arrays with bioactive capability. *IEEE Trans. Biomed. Eng.* 48, 361–370. doi: 10.1109/10.914800

Rubehn, B., and Stieglitz, T. (2010). In vitro evaluation of the long-term stability of polyimide as a material for neural implants. *Biomaterials* 31, 3449–3458. doi: 10.1016/j.biomaterials.2010.01.053

Saeed, M., Ren, W., and Wu, A. (2018). Therapeutic applications of iron oxide based nanoparticles in cancer: basic concepts and recent advances. *Biomater. Sci.* 6, 708–725. doi: 10.1039/c7bm00999b

Salazar-Montes, A. M., Hernández-Ortega, L. D., Lucano-Landeros, M. S., and Armendariz-Borunda, J. (2015). New gene therapy strategies for hepatic fibrosis. *World J. Gastroenterol.* 21, 3813–3825. doi 10.3748/wjg.v21.i13.3813

Salthouse, T. N. (1984). Some aspects of macrophage behavior at the implant interface. *J. Biomed. Mater. Res.* 18, 395–401. doi: 10.1002/jbm.820180407

Samba, R., Herrmann, T., and Zeck, G. (2015). PEDOT - CNT coated electrodes stimulate retinal neurons at low voltage amplitudes and low charge densities. *J. Neural Eng.* 12, 480–488. doi: 10.1088/1741-2560/12/1/016014

Sergi, P. N., del Oliva Valle, N. J., de la Micera, S., and Navarro, X. (2020). A data-driven polynomial approach to reproduce the scar tissue outgrowth around neural implants. *J. Mater. Sci. Mater. Med.* 31:59. doi: 10.1007/s10856-020-06396-4

Serino, A., Akselrod, M., Salomon, R., Martuzzi, R., Blefari, M. L., Canzoneri, E., et al. (2017). Upper limb cortical maps in amputees with targeted muscle and sensory reinnervation. *Brain* 140, 2993–3011. doi: 10.1093/brain/awx242

Sharifi, F., Htwe, S. S., Righi, M., Liu, H., Pietralunga, A., Yesil-Celiktas, O., et al. (2019). A Foreign body response-on-a-chip platform. *Adv. Healthc. Mater.* 8:e1801425. doi: 10.1002/adhm.201801425

Simon, D. T., Kurup, S., Larsson, K. C., Hori, R., Tybrandt, K., Goiny, M., et al. (2009). Organic electronics for precise delivery of neurotransmitters to modulate mammalian sensory function. *Nat. Mater.* 8, 742–746. doi: 10.1038/nmat2494

Sin, M. C., Chen, S. H., and Chang, Y. (2014a). Hemocompatibility of zwitterionic interfaces and membranes. *Polym. J.* 46, 436–443. doi: 10.1038/pj.2014.46

Sin, M. C., Sun, Y. M., and Chang, Y. (2014b). Zwitterionic-based stainless steel with well-defined polysulfobetaine brushes for general bioadhesive control. *ACS Appl. Mater. Interf.* 6, 861–873. doi: 10.1021/am4041256

Smiley, S. T., King, J. A., and Hancock, W. W. (2001). Fibrinogen stimulates macrophage chemokine secretion through toll-like receptor 4. *J. Immunol.* 167, 2887–2894. doi: 10.4049/jimmunol.167.5.2887

Smith, R. S., Zhang, Z., Bouchard, M., Li, J., Lapp, H. S., Brotske, G. R., et al. (2012). Vascular catheters with a nonleaching poly-sulfobetaine surface modification reduce thrombus formation and microbial attachment. *Sci. Transl. Med.* 4:153ra132. doi: 10.1126/scitranslmed.3004120

Sohal, H. S., Jackson, A., Jackson, R., Clowry, G. J., Vassilevski, K., O'Neill, A., et al. (2014). The sinusoidal probe: a new approach to improve electrode longevity. *Front. Neuroeng.* 7:10. doi: 10.3389/fneng.2014.00010

Soltanzadeh, R., Afsharipour, E., Anssari, N., Mansouri, B., and Shafai, C. (2020). Structural and performance comparison between SU-8 microfabricated and 3D-printed microneedle electrodes. *J. 3D Print. Med.* 4, 29–44. doi: 10.2217/3dp-2019-0020

Spataro, L., Dilgen, J., Retterer, S., Spence, A. J., Isaacson, M., Turner, J. N., et al. (2005). Dexamethasone treatment reduces astroglia responses to inserted neuroprosthetic devices in rat neocortex. *Exp. Neurol.* 194, 289–300. doi: 10.1016/j.expneurol.2004.08.037

Spencer, K. C., Sy, J. C., Ramadi, K. B., Graybiel, A. M., Langer, R., and Cima, M. J. (2017). Characterization of mechanically matched hydrogel coatings to improve the biocompatibility of neural implants. *Sci. Rep.* 7:1952. doi: 10.1038/s41598-017-02107-2

Staples, N. A., Goding, J. A., Gilmour, A. D., Aristovich, K. Y., Byrnes-Preston, P., Holder, D. S., et al. (2018). Conductive hydrogel electrodes for delivery of long-term high frequency pulses. *Front. Neurosci.* 11:748. doi: 10.3389/fnins.2017.00748

Stubbs, E. B. (2020). Targeting the blood-nerve barrier for the management of immune-mediated peripheral neuropathies. *Exp. Neurol.* 331:113385. doi: 10.1016/j.expneurol.2020.113385

Surendran, S. P., Thomas, R. G., Moon, M. J., and Jeong, Y. Y. (2017). Nanoparticles for the treatment of liver fibrosis. *Int. J. Nanomed.* 12, 6997–7006. doi: 10.2147/IJN.S145951

Svennersten, K., Berggren, M., Richter-Dahlfors, A., and Jager, E. W. H. (2011). Mechanical stimulation of epithelial cells using polypyrrole microactuators. *Lab Chip* 11, 3287–3293. doi: 10.1039/c1lc20436j

Szaba, F. M., and Smiley, S. T. (2002). Roles for thrombin and fibrin(ogen) in cytokine/chemokine production and macrophage adhesion in vivo. *Blood* 99, 1053–1059. doi: 10.1182/blood.V99.3.1053

Szarowski, D. H., Andersen, M. D., Retterer, S., Spence, A. J., Isaacson, M., Craighead, H. G., et al. (2003). Brain responses to micro-machined silicon devices. *Brain Res.* 983, 23–35. doi: 10.1016/S0006-8993(03)03023-3

Szostak, K. M., Grand, L., and Constandinou, T. G. (2017). Neural interfaces for intracortical recording: requirements, fabrication methods, and characteristics. *Front. Neurosci.* 11:665. doi: 10.3389/fnins.2017.00665

Takehara, H., Nagaoka, A., Noguchi, J., Akagi, T., Kasai, H., and Ichiki, T. (2014). Lab-on-a-brain: implantable micro-optical fluidic devices for neural cell analysis in vivo. *Sci. Rep.* 4:6721. doi: 10.1038/srep06721

Tang, L., and Eaton, J. W. (1993). Fibrin(ogen) mediates acute inflammatory responses to biomaterials. *J. Exp. Med.* 178, 2147–2156. doi: 10.1084/jem.178.6.2147

Tang, L., Jennings, T. A., and Eaton, J. W. (1998). Mast cells mediate acute inflammatory responses to implanted biomaterials. *Proc. Natl. Acad. Sci. U.S.A.* 95, 8841–8846. doi: 10.1073/pnas.95.15.8841

Tao, F., and Kobzik, L. (2002). Lung macrophage-epithelial cell interactions amplify particle-mediated cytokine release. *Am. J. Respir. Cell Mol. Biol.* 26, 499–505. doi: 10.1165/ajrcmb.26.4.4749

Teixeira, A. I., Ilkhanizadeh, S., Wigenius, J. A., Duckworth, J. K., Inganäs, O., and Hermanson, O. (2009). The promotion of neuronal maturation on soft substrates. *Biomaterials* 30, 4567–4572. doi: 10.1016/j.biomaterials.2009.05.013

Thull, R. (2002). Physicochemical principles of tissue material interactions. *Biomolecu. Eng.* 19, 43–50. doi: 10.1016/S1389-0344(02)00009-6

Tian, F., Cui, D., Schwarz, H., Estrada, G. G., and Kobayashi, H. (2006). Cytotoxicity of single-wall carbon nanotubes on human fibroblasts. *Toxicol. Vitr.* 20, 1202–1212. doi: 10.1016/j.tiv.2006.03.008

Trel'Ová, D., Salgarella, A. R., Ricotti, L., Giudetti, G., Cutrone, A., Šrámková, P., et al. (2019). Soft hydrogel zwitterionic coatings minimize fibroblast and macrophage adhesion on polyimide substrates. *Langmuir* 35, 1085–1099. doi: 10.1021/acs.langmuir.8b00765

Tyler, D. J., and Durand, D. M. (2002). Functionally selective peripheral nerve stimulation with a flat interface nerve electrode. *IEEE Trans. Neural Syst. Rehabil. Eng.* 10, 294–303. doi: 10.1109/TNSRE.2002.806840

Uguz, I., Proctor, C. M., Curto, V. F., Pappa, A. M., Donahue, M. J., Ferro, M., et al. (2017). A microfluidic ion pump for in vivo drug delivery. *Adv. Mater.* 29:1701217. doi: 10.1002/adma.201701217

Valle, G., Mazzoni, A., Iberite, F., D'Anna, E., Strauss, I., Granata, G., et al. (2018). Biomimetic intraneural sensory feedback enhances sensation naturalness, tactile sensitivity, and manual dexterity in a bidirectional prosthesis. *Neuron* 100, 37–45.e7. doi: 10.1016/j.neuron.2018.08.033

Vegas, A. J., Veiseh, O., Gürtler, M., Millman, J. R., Pagliuca, F. W., Bader, A. R., et al. (2016). Long-term glycemic control using polymer-encapsulated human stem cell-derived beta cells in immune-competent mice. *Nat. Med.* 22, 306–311. doi: 10.1038/nm.4030

Veiseh, O., Doloff, J. C., Ma, M., Vegas, A. J., Tam, H. H., Bader, A. R., et al. (2015). Size- and shape-dependent foreign body immune response to materials implanted in rodents and non-human primates. *Nat. Mater.* 14, 643–651. doi: 10.1038/nmat4290

Vitale, F., Vercosa, D. G., Rodriguez, A. V., Pamulapati, S. S., Seibt, F., Lewis, E., et al. (2018). Fluidic microactuation of flexible electrodes for neural recording. *Nano Lett.* 18, 326–335. doi: 10.1021/acs.nanolett.7b04184

Von Der Mark, K., Park, J., Bauer, S., and Schmuki, P. (2010). Nanoscale engineering of biomimetic surfaces: cues from the extracellular matrix. *Cell Tissue Res.* 339, 131–153. doi: 10.1007/s00441-009-0896-5

Wadhwa, R., Lagenaur, C. F., and Cui, X. T. (2006). Electrochemically controlled release of dexamethasone from conducting polymer polypyrrole coated electrode. *J. Control. Release* 110, 531–541. doi 10.1016/j.jconrel.2005.10.027

Wang, J., Thow, X. Y., Wang, H., Lee, S., Voges, K., Thakor, N. V., et al. (2018). A highly selective 3D Spiked Ultraflexible Neural (SUN) interface for decoding peripheral nerve sensory information. *Adv. Healthc. Mater.* 7:987. doi: 10.1002/adhm.201700987

Wang, M., Mi, G., Shi, D., Bassous, N., Hickey, D., and Webster, T. J. (2018). Nanotechnology and nanomaterials for improving neural interfaces. *Adv. Funct. Mater.* 28:1700905. doi: 10.1002/adfm.201700905

Ward, W. K. (2008). A review of the foreign-body response to subcutaneously-implanted devices: the role of macrophages and cytokines in biofouling and fibrosis. *J. Diabetes Sci. Technol.* 2, 768–777. doi: 10.1177/193229680800200504

Ward, W. K., Slobodzian, E. P., Tiekotter, K. L., and Wood, M. D. (2002). The effect of microgeometry, implant thickness and polyurethane chemistry on the foreign body response to subcutaneous implants. *Biomaterials* 23, 4185–4192. doi: 10.1016/S0142-9612(02)00160-6

Ware, T., Simon, D., Rennaker, R. L., and Voit, W. (2013). Smart polymers for neural interfaces. *Polym. Rev.* 53, 108–129. doi: 10.1080/15583724.2012.751924

Weaver, C. L., Larosa, J. M., Luo, X., and Cui, X. T. (2014). Electrically controlled drug delivery from graphene oxide nanocomposite films. *ACS Nano* 8, 1834–1843. doi: 10.1021/nn406223e

Wichterle, O., and Lím, D. (1960). Hydrophilic gels for biological use. *Nature* 185, 117–118. doi: 10.1038/185117a0

Wilks, S. J., Woolley, A. J., Ouyang, L., Martin, D. C., and Otto, K. J. (2011). In vivo polymerization of poly(3,4-ethylenedioxythiophene) (PEDOT) in rodent cerebral cortex. *Annu. Int. Conf. IEEE Eng. Med. Biol. Soc.* 2011, 5412–5415. doi: 10.1109/IEMBS.2011.6091338

Winslow, B. D., and Tresco, P. A. (2010). Quantitative analysis of the tissue response to chronically implanted microwire electrodes in rat cortex. *Biomaterials* 31, 1558–1567. doi: 10.1016/j.biomaterials.2009.11.049

Woeppel, K., Yang, Q., and Cui, X. T. (2017). Recent advances in neural electrode-tissue interfaces. *Curr. Opin. Biomed. Eng.* 4, 21–31. doi: 10.1016/j.cobme.2017.09.003

Wu, J., Xiao, Z., Chen, A., He, H., He, C., Shuai, X., et al. (2018). Sulfated zwitterionic poly(sulfobetaine methacrylate) hydrogels promote complete skin regeneration. *Acta Biomater.* 71, 293–305. doi: 10.1016/j.actbio.2018.02.034

Wu, W., He, Q., and Jiang, C. (2008). Magnetic iron oxide nanoparticles: synthesis and surface functionalization strategies. *Nanoscale Res. Lett.* 3, 397–415. doi: 10.1007/s11671-008-9174-9

Wünsche, J., Cardenas, L., Rosei, F., Cicoira, F., Gauvin, R., Graeff, C. F. O., et al. (2013). In situ formation of dendrites in eumelanin thin films between gold electrodes. *Adv. Funct. Mater.* 23, 5591–5598. doi: 10.1002/adfm.201300715

Wurth, S., Capogrosso, M., Raspopovic, S., Gandar, J., Federici, G., Kinany, N., et al. (2017). Long-term usability and bio-integration of polyimide-based intra-neural stimulating electrodes. *Biomaterials* 122, 114–129. doi: 10.1016/j.biomaterials.2017.01.014

Xavier, N., and Jaume, D. V. (2014). Regenerative neural interfaces for neuroprosthetic applications. *Front. Neuroeng.* 7:3. doi: 10.3389/conf.fneng.2014.11.00003

Xiao, S., Castro, R., Rodrigues, J., Shi, X., and Tomá, H. (2014). PAMAM dendrimer/pDNA functionalized-magnetic iron oxide nanoparticles for gene delivery. *J. Biomed. Nanotechnol.* 11, 1418–1430. doi: 10.1166/jbn.2015.2101

Xiao, Y., He, L., and Che, J. (2012). An effective approach for the fabrication of reinforced composite hydrogel engineered with SWNTs, polypyrrole and PEGDA hydrogel. *J. Mater. Chem.* 22, 8076–8082. doi: 10.1039/c2jm30601h

Xie, X., Rieth, L., Williams, L., Negi, S., Bhandari, R., Caldwell, R., et al. (2014). Long-term reliability of Al2O3 and Parylene C bilayer encapsulated utah electrode array based neural interfaces for chronic implantation. *J. Neural Eng.* 11:026016. doi: 10.1088/1741-2560/11/2/026016

Xu, H., Belkacemi, L., Jog, M., Parrent, A., and Hebb, M. O. (2013). Neurotrophic factor expression in expandable cell populations from brain samples in living patients with Parkinson's disease. *FASEB J.* 27, 4157–4168. doi: 10.1096/fj.12-226555

Yamato, H., Ohwa, M., and Wernet, W. (1995). Stability of polypyrrole and poly(3,4-ethylenedioxythiophene) for biosensor application. *J. Electroanal. Chem.* 397, 163–170. doi: 10.1016/0022-0728(95)04156-8

Yang, C., and Suo, Z. (2018). Hydrogel ionotronics. *Nat. Rev. Mater.* 3, 125–142. doi: 10.1038/s41578-018-0018-7

Yang, H., Rahman, M. T., Du, D., Panat, R., and Lin, Y. (2016). 3-D printed adjustable microelectrode arrays for electrochemical sensing and biosensing. *Sens. Actuat. B Chem.* 230, 600–606. doi: 10.1016/j.snb.2016.02.113

Yesilyurt, V., Veiseh, O., Doloff, J. C., Li, J., Bose, S., Xie, X., et al. (2017). A facile and versatile method to endow biomaterial devices with zwitterionic surface coatings. *Adv. Healthc. Mater.* 6:1601091. doi: 10.1002/adhm.201601091

Yildiz, K. A., Shin, A. Y., and Kaufman, K. R. (2020). Interfaces with the peripheral nervous system for the control of a neuroprosthetic limb: a review. *J. Neuroeng. Rehabil.* 17:43. doi: 10.1186/s12984-020-00667-5

Yoshida, K., and Stein, R. B. (1999). Characterization of signals and noise rejection with bipolar longitudinal intrafascicular electrodes. *IEEE Trans. Biomed. Eng.* 46, 226–234. doi: 10.1109/10.740885

Yu, Q., Xiong, X., Zhao, L., Xu, T., and Wang, Q. (2020). Antifibrotic effects of specific siRNA targeting connective tissue growth factor delivered by polyethyleneimine-functionalized magnetic iron oxide nanoparticles on LX-2 cells. *Mol. Med. Rep.* 21, 181–190. doi: 10.3892/mmr.2019.10834

Zeglio, E., Rutz, A. L., Winkler, T. E., Malliaras, G. G., and Herland, A. (2019). Conjugated polymers for assessing and controlling biological functions. *Adv. Mater.* 31:1806712. doi: 10.1002/adma.201806712

Zhang, L., Cao, Z., Bai, T., Carr, L., Ella-Menye, J. R., Irvin, C., et al. (2013). Zwitterionic hydrogels implanted in mice resist the foreign-body reaction. *Nat. Biotechnol.* 31, 553–556. doi: 10.1038/nbt.2580

Zhang, Y., An, D., Pardo, Y., Chiu, A., Song, W., Liu, Q., et al. (2017). High-water-content and resilient PEG-containing hydrogels with low fibrotic response. *Acta Biomater.* 53, 100–108. doi: 10.1016/j.actbio.2017.02.028

Zheng, X., Woeppel, K. M., Griffith, A. Y., Chang, E., Looker, M. J., Fisher, L. E., et al. (2019). Soft conducting elastomer for peripheral nerve interface. *Adv. Healthc. Mater.* 8:1311. doi: 10.1002/adhm.201801311

Zhu, Z., Yang, G., Li, R., and Pan, T. (2017). Photopatternable pedot:Pss/peg hybrid thin film with moisture stability and sensitivity. *Microsyst. Nanoeng.* 3:17004. doi: 10.1038/micronano.2017.4

Ziegler, D., Suzuki, T., and Takeuchi, S. (2006). Fabrication of flexible neural probes with built-in microfluidic channels by thermal bonding of Parylene. *J. Microelectromech. Syst.* 15, 1477–1482. doi: 10.1109/JMEMS.2006.879681

Zollo, L., Pino, G. D., Ciancio, A. L., Ranieri, F., Cordella, F., Gentile, C., et al. (2019). Restoring tactile sensations via neural interfaces for real-time force-and-slippage closed-loop control of bionic hands. *Sci. Robot.* 4:aau9924. doi: 10.1126/scirobotics.aau9924

Conflict of Interest: The authors declare that the research was conducted in the absence of any commercial or financial relationships that could be construed as a potential conflict of interest.

frontiers in Bioengineering and Biotechnology

REVIEW
published: 10 June 2021
doi: 10.3389/fbioe.2021.678048

The Rheology of the Carotid Sinus: A Path Toward Bioinspired Intervention

Andrew Iskander[1], Coskun Bilgi[2], Rotem Naftalovich[3,4], Ilker Hacihaliloglu[5], Tolga Berkman[3], Daniel Naftalovich[6,7] and Niema Pahlevan[2,7]*

[1] Department of Anesthesiology, Westchester Medical Center, New York Medical College, Valhalla, NY, United States, [2] Department of Aerospace and Mechanical Engineering, University of Southern California, Los Angeles, CA, United States, [3] Department of Anesthesiology, New Jersey Medical School, University Hospital, Rutgers University, Newark, NJ, United States, [4] Medical Corps of the U.S. Army, U.S. Army Medical Department, Fort Sam Houston, San Antonio, TX, United States, [5] Department of Biomedical Engineering, Rutgers School of Engineering, Rutgers University, Piscataway, NJ, United States, [6] Department of Computational and Mathematical Sciences, California Institute of Technology, Pasadena, CA, United States, [7] Keck School of Medicine, University of Southern California, Los Angeles, CA, United States

The association between blood viscosity and pathological conditions involving a number of organ systems is well known. However, how the body measures and maintains appropriate blood viscosity is not well-described. The literature endorsing the function of the carotid sinus as a site of baroreception can be traced back to some of the earliest descriptions of digital pressure on the neck producing a drop in blood delivery to the brain. For the last 30 years, improved computational fluid dynamic (CFD) simulations of blood flow within the carotid sinus have demonstrated a more nuanced understanding of the changes in the region as it relates to changes in conventional metrics of cardiovascular function, including blood pressure. We suggest that the unique flow patterns within the carotid sinus may make it an ideal site to transduce flow data that can, in turn, enable real-time measurement of blood *viscosity*. The recent characterization of the PIEZO receptor family in the sinus vessel wall may provide a biological basis for this characterization. When coupled with other biomarkers of cardiovascular performance and descriptions of the blood rheology unique to the sinus region, this represents a novel venue for bioinspired design that may enable end-users to manipulate and optimize blood flow.

Keywords: baroreceptor, blood flow, viscosity, PIEZO receptor, carotid sinus

OPEN ACCESS

Edited by:
Jian Yang,
Wuyi University, China

Reviewed by:
Nitesh Kumar,
Manipal Institute of Technology, India
Salvatore Andrea Pullano,
University Magna Graecia of Catanzaro, Italy

****Correspondence:***
Andrew Iskander
andrew.iskander@wmchealth.org

Specialty section:
This article was submitted to Bionics and Biomimetics, a section of the journal Frontiers in Bioengineering and Biotechnology

Received: *08 March 2021*
Accepted: *05 May 2021*
Published: *10 June 2021*

Citation:
Iskander A, Bilgi C, Naftalovich R, Hacihaliloglu I, Berkman T, Naftalovich D and Pahlevan N (2021) The Rheology of the Carotid Sinus: A Path Toward Bioinspired Intervention. Front. Bioeng. Biotechnol. 9:678048. doi: 10.3389/fbioe.2021.678048

DESCRIPTIONS OF THE CAROTID SINUS PHYSIOLOGY THROUGHOUT HISTORY

"I have gained the conviction through repeated and careful observations, that the slowing of the pulse when pressure is applied on the carotid is a frequent finding, in healthy, as well as in sick persons." (Huth and Murray, 2006).

-Heinrich Irenaeus Quincke

The Carotid Bifurcation Before the "Carotid Sinus"

In 1875 Quincke, a German physician responsible for introducing the lumbar puncture, spoke of the commonly held association between compression of the carotid bifurcation and decreased cardiac output. The association between the very immediate effects of compression of the vessels in the neck and a drop in global blood flow has been noted for a very long time. (The Greek word for "stupefy", "karos", provides the basis for our modern "carotid."). Indeed, Rufus of Ephesus, circa

50 AD, described the almost immediate change in blood flow and mentation when the vessels in the neck were compressed (Munster et al., 2016). For the 1,800 years that ensued, the notion that there was a profound slowing of the heart rate with compression of the neck vessels was attributed, somewhat correctly, to the nerves adjacent to the carotid (Glick and Covell, 1968; Persson and Kirchheim, 1991). As the heart rate was noted to decrease with manipulation of the dilated portion of the internal carotid, the vagus nerve was taken for granted up until the 1920s as being responsible for transmitting this signal to the autonomic nervous system.

The Current Paradigm of the Carotid Sinus as a Baroreceptor

It was Heinrich Ewald Hering in 1924 (Zimmer, 2004) who, through a series of experiments with over a hundred dogs, rationalized the anatomy and function of the carotid sinus and its nerve as it is currently understood. He observed that internal direct mechanical application of a pressure stimulus to the carotid sinus region using a brass probe had similar effects as direct electrical stimulation to the sinus. He realized that the nerve found to insert in the adventitia was distinct from the vagus nerve. Furthermore, he demonstrated that the electrical stimulation of this nerve also elicited the same effect as a clamp applied to the sinus–a reduction of heart rate and vasodilation with a resultant drop in blood pressure. The presumption is that this "vagal" parasympathetic effect does not originate in the vagus nerve. The role of the carotid sinus in global perfusion was further supported by Hering's observation that systemic blood pressure reduced with increased pressure within the sinus itself (Persson and Kirchheim, 1991). His pursuit of a nerve responsible for mediating these observed cardiovascular responses led him to the eponymous Hering's nerve, also known as the carotid sinus nerve, and helped complete our contemporary understanding of baroreception.

The Clinical Need for a Novel Biomarker of Blood Viscosity

The predictive relevance of blood viscosity in the literature has been suspected to be intrinsically germane to many disease processes. Types of problems where blood viscosity appears to play some pathophysiologic role include immunologic diseases (Gudmundsson et al., 1993), inflammatory diseases (Nwose, 2010), hemolytic anemias (Bowers et al., 2013, 2018; Kucukal et al., 2020), hearing loss (Hildesheimer et al., 1990; Garcia Callejo et al., 2006), diabetes (Nakanishi et al., 2004; Richards and Nwose, 2010; Schiapaccassa et al., 2019), renal disorders (Jung et al., 2017), sickle cell disease (Klug et al., 1974), and cerebrovascular disease (Song et al., 2017). However, the association between cardiovascular disease and blood viscosity has been looked at most extensively throughout the literature (Lowe, 1992; Kenyeres et al., 2008; Chevalier et al., 2013; Buyan et al., 2017; Celik et al., 2017; Peters et al., 2017; Sloop et al., 2018; Cekirdekci and Bugan, 2020; Engin and Guvenc, 2020).

In an attempt to determine whether increased blood viscosity has any predictive value as a biomarker in the setting of cardiovascular disease, Peters (Peters et al., 2017) compiled blood viscosity data from the Scottish Heart Health Extended Cohort (SHHEC). The SHEEC (Woodward et al., 2007) included participants without known cardiovascular disease recruited across Scotland from two different cohorts of men and women, one group from 1984–1987 and the other from north Glasgow in 1989, 1992, and 1995. For this prospective study, they compiled the data in the hopes of creating an ASSIGN (Assessing Cardiovascular Risk Using SIGN Guidelines) cardiovascular morbidity and mortality risk score. By taking venous blood samples, they calculated the relative blood and plasma viscosities. They uncovered a statistically significant association between cardiovascular and all-cause risk with blood viscosity, particularly plasma viscosity. More importantly, the study demonstrated that even when controlling for the normal increases in viscosity associated with age, sex, and other known cardiovascular risks, viscosity had predictive value in ultimate scoring for mortality risk.

In another study (Skretteberg et al., 2010) from Sweden, patients with no known cardiovascular disease were recruited into a study whereby hematocrit was related to long-term outcomes. After controlling for other known causes of cardiovascular mortality, they found an association between elevated sedimentation rate – a broad measure of inflammation – and elevated hematocrit. Remarkably, the association remained nearly as robust 26 years after enrollment as it did 10 years after enrollment. This study further corroborates the notion that blood viscosity may have predictive value independent of other known causes of cardiovascular mortality. The authors conclude that their findings support the theory that "hematocrit, plasma viscosity, and inflammation may increase... morbidity and mortality by promoting thrombotic complications and... atherosclerosis." Based on its robust and long-lasting association, the authors argue that blood viscosity should be an independent prognostic indicator for cardiovascular events and mortality.

While increasing plasma viscosity leading to increased end-organ dysfunction may make intuitive sense, the question arises: "How does the body detect 'optimal' blood viscosity?" Is there an apparatus that can be described as the body's own viscometer? Is that structure able, by virtue of its structure and function, to shed light on the rheology of global blood flow? Is this structure involved in the function of other organs whose functions titrate the fluid components involved in comprising blood viscosity?

THE CAROTID SINUS AS A VISCOMETER

The role of the carotid sinus as a pressure sensor is well-known (Andani and Khan, 2020). The present review discusses the intrinsic function of the carotid sinus as it relates to blood rheology and to the microanatomical apparatus responsible for initiation of its action. This review does not focus on the extensive and important work by many in the field of endothelial mechanobiology (a field which owes a great deal to Peter F. Davies for much of our understanding of the mechanics of endothelial transduction). This review is not a comprehensive review of the

entire downstream pathway that follows after sinus activation – a pathway that we believe involves the vagus nerve and further neuromodulation by the central nervous system. Here, we aim to present aspects of the structure and function of the carotid sinus that may support its role as a blood viscometer.

As applied physiologists, clinicians manipulate cardiovascular homeostasis on a gross scale. For example, during carotid endarterectomy surgeries, glycopyrrolate is often given at the time of anesthetic induction to attenuate the reflex bradycardia that often ensues after carotid stent deployment. Despite our familiarity with this mechanism, clinicians often overlook the blood flow characteristics within the carotid sinus that may have a role in maintaining hemodynamics. This review presents recent improvements in our understanding of the blood rheology and microphysiology of the carotid sinus to enhance the clinician's working knowledge. Considering the function of the carotid sinus and its possible role as a sensory organ may provide the basis for bioinspired design of devices that better enable clinicians to read, interpret, and manage blood viscosity.

THE UNIQUE FLOW AND SHEAR STRESS CHARACTERISTICS OF THE CAROTID SINUS

The salience of carotid ultrasound to anesthetic management is increasing. In many centers, carotid Doppler studies are part of the preoperative workup for many major surgeries. For patients undergoing cardiac surgery, carotid ultrasound is a cost-effective, non-invasive screening tool that most anesthesiologists probably take for granted and view as having somewhat of a distant relevance to patient evaluation. However, data obtained by carotid Doppler is now used to guide blood flow (Weber et al., 2016) and stratify delirium risk (Bernardi et al., 2019) in the immediate postoperative period, as well as for a longer-term perspective relating to post-operative cognitive dysfunction (Elias et al., 2019).

The Flow Dynamics Within the Carotid Sinus

The advent of clinically useful ultrasound examinations of the carotids created a need for a greater in-depth appreciation for the hemodynamic uniqueness of the sinus region. The very specific location of the sinus, immediately distal to the carotid bifurcation at the internal carotid artery inlet and above the level of the heart, lends its flow characteristics to vary over the cardiac cycle. The first comprehensive descriptions of the unique flow within the carotid sinus were first consolidated in 1983 (Ku and Giddens, 1983). The sinus is unique for the region of "flow separation" from the non-dividing wall at the origin of the internal carotid (Ku et al., 1985a,b; Ku and Giddens, 1987). Firstly, there is an effective coalescing of the flow streamlines in the origin of the internal carotid that results from the flow separation away from the non-dividing wall (**Figure 1**). Essentially, the flow vectors orient toward the carotid dividing wall and "make room" for the region of swirling, or recirculation, within the dilated region (**Figure 2**; Karner et al., 1999). This results in constant flow shear against the dividing wall throughout the cardiac cycle. Secondly, this high-velocity flow (**Figure 2A**) at the dividing wall leads to persistent reduced shear stress at the

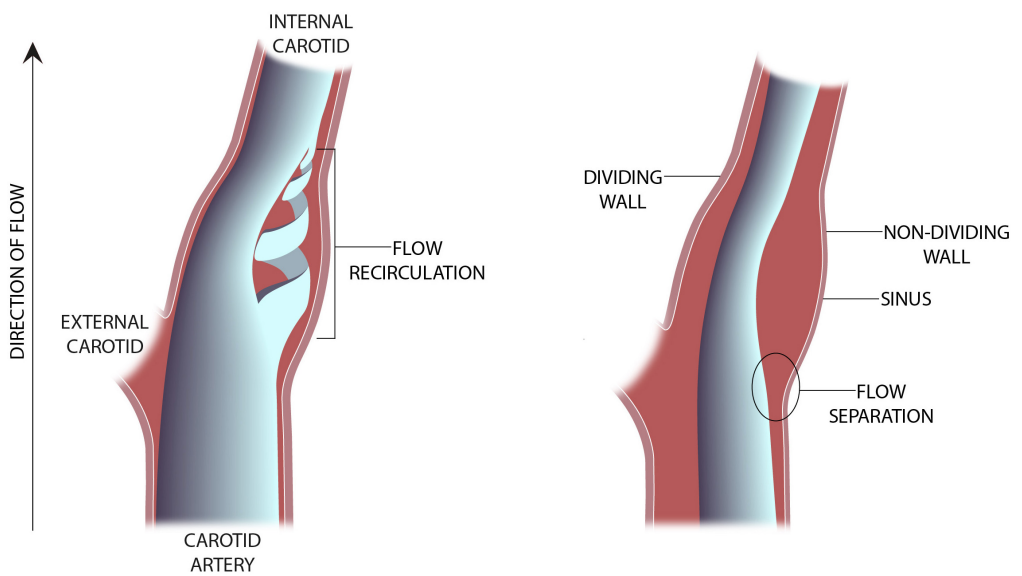

FIGURE 1 | Schematic representation of an in-vitro experimental model of the carotid sinus (Ku and Giddens, 1983). **(A)** The presence of vortical or flow recirculation during the peak of systole results in sheer stress "impulses" against the sinus wall. **(B)** The anatomy of the sinus causes flow separation from the non-dividing wall resulting in a region of low wall shear stress.

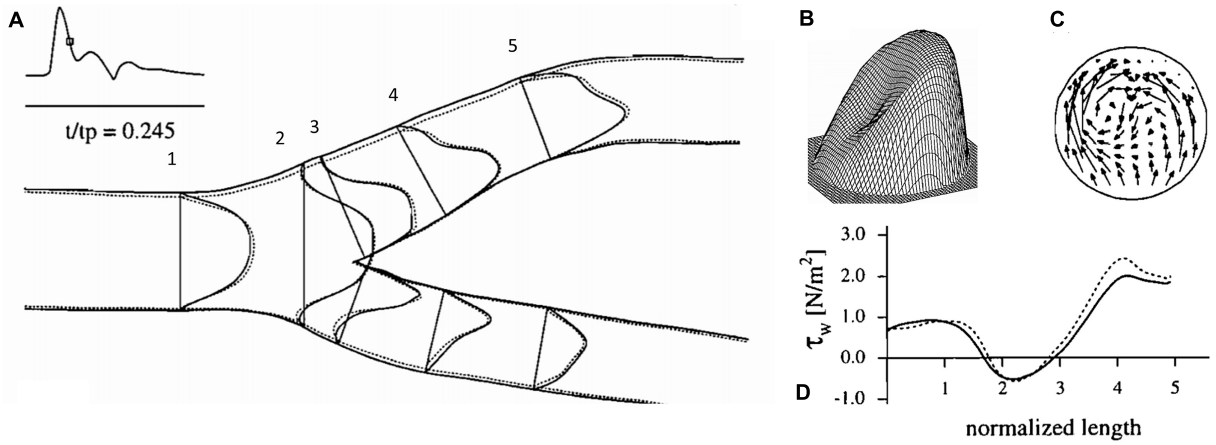

FIGURE 2 | Flow dynamics inside the carotid artery at deceleration, **(A)** axial velocity profiles, **(B)** three-dimensional representation of axial velocity profile at 4, **(C)** representation of circulatory flow vectors at 4, **(D)** wall shear stress values along the outer carotid wall (Karner et al., 1999).

non-dividing wall of the sinus where the carotid sinus inserts into the adventitia. Lastly, the vortex of the fluid within the sinus, **Figures 2B,C**, causes alternating levels of shear stress "impulses" that change in the magnitude and polarity over the cardiac cycle. Direction change of wall shear stress (WSS) can be observed in **Figure 2D**, which results in oscillations of stress throughout the cardiac cycle. Interestingly, it is the oscillations from WSS that have long been accepted as the inciting factor for atheroma formation in this portion of the internal carotid (de Vecchis et al., 2010; Hirata et al., 2011; Leisser et al., 2015; Saba et al., 2015). It is therefore not surprising that the carotid atherosclerotic plaque is often found in the sinus (Gulevskaia et al., 2007).

The advent of open-source platforms for computational fluid dynamic (CFD) simulations led to a more quantitative, data-driven understanding of the flow characteristics of the carotid vessels, especially of the shear stress-related flow patterns within the sinus (Marshall et al., 2004; Milos et al., 2011; Dong et al., 2013; Zhang et al., 2013; Sui et al., 2015; Cibis et al., 2016; Guo et al., 2018; Xu et al., 2018; Zhang D. et al., 2018; Dai et al., 2019; Iskander et al., 2020). Enabling visualization of flow makes this information more translatable to clinical practice by emphasizing the possible role of the shear-thinning aspects of blood flow. Patient-specific CFD studies suggest that the non-Newtonian behavior–including shear-thinning–of blood is negligible in large arteries (Lee and Steinman, 2007; Arzani, 2018). However, recent studies on simplified dilation geometries, such as is seen in the sinus, reveals the significant differences in WSS-related parameters seen with even small changes in the viscoelastic and shear-thinning behavior of blood (Bilgi and Atalik, 2019, 2020). Furthermore, experiments on Fontan hemodynamics highlight that neglecting non-Newtonian behavior like shear-thinning can produce significant errors and misinterpretation of the hemodynamics (Cheng et al., 2018a,b, 2019; Wei H. et al., 2020; Wei Z. et al., 2020). These studies demonstrate the important role of shear-thinning relevant to specific clinical problems such as Fontan flows and aneurysms.

The key parameter in triggering non-Newtonian effects is the shear rate, which depends on local fluid dynamics of the blood at any specific location. Shear-thinning is a property observed during low shear rate (low velocity gradient) in which the apparent viscosity increases as the velocity gradient (shear rate) decreases. Alternatively, at high shear rate, the apparent viscosity decreases until it reaches a constant viscosity value and it behaves Newtonian. Due to the Fahraeus-Lindqvist effect, the apparent viscosity further decreases in smaller vessels with diameters between 30 to 300 μm (Truskey et al., 2004). Ku and Giddens (1983) also demonstrated that in the sinus region, the wall is under *less* WSS throughout the cardiac cycle. This occurs since the sinus wall is drawn away from the opposing streamlined flow whose vector orients more toward the dividing wall than toward the sinus. Lee and Steinman (2007) developed a CFD model of the bifurcation and related changes in hematocrit to changes in the sinus region. In agreement with other models of the sinus, this area of low WSS corresponds to a zone of increased shear oscillation resulting from the vortical swirling characteristic of that region. They demonstrated that changes in the modeled root mean square WSS of 5–15% corresponded to hematocrit changes of 20% in the same direction. In short, they showed that the shear-thinning aspect of blood can be considered when modeling blood flow, and that this aspect is relatable to the velocity and hematocrit of blood, two immediately measurable clinical parameters.

Milos (Milos et al., 2011), looked at the CFD models of over 1,400 carotid arteries using data mining methods and began to draw generalizations about carotid geometry, blood viscosity, velocity, density, and several other clinically relevant parameters which correlates to the region of recirculation in the sinus. They aimed to determine the feasibility and logistics of using different machine learning models to associate local WSS and the region of recirculation with precision. **Figure 3** shows a comparison of the WSS values of conventional CFD with their multilayer perceptron neural network (MPL) and k-nearest neighbors (k-NN) algorithms. They ultimately demonstrated the availability of

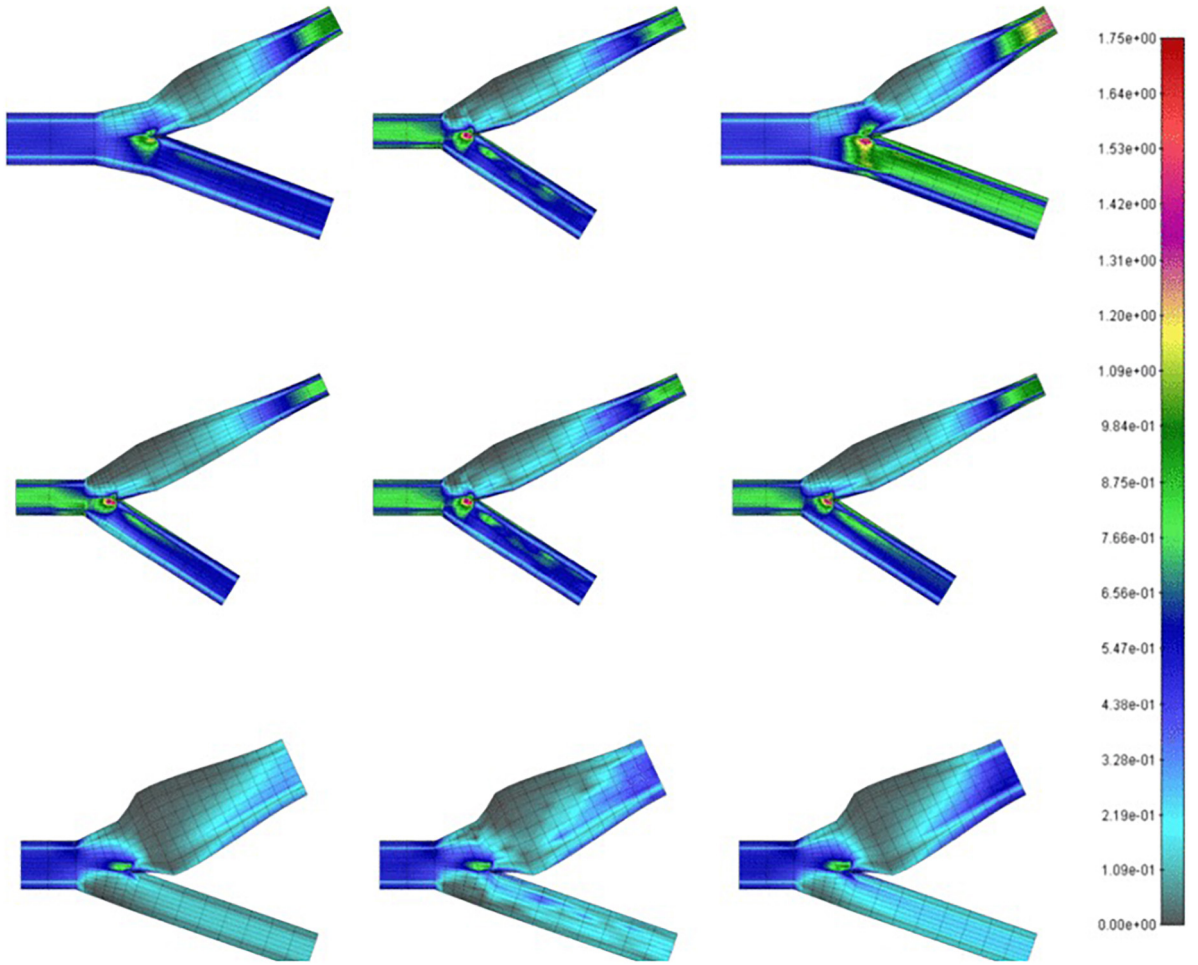

FIGURE 3 | Wall shear stress (in Pa) on carotid bifurcations of differing geometries obtained by CFD (left), MPL (middle), k-NN (right) algorithms (Milos et al., 2011).

clinically useful machine learning algorithms that can accurately predict the flow and stress fields by using anatomical data from ultrasound imaging. The required parameters like sinus diameter, sinus length, angle of the internal carotid relative to the common carotid, blood density, and velocity and clinically relevant proxies for hematocrit and cardiac output, can be easily and non-invasively collected from a patient.

Extracting data from simulations has also led to parameters previously only available from Doppler data (Gates et al., 2018; Zhang B. et al., 2018). In the work by Zhang B. et al. (2018), they obtained ultrasounds of two groups of fifty patients. One group had "normal" intimal-media thickness ratios and the other was "thickened." By taking dimensional measurements in and around the carotid sinus, they used conventional Doppler data to calculate values previously only available in a simulated setting: blood viscosity, WSS, and velocity gradients within the carotid sinus. When these parameters were correlated with blood pressure and cardiac output, in patients with higher blood pressures, the region of greatest WSS was smaller in volume and made contact with less area of the carotid sinus wall along the longitudinal orientation.

A more recent advancement is Vector Flow Imaging (VFI) which utilizes the Doppler data to visually construct the flow lines within the sinus. VFI is a robust method for obtaining 2D images of the velocity vector profiles well-suited for areas with vortical flow such as the sinus. The real advantage to this method is that the forward (i.e., toward the brain) vs. reverse flow can be depicted simultaneously, allowing for measurement of the degree of turbulence within the region of recirculation (Goddi et al., 2017). As VFI finds greater availability, more precise quantification of the non-laminar flow in the sinus is expected.

MECHANOTRANSDUCTION BY THE CAROTID SINUS

The Role of Shear Stress Mechanotransduction

The unique blood flow at the sinus creates flow patterns and shear forces that are transduced to the central nervous system. The term *mechanotransduction* refers to the transmission

of a physical extracellular input or trigger to a cellular output. The physical forces that lead to these biological responses include direct cellular contact with shear forces, changes in transmembrane voltage, and mechanical stretch. The pervasive role of mechanotransduction in so many *in vivo* processes cannot be overstated. In the literature, there is a role for mechanotransduction in voluntary urination (Mukhopadhyay and Stowers, 2020), guiding cell proliferation during embryological development (Wozniak and Chen, 2009), cardiomyocyte shape and function (McCain and Parker, 2011), renal tubule function (Weinbaum et al., 2011), touch (Sanzeni et al., 2019), regulation of vascular smooth muscle tone (Sazonova et al., 2015), pulmonary smooth muscle tone (Noble et al., 2014), pain (Feng and Guo, 2019), and many others. As applied physiologists, the modulation of these mechanisms is likely to have an increased role in the management of patients undergoing anesthesia. A classic example is utilizing mechanical ventilation settings that mitigate lung injury from shear forces due to positive pressure ventilation (Jamaati et al., 2016).

Amongst the physical phenomena that serve as the triggers for mechanotransduction in endothelial cells, the most important is shear stress. Shear stress is defined as the force created when two adjacent parcels of fluid are traveling adjacent to each other at different velocities. The force created between the parcels by this difference in speed at the point of contact between them is shear. In the case of simple laminar flow (i.e., blood flow direction parallels the vessel wall), the blood velocity profile is fastest at the center of the lumen, and the velocity decreases in a series of concentric circles approaching zero flow when in contact with the endothelial surface.

The local environment of the sinus leads to a region of recirculation which makes one ponder the relationship between its structure and function. The structure of the sinus is a dilation just distal to a bifurcation. This dilation creates a sudden expansion, and it leads to disturbance of the flow and vortex formation (Nguyen et al., 2008). This geometry, together with the cardiac cycle, leads to a pulsatile wash-out of the carotid stretch that accompanies each systolic pressure peak with every beat (Ku and Giddens, 1983). In other words, the sinus, due to the dilation geometry, is also experiencing a non-uniform stress field with pulsatile flow (Bilgi and Atalik, 2020). These stress fields lead to the development of recirculation regions inside the sinus. The types of forces that act on vascular endothelium are broadly thought of as WSS or circumferential stretch (Lu and Kassab, 2011). Whereas circumferential stretch reflects blood pressure, WSS depends on fluid properties and flow conditions, *and it is highly affected by viscosity* (Lee et al., 2020). Therefore, the unique presence of such stress fields suggests that transduction at the sinus may be biased toward shear stress as it carries more information on the overall hemodynamics than just pulsatile pressure.

The characteristics of the shear stress patterns specific to the sinus have been studied extensively since these patterns are believed to underlie the pathophysiology for atherogenesis in the carotid. The regions noted to have the highest incidence are often associated with the *lowest* WSS (Zhang et al., 2012). The region of low WSS may *independently* cause intimal-medial thickening (Irace et al., 2004; Liu et al., 2016; Zhang H. et al., 2018). Also it is thought to be a contributing nidus in the inflammatory cascade that ultimately leads to atherogenesis, as endothelial cells at the arterial vessels require WSS values of $\approx$2 Pa to avoid morphological changes (Malek et al., 1999). As a result, there are many efforts to utilize non-invasive quantification of WSS aimed at identifying patients who will develop carotid plaques (Katakami, 2016).

The region of the lowest WSS is a consequence of the disruption of laminar flow in the sinus described by Ku. This area of lowest WSS correlates with the region of highest shear oscillation (Zhang et al., 2012). To describe this, Ku posited the Oscillatory Shear Index (OSI) (Ku and Giddens, 1983) metric to describe the degree of the WSS direction persistency during a cardiac cycle. Essentially, the OSI quantifies the amount of WSS deflection from the average over a cardiac cycle, due to flow disturbance, and OSI is reported between 0 and 0.5, where 0 denotes no change in the vector direction. In an idealized Y-shaped carotid bifurcation model, OSI peak corresponded to the region of greatest intimal thickening in the inner and outer wall of the sinus. However, there was a weaker correlation along the sides of the sinus, where plaque development still occurs. To Ku's model, Ding et al. (2001) utilized a "tuning fork" shaped model more representative of actual carotid angiograms. He found that high OSI ($>$0.20) also correlated well with regions of the recirculation zones inside the carotid sinus and at the side-walls. As expected, a more anatomically realistic carotid model better reflected the accompanying sinus flow patterns. Furthermore, it demonstrated that flow changes throughout the cardiac cycle correspond to specific oscillation patterns in the low WSS region. The anatomy of the carotid sinus creates local secondary flows that "enhances the pulsation of WSS under pulsatile conditions" such as when the heart is beating and hence is a site well-suited for flow transduction. A patient-specific study supporting the relation between low WSS and high OSI regions can be seen in **Figure 4**. Here, the reader can note the discreet overlap between the region of lowest WSS and the region of most apparent shear oscillation. In that study, this region of low WSS may enhance the ability to detect and transduce the smaller oscillatory shear forces that result from recirculation. The low WSS environment makes it EASIER to transmit the oscillatory forces through the thinner medial layers where the carotid sinus nerve inserts (Porzionato et al., 2019).

The Role of PIEZO Receptors in Mechanotransduction of Flow

The roles of the carotid sinus apparatus in various homeostatic functions such as "cross-talk" (Wilson et al., 1990; Chen et al., 2007) between the cardiopulmonary and arterial reflexes, renal control of free water (Barger et al., 1984; Ouisuwan and Buranakarl, 2005), and regulation of vessel capacitance via smooth muscle tone (Risoe et al., 1994) suggest that mechanotransduction of blood flow in the sinus region plays a role in these processes. The breadth of functions underpinned by blood flow mechanotransduction across organ systems has led to increased interest in the relationship between shear force-gated

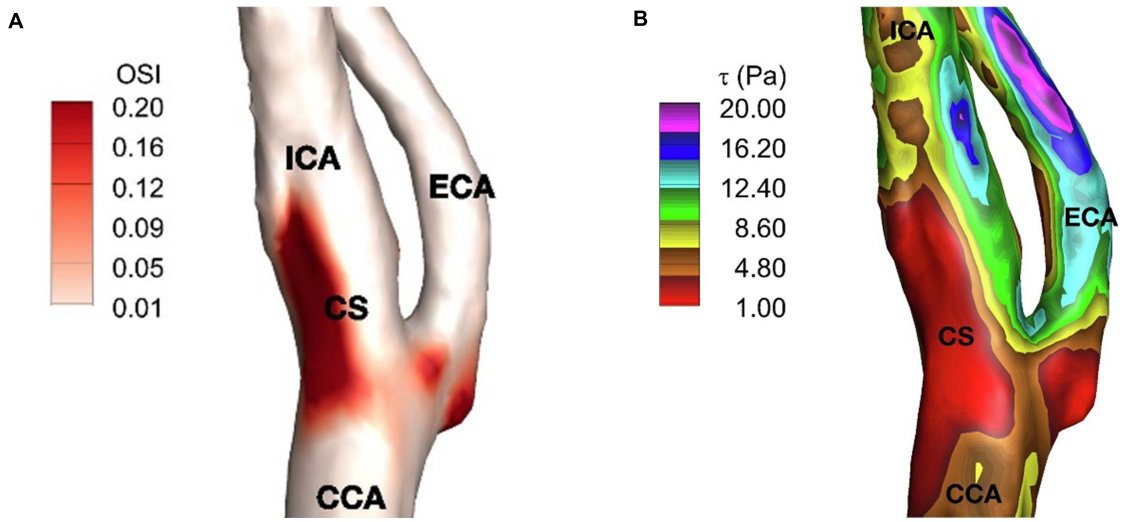

FIGURE 4 | (A) Time-averaged wall shear stress**, (B)** oscillatory shear index on carotid artery. ICA, internal carotid artery; ECA, external carotid artery; CCA, common carotid artery; and CS, carotid sinus (Iskander et al., 2020).

receptors and blood rheology. An important family of shear-force gated channels are the PIEZO receptors. In vertebrates, this group is comprised only of the PIEZO1 and PEIZO2 receptors (Coste, 2012). The PIEZO1 receptor is involved in endothelial function and development (Li et al., 2014; Rode et al., 2017) as well as cardiovascular homeostasis (Rode et al., 2017). PIEZO2 receptors have a role in the function of the somatosensory apparatus involved in proprioception (Yang et al., 2016), pain sensation (Bai et al., 2017), and possibly as a coreceptor with PIEZO1 in the carotid sinus (Zeng et al., 2018).

To further support the basis of the role of the PIEZO receptors in a model of cellular transduction of mechanical stimulus, Coste et al. (2010) determined the numbers of PIEZO-containing cells in adult mice organs by mRNA quantitative polymerase chain reaction. Importantly, the average number of detected PIEZO2 cells shown in **Table 1** are markedly increased for the cells that project from the dorsal root ganglia where mechanosenstive neurons originate and project to blood vessels in order to maintain vasomotor tone as shown by the presence of 478 PIEZO2 cells out of a total 2391 cells. The relative number of PIEZO cells are benchmarked on the assumption that bladder tissue has the same number of PIEZO1 cells as PIEZO2 cells. When the PIEZO2 cells were essentially deactivated, the dorsal root ganglion (DRG) cells were rendered insensitive to mechanical stimuli. Furthermore, when the PIEZO 1 and 2 receptors were *over*-expressed, the response to mechanical stimuli was increased exponentially. The origin of these neurons in a known mechanosensitive region of the DRG is consistent with previous studies (Coleridge and Coleridge, 1980; Westcott and Segal, 2013). Therefore, they concluded that the PIEZO receptors "are both necessary and sufficient" for mechanotransduction for cells in which they are expressed.

TABLE 1 | PIEZO-containing cell numbers found in adult mice organs (Coste et al., 2010).

Organ	PIEZO1 Cells	PIEZO2 Cells
Bladder	206	206
Brain	23	9
Cerebellum	8	9
Colon	69	66
Dorsal Root Ganglia	13	478
Heart	15	6
Kidney	74	13
Lung	407	506
Skeletal Muscle	13	6
Skin	165	16
Small Intestine	25	19
Stomach	43	35

PIEZO Receptor and Shear Stress From Blood Flow

There is increasing emphasis on the fundamental role of the PEIZO1 receptor in health and disease. In the commentary by Li et al. (2015) titled *Endothelial Piezo1: life depends on it*, he makes the argument that cation influx through the receptor results from shear force outside of the cell and leads to membrane tension proximal to the PIEZO channel. This triggers cation influx through the receptor into the cell. The resulting action depends on the cell in question. For example, if the relevant cell is a red blood cell, then the action may be to trigger downstream pathways meant to maintain the appropriate hydration (Cahalan et al., 2015) and turgidity of the cell, or the amount of iron turn-over from red blood cell turnover (Andolfo et al., 2020).

Similarly, in the case of the endothelial cell, the PIEZO1 receptor may enable the endothelium to serve its role as both a

responder to and shaper of blood flow necessary for development and function throughout life. In a mouse model with mutated PIEZO1 activity (Li et al., 2015), the alignment of endothelial cells needed for vascular maturation was aberrant. In these embryos, the heart is developed and beating and the endothelial cells are present, yet are unable to align themselves to create mature vasculature in the direction of blood flow, leading to embryonic lethality. Without the maturation of major vessels, the development of downstream organs cannot complete. In adulthood, the alignment of endothelial cells may offer protection against atherosclerosis by reducing the local atherogenic effects of disturbed flow (Coleman et al., 2020). The alignment of endothelial cells, as mediated by mechanisms including the PIEZO protein within the cell membrane, supports the notion that the goal of transducing shear stress is highly dependent on the time and place of the cell in question.

When detecting regions of locally created secondary flows, the PIEZO receptors are well suited to detecting endothelial flow data (Murthy et al., 2017; Douguet et al., 2019). In the work by Li et al. (2014), they demonstrate that the PIEZO1 receptors mediate shear stress-related events in human and mouse embryonic endothelial cells (**Figure 5**). In the *in vitro* setting, the human endothelial cells deficient in PIEZO activity were unable to align themselves in the direction of an applied shear force as seen *in vivo*. They first attached Green Fluorescent Protein to PIEZO1 proteins and found that they aggregated near the apical lamellipodia of the endothelial cells. The cells that were +/+ for the PEIZO1 genotype linearly aligned in the direction of the applied shear force. Those that were +/− were aligned in a cobble-stone fashion, and those that were −/− demonstrated no alignment. Furthermore, they demonstrated that the lack of piezo activity eliminated shear stress-induced entry of Ca^{2+} into the human endothelial cells entirely. They isolated human embryonic kidney cells that lacked PIEZO1. It was only after adding exogenous PIEZO1 activity that Ca^{2+} entry was seen in these cells. This supports the hypothesis that the PIEZO1 receptor has an important role in the detection and cellular response to shear stress.

The pivotal role of the PIEZO receptor in the detection of endothelial flow data rather than blood pressure, *per se*, is demonstrated when considering how vasculature will remodel in response to chronic changes. In the study by Retailleau et al. (2015), a murine model of PIEZO knockout was developed. Importantly, they found that the PIEZO1 receptors were located primarily in the media of the smooth muscle portion of the smaller diameter arteries, particularly the cutaneous caudal artery and the cerebral arteries, but not the larger diameter arteries including the renal artery and the aorta. In the PIEZO knockout mice where both alleles for the receptor were absent, all stretch-activated channel activity (where a patch-clamp is applied to the cell membrane as a shear stimulus) was absent. This suggests an important role for the PIEZO1 in vessel myocyte mechanotransduction. But when vasoactive substances were used, they found that the PIEZO knockout tissue from the caudal and cerebral arteries did not require the receptor to respond to vaso-constricting or vaso-dilating drugs. They did find that in the small diameter-arterial smooth muscle tissue, the PIEZO receptor was a necessary requirement to respond to the patch clamp stimulus, however. In order to examine smooth muscle remodeling in a model of hypertension, their model used an infusion of angiotensin II (AT II) infusion versus a saline as a normotensive control. They found that the arterial diameter, wall thickness, and cross-sectional area (CSA) was unchanged in the PIEZO-absent mice under normotensive conditions. In the knockout mice who underwent AT II infusions, there was a significant decrease in diameter, thickness and in CSA. Finally, they used cells where "mechanoprotection" was removed in which the actin cross-linking element Filament A (FlnA) was deleted in vascular smooth muscle. Those "unprotected" cells with the FlnA deletion resulted in PIEZO receptors that were open even without hypertension–essentially reducing the shear stimulus threshold needed for them to open–demonstrating that

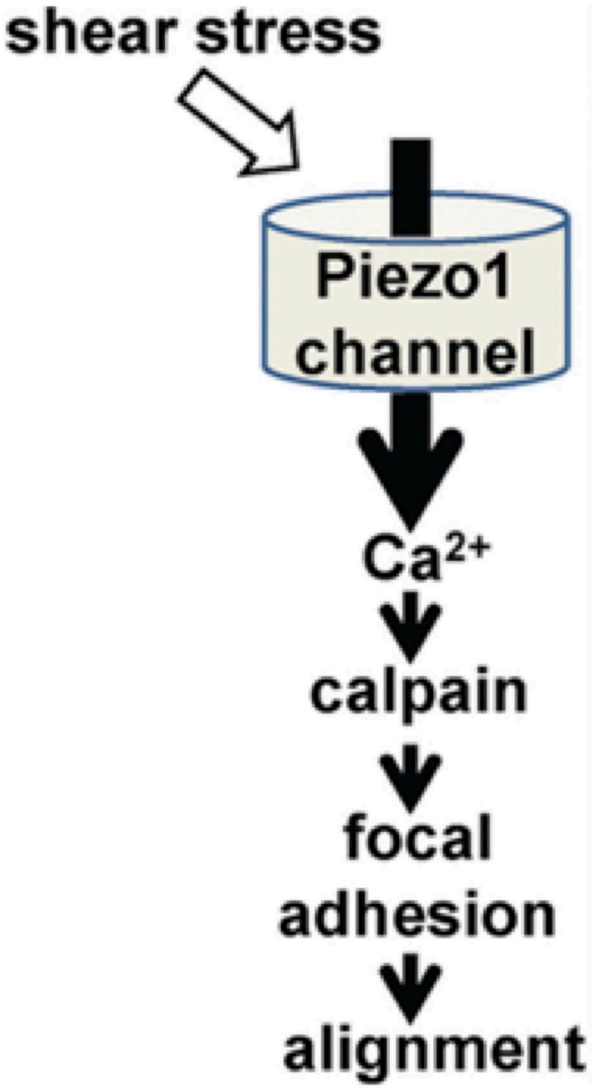

FIGURE 5 | The role of PIEZO1 receptors in alignment of endothelial cells during cardiovascular embryological development (Li et al., 2014).

remodeling of smooth muscle occurred in the caudal artery without hypertension and only with activated PIEZO receptors. Just replacing one of the PIEZO alleles in these unprotected cells was enough to reverse the increase in wall thickness seen from hypertension or the removal of the FlnA. This further supported the notion that the PIEZO receptor is central to the transduction and endothelial response to shear stress and not necessarily to blood pressure.

In addition to the possible role of the PIEZO receptor in vascular remodeling, elucidating the possible role of the PIEZO receptor in the proper functioning of the endothelium may suggest a line of inquiry aimed at examining the pathophysiology of atherosclerotic disease in the carotid sinus that results from the blood flow patterns unique to it. In the comprehensive review by Gimbrone, they discuss studies that compared atheroprone geometries such as the carotid sinus with its "oscillatory" flow patterns to atheroprotective geometries such as the distal internal carotid that have more consistent laminar flow (Gimbrone and Garcia-Cardena, 2016). In the region of atheroprone endothelium such as in the sinus, flow appears to demonstrate an "absence of undisturbed laminar shear stresses". Just upstream, however, endothelium in the distal internal carotid demonstrated upregulation of those factors associated with an atheroprotective phenotype, particularly of Kruppel-like Factor 2 (KLF2). Importantly, KLF2 has also been demonstrated to regulate production of vasoactive substances used to mediate locally mediated vasomotor tone such as nitric oxide. This locally mediated sensing and responding to shear force is essential to the role of PIEZO channels in sensing of cardiovascular force as described by Li et al. (2014) More specifically, it appears that the PIEZO receptors could be the primary players in coupling endothelial response to regulation of blood flow. As such, when PIEZO genes were disrupted, the endothelial response to increased blood flow appears to be diminished (Beech and Kalli, 2019). Given the central role of the PIEZO in sensing shear forces and the apparent importance of shear forces in atheroma prohibition and formation, PIEZO dysfunction may have a role in the development of the atheroprone phenotype.

The activation physics of the PIEZO receptor is also particularly well-suited to the type of flow unique to the sinus region described above. The recirculatory region results in secondary flows that repeatedly cause shear oscillation patterns that create a cohort of vibrations detected at the endothelium (Ku et al., 1985b). This creates a composite picture of the blood flow that reflects the particular rheological state of blood for a given cardiac output. Factors that change the oscillatory footprint of blood in the sinus region, including viscosity, blood pressure, and temperature, may only exhibit subtle changes in corresponding shear stress peaks and troughs from beat to beat. The PIEZO1 receptors have the distinctive feature of a particularly short inactivation time (Zheng et al., 2019). This is due to what Zheng et al. (2019) describes as the physical constriction within the lumen of the receptor tubule and a hydrophobic layer across the pore. This yields inactivation kinetics that are incredibly fast with time to cessation of activation of the receptor in as little as 50 ms (Wu et al., 2017b). Indeed, disease may result from slower time to inactivation (Demolombe et al., 2013). Such inactivation kinetics having few receptor channels open at a given time leads to a "temporal frequency filtering" phenomenon in which repeated vibrational stimuli can be transduced with high precision by filtering out background frequencies (Lewis and Grandl, 2015; Lewis et al., 2017). This may explain the unique suitability of the PIEZO receptor to reacting to infinitesimally small, discrete changes in the shear-force waveform in a region of vortical flow as in the carotid sinus.

PIEZO and the Effect on Red Blood Cell Morphology

The role of the PIEZO1 receptor in blood rheology may be seen in the effects on the red blood cells themselves when the receptor function is altered. Blood viscosity and other flow parameters change with blood temperature, local microenvironments both inside and outside the cell, iron and hemoglobin state, as well as the size of the vessel and flow rate (Dupire et al., 2012). A major determinant of the intrinsic ability of a red blood cell, whose diameter ranges from 6–8 μm, to sufficiently contort itself through capillaries around 5 μm in diameter, Godwin et al. (2020) is intracellular hydration status.

The possible role of the PIEZO receptor in blood flow homeostasis is supported by PIEZO1 mutations that lead to erythrocyte changes. In the work by Cahalan (Cahalan et al., 2015), they demonstrate a relationship between PIEZO1 function and appropriate hydration of red blood cells. They showed that mechanical force applied to red blood cells by a pipette initiated entry of Ca^{2+} into cells through the PIEZO1 channel, leading to osmotic changes. Furthermore, the red blood cells of PIEZO1-deficient mice were overhydrated, more fragile, and underwent greater splenic sequestration. This suggests a role for shear forces acting on the red blood cells themselves in maintaining rheological homeostasis. This further supports the notion that PIEZO channels represent a major means by which shear forces are transduced into cellular responses.

The PIEZO Receptor and the Carotid Sinus

More specific to the sinus region, the recent evidence produced by Zeng et al. (2018) for the preponderance of PEIZO1 and PEIZO2 receptors in the carotid sinus represents a significant shift in researchers' understanding the role of mechanotransduction in baroreception. Using a murine model, they injected fluorescent Cholera Toxin B (CTB) underneath the serosa of the sinus region. With the understanding of the location of the baroreceptor cell bodies in the nodose and petrosal ganglia, they quantified the number of CTB-labeled cells that expressed PIEZO1 or PIEZO2 transcripts. Of the total 95 cells that were labeled, six were *PIEZO1* positive, and eight were *PIEZO2* positive. Then they took knock-out mice for both alleles of the PIEZO genes and administered both phenylephrine and sodium nitroprusside. Essentially, the expected baroreceptor reflex was abolished with either drug. Knock-out mice with wild type PIEZO-intact phenotype who were awake and ambulating had a significantly

higher average blood pressure and lability with a slightly higher average heart rate than their normal counterparts. This clinical picture is similar to the syndrome of "baroreceptor failure" described in the literature. Given this, the presence of the PIEZO receptor may be fundamental to the function of the carotid sinus.

DISCUSSION

With the discovery of PIEZO channel aggregation in the sinus region, the carotid sinus may eventually be characterized as a sensory organ in its own right. The uniqueness of the flow in that region combined with the receptor population exquisitely suited to detect it lends itself well to efforts to modulate the action of the carotid sinus to effect cardiovascular changes. The PIEZO receptor family was described by Coste in 2010 and has since been recognized in a remarkable array of cells in which mechanotransduction serves as a nidus for cellular activity. More developments in the PIEZO receptor's role in baroreceptor mechanism are anticipated.

The variety of organ systems now known to employ the PIEZO channel in converting shear forces into physiologic responses has led to a better understanding of mediators of its activation (Wu et al., 2017a). Wu categorizes the effectors of PIEZO function into those that affect the shear effects on the membrane (i.e., the cell) to which the channel is attached, or the channel itself. Examples of known mediators of PIEZO function that alter the membrane and therefore shear properties include pH, cell hydration, osmotic pressure, and lipid composition. Direct channel mediators include pH, voltage, resting membrane potential, and isolated protein and pharmacologic mediators. For example, the isolation of a molecular agonist named Yoda1 (Syeda et al., 2015), which shortens the inactive state of PIEZO1, raises the possibility that there may be a method by which its inactivation kinetics may be manipulated. These mediators each represent potential methods by which the sinus region can be monitored and altered, and therefore another venue by which carotid sinus effects can be studied.

Furthermore, thanks to advances in researchers' ability to mine large datasets, biological associations between the PIEZO gene and the carotid sinus can uncover other potential avenues for inquiry. An example of this is Phenoscanner (Staley et al., 2016; Kamat et al., 2019)[1], with which traits can be cross-referenced with specific genes and gene variants. When examining the PIEZO1 gene, hemodynamically-relevant traits include mean corpuscular volume, hemoglobin concentration, red cell count, whole body water mass, and metabolic rate. It suggests at least a genetic link between blood composition homeostasis and PIEZO-mediated mechanotransduction. As for how and where that transduction of shear force to blood homology takes place, time will tell.

Numerous rheology studies have been conducted to understand the complex properties of blood (Thurston, 1973, 1976, 1979; Chien, 1975; Yeleswarapu, 1996). In Thurston's work, an oscillating piston cylinder assembly was used to obtain the viscosity curves and showed that blood has both viscoelastic and shear-thinning properties. Blood was centrifuged to disturb any formation between the cells, and then plasma and cells were mixed to ensure certain hematocrit levels. Despite using an oscillatory piston-cylinder system in which fluid cannot experience high residence times–a reflection of the amount of flow recirculation as seen in the sinus–other complex rheological properties were captured in these experiments. In the work by Chien (1975), a Couette viscometer was used to demonstrate the association between hematocrit concentration and viscosity curves. Although more recent studies claimed that non-Newtonian behavior can be neglected in large arteries (Lee and Steinman, 2007; Khan et al., 2017; Arzani, 2018), this assumption for whole blood shall only be valid when the overall shear rate is higher than 100 s^{-1}, which is similar to these older rheological experiments (Thurston, 1973, 1976, 1979; Chien, 1975; Yeleswarapu, 1996). Indeed, more recent studies of minimally dissipative CFD schemes have shown the importance of shear-thinning properties in pathological conditions (Bilgi and Atalik, 2019, 2020). An exquisite example of this is the decrease in shear rate with decreased cardiac function in Fontan circulation (Wei H. et al., 2020).

Understanding the Carotid Sinus to Achieve Homeostatic State and Future Directions

By quantifying the means by which the body "sees" blood *flow*, novel and more precise viscosity biomarkers may one day be available to clinicians. These, in turn, could facilitate care of patients undergoing resuscitation of their blood volume in order to better meet their needs. For example, when reconstituting blood volume lost during surgery, consideration for blood *viscosity* (itself a main component of the shear properties of blood)–in addition to volume and oxygen delivery–may facilitate improved outcomes and more cost-effective administration. Further supporting the sinus region's possible suitability in this regard, Lee et al. (2020) performed a very elegant study in which they studied changing flow patterns that result from blood *viscosity* after a bolus of crystalloid. To eight healthy subject they administered a one-liter bolus of normal saline. Obtaining viscosity values before and after the bolus, they then simulated the blood flow at the carotid bifurcation and studied the effects on the region of recirculation due to changes in viscosity from the infusion. They observed that the bolus resulted in the accentuation of the shear rate and velocity in the region of recirculation with a measurable decrease in viscosity.

When considering the parameters that affect the activity of the PIEZO receptor and their location, possibly useful endpoints that reflect shear forces caused by blood flow can be studied. One means to approach this is to consider the known mutations in PIEZO genes and the diseases with which they are associated. Any reader with an interest in a more comprehensive review beyond the scope of this piece on physiologic force transduction as mediated by the PIEZO receptor is encouraged to read the

[1] http://www.phenoscanner.medschl.cam.ac.uk/

review of the current state of knowledge by Beech and Kalli (2019). They include comprehensive descriptions of the PIEZO receptor and its genomic and protein structure and function as it relates to cardiovascular performance. Significantly, they point out that both PIEZO subtypes act as Ca^{2+} ion channels that appear exquisitely sensitive to fluid flows adjacent to cell membranes in which they are incorporated. They go on to suggest that this construct may be used to explain a possible role in the pathophysiology of diseases including lymphatic dysplagia, types of heart failure, hypertension, vascular diseases including aneurysmal ruptures, varicose veins, and anemia.

Looking at the location, morphology, distinctive flow patterns, and PIEZO receptor population of the carotid sinus, we are suggesting that the sinus may be a site of blood viscosity transduction. Given the presence on both the red blood cells and well as the vessel walls, a mutation of the PIEZO receptor may associate comorbid conditions such as anemia with cardiovascular disease that markedly alters blood viscosity–something we see when seeking links in genotype with phenotype. A mutation in the PIEZO receptor that affects the ability to accurately capture the fluid dynamics inside the sinus can alter feedback mechanisms mediated by the autonomic nervous system. This, in turn, can lead to a cardiovascular response that does not appropriately meet the real blood flow and metabolic needs of the patient.

Consider a theoretical mutation in the PIEZO1 receptor where the decrease in blood viscosity with decreased hematocrit is a well-described association (Quemada, 1981). Such a mutation would render a diminished/blunted signal that under normal conditions would correspond with a higher viscosity which would be perceived as a higher hematocrit when, in fact, it is normal or low. In order to increase sinus recirculation and decrease perceived viscosity (Perktold et al., 1991), other organ systems including the renal system, hepatic system, and cardiovascular system would act to retain free water, reduce the viscosity of blood, and increase blood velocity in order to reacquire a "normal" value.

In patients with aberrant blood viscosity of various etiologies, optimization of rheologic parameters, in addition to titrating to pressures, may enable more patient-specific management of blood flow. When trying to understand the physiological machinery the human body uses to detect and maintain hematologic homeostasis, clinicians may better mimic what the autonomic nervous system does to optimize viscosity and, therefore, perfusion. In emulating the apparent physiology utilized at the sinus to characterize blood's viscometric and shear stress properties, we can design devices that better aid management of patients with compromised blood delivery, or mitigate the effects pathophysiologic shear patterns have on the carotid vessel walls. Certainly, the fact that the location of the carotid vessels in the neck lends itself to easy visualization by non-invasive methods, including ultrasound, facilitates this. By using parameters like sinus geometry and blood velocity that can be easily obtained by a Doppler scan, recent machine learning algorithms based on deep learning can be used to guide physicians. Administration of blood products, blood expanders, and other agents to either increase or decrease blood viscosity can be titrated to specific WSS parameters and, ultimately, affect viscosity homeostasis.

AUTHOR CONTRIBUTIONS

AI and CB contributed to the conceptualization, writing (original draft), manuscript review, and editing. RN, TB, DN, and NP contributed to conceptualization, manuscript review, and editing. All authors contributed to the article and approved the submitted version.

REFERENCES

Andani, R., and Khan, Y. S. (2020). "Anatomy, head and neck, carotid sinus," in *StatPearls*, (Treasure Island, FL: StatPearls Publishing).

Andolfo, I., Rosato, B. E., Manna, F., De Rosa, G., Marra, R., Gambale, A., et al. (2020). Gain-of-function mutations in PIEZO1 directly impair hepatic iron metabolism via the inhibition of the BMP/SMADs pathway. *Am. J. Hematol.* 95, 188–197. doi: 10.1002/ajh.25683

Arzani, A. (2018). Accounting for residence-time in blood rheology models: do we really need non-Newtonian blood flow modelling in large arteries? *J. R. Soc. Interface* 15:20180486. doi: 10.1098/rsif.2018.0486

Bai, T., Li, Y., Xia, J., Jiang, Y., Zhang, L., Wang, H., et al. (2017). Piezo2: a candidate biomarker for visceral hypersensitivity in irritable bowel syndrome? *J. Neurogastroenterol. Motil.* 23, 453–463. doi: 10.5056/jnm16114

Barger, A. C., Farhi, E. R., and Cant, J. R. (1984). Modulation of renal baroreceptor function by catecholamines and salt intake in the conscious dog. *Clin. Exp. Hypertens. A* 6, 287–298. doi: 10.3109/10641968409062566

Beech, D. J., and Kalli, A. C. (2019). Force sensing by piezo channels in cardiovascular health and disease. *Arterioscler. Thromb. Vasc. Biol.* 39, 2228–2239. doi: 10.1161/ATVBAHA.119.313348

Bernardi, M. H., Wahrmann, M., Dworschak, M., Kietaibl, C., Ristl, R., Edlinger-Stanger, M., et al. (2019). Carotid artery blood flow velocities during open-heart surgery and its association with delirium: a prospective, observational pilot study. *Medicine (Baltimore)* 98:e18234. doi: 10.1097/MD.0000000000018234

Bilgi, C., and Atalik, K. (2019). Numerical investigation of the effects of blood rheology and wall elasticity in abdominal aortic aneurysm under pulsatile flow conditions. *Biorheology* 56, 51–71. doi: 10.3233/BIR-180202

Bilgi, C., and Atalik, K. (2020). Effects of blood viscoelasticity on pulsatile hemodynamics in arterial aneurysms. *J. Nonnewtonian Fluid Mech.* 279:104263. doi: 10.1016/j.jnnfm.2020.104263

Bowers, A. S., Reid, H. L., Greenidge, A., Landis, C., and Reid, M. (2013). Blood viscosity and the expression of inflammatory and adhesion markers in homozygous sickle cell disease subjects with chronic leg ulcers. *PLoS One* 8:e68929. doi: 10.1371/journal.pone.0068929

Bowers, A. S. A., Duncan, W. W., and Pepple, D. J. (2018). Erythrocyte aggregation and blood viscosity is similar in homozygous sickle cell disease patients with and without leg ulcers. *Int. J. Angiol.* 27, 35–38. doi: 10.1055/s-0037-1608901

Buyan, N., Akcaboy, M., Goktas, T., Kula, S., Nazliel, B., Cakar, N., et al. (2017). Effects of whole blood viscosity and plasma NOx on cardiac function and cerebral blood flow in children with chronic kidney disease. *Turk. J. Med. Sci.* 47, 1482–1491. doi: 10.3906/sag-1609-33

Cahalan, S. M., Lukacs, V., Ranade, S. S., Chien, S., Bandell, M., and Patapoutian, A. (2015). Piezo1 links mechanical forces to red blood cell volume. *Elife* 4:e07370. doi: 10.7554/eLife.07370

Cekirdekci, E. I., and Bugan, B. (2020). Whole blood viscosity in microvascular angina and coronary artery disease: significance and utility. *Rev. Port. Cardiol.* 39, 17–23. doi: 10.1016/j.repc.2019.04.008

Celik, T., Yilmaz, M. I., Balta, S., Ozturk, C., Unal, H. U., Aparci, M., et al. (2017). The relationship between plasma whole blood viscosity and cardiovascular

events in patients with chronic kidney disease. *Clin. Appl. Thromb. Hemost.* 23, 663–670. doi: 10.1177/1076029616634888

Chen, X., Kim, J. K., Sala-Mercado, J. A., Hammond, R. L., Swamy, G., Scislo, T. J., et al. (2007). Identification of the total peripheral resistance baroreflex impulse response from spontaneous hemodynamic variability: validation by chronic arterial baroreceptor denervation. *Conf. Proc. IEEE Eng. Med. Biol. Soc.* 2007, 1051–1054. doi: 10.1109/IEMBS.2007.4352475

Cheng, A. L., Pahlevan, N. M., Rinderknecht, D. G., Wood, J. C., and Gharib, M. (2018a). Experimental investigation of the effect of non-Newtonian behavior of blood flow in the Fontan circulation. *Eur. J. Mech. B Fluids* 68, 184–192. doi: 10.1016/j.euromechflu.2017.12.009

Cheng, A. L., Pahlevan, N. M., and Wood, J. C. (2018b). Non-newtonian behavior significantly affects hemodynamic efficiency in a four-dimensional flow magnetic resonance Fontan model. *J. Am. Coll. Cardiol.* 71:A622.

Cheng, A. L., Wee, C. P., Pahlevan, N. M., and Wood, J. C. (2019). A 4D flow MRI evaluation of the impact of shear-dependent fluid viscosity on in vitro Fontan circulation flow. *Am. J. Physiol. Heart Circ. Physiol.* 317, H1243–H1253.

Chevalier, G., Sinatra, S. T., Oschman, J. L., and Delany, R. M. (2013). Earthing (grounding) the human body reduces blood viscosity-a major factor in cardiovascular disease. *J. Altern. Complement Med.* 19, 102–110. doi: 10.1089/acm.2011.0820

Chien, S. (1975). Biophysical behavior of red cells in suspensions. *Red Blood Cell* 2, 1031–1133. doi: 10.1016/b978-0-12-677202-9.50019-8

Cibis, M., Potters, W. V., Selwaness, M., Gijsen, F. J., Franco, O. H., Arias Lorza, A. M., et al. (2016). Relation between wall shear stress and carotid artery wall thickening MRI versus CFD. *J. Biomech.* 49, 735–741. doi: 10.1016/j.jbiomech.2016.02.004

Coleman, P. R., Lay, A. J., Ting, K. K., Zhao, Y., Li, J., Jarrah, S., et al. (2020). YAP and the RhoC regulator ARHGAP18, are required to mediate flow-dependent endothelial cell alignment. *Cell Commun. Signal.* 18:18. doi: 10.1186/s12964-020-0511-7

Coleridge, H. M., and Coleridge, J. C. (1980). Cardiovascular afferents involved in regulation of peripheral vessels. *Annu. Rev. Physiol.* 42, 413–427. doi: 10.1146/annurev.ph.42.030180.002213

Coste, B. (2012). [Piezo proteins form a new class of mechanically activated ion channels]. *Med. Sci. (Paris)* 28, 1056–1057. doi: 10.1051/medsci/20122812012

Coste, B., Mathur, J., Schmidt, M., Earley, T. J., Ranade, S., Petrus, M. J., et al. (2010). Piezo1 and Piezo2 are essential components of distinct mechanically activated cation channels. *Science* 330, 55–60. doi: 10.1126/science.1193270

Dai, Y., Qian, Y., Zhang, M., Li, Y., Lv, P., Tang, X., et al. (2019). Associations between local haemodynamics and carotid intraplaque haemorrhage with different stenosis severities: a preliminary study based on MRI and CFD. *J. Clin. Neurosci.* 66, 220–225. doi: 10.1016/j.jocn.2019.05.041

de Vecchis, R., Ciccarelli, A., and Cioppa, C. (2010). Intima-media thickness of internal carotid arteries and total carotid plaque area: two surrogate endpoints of which the former has to be considered a weaker putative measure of subclinical atherosclerosis compared with the latter. *J. Cardiovasc. Med. (Hagerstown)* 11:325. doi: 10.2459/01.JCM.0000369376.83887.7b

Demolombe, S., Duprat, F., Honore, E., and Patel, A. (2013). Slower Piezo1 inactivation in dehydrated hereditary stomatocytosis (xerocytosis). *Biophys. J.* 105, 833–834. doi: 10.1016/j.bpj.2013.07.018

Ding, Z., Wang, K., Li, J., and Cong, X. (2001). Flow field and oscillatory shear stress in a tuning-fork-shaped model of the average human carotid bifurcation. *J. Biomech.* 34, 1555–1562. doi: 10.1016/s0021-9290(01)00148-8

Dong, J., Wong, K. K., and Tu, J. (2013). Hemodynamics analysis of patient-specific carotid bifurcation: a CFD model of downstream peripheral vascular impedance. *Int. J. Numer. Method. Biomed. Eng.* 29, 476–491. doi: 10.1002/cnm.2529

Douguet, D., Patel, A., Xu, A., Vanhoutte, P. M., and Honore, E. (2019). Piezo ion channels in cardiovascular mechanobiology. *Trends Pharmacol. Sci.* 40, 956–970. doi: 10.1016/j.tips.2019.10.002

Dupire, J., Socol, M., and Viallat, A. (2012). Full dynamics of a red blood cell in shear flow. *Proc. Natl. Acad. Sci. U.S.A.* 109, 20808–20813. doi: 10.1073/pnas.1210236109

Elias, M. F., Torres, R. V., and Davey, A. (2019). Carotid artery blood flow velocities and cognitive performance: forecasting cognitive decline. *Am. J. Hypertens.* 32, 237–239. doi: 10.1093/ajh/hpy184

Engin, M., and Guvenc, O. (2020). Investigation of the predictive values of triglyceride/HDL cholesterol ratio and whole blood viscosity with regard to severe peripheral or carotid artery disease in patients scheduled for coronary bypass. *Heart Surg. Forum* 23, E310–E314. doi: 10.1532/hsf.2991

Feng, B., and Guo, T. (2019). Visceral pain from colon and rectum: the mechanotransduction and biomechanics. *J. Neural Transm. (Vienna).* 127, 415–429. doi: 10.1007/s00702-019-02088-8

Garcia Callejo, F. J., De Paula Vernetta, C., Platero Zamarreno, A., Orts, A. M., Velert Vila, M. M., Morera Perez, C., et al. (2006). [Blood viscosity profile in rapidly progressive sensorineural hearing loss with positive Western-blot]. *Acta Otorrinolaringol. Esp.* 57, 90–95. doi: 10.1016/s0001-6519(06)78668-x

Gates, P. E., Gurung, A., Mazzaro, L., Aizawa, K., Elyas, S., Strain, W. D., et al. (2018). Measurement of wall shear stress exerted by flowing blood in the human carotid artery: ultrasound doppler velocimetry and echo particle image velocimetry. *Ultrasound Med. Biol.* 44, 1392–1401. doi: 10.1016/j.ultrasmedbio.2018.02.013

Gimbrone, M. A. Jr., and Garcia-Cardena, G. (2016). Endothelial cell dysfunction and the pathobiology of atherosclerosis. *Circ. Res.* 118, 620–636. doi: 10.1161/CIRCRESAHA.115.306301

Glick, G., and Covell, J. W. (1968). Relative importance of the carotid and aortic baroreceptors in the reflex control of heart rate. *Am. J. Physiol.* 214, 955–961. doi: 10.1152/ajplegacy.1968.214.5.955

Goddi, A., Bortolotto, C., Fiorina, I., Raciti, M. V., Fanizza, M., Turpini, E., et al. (2017). High-frame rate vector flow imaging of the carotid bifurcation. *Insights Imaging* 8, 319–328. doi: 10.1007/s13244-017-0554-5

Godwin, L., Tariq, M. A., and Crane, J. S. (2020). "Histology, capillary," in *StatPearls*, (Treasure Island, FL: StatPearls Publishing).

Gudmundsson, M., Nordborg, E., Bengtsson, B. A., and Bjelle, A. (1993). Plasma viscosity in giant cell arteritis as a predictor of disease activity. *Ann. Rheum. Dis.* 52, 104–109. doi: 10.1136/ard.52.2.104

Gulevskaia, T. S., Morgunov, V. A., and Anufriev, P. L. (2007). [Carotid sinus atherosclerosis]. *Arkh. Patol.* 69, 25–32. doi: 10.1016/0021-9150(89)90155-x

Guo, S., Jiang, P., Liu, J., Yang, X., Jiang, C., Li, Y., et al. (2018). A comparative CFD analysis of common carotid fusiform aneurysm in canine models and vertebrobasilar fusiform aneurysm in human patients. *Int. Angiol.* 37, 32–40. doi: 10.23736/S0392-9590.17.03869-X

Hildesheimer, M., Bloch, F., Muchnik, C., and Rubinstein, M. (1990). Blood viscosity and sensorineural hearing loss. *Arch. Otolaryngol. Head Neck Surg.* 116, 820–823. doi: 10.1001/archotol.1990.01870070068012

Hirata, Y., Sakata, N., Inoue, T., Yasumori, K., Yasaka, M., and Okada, Y. (2011). Histopathological features with angiographic correlates of internal carotid artery pseudo-occlusion: impact of plaque compositions. Clinical article. *J. Neurosurg.* 115, 350–358. doi: 10.3171/2011.3.JNS101434

Huth, E. J., and Murray, T. J. (2006). *Medicine in Quotations : Views of Health and Disease Through the Ages*. Philadelphia, PA: American College of Physicians.

Irace, C., Cortese, C., Fiaschi, E., Carallo, C., Farinaro, E., and Gnasso, A. (2004). Wall shear stress is associated with intima-media thickness and carotid atherosclerosis in subjects at low coronary heart disease risk. *Stroke* 35, 464–468. doi: 10.1161/01.STR.0000111597.34179.47

Iskander, A. J., Naftalovich, R., and Yang, X. (2020). The carotid sinus acts as a mechanotransducer of shear oscillation rather than a baroreceptor. *Med. Hypotheses* 134:109441. doi: 10.1016/j.mehy.2019.109441

Jamaati, H., Nazari, M., Darooei, R., Ghafari, T., and Raoufy, M. R. (2016). Role of shear stress in ventilator-induced lung injury. *Lancet Respir. Med.* 4, e41–e42. doi: 10.1016/S2213-2600(16)30159-X

Jung, J. H., Chae, Y. J., Lee, D. H., Cho, Y. I., Ko, M. M., Park, S. K., et al. (2017). Changes in whole blood viscosity during hemodialysis and mortality in patients with end-stage renal disease. *Clin. Hemorheol. Microcirc.* 65, 285–297. doi: 10.3233/CH-16183

Kamat, M. A., Blackshaw, J. A., Young, R., Surendran, P., Burgess, S., Danesh, J., et al. (2019). PhenoScanner V2: an expanded tool for searching human genotype-phenotype associations. *Bioinformatics* 35, 4851–4853. doi: 10.1093/bioinformatics/btz469

Karner, G., Perktold, K., Hofer, M., and Liepsch, D. (1999). Flow characteristics in an anatomically realistic compliant carotid artery bifurcation model. *Comput. Methods Biomech. Biomed. Engin.* 2, 171–185. doi: 10.1080/10255849908907986

Katakami, N. (2016). Utility of carotid wall shear stress as a predictor of coronary atherosclerosis. *J. Atheroscler. Thromb.* 23, 290–291. doi: 10.5551/jat.ED029

Kenyeres, P., Juricskay, I., Tarsoly, P., Kesmarky, G., Muhl, D., Toth, K., et al. (2008). Low hematocrit per blood viscosity ratio as a mortality risk factor in coronary heart disease. *Clin. Hemorheol. Microcirc.* 38, 51–56.

Khan, M. O., Steinman, D. A., and Valen-Sendstad, K. (2017). Non-Newtonian versus numerical rheology: practical impact of shear-thinning on the prediction of stable and unstable flows in intracranial aneurysms. *Int. J. Numer. Method Biomed. Eng.* 33. doi: 10.1002/cnm.2836

Klug, P. P., Lessin, L. S., and Radice, P. (1974). Rheological aspects of sickle cell disease. *Arch. Intern. Med.* 133, 577–590. doi: 10.1001/archinte.1974.00320160071007

Ku, D. N., and Giddens, D. P. (1983). Pulsatile flow in a model carotid bifurcation. *Arteriosclerosis* 3, 31–39. doi: 10.1161/01.atv.3.1.31

Ku, D. N., and Giddens, D. P. (1987). Laser Doppler anemometer measurements of pulsatile flow in a model carotid bifurcation. *J. Biomech.* 20, 407–421. doi: 10.1016/0021-9290(87)90048-0

Ku, D. N., Giddens, D. P., Phillips, D. J., and Strandness, D. E. Jr. (1985a). Hemodynamics of the normal human carotid bifurcation: in vitro and in vivo studies. *Ultrasound Med. Biol.* 11, 13–26. doi: 10.1016/0301-5629(85)90003-1

Ku, D. N., Giddens, D. P., Zarins, C. K., and Glagov, S. (1985b). Pulsatile flow and atherosclerosis in the human carotid bifurcation. Positive correlation between plaque location and low oscillating shear stress. *Arteriosclerosis* 5, 293–302. doi: 10.1161/01.atv.5.3.293

Kucukal, E., Man, Y., Hill, A., Liu, S., Bode, A., An, R., et al. (2020). Whole blood viscosity and red blood cell adhesion: potential biomarkers for targeted and curative therapies in sickle cell disease. *Am. J. Hematol.* 95, 1246–1256. doi: 10.1002/ajh.25933

Lee, S. W., and Steinman, D. A. (2007). On the relative importance of rheology for image-based CFD models of the carotid bifurcation. *J. Biomech. Eng.* 129, 273–278. doi: 10.1115/1.2540836

Lee, U. Y., Kim, C. I., Chung, G. H., Jung, J., and Kwak, H. S. (2020). Hemodynamic changes in the carotid artery after infusion of normal saline using computational fluid dynamics. *Diagnostics (Basel)* 10:473. doi: 10.3390/diagnostics10070473

Leisser, C., Kaufmann, T. A., Feltgen, N., Schumacher, M., Schmoor, C., and Meckel, S. (2015). Distribution of internal carotid artery plaque locations among patients with central retinal artery occlusion in the Eagle study population. *Graefes Arch. Clin. Exp. Ophthalmol.* 253, 1227–1230. doi: 10.1007/s00417-014-2804-2

Lewis, A. H., Cui, A. F., McDonald, M. F., and Grandl, J. (2017). Transduction of repetitive mechanical stimuli by Piezo1 and Piezo2 ion channels. *Cell Rep.* 19, 2572–2585. doi: 10.1016/j.celrep.2017.05.079

Lewis, A. H., and Grandl, J. (2015). Mechanical sensitivity of Piezo1 ion channels can be tuned by cellular membrane tension. *Elife* 4:e12088. doi: 10.7554/eLife.12088

Li, J., Hou, B., and Beech, D. J. (2015). Endothelial Piezo1: life depends on it. *Channels (Austin)* 9, 1–2. doi: 10.4161/19336950.2014.986623

Li, J., Hou, B., Tumova, S., Muraki, K., Bruns, A., Ludlow, M. J., et al. (2014). Piezo1 integration of vascular architecture with physiological force. *Nature* 515, 279–282. doi: 10.1038/nature13701

Liu, Z., Zhao, Y., Wang, X., Zhang, H., Cui, Y., Diao, Y., et al. (2016). Low carotid artery wall shear stress is independently associated with brain white-matter hyperintensities and cognitive impairment in older patients. *Atherosclerosis* 247, 78–86. doi: 10.1016/j.atherosclerosis.2016.02.003

Lowe, G. D. (1992). Blood viscosity and cardiovascular disease. *Thromb. Haemost.* 67, 494–498. doi: 10.1055/s-0038-1648479

Lu, D., and Kassab, G. S. (2011). Role of shear stress and stretch in vascular mechanobiology. *J. R. Soc. Interface* 8, 1379–1385. doi: 10.1098/rsif.2011.0177

Malek, A. M., Alper, S. L., and Izumo, S. (1999). Hemodynamic shear stress and its role in atherosclerosis. *JAMA* 282, 2035–2042. doi: 10.1001/jama.282.21.2035

Marshall, I., Zhao, S., Papathanasopoulou, P., Hoskins, P., and Xu, Y. (2004). MRI and CFD studies of pulsatile flow in healthy and stenosed carotid bifurcation models. *J. Biomech.* 37, 679–687. doi: 10.1016/j.jbiomech.2003.09.032

McCain, M. L., and Parker, K. K. (2011). Mechanotransduction: the role of mechanical stress, myocyte shape, and cytoskeletal architecture on cardiac function. *Pflugers Arch.* 462, 89–104. doi: 10.1007/s00424-011-0951-4

Milos, R., Dejan, P., and Nenad, F. (2011). Mining data from CFD simulation for aneurysm and carotid bifurcation models. *Conf. Proc. IEEE Eng. Med. Biol. Soc.* 2011, 8311–8314. doi: 10.1109/IEMBS.2011.6092049

Mukhopadhyay, S., and Stowers, L. (2020). Choosing to urinate. Circuits and mechanisms underlying voluntary urination. *Curr. Opin. Neurobiol.* 60, 129–135. doi: 10.1016/j.conb.2019.11.004

Munster, A. B., Thapar, A., and Davies, A. H. (2016). History of carotid stroke. *Stroke* 47, e66–e69. doi: 10.1161/STROKEAHA.115.012044

Murthy, S. E., Dubin, A. E., and Patapoutian, A. (2017). Piezos thrive under pressure: mechanically activated ion channels in health and disease. *Nat. Rev. Mol. Cell Biol.* 18, 771–783. doi: 10.1038/nrm.2017.92

Nakanishi, N., Suzuki, K., and Tatara, K. (2004). Haematocrit and risk of development of Type 2 diabetes mellitus in middle-aged Japanese men. *Diabet. Med.* 21, 476–482. doi: 10.1111/j.1464-5491.2004.01152.x

Nguyen, K. T., Clark, C. D., Chancellor, T. J., and Papavassiliou, D. V. (2008). Carotid geometry effects on blood flow and on risk for vascular disease. *J. Biomech.* 41, 11–19. doi: 10.1016/j.jbiomech.2007.08.012

Noble, P. B., Pascoe, C. D., Lan, B., Ito, S., Kistemaker, L. E., Tatler, A. L., et al. (2014). Airway smooth muscle in asthma: linking contraction and mechanotransduction to disease pathogenesis and remodelling. *Pulm. Pharmacol. Ther.* 29, 96–107. doi: 10.1016/j.pupt.2014.07.005

Nwose, E. U. (2010). Whole blood viscosity assessment issues IV: prevalence in acute phase inflammation. *N. Am. J. Med. Sci.* 2, 353–358. doi: 10.4297/najms.2010.2353

Ouisuwan, S., and Buranakarl, C. (2005). Effects of cyclosporin A on blood pressure, baroreceptor reflex and renal function in dogs. *Vet. Res. Commun.* 29, 201–213. doi: 10.1023/b:verc.0000047507.85689.90

Perktold, K., Resch, M., and Florian, H. (1991). Pulsatile non-Newtonian flow characteristics in a three-dimensional human carotid bifurcation model. *J. Biomech. Eng.* 113, 464–475. doi: 10.1115/1.2895428

Persson, P. B., and Kirchheim, H. R. (1991). *Baroreceptor Reflexes : Integrative Functions and Clinical Aspects*. New York, NY: Springer-Verlag.

Peters, S. A., Woodward, M., Rumley, A., Tunstall-Pedoe, H. D., and Lowe, G. D. (2017). Plasma and blood viscosity in the prediction of cardiovascular disease and mortality in the Scottish Heart Health Extended Cohort Study. *Eur. J. Prev. Cardiol.* 24, 161–167. doi: 10.1177/2047487316672004

Porzionato, A., Macchi, V., Stecco, C., and De Caro, R. (2019). The carotid sinus nerve-structure, function, and clinical implications. *Anat. Rec. (Hoboken)* 302, 575–587. doi: 10.1002/ar.23829

Quemada, D. (1981). A rheological model for studying the hematocrit dependence of red cell-red cell and red cell-protein interactions in blood. *Biorheology* 18, 501–516. doi: 10.3233/bir-1981-183-615

Retailleau, K., Duprat, F., Arhatte, M., Ranade, S. S., Peyronnet, R., Martins, J. R., et al. (2015). Piezo1 in smooth muscle cells is involved in hypertension-dependent arterial remodeling. *Cell Rep.* 13, 1161–1171. doi: 10.1016/j.celrep.2015.09.072

Richards, R. S., and Nwose, E. U. (2010). Blood viscosity at different stages of diabetes pathogenesis. *Br. J. Biomed. Sci.* 67, 67–70. doi: 10.1080/09674845.2010.11730293

Risoe, C., Tan, W., and Smiseth, O. A. (1994). Effect of carotid sinus baroreceptor reflex on hepatic and splenic vascular capacitance in vagotomized dogs. *Am. J. Physiol.* 266(4 Pt 2), H1528–H1533. doi: 10.1152/ajpheart.1994.266.4.H1528

Rode, B., Shi, J., Endesh, N., Drinkhill, M. J., Webster, P. J., Lotteau, S. J., et al. (2017). Piezo1 channels sense whole body physical activity to reset cardiovascular homeostasis and enhance performance. *Nat. Commun.* 8:350. doi: 10.1038/s41467-017-00429-3

Saba, L., Bhavsar, A. V., Gupta, A., Mtui, E. E., Giambrone, A. E., Baradaran, H., et al. (2015). Automated calcium burden measurement in internal carotid artery plaque with CT: a hierarchical adaptive approach. *Int. Angiol.* 34, 290–305.

Sanzeni, A., Katta, S., Petzold, B., Pruitt, B. L., Goodman, M. B., and Vergassola, M. (2019). Somatosensory neurons integrate the geometry of skin deformation and mechanotransduction channels to shape touch sensing. *Elife* 8:e43226. doi: 10.7554/eLife.43226

Sazonova, O. V., Isenberg, B. C., Herrmann, J., Lee, K. L., Purwada, A., Valentine, A. D., et al. (2015). Extracellular matrix presentation modulates vascular smooth muscle cell mechanotransduction. *Matrix Biol.* 41, 36–43. doi: 10.1016/j.matbio.2014.11.001

Schiapaccassa, A., Maranhao, P. A., de Souza, M., Panazzolo, D. G., Nogueira Neto, J. F., Bouskela, E., et al. (2019). 30-days effects of vildagliptin on vascular function, plasma viscosity, inflammation, oxidative stress, and intestinal peptides on drug-naive women with diabetes and obesity: a randomized head-to-head metformin-controlled study. *Diabetol. Metab. Syndr.* 11:70. doi: 10.1186/s13098-019-0466-2

Skretteberg, P. T., Bodegard, J., Kjeldsen, S. E., Erikssen, G., Thaulow, E., Sandvik, L., et al. (2010). Interaction between inflammation and blood viscosity predicts cardiovascular mortality. *Scand. Cardiovasc. J.* 44, 107–112. doi: 10.1080/14017430903171248

Sloop, G. D., Weidman, J. J., and St Cyr, J. A. (2018). Perspective: interesterified triglycerides, the recent increase in deaths from heart disease, and elevated blood viscosity. *Ther. Adv. Cardiovasc. Dis.* 12, 23–28. doi: 10.1177/1753944717745507

Song, S. H., Kim, J. H., Lee, J. H., Yun, Y. M., Choi, D. H., and Kim, H. Y. (2017). Elevated blood viscosity is associated with cerebral small vessel disease in patients with acute ischemic stroke. *BMC Neurol.* 17:20. doi: 10.1186/s12883-017-0808-3

Staley, J. R., Blackshaw, J., Kamat, M. A., Ellis, S., Surendran, P., Sun, B. B., et al. (2016). PhenoScanner: a database of human genotype-phenotype associations. *Bioinformatics* 32, 3207–3209. doi: 10.1093/bioinformatics/btw373

Sui, B., Gao, P., Lin, Y., Jing, L., Sun, S., and Qin, H. (2015). Hemodynamic parameters distribution of upstream, stenosis center, and downstream sides of plaques in carotid artery with different stenosis: a MRI and CFD study. *Acta Radiol.* 56, 347–354. doi: 10.1177/0284185114526713

Syeda, R., Xu, J., Dubin, A. E., Coste, B., Mathur, J., Huynh, T., et al. (2015). Chemical activation of the mechanotransduction channel Piezo1. *Elife* 4:e07369. doi: 10.7554/eLife.07369

Thurston, G. B. (1973). Frequency and shear rate dependence of viscoelasticity of human blood. *Biorheology* 10, 375–381. doi: 10.3233/bir-1973-10311

Thurston, G. B. (1976). The effects of frequency of oscillatory flow on the impedance of rigid, blood-filled tubes. *Biorheology* 13, 191–199. doi: 10.3233/bir-1976-13306

Thurston, G. B. (1979). Rheological parameters for the viscosity viscoelasticity and thixotropy of blood. *Biorheology* 16, 149–162. doi: 10.3233/bir-1979-16303

Truskey, G. A., Yuan, F., and Katz, D. F. (2004). *Transport Phenomena in Biological Systems*. Upper Saddle River, NJ: Pearson Prentice Hall.

Weber, U., Glassford, N. J., Eastwood, G. M., Bellomo, R., and Hilton, A. K. (2016). A Pilot assessment of carotid and brachial artery blood flow estimation using ultrasound doppler in cardiac surgery patients. *J. Cardiothorac. Vasc. Anesth.* 30, 141–148. doi: 10.1053/j.jvca.2015.06.025

Wei, H., Cheng, A. L., and Pahlevan, N. M. (2020). On the significance of blood flow shear-rate-dependency in modeling of Fontan hemodynamics. *Eur. J. Mech. B Fluids* 84, 1–4. doi: 10.1016/j.euromechflu.2020.05.011

Wei, Z., Singh-Gryzbon, S., Trusty, P. M., Huddleston, C., Zhang, Y., Fogel, M. A., et al. (2020). Non-Newtonian effects on patient-specific modeling of fontan hemodynamics. *Ann. Biomed. Eng.* 48, 2204–2217. doi: 10.1007/s10439-020-02527-8

Weinbaum, S., Duan, Y., Thi, M. M., and You, L. (2011). An integrative review of mechanotransduction in endothelial, epithelial (Renal) and dendritic cells (Osteocytes). *Cell. Mol. Bioeng.* 4, 510–537. doi: 10.1007/s12195-011-0179-6

Westcott, E. B., and Segal, S. S. (2013). Perivascular innervation: a multiplicity of roles in vasomotor control and myoendothelial signaling. *Microcirculation* 20, 217–238. doi: 10.1111/micc.12035

Wilson, J. R., Lanoce, V., Frey, M. J., and Ferraro, N. (1990). Arterial baroreceptor control of peripheral vascular resistance in experimental heart failure. *Am Heart J* 119, 1122–1130. doi: 10.1016/s0002-8703(05)80243-1

Woodward, M., Brindle, P., Tunstall-Pedoe, H., and SIGN Group on Risk Estimation (2007). Adding social deprivation and family history to cardiovascular risk assessment: the ASSIGN score from the Scottish Heart Health Extended Cohort (SHHEC). *Heart* 93, 172–176. doi: 10.1136/hrt.2006.108167

Wozniak, M. A., and Chen, C. S. (2009). Mechanotransduction in development: a growing role for contractility. *Nat. Rev. Mol. Cell Biol.* 10, 34–43. doi: 10.1038/nrm2592

Wu, J., Lewis, A. H., and Grandl, J. (2017a). Touch, tension, and transduction–the function and regulation of Piezo Ion Channels. *Trends Biochem. Sci.* 42, 57–71. doi: 10.1016/j.tibs.2016.09.004

Wu, J., Young, M., Lewis, A. H., Martfeld, A. N., Kalmeta, B., and Grandl, J. (2017b). Inactivation of mechanically activated Piezo1 ion channels is determined by the C-terminal extracellular domain and the inner pore helix. *Cell Rep.* 21, 2357–2366. doi: 10.1016/j.celrep.2017.10.120

Xu, P., Liu, X., Zhang, H., Ghista, D., Zhang, D., Shi, C., et al. (2018). Assessment of boundary conditions for CFD simulation in human carotid artery. *Biomech. Model. Mechanobiol.* 17, 1581–1597. doi: 10.1007/s10237-018-1045-4

Yang, J., Zhang, J., Yang, H., Li, K., Lei, X., and Xu, C. (2016). The potential role of Piezo2 in the mediation of visceral sensation. *Neurosci. Lett.* 630, 158–163. doi: 10.1016/j.neulet.2016.07.058

Yeleswarapu, K. K. (1996). *Evaluation of Continuum Models for Characterizing the Constitutive Behavior of Blood.* Ph.D. Thesis. Pittsburgh, PA: University of Pittsburgh.

Zeng, W. Z., Marshall, K. L., Min, S., Daou, I., Chapleau, M. W., Abboud, F. M., et al. (2018). PIEZOs mediate neuronal sensing of blood pressure and the baroreceptor reflex. *Science* 362, 464–467. doi: 10.1126/science.aau6324

Zhang, B., Ma, Y., and Ding, F. (2018). Evaluation of spatial distribution and characterization of wall shear stress in carotid sinus based on two-dimensional color Doppler imaging. *Biomed. Eng. Online* 17:141. doi: 10.1186/s12938-018-0589-y

Zhang, C., Xie, S., Li, S., Pu, F., Deng, X., Fan, Y., et al. (2012). Flow patterns and wall shear stress distribution in human internal carotid arteries: the geometric effect on the risk for stenoses. *J. Biomech.* 45, 83–89. doi: 10.1016/j.jbiomech.2011.10.001

Zhang, D., Xu, P., Qiao, H., Liu, X., Luo, L., Huang, W., et al. (2018). Carotid DSA based CFD simulation in assessing the patient with asymptomatic carotid stenosis: a preliminary study. *Biomed. Eng. Online* 17:31. doi: 10.1186/s12938-018-0465-9

Zhang, H., Liu, H., Dong, Y., Wang, J., Zhao, Y., Cui, Y., et al. (2018). Low carotid wall shear stress independently accelerates the progression of cognitive impairment and white matter lesions in the elderly. *Oncotarget* 9, 11402–11413. doi: 10.18632/oncotarget.23191

Zhang, Y., Furusawa, T., Sia, S. F., Umezu, M., and Qian, Y. (2013). Proposition of an outflow boundary approach for carotid artery stenosis CFD simulation. *Comput. Methods Biomech. Biomed. Engin.* 16, 488–494. doi: 10.1080/10255842.2011.625358

Zheng, W., Gracheva, E. O., and Bagriantsev, S. N. (2019). A hydrophobic gate in the inner pore helix is the major determinant of inactivation in mechanosensitive Piezo channels. *Elife* 8:e44003. doi: 10.7554/eLife.44003

Zimmer, H. G. (2004). Heinrich Ewald Hering and the carotid sinus reflex. *Clin. Cardiol.* 27, 485–486. doi: 10.1002/clc.4960270813

Conflict of Interest: The authors declare that the research was conducted in the absence of any commercial or financial relationships that could be construed as a potential conflict of interest.

frontiers in Bioengineering and Biotechnology

ORIGINAL RESEARCH
published: 23 June 2021
doi: 10.3389/fbioe.2021.703048

An Ear Wearable Device System for Facial Emotion Recognition Disorders

Zhengxu Lian[1]†, Yingjie Guo[1†], Xinyu Cao[1†] and Wendi Li[2]*

[1] School of Medicine and Bioinformatics Engineering, Northeastern University, Shenyang, China, [2] Software College of Northeastern University, Shenyang, China

A wearable device system was proposed in the present work to address the problem of facial emotion recognition disorders. The proposed system could comprehensively analyze the user's own stress status, emotions of people around, and the surrounding environment. The system consists of a multi-dimensional physiological signals acquisition module, an image acquisition and transmission module, a user interface of the user mobile terminal, and a cloud database for data storage. Moreover, a deep learning based multi-model physiological signal pressure recognition algorithm and a facial emotion recognition algorithm were designed and implemented in the system. Some publicly available data sets were used to test the two algorithms, and the experiment results showed that the two algorithms could well realize the expected functions of the system.

Keywords: facial emotion recognition, pressure recognition, multi-modal physiological signal, wearable device, facial emotion recognition disorder

OPEN ACCESS

Edited by:
Xiaoguang Zhou,
Beijing University of Posts and Telecommunications, China

Reviewed by:
Xiaowei Ma,
China Agricultural University, China
Yuhan Zhu,
Capital Medical University, China

***Correspondence:**
Zhengxu Lian
Shelleicemlian1@163.com

† These authors have contributed equally to this work and share first authorship

Specialty section:
This article was submitted to Bionics and Biomimetics, a section of the journal Frontiers in Bioengineering and Biotechnology

Received: *30 April 2021*
Accepted: *26 May 2021*
Published: *23 June 2021*

Citation:
Lian Z, Guo Y, Cao X and Li W (2021) An Ear Wearable Device System for Facial Emotion Recognition Disorders. Front. Bioeng. Biotechnol. 9:703048. doi: 10.3389/fbioe.2021.703048

INTRODUCTION

As an important way of emotional expression and cognition, facial expressions are an indispensable part of our daily activities. Being a form of one's response to happenings in the objective world, emotions play an important role in people's real life and spiritual life. Obstacles in recognition of facial emotions will inevitably lead to problems in interpersonal communication. Shen et al. (2015) have found that the mechanisms of facial emotions recognition are complex and are not the functions of one single area in the brain; instead, different loops are formed between different regions, and damages to these loops would lead to facial emotion recognition disorders, manifested by such diseases as schizophrenia, cerebrovascular accidents, dementia syndrome, Parkinson's disease, depression, autism, epilepsy, traumatic brain injury, and multiple sclerosis. Therefore, early detection and identification of potential facial emotion recognition disorders will facilitate the judgment, treatment and community management of nervous system diseases.

At the same time, with the rapid development of the wearable technology in recent years, wearable devices have provided a popular solution and played an important role in health monitoring, safety monitoring, family rehabilitation, efficacy evaluation, early detection of diseases, and other related fields (Jia et al., 2017). The purpose of this research is to design a wearable device system for facial emotion recognition disorders, and the system could comprehensively analyze the user's own psychological stress, other people's emotions and surrounding environment, thus contributing to the prevention, monitoring, and management of related diseases.

This system is expected to provide a solution to the following fields. (1) It can be used as a monitoring system for early diagnosis, prevention and treatment of diseases related to facial emotion recognition, such as anxiety, to prevent it from escalating into more serious diseases like depression. (2) The system can provide a technical basis for treatment of specific diseases. For example, in the case of patients with autism who are sensitive to mathematical laws, the system can transform the emotional data of others into more regular games to help autistic patients better recover and recognize their emotional recognition capacity. (3) The system can also be used as a data collection platform to provide more sample data for the research on neurological diseases.

Wearable devices for monitoring of users' physiological signals and detection of psychological pressure have drawn wide attention from researchers around the world. Such signals come from all parts of the body, such as Electrocardiograph (ECG), Electro- myogram (EMG), Electroencephalogram (EEG), and respiration. A new wearable ECG monitoring system based on active cables and smart electrodes developed by the KTH Royal Institute of Technology includes a hand-held personal health assistant, an active cable and 10 smartelectrodes, which are attached to specific parts of the patient's body from chest to calf, and can obtain high-quality ECG data (Yang et al., 2008). In a study by Hasanbasic et al. (2019), they monitored students' ECG and skin electrical activity signals by wearable sensors in real time, and classified by machine learning algorithms such as SVM to identify the students' stress level in a specific environment such as during exams (Hasanbasic et al., 2019). Montesinos et al. (2019) employed multi-modal machine learning and sensor fusion technology to detect the occurrence of acute stress events.

In these previous publications, researchers employed wearable sensors to collect physiological signals, discriminated and classified psychological pressure through machine learning. However, physiological-signal monitoring devices mentioned in the above studies are expensive and cumbersome. As a result, ordinary users often find it hard to afford these expensive devices and inconvenient to wear these devices in daily life, which makes it impossible to popularize these devices. Moreover, the previous studies have failed to measure the surrounding environment when stress occurs, and hence could not assess the impact of the surrounding environment on facial emotion recognition disorders.

Machine learning models, especially deep learning algorithms, are popular solutions to classification of physiological information and it is assumed that these models could bring new breakthroughs to facial emotion recognition disorders. In fact, research on facial emotion recognition based on deep learning has been relatively mature. Arriaga et al. (2017) proposed a lightweight convolutional neural network, which reached an emotion recognition accuracy close to human on the FER2013 database. Therefore, it is feasible to achieve the goal of recognizing emotions in interpersonal scenarios by improving machine learning models.

The present work proposes a wearable device system that is cost effective and can keep track of changes in the surrounding environment. The system achieves the expected functions by a self-designed multi-modal psychological signal-based stress recognition deep learning algorithm and an improved facial emotion recognition algorithm.

The software of the proposed system was designed as follows. A multi-modal psychological signal-based stress recognition multi-head Convolutional Neural Networks (CNN) model was designed, the facial emotion recognition model based on the mini_Xception CNN was improved; and the algorithms were deployed on the cloud server; A cloud database was constructed to store the physiological signals and analysis results obtained by the above-mentioned algorithms, and a mobile interface for user interaction was developed. The hardware of the system was developed as follows. An ergonomic ear wearable device was designed, which comprised of sensors for the photoelectric volumetric heart rate, triaxial acceleration, skin electricity and body temperature, cameras used for collection of the facial images of the people whom users interact with and the surrounding environment, and a Wi-Fi module for data transfer with the cloud server.

MATERIALS AND METHODS

Overall Framework of Wearable Device System

This system is composed of five sub-systems: an image acquisition and transmission system, a human physiological signal collection and transmission system, an algorithm analysis system deployed on cloud server, a cloud database and an user mobile APP, as shown in **Figure 1**. (1) The image acquisition and transmission system realizes real-time image acquisition through cameras, and transmits videos to the cloud server via intranet transparent transmission technology through module integrated WI-FI chips, thus completing wireless image transmission. (2) In the human physiological signal acquisition and transmission system, small-sized sensors are used to make the device portable and easy to use; the physiological signals collected by the sensors are input into the ESP8266 WI-FI communication module connected with the serial communication ports through the main development board, and the module further uploads the data to the cloud server using the Transmission Control Protocol (TCP) transmission protocol. (3) On the cloud server, a multi-modal physiological signal-based stress recognition model and a facial emotion recognition model are deployed to acquire and analyze data, and provide feedback to the cloud database. (4) The cloud database records the collects raw data and algorithm analysis results, and returns the user stress state and the facial emotion prediction result of people around to the user through the mobile APP. (5) The mobile APP receives the algorithm analysis results returned by the cloud database and displays them on the user interface for users to view.

Hardware Circuit and Appearance Design

In the hardware circuit design, the image acquisition and transmission system and the human physiological signal

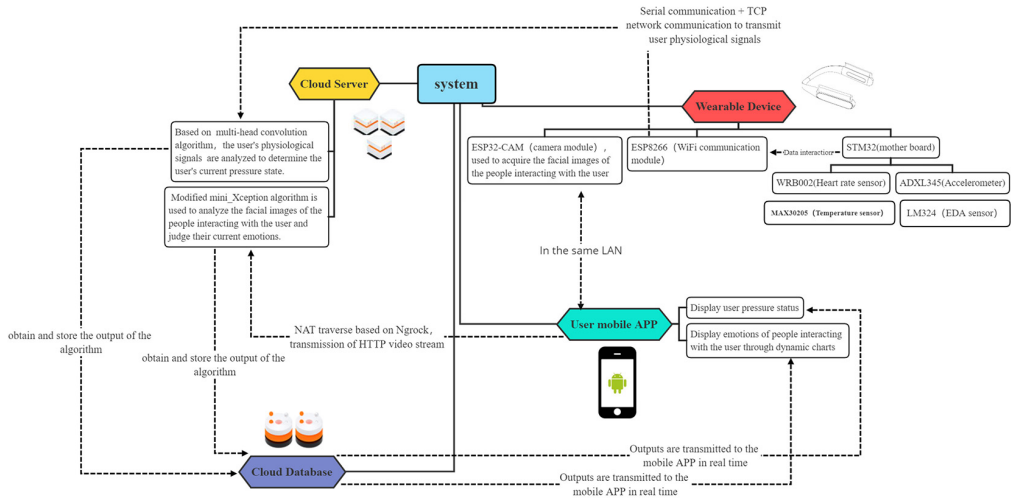

FIGURE 1 | Relations between the sub-systems in the proposed wearable device system.

acquisition system are independent of each other. As shown in **Figure 2**, the image acquisition and transmission system is composed of the ESP32CAM module with integrated cameras and WI-FI chips powered by lithium batteries. In the human physiological signal acquisition system, STM32 is used as the main development board, and ADXL345 acceleration sensor, LM324 skin electrical sensor, MAX30205 body temperature sensor and photoelectric volumetric WRB002 heart rate sensor are connected to the corresponding serial ports of the development board, and are also powered by lithium batteries. The serial port data exchange end of the motherboard is connected to the WI-FI module ESP8266, through which physiological signals can be transmitted to the cloud server.

The wearable device presents a U-shaped elastic ring structure, which is placed above the ear and close to the head. Each sensor opening is arranged on the side to facilitate physiological signal acquisition. U-shaped front-end cameras can collect the facial images of the people whom users interact with and the surrounding environment. **Figure 3** presents the appearance and internal structure of the device.

Software Design

The experimental software includes a mobile APP, a cloud database and algorithm analysis system deployed on the cloud server. The mobile APP interface is written in Java and can be used on Android mobile devices. By receiving the algorithm analysis results returned from the cloud database, the app presents the user's psychological stress status and the facial emotion recognition results of people around in real time (**Figure 4**). The cloud database uses MySQL language to record and store the raw physiological signals from sensors and algorithm analysis results. In order to facilitate the follow-up studies about the impacts of the scenes on the user's stress state, the cloud database will also store the images collected by the camera module when the algorithm judges that the user is under stress. The cloud server adopts the Windows Server 2012 system. The working principles of the multi-modal physiological signal-based stress recognition model and the facial emotion recognition model deployed on the cloud server will be discussed in detail in Sections "Facial Emotion Recognition Algorithm Description" and "Multi-modal Physiological Signal-based Stress Recognition Algorithm."

Facial Emotion Recognition Algorithm Description

Image Texture Feature Extraction

Texture, a common feature of images, has been widely used in various image segmentation, classification and recognition tasks. Tyagi (2018) points out that there is no universally-accepted definition for the image texture at present. However, in some studies (Smith and Chang, 1996; Hall-Beyer, 2007), texture is defined as the surface roughness and roughness of objects, which are unique and show certain patterns. Texture features are reflected by gray intensity distribution pattern in images, and these features have been described in diverse forms in the field of digital image processing. Khaldi et al. (2019) points out that gray level co-occurrence matrix (GLCM) is often considered as an accurate method of texture feature extraction, and has seen wide adoption in various fields because of its simplicity and high efficiency. For an image I of the size of $N \times M$, with a given displacement vector $(\Delta x, \Delta y)$, the gray level co-occurrence matrix M can be obtained by Eq. 1.

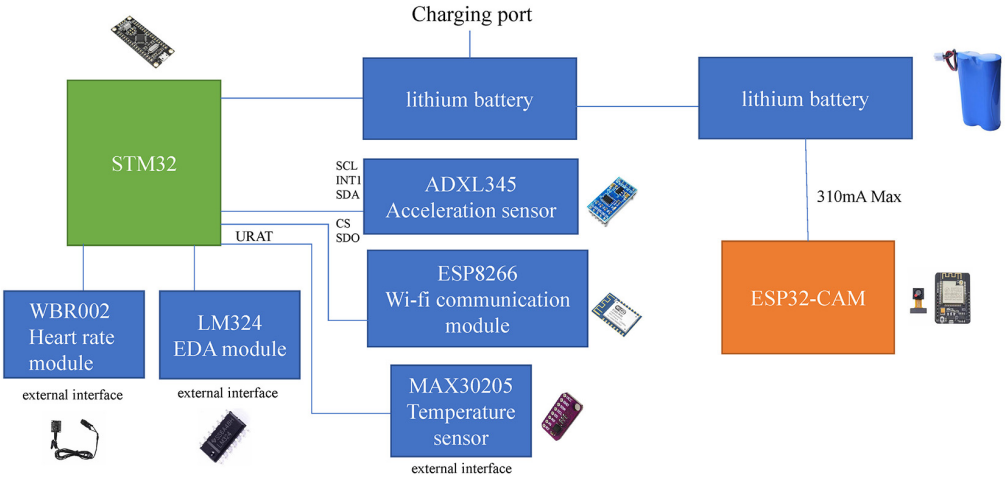

FIGURE 2 | The hardware circuit.

$$M(p,q) = \sum_{i=1}^{N}\sum_{j=1}^{M}\begin{cases} 1 & \text{if } I(i,j) = p \text{ and} \\ & I(i+\Delta x, j+\Delta y) = q \\ 0 & \text{otherwise} \end{cases} \quad (1)$$

Usually, some statistical indicators are used to characterize the gray level co-occurrence matrix and hence reflect that texture features of images. In the present work, the following statistical indicators were employed to calculate the eigenvalue of the local gray level co-occurrence matrix of the images: the mean, standard deviation (std), contrast, dissimilarity, homogeneity, angular second moment (ASM), energy, maximum and entropy, so as to generate images that reflect the texture features of the image.

Figure 5 shows the pseudo-color images of a human face after extraction of texture features. An image with a size of 48 × 48 and a gray scale range of 0–255 is used for testing. The lighter colors corresponds to the higher gray values. The pseudo-color images clearly presents the texture features extracted by the gray level co-occurrence matrix based on different statistical indicators.

Algorithm Description

To solve the problem of parameter redundancy, improve the model's generalization capacity, and reduce the processing burden of the hardware, Arriaga et al. (2017) proposed a lightweight CNN: mini_Xception. This network borrowed the ideas of deep segmentable volume and residual network from the Google mainstream CNN Xception (Chollet, 2017), to achieve higher accuracy under small model complexity.

In order to improve the performance of mini_Xception in facial emotion recognition task, the gray level co-occurrence matrix was introduced in our method to extract texture features from the input images so as to enrich the types and scale of data for the model. The algorithm implementation flow is shown in **Figure 6**.

As **Figure 6** shows, the algorithm first extracts the texture features of the input image to generate nine texture-feature images. After that, ten images including the original image are input into the algorithm through 10 separate channels, and are filtered by 3 × 3 convolution networks with the 16 dimensions. After passing the activation layer of the Rectified Linear Unit (ReLu) function, the features of each channel are fused and input into the mini_Xception model. At last, the mini_Xception model outputs the probabilities of seven predicted emotions through the softmax activation layer, and takes the emotion with the largest probability as the final predition outcome. The Adam optimizer is used as the weight optimizer of the algorithm network in the training process.

Multi-Modal Physiological Signal-Based Stress Recognition Algorithm

Batch Standardization

Firstly, the physiological signals of the input model are standardized in batches. The mean and variance of a batch of data can be calculated by Eqs 2 and 3, respectively, and then each indicator in the batch of data is standardized by Eq. 4, and finally the weight of the data is corrected to achieve the result. By standardizing the variance of the training set data, the values of feature vectors in each dimension are treated equivalently, and are made to follow the normal distribution with the mean value of 0 and the variance of 1. Thus the problem of unbalanced weight caused by the difference in the values of feature vectors can be avoided (Tang, 2017).

$$\mu_B = \frac{1}{m}\sum_{i=1}^{m} x_i \quad (2)$$

$$\sigma_B^2 = \frac{1}{m}\sum_{i=1}^{m}(x_i - \mu_B)^2 \quad (3)$$

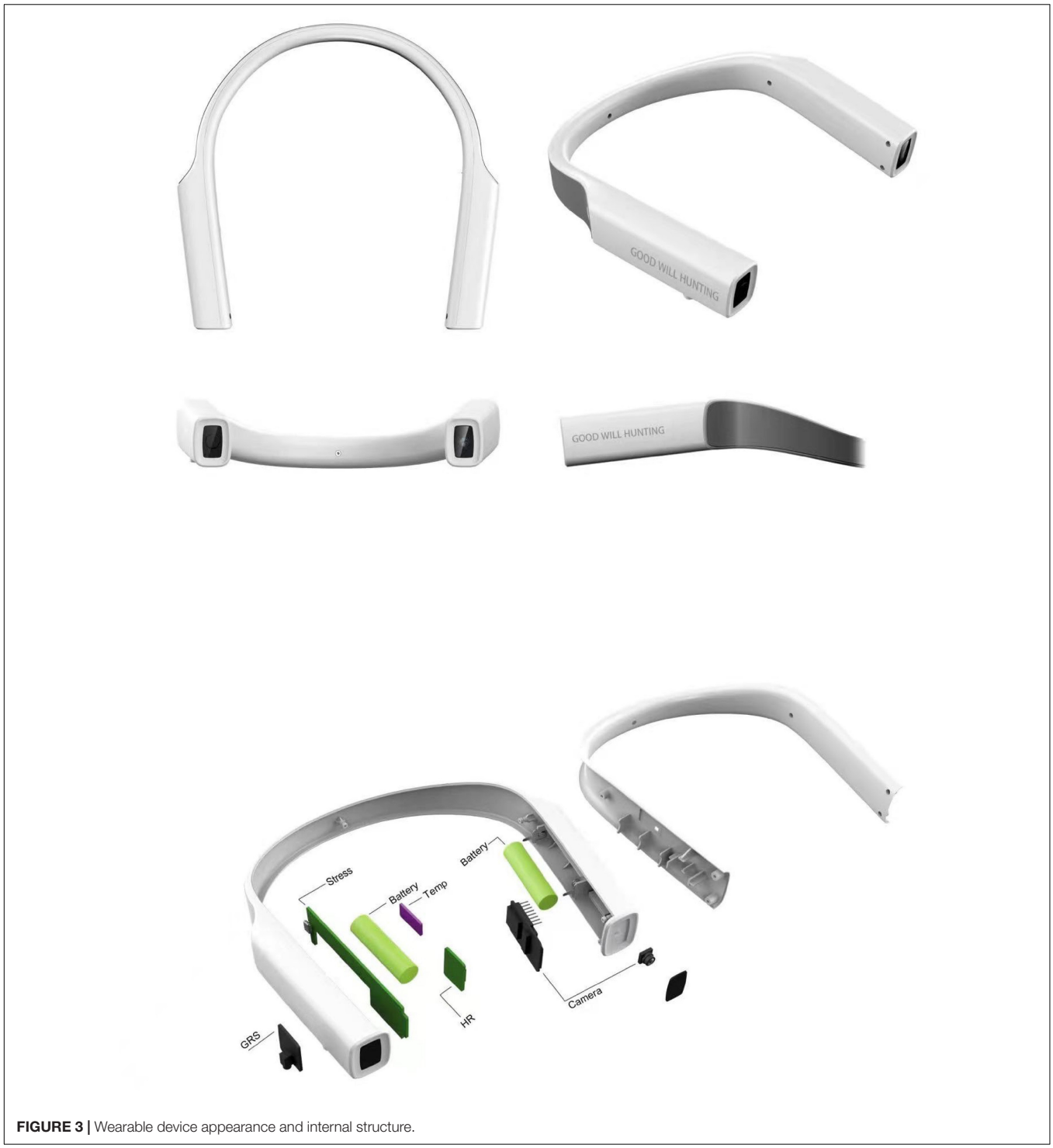

FIGURE 3 | Wearable device appearance and internal structure.

$$\hat{x}_i = \frac{x_i - \mu_B}{\sqrt{\sigma_B^2 + \varepsilon}} \tag{4}$$

Slicing

Usually, Eq. 5 is used to transform single-row single-dimension inputs into multi-row and multi-dimension. In Eq. 5, "input" is the input value of the model, "slice" is the slice length, and a_k is a row of vector of the original data. The purpose of this method is to change the input from single time point to multi-points time period, and to provide the data with continuous physiological information. Because of the large individual differences of one-dimensional physiological data, it has poor robustness in model adaptation. In addition, the separate time points of physical

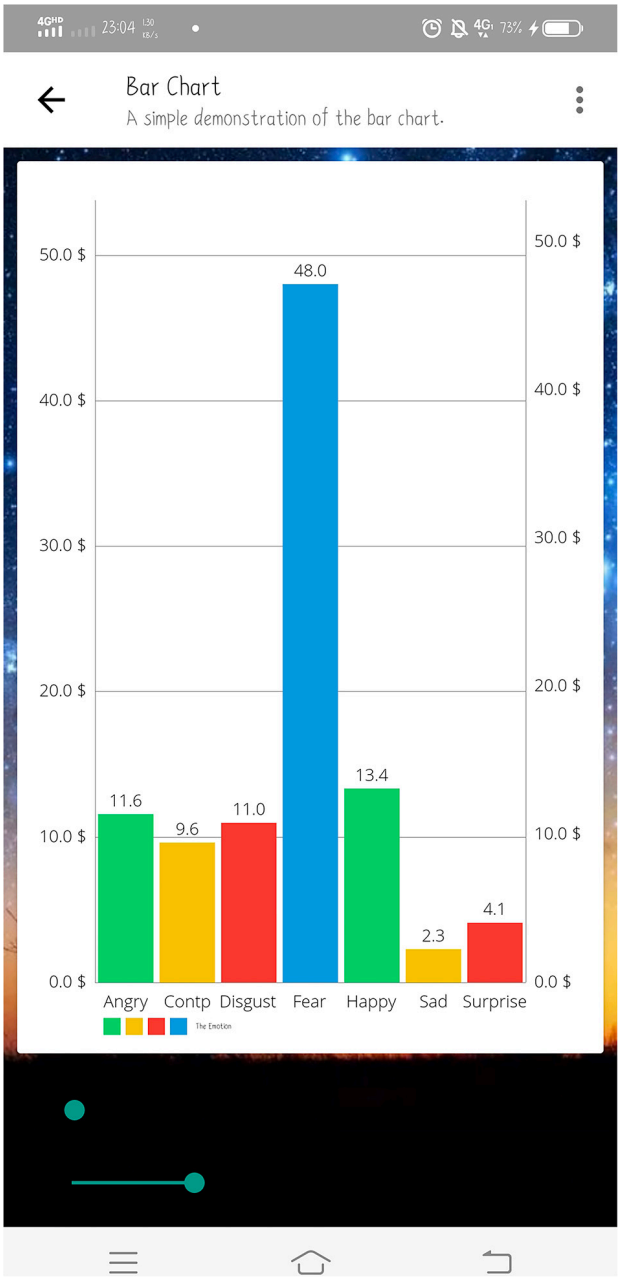

FIGURE 4 | Display of analysis results on the mobile app.

signals are not all index data, and cannot be used to indicate a certain physiological state just because the value of which reach a specific threshold. Therefore, the input of multi-dimensional time period data is needed to ensure the introduction of continuous characteristics of signals, so as to make the model more robust and practical (Jia et al., 2017).

$$\text{Input} = (a1, a2, a3 \ldots a_k)T(k = 1, 2, 3 \ldots \text{Slice}) \tag{5}$$

Model Design

In the model proposed in this study, the multi-channel concatenate layer fusion model was used for training.

The main working principle is shown in Eq. 6.

$$\text{Zconact} = \sum_{i=1}^{c} Xi * Ki + \sum_{i=1}^{c} Xi * Ki + c + \cdots \tag{6}$$

The model structure is shown in **Figure 7**.

As shown in **Figure 7**, there are four basic input channels of the model in this experiment. The first three channels share the same workflow, all consisting of an input layer, a one-dimensional convolution layer, a random inactivation layer, a maximum pooling layer and a flattening layer. The convolution kernel size was set at 3, 5, and 11 to extract features from different scales. The fourth channel is composed of a Convolution+Long Short-Term Memory-2D (ConvLSTM-2D) model and a flatten layer. Among them, the traditional two-stream LSTM model cannot only improve the performance of the neural network by making better use of the dependency product between sequence frame data (Jie et al., 2021), but also introduce the long-term and short-term memory mechanism to the model. Through the convolution layer, the relationship between time series can be obtained, and at the same time, the spatial features can be extracted, and thus the spatio-temporal features are obtained. Therefore, the two-stream convolution of LSTM combined with Attention-Conv can better analyze the spatio-temporal relationship of local features. Then, the data from the four input channels are weighted and fused, and the feature dimension is reduced through the full connection layer, after which four kinds of stress recognition results are output: physiological stress, cognitive stress, emotional stress and relaxed state.

Evaluation Indicators

To evaluate the experimental results, the following evaluation criteria are defined and used.

Loss Function

In multi-classification problems, the cross entropy loss functions of Eqs 7 and 8 are often used, where *y* is the predicted value, and *y_hat* is the label value. By continuously reducing the value of the loss function *L* to 0, the predicted result and the actual label value could be matched.

$$\text{Soft max}\left(y_i\right) = \frac{e^{y_i}}{\sum_{i=1}^{n} e^{y_i}} \tag{7}$$

$$L\left(y, y\_hat\right) = -\frac{1}{n}\sum_{i=1}^{n} y\_hat_i \times \log\left(\text{Soft max}\left(y_i\right)\right) \tag{8}$$

Accuracy

In evaluation of multi-classification tasks, multi-classification problems are often transformed into multiple two-classification problems. The selected class is set as positive (P), while the rest is set as negative (N). If the prediction result matches the label, the classified target is marked by a prefix T; otherwise, it is marked by the prefix F.

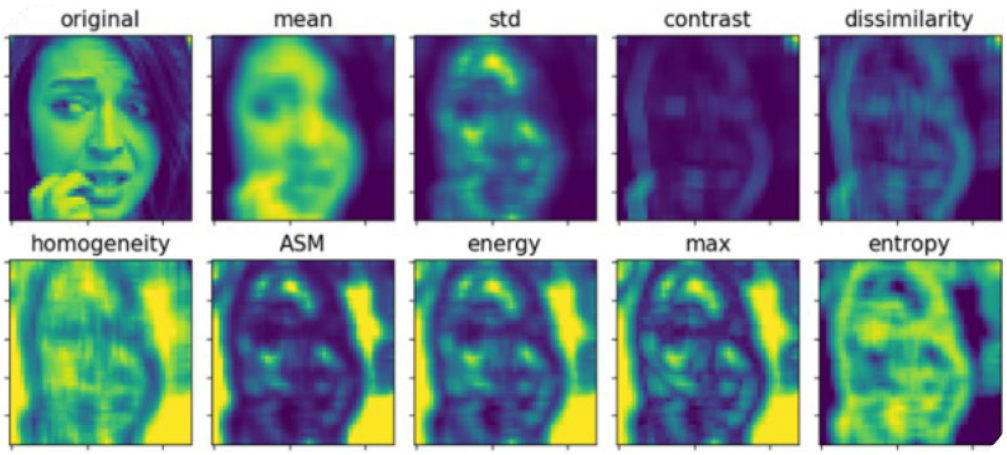

FIGURE 5 | Grayscale pseudo-color images for nine features.

Equation 9 shows the calculation of the classification accuracy, which represents the ratio of correct prediction times to all prediction times.

$$\text{Accuracy} = \frac{\text{TP} + \text{TN}}{\text{TP} + \text{TN} + \text{FP} + \text{FN}} \tag{9}$$

Evaluation Indicators of Test Set

Equation 10 is used to calculate the classification precision of a random class *i*, which describes the proportion of true positives in samples predicted to be positives.

$$\text{Precision}_i = \frac{\text{TP}_i}{\text{TP}_i + \text{FP}_i} \tag{10}$$

Equation 11 is the recall rate of classification of Class *i*, which represents the number of samples predicted to be positive among the samples that are really positive.

$$\text{Recall}_i = \frac{\text{TP}_i}{\text{TP}_i + \text{FN}_i} \tag{11}$$

Equation 12 is the F1 score of the classification of Class *i*, which is the harmonic mean of the precision and recall rate.

$$\text{F1}_i = \frac{2 \cdot \text{Precision}_i \cdot \text{Recall}_i}{\text{Precision}_i + \text{Recall}_i} \tag{12}$$

Equations 13–15 are the macro average calculation formulae of the precision, recall rate and F1 score, which are obtained as the arithmetic average of various components.

$$\text{Precision}_{\text{macro}} = \frac{\sum_{i=1}^{L} \text{Precision}_i}{|L|} \tag{13}$$

$$\text{Recall}_{\text{macro}} = \frac{\sum_{i=1}^{L} \text{Recall}_i}{|L|} \tag{14}$$

$$\text{Macro F1} = \frac{2 \cdot \text{Precision}_{\text{macro}} \cdot \text{Recall}_{\text{macro}}}{\text{Precision}_{\text{macro}} + \text{Recall}_{\text{macro}}} \tag{15}$$

Equations 16–18 are the weighted average calculation formulae of the precision, recall rate and F1 score, which represent the weighted coefficients of a certain class in the total sample.

$$\text{Precision}_{\text{macro}} = \frac{\sum_{i=1}^{L} \text{Precision}_i \times w_i}{|L|} \tag{16}$$

$$\text{Recall}_{\text{macro}} = \frac{\sum_{i=1}^{L} \text{Recall}_i \times w_i}{|L|} \tag{17}$$

$$\text{Macro weighted F1} = \frac{2 \cdot \text{Precision}_{\text{macro}} \cdot \text{Recall}_{\text{macro}}}{\text{Precision}_{\text{macro}} + \text{Recall}_{\text{macro}}} \tag{18}$$

EXPERIMENTAL VERIFICATION

Experimental Verification of Facial Emotion Recognition Algorithm

Data Selection

In order to evaluate the performance of the proposed model, an evaluation experiment was designed. In the experiment, the CK+ data set of face emotion recognition was used. This data set has been widely used in experiments to evaluate the performance of facial emotion recognition algorithms, and consists of 593 video clips collected from 123 subjects of various races. Among them, 327 samples were marked with seven emotional labels: anger, contempt, disgust, fear, happy, sad and surprise. According to the recommendation of the data set, three frames from the middle of each video clip were intercepted as samples in our experiment to form a data set. This dataset is available online[1].

As the number of data in the CK+ data set is limited, to enhance the generalization capacity of the model, the samples were rotated and balanced, and finally the data set was expanded to 16,890 samples.

[1]http://www.pitt.edu/~emotion/ck-spread.htm

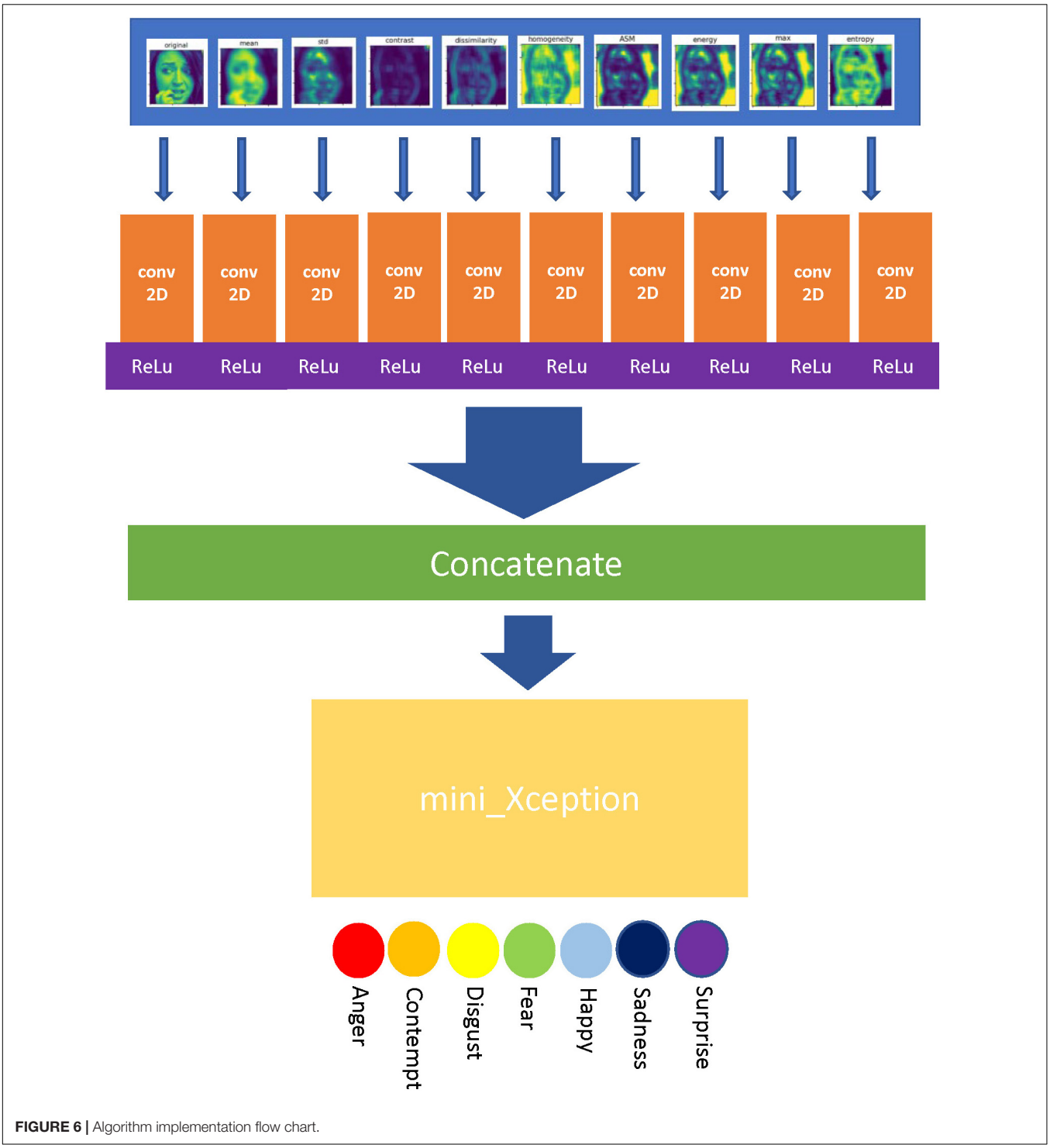

FIGURE 6 | Algorithm implementation flow chart.

Experimental Process

In the experiment, the data set to be tested was divided into a training set, a test set and a verification set by a ratio of 7:2:1, the data were randomly divided to ensure that the experimental results are reasonable and effective. In order to make the input samples compatible with the model, the images in the dataset were transformed into 8–8 bit gray images in 48 × 48 format prior to the experiment, and the label values were digitally encoded: 0–anger, 1–contempt, 2–disgust, 3–fear, 4–happy, 5–sad, and 6–surprise. The model was written in Python and trained with RTX-2070 graphics card. The number of training rounds were set to 500 rounds, but the training would be terminated if the loss function of verification set exceeded 50 rounds in the callback function, and the actual training rounds were about 60.

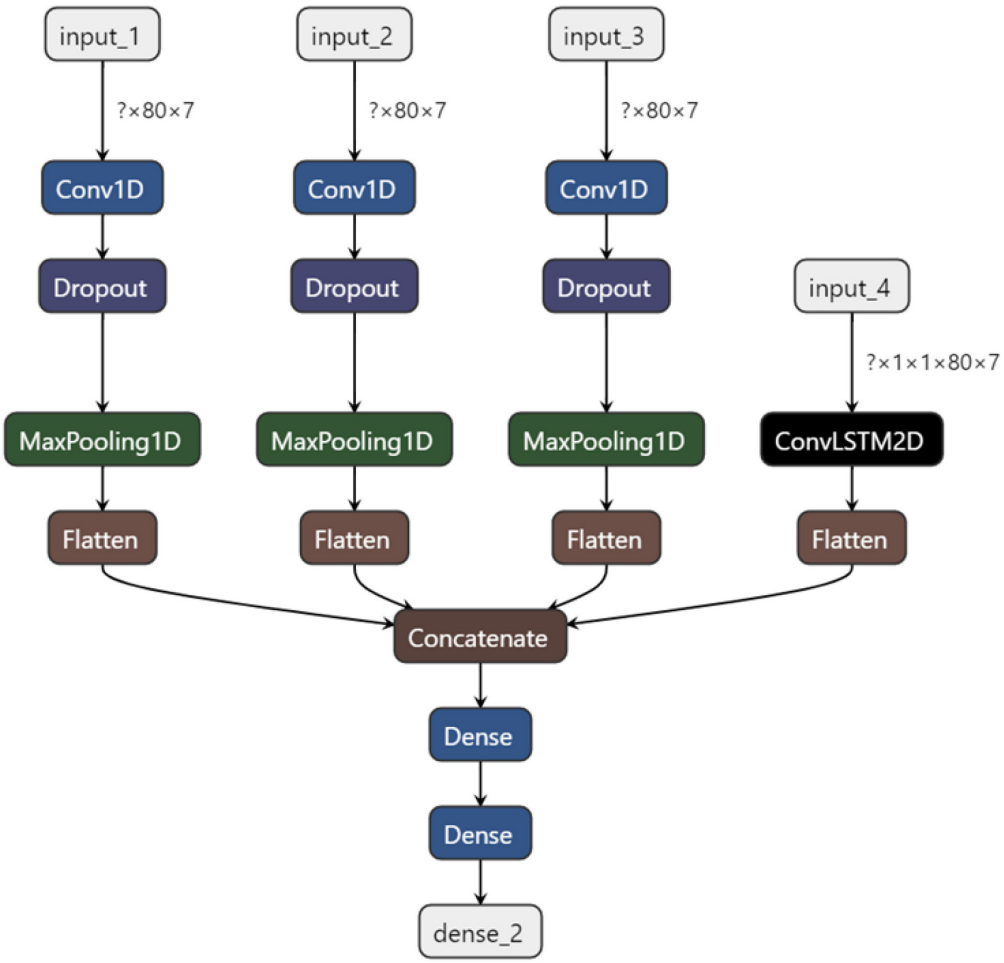

FIGURE 7 | Model structure.

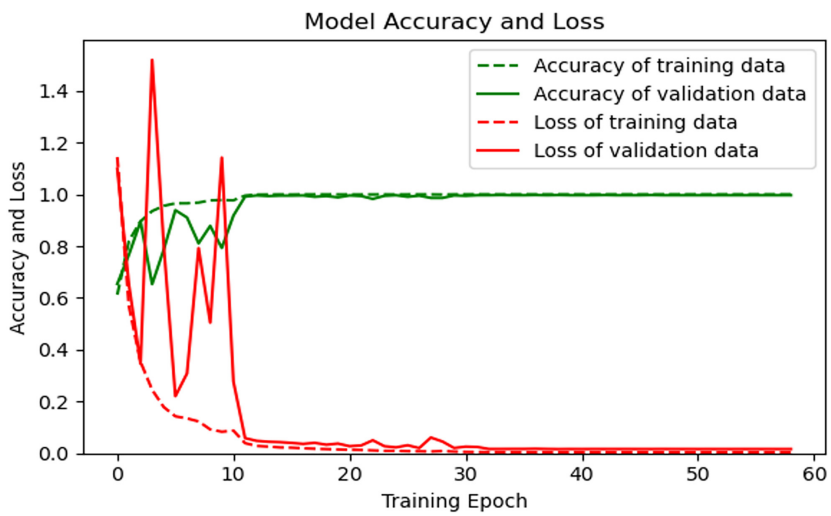

FIGURE 8 | Loss and accuracy of the model on the training set and the verification set.

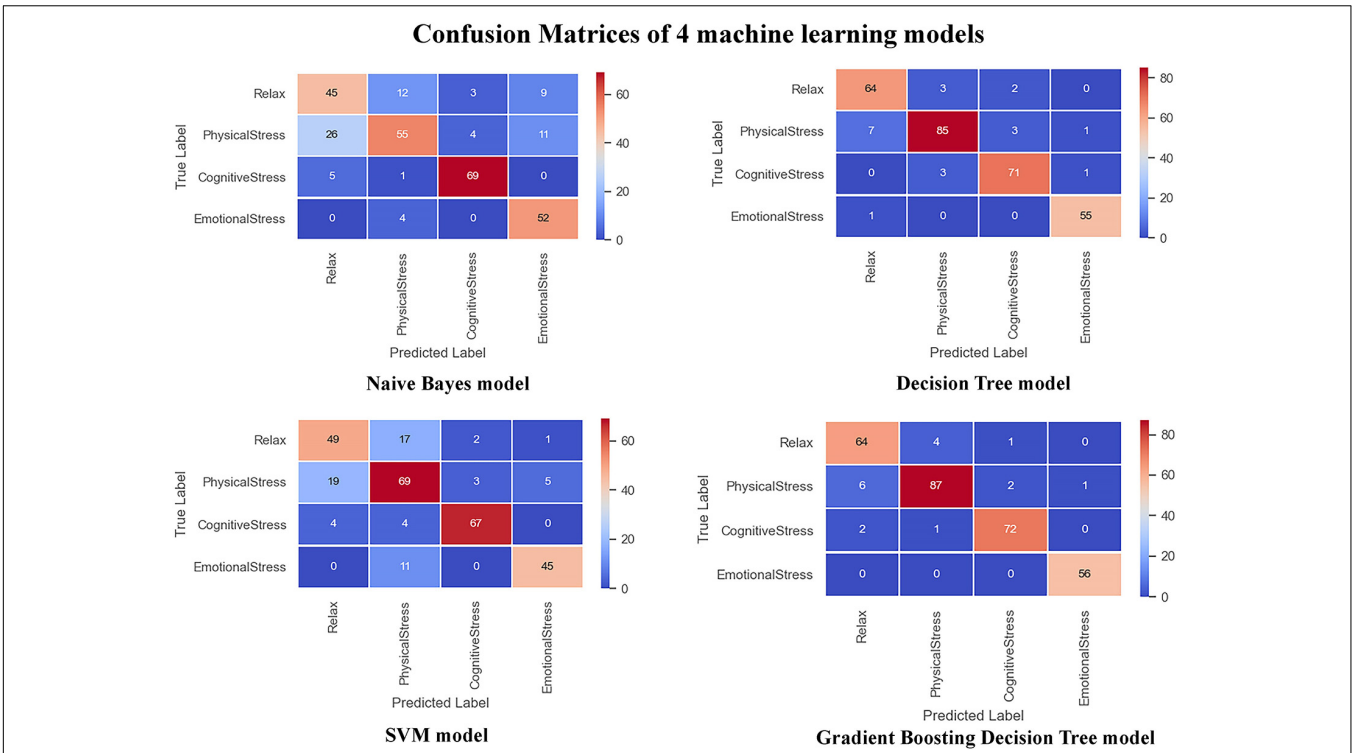

FIGURE 9 | Confusion matrices of test set.

The loss function and accuracy curve of the training set and the verification set are shown in **Figure 8**.

As shown in **Figure 8**, after 20 rounds of training, the loss function curves and accuracy curves of the training set and the verification set tend to flatten out, and there is no obvious decline. After 50 training rounds, the accuracy of the training set and verification set has reached more than 99%, which proves the good performance of our proposed algorithm.

Experimental Verification of Multi-Modal Physiological Signal-Based Stress Identification Algorithm

Data Selection and Preprocessing

In order to verify the effect of the proposed model, the published data set of multi-modal physiological stress identification (Birjandtalab et al., 2016) by the University of Texas was employed to test the model. This data set has collected five kinds of physiological signals from 20 college students (16 males and four females): triaxial acceleration, body temperature, galvanic skin response (GSR), Saturation of Peripheral Oxygen (SPO_2) and heart rate, and in a period of time, a series of external environmental stimuli were applied to the subjects to direct them into four psychological stress states: physiological stress, cognitive stress, emotional stress and relaxed state. The relaxed state, as described in the work (Birjandtalab et al., 2016), was controlled to stay only within the first time period to make the quantity of data in each class of state more balanced. In addition, in the dataset, the sampling frequency of heart rate and blood oxygen signal in this data set is 1 HZ, while the sampling frequency of other physiological signals is 8 HZ. To make the sampling frequency of each physiological signal consistent, other physiological signals except the heart rate and the blood oxygen were down-sampled to a frequency of 1 HZ. After the above operations, four kinds of labels of physiological signals from 20 samples at 29,582 time points were obtained from the data set. In order to meet the requirements of the model input, the data was extracted by slices with 5 s as a unit. Label values were digitally coded beforehand: 0–relaxation, 1–physiological stress, 2–cognitive stress, and 3–emotional stress. This dataset is available online[2].

Experimental Process

In the experimental, the data to be tested were divided into a training set and a test set by a ratio of 19:1; then, the verification set was separated from the training set by a ratio of 9:1. The data were randomly divided into different sets to ensure that the experimental results were reasonable and effective. The model was written in Python language, and RTX-2070 graphics card was used in the training process. The number of training rounds was set to 300, and the training would be terminated if the loss function of verification set exceeded 60 rounds in the callback function, and the actual training rounds were about 110 rounds. **Figure 10** shows the loss and accuracy curves of the model on

[2]https://physionet.org/content/noneeg/1.0.0/

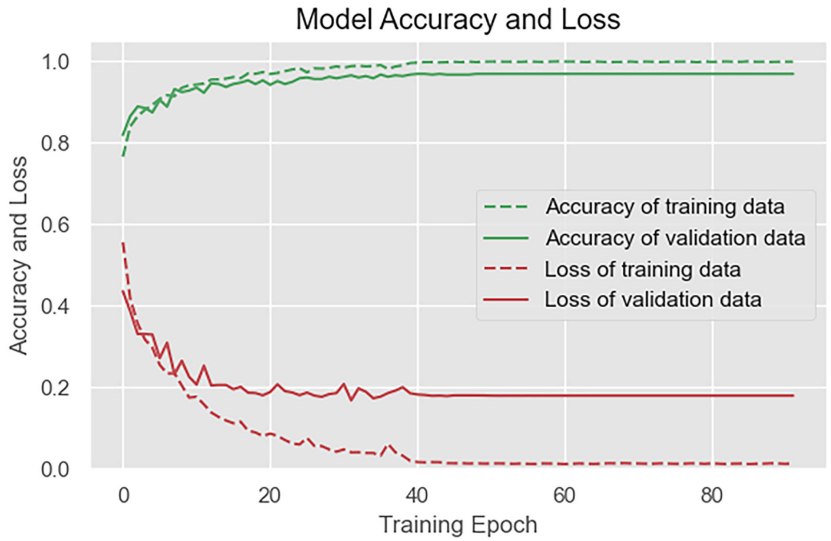

FIGURE 10 | Loss and accuracy of the model on the training set and the verification set.

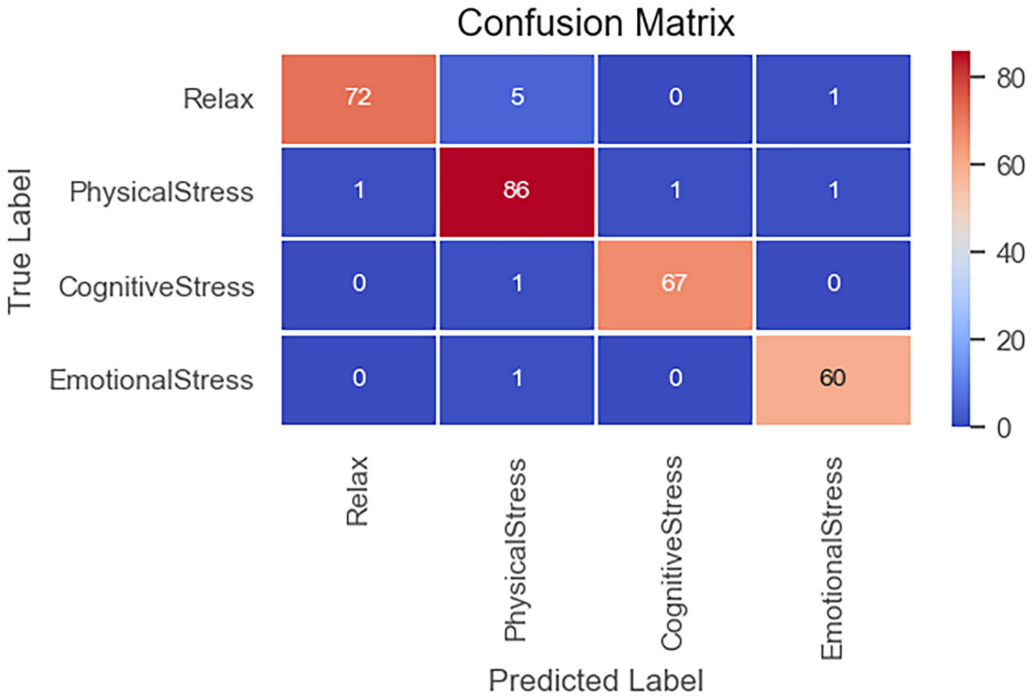

FIGURE 11 | Confusion matrix of test set.

the training set and the verification set, and **Figure 11** shows the confusion matrix on the test set.

As **Figure 10** shows, the model achieves a good fitting effect, with an accuracy of 99.3% on the training set and 96.2% on the verification set, without overfitting. After 40 rounds of training, the loss and accuracy curves flatten out. As **Figure 11** shows, cognitive stress marks the highest classification accuracy among all stress states.

DISCUSSION

Discussion of of Facial Emotion Recognition Algorithm Experimental Results

Furthermore, the confusion matrix obtained by using the test set is shown in **Figure 12**.

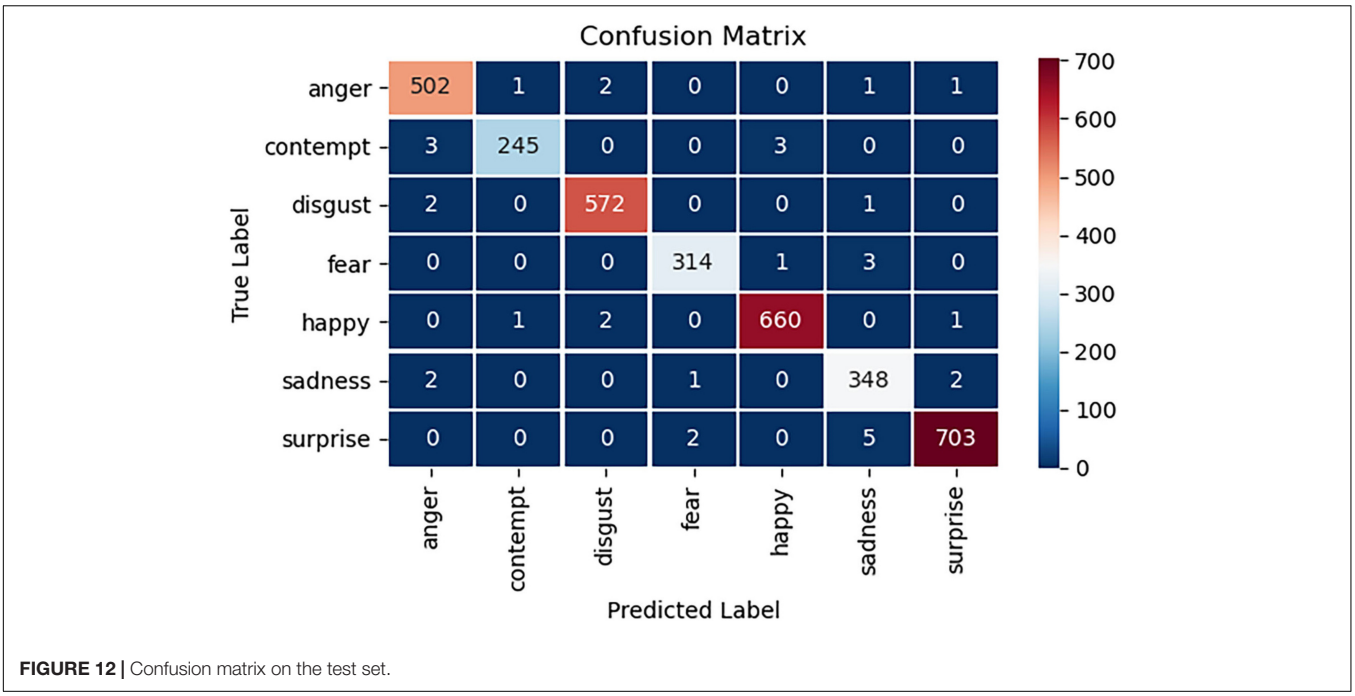

FIGURE 12 | Confusion matrix on the test set.

As **Figure 12** shows, the model also achieves high accuracy on the test set. **Table 1** shows the specific results on the test set.

As **Table 1** reveals, the results of the test set have reached an ideal range in terms of accuracy, F1 score and recall rate. Among them, the model performs best in classification of the emotions of anger and surprise. The accuracy of the test set is 99%, and the weighted F1 score is 0.99.

Comparisons between our model and previous works are shown in **Table 2**. As it suggests, our model gain an advantage over the previous advanced methods, thus rationalizing the application of the improved algorithm of mini_Xception in face emotion recognition and classification. Besides, because the mini_Xception model has a small scale of parameters and is applicable to low-performance platforms, the proposed improved algorithm can be well applied to the system, providing support for the facial emotion recognition function. The future research work can make breakthroughs in these aspects: (1) The parameter scale of feature extraction and the running time of the algorithm can be reduced to improve the efficiency of the system. (2) The model can be further improved and applied to continuous emotion recognition to enhance the universality of the model. (3) The performance of the model on emotion recognition accuracy under the condition of partial occlusion of the face can be tested and improved to enhance the generalization capacity of the algorithm.

TABLE 1 | Specific evaluation results on the test set.

Class	Precision	Recall	F1-score
Angry	0.99	0.99	0.99
Contempt	0.99	0.98	0.98
Disgust	0.99	0.99	0.99
Fear	0.99	0.99	0.99
Happy	0.99	0.99	0.99
Sad	0.97	0.99	0.98
Surprise	0.99	0.99	0.99
Macro average	0.99	0.99	0.99
Weighted mean	0.99	0.99	0.99

Discussion of Multi-Modal Physiological Signal-Based Stress Identification Algorithm Experimental Results

To verify the advantages of our model, it was compared with other machine learning models, including the support vector machine (SVM) model, decision tree model, classical Naive Bayes (NB) model, and gradient boosting decision tree (GBT) model. The form of data input remained the same on all the models for comparison. In addition, in order to better reflect the advantages of the proposed model, we compare with the Gaussian Mixture Model (GMM) used in the paper containing the original database and the Ensemble classifier based on statistical feature used in a research adopting the same database (Xin et al., 2019). **Table 3** shows the comparison result between our model and the machine learning models as well as advanced methods from previous works, and **Figure 9** show the performance of all the machine learning models that were compared.

As **Table 3** shows, our model has absolute advantages over the classical Naive Bayes and SVM models, and it outperforms the random forest model and the gradient boosting decision-tree model in terms of accuracy. It could be also found that the proposed method outweights that of the previous works in terms of several crucial parameters. In addition, the variables input in the models are sliced and extracted, which contain

TABLE 2 | Comparison of performance on the dataset between different algorithms.

Source	Method	Accuracy	F1-score
Lopes et al. (2017)	7-Layers CNN	0.99	0.98
Lu et al. (2016)	LeNet-5	0.84	0.8456
Yong et al. (2018)	5-Layers CNN	0.97	0.9645
Xi et al. (2020)	CCRNet	0.98	0.9801
Our model	mini_Xception+GLCM feature extraction	0.99	0.99

TABLE 3 | Model performance comparison.

Models	Accuracy	Weighted-recall	Weighted-F1 score
SVM	0.78	0.78	0.77
NB	0.75	0.75	0.75
GBT	0.94	0.94	0.94
Decision tree	0.93	0.93	0.93
This model	0.96	0.96	0.96
GMM	0.84	NA	NA
Ensemble classifier	0.94	0.94	NA

more time features, so the model is expected to have better robustness in real-world scenarios. Nonetheless, as the model merges inputs from diverse channels, which increases the number of parameters. Convolutional layers dominate the computation complexity and consequently affects the latency and throughput (Jafari et al., 2018). In the future, more research work needs to be devoted to achieve a balance between the complexity and accuracy of the model.

Discussion of Wearable Device System

Compared with previous work, the proposed wearable device has the following advantages: (1) a good balance is achieved between cost and functional effectiveness of the wearable device system; (2) the proposed device is portable and comfortable, thus making its application scenarios more general; (3) the system pays attention to the influence of external environment information, providing the basis for the follow-up research; (4) the integrated system could monitor both users' stress and facial emotions of people around, which is suitable for research on facial emotion recognition disorders; (5) an original multi-modal physiological signal-based stress identification algorithm as well as an improved facial emotion recognition algorithm is carefully designed for the system.

However, this research also has many shortcomings. First of all, because facial emotion recognition disorders are related to mental illness, it is necessary to analyze the specific situation of different types of users to avoid the following problems: the users may not want to wear this device, and significant differences among specific users in the physiological signals would result in reduced accuracy of the model. In the future, surveys will be performed on the users to improve the shape, appearance and size of the device to increase its appeal to users. Moreover, more data on different groups of people should be collected to improve the model's performance. Secondly, collecting information about emotions of people around and the surrounding environment by cameras may incur privacy disputes. Thus, in the future, it is necessary to improve the rules concerning the use of the device and the collected information to conform to the law and protect the privacy of users. Finally, the mobile APP designed in our system can provide only the result feedback function. Thus, it is necessary to expand the functions of the app to monitoring and analysis of the user's movements, automatic emergency alarming and the like to improve user experience.

CONCLUSION

In the present work, an ear wearable device system was proposed. The system can analyze the user's own stress state and recognize the facial emotions of people around the user. It will provide a solution to long-term supervision of patients with facial emotion recognition disorders. The contributions of this work are as follows: A new platform is proposed, which can be used to assist and study facial emotion recognition disorders. The system is expected to provide help for patients or potential sufferers of facial emotion recognition disorders. Specifically, it can collect information and keep track of the stress state of the user, the surrounding environment, the emotions of people whom users interact with through sensors and cameras to realize real-time monitoring of the user's psychological stress and allow the user to identify emotions of people around. The system can also be used by hospitals to analyze the patients' specific conditions and make corresponding treatment plans. Moreover, a novel multi-modal physiological signal-based stress identification algorithm and an improved facial emotion recognition algorithm are put forward in this work, and experimental results show that these two algorithms could well meet the functional requirements of the system.

DATA AVAILABILITY STATEMENT

The original contributions presented in the study are included in the article/supplementary material, further inquiries can be directed to the corresponding author.

AUTHOR CONTRIBUTIONS

As the project leader and the first author, ZL was responsible for project establishment and assignment, modeling, heart rate data, facial expression data collection and analysis, and paper writing. YG was responsible for appearance design, experimental data processing, and paper revision. XC was responsible for hardware module design, experimental data processing, and paper revision. WL was responsible for communications and APP interface design. All authors contributed to the article and approved the submitted version.

REFERENCES

Arriaga, O., Valdenegro-Toro, M., and Plöger, P. (2017). Real-time convolutional neural networks for emotion and gender classification. *arXiv* [preprint] arXiv:1710.07557

Birjandtalab, J., Cogan, D., Pouyan, M. B., and Nourani, M. (2016). "A Non-EEG biosignals dataset for assessment and visualization of neurological status," in *Proceedings of the IEEE International Workshop on Signal Processing Systems*, Piscataway, NJ: IEEE. doi: 10.1109/SiPS.2016.27

Chollet, F. (2017). "Xception: deep learning with depthwise separable convolutions," in *Proceedings of the 2017 IEEE Conference on Computer Vision and Pattern Recognition (CVPR)*, Piscataway, NJ: IEEE. doi: 10.1109/CVPR.2017.195

Hall-Beyer, M. (2007). *The GLCM Tutorial Home Page. Current Version 2.10*. Calgary: University of Calgary

Hasanbasic, A., Spahic, M., Bosnjic, D., Adzic, H. H., Mesic, V., and Jahic, O. (2019). "Recognition of stress levels among students with wearable sensors," in *Proceedings of the 18th International Symposium INFOTEH-JAHORINA*, Piscataway, NJ: IEEE. doi: 10.1109/INFOTEH.2019.8717754

Jafari, A., Ganesan, A., Thalisetty, C. S. K., Sivasubramanian, V., Oates, T., and Mohsenin, T. (2018). "SensorNet: a scalable and low-power deep convolutional neural network for multi-modal data classification," in *Proceedings of the IEEE Transactions on Circuits and Systems I: Regular Papers*, Vol. 66, Piscataway, NJ: IEEE, 274–287. doi: 10.1109/TCSI.2018.2848647

Jia, Z., Wang, W., Wang, C., and Xu, W. (2017). Application and development of wearable devices in medical field. *Chin. Med. Dev.* 32, 96–99.

Jie, Z., Zeng, M., Zhou, X., and He, Q. (2021). Two stream CNN with attention-ConvLSTM on human behavior recognition[J]. *J. Chin. Mini Micro Comput. Syst.* 42, 405–408.

Khaldi, B., Aiadi, O., and Kherfi, M. L. (2019). Combining colour and grey-level co-occurrence matrix features: a comparative study. *IET Image Process.* 13, 1401–1410. doi: 10.1049/iet-ipr.2018.6440

Lopes, A. T., Aguiar, E. D., Souza, A., and Oliveira-Santos, T. (2017). Facial expression recognition with convolutional neural networks: coping with few data and the training sample order. *Pattern Recognit.* 61, 610–628. doi: 10.1016/j.patcog.2016.07.026

Lu, G., He, J., Yan, J., and Li, H. (2016). Convolutional neural network for facial expression recognition[J]. *J. Nanjing Univ. Posts Telecommun.* 36, 16–22.

Montesinos, V., Dell'Agnola, F., Arza, A., Aminifar, A., and Atienza, D. (2019). "Multi-Modal acute stress recognition using off-the-shelf wearable devices," in *Proceedings of the Annual International Conference of the IEEE Engineering in Medicine and Biology Society. Annual Conference*, Piscataway, NJ: IEEE, 2196–2201. doi: 10.1109/EMBC.2019.8857130

Shen, H., Kong, F., and Liu, S. (2015). Research progress of facial emotion cognitive impairment. *Chin. J. Diffic. Compl. Cas.* 14, 643–647.

Smith, J. R., and Chang, S. F. (1996). "Automated binary texture feature sets for image retrieval," in *Proceedings of the IEEE International Conference on Acoustics, Speech, and Signal Processing Conference Proceedings, Atlanta, GA*, Piscataway, NJ: IEEE, 2239–2242.

Tang, R. Z. (2017). *Research on Improving SVM Training Efficiency by Data Normalization Method*. Jinan: Shandong Normal University.

Tyagi, V. (2018). *Content-Based Image Retrieval: Ideas, Influences, and Current Trend[M]*, 1st Edn, Vol. 8. Singapore: Springer, 162–163.

Xi, Z., Niu, Y., Chen, J., Kan, X., and Liu, H. (2020). Facial expression recognition of industrial internet of things by para-llel neural networks combining texture features. *IEEE Trans. Ind. Inform.* 17, 2784–2793. doi: 10.1109/tii.2020.3007629

Xin, S. Q., Yahya, N., and Izhar, L. I. (2019). "Classification of neurological states from biosensor signals based on statistical features," in *Proceedings of the 2019 IEEE Student Conference on Research and Development(SCOReD)*, Piscataway, NJ: IEEE, 231–236. doi: 10.1109/SCORED.2019.8896286

Yang, G., Chen, J., Cao, Y., Tenhunen, H., and Zheng, L. R. (2008). "A novel wearable ECG monitoring system based on active-cable and intelligent electrodes," in *Proceedings of the 10th International Conference on E-health Networking*, Piscataway, NJ: IEEE.

Yong, L. I., Lin, X. Z., and Jiang, M. Y. (2018). Facial expression recognition with cross-connect LeNet-5 network. *Acta Automat. Sin.* 44, 176–182.

Conflict of Interest: The authors declare that the research was conducted in the absence of any commercial or financial relationships that could be construed as a potential conflict of interest.

frontiers in Bioengineering and Biotechnology

ORIGINAL RESEARCH
published: 02 July 2021
doi: 10.3389/fbioe.2021.696166

Bioaugmentation Technology for Treatment of Toxic and Refractory Organic Waste Water Based on Artificial Intelligence

Jiang Yanbo[1,2], Jiang Jianyi[1], Wei Xiandong[1], Ling Wei[1] and Jiang Lincheng[3]*

[1] Research Center of Wastewater Engineering Treatment and Resource Recovery, Guangxi Beitou Environmental Protection and Water Group, Nanning, China, [2] Institute of Ecological Engineering, Guangxi University, Nanning, China, [3] Guangxi Civil and Environment Co., Ltd., Nanning, China

OPEN ACCESS

Edited by:
Xiaoguang Zhou, Beijing University of Posts and Telecommunications, China

Reviewed by:
Guanglong Chen, South China Agricultural University, China
Hao Du, South China Agricultural University, China
Kai Huang, Guangxi Academy of Sciences, China

***Correspondence:**
Jiang Yanbo
yamboo@gxu.edu.cn

Specialty section:
This article was submitted to Bionics and Biomimetics, a section of the journal Frontiers in Bioengineering and Biotechnology

Received: *16 April 2021*
Accepted: *26 May 2021*
Published: *02 July 2021*

Citation:
Yanbo J, Jianyi J, Xiandong W, Wei L and Lincheng J (2021) Bioaugmentation Technology for Treatment of Toxic and Refractory Organic Waste Water Based on Artificial Intelligence. Front. Bioeng. Biotechnol. 9:696166. doi: 10.3389/fbioe.2021.696166

With the development of modern chemical synthesis technology, toxic and harmful compounds increase sharply. In order to improve the removal efficiency of refractory organic matter in waste water, the method of adding powdered activated carbon (PAC) to the system for adsorption was adopted. Through the analysis of organic matter removal rule before and after waste water treatment, it can be found that PAC is easy to adsorb hydrophobic organic matter, while activated sludge is easy to remove hydrophilic and weakly hydrophobic neutral organic matter. Powdered activated carbon-activated sludge SBR system (PAC-AS) system is obviously superior to AS and PAC system in removing organic matter of hydrophilic and hydrophobic components, that is, biodegradation and PAC adsorption are additive. Compared with the control system, the Chemical Oxygen Demand (COD) removal rate of refractory substances increased by 8.36%, and PAC had a good adsorption effect on small molecular weight organic compounds, but with the increase of molecular weight of organic compounds, the adsorption effect of PAC gradually weakened, and it had no adsorption effect on macromolecular organic compounds. Based on the research of fuzzy control theory, an Agent control system for ozone oxidation process of industrial waste water based on Mobile Agent Server (MAS) theory was established, which was realized by fuzzy control method. The simulation results showed strong stability and verified the feasibility and adaptability of the distributed intelligent waste water treatment system based on MAS theory in the actual control process.

Keywords: artificial intelligence, intelligent control, waste water treatment, biofortification, fuzzy neural network

INTRODUCTION

In recent years, with the rapid development of economy, a large number of domestic industrial parks have emerged. The emergence of various industrial parks has caused a large amount of industrial waste water discharge, while most of the industrial parks in China are chemical industrial parks (Wu et al., 2018). Chemical enterprises produce various chemical industrial waste water in their production activities, the main sources of which are as follows (Boonnorat et al., 2018;

Zhang et al., 2018): (1) raw materials for production; (2) By-products discharged in the production process; (3) Part of the final products in the production process; and (4) The waste water produced in the above production process due to transportation, washing, rain erosion, or other accidental factors, such as leakage. The waste water produced by various chemical enterprises is discharged and collected into comprehensive chemical waste water through the pipeline network. Therefore, comprehensive chemical waste water usually contains a large number of chemical inorganic or organic pollutants.

In recent decades, a large number of synthetic compounds have entered the environment. Due to their structural complexity and biological strangeness, it is difficult for them to be utilized by microorganisms and enter the material circulation in a short time. Refractory organic compounds are the main components of these compounds, and their treatment challenges the original treatment facilities and technologies. Aniline is an important chemical raw material, which is widely used in national defense, printing and dyeing, plastics, pesticides and pharmaceutical industries. At the same time, it is also a harmful substance that seriously pollutes the environment and endangers human health. Due to the toxicity of aniline to ecological organisms, aniline has been listed in the "blacklist of China's environmental priority pollutants," which requires strict control in industrial drainage. At present, the treatment of aniline waste water at home and abroad mainly includes physical, chemical and biological methods (Fan et al., 2017; Ke et al., 2018), and the research results in recent years show that biological enhanced treatment is one of the important ways to eliminate amine in the environment (Weiwei et al., 2017; Santos and Daniel, 2020). Bioaugmentation technology can effectively remove target pollutants (Weiwei et al., 2019), accelerate system startup (Abbaslou et al., 2018), improve the system's ability to resist hydraulic and organic loads (Jasper et al., 2017), and enhance the stability of system flora structure and function (Ying et al., 2018).

In industrial production, a considerable number of complex control processes are still dominated by manual operation and control, such as the control of some nonlinear objects with large time delay. In this way, not only the technology is imperfect, but also the error in operation is large, and the data detection cannot achieve the expected effect. The control object of waste water treatment system is also nonlinear and unstable, which limits the treatment efficiency and results of waste water treatment process. Artificial intelligence has gradually become an independent branch (Wang et al., 2018; Hong et al., 2020). In this paper, Mobile Agent Server (MAS) theory is applied to the field of waste water treatment combined with bioaugmentation technology, and a distributed waste water treatment intelligent system based on Multi-Agent is established, so that agents can run in parallel and cooperate with each other in distributed environment, and comprehensively realize the functions of measurement and analysis, intelligent control and fault diagnosis in waste water treatment process from the system point of view. Multi-level and multi-sided integrated research is not only beneficial to cross-infiltration among disciplines, but also of great significance to solve the problems faced by waste water treatment process control and keep up with the development of the frontier disciplines.

THE INNOVATION OF THIS RESEARCH

In this paper, the water quality and biodegradability of comprehensive chemical waste water in a chemical industry park are deeply analyzed, the treatment effect of conventional biological process on toxic and refractory organic waste water is evaluated, and feasible strengthening schemes are put forward. The removal effect and removal mechanism of the system after the implementation of each strengthening scheme are investigated, which provides theoretical guidance and technical support for practical sewage treatment plants to treat this kind of refractory comprehensive chemical waste water.

RESEARCH STATUS AT HOME AND ABROAD

Research Status of Bioaugmentation Technology in Waste Water Treatment

Bioaugmentation technology is to enhance biomass by adding microorganisms with special functions to natural flora, so as to enhance the response of biomass to a specific environment or special pollutants. The effects between the input strains and the sediment mainly include:

Direct Action of High-Efficiency Degrading Bacteria

The most common way to apply bioaugmentation technology is to directly add microorganisms with specific degradation ability to target pollutants. In this mechanism of action, firstly, one or more efficient microbial strains with high tolerance and degradation and transformation ability, which use one or a certain kind of pollutants as the main carbon source and energy, need to be obtained through domestication, screening, enrichment, separation, mutagenesis and gene recombination. After repeated cultivation and domestication, the microbial population grows continuously, and finally, it is put into the waste water treatment system that needs targeted degradation or treatment.

Co-metabolism of Microorganisms

Co-metabolism of microorganisms means that some organic matters can not be oxidized as carbon source or energy source of microorganisms, but only when the growth substrate exists can microorganisms biodegrade or oxidize the non-growth substrate. Literature (Singh et al., 2021) found that the coexistence of o-dichlorobenzene and m-dichlorobenzene was beneficial to the degradation of chlorinated aromatic hydrocarbons in the whole system. The research results of Xiaojian et al. also show that in anaerobic treatment system, glucose and other easily degradable organic compounds as co-metabolism matrix can obviously improve the degradation effect of biphenyl.

Literature (Park and Oh, 2020) using SBR process to treat landfill leachate, the removal effects of COD, ammonia nitrogen,

chroma and total dissolved solids have been significantly improved after adding activated carbon into the system; Literature (Nath et al., 2018) used traditional activated sludge process to treat pharmaceutical waste water. By comparing the treatment effect of the system before and after adding activated carbon, the results showed that the treatment effect of the system after adding activated carbon was continuously improved, and antibiotic pollutants were better removed. Literature (Atashgahi et al., 2018) compares biological system with activated carbon, simple biological system and activated carbon system to treat waste water containing Cr. The results show that the removal effect of Cr is obviously improved after adding activated carbon.

One of the important benefits of bioaugmentation is that it can be processed on demand. Studies have shown that under the condition of limited space, direct inoculation of microorganisms can provide an immediate solution for a series of failed treatment systems without adding equipment or adding less equipment, which can maximize the operation of the treatment system and enhance the degradation ability of the system to organic pollutants (Rodriguez-Rodriguez et al., 2017), and may also be the only way to ensure closed circulation and zero emission of waste water without stopping production (Tigini et al., 2018).

Application Status of Artificial Intelligence Technology in Waste Water Treatment System

Artificial Intelligence (AI) is a discipline that simulates human intelligence. Since the rapid development of AI theory and technology in 1970s, foreign scholars began to explore the application of AI technology in waste water treatment field, in order to solve the key problems that depend on knowledge highly and determine the operation control effect of waste water treatment. After decades of development, many effective research results have been obtained.

Among many intelligent control methods, fuzzy control, expert control and neural network control are the three most typical methods.

At present, the application of fuzzy control in China mainly focuses on the design of lower-level fuzzy controller, while foreign countries have many successful experiences in upper-level and lower-level applications, and pay more attention to upper-level reasoning and decision-making applications. For example, literature (Boonnorat et al., 2018) proposed that six variables, such as effluent substrate concentration, effluent SS, MLSS, effluent ammonia nitrogen concentration, DO concentration and sludge discharge rate, were used in the upper reasoning of the control system, and the set values of DO, sludge reflux ratio and sludge discharge were given by fuzzy decision-making, which were implemented by the bottom control. Literature (Correa and Maranho, 2021) developed a simple, reliable, cheap and PLC-embedded fuzzy controller for waste water treatment. After fuzzification of input variables, the output of the controller was calculated by inference engine, and then the control quantity was obtained after anti-fuzzification.

From the current application point of view, there are few reports on the application of expert control in the field of waste water treatment and control in China, and expert systems are used more in the upper layer of control system in foreign countries to carry out reasoning and optimization calculation and generate the set value of the controlled quantity; The lower layer uses switch control, PID control, fuzzy control and other methods to control the set value. For example, in reference (Poddar et al., 2020), the expert system is used to monitor and diagnose the anaerobic treatment process of sewage; Document (Aparicio et al., 2020; Martinez-Gallardo et al., 2020; Raimondo et al., 2020) uses rule-based expert system to calculate the set value of DO according to influent flow rate and influent COD.

From the current application point of view, in the waste water treatment process control, ANN control mostly acts as a controller directly. For example, the real-time control of continuous flow SBR process was studied by using BP neural network to monitor ORP and pH on line in document (Tigini et al., 2019). The results show that BP network can not only accurately predict information for real-time process control, but also reduce hydraulic retention time and aeration energy consumption compared with fixed-time control, and at the same time improve total nitrogen removal rate and denitrification effect.

RESEARCH TECHNIQUE

Waste Water Treatment Control System Based on MAS

Distributed Control Design Idea

The problems to be solved by distributed control system are the coordination and scheduling among control flow systems, the synchronization of process data and the maintenance of process status in distributed control system because the control subsystems are distributed on different devices (Yue et al., 2018). The reason why the distributed control system is more complex than the centralized control flow system is that it has many nodes, and there may be various errors or anomalies in the process of coordinating various control flow subsystems to work together. The sources of these problems can be roughly divided into: 1) the problems of the control management system itself; 2) External factors, including human error, network or hardware abnormality. Designing a robust step-by-step control framework can deal with errors and recover from them, thus ensuring that the control process is not interrupted.

Mobile Agent Server Structure of Distributed Control System

Considering the initiative and mobility of Agent technology, according to the specific requirements of control tasks, the control MAS (Mobile Agent Server) system structure is constructed, as shown in **Figure 1**.

Among them, the functions of the control task cooperative Agent include: receiving the control plan of the control plan MAS and transforming it into a control task list; Maintain task list information, including the number, quantity and start time of controlled equipment, track the execution process, and send status information to the control decision MAS in real

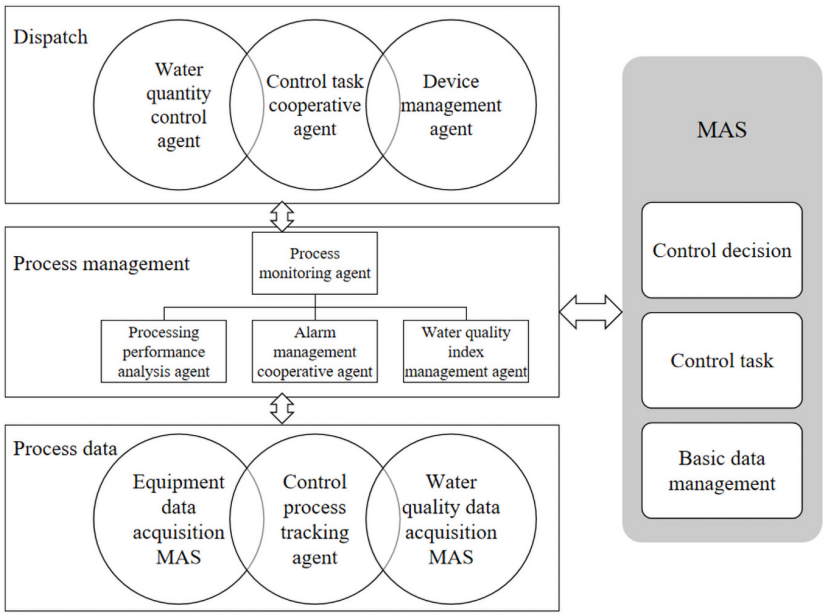

FIGURE 1 | Mobile Agent Server (MAS) structure of distributed control system.

time. The functions of standby management Agent include: Store the control parameters and usage amount representing the control system, and maintain the basic information of equipment, including equipment functions, attributes, capability levels, subordinate units, historical records, use depreciation, etc.; After the equipment obtains the task control list information, record the task information that the equipment needs to complete; When the equipment status changes, the equipment Agent can obtain the real-time information of the equipment operation through the basic data management MAS interaction, and automatically update the data.

Operation Model of Distributed Control System MAS

Distributed control MAS can realize three functions: collaborative dispatching of control tasks, management of processing equipment Agent real-time data collection through multi-agent running process. In the process of control task collaboration, the control task collaboration Agent receives the control plan of the control decision MAS, sends a control task list and sends it to the equipment management Agent. At the same time, the water quantity distribution request is sent to the water quantity control Agent, which distributes the sewage to be treated. The equipment management Agent performs the operation tasks such as starting, stopping and numerical control adjustment of the control equipment, and feeds back the task execution. The interaction flow between Agent is shown in **Figure 2**.

Fuzzy Neural Network Control System Model

The structure of fuzzy neural network control system combined with waste water treatment system is shown in **Figure 3**. The nonlinear state equation obtained by the following formula is taken as the controlled model, and the adaptive fuzzy neural network controller optimized by the above parameters is applied to the system structure.

According to the law of material balance, based on the first and second equations of Lawrence-McCarty model and Mckinney model, the following nonlinear state equation of waste water treatment system is obtained through analysis and calculation (Changotra et al., 2019; Wang and Chen, 2020):

$$\begin{cases} \frac{dO}{dt} = 0.57\lambda\,(S_o, S_e) + 1.1K_eX + \mu \\ \frac{dS}{dt} = \frac{KSX}{K_s+S} \\ \frac{dX}{dt} = \eta\frac{KSX}{K_s+S} - K_dX \end{cases} \quad (1)$$

In which:

S–aeration tank volume, m^3;
η–the real yield of activated sludge microorganisms is obtained according to the empirical value of waste water treatment plant;
K_e–endogenous respiration rate constant, h^{-1};
K–maximum specific substrate concentration utilization rate, constant, d^{-1};
K_s–it is called half speed constant, and its value is equal to the substrate concentration at the maximum specific growth rate of half of microorganisms, mg/L;
λ–the reciprocal of water inflow time can be given according to the actual situation of waste water treatment plant, h^{-1};
K_d–microbial attenuation constant of activated sludge, constant, d^{-1};
μ –air flow in aeration tank, m^3/h;

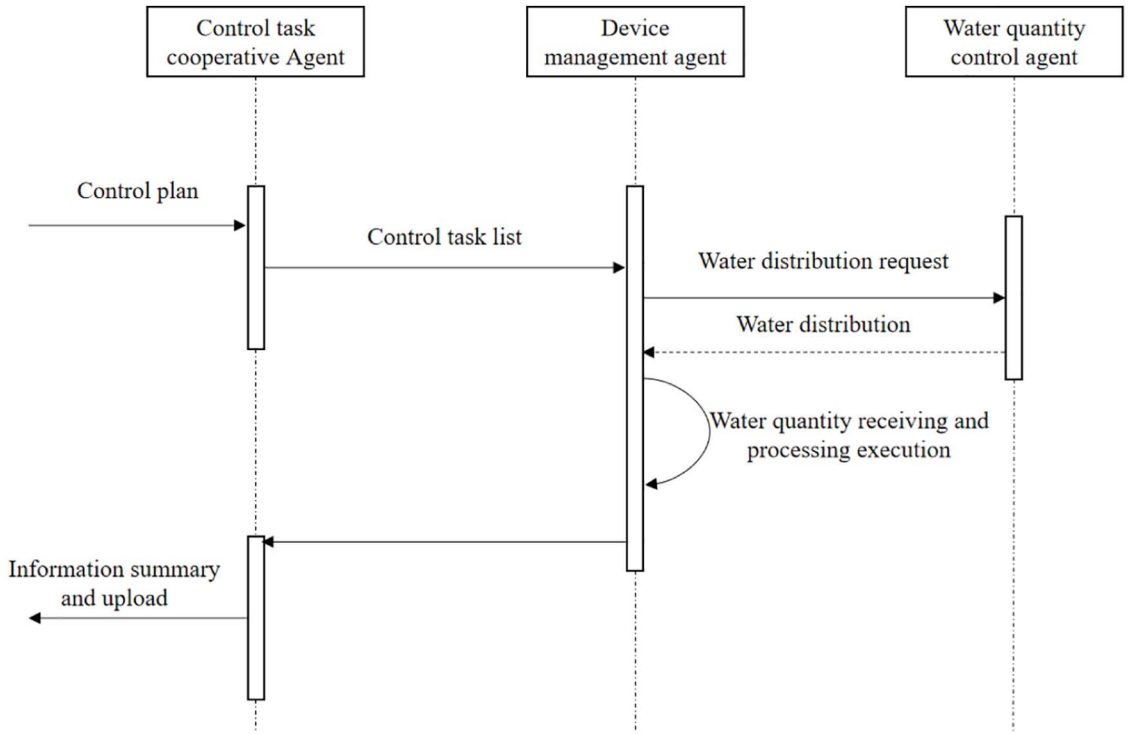

FIGURE 2 | Information processing flow of MAS task dispatching in distributed control system.

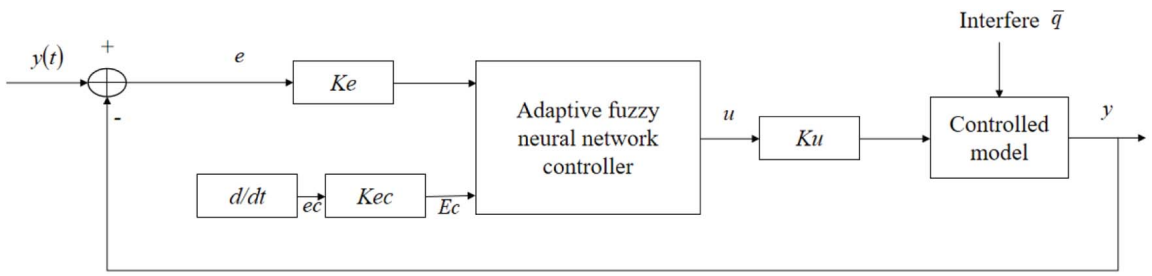

FIGURE 3 | Fuzzy neural network control simulation system.

O–concentration of dissolved oxygen in aeration tank, mg/L.

In the figure:

e, *ec*–error and error rate of change;
Ke, *Kec*–quantization factors input by the controller, respectively;
E, *Ec*–respectively, expressed as the error and error change rate after system quantization;
Ku–the quantization factor expressed as the output of the controller;
$y(t)$–expressed as the concentration of a given dissolved oxygen;
u–expressed as controller output;
y–expressed as the actual output dissolved oxygen concentration.

There is the following formula for calculating *Ke*, *Kec*, *Ku*:

$$\begin{aligned} Ke &= \frac{n}{e} \\ Kec &= \frac{n}{ec} \\ Ku &= \frac{u}{n} \end{aligned} \tag{2}$$

Set the physical domain:

$N = [-n, n+1, \cdots, -1, 0, 1 \cdots, n]$,

$n = 6, e = [-2, +2], ec = [-1.5, +1.5], u = [-1, 1]$.

According to formula (2), the values of *qKe*, *Kec*, *Ku* are: $Ke = 3$, $Kec = 3$, $Ku = \frac{1}{6}$.

Bioaugmentation

In order to further improve the removal efficiency of waste water, physical and chemical methods and biological processes are generally used to improve the removal efficiency.

Activated carbon adsorption, because of its large adsorption capacity and wide application range, is widely used in waste water and drinking water treatment. Activated carbon-activated sludge process, due to the simultaneous physical adsorption and biodegradation, further improves the treatment effect of the system.

Source and Characteristics of Sewage

The waste water studied was taken from the actual industrial waste water of a comprehensive waste water treatment plant in a chemical industry park. There are more than 50 different types of chemical enterprises in the industrial park, such as pharmaceutical, petrochemical, electronics, machinery manufacturing, daily chemicals, chemical reagents and so on. The waste water produced by these enterprises is discharged into the pipe network after preliminary treatment, and then collected into the comprehensive waste water treatment plant, and finally discharged into the polluted river after treatment by the waste water treatment plant. The waste water discharged into the pipe network after preliminary treatment by chemical enterprises is comprehensive chemical waste water, which has the characteristics of high pollutant concentration, poor biodegradability, toxicity and inhibition.

Test Equipment and Operating Conditions

The research on the removal effect and law of organic matter by adding powdered activated carbon (PAC) into activated sludge system is realized by three groups of SBR reactors, namely activated carbon-activated sludge SBR system (PAC-AS), activated sludge SBR system (AS) and activated carbon SBR system (PAC). The effective volume of each reactor is 2 L, and it runs for 24 h in each cycle. The operation mode is as follows: 1.2 l (15 min) water is fed; Anaerobic stirring (6 h); Aerobic aeration (14 h); Sedimentation (2 h); Drainage 1.2 l (15 min); and Idle (1.5 h).

Experimental Method

Microbic growth curve

Under aseptic operation conditions, EM bacteria, PP bacteria, and sukehan biological bacteria were mixed with glucose and distilled water according to the ratio of 1:1:100. 200 mL of the mixed solution was sealed in a 250 mL conical flask, and was placed in a shaking table at 25.0°C for shaking culture. Then, 4 mL of bacterial liquid is taken every 2 h, and the OD600 value is measured after dilution. If the OD600 value is within the confidence interval of 0.2–0.8, the final value is measured as x dilution multiple, and if the measured value is not within the interval, the dilution multiple is adjusted for re-measurement.

Activation method of microbial agent

According to the mass ratio of 1:9, brown sugar and water were mixed into the culture solution, PP and EM bacteria were inoculated into the brown sugar solution according to the inoculation amount of 10%, then mixed and shaken evenly, and then cultured in a water bath at a constant temperature of 30°C in a shaker at 120 r/min, and centrifuged at 10,000 r/min for 10 min to obtain the bacterial cake. Dilute the bacterial cake with distilled water to prepare bacterial suspension with OD of about 0.2. All centrifuge tubes were sterilized by high pressure steam (121°C, 30 min) before use. The following microbial agents have been activated.

Addition of strains

Take a reactor with a volume of 4.5 L and an effective volume of 3 L, clean and autoclave the reactor before use, inoculate the bacterial suspension prepared above into the experimental sewage according to the proportion in **Table 1** with an inoculation amount of 10%, set the dissolved oxygen at 3.0 mg/L, react at 30°C for 48 h, take the mud-water mixed sample from the top with a syringe every 3 h, and measure the chroma, viscosity, and lignin after centrifugal separation.

EXPERIMENTAL ANALYSIS AND DISCUSSION

Bioenhanced Degradation of Toxic and Refractory Organic Waste Water

The activated sludge is put into a dynamic simulation reactor, and the sludge is cultured and domesticated with nutrients and toxic and refractory organic waste water until it matures. Toxic and refractory organic waste water is prepared from phenol, pyridine and naphthalene, in which pyridine concentration is 40 mg/L and naphthalene concentration is 30 mg/L. Co-metabolism primary matrix is added according to the experimental scheme. Measure COD concentration, MLVSS and dissolved oxygen concentration of inlet and outlet water regularly after the system runs stably. The test results are discussed below.

The test results are shown in **Figures 4–6** and **Table 1**.

It can be seen from **Figures 4–6** and **Table 1**:

(1) Each treatment system has a high COD removal rate for toxic and refractory organic waste water, and the average COD removal rate in 21 days is above 85%, and the operation is stable. The COD removal rate of treatment system 3 is between 83.21 and 86.15%, and the average COD removal rate is 86.33%; 20% glucose was added in the treatment system 1, and the removal rate of COD of refractory substances was 85.33–89.21%, with an average of 88.01%. When 20% rice washing water is added into the treatment system 2, the COD removal rate of refractory substances is between 91.9 and 95.7%. The average is 93.14.

From the above data, it can be seen that adding co-metabolizing primary matrix can improve the COD removal rate of coking waste water in biological treatment system, which may be because the primary matrix promotes the growth of co-metabolizing degradation bacteria and improves the co-metabolizing degradation efficiency of refractory substances.

(2) When rice washing water was used as the primary matrix, the COD removal rate of refractory substances increased

by 8.36% compared with the control system, while when glucose was used as the primary matrix, the COD removal rate only increased by 1.87%, indicating that rice washing water was better than glucose in co-metabolism primary matrix.

Analysis of Removal Characteristics of Organic Matter in Waste Water by Adding PAC

Removal Characteristics of Organic Compounds With Different Molecular Weights by Adding PAC

Comparison of molecular weight distribution changes of organic matter in waste water before and after being treated by PAC-AS, AS, and PAC system can reveal the removal rule of organic matter with different molecular weights in waste water by PAC-AS system, as shown in **Figure 7**. Among them, PAC-AS, AS, and PAC systems are running continuously, and PAC is added continuously. PAC dosing conditions: the initial concentration of PAC is 2 g/l; PAC continuous dosage is 0.25 g/L (0.25 gPAC/L per 4 days) every 4 days. Under this condition, the system can maintain a stable removal effect.

As can be seen from **Figure 7**:

The AS system has obvious removal effect on organic matters with molecular weights less than 500 Da and 1 k–500 Da, slightly removes organic matters with molecular weights of 0.45 μm–100 kDa, and does not remove organic matters with molecular weights of 10 k–1 kDa and 100 k–10 kDa obviously. Therefore, activated sludge can remove biodegradable parts of organic matters with molecular weights less than 500 Da, 1 k–500 Da, and 0.45 μm–100 kDa, while organic matters with molecular weights of 10 k–1 kDa and 100 k–10 kDa are mainly difficult to biodegrade, so the removal is not obvious.

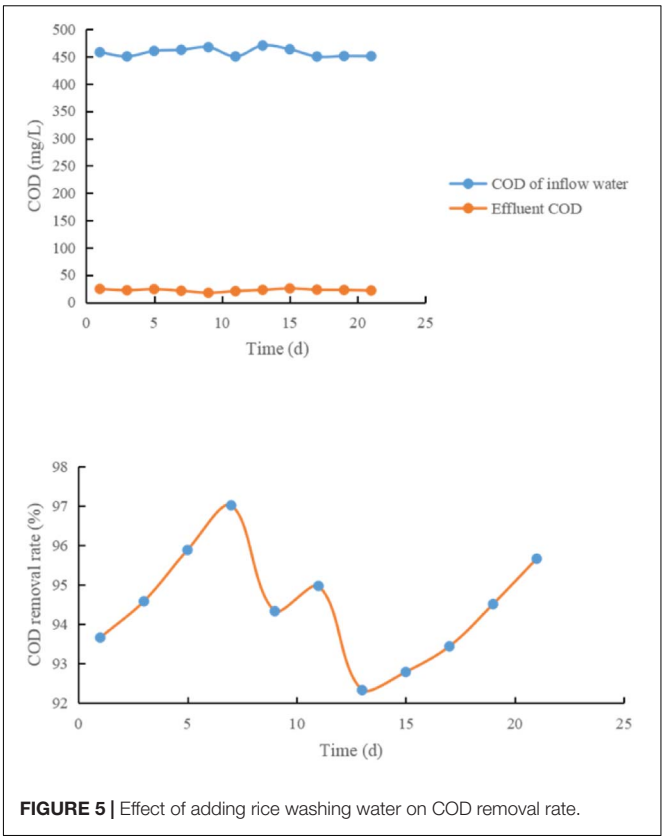

FIGURE 5 | Effect of adding rice washing water on COD removal rate.

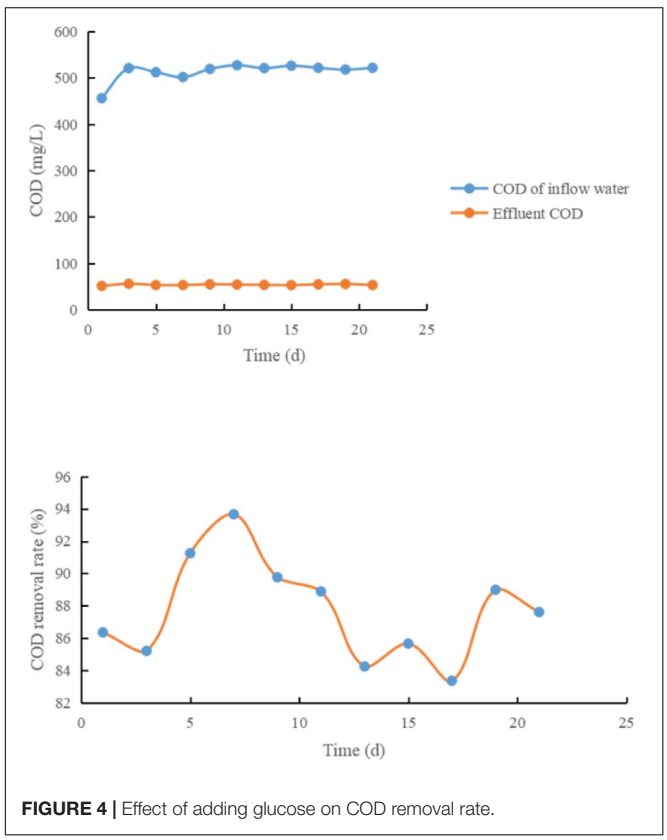

FIGURE 4 | Effect of adding glucose on COD removal rate.

PAC system has obvious removal effect on organic matter with molecular weight less than 500 Da, and slightly removes organic matter with molecular weights of 1 k–500 Da and 10 k–1 kDa, but has no obvious removal effect on organic matter with molecular weights of 100 k–10 kDa and 0.45 μm–100 kDa. It shows that PAC has a good adsorption effect on small molecular weight organic matter, but with the increase of molecular weight of organic matter, the adsorption effect of PAC decreases gradually, and it has no adsorption effect on large molecular weight organic matter.

Powdered activated carbon-activated sludge SBR system system is obviously superior to AS and PAC system in removing organic matter with molecular weight less than 500 Da, indicating that PAC-AS system is superior to the combined action of PAC adsorption and biodegradation, which makes the removal of organic matter in this molecular weight range show the additive action of PAC adsorption and biodegradation.

Removal Characteristics of Different Hydrophilic and Hydrophobic Organic Compounds by Adding PAC

The analysis of changes in hydrophilicity and hydrophobicity of organic matter before and after waste water treatment can further

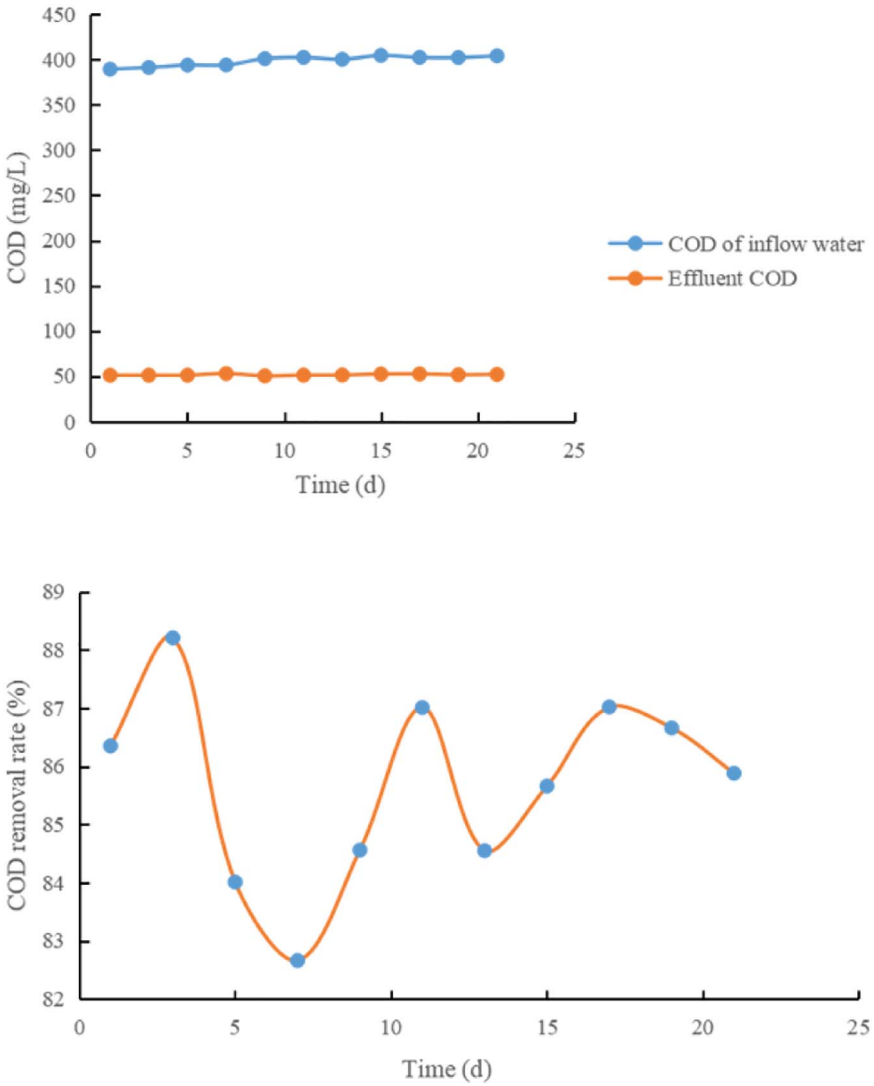

FIGURE 6 | Change curve of COD removal rate of control system.

TABLE 1 | Operation of simulated waste water treatment by biological enhancement.

Number	Reinforcer	Water penetration COD (mg/L)	Refractory substance COD (mg/L)	Effluent COD (mg/L)	COD removal rate of refractory substances (%)	MLVSS (g/L)	U_s (kg/kg·d)	Dissolved oxygen (mg/L)
1	20% glucose + 0.25 mg/L Fe^{3+}	456.33	387.01	48.36	88.01	2.6	0.55	2.1
2	20% rice washing water + 0.25 mg/L Fe^{3+}	458.01	379.05	25.58	93.14	2.4	0.52	2.8
3	Contrast	389.36	381.25	55.33	86.33	1.7	0.56	2.4

reveal the removal rule of organic matter after adding PAC into biological system, as shown in **Figure 8** and **Table 2**.

Comparing the raw water with the effluent of AS system, it can be seen that the biodegradable part of each hydrophilic and hydrophobic component can be removed by AS system to a certain extent, and the order of removal rate of each hydrophilic and hydrophobic component from large to small is as follows: TPI-N (73%) > HPI (60%) > HPO-N (55%) > HPO-A

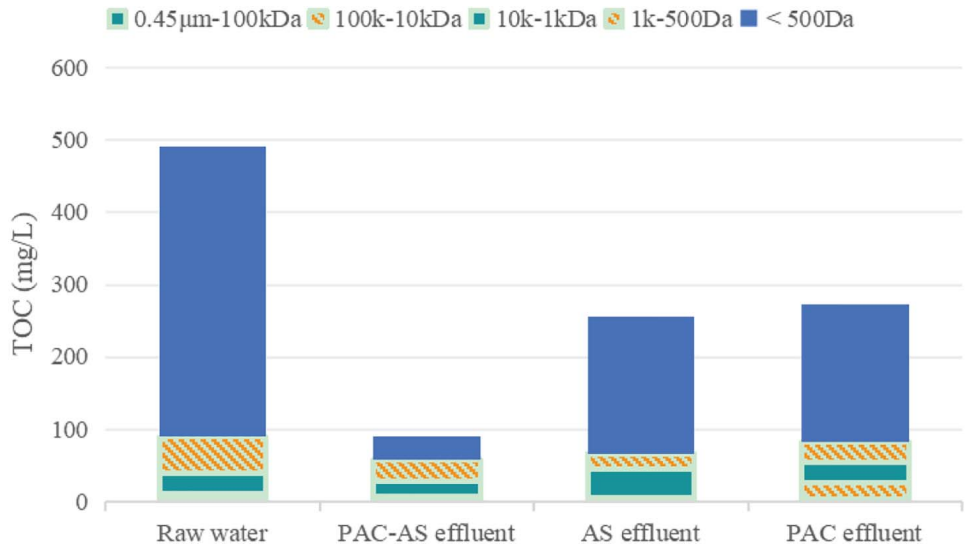

FIGURE 7 | Comparison of molecular weight distribution of organic matter in waste water before and after treatment.

FIGURE 8 | Changes of hydrophilicity and hydrophobicity of organic matter before and after waste water treatment.

(49%) > TPI-A (<2%), That is, TPI-N and HPI are easy to biodegrade, followed by HPO-N and HPO-A, while TPI-A is difficult to biodegrade. It can be seen that hydrophilic components in organic matter are easily degraded and removed by activated sludge, while hydrophobic organic matter is difficult to be degraded by microorganisms. Therefore, the effluent from AS system is mainly hydrophobic organic matter.

Comparing the analysis results of hydrophilic and hydrophobic properties of raw water and PAC system effluent, it can be seen that the removal rate of hydrophilic and hydrophobic components in descending order is HPO-A (72.33%) > HPO-N (62.01%) > TPI-N (48.77%) > TPI-A (26.01%) > HPI (22.01%). It can be seen that PAC has strong adsorption capacity for hydrophobic organic matter (HPO-A and HPO-N), but poor adsorption capacity for hydrophilic organic matter (HPI). Therefore, the effluent from PAC system is mainly HPI component. This is similar to the results obtained in literature (Ran and Li, 2020; Wang et al., 2020), that is, activated carbon mainly adsorbs hydrophobic organic matters, while activated sludge mainly removes hydrophilic organic matters.

After the waste water is treated by PAC-AS system, the order of removal rate of hydrophilic and hydrophobic components is TPI-N (82.01%) > HPO-A (77.86%) > HPO-N (74.33%) > HPI (68.21%) > TPI-A (29.04%) It can be seen that all the components are well removed, and the removal effect is better than that of AS and PAC systems. This is because PAC adsorption

TABLE 2 | Removal effect of organic matter in waste water by classification of hydrophilicity and hydrophobicity.

Classify	PAC-AS system	AS system	PAC system
HPO-A	**++**	**++**	**++**
HPO-N	++	+	++
TPI-A	++	-	+
TPI-N	+	+	+
HPI	++	++	+

Note "++" means that most of them are removed; "+" means part is removed. "-" means difficult to remove.

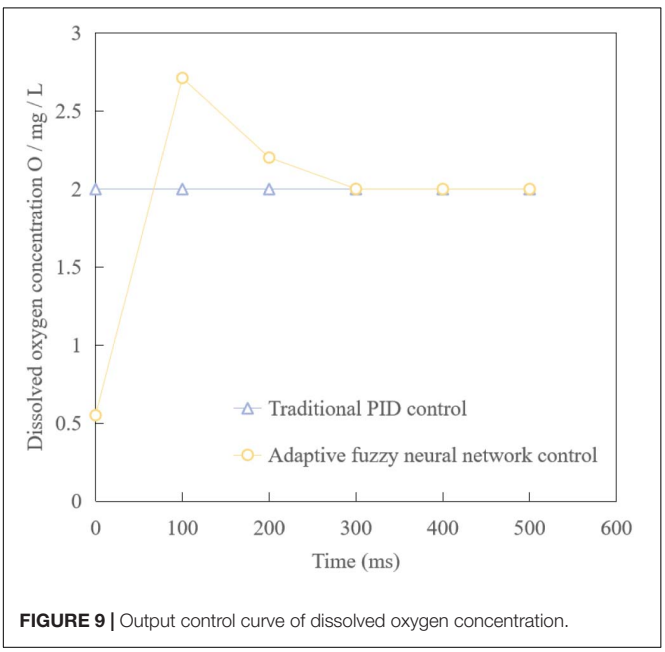

FIGURE 9 | Output control curve of dissolved oxygen concentration.

and biodegradation can complement each other's deficiencies in the removal of aqueous organic matter from different relatives, and the two removal effects are additive (Zhang, 2020). For TPI-A component, this part of organic matter is mainly difficult to biodegrade, so in PAC-AS system, the organic matter of this component is mainly removed by PAC adsorption.

Simulation Result Analysis of Waste Water Treatment System

The optimized adaptive fuzzy neural network control is applied to the established simplified model of waste water treatment. A given dissolved oxygen concentration is 2.0 mg/L, that is, a step signal with a value of 2 is added to the input of the control system, and an interference signal is added to the control model, and simulation experiments are carried out.

The control method is applied to the simplified mathematical model formula (1), that is, when the substrate concentration is high and the growth rate of microorganisms is fast, the simulation experiment is carried out, in which each coefficient in the dynamic parameter value of the state equation is uncertain and

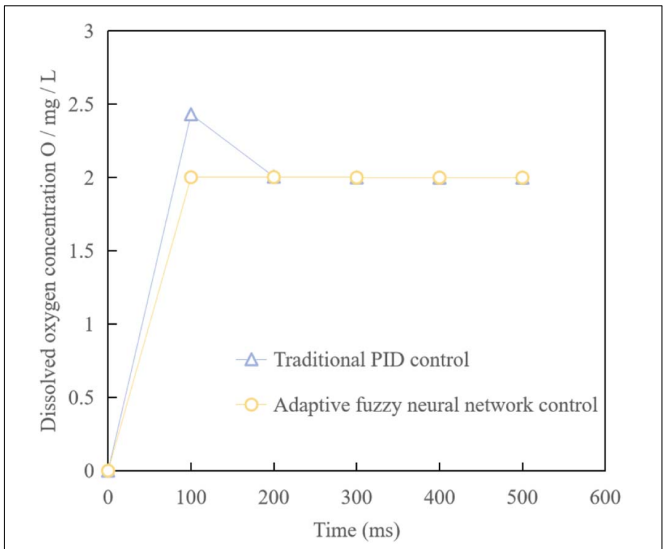

FIGURE 10 | Output control curve of dissolved oxygen concentration.

bounded, and the simulation result is shown in **Figure 9**. We can see that the controlled object can quickly reach the set value, and has strong anti-interference and the simulation result is stable.

In the practical application of waste water treatment, traditional control methods (such as PID control) are still adopted in most automatic control links at present, so taking simplified model formula (1) as an example, comparing the control method in this paper with the traditional control method, the simulation results can be obtained as shown in **Figure 10**. It can be seen from the figure that the optimized adaptive fuzzy neural network control can achieve the control requirements faster than the traditional control method.

CONCLUSION

In this paper, aiming at the time-varying and unstable system in the treatment process of toxic and refractory organic waste water, taking the aeration tank of the toxic and refractory organic waste water treatment system as the research object, the architecture of MAS distributed intelligent control waste water treatment system is determined from two aspects of hierarchical structure and model structure, and the system is divided into two parts: control decision system and treatment control system. By comparing the treatment effects of PAC-AS, AS, and PAC systems, the law and characteristics of organic removal after adding PAC into biological system are investigated, and the conclusions are as follows:

(1) Adding co-metabolism primary matrix plays an important role in improving COD removal rate of toxic and refractory organic waste water. The effect of rice washing water as primary substrate is better than that of glucose, and its average COD removal rate is increased by 8.36%, while the average COD removal rate of glucose dosing system is only increased by 1.87%.

(2) According to the classification and analysis of hydrophilicity and hydrophobicity of organic matter before and after waste water treatment, PAC mainly removes hydrophobic organic matter, while activated sludge mainly removes hydrophilic and weakly hydrophobic neutral organic matter. In PAC-AS system, the organic matter of each hydrophilic and hydrophobic component can be removed by microbial degradation and PAC adsorption, so the removal effect of organic matter of each component is further improved.
(3) Compared with the traditional control method, it shows that the fuzzy neural network controller with optimized parameters can achieve better stability when applied to this system, which further shows that the fuzzy neural network control has strong robustness.

DATA AVAILABILITY STATEMENT

The original contributions presented in the study are included in the article/supplementary material, further inquiries can be directed to the corresponding author.

AUTHOR CONTRIBUTIONS

JY conceptualization, investigation, methodology, validation, software, formal analysis, data curation, writing–original draft, and project administration. JJ methodology, writing–review and editing, formal analysis, validation, and funding acquisition. WX resources, writing–review and editing, and language. LW visualization, investigation, writing–review and editing, and formal analysis. JL visualization and investigation. All authors contributed to the article and approved the submitted version.

FUNDING

Funding for this research was provided by National Natural Science Foundation of China (No. 31800530), Natural Science Foundation of Guangxi Province (No. 2018GXNSFBA281009), Science and Technology Base and Talent Project of Guangxi Province (No. AD19110124), and Innovation Project for Graduate Education of Guangxi Province (No. YCSW2019037).

REFERENCES

Abbaslou, H., Bakhtiari, S., and Hashemi, S. S. (2018). Rehabilitation of iron ore mine soil contaminated with heavy metals using rosemary phytoremediation-assisted mycorrhizal arbuscular fungi bioaugmentation and fibrous clay mineral immobilization. *Iran. J. Sci. Technol.* 42, 431–441. doi: 10.1007/s40995-018-0543-7

Aparicio, J. D., Lacalle, R. G., Artetxe, U., Urionabarrenetxea, E., and Soto, M. (2020). Successful remediation of soils with mixed contamination of chromium and lindane: Integration of biological and physico-chemical strategies. *Environ. Res.* 194:110666. doi: 10.1016/j.envres.2020.110666

Atashgahi, S., Sanchez-Andrea, I., Heipieper, H. J., Van, d. M. J. R, Stams, A. J. M., and Smidt, H. (2018). Prospects for harnessing biocide resistance for bioremediation and detoxification. *Science* 360, 743–746. doi: 10.1126/science.aar3778

Boonnorat, J., Techkarnjanaruk, S., Honda, R., Angthong, S., Boonapatcharoen, N., and Muenmee, S. (2018). Use of aged sludge bioaugmentation in two-stage activated sludge system to enhance the biodegradation of toxic organic compounds in high strength waste water. *Chemosphere* 202:208. doi: 10.1016/j.chemosphere.2018.03.084

Changotra, R., Rajput, H., Guin, J. P., Varshney, L., and Dhir, A. (2019). Hybrid coagulation, gamma irradiation and biological treatment of real pharmaceutical wastewater. *Chem. Eng. J.* 370, 595–605. doi: 10.1016/j.cej.2019.03.256

Correa, H., and Maranho, L. T. (2021). The potential association of *Echinochloa polystachya* (Kunth) Hitchc. with bacterial consortium for petroleum degradation in contaminated soil. *SN Appl. Sci.* 3, 1–12.

Fan, M., Yang, A., Wang, H., Zhang, G., and Zou, Z. (2017). One-step treatment and resource recovery of high-concentration non-toxic organic waste water by photosynthetic bacteria. *Bioresour. Technol.* 251:121. doi: 10.1016/j.biortech.2017.12.002

Hong, P., Wu, X., Shu, Y., Wang, C., and Xiao, B. (2020). Bioaugmentation treatment of nitrogen-rich waste water with a denitrifier with biofilm-formation and nitrogen-removal capacities in a sequencing batch biofilm reactor. *Bioresour. Technol.* 303:122905. doi: 10.1016/j.biortech.2020.122905

Jasper, J. T., Yang, Y., and Hoffmann, M. R. (2017). Toxic byproduct formation during electrochemical treatment of latrine waste water. *Environ. Sci. Technol.* 51, 7111–7119. doi: 10.1021/acs.est.7b01002

Ke, Y., Song, H., and Li, S. (2018). Application of bioaugmentation technology in cold-rolling emulsion waste water treatment and analysis of microbial community. *IOP Conf. Ser. Mater. Sci. Eng.* 392:052029. doi: 10.1088/1757-899x/392/5/052029

Martinez-Gallardo, M. R., Lopez, M. J., Jurado, M. M., Suarez-Estrella, F., Lopez-Gonzalez, J. A., and Saez, J. A. (2020). Bioremediation of Olive Mill waste water sediments in evaporation ponds through in situ composting assisted by bioaugmentation. *Sci. Total Environ.* 703(Pt 2), 135537.1–135537.9. doi: 10.1016/j.scitotenv.2019.135537

Nath, S., Deb, B., and Sharma, I. (2018). Isolation of toxic metal-tolerant bacteria from soil and examination of their bioaugmentation potentiality by pot studies in cadmium- and lead-contaminated soil. *Int. Microbiol.* 21, 35–45. doi: 10.1007/s10123-018-0003-4

Park, S., and Oh, S. (2020). Detoxification and bioaugmentation potential for acetaminophen and its derivatives using *Ensifer* sp. isolated from activated sludge. *Chemosphere* 260:127532. doi: 10.1016/j.chemosphere.2020.127532

Poddar, K., Sarkar, D., and Sarkar, A. (2020). Bacterial hydrocarbon contaminants degradation: a cleaner perspective of bioremediation. *Rem. Toxic Pollut. Through Microbiol. Tert. Treat.* 261–278. doi: 10.1016/b978-0-12-821014-7.00010-1

Raimondo, E. E., Aparicio, J. D., Bigliardo, A. L., Fuentes, M. S., and Benimeli, C. S. (2020). Enhanced bioremediation of lindane-contaminated soils through microbial bioaugmentation assisted by biostimulation with sugarcane filter cake. *Ecotoxicol. Environ. Saf.* 190:110143. doi: 10.1016/j.ecoenv.2019.110143

Ran, G., and Li, Q. (2020). Degradation of refractory organic compounds from dinitrodiazophenol containingindustrial wastewater through UV/H 2 O 2 and UV/PS processes. *Environ. Sci. Pollut. Res.* 27, 6042–6051. doi: 10.1007/s11356-019-07367-1

Rodriguez-Rodriguez, C. E., Madrigal-Leon, K., Masis-Mora, M., Perez-Villanueva, M., and Salvador Chin-Pampillo, J. (2017). Removal of carbamates and detoxification potential in a biomixture: Fungal bioaugmentation versus traditional use. *Ecotoxicol. Environ. Saf.* 135, 252–258. doi: 10.1016/j.ecoenv.2016.10.011

Santos, P., and Daniel, L. A. A. (2020). review: organic matter and ammonia removal by biological activated carbon filtration for water and waste water treatment. *Int. J. Environ. Sci. Technol.* 17, 591–606. doi: 10.1007/s13762-019-02567-1

Singh, A. K., Bilal, M., Iqbal, H., Meyer, A. S., and Raj, A. (2021). Bioremediation of lignin derivatives and phenolics in waste water with lignin modifying enzymes: Status, opportunities and challenges. *Sci. Total Environ.* 145988. doi: 10.1016/j.scitotenv.2021.145988

Tigini, V., Bevione, F., Prigione, V., Poli, A., Ranieri, L., and Spennati, F. (2019). Waste water-Agar as a selection environment: a first step towards a fungal in-situ bioaugmentation strategy. *Ecotoxicol. Environ. Saf.* 171, 443–450. doi: 10.1016/j.ecoenv.2018.12.072

Tigini, V., Federico, B., and Poli, P. (2018). Tannery mixed liquors from an ecotoxicological and mycological point of view: risks vs. potential biodegradation application. *Sci. Total Environ.* 627, 835–843. doi: 10.1016/j.scitotenv.2018.01.240

Wang, F., Wu, C., and Li, Q. (2020). Treatment of refractory organics in strongly alkaline dinitrodiazophenol wastewater with microwave irradiation-activated persulfate. *Chemosphere* 254:126773. doi: 10.1016/j.chemosphere.2020.126773

Wang, J., and Chen, H. (2020). Catalytic ozonation for water and wastewater treatment: recent advances and perspective. *Sci. Total Environ.* 704, 135249.1–135249.17. doi: 10.1016/j.scitotenv.2019.135249

Wang, R., Tai, Y., Wan, X., Ruan, W., Man, Y., and Wang, J. (2018). Enhanced removal of Microcystis bloom and microcystin-LR using microcosm constructed wetlands with bioaugmentation of degrading bacteria. *Chemosphere* 210, 29–37. doi: 10.1016/j.chemosphere.2018.06.140

Weiwei, Y., Wencheng, H., and Chunyan, H. (2017). Treatment of the acrylic fibre waste water by Fenton process. *Nat. Environ. Pollut. Technol.* 16, 623–626.

Weiwei, Y., Wencheng, H., and Chunyan, H. (2019). Simultaneous nitrification and denitrification (SND) bioaugmentation with. *Water Sci. Technol. J. Int. Associat. Water Pollut. Res.* 80, 1512–1523. doi: 10.2166/wst.2019.399

Wu, H., Shen, J., Jiang, X., Liu, X., Sun, X., and Li, J. (2018). Bioaugmentation potential of a newly isolated strain *Sphingomonas* sp. NJUST37 for the treatment of waste water containing highly toxic and recalcitrant tricyclazole. *Bioresour. Technol.* 264, 98–105. doi: 10.1016/j.biortech.2018.05.071

Ying, H., Haipeng, W., Chunyan, W., Shuai, W., and Jing, Z. (2018). Characteristics of bioaugmentation technology and waste water treatment process. *North. Environ.* 30, 61–62.

Yue, W., Chen, M., Cheng, Z., Xie, L., and Li, M. (2018). Bioaugmentation of strain *Methylobacterium* sp. C1 towards p-nitrophenol removal with broad spectrum coaggregating bacteria in sequencing batch biofilm reactors. *J. Hazard. Mater.* 344, 431–440. doi: 10.1016/j.jhazmat.2017.10.039

Zhang, X., Yang, Y. S., Lu, Y., Wen, Y. J., Li, P. P., and Zhang, G. (2018). Bioaugmented soil aquifer treatment for P-nitrophenol removal in waste water unique for cold regions. *Water Res.* 144, 616–627. doi: 10.1016/j.watres.2018.08.004

Zhang, Y. (2020). Research on the Stability of Pd-catalysts based on the treatment of refractory biodegrading organic wastewater. *IOP Conf. Ser. Earth Environ. Sci.* 495:012066.

Conflict of Interest: JL was employed by the company Guangxi Civil & Environment Co., Ltd.

The remaining authors declare that the research was conducted in the absence of any commercial or financial relationships that could be construed as a potential conflict of interest.

frontiers in Bioengineering and Biotechnology

ORIGINAL RESEARCH
published: 05 July 2021
doi: 10.3389/fbioe.2021.698390

An Optimization Algorithm for Computer-Aided Diagnosis of Breast Cancer Based on Support Vector Machine

Yifeng Dou[1,2] *and Wentao Meng*[1]*

[1] Network Information Center, Tianjin Baodi Hospital, Tianjin, China, [2] Baodi Clinical College, Tianjin Medical University, Tianjin, China

As one of the most vulnerable cancers of women, the incidence rate of breast cancer in China is increasing at an annual rate of 3%, and the incidence is younger. Therefore, it is necessary to conduct research on the risk of breast cancer, including the cause of disease and the prediction of breast cancer risk based on historical data. Data based statistical learning is an important branch of modern computational intelligence technology. Using machine learning method to predict and judge unknown data provides a new idea for breast cancer diagnosis. In this paper, an improved optimization algorithm (GSP_SVM) is proposed by combining genetic algorithm, particle swarm optimization and simulated annealing with support vector machine algorithm. The results show that the classification accuracy, MCC, AUC and other indicators have reached a very high level. By comparing with other optimization algorithms, it can be seen that this method can provide effective support for decision-making of breast cancer auxiliary diagnosis, thus significantly improving the diagnosis efficiency of medical institutions. Finally, this paper also preliminarily explores the effect of applying this algorithm in detecting and classifying breast cancer in different periods, and discusses the application of this algorithm to multiple classifications by comparing it with other algorithms.

Keywords: breast cancer, computer-aided diagnosis, support vector machine, optimization, machine learning, classification

OPEN ACCESS

Edited by:
Zhiwei Luo,
Kobe University, Japan

Reviewed by:
Krishna Chandra Persaud,
The University of Manchester, United Kingdom
Laurent Simon,
New Jersey Institute of Technology, United States

***Correspondence:**
Wentao Meng
network0828@163.com

Specialty section:
This article was submitted to Bionics and Biomimetics, a section of the journal Frontiers in Bioengineering and Biotechnology

Received: *21 April 2021*
Accepted: *11 June 2021*
Published: *05 July 2021*

Citation:
Dou Y and Meng W (2021) An Optimization Algorithm for Computer-Aided Diagnosis of Breast Cancer Based on Support Vector Machine. Front. Bioeng. Biotechnol. 9:698390. doi: 10.3389/fbioe.2021.698390

INTRODUCTION

Health is the foundation of all-round development of human beings. The incidence rate of breast cancer worldwide has been increasing since the end of 1970s. Breast Cancer is a malignant tumor of abnormal breast cell division and proliferation. The incidence of breast cancer is more prominent in female patients. A United States survey shows that in 2016, 16,85,210 cases of new cancer and 595 cases of cancer were found. Among 690 cancer deaths, breast cancer is the main cause of cancer death in women aged 20–59 (Siegel et al., 2016). Each year, the number of new breast cancer cases and deaths in China account for 12.2 and 9.6% of the world's total, respectively. In view of this serious social reality, there is an urgent need to carry out research on the risk of breast cancer, including the cause analysis and prediction of breast cancer risk diagnosis based on historical data

(Li Y. et al., 2020). In the examination, the characteristics of cell size, shape, and mass thickness are considered as the criteria to distinguish benign from malignant tumors, while the characteristics of age, tumor size, menopause, number of lymph nodes involved and radiotherapy are considered as the factors influencing the recurrence of breast cancer. It is difficult for doctors to manually determine whether breast cancer is benign or not and the recurrence of breast cancer according to the complex characteristic data, but computer technology can analyze and predict the existing data.

Artificial intelligence (AI) is the product of the rapid development of computer technology. It has a profound impact on the development of human society and the progress of science and technology. At this stage, artificial intelligence has been widely used in clinic. With the development of technology and the availability of big data, the application and development of artificial intelligence in medical disease diagnosis has become a research hotspot in today's era. As one of the important means in artificial intelligence, in 1959, Arthur Samuel proposed the concept of machine learning, that is, using algorithms to make machines learn from a large number of data, to obtain the method of new data analysis and research (Skoff, 2017).

At present, researchers have used deep learning or machine learning methods to study different breast cancer data. Khan et al. (2019) used the method of combining transfer learning and deep learning to detect and classify breast cancer cells, and achieved high accuracy. Abbass (2002) proposed a neural network method based on differential evolution algorithm and local search to predict breast cancer, and the standard deviation of its test accuracy is 0.459 lower than that of Fogel et al. (1995). Abdikenov et al. (2019) used the evolutionary algorithm NSGA III (non-dominated sorting genetic algorithm – III) to initialize the deep neural network and optimize its super parameters for the prognosis of breast cancer. Liu et al. (2019) proposed an end-to-end deep learning system combined with full convolution network to extract breast region data, and the results are highly correlated with the diagnosis made by pathologists. Lu et al. (2019) proposed a novel genetic algorithm based online gradient boosting (GAOGB) model to predict the diagnosis and prognosis of breast cancer in real time through online learning (Oza, 2005) technology. The above research shows that the application of artificial intelligence in the medical field is practical and effective. The application of existing machine learning methods in the medical field helps medical workers improve work efficiency and reduce work burden. People are trying to improve the traditional algorithm while applying computer technology to the medical field.

In this paper, Support Vector Machine (SVM) is taken as a breakthrough point. The choice of penalty parameter c and g in SVM kernel function is directly related to the effectiveness and accuracy of SVM algorithm in solving dichotomy. According to previous research methods, there are mainly 5 optimization methods for the above two important parameters, namely, empirical selection method, grid selection method, genetic optimization algorithm, particle swarm optimization algorithm, and ant colony optimization algorithm so on (Ali and Abdullah, 2020; Kouziokas, 2020; Li X. et al., 2020; Arya Azar et al., 2021; Ramkumar et al., 2021). Although these optimization algorithms have been applied to some extent and achieved some effects, they all have problems of different degrees. For example, the empirical selection method is highly experienced by users and highly dependent on samples, which lacks sufficient theoretical support. The disadvantage of grid selection method lies in the step size selection. If the step size selection is too large, it is easy to fall into the local optimum; if the step size selection is too small, the calculation amount will be too large. The genetic optimization algorithm needs to go through three steps of selection, crossover and mutation. The parameter setting is relatively complex, the convergence speed is slow, and it is easy to fall into the local optimal solution. Particle swarm optimization (PSO) SVM has the advantage of faster convergence speed and fewer parameters, but it is also easy to fall into local optimal. The combination of genetic or particle swarm optimization and simulated annealing (SA) to optimize SVM parameters improves the convergence speed and improves the poor local optimization ability to some extent. However, poor stability may occur in some practical applications. Therefore, how to use the advantages of three heuristic algorithms to optimize the selection of parameters in support vector machines, so that the algorithm to achieve the best classification performance is the focus of this paper.

CONCEPTUAL PRINCIPLE

Support Vector Machine

Support vector machine was proposed by Vapnik (1995). The basic idea of the algorithm is to map the input data into a high-dimensional space through non-linear transformation and establish the optimal linear classification surface to classify the two sample categories correctly. Based on the principle of structural risk minimization, the SVM model is classified by calculating the optimal separating hyperplane (OSH) (Zhou et al., 2018). The larger the interval between the optimal hyperplanes, the stronger the generalization ability of the established SVM model. Suppose that the training sample set $\{(x_i, y_i), i = 1,2,\ldots,l\}$ with the size of 1, its data samples can only be divided into two categories. If it belongs to the first type of samples, it is recorded as positive ($y_i = 1$), otherwise it belongs to the second category and is recorded as a negative value ($y_i = -1$). At this time, we need to construct a discriminant function to make the function classify the test data samples as correctly as possible. If there is a classification hyperplane

$$w \cdot x + b = 0 \tag{2-1}$$

bring

$$\begin{cases} w \cdot x_i + b \geq 1, \ y_i = 1 \\ w \cdot x_i + b \leq -1, \ y_i = -1, \ i = 1, 2, \ldots, l \end{cases} \tag{2-2}$$

We call the training sample set is linearly separable. $w \cdot x$ is called the inner product of vector $w \in R^N$ and vector $x \in R^N$,

and $w \in R^N$ and $b \in R$ in formula (2-1) and formula (2-2) are normalized. For formula (2-2), it can be rewritten as follows:

$$y_i(w \cdot x_i + b) \geq 1,\ i = 1, 2, ..., l \tag{2-3}$$

According to the definition of the optimal hyperplane, the following discriminant functions can be obtained

$$y(x) = sign(w \cdot x + b) \tag{2-4}$$

Its generalization ability is the best, and sign $(\cdot)$ is the symbol function. The solution of the optimal hyperplane needs to maximize $2/||w||$, that is to say it can be transformed into the following quadratic programming problem composed of objective function and constraint conditions

$$\begin{aligned} &\min_{w,b} \frac{||w||^2}{2} \\ &s.t.\ \ y_i(w \cdot x_i + b) \geq 1,\ i = 1, 2, ..., l \end{aligned} \tag{2-5}$$

When the training sample set is linear and indivisible, it is necessary to introduce a non-negative parameter, i.e., relaxation variable ξ_i, i = 1,2,. . ., l. at this time, the optimization problem of classification hyperplane is transformed into the form shown in formula (2-6).

$$\begin{aligned} &\min_{w,b,\xi} \frac{||w||^2}{2} + c\sum_{i=1}^{l} \xi_i \\ &s.t.\ \begin{cases} y_i(w \cdot x_i + b) \geq 1 - \xi_i \\ \xi_i \geq 0,\ i = 1, 2, ..., l \end{cases} \end{aligned} \tag{2-6}$$

Where c is the constraint parameter, also known as the penalty parameter. The higher the value of c, the greater the penalty for error classification. Using Lagrange multiplier method to solve the problem

$$\begin{aligned} &\max_{\alpha,\beta,w,b,\xi} \min\{L_p = \frac{||w||^2}{2} + c\sum_{i=1}^{l} \xi_i - \sum_{i=1}^{l} \alpha_i \left[y_i(w \cdot x_i + b)\right. \\ &\left. -1 + \xi_i\right] - \sum_{i=1}^{l} \beta_i \xi_i\} \\ &s.t.\ \begin{cases} \alpha_i \geq 0 \\ \beta_i \geq 0 \end{cases} \end{aligned} \tag{2-7}$$

Where α_i and β_i are Lagrange multipliers

$$\frac{\partial L_p}{\partial w} = 0 \rightarrow w = \sum_{i=1}^{l} \alpha_i y_i x_i \tag{2-8}$$

$$\frac{\partial L_p}{\partial b} = 0 \rightarrow \sum_{i=1}^{l} \alpha_i y_i = 0 \tag{2-9}$$

$$\frac{\partial L_p}{\partial \xi_i} = 0 \rightarrow c - \alpha_i - \beta_i = 0 \tag{2-10}$$

By substituting formula (2-8) to (2-10) into formula (2-7), the dual optimization problem form is obtained

$$\begin{aligned} &\max_{\alpha}\{L_D = \sum_{i=1}^{l} \alpha_i - \frac{1}{2}\sum_{i=1}^{l}\sum_{j=1}^{l} \alpha_i \alpha_j y_i y_j x_i x_j\} \\ &s.t.\ \begin{cases} 0 \leq \alpha_i \leq c \\ \sum_{i=1}^{l} \alpha_i y_i = 0 \end{cases} \end{aligned} \tag{2-11}$$

The α_i obtained by optimization may be (a) $\alpha_i = 0$; (b) $0 < \alpha_i < c$; (c) $\alpha_i = c$. According to formula (2-8), only when the support vector has a positive effect on the optimal hyperplane and discriminant function, the corresponding learning method is called support vector machine algorithm. In support vector, x_i corresponding to c is called boundary support vector (BSV), which is actually the training sample points that are misclassified; (b) The corresponding x_i is called normal support vector (NSV). According to Karush–Kuhn–Tucher condition (Chauhan and Ghosh, 2021), the product between Lagrange multiplier and corresponding constraint is equal to 0 when the sample point is optimal

$$\begin{cases} \alpha_i[y_i(w \cdot x_i + b) - 1 + \xi_i] = 0 \\ \beta_i \xi_i = 0 \end{cases} \tag{2-12}$$

For the standard support vector $(0 < \alpha_i < c)$, $\beta_i > 0$ is obtained from formula (2-10). Therefore, $\beta_i = 0$ can be obtained from formula (2-12). Therefore, it can be seen that all the criteria satisfy the following requirements for any standard support vector x_i,

$$y_i(w \cdot x_i + b) = 1 \tag{2-13}$$

the parameter b is calculated

$$b = y_i - w \cdot x_i = y_i - \sum_{x_i \in NSV, x_j \in SV} \alpha_j y_j x_j x_i \tag{2-14}$$

The value of b is calculated for all standard support vectors, and then the average value of the results is obtained

$$b = \frac{1}{N_{NSV}} \sum_{x_i \in NSV} (y_i - \sum_{x_i \in SV} \alpha_j y_j x_j x_i) \tag{2-15}$$

Where N_{NSV} is the number of the standard support vectors. According to formula (2-13), the support vector machine model is the sample data that meets the requirements of formula (2-3).

Kernel Function Selection for Support Vector Machine Algorithm

The use of support vector machines to solve pattern classification problems usually requires the selection of an appropriate kernel function. Since the low-dimensional space vector sample set is usually difficult to divide, we usually use to map the low-dimensional space vector sample set into the high-dimensional feature space, but the consequent problem is to increase the computational complexity, and the emergence of the kernel function is a good solution to the problem. Theoretically, any function that can satisfy the Merce condition can be used as the kernel function of a support vector machine algorithm, but the different choices of kernel functions can lead to different algorithms and directly lead to different performance of their classifiers. Therefore, the selection of the appropriate kernel function is crucial to effectively improve the distribution of feature vectors in the high-dimensional feature space, thus making the structure of the classifier simpler; at the same time, even if a certain kernel function is selected, the selection of the corresponding parameters in the kernel function, such as the

order in the polynomial kernel function and the width parameter in the Gaussian kernel function, also needs to be deliberated.

The most studied kernel functions are mainly of the following types, one is linear kernel function, as shown in formula (2-16), which mainly solves linear classification problems.

$$K(x_i, x_j) = x_i \cdot x_j \tag{2-16}$$

Second, the polynomial kernel function, as shown in formula (2-17), is obtained as a polynomial classifier of order q.

$$K(x_i, x) = (x_i \cdot x + 1)^d \tag{2-17}$$

Third, the radial basis function (referred to as the RBF kernel function), as shown in formula (2-18).

$$K(x, x_i) = \exp(-\frac{||x\text{-}x_i||^2}{\sigma^2}) \tag{2-18}$$

The resulting classifier differs from the traditional RBF method in that it has a support vector corresponding to the center of each basis function, where the weights of the output are determined automatically by the algorithm. A Sigmoid function can also be used as the inner product, i.e.,

$$K(x, x_i) = \tanh(v(x \cdot x_i) + c) \tag{2-19}$$

The support vector machine algorithm implemented in this case is equivalent to a multilayer perceptron network with hidden layers, in which the number of hidden layer nodes is also determined automatically by the algorithm, and it is also able to better solve the problem of local minima in neural networks. Based on this, and also considering that the SVM algorithm is not sensitive to the selection of the kernel, this paper uses the radial basis kernel function, which is also called Gaussian Kernel. The classification accuracy factor $_\sigma$ in the RBF kernel is the parameter that needs to be adjusted, and the different values of $_\sigma$ will also have a great impact on the nature of the classifier and the correct recognition rate, etc.

Optimization Algorithm

For the improvement of local optimization and global optimization, this paper uses the genetic algorithm and particle swarm optimization algorithm in the algorithm to determine the respective population optimal solution, so as to seek the global optimal solution as the parameter input of SVM, so as to achieve a good balance between global and local search optimization. Through the assignment between the optimal particle and the worst chromosome or between the worst particle and the optimal chromosome, the two search algorithms complement each other and accelerate the convergence speed of the algorithm.

For the improvement that particle swarm optimization algorithm is easy to fall into local optimum, this paper takes into account the role of inertia factor ω in particle velocity and position update in formula (2-20), Because ω reflects the ability of particles to inherit the previous velocity, when the value is large, the particle swarm optimization has strong search ability in the early stage, but it is not conducive to ensure the optimal solution when the search enters the late stage; When the value of ω is small, the effect is just the opposite. When the value is small, the search ability of particle swarm optimization is enhanced, but the ability of global search for optimal solution is decreased. Therefore, in order to improve this deficiency, the harmonic inertia factor is adopted, as shown in formula (2-22).

$$v_{i,j}(t+1) = \omega v_{i,j}(t) + c_1 r_1 [p_{i,j} - x_{i,j}(t)] + c_2 r_2 [p_{g,j} - x_{i,j}(t)] \tag{2-20}$$

$$x_{i,j}(t+1) = x_{i,j}(t) + v_{i,j}(t+1) \tag{2-21}$$

The meanings of parameters in the above two formulas are as follows:

ω represents the inertia weight of particles, and c_1 and c_2 represent the self-learning factor and global learning factor of particles, respectively. r_1 and r_2 represent random numbers between [0–1]. In order to make particles search in effective space, it is generally necessary to limit the search space of particles, that is to limit the position to $[x_{min}, x_{max}]$. At the same speed, a range $[v_{min}, v_{max}]$ should be set instead of blindly optimizing. This setting can control the movement of particles.

$$\omega_m = \omega_1 - \frac{(\omega_1 - \omega_2)(m-1)^2}{t^2} \tag{2-22}$$

Where m is the number of iterations and t is the maximum evolution algebra.

In order to improve the local search ability of particle swarm optimization (PSO), a simulated annealing algorithm is introduced in this paper. Metropolis criterion (Wang et al., 2019) is used to determine whether to accept the new location of particles, suppose that the change of fitness of the particle in the new position is Δf, if $\Delta f \geq 0$, then accept the new position of the particle at time t;If $\Delta f < 0$, the acceptance probability is calculated according to formula (2-23). By comparing with the threshold value, it is a standard normal distribution random quantity with a mean value of 0 and a standard deviation of 1. When $_{P_a > P}$ the bad position is accepted.

$$P_a = \exp(\frac{\Delta f}{t}), \ t = KT \tag{2-23}$$

Where t is the control parameter, K is the Boltzmann constant in physics, and T is the temperature of the material.

Both genetic algorithm and particle swarm optimization belong to the branch of evolutionary algorithm. Both of them are suitable for solving discrete problems, especially 0–1 non-linear optimization, integer programming and mixed integer programming. Therefore, this paper selects GA and PSO as basic algorithms. At the same time, in order to make full use of the local search solution space of GA and the fast convergence ability of PSO algorithm, and to improve the poor local search ability of PSO algorithm in the later stage, the simulated annealing algorithm is introduced f or optimization. In this paper, a new algorithm combining three classical algorithms to optimize support vector machine (GSP_SVM) is proposed. By comparing the population optimal solutions obtained from GA and PSO algorithm, the overall optimal solution is found. In this paper, the accuracy of training classification is taken as fitness value. If

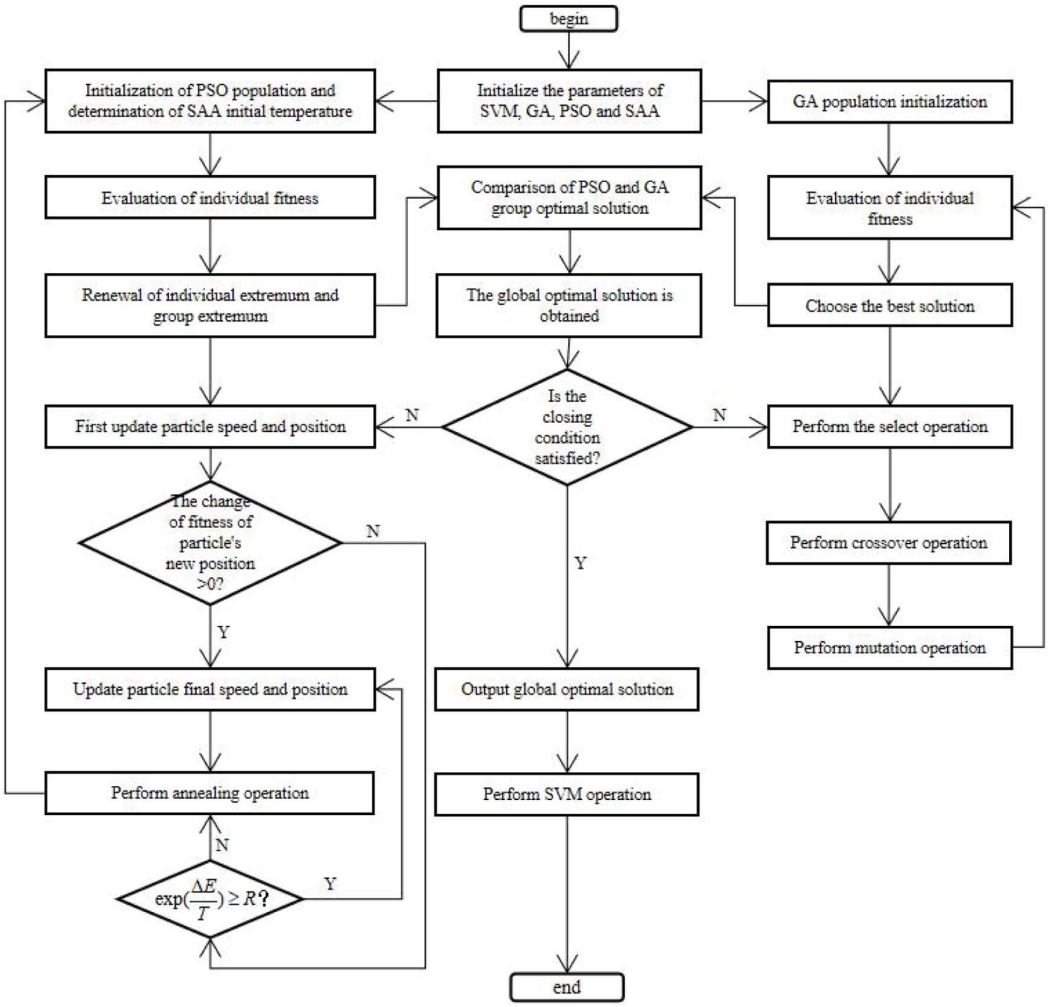

FIGURE 1 | Flow chart of GSP_SVM algorithm.

the fitness of PSO optimal solution is higher than that of GA, it is regarded as the global optimal solution and assigned to the worst chromosome in GA. however, if the fitness of PSO optimal solution is lower than that of GA, the chromosome with the highest fitness is regarded as the global optimal solution and assigned to the particle with the worst fitness, and then iterative calculation is carried out until the algorithm is implemented Termination. The overall framework of the algorithm is shown in **Figure 1**.

EXPERIMENT

Data Set

In order to verify the effectiveness and feasibility of the gsposvm algorithm proposed in this paper, we use the breast cancer data set[1] provided by Dr. William H. wolberg of the Wisconsin Medical School in the United States. Each data sample in the medical data set has 10 attribute variables, which are case code number, tumor thickness value, cell size uniformity, cell shape uniformity, edge viscosity, single epithelial cell size, naked nucleus, boring chromosome, normal nucleus and mitotic number. Except the case code number, the values of the other 9 attributes were all [1,10]. The binary variable was to judge the characteristics of breast cancer. 1 was malignant and 2 was benign. In order to get a better prediction effect, this section makes a study on the original data set of "breast cancer"- wisconsin.data to preserve the authenticity of the data, the redundant attributes are removed 16 data samples were eliminated, and the final experimental data samples were 683. Finally, in order to reduce the value range of some attributes which are too large while others are too small, so that the large number will submerge the decimal. At the same time, in order to avoid the difficulties in numerical calculation due to the calculation of kernel function, the data of training set and test set are normalized, and the data is scaled to [0,1].

[1]http://www.csie.ntu.edu.tw/~cjlin/libsvmtools/datasets/binary.html#breast-cancer

Evaluating Indicators

In order to better explain the evaluation index used in this paper, we first give a confusion matrix about binary classification problem, as shown in **Table 1**.

Based on the Precision and recall rate, the receiver characteristic curve, namely AUC, F-measure, total accuracy G are used to evaluate the application effect of the proposed optimization algorithm in unbalanced data sets.

Precision: refers to the ratio of the number of records that the classifier can correctly determine as the category and the total number of records that should be determined as the category. As shown in formula (3-1), the precision rate represents the classification accuracy of the classifier itself. If the TP_i is larger and the FP_i is smaller, the precision value will be larger, which means that the probability of the classifier's misclassification on this category will be smaller.

$$Precision = \frac{TP_i}{TP_{\mathrm{i}} + FP_{\mathrm{i}}} \times 100\% \tag{3-1}$$

Recall: refers to the ratio of the number of records that can be correctly determined by the classifier to the total number of records in the classification records that should be the category. As shown in formula (3-2), recall reflects the completeness of the classification results of the classifier. If the greater the TP_i is, the smaller the FN_i is, the greater the recall value is, which means that the fewer records should have been missed by the classification system.

$$Recall = \frac{TP_{\mathrm{i}}}{TP_{\mathrm{i}} + FN_{\mathrm{i}}} \times 100\% \tag{3-2}$$

Sensitivity: the proportion of correct number of multi class discrimination in all multi class samples, and the calculation method is consistent with the calculation formula of recall rate.

Specificity: the proportion of the correct number of minority discrimination in all minority samples. The calculation method is shown in formula (3-3).

$$Specificity = \frac{TN_{\mathrm{i}}}{TN_{\mathrm{i}} + FP_{\mathrm{i}}} \times 100\% \tag{3-3}$$

Total accuracy *G*: considering the classification performance of minority and majority records, the calculation method is the geometric average of specificity and sensitivity. It can be seen from formula (3-4) for details. Therefore, *G* is also called geometric average, and the accuracy increases monotonically with the values of specificity and sensitivity in [0,1].

$$G = \sqrt{Specificity{*}Sensitivity} \tag{3-4}$$

TABLE 1 | Contingency table for binary classification problems.

Actual $Class_i$	Prediction	
	Judged as $Class_i$	Not $Class_i$
The record belongs to $Class_i$	*True Positive* (TP_i)	*False Negative* (FN_i)
The record does not belongs to $Class_i$	*False Positive* (FP_i)	*True Negative* (TN_i)

F_β: considering the difference between precision rate and recall rate, the formula is as follows:

$$F_\beta = \frac{(\beta^2 + 1) \times Precision \times Recall}{\beta^2 \times Precision + Recall} \tag{3-5}$$

$$F{-}measure = \frac{2{*}Precision{*}Recall}{Precision + Recall} = \frac{2{*}Precision{*}Sensitivity}{Precision + Sensitivity} \tag{3-6}$$

The F_β measure value represents the trade-off between accuracy and recall when evaluating the performance of classifiers. β is used to adjust the proportion of precision and recall in the formula. Usually, when it is used in practice, it is taken as $_\beta$ = 1 to get the performance evaluation index *F*-measure of our common classifier. The calculation formula is as follows (3-6). F-measure is the harmonic mean of precision and recall. When the accuracy and recall are both high, the *F*-measure value will also increase. This index takes into account the recall and precision of minority records. Therefore, any change of any value can affect the size of *F*-measure. Therefore, it can show the classification effect of the classifier on the majority class and minority class, but it focuses on the classification effect of minority records is also discussed.

MCC: Matthew's correlation coeffcient (3-7):

$$MCC = \frac{TP \times TN - FP \times FN}{\sqrt{(TP + FN)(TP + FP)(TN + FP)(TN + FN)}} \tag{3-7}$$

AUC (area under the ROC curve): the area under the ROC curve, between 0.1 and 1. It can quantify the ROC curve and present the algorithm performance more intuitively. The larger the value is better. The larger the value is, the more likely the positive samples will be placed before the negative samples, so as to better classify.

Results

Discussion of the Binary Classification Problems

In this paper, we use radial basis function, which is also known as Gaussian kernel function. The classification accuracy factor in RBF kernel is a parameter σ that needs to be adjusted. Different σ values will have a great impact on the properties of classifier and recognition accuracy. In this paper, a heuristic search method is used to find the optimal parameters in the model selection, so as to achieve the optimal performance for the classification and prediction.

In order to verify the effect of different optimization algorithms on the optimization of support vector machine parameters, this paper uses several algorithms for experimental comparison: (1) Based on the most original support vector machine algorithm; (2) Based on principal component analysis support vector machine algorithm (PCA_SVM) (Tao and Cuicui, 2020); (3) Support vector machine algorithm based on grid search optimization (GS_SVM) (Fayed and Atiya, 2019); (4) Support vector machine algorithm based on genetic algorithm optimization (GA_SVM) (Guan et al., 2021); (5)

Particle swarm optimization based support vector machine algorithm (PSO_SVM) (Zhang and Su, 2020), in order to compare the genetic algorithm, particle swarm optimization algorithm and simulated annealing algorithm based on the fusion algorithm to optimize the parameters of support vector machine (GSP_SVM).

For better performance comparison and algorithm verification, we randomly take 50, 60, 70, and 80% of the data as labeled data and training data, and the remaining data as unlabeled sample data and test sample set. In order to balance the random effect, the average value of 10 repeated independent running results is used for the reported experimental results. The specific results are shown in **Table 2**.

Since the parameters of SVM and PCA_SVM algorithms are set to fixed values, c is 100 and g is 4, all the other algorithms are optimized for SVM parameters except these two algorithms. On the whole, with the increase of training sample data, most of the values of the evaluation matrix have a positive growth

TABLE 2 | Experimental results.

Evaluating indicator	Proportion of training data	SVM	PCA_SVM	GA_SVM	GS_SVM	PSO_SVM	GSP_SVM
Precision	50%	0.9853	0.9417	0.9906	0.9804	0.9450	0.9716
	60%	0.9695	0.9519	0.9708	0.9711	0.9586	**0.9818**
	70%	0.9841	0.9697	0.9853	0.9924	**0.9927**	0.9699
	80%	0.9878	0.9667	0.9865	0.9667	0.9778	**1.0000**
	90%	0.9773	0.9524	0.9722	0.9778	0.9778	**1.0000**
Recall	50%	0.9526	0.9713	0.9251	0.9524	**0.9810**	0.9716
	60%	0.9578	0.9700	0.9595	0.9711	0.9701	**0.9759**
	70%	0.9612	0.9771	0.9710	0.9489	0.9577	**0.9847**
	80%	0.9529	0.9667	0.9359	**0.9886**	0.9670	0.9655
	90%	0.9556	0.9756	0.9722	0.9565	**0.9778**	0.9762
G	50%	1.0009	0.9061	**1.0214**	0.9934	0.9172	0.9677
	60%	0.9740	0.9112	0.9698	0.9640	0.9483	**0.9839**
	70%	0.9928	0.9562	0.9841	**1.0112**	1.0053	0.9525
	80%	1.0039	0.9508	1.0159	0.9429	0.9717	**1.0177**
	90%	0.9785	0.9374	0.9825	0.9760	0.9673	**1.0121**
F-measure	50%	0.9687	0.9611	0.9567	0.9662	0.9626	**0.9716**
	60%	0.9636	0.9648	0.9651	0.9711	0.9643	**0.9789**
	70%	0.9725	0.9734	**0.9781**	0.9701	0.9749	0.9773
	80%	0.9701	0.9667	0.9605	0.9775	0.9724	**0.9825**
	90%	0.9663	0.9639	0.9722	0.9670	0.9778	**0.9880**
MCC	50%	0.9209	0.8933	0.8828	0.9146	0.9008	**0.9254**
	60%	0.9082	0.8921	0.9058	0.9211	0.9073	**0.9463**
	70%	0.9273	0.9252	0.9336	0.9150	0.9222	**0.9358**
	80%	0.9226	0.9014	0.9122	0.9355	0.9176	**0.9538**
	90%	0.9030	0.9077	0.9410	0.9009	0.9343	**0.9696**
AUC	50%	0.9707	0.9652	0.9561	0.9695	0.9681	**0.9708**
	60%	0.9592	0.9761	0.9688	0.9705	0.9652	**0.9865**
	70%	0.9737	0.9648	0.9758	0.9573	0.9752	**0.9782**
	80%	0.9812	0.9708	0.9651	0.9711	0.9731	**0.9864**
	90%	0.9729	0.9512	0.9679	0.9605	0.9720	**0.9890**

Bolded values represent the optimal values obtained by the algorithm for the evaluation metrics on this training set.

TABLE 3 | The experimental results of classification accuracy of algorithms.

	SVM	PCA_SVM	GA_SVM	GS_SVM	PSO_SVM	GSP_SVM
50%	0.9619	0.9501	0.9443	0.9589	0.9531	0.9648
60%	0.9560	0.9524	0.9560	0.9634	0.9560	**0.9744**
70%	0.9657	0.9657	**0.9706**	0.9608	0.9657	**0.9706**
80%	0.9630	0.9559	0.9559	0.9706	0.9632	**0.9779**
90%	0.9559	0.9559	0.9706	0.9559	0.9706	**0.9853**
Avg	0.9605	0.9560	0.9595	0.9619	0.9617	**0.9746**

Bolded values represent the optimal values obtained by the algorithm for the evaluation metrics on this training set.

TABLE 4 | Evaluation results of multicategorical indicators.

Evaluating indicator	Proportion of training data	SVM	PCA_SVM	GA_SVM	GS_SVM	PSO_SVM	GSP_SVM
Accuracy_score	50%	0.8768	0.8261	0.8551	0.8478	0.8261	0.8957
	60%	0.9455	0.9273	0.9364	0.8455	0.8273	**0.9527**
	70%	0.9518	**0.9639**	**0.9639**	0.9157	0.8193	**0.9639**
	80%	**0.9636**	**0.9636**	0.9455	0.8909	0.9455	**0.9636**
	90%	0.9630	0.9630	0.9630	0.9630	0.8889	**0.9852**
Precision_score	50%	0.8768	0.8261	0.8551	0.8478	0.8261	**0.8957**
	60%	0.9455	0.9273	0.9364	0.8455	0.8273	**0.9527**
	70%	0.9518	**0.9639**	**0.9639**	0.9157	0.8193	**0.9639**
	80%	**0.9636**	**0.9636**	0.9455	0.8909	0.9455	**0.9636**
	90%	0.9630	0.9630	0.9630	0.9630	0.8889	**0.9852**
Recall_score	50%	0.8768	0.8261	0.8551	0.8478	0.8261	**0.8957**
	60%	0.9455	0.9273	0.9364	0.8455	0.8273	**0.9527**
	70%	0.9518	**0.9639**	**0.9639**	0.9157	0.8193	**0.9639**
	80%	**0.9636**	**0.9636**	0.9455	0.8909	0.9455	**0.9636**
	90%	0.9630	0.9630	0.9630	0.9630	0.8889	**0.9852**
F1_score	50%	0.8768	0.8261	0.8551	0.8478	0.8261	**0.8957**
	60%	0.9455	0.9273	0.9364	0.8455	0.8273	**0.9527**
	70%	0.9518	**0.9639**	**0.9639**	0.9157	0.8193	**0.9639**
	80%	**0.9636**	**0.9636**	0.9455	0.8909	0.9455	**0.9636**
	90%	0.9630	0.9630	0.9630	0.9630	0.8889	**0.9852**
Hamming_loss↓	50%	0.1232	0.1739	0.1449	0.1522	0.1739	**0.1043**
	60%	0.0545	0.0727	0.0636	0.1545	0.1727	**0.0473**
	70%	0.0482	0.0361	0.0361	0.0843	0.1807	**0.0361**
	80%	0.0482	0.0361	0.0361	0.0843	0.1807	**0.0361**
	90%	0.0370	0.0370	0.0370	0.0370	0.1111	**0.0148**
Cohen_kappa_score	50%	0.8053	0.7170	0.7647	0.7533	0.7205	**0.8313**
	60%	0.9132	0.8896	0.8952	0.7553	0.7149	**0.9255**
	70%	0.9224	0.9412	0.9397	0.8602	0.7107	**0.9434**
	80%	0.9403	0.9369	0.9142	0.8291	0.9127	**0.9428**
	90%	0.9444	0.9429	0.9330	0.9363	0.8273	**0.9764**
Jaccard_score	50%	0.7899	0.7108	0.7452	0.7358	0.7006	**0.8145**
	60%	0.8966	0.8648	0.8809	0.7264	0.6987	**0.9111**
	70%	0.9357	0.9293	**0.9359**	0.8478	0.6901	0.9348
	80%	0.9300	**0.9386**	0.8961	0.8110	0.8978	0.9340
	90%	0.9444	0.9383	0.9288	0.9290	0.8008	**0.9716**

Bolded values represent the optimal values obtained by the algorithm for the evaluation metrics on this training set.

trend. It can be seen from the above table that among all the optimization algorithms, the support vector machine algorithm (GSP_SVM) based on the fusion of three classical optimization algorithms has improved the value of each evaluation index to varying degrees compared with other algorithms. The accuracy rate, recall rate, sensitivity, *F*-measure measurement value and other four evaluation indicators are presented in 60, 70, and 80% training data, respectively, the best result, in AUC, the best is in 70 and 80% training data.

This paper also investigates the accuracy, the most basic evaluation index of classification algorithm. The calculation method is shown in formula (3-8). No matter which category, as long as the prediction is correct, the number is placed on the numerator, and the denominator is the number of all the data. It shows that the accuracy is the judgment of all the data, and it is the evaluation index that can directly reflect the advantages and disadvantages of the algorithm. The accuracy of each algorithm on the training data set with different proportions can be seen from **Table 3**.

$$Accuracy = \frac{TP + TN}{TP + TN + FP + FN} \tag{3-8}$$

According to the above table, the results of the experiment on 50, 60, 80, and 90% training proportion data sets are the best, especially in the 90%, the training proportion data set reaches 0.9853. Therefore, combined with the experimental results of evaluation indexes in **Table 2**, it can be concluded that the algorithm proposed in this paper can obtain the optimal parameter values and classify more accurately.

Discussion of the Multiclass Problems

In the above study, we considered the effectiveness of the algorithm for evaluation on the dichotomous classification problem, and next, in this paper, we will initially explore the classification of the algorithm on the multiclassification problem. We use the dataset proposed by M. Zwitter and M. Soklic from

the Institute of Oncology, University of Ljubljana, Yugoslavia (Bennett et al., 2002), which has 286 instances, each containing 10 attributes such as tumor size, number of invaded lymph nodes, presence or absence of nodal adventitious, mass location, etc., all of which are of enumerated type, according to which we ask experts to manually annotate The defective instances accounted for only 0.3% of the total data set, so they were directly discarded. A total of 277 instances consisting of 10 independent variables and 1 multicategorical variable were finally used for the experiment.

For the binary classification problem, we have many evaluation metrics because there are only two types of positive and negative classes, but they are not applicable for the multi-classification problem. In this paper, we choose the following evaluation metrics for the multi-classification problem: (1) Accuracy_score, which is the ratio of the total number of correctly classified data in the classification result. (2) Precision_score, i.e., the proportion of positive cases in the prediction results. (3) Recall_score, i.e., the proportion of true positive cases that are finally predicted to be positive. (4) F1_score, as a combination of accuracy and recall, is often used as a metric for multi-classification model selection. (5) Hamming_loss, which is a measure of the distance between the predicted label and the true label, takes a value between 0 and 1, the smaller the value the better, and a distance of 0 indicates that the predicted result is exactly the same as the true result. (6) Cohen_kappa_score, the value range is [0,1], the higher the value of this coefficient, the higher the accuracy of the classification achieved by the model. It is calculated as $k = (P_o - P_e)/(1 - P_e)$, Where P_o denotes the overall classification accuracy and P_e denotes SUM (the number of true samples in class i * number of samples predicted in class i)/total number of samples squared. (7) Jaccard_score, which is used to compare the similarity and difference between the true and predicted values. The larger the coefficient value, the higher the sample similarity, indicating the more accurate prediction.

The experiments in this section are in the form of ten-fold cross-validation, and the average of five experiments is calculated as the indicator results, where for the average price indicators (2)–(4) a micro-averaging approach is used, i.e., a global confusion matrix is established for each instance in the dataset without categorizing the statistics, and then the corresponding indicators are calculated. The experimental results are shown in **Table 4**.

TABLE 5 | The optimal parameters of algorithms.

Parameters	GA_SVM	GS_SVM	PSO_SVM	GSP_SVM
bestc	0.84731	0.0625	77.691	0.1
bestg	4.0526	0.7579	0.01	1.0164

DISCUSSION

Discussion of the Binary Classification Problems

In this experiments, we all assume that the range of penalty factor c is [0.1, 100], which is mainly used to control the tradeoff between model complexity and approximation error of classification model. If the penalty factor c is larger, the better the fitting degree of the algorithm is, but at the same time, the generalization ability of the algorithm will be reduced, which is not conducive to the popularization and application of the algorithm. At the same time, we also assume that the value range of parameter g in the selected Gaussian kernel function is [0.01,1000], which determines the classification accuracy of the algorithm. Through parameter optimization, we get the optimal parameter values of each algorithm, as shown in **Table 5**. **Figure 2** also shows the visualization of iterative optimization of parameters c and g based on the algorithm of optimizing support vector machine parameters based on GA_SVM and PSO_SVM.

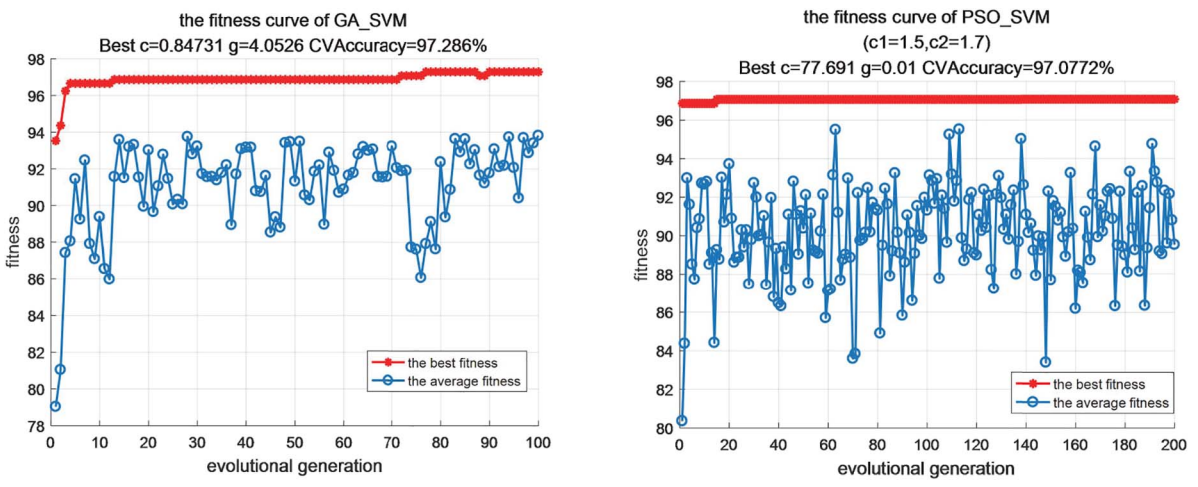

FIGURE 2 | The visualization of iterative optimization.

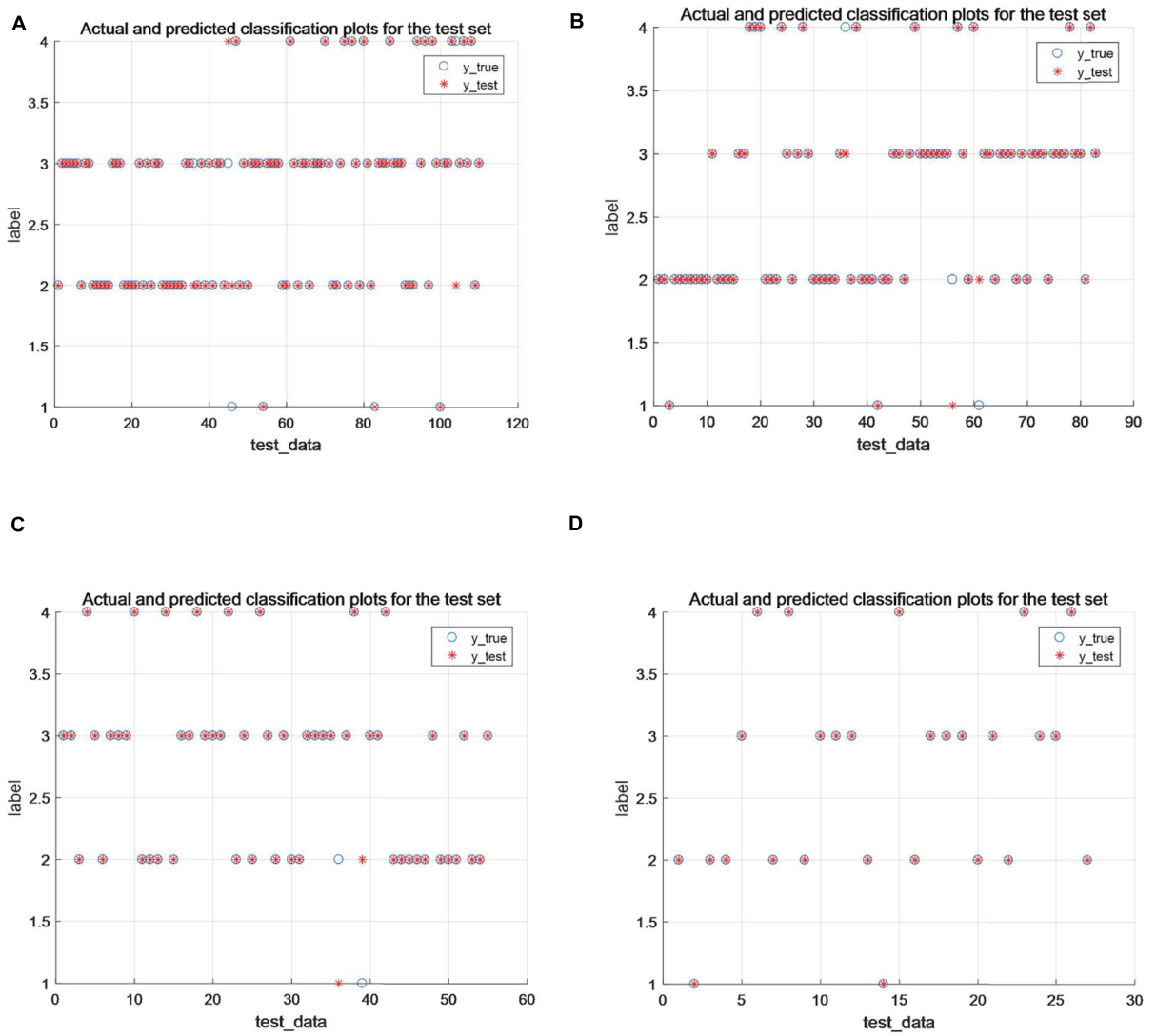

FIGURE 3 | (A–D) Classification results under 60, 70, 80, and 90% training percentages, respectively.

From the above analysis, this paper uses the advantages of GA, PSO and SAA to improve the parameter optimization algorithm of support vector machine, which can balance the difference between global search optimization and local search optimization. Through the mutual assignment between the optimal particle and the worst chromosome or between the worst particle and the optimal dye, the genetic algorithm and particle swarm optimization algorithm complement each other. In the later stage, the local search ability of the sub group algorithm is insufficient, and the simulated annealing method is used to enhance it, the Metropolis criterion is used to select whether to accept new particles. According to the experimental results, we can also see that the improved SVM optimization algorithm can show good performance in the case of small samples and non-linear, and its robustness is high, the generalization ability is strong, and there is no problem of under fitting and over fitting.

Extension to Multiclass Problems

From **Table 4**, it can be seen that, overall, the performance of this paper's algorithm is optimal compared with other algorithms on data with 50, 60, and 90% training share, and the algorithm of this paper applied on 70% of the training dataset is consistent with Accuracy_score, Precision_score, Recall_score, and F1_score metrics with PCA_SVM and GA_SVM exhibit consistent results with SVM and PCA_SVM on 80% of the training set datasets. As the most commonly used metrics in evaluating multi-classification problems, the smaller the value of Hamming_loss, the closer the predicted label is to the true label, and the higher the value of Cohen_kappa_score, the better the classification accuracy of the algorithm. The algorithm in this paper shows optimal results in both metrics, especially in the 90% training data share, the Hamming_loss decreases to 0.0148 and Cohen_kappa_score

reaches 97.64%, and **Figure 3** shows the classification results of the algorithm in this paper on different training sets. Therefore, the algorithm proposed in this paper can also show better classification results when extended to multi-classification problems.

CONCLUSION

In this paper, through the simultaneous interpretation of traditional optimization algorithms and machine learning methods, an algorithm combining three classical algorithms for optimization of support vector machines is proposed and trained and tested based on different breast cancer datasets, and the experimentally obtained classification accuracy, MCC, AUC, and other indexes reach high levels on the binary dataset. On the multiclassification dataset, the experimentally obtained metrics such as Hamming_loss minimum, Cohen_kappa_score and classification accuracy are optimal, which fully demonstrate that the method can provide decision support for breast cancer assisted diagnosis and thus significantly improve the diagnostic efficiency of medical institutions. Our research work will be based on this and will be developed into a breast cancer diagnosis recognition system, using artificial intelligence methods and combined with computer visualization to provide an auxiliary diagnostic basis for clinicians' decision making through a graphical interface.

From the perspective of medical risk, in order to maximize the accuracy of the classification of malignant tumors, further research can be done on the combination of more complex kernel functions for different classifications. At the same time, medical institutions need to collect typical sample data purposefully to prevent the serious asymmetry of the two types of sample data. Of course, if we want to comprehensively improve the level of computer-aided diagnosis of diseases in medical institutions, we need to do further research on other high-risk diseases.

DATA AVAILABILITY STATEMENT

The original contributions generated for this study are included in the article/**Supplementary Material**, further inquiries can be directed to the corresponding author.

AUTHOR CONTRIBUTIONS

YD and WM conceived and designed the experimental protocol. YD involved in the analysis and designed the model of improved SVM. WM performed operations. YD wrote the first draft of the manuscript. WM reviewed and revised the manuscript. Both authors read and approved the final manuscript.

FUNDING

This work was supported by the Scientific Research Project of Tianjin Health Information Association under Grant No. TJHIA-2020-001.

ACKNOWLEDGMENTS

We thank Tianjin Baodi Hospital for providing the experimental platform.

SUPPLEMENTARY MATERIAL

The Supplementary Material for this article can be found online at: https://www.frontiersin.org/articles/10.3389/fbioe.2021.698390/full#supplementary-material

REFERENCES

Abbass, H. A. (2002). An evolutionary artificial neural networks approach for breast cancer diagnosis. *Artif. Intell. Med.* 25, 265–281. doi: 10.1016/s0933-3657(02)00028-3

Abdikenov, B., Iklassov, Z., Sharipov, A., Hussain, S., and Jamwal, P. K. (2019). Analytics of heterogeneous breast cancer data using neuroevolution. *IEEE Access* 7, 18050–18060. doi: 10.1109/access.2019.2897078

Ali, A. H., and Abdullah, M. Z. (2020). A parallel grid optimization of SVM hyperparameter for big data classification using spark radoop. *Karbala Int. J. Modernence* 6:3.

Arya Azar, N., Ghordoyee Milan, S., and Kayhomayoon, Z. (2021). The prediction of longitudinal dispersion coefficient in natural streams using LS-SVM and ANFIS optimized by Harris hawk optimization algorithm. *J. Contam. Hydrol.* 240:103781. doi: 10.1016/j.jconhyd.2021.103781

Bennett, K. P., Demiriz, A., and Maclin, R. (2002). "Exploiting unlabeled data in ensemble methods," in *Proceedings of the Eighth ACM SIGKDD International Conference on Knowledge Discovery and Data Mining (KDD '02)*, (New York, NY: Association for Computing Machinery), 289–296.

Chauhan, R. S., and Ghosh, D. (2021). An erratum to "Extended Karush-Kuhn-Tucker condition for constrained interval optimization problems and its application in support vector machines". *Inform. Sci.* 559, 309–313. doi: 10.1016/j.ins.2020.12.034

Fayed, H. A., and Atiya, A. F. (2019). Speed up grid-search for parameter selection of support vector machines. *Appl. Soft Comput.* 80, 202–210. doi: 10.1016/j.asoc.2019.03.037

Fogel, D. B., Wasson, E. C. III, and Boughton, E. M. (1995). Evolving neural networks for detecting breast cancer. *Cancer Lett.* 96, 49–53. doi: 10.1016/0304-3835(95)03916-k

Guan, S., Wang, X., Hua, L., and Li, L. (2021). Quantitative ultrasonic testing for near-surface defects of large ring forgings using feature extraction and GA-SVM. *Appl. Acoust.* 173:107714. doi: 10.1016/j.apacoust.2020.107714

Khan, S. U., Islam, N., Jan, Z., Din, I. U., and Rodrigues, J. J. (2019). A novel deep learning based framework for the detection and classification of breast cancer using transfer learning. *Pattern Recognit. Lett.* 125, 1–6. doi: 10.1016/j.patrec.2019.03.022

Kouziokas, G. N. (2020). SVM kernel based on particle swarm optimized vector and Bayesian optimized SVM in atmospheric particulate matter forecasting. *Appl. Soft Comput.* 93:106410. doi: 10.1016/j.asoc.2020.106410

Li, X., Guo, Y., and Li, Y. (2020). Particle swarm optimization-based SVM for classification of cable surface defects of the cable-stayed

bridges. *IEEE Access* 8, 44485–44492. doi: 10.1109/access.2019.2961755

Li, Y., Chen, S. X., Jia, H., and Wang, X. (2020). Prediction of breast cancer based on C-AdaBoost model. *Comput. Eng. Sci.* 42, 1414–1422.

Liu, J., Xu, B., Zhang, C., Gong, Y., Garibaldi, J., Soria, D., et al. (2019). An end-to-end deep learning histochemical scoring system for breast cancer tissue microarray. *IEEE Trans. Med. Imaging* 38, 617–628. doi: 10.1109/tmi.2018.2868333

Lu, H., Wang, H., and Yoon, S. W. (2019). A dynamic gradient boosting machine using genetic optimizer for practical breast cancer prognosis. *Expert Syst. Appl.* 116, 340–350. doi: 10.1016/j.eswa.2018.08.040

Oza, N. C. (2005). "Online bagging and boosting," in *Proceedings of the 2015 IEEE International Conference on Systems, Man and Cybernetics*, (Waikoloa, HI), 2340–2345.

Ramkumar, M., Babu, C. G., Priyanka, G. S., and Sarath Kumar, R. (2021). Ecg arrhythmia signals classification using particle swarm optimization-support vector machines optimized with independent component analysis. *IOP Conf. Ser. Mater. Sci. Eng.* 1084:012009. doi: 10.1088/1757-899x/1084/1/012009

Siegel, R. L., Miller, K. D., and Jemal, A. (2016). Cancer statistics. *CA Cancer J. Clin.* 66, 7–30.

Skoff, D. N. (2017). Exploring potential flaws and dangers involving machine learning technology. *S & T's Peer to Peer* 1:4.

Tao, Y., and Cuicui, L. (2020). Recognition system for leaf diseases of *Ophiopogon japonicus* based on PCA-SVM. *Plant Dis. Pests* 11, 11–15.

Vapnik, V. N. (1995). "Controlling the generalization ability of learning processes," in *The Nature of Statistical Learning Theory*, (New York, NY: Springer), 89–118. doi: 10.1007/978-1-4757-2440-0_5

Wang, C., Wang, Y., Wang, K., Yang, Y., and Tian, Y. (2019). An improved biogeography/complex algorithm based on decomposition for many-objective optimization. *Int. J. Mach. Learn. Cybern.* 10, 1961–1977. doi: 10.1007/s13042-017-0728-y

Zhang, H., and Su, M. (2020). Hand gesture recognition of double-channel EMG signals based on sample entropy and PSO-SVM. *J. Phys. Conf. Ser.* 1631:012001. doi: 10.1088/1742-6596/1631/1/012001

Zhou, S., Qian, S., Chang, W., Xiao, Y., and Cheng, Y. (2018). A novel bearing multi-fault diagnosis approach based on weighted permutation entropy and an improved SVM ensemble classifier. *Sensors* 18:1934. doi: 10.3390/s18061934

Conflict of Interest: The authors declare that the research was conducted in the absence of any commercial or financial relationships that could be construed as a potential conflict of interest.

frontiers in Bioengineering and Biotechnology

ORIGINAL RESEARCH
published: 06 July 2021
doi: 10.3389/fbioe.2021.662749

Prediction of Tumor Shrinkage Pattern to Neoadjuvant Chemotherapy Using a Multiparametric MRI-Based Machine Learning Model in Patients With Breast Cancer

Yuhong Huang[1†], Wenben Chen[2†], Xiaoling Zhang[3†], Shaofu He[3], Nan Shao[1], Huijuan Shi[4], Zhenzhe Lin[2], Xueting Wu[5], Tongkeng Li[5], Haotian Lin[2,6] and Ying Lin[1*]*

[1] Breast Disease Center, The First Affiliated Hospital, Sun Yat-sen University, Guangzhou, China, [2] State Key Laboratory of Ophthalmology, Zhongshan Ophthalmic Center, Sun Yat-sen University, Guangzhou, China, [3] Department of Radiology, The First Affiliated Hospital, Sun Yat-sen University, Guangzhou, China, [4] Department of Pathology, The First Affiliated Hospital, Sun Yat-sen University, Guangzhou, China, [5] Zhongshan School of Medicine, Sun Yat-sen University, Guangzhou, China, [6] Center for Precision Medicine, Sun Yat-sen University, Guangzhou, China

OPEN ACCESS

Edited by:
Sandro Mussa-Ivaldi,
Northwestern University, United States

Reviewed by:
Hung-Yin Lin,
National University of Kaohsiung, Taiwan
Giovanni Badiali,
University of Bologna, Italy

***Correspondence:**
Haotian Lin
gddlht@aliyun.com
Ying Lin
linying3@mail.sysu.edu.cn

[†]These authors have contributed equally to this work and share first authorship

Specialty section:
This article was submitted to Bionics and Biomimetics, a section of the journal Frontiers in Bioengineering and Biotechnology

Received: 01 February 2021
Accepted: 07 June 2021
Published: 06 July 2021

Citation:
Huang Y, Chen W, Zhang X, He S, Shao N, Shi H, Lin Z, Wu X, Li T, Lin H and Lin Y (2021) Prediction of Tumor Shrinkage Pattern to Neoadjuvant Chemotherapy Using a Multiparametric MRI-Based Machine Learning Model in Patients With Breast Cancer. Front. Bioeng. Biotechnol. 9:662749. doi: 10.3389/fbioe.2021.662749

Aim: After neoadjuvant chemotherapy (NACT), tumor shrinkage pattern is a more reasonable outcome to decide a possible breast-conserving surgery (BCS) than pathological complete response (pCR). The aim of this article was to establish a machine learning model combining radiomics features from multiparametric MRI (mpMRI) and clinicopathologic characteristics, for early prediction of tumor shrinkage pattern prior to NACT in breast cancer.

Materials and Methods: This study included 199 patients with breast cancer who successfully completed NACT and underwent following breast surgery. For each patient, 4,198 radiomics features were extracted from the segmented 3D regions of interest (ROI) in mpMRI sequences such as T1-weighted dynamic contrast-enhanced imaging (T1-DCE), fat-suppressed T2-weighted imaging (T2WI), and apparent diffusion coefficient (ADC) map. The feature selection and supervised machine learning algorithms were used to identify the predictors correlated with tumor shrinkage pattern as follows: (1) reducing the feature dimension by using ANOVA and the least absolute shrinkage and selection operator (LASSO) with 10-fold cross-validation, (2) splitting the dataset into a training dataset and testing dataset, and constructing prediction models using 12 classification algorithms, and (3) assessing the model performance through an area under the curve (AUC), accuracy, sensitivity, and specificity. We also compared the most discriminative model in different molecular subtypes of breast cancer.

Results: The Multilayer Perception (MLP) neural network achieved higher AUC and accuracy than other classifiers. The radiomics model achieved a mean AUC of 0.975 (accuracy = 0.912) on the training dataset and

0.900 (accuracy = 0.828) on the testing dataset with 30-round 6-fold cross-validation. When incorporating clinicopathologic characteristics, the mean AUC was 0.985 (accuracy = 0.930) on the training dataset and 0.939 (accuracy = 0.870) on the testing dataset. The model further achieved good AUC on the testing dataset with 30-round 5-fold cross-validation in three molecular subtypes of breast cancer as following: (1) HR+/HER2–: 0.901 (accuracy = 0.816), (2) HER2+: 0.940 (accuracy = 0.865), and (3) TN: 0.837 (accuracy = 0.811).

Conclusions: It is feasible that our machine learning model combining radiomics features and clinical characteristics could provide a potential tool to predict tumor shrinkage patterns prior to NACT. Our prediction model will be valuable in guiding NACT and surgical treatment in breast cancer.

Keywords: breast cancer, multi-parametric MRI, neoadjuvant chemotherapy, radiomics, machine learning, tumor shrinkage pattern

INTRODUCTION

Neoadjuvant chemotherapy (NACT) has been used as the standard treatment to downstage tumor in inoperable patients with locally advanced breast cancer, while for operable patients, it is increasingly being used to reduce tumor size and increase the possibility of breast-conserving surgery (BCS) (Hennessy et al., 2005; Mathew et al., 2009; Mougalian et al., 2016). The 2017 St. Gallen International Expert Consensus Conference showed that NACT had been extensively used in patients with human epidermal growth factor receptor 2 positive (HER2+) and triple-negative (TN) breast cancer, especially those with axillary lymph node metastasis, to improve survivals (Curigliano et al., 2019). Pathological complete response (pCR), which is defined as ypT0/is after NACT according to the *American Joint Committee on Cancer (AJCC) TNM Staging Manual*, 8th Edition, has been proven as a good prognostic marker to predict a successful long-term survival in breast cancer (Kong et al., 2011; Giuliano et al., 2018). But only about 30% of the patients achieved pCR after NACT, and the pCR rate varied in different molecular subtypes, as tumor size and treatment regimen influence the treatment response (Chen et al., 2014; Cortazar et al., 2014; Goorts et al., 2017).

After NACT, breast cancer shows different shrinkage patterns as follows: (a) no residual tumor, (b) no invasive tumor but residual ductal carcinoma in situs (DCIS), (c) concentric shrinkage, (d) a main residual invasive focus with surrounding DCIS, (e) multicentric shrinkage (i.e., more than two invasive lesions), (f) stable disease (SD), and (g) progressive disease (PD). The former two patterns are considered as pCR after NACT while pCR and concentric shrinkage are both considered as sufficient tumor responses which can benefit from BCS, and the negative surgical margins are easier to achieve for them. The mechanism of how some biological factors such as tumor subtypes influence tumor shrinkage pattern is still unclear. Earlier studies showed that HER2+ and TN breast cancer had a higher possibility to achieve a sufficient tumor response than hormone receptor positive (HR+) but HER2– breast cancer after NACT. Breast pCR is rarely achieved in HR+/HER2– breast cancer due to the low chemosensitivity, but such molecular subtype of cancer can also benefit from BCS (Ballesio et al., 2017; Eom et al., 2017). The assessment of pCR is insufficient to determine patients suitable for BCS since tumor concentric shrinkage is also suitable. Hence, the tumor shrinkage pattern is a more reasonable marker than pCR to choose candidates for BCS. Another study has shown that about 10–35% of patients had a poor response to NACT (SD/PD), which indicates a high risk of local recurrence after surgery (Li et al., 2020). For these patients, it is imperative to avoid the associated adverse toxicity of chemo-drug and overtreatment.

In order to identify the patients who have a sufficient response to NACT and can benefit from BCS, it is essential to predict tumor shrinkage pattern prior to treatment. Lobbes et al. revealed that magnetic resonance imaging (MRI) has better accuracy in assessing residual tumor after NACT than physical examination, mammography, and ultrasonography in patients with breast cancer (Lobbes et al., 2013). The ACRIN 6657/I-SPY Trial has reported that MRI in the early stage of NACT could provide much helpful information about tumor pathological response (Hylton et al., 2012). Some studies have revealed that dynamic contrast-enhanced imaging (DCE) could distinguish residual tumor from therapy-induced non-vascularized fibrosis (Pickles et al., 2005; Manton et al., 2006; Padhani et al., 2006; Loo et al., 2008). The pre-NACT MRI can be used to assess the extent and morphology of primary breast cancer and may provide useful information about tumor shrinkage patterns. However, a meta-analysis reported that

Abbreviations: NACT, neoadjuvant chemotherapy; BCS, breast-conserving surgery; DCIS, ductal carcinoma *in situ*; IHC, immunohistochemistry; FISH, fluorescence *in situ* hybridization; mpMRI, multiparametric MRI; T1-DCE, T1-weighted dynamic contrast-enhanced imaging; T2WI, T2-weighted imaging; ADC, apparent diffusion coefficient; ROI, regions of interest; LASSO, least absolute shrinkage and selection operator; MLP, Multilayer Perception; HER2, human epidermal growth factor receptor 2; TN, triple-negative; HR, hormone receptor; ROC, receiver operating characteristic; AUC, area under the ROC curve; SLNB, sentinel lymph node biopsy; ALND, axillary lymph node dissection; pCR, pathological complete response; SD, stable disease; PD, progressive disease; PCCM, Pearson's correlation coefficient matrix.

the MRI data had limited value for the prediction of pCR with the sensitivity of 64% in breast cancer (Yuan et al., 2010).

Radiomics is a frontier interdiscipline of medical imaging and computer field, and it has been used to extract much quantitative information from medical images (Lambin et al., 2012; Aerts et al., 2014; Yip and Aerts, 2016). The radiomics information has shown a great potential to assist clinicians, and several radiomics models had been constructed to better diagnose disease and monitor tumor response to treatment in breast cancer (Antunovic et al., 2019; Li et al., 2020; Zheng et al., 2020; Zhuang et al., 2020). Liu et al. developed a radiomics model for predicting pCR after NACT in breast cancer based on mpMRI and validated the model by multicenter datasets with the AUCs of 0.71–0.80 (Liu et al., 2019). Radiomics can help acquire more information from MRI to better predict tumor shrinkage patterns prior to NACT. However, to our knowledge, the feasibility of radiomics to predict tumor shrinkage pattern based on mpMRI and clinicopathologic characteristics prior to NACT still remains to be tested, and no study investigated the correlation between the tumor shrinkage pattern and the mpMRI radiomics features in different molecular subtypes of breast cancer using the machine learning method. Therefore, the purpose of our study is to explore the radiomics biomarkers of tumor shrinkage pattern from mpMRI, construct a prediction model combined with the clinicopathologic characteristics, and investigate the predictor based on the molecular subtype of breast cancer.

MATERIALS AND METHODS

Study Population

We retrieved 503 consecutive patients with breast cancer who were treated with NACT and followed by surgery in our center between March 2016 and July 2020. The inclusion criteria for this study were as follows: (1) the patient had a biopsy-proven unilateral breast cancer, (2) the patient successfully completed NACT and following breast surgery in our center, (3) the MRI examination of the breast was performed before the initiation of NACT in our hospital within 2 weeks, and (4) the baseline data were complete. The exclusion criteria were as follows: (1) the patient had prior treatment to breast cancer, (2) the pathological results or clinical data were unavailable, (3) the patient did not complete standard NACT, or the surgery was not performed in our center, (4) the MRI data were unavailable, or imaging quality was insufficient, and (5) the patient had a metastatic disease or other malignance. Finally, a total of 199 patients met the criteria. The clinicopathologic characteristics of each patient including age, menstrual state, clinical anatomical TNM staging according to the *AJCC Manual*, 8th Edition, and the pathological biopsy results including tumor type, receptor status, and tumor proliferation rate (i.e., Ki-67 index) were derived from the electronic medical records. The characteristics of all patients are summarized in **Table 1**.

Treatment to Patients

All patients completed 6–8 cycles of chemotherapy and underwent breast surgery based on the current National

TABLE 1 | Clinical and histopathological characteristics of study population grouped by tumor shrinkage pattern.

Characteristics	Total patients (n = 199)	Type 1 shrinkage (n = 105)	Type 2 shrinkage (n = 94)	p-value
Age (mean ± SD)	46.85 ± 10.13	47.95 ± 10.19	45.62 ± 9.97	0.105
Menopausal status				0.819
Premenopausal	116 (58.3%)	62 (59.0%)	54 (57.4%)	
Postmenopausal	83 (41.7%)	43 (41.0%)	40 (42.6%)	
Histology				0.152
IDC	191 (96.0%)	103 (98.1%)	88 (93.6%)	
Other	8 (4.0%)	2 (1.9%)	6 (6.4%)	
Clinical stage				0.133
II	98 (49.2%)	57 (54.3%)	41 (43.6%)	
III	101 (50.8%)	48 (45.7%)	53 (56.4%)	
Clinical T stage				0.139
1	5 (2.5%)	3 (2.9%)	2 (2.1%)	
2	127 (63.8%)	73 (69.5%)	54 (57.4%)	
3	50 (25.1%)	24 (22.9%)	26 (27.7%)	
4	17 (8.6%)	5 (4.7%)	12 (12.8%)	
Clinical N stage				0.829
cN0	24 (12.1%)	14 (13.3%)	10 (10.6%)	
cN1	105 (52.8%)	54 (51.4%)	51 (54.3%)	
cN2 or cN3	70 (35.2%)	37 (35.3%)	33 (35.1%)	
ER				0.026
Positive	117 (58.8%)	54 (51.4%)	63 (67.0%)	
Negative	82 (41.2%)	51 (48.6%)	31 (33.0%)	
PR				0.019
Positive	101 (50.8%)	45 (42.9%)	56 (59.6%)	
Negative	98 (49.2%)	60 (57.1%)	38 (40.4%)	
HER2				0.102
Positive	99 (49.7%)	58 (55.2%)	41 (43.6%)	
Negative	100 (50.3%)	47 (44.8%)	53 (56.4%)	
Molecular subtype				0.239
HR+/HER2−	66 (33.2%)	30 (28.6%)	36 (38.3%)	
HER2+	99 (49.7%)	58 (55.2%)	41 (43.6%)	
TN	34 (17.1%)	17 (16.2%)	17 (18.1%)	

(Continued)

TABLE 1 | Continued

Characteristics	Total patients ($n = 199$)	Type 1 shrinkage ($n = 105$)	Type 2 shrinkage ($n = 94$)	p-value
Ki-67				0.048
<30	83 (41.7%)	37 (35.2%)	46 (48.9%)	
≥30	116 (58.3%)	68 (64.8%)	48 (51.1%)	

Comprehensive Cancer Network (NCCN) guideline (Goetz et al., 2019). All patients with HER2– breast cancer received four cycles of epirubicin and cyclophosphamide and then followed by four cycles of taxotere (EC-T regimen), whereas patients with HER2+ breast cancer were treated with four cycles of epirubicin and cyclophosphamide and followed by four cycles of taxotere and trastuzumab (EC-TH regimen), or received six cycles of taxotere, carboplatin, and trastuzumab (TCH regimen). For HER2+ breast cancer, some patients received trastuzumab and pertuzumab dual-target therapy during their NACT (EC-THP or TCbHP regimen). After NACT, BCS, or mammectomy were performed. The staging of axillary nodes included sentinel lymph node biopsy (SLNB) or axillary lymph node dissection (ALND).

Pathological Assessment

All pre-NACT biopsy and postoperative pathological results were analyzed by a breast pathologist with more than 10 years of experience. The receptor status and Ki-67 index of the tumor were determined based on immunohistochemistry (IHC) staining. The HR was defined as positive for estrogen receptor (ER) or progesterone receptor (PR) expression when ≥1% of the tumor cells showed nuclear staining, and the HER2 expression graded 3+ was defined as positive while 0 and 1+ were negative (Hammond et al., 2010; Wolff et al., 2013). When the HER2 expression graded 2+ was reported, the gene amplification by the fluorescence *in situ* hybridization (FISH) was used to determine the HER2 status. Tumors were classified into three molecular subtypes as follows: (1) HR+/HER2–, (2) HER2+, and (3) TN. For Ki-67 index, we defined tumor cells with ≥30% staining as high expression and those with <30% staining as low expression.

The specimen pathology was used as the gold standard of tumor shrinkage pattern, and the largest diameter of the invasive tumor region on slides was measured by two pathologists in consensus. According to the surgical pathology, tumor shrinkage patterns were classified as follows: (a) pCR (i.e., no residual tumor or only residual ductal carcinoma in situs, defined as $ypT_{0/is}$), (b) concentric shrinkage (i.e., only one residual invasive tumor focus, without DCIS), (c) diffuse shrinkage (i.e., a main residual invasive focus with surrounding satellite DCIS), (d) multifocal shrinkage (≥ 2 invasive tumor foci, with/without DCIS), (e) SD, and (f) PD. The former two are classified into type 1 shrinkage, which is called favorable shrinkage pattern, and the last four are classified into type 2 shrinkage, which is called the poor shrinkage pattern. **Figure 1** shows the tumor shrinkage patterns after NACT.

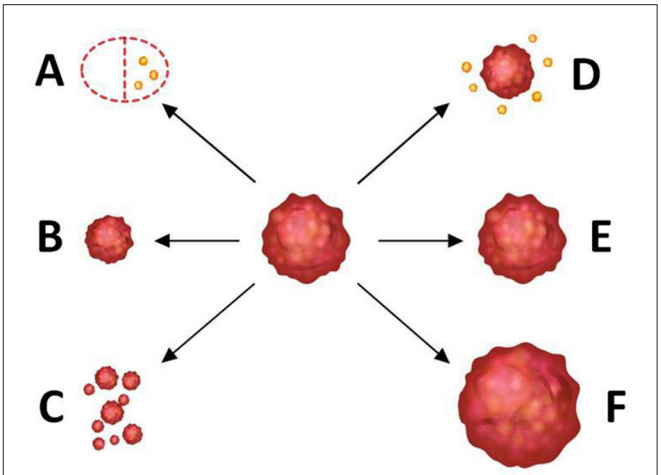

FIGURE 1 | Tumor shrinkage patterns after neoadjuvant chemotherapy. **(A)** Pathological complete response [i.e., no residual tumor or only residual ductal carcinoma *in situ* (DCIS), defined as $ypT_{0/is}$], **(B)** concentric shrinkage (i.e., only one residual invasive tumor focus, without DCIS), **(C)** multifocal shrinkage (i.e., more than 2 invasive tumor foci, with/without DCIS), **(D)** diffuse shrinkage (i.e., a main residual invasive focus with surrounding satellite DCIS), **(E)** stable disease (SD), and **(F)** progressive disease (PD). **(A,B)** belong to type 1 shrinkage pattern. **(C–F)** belong to type 2 shrinkage pattern.

The longest diameter of the primary tumor on the segmented 3D regions of interest (ROI) was measured in the MRI workstation as well. According to the Response Evaluation Criteria in Solid Tumors (RECIST 1.1) guideline, patients were classified into response or non-response group to NACT as the following: patients who responded to NACT were determined when the invasive tumor area showed a decrease of largest diameter ≥30% compared with that in the MRI, while SD indicated a decrease of largest diameter <30% or an increase of largest diameter <20%, and PD indicated an increase of largest diameter ≥20% (Chalian et al., 2011; Schwartz et al., 2016). Concentric shrinkage is defined as only one invasive tumor focus without DCIS, and such a shrinkage pattern is more likely to achieve the negative surgical margins in BCS, while multifocal and diffuse shrinkages are both considered as significant responses to NACT but still unsuitable for BCS.

MRI Acquisition

All patients underwent MRI examination using a 3.0 Tesla system (Siemens Verio, syngo MR B17, Erlangen, Germany) with a dedicated 16-channel breast coil within 2 weeks prior to the initiation of NACT. The MRI sequences of each patient included as follows: an axial fat-suppressed T2-weighted imaging (T2WI), an axial T1-weighted DCE (T1-DCE), and an apparent diffusion coefficient (ADC) map derived from diffusion-weighted imaging. The details of the MRI examination and parameters for MRI images are shown in the **Supplementary Material**.

Tumor Segmentation and Features Extraction

Two radiologists with more than 10 years of experience in breast imaging performed the tumor segmentation with

Segmentation Module in 3D Slicer software (version 4.10.2, www.slicer.org) (Fedorov et al., 2012; Cheng et al., 2016). On T1-DCE images, the high signal intensity of the tumor region after injection of the contrast agent allows an accurate delineation to the tumor margins. The semi-automatic algorithms did the preliminary segmentation according to the intensity threshold segmentation, and then, manual corrections such as relabeling and hole-filling were done by two professional radiologists in consensus. The masks of ROI on T1-DCE were then registered to the other two MRI sequences (i.e., T2WI and ADC map). Finally, we got three segmentation ROI masks per patient. More details about the tumor segmentation are shown in the **Supplementary Material**.

Feature extraction of ROI was performed with Pyradiomics Module in 3D Slicer software (https://github.com/Radiomics/pyradiomics) (van Griethuysen et al., 2017; Zwanenburg et al., 2020). Before features extraction, the voxel size of each sequence was resampled to $1 \times 1 \times 1$ mm, and the bin width of the gray-level histogram was fixed as 25. Six Laplacian of Gaussian filters (i.e., kernel sizes were set as 1, 2, 3, 4, 5, and 6) and a wavelet-based filter were used to process the original MRI images. Then, 1,424 quantitative radiomics features could be extracted from each MRI sequence, and the features were divided into seven categories: (1) first-order statistics features, (2) shape-based features, (3) gray-level co-occurrence matrix (GLCM), (4) gray-level size zone matrix (GLSZM), (5) gray-level run length matrix (GLRLM), (6) neighboring gray-tone difference matrix (NGTDM), and (7) gray-level dependence matrix (GLDM). After removing the duplicate shape of features, a total of 4,198 radiomics features from three MRI sequences could be extracted per patient. The information of the various features is shown in **Supplementary Material**. The clinical characteristics such as age, menopausal status, histological type, clinical anatomical TNM stage, ER status, PR status, HER2 status, and Ki-67 index were also added in the feature set.

Feature Selection

Features selection was performed with Python 3.70 (https://www.python.org/). Before feature selection, the feature normalization was performed to ensure a relatively uniform range of all the radiomics features. The z-score normalization process is shown in the **Supplementary Material**. To achieve the dimensionality reduction, we used ANOVA and the least absolute shrinkage and selection operator (LASSO) logistic regression with 10-fold cross-validation to select the most significant features corresponding to the tumor shrinkage pattern. Then, the Pearson's correlation coefficient matrix (PCCM) was used to identify the multicollinearity between features. If there is any pair of features with a correlation coefficient of more than 0.85 or less than −0.85, then only one feature with a higher discriminative ability was selected. Finally, we selected the most significant features to make a combination with the best prediction performance.

Establishment and Assessment of Models

The establishment and evaluation of the machine learning model were performed with Scikit-learn 0.18 package in Python 3.70. All patients were randomly allocated to the training dataset and testing dataset by stratified cross-validation, which included a 6-fold outer loop and a 5-fold inner loop. The positive/negative sample ratio was similar in the training dataset and testing dataset. In the outer loop, 5-fold (83.4%, 166 patients) dataset was used as the training dataset to develop the model, and the independent testing dataset (16.6%, 33 patients) was used to evaluate the model performance. To determine the best optimal hyperparameters, grid searching, and cross-validation were employed in the inner loop, and 1-fold (16.6%, 33 patients) dataset, also called the inner validation dataset, was assessed to choose the best hyperparameters. The whole process (i.e., stratified splitting, subsequent model development, hyperparameters optimization, and performance evaluation) was repeated by a 30-round bootstrap method to assess the robustness.

The clinical model and radiomics model were constructed with selected significant clinicopathologic and radiomics features, respectively, and then, the total features were combined to establish a combined model. As our model construction was a task for the labeled data, we used 12 robust supervised classification algorithms as following: Logistic Regression, Support Vector Machine (i.e., linear or radial kernel), Linear Discriminant Analysis, Random Forest, Extreme Gradient Boosting, Gaussian Naïve Bayes, AdaBoost, Decision Tree, K-Nearest Neighbors, AdaBoost, and Multilayer Perception (MLP) neural network. Then, the performance of each model was evaluated using the receiver operating characteristic (ROC) curves, the area under the ROC curve (AUC), accuracy, sensitivity, and specificity. Each specific algorithm was designed to fit the training dataset in the inner loop and to correctly predict the independent testing dataset in the outer loop. The prediction results were used to assess the performance and generalization ability of the models. We divided our patients into three subgroups according to molecular subtypes as follows: (1) HR+/HER2−, (2) HER2+, and (3) TN. The stratified 5-fold cross-validation was used to evaluate the model performance for each subtype. **Figure 2** shows the workflow of data input, feature extraction, selection, model construction, and performance assessment.

Statistical Analysis

The baseline data of the patient were evaluated with professional statistics packages in Python 3.7.0 and SPSS (version 20.0). The quantitative data were calculated and recorded as mean ± SD, and the qualitative data were summarized as frequencies and percentages. The Mann–Whitney *U*-test or Student's *t*-test was used for quantitative variables, and the chi-squared test or Fisher's exact test was used for qualitative variables. The normality test and *Z*-test were done for the comparison of performance indexes. The discrimination metrics of models, such as AUC, accuracy, sensitivity, and specificity, were also

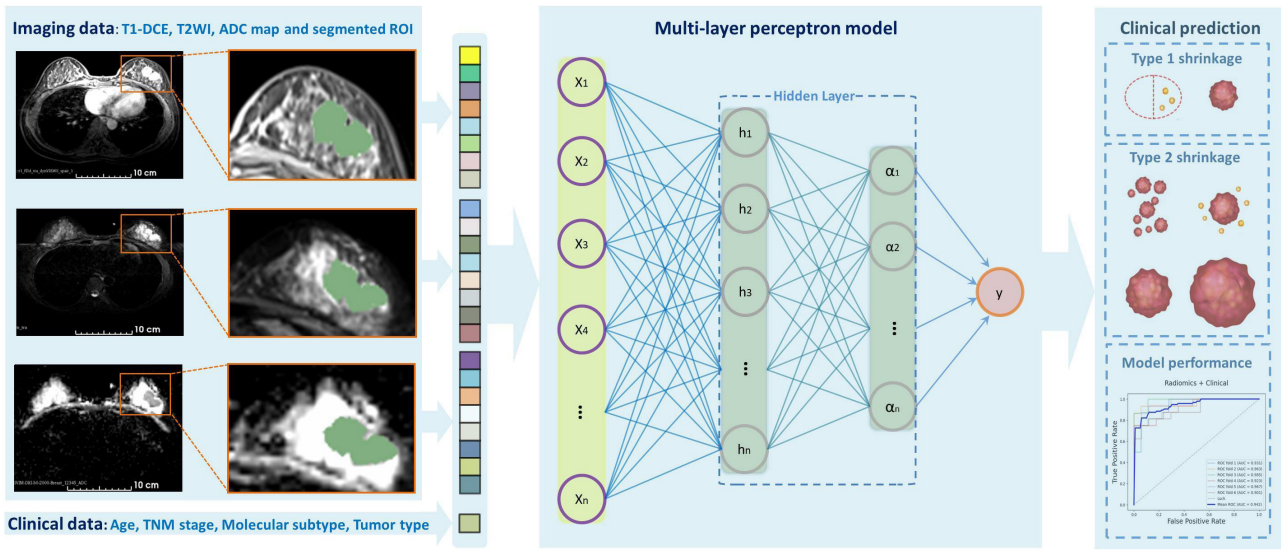

FIGURE 2 | Outline of the workflow from the data input, feature extraction, selection, model construction, and performance assessment.

calculated. A two-sided $p < 0.05$ is considered statistically significant. The Wilson score interval method was used to calculate the CI of AUC.

RESULTS

Baseline Characteristics of Patients

In total, 199 eligible patients were enrolled in this study. The baseline data are presented in **Table 1**. The mean age was 46.85 ± 10.13 years (range 23–78 years), and 116 patients (58.3%) were premenopausal women. Among all patients, 66 were HR+/HER2− (33.2%), 99 were HER2+ (49.7%), and 34 were TN (17.1%). After NACT, 105 patients had achieved type 1 tumor shrinkage pattern (52.8%), whereas 94 had achieved type 2 tumor shrinkage pattern (47.2%) according to the histological confirmation. Significant differences of some baseline characteristics were detected between two groups, including ER, PR, and Ki-67 ($p = 0.026$, 0.019, and 0.049, respectively).

Feature Extraction and Selection

For each patient, 4,198 radiomics features and 10 clinical features were used in the followed machine learning process. The ANOVA and LASSO logistic regression were used to reduce dependency and redundancy, and finally, the 50 most optimal features were selected as follows: 2 clinicopathologic characteristics (ER and Ki-67), and 48 radiomics features, including 11, 16, and 21 features from T1-DCE, T2WI, and ADC map, respectively. The associations of these features were assessed using the PCCM Heatmap, which is shown in **Figure 3**. The features were considered independent of each other as there was no PCC value over 0.85 or < -0.85.

Development and Performance of Models

In order to find the most suitable algorithm for the prediction of tumor shrinkage patterns, 12 robust machine learning algorithms were applied based on the total features we selected. **Table 2** summarizes the performances of each algorithm. The MLP neural network outperformed all other classifier algorithms, with a mean AUC value of 0.939 (95% CI: 0.896–0.965), a mean accuracy of 0.870 (95% CI: 0.815–0.910), a mean sensitivity of 0.840 (95% CI: 0.781–0.885), and a mean specificity of 0.897 (95% CI: 0.846–0.933) in the testing dataset based on the 30-round bootstrap validation. Then, we chose the MLP neural network as the basic algorithm to construct the machine learning models. The MLP neural network contained input, hidden, and output layers, and the hyperparameters in each layer were trained in the inner loop. The prediction workflow of MLP classifier was as follows: all features of one patient were input to the first layer, and finally, the output layer provided a prediction result.

Based on the MLP neural network, nine various models based on feature type were constructed and the prediction performances of various models were shown in **Table 3**. The accuracy of $\text{Model}_{\text{Radiomics}}$ was 0.828 (95% CI: 0.767–0.874), which demonstrated a better performance than that in $\text{Model}_{\text{T1-DCE}}$ (0.644, 95% CI: 0.573–0.708), $\text{Model}_{\text{T2WI}}$ (0.606, 95% CI: 0.534–0.672), $\text{Model}_{\text{ADCmap}}$ (0.709, 95% CI: 0.641–0.768), and $\text{Model}_{\text{Clinical}}$ (0.561, 95% CI: 0.490–0.629). The AUC value (0.900, 95% CI: 0.849–0.935) of $\text{Model}_{\text{Radiomics}}$ also outperformed that in the other four models (i.e., $\text{Model}_{\text{T1-DCE}}$: 0.712, 95% CI: 0.644–0.771; $\text{Model}_{\text{T2WI}}$: 0.661, 95% CI: 0.591–0.724; $\text{Model}_{\text{ADCmap}}$: 0.795, 95% CI: 0.732–0.846; and $\text{Model}_{\text{Clinical}}$: 0.611, 95% CI: 0.540–0.677) on testing dataset. On the training dataset, the $\text{Model}_{\text{Radiomics}}$ achieved a mean accuracy of 0.912 and a mean AUC of 0.975. When the clinicopathologic characteristics were added to

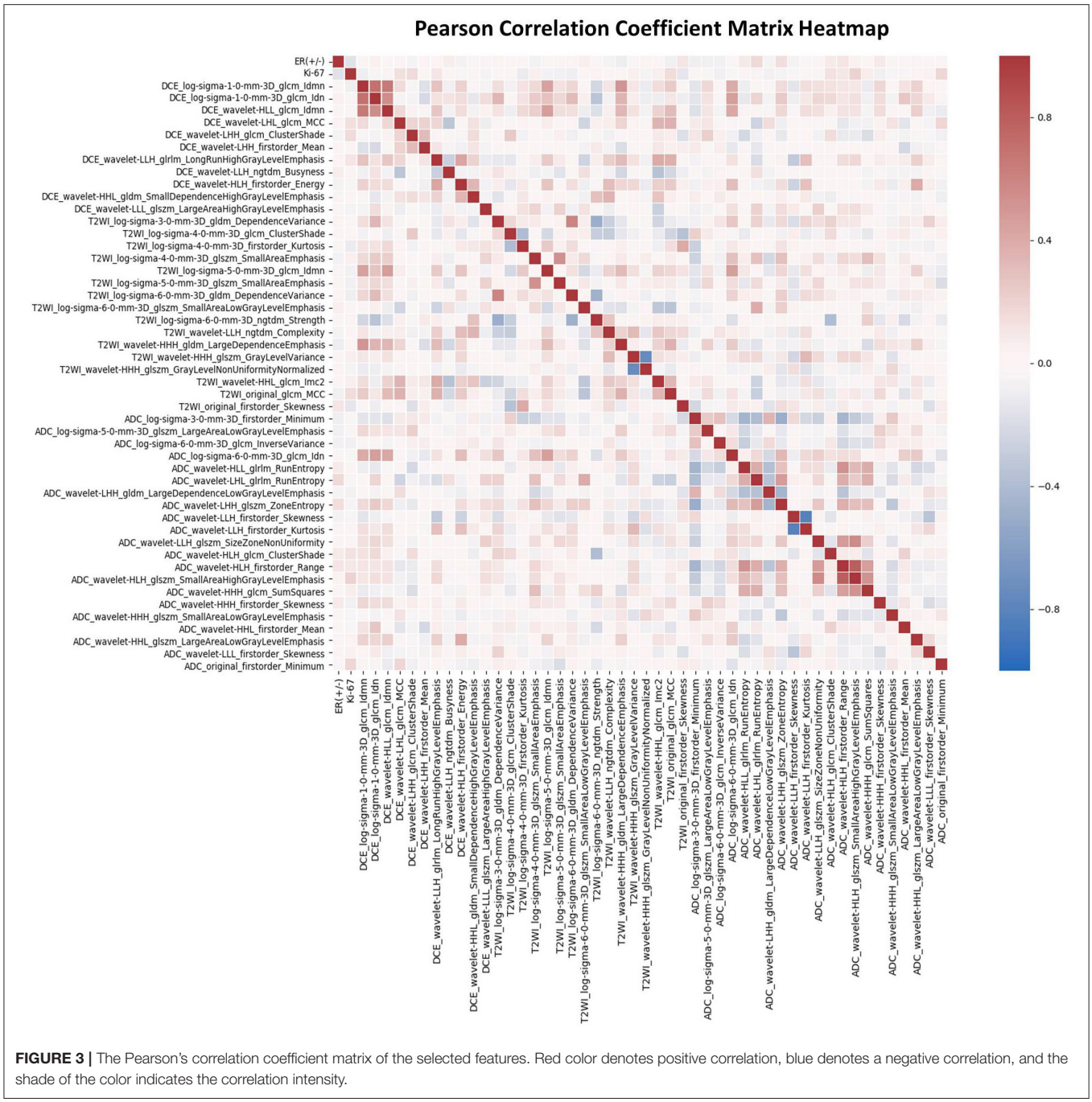

FIGURE 3 | The Pearson's correlation coefficient matrix of the selected features. Red color denotes positive correlation, blue denotes a negative correlation, and the shade of the color indicates the correlation intensity.

construct $Model_{Radiomics+Clinical}$, the accuracy was improved to 0.870 (95% CI: 0.815–0.911) and the AUC was improved to 0.939 (95% CI: 0.896–0.965) on testing dataset, which showed the highest performance in differentiating tumor shrinkage pattern. On the training dataset, the $Model_{Radiomics+Clinical}$ achieved a mean accuracy of 0.930 and a mean AUC of 0.985.

The results of 1-round 6-fold cross-validation of ROC curves of three representative models (i.e., $Model_{Clinical}$, $Model_{Radiomics}$, and $Model_{Radiomics+Clinical}$) are shown in **Figure 4**. For the different molecular subtypes, the predictive performance was evaluated, respectively, and the results were shown in **Table 4**. The HER2+ subtype achieved the highest performance in $Model_{Radiomics+Clinical}$ with an AUC value of 0.940 (95% CI: 0.873–0.973), while the TN subtype had a relatively low performance with an AUC value of 0.837 (95% CI: 0.699-1.0) in the testing dataset. The results of 1-round 5-fold cross-validation of ROC curves for three molecular subtypes are shown in **Figure 5**.

TABLE 2 | Performances of the 12 machine learning classifiers on 30-round 6-fold cross-validation in testing dataset for predicting tumor shrinkage pattern based on all the selected features.

Algorithm	AUC (95% CI)	Accuracy (95% CI)	Sensitivity (95% CI)	Specificity (95% CI)
MLP neural network	0.939 (0.896–0.965)	0.870 (0.815–0.910)	0.840 (0.781–0.885)	0.897 (0.846–0.932)
Logistic Regression	0.922 (0.874–0.952)	0.847 (0.789–0.891)	0.817 (0.756–0.865)	0.874 (0.819–0.913)
SVM (radial kernel)	0.909 (0.859–0.941)	0.823 (0.761–0.869)	0.784 (0.720–0.836)	0.855 (0.798–0.898)
Linear discriminant analysis	0.902 (0.851–0.936)	0.815 (0.753–0.863)	0.789 (0.725–0.840)	0.838 (0.779–0.883)
SVM (linear kernel)	0.890 (0.837–0.926)	0.809 (0.747–0.858)	0.780 (0.715–0.832)	0.835 (0.775–0.880)
Random forest	0.803 (0.740–0.852)	0.731 (0.663–0.788)	0.664 (0.594–0.727)	0.790 (0.726–0.841)
Gradient boosting	0.786 (0.722–0.838)	0.712 (0.644–0.771)	0.650 (0.580–0.714)	0.769 (0.703–0.822)
K neighbors	0.782 (0.718–0.834)	0.722 (0.654–0.780)	0.633 (0.562–0.698)	0.802 (0.739–0.852)
Gaussian NB	0.776 (0.711–0.829)	0.667 (0.597–0.730)	0.775 (0.710–0.828)	0.570 (0.499–0.638)
AdaBoost	0.769 (0.704–0.823)	0.708 (0.640–0.768)	0.679 (0.610–0.741)	0.734 (0.667–0.791)
XGB	0.758 (0.692–0.813)	0.677 (0.607–0.739)	0.639 (0.568–0.703)	0.711 (0.643–0.770)
Decision tree	0.630 (0.559–0.695)	0.630 (0.559–0.694)	0.630 (0.559–0.695)	0.629 (0.559–0.694)

TABLE 3 | Diagnostic performances to classify tumor shrinkage pattern in testing dataset of different models based on the type of features using the Multilayer Perception (MLP) neural network.

Model	AUC (95%CI)	Accuracy (95%CI)	Sensitivity (95%CI)	Specificity (95%CI)
$Model_{T1-DCE}$	0.712 (0.644–0.771)	0.644 (0.573–0.708)	0.489 (0.418–0.558)	0.783 (0.719–0.835)
$Model_{T2WI}$	0.661 (0.591–0.724)	0.606 (0.534–0.672)	0.562 (0.491–0.630)	0.645 (0.575–0.709)
$Model_{ADCmap}$	0.795 (0.732–0.846)	0.709 (0.641–0.768)	0.699 (0.630–0.759)	0.718 (0.650–0.777)
$Model_{Clinical}$	0.611 (0.540–0.677)	0.561 (0.489–0.629)	0.653 (0.582–0.716)	0.480 (0.410–0.550)
$Model_{Radiomics}$	0.900 (0.849–0.935)	0.828 (0.767–0.874)	0.788 (0.724–0.839)	0.864 (0.807–0.905)
$Model_{T1-DCE+Clinical}$	0.743 (0.676–0.799)	0.687 (0.618–0.748)	0.713 (0.644–0.771)	0.665 (0.595–0.727)
$Model_{T2WI+Clinical}$	0.708 (0.640–0.768)	0.649 (0.579–0.713)	0.627 (0.556–0.692)	0.670 (0.599–0.732)
$Model_{ADCmap+Clinical}$	0.809 (0.746–0.858)	0.729 (0.662–0.787)	0.699 (0.630–0.759)	0.757 (0.690–0.811)
$Model_{Radiomics+Clinical}$	0.939 (0.896–0.965)	0.870 (0.815–0.910)	0.840 (0.781–0.885)	0.897 (0.846–0.932)

TABLE 4 | Performance to classify tumor shrinkage pattern in three molecular subtypes.

Molecular subtype	Training dataset				Testing dataset			
	AUC (95%CI)	Accuracy (95%CI)	Sensitivity (95%CI)	Specificity (95%CI)	AUC (95%CI)	Accuracy (95%CI)	Sensitivity (95%CI)	Specificity (95%CI)
HR+/HER2-	0.999 (0.980–0.999)	0.991 (0.899–0.995)	0.999 (0.850–0.991)	0.986 (0.930–1.0)	0.901 (0.866–0.936)	0.816 (0.715–0.917)	0.729 (0.546–0.912)	0.883 (0.799–0.967)
HER+	0.999 (0.986–0.997)	0.987 (0.926–0.996)	0.997 (0.956–1.0)	0.980 (0.886–0.994)	0.940 (0.886–0.994)	0.865 (0.761–0.986)	0.912 (0.701–0.994)	0.799 (0.707–0.891)
TN	1.0 (0.913–1.0)	0.999 (0.767–0.967)	0.999 (0.688–1.0)	1.0 (0.773–1.0)	0.837 (0.699–0.975)	0.811 (0.614–0.993)	0.777 (0.456–0.993)	0.851 (0.558–0.996)

The Stability and Interpretability of Models

The differences in accuracy and AUC between the validation dataset in the inner loop and the testing dataset in the outer loop were calculated 30 times to assess the reproducibility of the results. There are no significant difference in AUC and accuracy between the outer loop and inner loop (**Figures 6**, **7**), so we considered that the results of our models are stabilized and representative. To evaluate the feature importance and predictive workflow of our model, the SHapley Additive exPlanations (SHAP) values were calculated (Rodríguez-Pérez and Bajorath, 2020a,b). The mean SHAP value of each feature was summarized based on its weight importance to the model, which calculated the number of times a feature was used to split the dataset in the model. For the prediction of tumor shrinkage pattern, each selected feature had a significant impact on the model output. **Figure 8** lists the weight importance

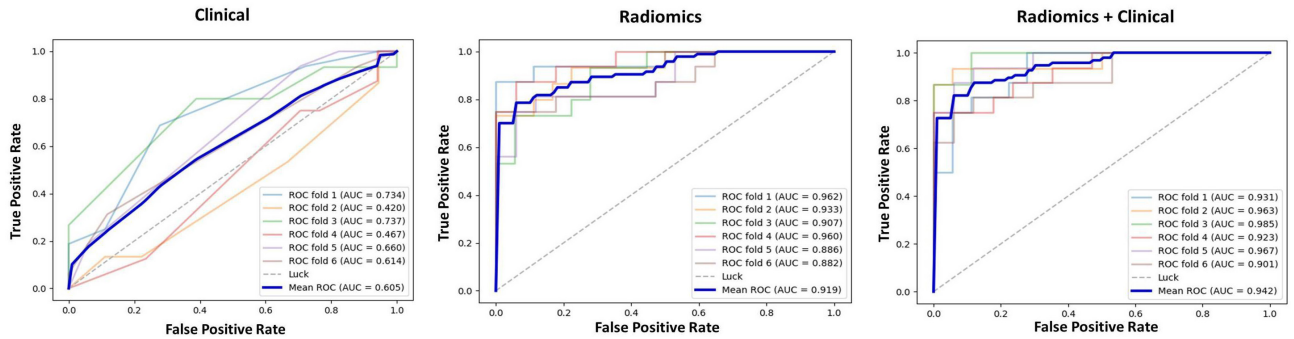

FIGURE 4 | Receiver operating characteristic (ROC) curves of clinical prediction model, radiomics prediction model, and combined prediction model in testing dataset for 1-round cross-validation.

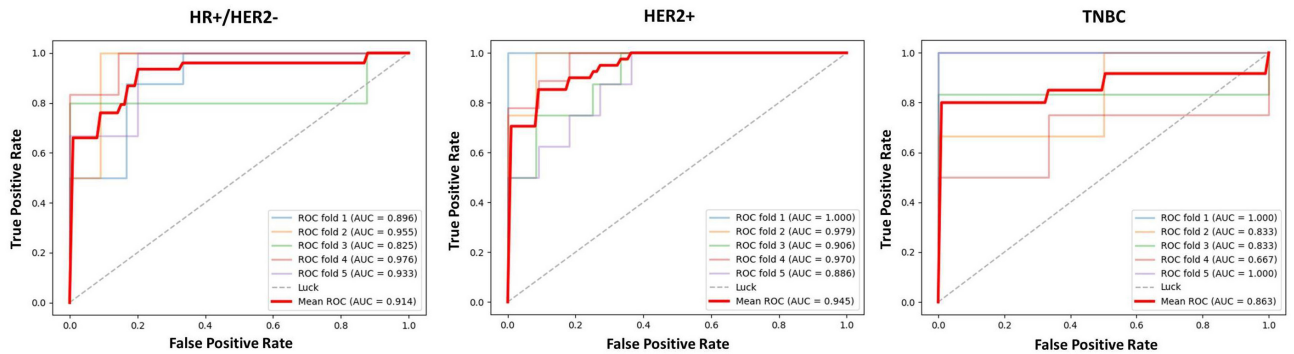

FIGURE 5 | The ROC curves of prediction model based on three molecular subtypes in testing dataset for 1-round cross-validation.

rank of the total features. **Figure 9** shows the decision curve reflecting how each feature affects the predictive output for the patients in the testing dataset (i.e., one round of classical splitting method with a ratio of 7:3). The baseline SHAP value was set as 0, and in the workflow of our model, each feature has a positive or negative impact on the final output value. When the output value was over 0, the patient was considered achieving type 1 shrinkage pattern after NACT, and when the value was <0, type 2 shrinkage pattern was more likely considered.

DISCUSSION

As there is an increasing need for BCS in patients with breast cancer, the accurate evaluation of tumor shrinkage patterns prior to NACT in a non-invasive way is essential. The aim of this study was to investigate the relationship among tumor shrinkage patterns, clinicopathologic characteristics, and MRI-derived radiomics features. We aimed to develop a model to assess tumor shrinkage patterns prior to NACT. The radiomics method could improve the diagnostic accuracy of MRI for tumor response to NACT. Enabling the prediction of tumor shrinkage pattern prior to treatment would help determine the feasibility of BCS and may lead to alterations in chemotherapy regimen or performing surgery earlier than initially planned.

The NACT benefits those patients who are willing to have BCS but the tumor size is large and not suitable for the surgery (Hennessy et al., 2005; Mathew et al., 2009; Mougalian et al., 2016). Wolmark et al. have reported that the ipsilateral recurrence rate of patients treated with BCS after NACT was 10.7%, and the rates were 7.6% in patients with primary tumors fit for BCS and 15.9% in patients with primary breast cancer unfit for BCS (Wolmark et al., 2001). Tumor downstaged by NACT and followed by BCS has a higher local recurrence rate than the primary tumor and is fit for BCS, which may be a result of incomplete resection of cancer cells. It has been clearly indicated that a clear surgical margin is essential to decrease the local recurrence rate. In clinical practice, however, the current criteria for the evaluation of tumor response, the RECIST 1.1, are used extensively to assess tumor response to NACT, but it cannot identify those patients with tumor concentric shrinkage (Chalian et al., 2011; Schwartz et al., 2016).

The MRI examination can accurately show the morphology and extent of breast cancer, and it guides surgical decisions to ensure a negative surgical margin. Several studies have divided tumor shrinkage into concentric shrinkage and dendritic shrinkage based on the MRI examination (Wang et al., 2013;

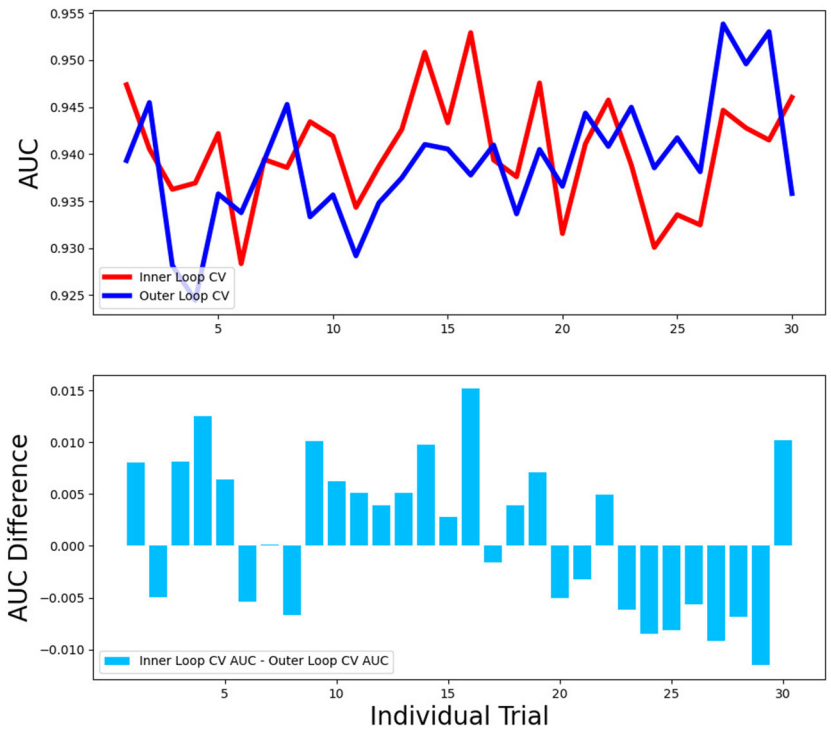

FIGURE 6 | The AUC between the validation dataset in the inner loop and testing dataset in the outer loop for 30-round cross-validation.

Ballesio et al., 2017; Fukada et al., 2018; Goorts et al., 2018; Zhang et al., 2018; Zhuang et al., 2020). According to earlier studies, after NACT, about 70% of residual tumors were concentric and 30% were dendritic in MRI images. Post-NACT tumors that showed pCR and concentric shrinkage were easier to obtain negative surgical margins, so those patients were the candidates of BCS (Chen et al., 2004). In general, the tumor that shows dendritic shrinkage has multicentric and discontinuous residual tumor, which can cause postoperative local recurrence and metastasis, so it is unfit for BCS. However, some solitary residual tumors may be missed by conventional histological sections, and negative margins are still observed in surgical specimens. Favorable tumor shrinkage patterns, such as pCR and concentric shrinkage tumor after NACT, were included in the standards for BCS, while patients with poor shrinkage pattern show either multifocal residual tumors or no significant decline in tumor size. The post-NACT pCR is more difficult to obtain in luminal breast cancer than other subtypes, and dendritic shrinkage and mixed shrinkage are also more common in the luminal subtype. The accurate assessment of tumor shrinkage pattern can help in choosing an optimal treatment option for patients. To find patients suitable for BCS, our study divided the tumor shrinkage patterns into two types as well. Patients with type 1 shrinkage pattern showed an adequate response to NACT, with tumor complete remission or a significant decline in size. In our study, the percentages of type 1 shrinkage pattern in three subtypes were as follows: HR+/HER2– (45.5%), HER2+ (58.6%), and TN (50%). Consistent with the earlier studies, the concentric shrinkage patterns were more likely to occur in patients with HER2+ and TN subtype tumors.

The assessment of tumor size using MRI during NACT is a good predictor of the tumor response to NACT. Loo et al. reported that MRI was useful to monitor tumor response during NACT and massive tumor regression was more easily observed in HER2+ and TN tumors than in HR+/HER2– tumors (Loo et al., 2011). In a meta-analysis of Yuan et al., MRI had high specificity (91%) and relatively low sensitivity (63%) in predicting pCR after NACT in patients with breast cancer (Yuan et al., 2010). Liu et al. had reported that a radiomics model combining T1-DCE, DWI, and T2WI images had a great performance to predict the tumor response to NACT and achieved an AUC of 0.71–0.80 in the testing cohort, but the literature did not identify those patients with concentric shrinkage after NACT (Liu et al., 2019). Zhuang et al. established a nomogram to predict the tumor regression pattern using T2WI, DWI sequences, and clinical factors, and their model achieved an AUC of 0.826 in the testing cohort (Zhuang et al., 2020). Some studies have shown that the radiomics models had diagnostic value in tumor response to NACT, and most of the literature aimed to distinguish

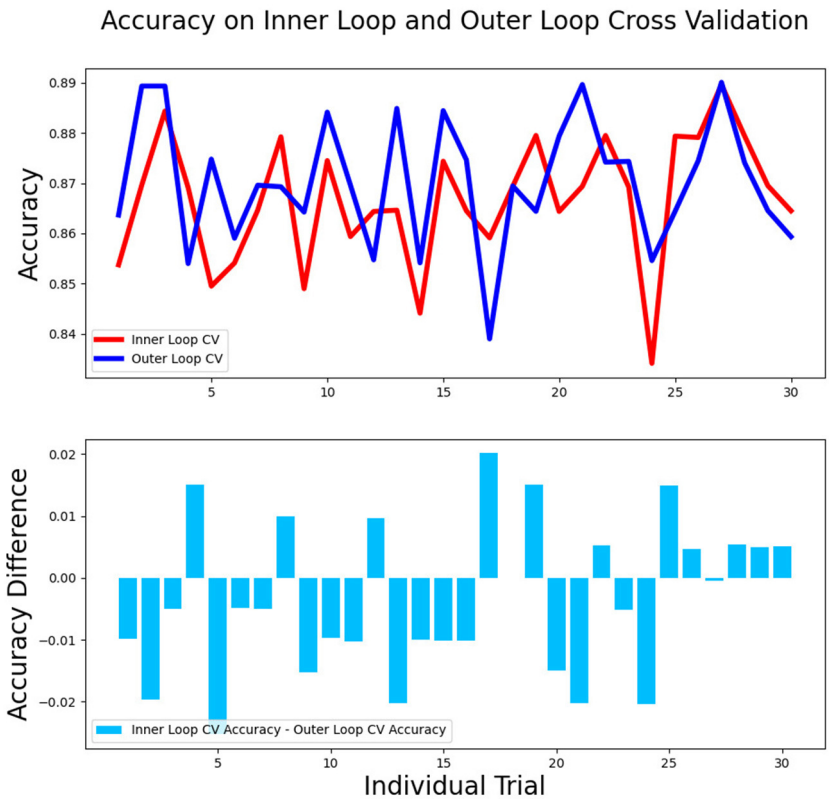

FIGURE 7 | The accuracy between the validation dataset in the inner loop and testing dataset in the outer loop for 30-round cross-validation.

pCR and non-pCR (Antunovic et al., 2019; Liu et al., 2019; Li et al., 2020; Zhuang et al., 2020). Fukada et al. reported that the shrinkage pattern at MRI during NACT was the significant independent predictor and the radiomics features based on MRI had closer associations with the risk of recurrence and prognosis in low-grade early-stage luminal breast cancer (Fukada et al., 2018). Assessing tumor response to NACT has been reported, which could predict the prognosis of patients with luminal breast cancer. Richard et al. found that the patients with breast cancer with a high pretreatment ADC in DWI were more likely to respond completely to NACT (Richard et al., 2013). From the earlier studies in the literature, we knew that mpMRI had the potential in assessing tumor shrinkage pattern, so in our study, we extracted radiomics features from three MRI sequences (i.e., T1-DCE, T2WI, and ADC map), and we also added the clinicopathologic characteristics into the feature set.

The radiomics method offers the great potential to identify the tumor shrinkage pattern prior to NACT, whereas the clinical characteristics provide limited information about the tumor. There continues to face a challenge for the success of BCS, and there is still a lack of effective methods to assess the tumor response during NACT and risk of local recurrence postoperatively. In our study, after the feature selection, 50 features, including the clinicopathologic characteristics and the radiomics features from MRI were selected to develop the machine learning model. The mean AUC of the $Model_{Clinical}$ in the testing set was 0.611 (95% CI: 0.540–0.677), while the result of $Model_{Radiomics}$ was 0.900 (95% CI: 0.849–0.935), and when combining the clinicopathologic characteristics with radiomics features, the result could rise to 0.939 (95% CI of the $Model_{Radiomics+Clinical}$: 0.896–0.965). We also found that when combining the clinical characteristics with radiomics features, the model had a more stable performance with a lower SD. Our radiomics model that combined the clinical and radiomics features might provide a more accurate assessment for tumor shrinkage pattern prior to NACT treatment and is worthy of further study.

This study has some limitations. First, our study was based on a retrospective design and the patient population is limited, and it is better if there are data from external institutions that could validate our model. Actually, NACT was mainly used in locally advanced breast cancer, and it spent several months of a patient to complete the standard NACT and followed surgery, so the patient population is limited in most studies. Second, the distribution of molecular subtypes was imbalanced due to less number of patients with TN breast cancer. But in the total population with breast cancer, the TN subtype occupied the lowest proportion, which could explain the imbalanced distribution of our patients. Third, only the pre-NACT MRI data were collected to construct models, and it is worthwhile to study further of the predictive potential to the tumor shrinkage

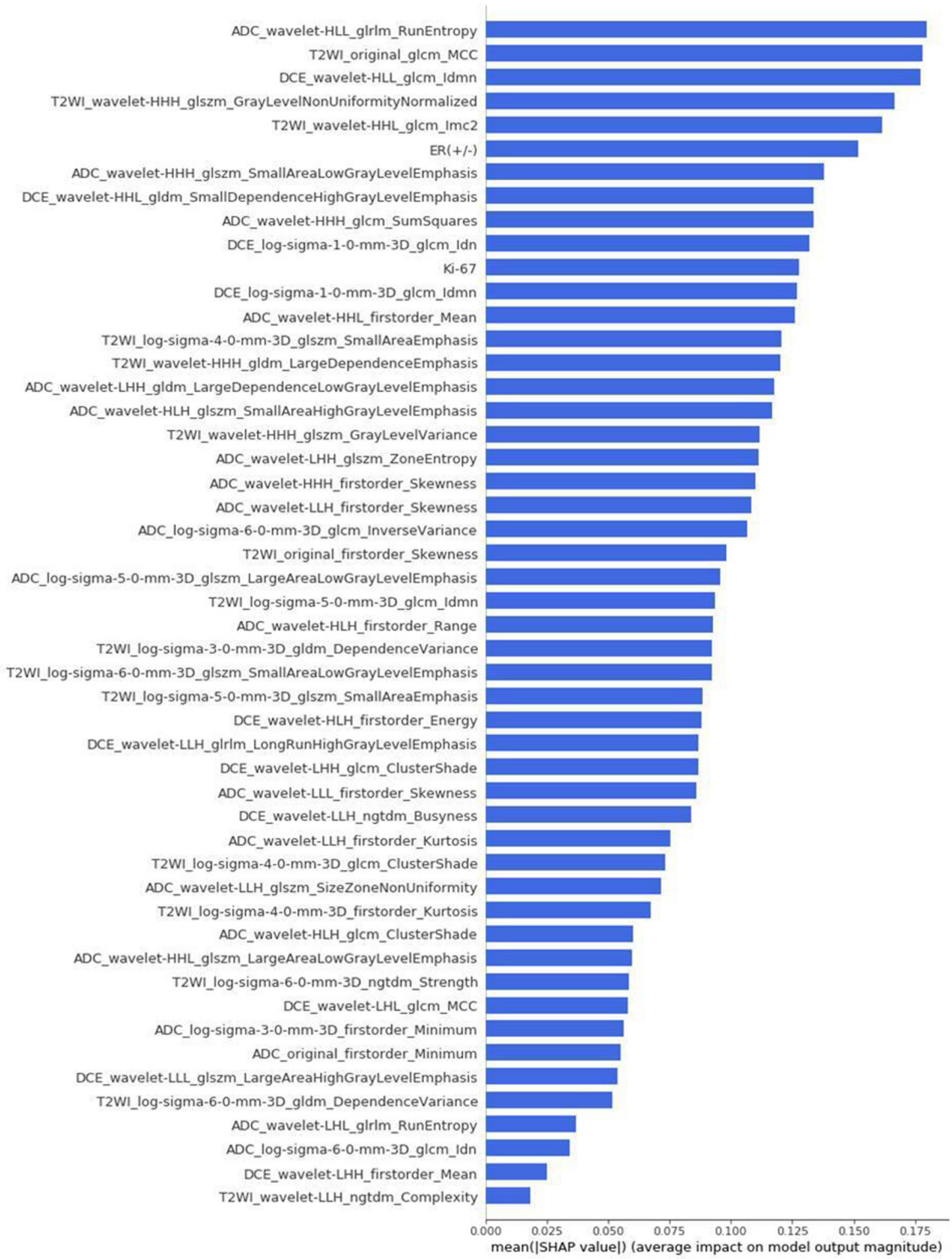

FIGURE 8 | The weight importance rank of selected features. The feature with a longer bar contributes more to the model.

patterns based on the sequential MRI examination during NACT. Delta-radiomics that combines pre-NACT with the early-NACT MRI data could provide tumor response information in the early stage of treatment, and that combines pre-NACT with the post-NACT MRI data could help distinguish pCR from radial complete response.

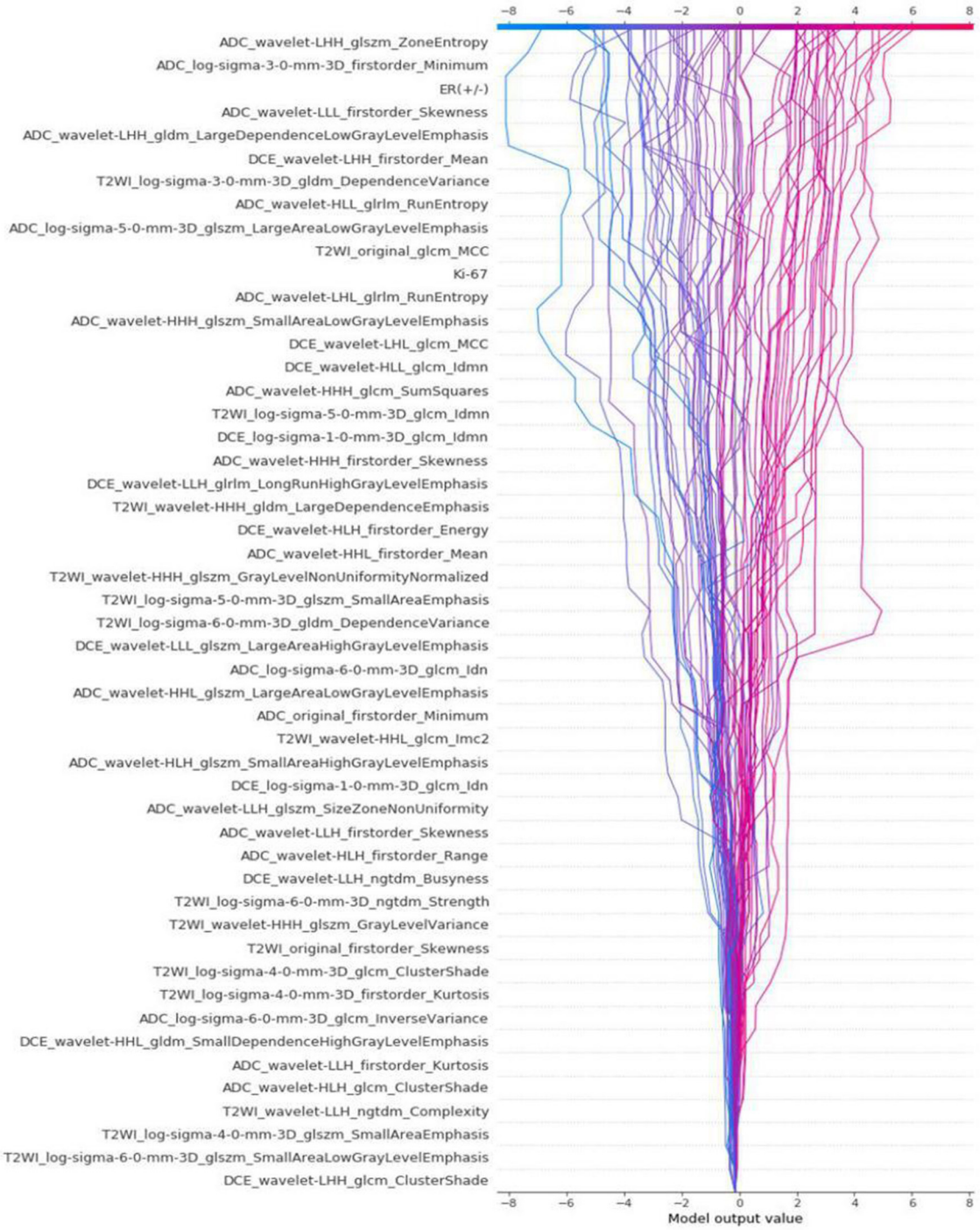

FIGURE 9 | The decision curve that reflects how each feature affects the predictive output for the patients in testing dataset by classical splitting with a ratio of 7:3.

CONCLUSIONS

We constructed a model combining clinicopathologic characteristics and radiomics features to accurately predict tumor shrinkage pattern prior to NACT using the mpMRI data. The model performed well in different molecular subtypes, and this early prediction model can help clinicians make a clinical decision with the potential to evaluate the feasibility of BCS after effective chemotherapy. Further multicenter study with larger datasets could improve our prediction model and

explore the potential for clinical application to the wider regions and population.

DATA AVAILABILITY STATEMENT

The datasets presented in this article are not readily available because of the privacy of patients and the huge amount of MRI data. Requests to access the datasets should be directed to linying3@mail.sysu.edu.cn.

ETHICS STATEMENT

The studies involving human participants were reviewed and approved by the Institutional Ethics Review Board of the first affiliated hospital of Sun Yat-sen University. The patients/participants provided their written informed consent to participate in this study.

AUTHOR CONTRIBUTIONS

YH contributed to concept development, study management, data curation, literature searching, and writing the original draft. WC contributed to the study management, literature searching, methodology, software using, and language editing. XZ contributed to the analysis of breast imaging and writing the original draft. SH contributed to the data curation, imaging processing, and methodology. NS contributed to the concept development, study management, and writing the original draft. HS contributed to the analysis of pathology. ZL contributed to the statistical analysis and writing statistics section of the manuscript. XW and TL contributed to the data curation. HL and YL contributed to the concept development, funding acquisition, and writing the original draft. All authors contributed to the critical review and approved the submitted version of the article.

FUNDING

This study was funded by the Sun Yat-sen University Clinical Research 5010 Program (2016007). The funder played no role in determining the content of the manuscript or in the decision regarding whether to submit the manuscript for publication.

SUPPLEMENTARY MATERIAL

The Supplementary Material for this article can be found online at: https://www.frontiersin.org/articles/10.3389/fbioe.2021.662749/full#supplementary-material

REFERENCES

Aerts, H. J., Velazquez, E. R., Leijenaar, R. T., Parmar, C., Grossmann, P., Carvalho, S., et al. (2014). Decoding tumour phenotype by noninvasive imaging using a quantitative radiomics approach. *Nat. Commun.* 5:4006. doi: 10.1038/ncomms5644

Antunovic, L., De Sanctis, R., Cozzi, L., Kirienko, M., Sagona, A., Torrisi, R., et al. (2019). PET/CT radiomics in breast cancer: promising tool for prediction of pathological response to neoadjuvant chemotherapy. *Eur. J. Nucl. Med. Mol. Imaging* 46, 1468–1477. doi: 10.1007/s00259-019-04313-8

Ballesio, L., Gigli, S., Di Pastena, F., Giraldi, G., Manganaro, L., Anastasi, E., et al. (2017). Magnetic resonance imaging tumor regression shrinkage patterns after neoadjuvant chemotherapy in patients with locally advanced breast cancer: correlation with tumor biological subtypes and pathological response after therapy. *Tumour Biol.* 39:1010428317694540. doi: 10.1177/1010428317694540

Chalian, H., Töre, H. G., Horowitz, J. M., Salem, R., Miller, F. H., and Yaghmai, V. (2011). Radiologic assessment of response to therapy: comparison of RECIST Versions 1.1 and 1.0. *Radiographics* 31, 2093–2105. doi: 10.1148/rg.317115050

Chen, A. M., Meric-Bernstam, F., Hunt, K. K., Thames, H. D., Oswald, M. J., Outlaw, E. D., et al. (2004). Breast conservation after neoadjuvant chemotherapy: the MD Anderson cancer center experience. *J. Clin. Oncol.* 22, 2303–2312. doi: 10.1200/JCO.2004.09.062

Chen, J. H., Bahri, S., Mehta, R. S., Carpenter, P. M., McLaren, C. E., Chen, W. P., et al. (2014). Impact of factors affecting the residual tumor size diagnosed by MRI following neoadjuvant chemotherapy in comparison to pathology. *J. Surg. Oncol.* 109, 158–167. doi: 10.1002/jso.23470

Cheng, G. Z., San Jose Estepar, R., Folch, E., Onieva, J., Gangadharan, S., and Majid, A. (2016). Three-dimensional printing and 3D slicer: powerful tools in understanding and treating structural lung disease. *Chest* 149, 1136–1142. doi: 10.1016/j.chest.2016.03.001

Cortazar, P., Zhang, L., Untch, M., Mehta, K., Costantino, J. P., Wolmark, N., et al. (2014). Pathological complete response and long-term clinical benefit in breast cancer: the CTNeoBC pooled analysis. *Lancet* 384, 164–172. doi: 10.1016/S0140-6736(13)62422-8

Curigliano, G., Burstein, H. J., E. P. W., Gnant, M., Dubsky, P., Loibl, S., et al. (2019). De-escalating and escalating treatments for early-stage breast cancer: the St. Gallen International expert consensus conference on the primary therapy of early breast cancer 2017. *Ann. Oncol.* 30:1181. doi: 10.1093/annonc/mdz235

Eom, H. J., Cha, J. H., Choi, W. J., Chae, E. Y., Shin, H. J., and Kim, H. H. (2017). Predictive clinicopathologic and dynamic contrast-enhanced MRI findings for tumor response to neoadjuvant chemotherapy in triple-negative breast cancer. *AJR Am. J. Roentgenol.* 208, W225–W230. doi: 10.2214/AJR.16.17125

Fedorov, A., Beichel, R., Kalpathy-Cramer, J., Finet, J., Fillion-Robin, J. C., Pujol, S., et al. (2012). 3D Slicer as an image computing platform for the Quantitative Imaging Network. *Magn. Reson. Imaging* 30, 1323–1341. doi: 10.1016/j.mri.2012.05.001

Fukada, I., Araki, K., Kobayashi, K., Shibayama, T., Takahashi, S., Gomi, N., et al. (2018). Pattern of tumor shrinkage during neoadjuvant chemotherapy is associated with prognosis in low-grade luminal early breast cancer. *Radiology* 286, 49–57. doi: 10.1148/radiol.2017161548

Giuliano, A. E., Edge, S. B., and Hortobagyi, G. N. (2018). Eighth edition of the AJCC cancer staging manual: breast cancer. *Ann. Surg. Oncol.* 25, 1783–1785. doi: 10.1245/s10434-018-6486-6

Goetz, M. P., Gradishar, W. J., Anderson, B. O., Abraham, J., Aft, R., Allison, K. H., et al. (2019). NCCN guidelines insights: breast cancer, version 3.2018. *J. Natl. Compreh. Cancer Network* 17, 118–126. doi: 10.6004/jnccn.2019.0009

Goorts, B., Dreuning, K. M. A., Houwers, J. B., Kooreman, L. F. S., Boerma, E. G., Mann, R. M., et al. (2018). MRI-based response patterns during neoadjuvant chemotherapy can predict pathological (complete) response in patients with breast cancer. *Breast Cancer Res.* 20:34. doi: 10.1186/s13058-018-0950-x

Goorts, B., van Nijnatten, T. J., de Munck, L., Moossdorff, M., Heuts, E. M., de Boer, M., et al. (2017). Clinical tumor stage is the most important predictor of pathological complete response rate after neoadjuvant chemotherapy in breast cancer patients. *Breast Cancer Res. Treat.* 163, 83–91. doi: 10.1007/s10549-017-4155-2

Hammond, M. E., Hayes, D. F., Dowsett, M., Allred, D. C., Hagerty, K. L., Badve, S., et al. (2010). American Society of Clinical Oncology/College Of American Pathologists guideline recommendations for immunohistochemical testing of estrogen and progesterone receptors in breast cancer. *J. Clin. Oncol.* 28, 2784–2795. doi: 10.1200/JCO.2009.25.6529

Hennessy, B. T., Hortobagyi, G. N., Rouzier, R., Kuerer, H., Sneige, N., Buzdar, A. U., et al. (2005). Outcome after pathologic complete eradication of cytologically proven breast cancer axillary node metastases following primary chemotherapy. *J. Clin. Oncol.* 23, 9304–9311. doi: 10.1200/JCO.2005.02.5023

Hylton, N. M., Blume, J. D., Bernreuter, W. K., Pisano, E. D., Rosen, M. A., Morris, E. A., et al. (2012). Locally advanced breast cancer: MR imaging for prediction of response to neoadjuvant chemotherapy–results from ACRIN 6657/I-SPY TRIAL. *Radiology* 263,663–672. doi: 10.1148/radiol.12110748

Kong, X., Moran, M. S., Zhang, N., Haffty, B., and Yang, Q. (2011). Meta-analysis confirms achieving pathological complete response after neoadjuvant chemotherapy predicts favourable prognosis for breast cancer patients. *Europ. J. Cancer* 47, 2084–2090. doi: 10.1016/j.ejca.2011.06.014

Lambin, P., Rios-Velazquez, E., Leijenaar, R., Carvalho, S., van Stiphout, R. G., Granton, P., et al. (2012). Radiomics: extracting more information from medical images using advanced feature analysis. *Europ. J. Cancer* 48, 441–446. doi: 10.1016/j.ejca.2011.11.036

Li, P., Wang, X., Xu, C., Liu, C., Zheng, C., Fulham, M. J., et al. (2020). (18)F-FDG PET/CT radiomic predictors of pathologic complete response (pCR) to neoadjuvant chemotherapy in breast cancer patients. *Eur. J. Nucl. Med. Mol. Imaging* 47, 1116–1126. doi: 10.1007/s00259-020-04684-3

Liu, Z., Li, Z., Qu, J., Zhang, R., Zhou, X., Li, L., et al. (2019). Radiomics of Multiparametric MRI for pretreatment prediction of pathologic complete response to neoadjuvant chemotherapy in breast cancer: a multicenter study. *Clin. Cancer Res.* 25, 3538–3547. doi: 10.1158/1078-0432.CCR-18-3190

Lobbes, M. B., Prevos, R., Smidt, M., Tjan-Heijnen, V. C., van Goethem, M., Schipper, R., et al. (2013). The role of magnetic resonance imaging in assessing residual disease and pathologic complete response in breast cancer patients receiving neoadjuvant chemotherapy: a systematic review. *Insights Imaging* 4, 163–175. doi: 10.1007/s13244-013-0219-y

Loo, C. E., Straver, M. E., Rodenhuis, S., Muller, S. H., Wesseling, J., Vrancken Peeters, M. J., et al. (2011). Magnetic resonance imaging response monitoring of breast cancer during neoadjuvant chemotherapy: relevance of breast cancer subtype. *J. Clin. Oncol.* 29, 660–666. doi: 10.1200/JCO.2010.31.1258

Loo, C. E., Teertstra, H. J., Rodenhuis, S., van de Vijver, M. J., Hannemann, J., Muller, S. H., et al. (2008). Dynamic contrast-enhanced MRI for prediction of breast cancer response to neoadjuvant chemotherapy: initial results. *AJR Am. J. Roentgenol.* 191, 1331–1338. doi: 10.2214/AJR.07.3567

Manton, D. J., Chaturvedi, A., Hubbard, A., Lind, M. J., Lowry, M., Maraveyas, A., et al. (2006). Neoadjuvant chemotherapy in breast cancer: early response prediction with quantitative MR imaging and spectroscopy. *Br. J. Cancer* 94, 427–435. doi: 10.1038/sj.bjc.6602948

Mathew, J., Asgeirsson, K. S., Cheung, K. L., Chan, S., Dahda, A., and Robertson, J. F. (2009). Neoadjuvant chemotherapy for locally advanced breast cancer: a review of the literature and future directions. *Europ. J. Surg. Oncol.* 35, 113–122. doi: 10.1016/j.ejso.2008.03.015

Mougalian, S. S., Hernandez, M., Lei, X., Lynch, S., Kuerer, H. M., Symmans, W. F., et al. (2016). Ten-year outcomes of patients with breast cancer with cytologically confirmed axillary lymph node metastases and pathologic complete response after primary systemic chemotherapy. *JAMA Oncol.* 2, 508–516. doi: 10.1001/jamaoncol.2015.4935

Padhani, A. R., Hayes, C., Assersohn, L., Powles, T., Makris, A., Suckling, J., et al. (2006). Prediction of clinicopathologic response of breast cancer to primary chemotherapy at contrast-enhanced MR imaging: initial clinical results. *Radiology* 239, 361–374. doi: 10.1148/radiol.2392021099

Pickles, M. D., Lowry, M., Manton, D. J., Gibbs, P., and Turnbull, L. W. (2005). Role of dynamic contrast enhanced MRI in monitoring early response of locally advanced breast cancer to neoadjuvant chemotherapy. *Breast Cancer Res. Treat.* 91, 1–10. doi: 10.1007/s10549-004-5819-2

Richard, R., Thomassin, I., Chapellier, M., Scemama, A., de Cremoux, P., Varna, M., et al. (2013). Diffusion-weighted MRI in pretreatment prediction of response to neoadjuvant chemotherapy in patients with breast cancer. *Eur. Radiol.* 23, 2420–2431. doi: 10.1007/s00330-013-2850-x

Rodríguez-Pérez, R., and Bajorath, J. (2020a). Interpretation of compound activity predictions from complex machine learning models using local approximations and shapley values. *J. Med. Chem.* 63, 8761–8777. doi: 10.1021/acs.jmedchem.9b01101

Rodríguez-Pérez, R., and Bajorath, J. (2020b). Interpretation of machine learning models using shapley values: application to compound potency and multi-target activity predictions. *J. Comput. Aided Mol. Des.* 34, 1013–1026. doi: 10.1007/s10822-020-00314-0

Schwartz, L. H., Litière, S., de Vries, E., Ford, R., Gwyther, S., Mandrekar, S., et al. (2016). RECIST 1.1-Update and clarification: From the RECIST committee. *Europ. J. Cancer* 62, 132–137. doi: 10.1016/j.ejca.2016.03.081

van Griethuysen, J. J. M., Fedorov, A., Parmar, C., Hosny, A., Aucoin, N., Narayan, V., et al. (2017). Computational radiomics system to decode the radiographic phenotype. *Cancer Res.* 77, e104–e7. doi: 10.1158/0008-5472.CAN-17-0339

Wang, S., Zhang, Y., Yang, X., Fan, L., Qi, X., Chen, Q., et al. (2013). Shrink pattern of breast cancer after neoadjuvant chemotherapy and its correlation with clinical pathological factors. *World J. Surg. Oncol.* 11:166. doi: 10.1186/1477-7819-11-166

Wolff, A. C., Hammond, M. E., Hicks, D. G., Dowsett, M., McShane, L. M., Allison, K. H., et al. (2013). Recommendations for human epidermal growth factor receptor 2 testing in breast cancer: American Society of Clinical Oncology/College of American Pathologists clinical practice guideline update. *J. Clin. Oncol.* 31, 3997–4013. doi: 10.1200/JCO.2013.50.9984

Wolmark, N., Wang, J., Mamounas, E., Bryant, J., and Fisher, B. (2001). Preoperative chemotherapy in patients with operable breast cancer: nine-year results from National Surgical Adjuvant Breast and Bowel Project B.- 18. *J. Natl. Cancer Inst. Monographs* 96–102. doi: 10.1093/oxfordjournals.jncimonographs.a003469

Yip, S. S., and Aerts, H. J. (2016). Applications and limitations of radiomics. *Phys. Med. Biol.* 61, R150–R166. doi: 10.1088/0031-9155/61/13/R150

Yuan, Y., Chen, X. S., Liu, S. Y., and Shen, K. W. (2010). Accuracy of MRI in prediction of pathologic complete remission in breast cancer after preoperative therapy: a meta-analysis. *AJR Am. J. Roentgenol.* 195, 260–268. doi: 10.2214/AJR.09.3908

Zhang, D., Zhang, Q., Suo, S., Zhuang, Z., Li, L., Lu, J., et al. (2018). Apparent diffusion coefficient measurement in luminal breast cancer: will tumour shrinkage patterns affect its efficacy of evaluating the pathological response? *Clin. Radiol.* 73, 909.e7–.e14. doi: 10.1016/j.crad.2018.05.026

Zheng, X., Yao, Z., Huang, Y., Yu, Y., Wang, Y., Liu, Y., et al. (2020). Deep learning radiomics can predict axillary lymph node status in early-stage breast cancer. *Nat. Commun.* 11:1236. doi: 10.1038/s41467-020-15027-z

Zhuang, X., Chen, C., Liu, Z., Zhang, L., Zhou, X., Cheng, M., et al. (2020). Multiparametric MRI-based radiomics analysis for the prediction of breast tumor regression patterns after neoadjuvant chemotherapy. *Transl. Oncol.* 13:100831. doi: 10.1016/j.tranon.2020.100831

Zwanenburg, A., Vallières, M., Abdalah, M. A., Aerts, H., Andrearczyk, V., Apte, A., et al. (2020). The image biomarker standardization initiative: standardized quantitative radiomics for high-throughput image-based phenotyping. *Radiology* 295, 328–338. doi: 10.1148/radiol.2020191145

Conflict of Interest: The authors declare that the research was conducted in the absence of any commercial or financial relationships that could be construed as a potential conflict of interest.

frontiers in Bioengineering and Biotechnology

ORIGINAL RESEARCH
published: 14 July 2021
doi: 10.3389/fbioe.2021.696251

MBFFNet: Multi-Branch Feature Fusion Network for Colonoscopy

Houcheng Su[1†], Bin Lin[1†], Xiaoshuang Huang[1†], Jiao Li[1], Kailin Jiang[2] and Xuliang Duan[1]*

[1] College of Information Engineering, Sichuan Agricultural University, Ya'an, China, [2] College of Science, Sichuan Agricultural University, Ya'an, China

Colonoscopy is currently one of the main methods for the detection of rectal polyps, rectal cancer, and other diseases. With the rapid development of computer vision, deep learning–based semantic segmentation methods can be applied to the detection of medical lesions. However, it is challenging for current methods to detect polyps with high accuracy and real-time performance. To solve this problem, we propose a multi-branch feature fusion network (MBFFNet), which is an accurate real-time segmentation method for detecting colonoscopy. First, we use UNet as the basis of our model architecture and adopt stepwise sampling with channel multiplication to integrate features, which decreases the number of flops caused by stacking channels in UNet. Second, to improve model accuracy, we extract features from multiple layers and resize feature maps to the same size in different ways, such as up-sampling and pooling, to supplement information lost in multiplication-based up-sampling. Based on mIOU and Dice loss with cross entropy (CE), we conduct experiments in both CPU and GPU environments to verify the effectiveness of our model. The experimental results show that our proposed MBFFNet is superior to the selected baselines in terms of accuracy, model size, and flops. mIOU, *F* score, and Dice loss with CE reached 0.8952, 0.9450, and 0.1602, respectively, which were better than those of UNet, UNet++, and other networks. Compared with UNet, the flop count decreased by 73.2%, and the number of participants also decreased. The actual segmentation effect of MBFFNet is only lower than that of PraNet, the number of parameters is 78.27% of that of PraNet, and the flop count is 0.23% that of PraNet. In addition, experiments on other types of medical tasks show that MBFFNet has good potential for general application in medical image segmentation.

Keywords: multi-branch feature, fusion network, colonoscopy, medical image segmentation, MBFFNet

OPEN ACCESS

Edited by:
Zhiwei Luo,
Kobe University, Japan

Reviewed by:
Atif Mehmood,
Xidian University, China
Shuwan Pan,
Huaqiao University, China

****Correspondence:***
Xuliang Duan
duanxuliang@sicau.edu.cn

† These authors have contributed equally to this work and share first authorship

Specialty section:
This article was submitted to Bionics and Biomimetics, a section of the journal Frontiers in Bioengineering and Biotechnology

Received: *16 April 2021*
Accepted: *25 May 2021*
Published: *14 July 2021*

Citation:
Su H, Lin B, Huang X, Li J, Jiang K and Duan X (2021) MBFFNet: Multi-Branch Feature Fusion Network for Colonoscopy. Front. Bioeng. Biotechnol. 9:696251. doi: 10.3389/fbioe.2021.696251

INTRODUCTION

Medical image processing is an important part of medical processes. At present, the main research directions in medical image processing include image segmentation, structure analysis, and image recognition. Among these, image segmentation is very important for the detection of lesions and organs, which significantly aids the development of medical automation, reduces the burden on medical workers, and reduces the incidence of medical accidents caused by human error (Litjens et al., 2017). In 2018, there were an estimated 4.8 million new cases of gastrointestinal (GI) cancers

and 3.4 million related deaths worldwide. GI cancers account for 26% of the global cancer incidence and 35% of all cancer-related deaths (Arnold et al., 2020). Endoscopy is the gold standard for GI examinations (Deeba et al., 2019; Li et al., 2021). Gastroscopy is an examination of the upper digestive tract, which includes the esophagus, stomach, and the first part of the small intestine, whereas colonoscopy covers the large intestine (colon) and rectum. Both tests involve the real-time viewing of the GI tract using a digital high-definition endoscope. Endoscopy is resource-intensive and requires expensive technical equipment and trained personnel (Pogorelov et al., 2017). Both endoscopy and the removal of potentially pre-cancerous lesions are essential for the prevention of colorectal cancer. The semantic segmentation method of artificial intelligence can be used to assist colonoscopy detection, which can significantly reduce the risk of misjudgment and the omission of medical workers for various reasons, resulting in polyp canceration, colorectal tumor lesions, and colorectal cancer from early to late stages, as well as delayed treatment (Akbari et al., 2018). It is thus important to achieve early prevention, early detection, and early treatment. A large number of experimental studies have shown that early colonoscopy can reduce the incidence of colorectal cancer by 30% (Haggar and Boushey, 2009). In clinical medical treatment, the accurate real-time segmentation of polyps is a challenging task. First, the same type of polyp may be due to different stages of colorectal cancer and may have a different constitution. In addition, there may be different sizes, shapes, and colors, which affects the actual segmentation result (Nguyen et al., 2020). Second, because polyps and surrounding mucosa possess similar characteristics, it is difficult to segment the boundary clearly, and commonly employed segmentation method cannot obtain ideal segmentation results (Ganz et al., 2012; Bernal et al., 2014). Third, owing to the specific nature of medical images, it is often difficult to achieve high accuracy and fast speed simultaneously. Therefore, commonly used medical image segmentation model often ignores the size of the model while ensuring accuracy, resulting in an oversized model and slow segmentation speed; it is thus unable to provide real-time segmentation for colonoscopy (Bernal et al., 2012, 2015). Therefore, in medical automation and to achieve the early prevention of colorectal cancer, it is important to propose a method that segments polyps with sufficient accuracy to prevent the missed detection of polyps and to ensure that the model will not be too bloated, leading to slow speed.

Based on the machine algorithm of manually extracted features, features such as color, shape, and appearance have been applied to the classifier to detect polyps (Armato et al., 2017). Because of the limitation of the expression ability of manually extracted features, sufficient features cannot be effectively obtained for classifier classification (Breier et al., 2011), and there is a high rate of missed detection, which cannot be effectively applied to accurately segment polyps. However, based on the depth study of the semantic segmentation method of the polyp segmentation method, there has been good progress so far. Armato et al. (2017) used the FCN8 (Long et al., 2015) semantic segmentation model to split polyps, but because FCN8 cannot effectively retain low-dimension detail characteristics, it cannot effectively segment polyps and membranes around the border, so the use of FCN8 polyp segmentation is mistakenly identified and residual (Xia, 2020). Other semantic segmentation models are applied to life scenarios, such as PSPNET (Zhao et al., 2017), and although they use a feature pyramid, retain as many low-dimensional features as possible, and improve the boundary extraction effect of FCN8, they still fail to meet the requirements of precision medicine. Meanwhile, other models, such as Deeplabv3 (Chen et al., 2017), Deeplabv3+ (Chen et al., 2018), LinkNet (Chaurasia and Culurciello, 2018), and FPN (Lin et al., 2017), all have similar problems. In UNet (Ronneberger et al., 2015), UNet++ (Zhou et al., 2018, 2020), ResUNet++ (Jha et al., 2019), and U^2Net (Qin et al., 2020), which are medical image segmentation models, the adoption of more detailed features has a good effect on the polyp boundary segmentation, but these methods with the characteristics of the UNet (Ronneberger et al., 2015) method to keep figure overlay information, model and quantity, and flop count are inevitable. In real-time polyp segmentation, there is still a disadvantage in that it is unable to meet real-time requirements. Fang et al. (2019) proposed a three-step selective feature aggregation network with area and boundary constraints, which was applied to the precise segmentation of polyps. Because the relationship between the area and boundary was considered in this network, excellent segmentation results were obtained. However, the PraNet (Fan et al., 2020) model proposed by Fan et al. (2020) adopted the reverse attention method and achieved excellent results in polyp segmentation. However, it aimed to achieve segmentation that was too precise, resulting in a large flow count, which could not be applied to general computer applications and could not be popularized on a large scale.

In this study, to better achieve the precise real-time segmentation task of polyps and considering these problems, we developed the following strategies:

(1) Avoid the loss of local low-dimensional features by large up-sampling directly, which leads to the loss of too many features on the segmenting boundary and the inability to restore complete edge information.
(2) Avoid superimposing feature information on channel dimensions only through feature maps to retain feature information, which will lead to an overbloated feature map in the last few layers of the feature map, resulting in the model requiring a large number of calculations.

Based on these strategies, we propose a multi-branching feature fusion network for polyp segmentation. We first propagated the context information to the higher-resolution layer through progressive up-sampling to obtain the preliminary polyp features. This method followed strategy 1, and we avoided the channel dimension superposition feature information of the UNet (Ronneberger et al., 2015) series-related models, and selected the method of feature graph multiplication to fuse features, which followed strategy 2. Thus, most of the feature information was well retained, and the boundary information could be obtained effectively. The accuracy is equal to that of UNet (Ronneberger et al., 2015), and the flop count was effectively reduced. Then, through the feature information of

another branch, the concat method was adopted to provide more detailed low-dimensional feature information as a complement for feature fusion in order to ensure that the accuracy is slightly better than that of UNet++ (Zhou et al., 2018, 2020), ResUNet++ (Jha et al., 2019), and other networks, whereas the actual running speed is much better than other models; in addition, it has the advantages of high training efficiency and strong generalization ability. This study makes the following contributions:

(1) We propose a model improvement approach that provides effective support for the efficient application of deep learning models in large-scale medical environments.
(2) An efficient polyp segmentation network is proposed that can accurately and effectively segment polyp images without the need for costly computer resources. Real-time colonoscopy detection can be guaranteed using existing computer resources.

Our proposed model shows good performance and generalization ability in a variety of different medical image datasets and can be extended to the detection of other medical issues.

In this article, the detailed model structure and parameter number verification are described in section "Materials and Methods," the experimental part of the model is discussed in section "Experiments," and a summary of the model is presented in section "Conclusion."

MATERIALS AND METHODS

In this section, we first introduce and analyze the advantages and disadvantages of PspNet (Zhao et al., 2017) and UNet (Ronneberger et al., 2015) models, and we make a detailed comparison with this model to provide a better understanding of our multi-branch feature fusion network (MBFFNet).

Baseline

With PspNet (Zhao et al., 2017), researchers believe that the existing models have segmentation errors owing to insufficient context information and global information under different receptive fields. PspNet model structure diagram as shown in **Figure 1**. Therefore, a hierarchical global priority containing information of different scales between different subareas is proposed, which is called the pyramid pooling module (Zhao et al., 2017). Four features of different pyramid scales are integrated, from the roughest feature in the first-row global pooling to a single output, and the next three are pooling features of different scales. After each level, a 1×1 convolution is used to reduce the level channel to the original 1/N. Then, it is converted to the pre-pooled size through bilinear interpolation, and finally, concatenation is carried out. In this way, the global features are obtained, the global information of different receptive fields is obtained, and good semantic segmentation results are obtained. However, as the pooled information of different scales is directly converted to the dimensions before pooling by an up-sampling method, the feature loss of the model is relatively large in the low-dimensional features. For medical image segmentation requiring accurate boundary results, although PspNet (Zhao et al., 2017) has a good overall effect, it is not suitable for application in medical image segmentation because of its incomplete retention of fine edge features and the inability to obtain complete boundary results.

To solve the problem of medical image segmentation and accurate boundary segmentation, UNet (Ronneberger et al., 2015) employs a completely different method of feature fusion. UNet uses VGG16 (Simonyan and Zisserman, 2014) as the backbone network backbone, and through the different location of the backbone for the characteristics of the different size chart, on the four double sampling, and after each sampling on a layer to obtain the characteristics of the figure for Mosaic, UNet (Ronneberger et al., 2015), researchers in order to retain more features, will feature in the channel dimension stitching together, forming thicker characteristics (Simonyan and Zisserman, 2014; Ronneberger et al., 2015). It is used in the same phase in the jumping connections, rather than to directly supervise and experiences loss with respect to high-level semantic features. These characteristics of a graph are a combination of more low-level image edge features and features with different scales, so the multi-scale prediction can be performed, making the model on the edge of the segmentation image restoration have more detailed information. However, because UNet (Ronneberger et al., 2015) employs the channel dimension splicing characteristic figure, combining to form the characteristics of the figure will result in many similar repeated characteristics, and characteristics of the severe figure redundancy phenomenon are costly in later calculations, requiring a large number of calculations and a high flop count, which affects the speed of the model. The model diagram of UNet (Ronneberger et al., 2015) is shown in **Figure 2**.

MBFFNet

Considering the above problems and the advantages and disadvantages of different models, we proposed the MBFFNet, which has a better lightweight network structure, and can simultaneously consider model accuracy and rapid deployment. Compared with UNet (Ronneberger et al., 2015) and its derivative versions, MBFFNet has better accuracy and requires fewer computations. In order to better validate the model of the network segmentation effect, we adopted the same approach as UNet (Ronneberger et al., 2015), with the VGG16 (Simonyan and Zisserman, 2014) network as the backbone, and multiple branch feature fusion network using the U-shaped structure of the UNet (Ronneberger et al., 2015) framework. We selected the Relu activation function to ensure that the model can reduce the flop count, and we abandoned the UNet (Ronneberger et al., 2015) channel dimension of the connection method. MBFFNet did not choose the method of FCN8 (Long et al., 2015) feature combination and fusion, but chose the method of feature multiplication for feature fusion. Therefore, there are two important advantages: (1) it avoids the burden of excessive computation owing to the excessive feature channels caused by the direct Mosaic of feature graphs; and (2) as the number

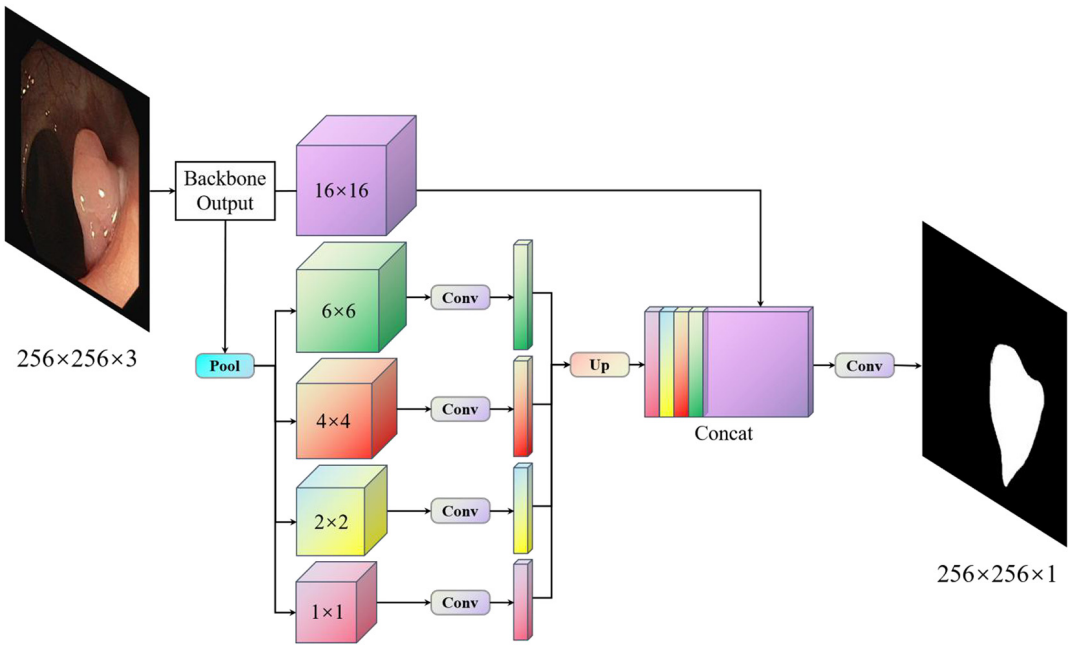

FIGURE 1 | Pspnet structure.

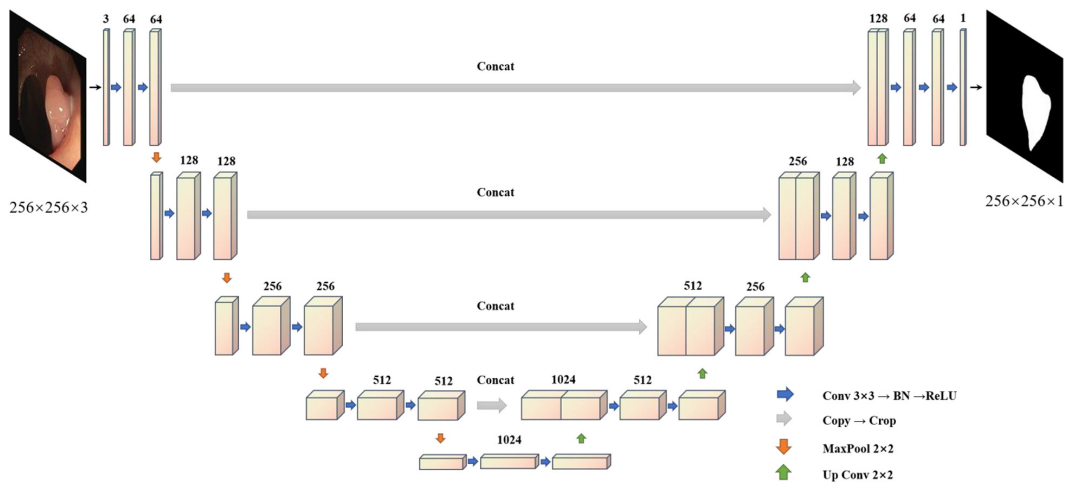

FIGURE 2 | Unet structure.

of network layers increases, overfitting is easily caused, but considering that the use of feature information between the upper and lower layers can solve this problem well. We weighted the normalized weight to the features of each pixel of the next layer through a dot product operation. This is no longer an attention mechanism based on channels, but an attention mechanism based on the pixel level (Jie et al., 2018). However, it is inevitable that low-dimensional feature information will be lost to a certain extent. Although the loss of such low-dimensional feature information is not serious after our experiment, the loss of some low-dimensional feature information may prevent the segmentation of a complete and detailed boundary image during the precise boundary division of polyps. Therefore, after using the original U-shaped structure, our model maximizes the characteristics of the five branches in the figure. Through pooling, without processing, the bilinear interpolation method is used for samples of the same size two/four/eight times. This will be an hourglass-like combination that will sample the functional layers at different times and then add low-dimensional edge feature information through convolution after the channel dimension concat has passed, adding second information to integrate features with other maps, a complete multi-branch feature fusion model network structure diagram, as shown in **Figure 3**. In this way, we can ensure that the information of low-dimensional

features is preserved as much as possible and avoid the loss of low-dimensional features caused by the direct use of single up-sampling. The continuous pixel-based attention mechanism makes the model more precise in the segmentation of image edges and other information. At the same time, it also avoids the excessive pursuit of keeping feature information of different scales as far as possible in UNet (Ronneberger et al., 2015), which adopts feature graphs to add channel dimensions, resulting in too many channels, the need for too many calculations, and increased computer burden.

EXPERIMENTS

Dataset

The polyp images used in this section were derived from the following datasets: ETIS, CVC-ClinicDB, CVC-ColonDB, Endoscene, and Kvasir. Kvasir is the largest and most extensive dataset released in 2017, and we selected polyp images from a subcategory of the Kvasir dataset (polyps). CVC-ClinicDB, which is also known as CVC-612, consists of 612 open-access images from obtained 31 colonoscopy clips. The CVC-ColonDB is a small database containing 380 images from 15 short colonoscopy sequences. ETIS is an established dataset containing 196 images of polyps for the early diagnosis of colorectal cancer. Endoscene is a combination of CVC-612 and CVC300. We integrated these data and eliminated the fuzzy images and finally obtained 1450 polyp images as the experimental data in this section.

To prove that the proposed model has better generalization ability, we collected a variety of medical image segmentation datasets for verification of our model. Common medical images share certain similarities. Therefore, we selected a larger number of medical image datasets to verify the robustness of our model.

In addition, our datasets are obtained from publicly available competitive medical datasets online, follow standard biosecurity and institutional safety procedures, and can be downloaded online. The raw data are available in articles, supplements, or repositories.

Corneal Nerve Dataset

This dataset consists of 30 images from the subbasal corneal nerve plexus obtained in normal and pathological subjects. Thirty images were obtained from 30 different normal or pathological subjects (diabetes mellitus, pseudoextirpation syndrome, and keratoconus). The instrument used to acquire these data was a Heidelberg Retina Tomograph II with a Rostock Corneal Module (HRTII32-RCM) confocal laser microscope.

Liver Dataset

This dataset was provided by the MICCAI 2018 LITS Challenge and consisted of 400 CT scans. Two distinct labels were provided for ground truth segmentation: liver and lesion. In our experiment, we treated only the liver as positive and the other parts as negative.

Lung Dataset

This dataset was provided by the Lung Image Database Consortium Image Collection (LIDCIDRI) and was collected by seven academic centers and eight medical imaging companies. To simplify the processing, only the lungs were segmented, and the remaining non-lung organs were treated as the background.

Electron Microscopy (EM) Dataset

This dataset was provided by the electron microscopy (EM) Segmentation Challenge as part of ISBI 2012. The dataset consisted of 30 (512 × 512 pixels) continuous slice transmission electron microscope images of the ventral nerve cord of the first instar larvae of *Drosophila melanogaster*. Referring to the example in **Figure 3**, each image has a corresponding fully annotated base-instance split map of the cell (white) and cell membrane (black).

Neums Dataset

The dataset was provided by the HE Data Science Bowl 2018 Segmentation Challenge and consisted of 670 segmenting nuclear images from different patterns (bright and fluorescent). This is the only dataset in this work that uses instance-level annotation, where each kernel is colored differently.

Ocular Vascular Dataset

This task is based on the DRIVE dataset, which uses photographs from the diabetic retinopathy screening program in Netherlands. The aim was to isolate the blood vessels in the fundus image.

Dataset of Esophageal Cancer

This dataset was provided by the First Affiliated Hospital of Sun Yat-sen University and comprised a total of 13,240 CT images (80 × 80) labeled by professional doctors. The goal of this dataset was to segment the esophageal cancer region in the CT image, with the non-esophageal cancer region as the background.

Experimental Setting

Environment

For the polyp segmentation experiment in this section, the framework used for the training model was TensorFlow (Abadi et al., 2016). Using the ADAM optimizer, the initial learning rate was set to 0.001. The experiment was carried out on a platform with an Intel (R) Xeon (R) Silver 4208 CPU at 2.10 GHz, 2.10 GHz (two processors), 64.0 GB RAM, Windows 64-bit operating system, NVidia Titan V graphics card, and 12 GB video memory capacity. In actual production, we can choose a better lightweight backbone, such as GhostNet (Han et al., 2020) and MobileNetv3 (Howard et al., 2017, 2020; Sandler et al., 2018).

Data Enhancement

Considering the polyps, liver, bowel, and medical images compared to natural images, medical imaging has the following characteristics. First, compared to a variety of modes, different imaging mechanisms of different modal medical images also have different characteristics, such as format, size, and quality, and it is necessary to better design the network to extract features of different modes. Second, the shape, size, and position of different tissues and organs vary greatly. Third, the texture feature is weak and requires a higher feature extraction module. Fourth, the boundary is fuzzy, which is not conducive to accurate segmentation.

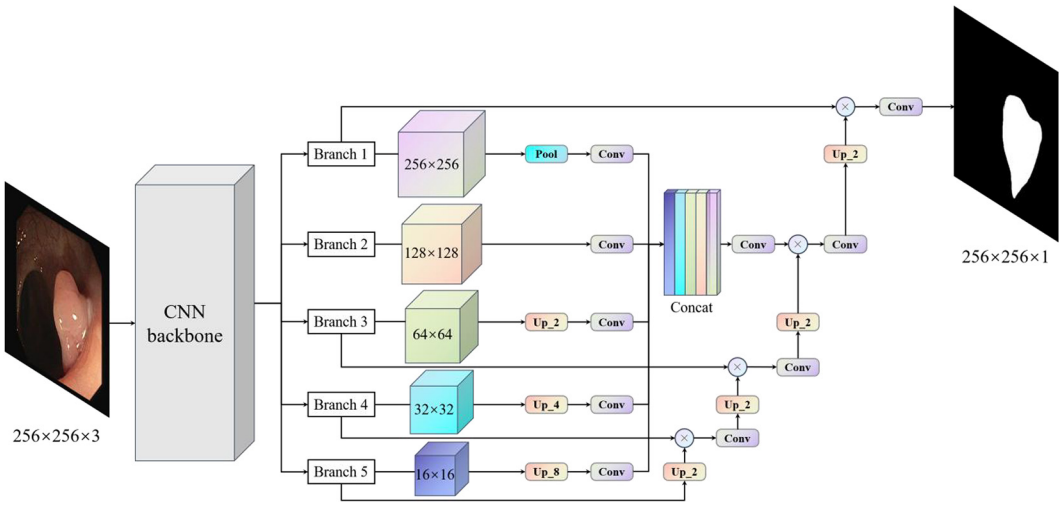

FIGURE 3 | Multi-branch feature fusion network. The backbone initially extracts the features of images, and images with different subsampling multiples are superimposed in an hourglass image pyramid (subsample images have a size larger than 128, and up-sample images have a size smaller than 128, which is equal to 1 × 1 standard convolution for images with size larger than 128). To maximize the use of cross-channel and cross-resolution image branches, each branch is up-sampled and multiplied by the previous layer. Finally, the predicted image of the original image size is obtained.

To train our model effectively, we divided the dataset into an 8:2 ratio. Eighty percent of the datasets were used for model training and 20% for model testing.

To improve the robustness of the model, appropriate image enhancement is required for the training image. In this study, brightness enhancement, scaling, horizontal flip, shift, rotation, and channel transformation were performed on the training image. Owing to the limited number of medical images, we could not use the limitation of commonly used image tasks, so we chose the most commonly used data enhancement parameters of existing medical images. The specific proportions and effects are listed in **Table 1** and **Figure 4**, respectively.

Accuracy Evaluation Index

To fully verify the accuracy of the proposed model, we chose three evaluation indicators to evaluate the model as a whole in order to more fully and intuitively prove the effect of our model. Three metrics are as follows.

mIOU

This calculates the ratio of the intersection and union of two sets of true and predicted values. This ratio is the sum of true positive (TP) divided by TP, false positive (FP), and false negative (FN). FN indicates that the prediction was negative, but the label result was positive; an FP is actually a negative case, and for a TP, the prediction is positive. In fact, it is also a positive example, indicating that the prediction result is correct, where p_{ij} represents the number of real values and is predicted to be j, and k+1 is the number of classes (including the background). P_{ii} is the number of values predicted correctly, and p_{ij}, and p_{ji} represent FP and FN, respectively (Kingma and Ba, 2015). The formula for calculating mIOU is as follows:

$$\mathrm{mIOU} = \frac{1}{k+1}\sum_{i=0}^{k}\frac{p_{ii}}{\sum_{j=0}^{k}p_{ij}+\sum_{j=0}^{k}p_{ji}-p_{ii}} \tag{1}$$

TABLE 1 | Image enhancement setting parameters.

Operation	Proportion
Brightness	−0.2 to 0.2
Zoom	−0.75 to 2
Horizontal flip	0.5
Shift	0.5
Rotation	−0.5 to 0.5
Channel transformation	10

F score

In an ideal situation, it would be best if both evaluation indexes were high. However, a high precision generally means low recall, and high recall means low precision. Therefore, in practice, it is often necessary to make a trade-off according to specific circumstances, such as the general search situation. To ensure the recall rate, the precision rate should be improved as much as possible. For example, for cancer detection, seismic detection, financial fraud, and so on, the recall rate should be increased as much as possible to ensure accuracy. A new index, the F score, is derived, which comprehensively considers the harmonic value of precision and recall (Flach and Kull, 2015). The calculation formula is as follows:

$$Precision = \frac{TP}{TP+FP}+\mathrm{FP} \tag{2}$$

$$Recall = \frac{TP}{TP+FN} \tag{3}$$

$$F-\mathrm{score} = \left(1+\beta^2\right)\cdot\frac{Precision\cdot Recall}{\beta^2\cdot Precision + Recall} \tag{4}$$

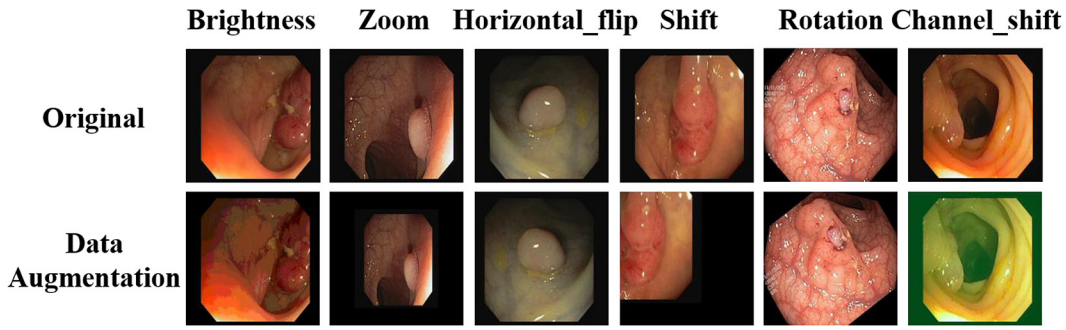

FIGURE 4 | Image enhancement renderings.

The Dice coefficient is a set similarity measurement function, which is usually used to calculate the similarity between two samples, and its value range is [0,1]. The inclusion of $|y \cap \hat{y}|$ is real labels, and predicting the intersection between $|y|$ and $|\hat{y}|$ indicates the number of elements in y and $\hat{y}$, respectively; among them, the coefficient of molecules is 2 because there is a common element in the denominator between the repeated calculation of y and $\hat{y}$

The loss function (Dice loss) is formulated according to the Dice coefficient because the real goal of segmentation is to maximize the degree of overlap between the real tag and the predicted one, that is, the similarity. However, when the Dice loss is used, there is severe shock when positive samples are generally small targets. In the case of only the foreground and background, once some pixels of small targets are predicted incorrectly, the loss value will change significantly, leading to a drastic gradient change. In the extreme case, it can be assumed that only one pixel is a positive sample. If the prediction of this pixel is correct, the prediction results of the other pixels will be ignored, and the loss is always close to 0. The prediction error causes the loss to approach 1. For the cross-entropy loss (CE loss) function, CE is a proxy form, and it is easy to maximize optimization in the network by virtue of its characteristics, which averages the value as a whole. Therefore, the loss function adopted in our experiment is to add CE loss based on the Dice loss. This can compensate for some deficiencies in the Dice loss (Li et al., 2020). The calculation formula is as follows:

$$\text{Dice loss with CE} = 1 - \frac{2|y \cap \hat{y}|}{|y| + |\hat{y}|} - [y \log \hat{y} + (1 - y)\log(1 - \hat{y})] \quad (5)$$

Model Accuracy on Polyp Datasets

This section discusses an experiment that was conducted on a dataset of polyps. In order to better verify the effectiveness of our proposed model on the CT images of polyp tumor lesions, we determine the effect on polyp segmentation. We compared popular medical image segmentation semantic segmentation models: UNet (Ronneberger et al., 2015), UNet++ (Zhou et al., 2018, 2020), UNet+++ (Huang et al., 2020), U^{2}Net (Qin et al., 2020), and PraNet (Fan et al., 2020), and we compared three general semantic segmentation models: PspNet (Zhao et al., 2017), Deeplabv3+ (Chen et al., 2018), and FCN8 (Long et al., 2015). To increase the reliability of our model, we added three new semantic segmentation networks: OcrNet (Yuan et al., 2020), DnlNet (Yin et al., 2020), and PointRend (Kirillov et al., 2019). For the experiment, the backbone of the model chooses the VGG16 (Simonyan and Zisserman, 2014) network as the comparison model. On the validation set data, the accuracy was analyzed based on two commonly used semantic segmentation evaluation indexes, mIOU and Dice loss with CE.

We randomly selected four test images from different angles and analyzed our model using multiple contrast models. The segmentation results are shown in **Figure 5**. The results of PspNet (Zhao et al., 2017), Deeplabv3+ (Chen et al., 2018), and FCN8 (Long et al., 2015), which are three general semantic segmentation models on the dataset segmentation effect, are poorer, produce serious false identification, and cannot effectively segment the region and segment the area completely, although the PraNet (Fan et al., 2020) effect is better; however, because its detection speed is much slower than MBFFNet, it does not have practical application value and is not suitable for rendering displays in the four models. As can be seen from the figure, UNet (Ronneberger et al., 2015), UNet++ (Zhou et al., 2018, 2020), U^{2}Net (Qin et al., 2020), and UNet+++ (Huang et al., 2020) all segment relatively good areas and can segment the contour of the area in which the polyp is located, but the precise boundary of the polyp cannot be obtained. There are some FN pixels, especially for small polyps, and the segmentation effect of MBFFNet is obviously better than that of the other models. OcrNet (Yuan et al., 2020), DnlNet (Yin et al., 2020), and PointRend (Kirillov et al., 2019) are semantic segmentation networks, but although they show relatively excellent performance, they cannot be properly segmented in the third line of small colonoscopy images, resulting in their omission. In this study, the multiple branches feature fusion network MBFFNet is compared with the multiple model above, although it significantly reduces the number of calculations and increases the detection speed; however, because of the way in which multi-branch feature fusion is used, even small polyps in segmentation, it still makes good corresponding image edges and accurately determines the image boundary. Therefore, the MBFFNet is more effective for segmenting polyps.

As shown in **Table 2**, the evaluation index shows that the polyp divides the dataset on the test set, multiple-branch fusion network

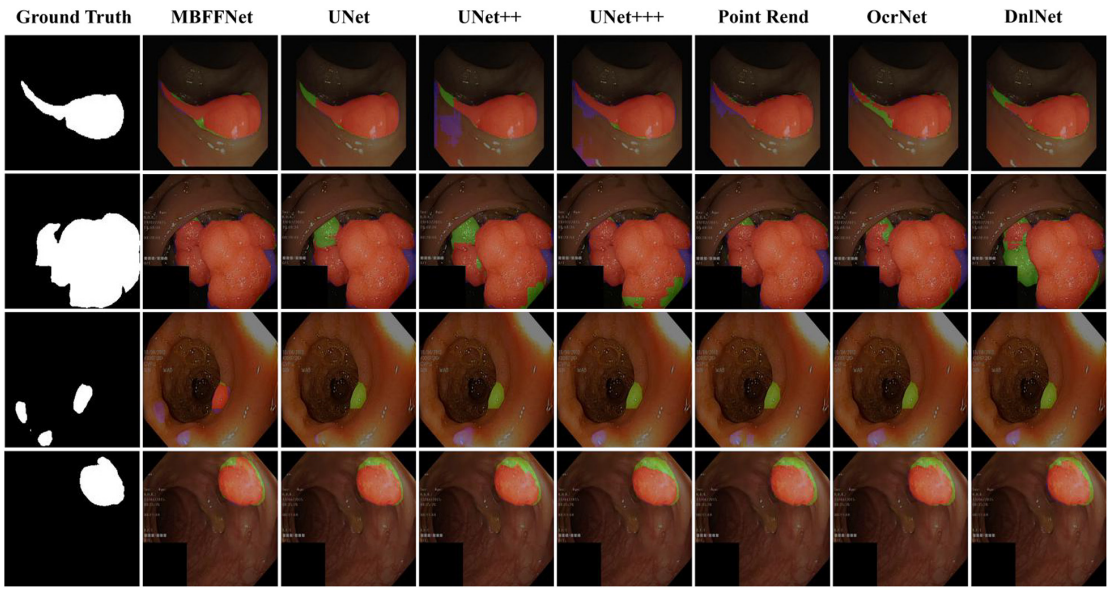

FIGURE 5 | Comparison of model effect. The red represents True Positive (TP), indicating that the predicted polyp area is actually a polyp area. Blue represents False Positive (FP), indicating that the predicted polyp area is actually a non-nuclear area. The green represents FN (False Negative), which means that the predicted polyp area is actually a polyp area.

MBFFNet mIOU above LinkNet (Chaurasia and Culurciello, 2018), PspNet (Zhao et al., 2017), Deeplabv3+(Chen et al., 2018) general semantic network segmentation, segmentation, and medical UNet (Ronneberger et al., 2015), and the optimization model of the polyp has the same order of magnitude. Image segmentation results in a reduction in the number of calculations. The model precision does not decrease, and it can be seen that the model reduces the UNet (Ronneberger et al., 2015) redundancy phenomenon, making the model more efficient. However, in the evaluation index of Dice loss with CE, the loss value of the MBFFNet is slightly higher than that of medical networks such as UNet (Ronneberger et al., 2015), and it is much lower than that of networks such as LinkNet (Chaurasia and Culurciello, 2018). OcrNet (Yuan et al., 2020), DnlNet (Yin et al., 2020), and PointRend (Kirillov et al., 2019), which are the latest semantic segmentation networks, and they show very good performance in general semantic segmentation and show much better segmentation performance than FCN8 (Long et al., 2015), Deeplabv3+ (Chen et al., 2018), and PspNet (Zhao et al., 2017) for the colonoscopy segmentation dataset. However, because they focus more on semantic segmentation in common scenes, the segmentation effect on colonoscopy was lower than that of our proposed model and other medical image segmentation networks. This shows that the optimization of the model did not significantly affect the accuracy. It can be seen that the MBFFNet reduces redundancy in polyp segmentation, while ensuring that the accuracy does not change significantly.

Parameter Number Verification

To better verify whether our model reduces the redundancy of the feature map and the number of parameters and flops of the model, we calculated the number of parameters and flops of the MBFFNet and LinkNet (Chaurasia and Culurciello, 2018), FCN8 (Long et al., 2015), U^{2}Net (Qin et al., 2020), UNet++ (Zhou et al., 2018, 2020), UNet+++ (Huang et al., 2020), PspNet (Zhao et al., 2017), and Deeplabv3+ (Chen et al., 2018). To better compare the differences between the model parameters and the number of computations, VGG16 (Simonyan and Zisserman, 2014) was used as the backbone for all semantic segmentation networks, and the same settings were used in all comparison experiments.

The number of parameters of the model mainly depends on the number of calculations of each convolution kernel in each convolution layer. Here, the size of each convolution kernel is $k_w \times k_h$, the size of the input feature graph is c^i, and the number

TABLE 2 | Evaluation index of polyp segmentation mIOU, *F*-score, and Dice loss with CE.

Model	mIOU	*F*-score	Dice loss with CE
UNet (Ronneberger et al., 2015)	0.8883	0.9354	0.1719
LinkNet (Chaurasia and Culurciello, 2018)	0.8711	0.9238	0.1911
U^{2}Net (Qin et al., 2020)	0.8950	0.9398	0.1528
UNet++ (Zhou et al., 2018, 2020)	0.8895	0.9364	0.1642
UNet+++ (Huang et al., 2020)	0.8831	0.9312	0.1827
PraNet (Fan et al., 2020)	0.9347	0.9612	0.1012
PspNet (Zhao et al., 2017)	0.8612	0.8972	0.2453
Deeplabv3+ (Chen et al., 2018)	0.8452	0.8872	0.3214
FCN8 (Long et al., 2015)	0.8563	0.8945	0.2752
DnlNet (Yin et al., 2020)	0.8657	0.9143	0.2064
OcrNet (Yuan et al., 2020)	0.8801	0.9210	0.1953
PointRend (Kirillov et al., 2019)	0.8585	0.9074	0.2153
MBFFNet	0.8952	0.9450	0.1602

of convolution kernels is the number of channels of the output feature graph, which is c^o. Therefore, the calculation formula for the number of parameters at each convolution layer is as follows:

$$Param = c^i c^o k_w k_h \tag{6}$$

The computation of the model is the sum of each convolution layer. The number of calculations of the convolutional layer is determined by the number of calculations of the convolutional kernel in each sliding window and the overall sliding duration. In each sliding window, the number of calculations of the convolution operation is approximately $c^i k_w k_h$, $l_w^o l_h^o$ is the size of the output feature graph, and the number of sliding times of the convolution kernel is the number of data of the output feature graph, that is, $c^o l_w^o l_h^o$, so the overall number of calculations is:

$$Flops = c^i c^o l_w^o l_h^o k_w k_h \tag{7}$$

Using the above formula, the number of parameters in the MBFFNet and the comparison model with flops are shown in **Table 3**. As can be seen in the table, our MBFFNet was compared with UNet (Ronneberger et al., 2015) because of the complex model structure. MBFFNET on FLOPS reduced to 26.79% of UNET's FLOPS; compared with U2Net (Qin et al., 2020), the quantity decreased to 24.67%, and flops to 39.51%. The results were analyzed and compared with the UNet (Ronneberger et al., 2015) model, multiple branching feature fusion network, and there was a significant reduction in the number of parameters of the model and the flop count, decreasing to a certain extent the redundancy of the model. Compared with other networks, FCN8 (Long et al., 2015) and other classical semantic segmentation networks fail to meet the requirements with respect to both precision and number of parameters. OcrNet (Yuan et al., 2020), PointRend (Kirillov et al., 2019), and DnlNet (Yin et al., 2020) have improved their accuracy, but their very high flop count requires extremely high configurations to achieve excellent performance, and they can only be applied to workstations and other environments in the future. In addition, to more comprehensively show the light weight and popularity of our model, we added the convergence time of the training model to the evaluation index of the model. It can be seen that although our model did not achieve the fastest convergence, its training time was much lower than that of UNet (Ronneberger et al., 2015), UNet++ (Zhou et al., 2018, 2020), and other networks.

TABLE 3 | Analysis of the number of parameters and the number of calculation.

Model	Training time (h)	Param (M)	Flops (B)
UNet (Ronneberger et al., 2015)	12	24.89	56.33
LinkNet (Chaurasia and Culurciello, 2018)	3	11.53	1.23
U^2Net (Qin et al., 2020)	18	96.25	40.24
UNet++ (Zhou et al., 2018, 2020)	20.5	36.16	135.24
UNet+++ (Huang et al., 2020)	16	18.27	211.09
PraNet (Fan et al., 2020)	13	16.16	20.37
PspNet (Zhao et al., 2017)	11.5	15.11	25.57
Deeplabv3+ (Chen et al., 2018)	16.5	134.27	27.78
FCN8 (Long et al., 2015)	78.5	30.34	6390
DnlNet (Yin et al., 2020)	15.5	50.13	50110
OcrNet (Yuan et al., 2020)	5	70.35	40530
PointRend (Kirillov et al., 2019)	37.5	47.69	14640
MBFFNet	5.5	23.74	15.09

To obtain a more intuitive understanding of the effects of different models, we used the flop count as the abscissa and mIOU as the ordinate, and we built a coordinate graph with the number of parameters to show the size of the model, as shown in **Figure 6**. From **Figure 6**, we observe that when the model is closer to the upper left corner, the model has a higher mIOU and a lower flop count. Although PraNet (Fan et al., 2020) possesses excellent mIOU precision, the high flop model in terms of the comprehensive income ratio is not ideal; further, although LinkNet (Chaurasia and Culurciello, 2018) has a very low flow count, the model does not have satisfactory accuracy and cannot meet the precision requirements of medical treatment, so it cannot be applied to health care.

Real-Time Analysis of the Model

To verify that the detection rate of our model is improved when the number of parameters and number of calculations are significantly decreased, images with sizes of 256 × 256 and 64 × 64 are selected for experiments, and it is determined whether the model can meet the application standards in different computing resource environments. According to the sales data, we choose mainstream graphics cards currently on the market. GTX1060 represents the graphics card having a midrange productivity, which is the one with the highest production and the widest coverage at present. The 2060s is the midrange and top end graphics card and is the one expected to be most in use in the next 20 years. To meet the requirements of our model, it can be used in a wider range of medical environments worldwide to effectively prevent colorectal cancer and accurately separate polyps and adenomas. To test the actual operation effect of MBFFNet and considering the equipment environment in economically underdeveloped areas, we added the R5-3600 with an AMD platform and the I7-8750H CPU environment with an Intel platform, which are commonly used at present. In addition, considering that our proposed model will be applied on a large scale in medical environments, we did not choose traditional segmentation networks with poor segmentation results, such as Deeplabv3+ (Chen et al., 2018), PspNet (Zhao et al., 2017), and LinkNet (Chaurasia and Culurciello, 2018); nor did we choose PraNet (Fan et al., 2020) with poor real-time performance to conduct related experiments.

First, we selected a common medical image size of 256 × 256 as a test, and the test results are presented in **Table 4**. It can be seen that at 256 × 256, our model runs much faster in the CPU environment than other U-shaped networks; at its actual running speed, FPS is 100% higher than UNet (Ronneberger et al., 2015), UNet++ (Zhou et al., 2018, 2020), etc. In a GPU environment, the actual segmentation approaches 30 FPS, even on today's midproductivity graphics cards; in real life, 30 FPS can achieve a smoother detection effect to the naked eye to meet the real-time requirements. However, other semantic segmentation models with better medical segmentation effects cannot meet

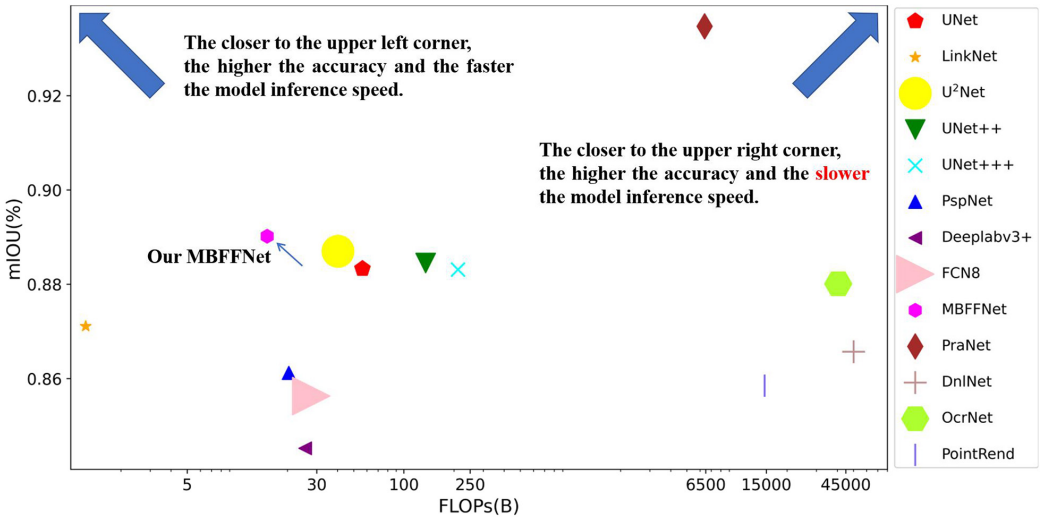

FIGURE 6 | Comparison between the accuracy of different models and flop count.

the real-time requirements. Although LinkNet (Chaurasia and Culurciello, 2018) has an excellent actual operating performance, its segmentation performance fails to meet the precision requirements. In accuracy verification, the LinkNet model (Chaurasia and Culurciello, 2018) cannot effectively segment the polyp boundary.

Subsequently, we conducted FPS test experiments on 64 × 64 images, and the experimental results are listed in **Table 5**. In the 64 × 64 image, our model can meet the real-time test requirement of 30 FPS even in a CPU environment, and the actual running fluency FPS is higher than that of other medical image segmentation networks. Thus, it can be seen that in existing common computer resources equipment, MBFFNet can meet the requirements of real-time observation of medical observation, even in economically underdeveloped areas. For low computer resources, it is seen that even in the case of infrequently used graphics resources configuration, our proposed model can also guarantee the real-time segmentation of polyps.

Based on the experiment results, it can be seen that owing to the advantages of low flop count, our model displays excellent real-time performance in an environment with low computer resources, while the advantages of our model are very significant in environments with lower computer resources. Under the current computer resources, our model MBFFNet has been able to deal with a variety of different conditions of accurate basic real-time polyp segmentation and achieved a relatively good effect.

Model Generalization Experiment

For all of the experiments in this section, we chose the same experimental environment and image processing method as the polyp segmentation dataset in *Dataset*. The final evaluation indexes mIOU, *F* score, and Dice loss with CE were also evaluated based on validation set data. We chose U^{2}Net (Qin et al., 2020), UNet++ (Zhou et al., 2018, 2020), and UNet+++ (Huang et al., 2020) as the semantic segmentation models for medical images; PraNet (Fan et al., 2020) as the semantic segmentation model for polyps; and PspNet (Zhao et al., 2017), Deeplabv3+ (Chen et al., 2018), and FCN8 (Long et al., 2015) as the comparison model for the experiment. For the demonstration, we selected the test sample for liver lesion segmentation, and the sample segmentation image is shown in **Figure 7**. It can be seen

TABLE 4 | 256 × 256 polyp image segmentation FPS.

Model	AMD	Inter	2060Super	1060
Unet (Ronneberger et al., 2015)	4	3	45	21
LinkNet (Chaurasia and Culurciello, 2018)	19	16	115	88
U^{2}Net (Qin et al., 2020)	2	2	23	14
UNet++ (Zhou et al., 2018, 2020)	2	2	22	10
UNet+++ (Huang et al., 2020)	2	1	16	8
MBFFNet	8	7	55	28

The image size is 256 × 256. AMD represents the FPS test on the CPU of the AMD platform (R5-3600), Inter represents the FPS test on the CPU of Intel platform (I7-8750H), 2060Super represents the FPS test in the GPU environment of the 2060Super graphics card, and 1060 represents the FPS test in the GPU environment of the RTX1060 graphics card.

TABLE 5 | FPS segmentation of 64 × 64 polyp images.

Model	AMD	Inter	2060Super	1060
Unet (Ronneberger et al., 2015)	20	19	152	90
LinkNet (Chaurasia and Culurciello, 2018)	84	68	138	141
U^{2}Net (Qin et al., 2020)	13	14	31	23
UNet++ (Zhou et al., 2018, 2020)	10	11	98	55
UNet+++ (Huang et al., 2020)	9	9	90	68
MBFFNet	33	31	163	112

The image size is 64 × 64. AMD stands for the FPS test on AMD CPU (R5-3600), Intel stands for the FPS test on an Intel CPU (I7-8750H), 2060Super stands for the FPS test in the GPU environment on a 2060Super graphics card, and 1060 stands for FPS test in the GPU environment on an RTX1060 graphics card.

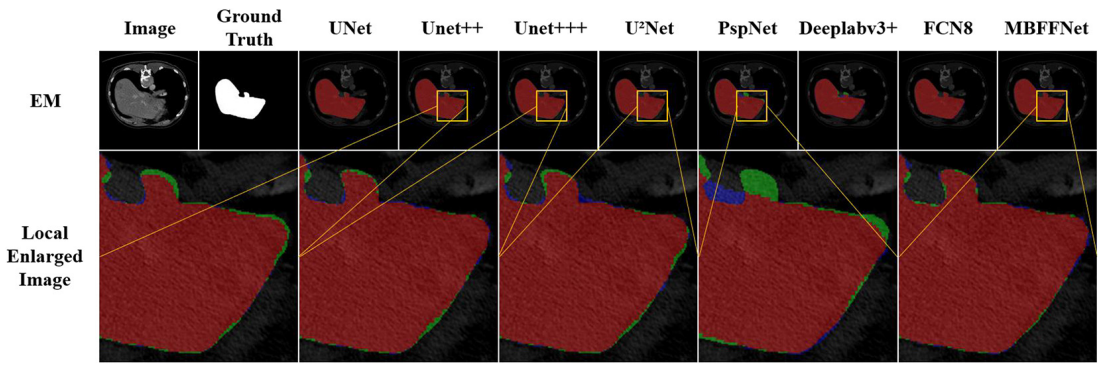

FIGURE 7 | Segmentation effect of liver lesions.

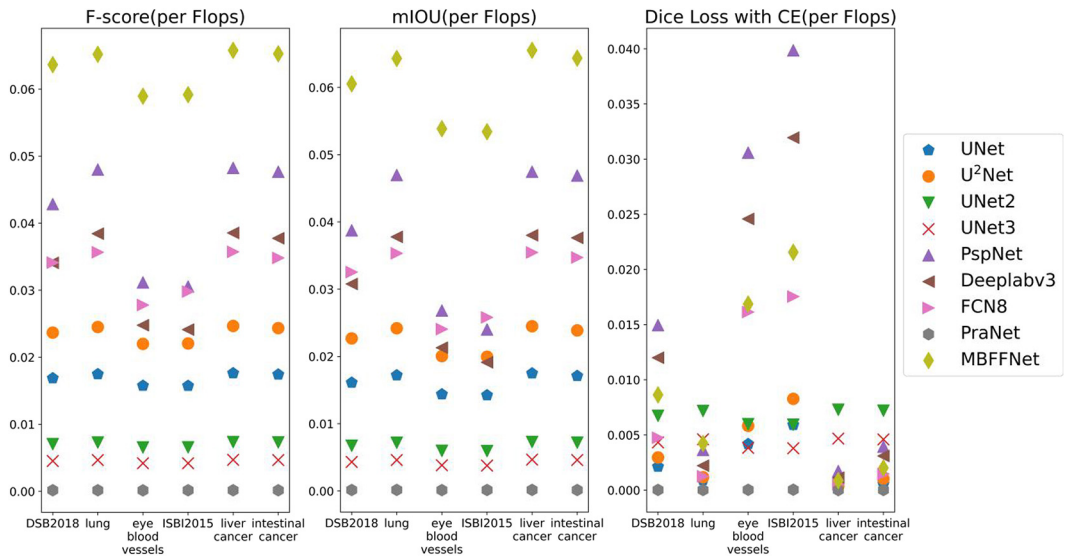

FIGURE 8 | Comparison between the accuracy of different models and Flop count.

that, compared with other models, MBFFNet retains the edge feature information better, which makes the boundary of liver lesion segmentation clearer and more accurate, and ensures the accuracy of medical images.

According to the analysis of the experimental results, similar to the results of colonoscopy segmentation, our model is better than PraNet (Fan et al., 2020), Deeplabv3+ (Chen et al., 2018), FCN8 (Long et al., 2015), and other general semantic segmentation models in various medical image segmentation datasets, but it is slightly better than UNet (Ronneberger et al., 2015), UNet++ (Zhou et al., 2018, 2020), and U^{2}Net (Qin et al., 2020) and basically equal to UNet+++ (Huang et al., 2020). The segmentation results of the model are worse than those of PraNet (Fan et al., 2020). As these medical models can all achieve good segmentation effects, mIOU, *F* score, Dice loss with CE, and other indicators show excellent effects in intestinal cancer, liver cancer, DSB2018, lung, and other datasets, with little difference. In the face of a more complex medical image segmentation environment, for example, only in the eye blood vessels and ISBI2015 datasets can PraNet (Fan et al., 2020) show relatively good results. It can be seen that the PraNet (Fan et al., 2020) model can achieve a good segmentation effect in a very complex segmentation environment, but its extremely large flop count makes it impossible to carry out an effective real-time segmentation model in a generally productive equipment. However, our MBFFnet model retains edge feature information owing to multi-branch feature fusion. In most circumstances, it can achieve excellent segmentation results and has good generalization ability, which is sufficient to deal with most of the image segmentation, and because our model with network model structure is compact and lightweight, it enables very convenient deployment in most of medical environments, lesion image segmented (see the **Appendix** for detailed experimental results in **Tables A1–A3**). Because the ultimate purpose of this study is to find a network that can be applied in practice and that considers both speed and precision, it is not ideal to talk about precision without speed alone. Therefore, the ratio of mIOU, *F* score, and Dice loss with CE to flops was taken as the index of the

new measurement model. It can be seen from mIOU (per flops) and *F* score (per flop) that our model has the highest return under the same computing resources (the higher the better), whereas the loss indicator indicates a faster and more stable convergence (the lower the better). The effect diagram is shown in **Figure 8**.

CONCLUSION

In this article, an MBFFNet is proposed to achieve the accurate and real-time segmentation of liver lesion images. A U-shaped structure such as UNet is used to gradually fuse shallow features with high-dimensional features. The method of superposition of feature graphs used by UNet is abandoned in the process of feature fusion, but the multiplication of feature graphs is chosen for feature fusion. A feature map with five branches is used, and then a pyramid feature map similar to PspNet is used to fuse the feature as a supplementary feature of the feature information. Finally, the two groups of features are fused to obtain the final segmentation result, and the experimental results show that the algorithm in the segmentation polyp area achieved the same results as the UNet segmentation results regardless of the polyp area size. In addition, it can complete the segmentation edge details such as features, get a better segmentation effect, and significantly reduce the network number and number of calculations, and it improved the real-time performance of the polyp of semantic segmentation model segmentation; at the same time, the segmentation experiments on other medical images show that MBFFNet has good robustness in medical image segmentation.

DATA AVAILABILITY STATEMENT

The original contributions presented in the study are included in the article/supplementary material, further inquiries can be directed to the corresponding author/s.

AUTHOR CONTRIBUTIONS

HS: writing–editing, conceptualization, investigation, and model validation. BL: project administration, writing–editing, and model improvement. XH: writing–original draft and visualization. JL: formal analysis and project improvement. KJ: writing–review. XD: funding acquisition and methodology. All authors contributed to the article and approved the submitted version.

ACKNOWLEDGMENTS

We thank Tao Liu, Xiaoyan Chen, Jun Li, Jiong Mu, and other teachers for their support and help in our life and contributions. Without their help, we would not have been able to carry out university life and related research so smoothly. We would like to thank Editage (www.editage.cn) for English language editing.

REFERENCES

Abadi, M., Barham, P., Chen, J., Chen, Z., Davis, A., Dean, J., et al. (2016). "TensorFlow: a system for large-scale machine learning," in *Proceedings of the 12th USENIX Conference on Operating Systems Design and Implementation*, Vol. 16, (Berkeley, CA: USENIX Association), 265–283.

Akbari, M., Mohrekesh, M., Nasr-Esfahani, E., Soroushmehr, S., Karimi, N., Samavi, S., et al. (2018). "Polyp segmentation in colonoscopy images using fully convolutional network," in *Proceedings of the 2018 40th Annual International Conference of the IEEE Engineering in Medicine and Biology Society (EMBC)*, Honolulu, HI: IEEE.

Armato, S. G., Petrick, N. A., Brandao, P., Mazomenos, E., Ciuti, G., Caliò, R., et al. (2017). "Fully convolutional neural networks for polyp segmentation in colonoscopy," in *Proceedings of the Medical Imaging 2017: Computer-Aided Diagnosis*, (Orlando, FL: SPIE Medical Imaging).

Arnold, M., Abnet, C. C., Neale, R. E., Vignat, J., and Bray, F. (2020). Global burden of 5 major types of gastrointestinal cancer. *Gastroenterology* 159, 335–349.e15. doi: 10.1053/j.gastro.2020.02.068

Bernal, J., Núñez, J., Sánchez, F., and Vilariño, F. (2014). Polyp segmentation method in colonoscopy videos by means of MSA-DOVA energy maps calculation. *Workshop Clin. Image-Based Proc.* 8680, 41–49. doi: 10.1007/978-3-319-13909-8_6

Bernal, J., Sánchez, F. J., Fernández-Esparrach, G., Gil, D., Rodríguez, C., and Vilariño, F. (2015). WM-DOVA maps for accurate polyp highlighting in colonoscopy: validation vs. saliency maps from physicians. *Comput. Med. Imaging Graph.* 43, 99–111.

Bernal, J., Sánchez, J., and Vilari, O. F. (2012). Towards automatic polyp detection with a polyp appearance model. *Pattern Recognit.* 45, 3166–3182. doi: 10.1016/j.patcog.2012.03.002

Breier, M., Summers, R. M., Ginneken, B. V., Gross, S., Behrens, A., Stehle, T., et al. (2011). "Active contours for localizing polyps in colonoscopic nbi image data," in *Proceedings of the 2011 International Society for Optics and Photonics*, Vol. 7963, (Lake Buena Vista, FL: SPIE), 79632M. doi: 10.1117/12.877986

Chaurasia, A., and Culurciello, E. (2018). "LinkNet: exploiting encoder representations for efficient semantic segmentation," in *Proceedings of the 2017 IEEE Visual Communications and Image Processing (VCIP)*, (St. Petersburg, FL: IEEE), 1–4. doi: 10.1109/VCIP.2017.8305148

Chen, L. C., Papandreou, G., Schroff, F., and Adam, H. (2017). Rethinking atrous convolution for semantic image segmentation. *arXiv* [Preprint] arXiv:1706.05587,

Chen, L. C., Zhu, Y., Papandreou, G., Schroff, F., and Adam, H. (2018). *Encoder-Decoder With Atrous Separable Convolution For Semantic Image Segmentation*. Cham: Springer, 833–851. doi: 10.1007/978-3-030-01234-2_49

Deeba, F., Bui, F. M., and Wahid, K. A. (2019). Computer-aided polyp detection based on image enhancement and saliency-based selection. *Biomed. Signal Process. Control* 55:101530. doi: 10.1016/j.bspc.2019.04.007

Fan, D. P., Ji, G. P., Zhou, T., Chen, G., Fu, H., Shen, J., et al. (2020). "Pranet: parallel reverse attention network for polyp segmentation," in *Proceedings of the Medical Image Computing and Computer Assisted Intervention (MICCAI). Lecture Notes in Computer Science*, Vol. 12266, (Cham: Springer), doi: 10.1007/978-3-030-59725-2_26

Fang, Y., Chen, C., Yuan, Y., and Tong, K. Y. (2019). "Selective feature aggregation network with area-boundary constraints for polyp segmentation," in *Proceedings of the International Conference on Medical Image Computing and Computer-Assisted Intervention*, (Cham: Springer), doi: 10.1007/978-3-030-32239-7_34

Flach, P., and Kull, M. (2015). "Precision-recall-gain curves: PR analysis done right," in *Advances in Neural Information Processing Systems 28*, Vol. 1, (Cambridge, MA: Massachusetts Institute of Technology (MIT) Press), 838–846. Avilable online at: https://papers.nips.cc/paper/5867-precision-recall-gain-curves-pr-analysis-done-right (accessed March, 2021).

Ganz, M., Yang, X., and Slabaugh, G. (2012). Automatic segmentation of polyps in colonoscopic narrow-band imaging data. *IEEE Trans. Biomed. Eng.* 59, 2144–2151. doi: 10.1109/TBME.2012.2195314

Haggar, F., and Boushey, R. (2009). Colorectal cancer epidemiology: incidence, mortality, survival, and risk factors. *Clin. Colon Rectal Surg.* 22, 191–197. doi: 10.1055/s-0029-1242458

Han, K., Wang, Y., Tian, Q., Guo, J., and Xu, C. (2020). "GhostNet: more features from cheap operations," in *Proceedings of the 2020 IEEE/CVF Conference on Computer Vision and Pattern Recognition (CVPR)*, (Seattle, WA: IEEE), 1577–1586. doi: 10.1109/CVPR42600.2020.00165

Howard, A., Sandler, M., Chen, B., Wang, W. J., Chen, L. C., Tan, M. X., et al. (2020). "Searching for mobileNetV3," in *Proceedings of the 2019 IEEE/CVF International Conference on Computer Vision (ICCV)*, (Seoul: IEEE), 1314–1324. doi: 10.1109/ICCV.2019.00140

Howard, A. G., Zhu, M., Chen, B., Kalenichenko, D., Wang, W., Weyand, T., et al. (2017). Mobilenets: efficient convolutional neural networks for mobile vision applications. *arXiv* [Preprint] arXiv:1704.04861 [cs.CV].

Huang, H., Lin, L., Tong, R., Hu, H., and Wu, J. (2020). "UNet 3+: a full-scale connected UNet for medical image segmentation," in *Proceedings of the ICASSP 2020 - 2020 IEEE International Conference on Acoustics, Speech and Signal Processing (ICASSP)*, (Barcelona: IEEE).

Jha, D., Smedsrud, P. H., Riegler, M. A., Johansen, D., De Lange, T., Halvorsen, P., et al. (2019). "ResUNet++: an advanced architecture for medical image segmentation," in *Proceedings of the 21st IEEE International Symposium on Multimedia*, (San Diego, CA: IEEE).

Jie, H., Li, S., and Gang, S. (2018). "Squeeze-and-excitation networks," in *Proceedings of the 2018 IEEE/CVF Conference on Computer Vision and Pattern Recognition (CVPR)*, (Salt Lake City, UT: IEEE)), 7132–7141. doi: 10.1109/CVPR.2018.00745

Kingma, D. P., and Ba, J. (2015). "Adam: a method for stochastic optimization[C]," in *Proceedings of the 3rd International Conference on Learning Representations*, 2015: arXiv:1412.6980.

Kirillov, A., Wu, Y., He, K., and Girshick, R. (2019). Pointrend: image segmentation as rendering. *arXiv* [Preprint] arXiv:1912.08193 [cs.CV].,

Li, J., Wang, P., Zhou, Y., Liang, H., and Luan, K. (2021). Different machine learning and deep learning methods for the classification of colorectal cancer lymph node metastasis images. *Front. Bioeng. Biotechnol.* 8:620257. doi: 10.3389/fbioe.2020.620257

Li, X., Sun, X., Meng, Y., Liang, J., and Li, J. (2020). "Dice loss for data-imbalanced NLP tasks," in *Proceedings of the 58th Annual Meeting of the Association for Computational Linguistics*, (Stroudsburg, PA: Association for Computational Linguistics).

Lin, T. Y., Dollar, P., Girshick, R., He, K., Hariharan, B., and Belongie, S. (2017). "Feature pyramid networks for object detection," in *Proceedings of the 2017 IEEE Conference on Computer Vision and Pattern Recognition (CVPR)*, (Washington, DC: IEEE Computer Society).

Litjens, G., Kooi, T., Bejnordi, B. E., Setio, A., and Sánchez, C. I. (2017). A survey on deep learning in medical image analysis. *Med. Image Anal.* 42, 60–88. doi: 10.1016/j.media.2017.07.005

Long, J., Shelhamer, E., and Darrell, T. (2015). Fully convolutional networks for semantic segmentation. *IEEE Trans. Pattern Anal. Mach. Intell.* 39, 640–651. doi: 10.1109/CVPR.2015.7298965

Nguyen, N. Q., Vo, D. M., and Lee, S. W. (2020). Contour-aware polyp segmentation in colonoscopy images using detailed upsamling encoder-decoder networks. *IEEE Access* 8, 99495–99508. doi: 10.1109/ACCESS.2020.2995630

Pogorelov, K., Randel, K. R., Griwodz, C., Lange, T. D., and Halvorsen, P. (2017). "KVASIR: a multi-class image dataset for computer aided gastrointestinal disease detection," in *Proceedings of the 8th ACM on Multimedia Systems Conference*, (New York, NY: ACM), 164–169. doi: 10.1145/3083187.3083212

Qin, X., Zhang, Z., Huang, C., Dehghan, M., Zaïane, O. R., and Jagersand, M. (2020). U2-Net: going deeper with nested U-structure for salient object detection. *Pattern Recognit.* 106:107404. doi: 10.1016/j.patcog.2020.107404

Ronneberger, O., Fischer, P., and Brox, T. (2015). "U-Net: convolutional networks for biomedical image segmentation," in *Proceedings of the International Conference on Medical Image Computing and Computer-Assisted Intervention*, (Cham: Springer), doi: 10.1007/978-3-662-54345-0_3

Sandler, M., Howard, A., Zhu, M., Zhmoginov, A., and Chen, L. C. (2018). "MobileNetV2: inverted residuals and linear bottlenecks," in *Proceedings of the 2018 IEEE/CVF Conference on Computer Vision and Pattern Recognition (CVPR)*, (Salt Lake City, UT: IEEE), 4510–4520. doi: 10.1109/CVPR.2018.00474

Simonyan, K., and Zisserman, A. (2014). Very deep convolutional networks for large-scale image recognition. *arXiv* [Preprint]

Xia, K. J. (2020). *A Study On The Assisted Diagnosis Of Liver Space Occupancy Based On Depth Feature Of Abdominal CT Imaging*. Beijing: China University of Mining and Technology.

Yin, M., Yao, Z., Cao, Y., Li, X., Zhang, Z., Lin, S., et al. (2020). "Disentangled non-local neural networks," in *Proceedings of the ECCV 2020. Lecture Notes in Computer Science*, Vol. 12360, (Cham: Springer), 191–207. doi: 10.1007/978-3-030-58555-6_12

Yuan, Y., Chen, X., and Wang, J. (2020). "Object-contextual representations for semantic segmentation," in *Proceedings of the ECCV 2020. Lecture Notes in Computer Science*, Vol. 12351, (Cham: Springer), 173–190. doi: 10.1007/978-3-030-58539-6_11

Zhao, H., Shi, J., Qi, X., Wang, X., and Jia, J. (2017). "Pyramid scene parsing network," in *Proceedings of the 2017 IEEE Conference on Computer Vision and Pattern Recognition (CVPR)*, Vol. 1, (Honolulu, HI), 6230–6239.

Zhou, Z., Siddiquee, M., Tajbakhsh, N., and Liang, J. (2018). "UNet++: a nested U-Net architecture for medical image segmentation," in *Proceedings of the Medical Image Computing and Computer-Assisted Intervention Workshop* (Berlin: Springer) 3–11.

Zhou, Z., Siddiquee, M., Tajbakhsh, N., and Liang, J. (2020). Unet++: redesigning skip connections to exploit multiscale features in image segmentation. *IEEE Trans. Med. Imaging* 39, 1856–1867. doi: 10.1109/TMI.2019.2959609

Conflict of Interest: The authors declare that the research was conducted in the absence of any commercial or financial relationships that could be construed as a potential conflict of interest.

APPENDIX

TABLE A1 | mIOU evaluation index of multi-class medical image segmentation.

Model	mIOU					
	DSB2018	**Lung**	**Eye blood vessels**	**ISBI2015**	**Liver cancer**	**Intestinal cancer**
UNet (Ronneberger et al., 2015)	0.9078	0.9691	0.8106	0.8020	0.9854	0.9641
LinkNet (Chaurasia and Culurciello, 2018)	0.8983	0.9166	0.7457	0.7711	0.9803	0.9279
U^2Net (Qin et al., 2020)	0.9126	0.9732	0.8070	0.8031	0.9854	0.9609
UNet++ (Zhou et al., 2018, 2020)	0.9108	0.9697	0.8083	0.8023	0.9849	0.9733
UNet+++ (Huang et al., 2020)	0.9134	0.9715	0.8077	0.7995	0.9858	0.9707
PraNet (Fan et al., 2020)	0.9453	0.9897	0.8762	0.8862	0.9903	0.9801
PspNet (Zhao et al., 2017)	0.7892	0.9568	0.5464	0.4891	0.9667	0.9551
Deeplabv3+ (Chen et al., 2018)	0.7871	0.9661	0.5449	0.4890	0.9721	0.9623
FCN8 (Long et al., 2015)	0.9041	0.9815	0.6687	0.7172	0.9853	0.9645
MBFFNet	0.9132	0.9704	0.8127	0.8061	0.9884	0.9709

TABLE A2 | Multi-class medical image segmentation *F*-score evaluation index.

Model	*F*-score					
	DSB2018	**Lung**	**Eye blood vessels**	**ISBI2015**	**Liver cancer**	**Intestinal cancer**
UNet (Ronneberger et al., 2015)	0.9502	0.9842	0.8872	0.8864	0.9926	0.9815
LinkNet (Chaurasia and Culurciello, 2018)	0.9446	0.9803	0.8379	0.8657	0.9900	0.9616
U^2Net (Qin et al., 2020)	0.9527	0.9864	0.8846	0.8873	0.9926	0.9798
UNet++ (Zhou et al., 2018, 2020)	0.9519	0.9845	0.8855	0.8865	0.9923	0.9863
UNet+++ (Huang et al., 2020)	0.9532	0.9855	0.8851	0.8846	0.9928	0.9850
PraNet (Fan et al., 2020)	0.9732	0.9912	0.9213	0.9274	0.9912	0.9883
PspNet (Zhao et al., 2017)	0.8729	0.9778	0.6350	0.6223	0.9828	0.9712
Deeplabv3+ (Chen et al., 2018)	0.8714	0.9827	0.6337	0.6170	0.9857	0.9653
FCN8 (Long et al., 2015)	0.9478	0.9906	0.7722	0.8278	0.9925	0.9671
MBFFNet	0.9604	0.9839	0.8895	0.8928	0.9926	0.9851

TABLE A3 | Dice loss with CE evaluation index for multi-class medical image segmentation.

Model	Dice Loss with CE					
	DSB2018	**Lung**	**Eye blood vessels**	**ISBI2015**	**Liver cancer**	**Intestinal cancer**
UNet (Ronneberger et al., 2015)	0.1264	0.0548	0.2222	0.3310	0.0146	0.0377
LinkNet (Chaurasia and Culurciello, 2018)	0.1423	0.0714	0.3258	0.3822	0.0215	0.0779
U^2Net (Qin et al., 2020)	0.1191	0.0471	0.2344	0.3327	0.0148	0.0411
UNet++ (Zhou et al., 2018, 2020)	0.1213	0.0547	0.2248	0.3202	0.0151	0.0276
UNet+++ (Huang et al., 2020)	0.1199	0.0514	0.2351	0.3331	0.0144	0.0307
PraNet (Fan et al., 2020)	0.0921	0.0321	0.1453	0.2145	0.0101	0.0219
PspNet (Zhao et al., 2017)	0.3046	0.0743	0.6231	0.8119	0.0351	0.0801
Deeplabv3+ (Chen et al., 2018)	0.3068	0.0565	0.6285	0.8169	0.0290	0.0792
FCN8 (Long et al., 2015)	0.1318	0.0350	0.4485	0.4874	0.0145	0.0407
MBFFNet	0.1303	0.0638	0.2545	0.3254	0.0130	0.0303

frontiers in Bioengineering and Biotechnology

ORIGINAL RESEARCH
published: 06 August 2021
doi: 10.3389/fbioe.2021.696227

A Dense RNN for Sequential Four-Chamber View Left Ventricle Wall Segmentation and Cardiac State Estimation

Yu Wang[1] *and Wanjun Zhang*[2]*

[1] Research Center for Physical Education Reform and Development, School of Physical Education, Henan University, Kaifeng, China, [2] Henan Key Laboratory of Big Data Analysis and Processing, School of Computer and Information Engineering, Henan University, Kaifeng, China

The segmentation of the left ventricle (LV) wall in four-chamber view cardiac sequential image is significant for cardiac disease diagnosis and cardiac mechanisms study; however, there is no successful reported work on sequential four-chambered view LV wall segmentation due to the complex four-chamber structure and diversity of wall motion. In this article, we propose a dense recurrent neural network (RNN) algorithm to achieve accurately LV wall segmentation in a four-chamber view MRI time sequence. In the cardiac sequential LV wall process, not only the sequential accuracy but also the accuracy of each image matters. Thus, we propose a dense RNN to provide compensation for the first long short-term memory (LSTM) cells. Two RNNs are combined in this work, the first one aims at providing information for the first image, and the second RNN generates segmentation result. In this way, the proposed dense RNN improves the accuracy of the first frame image. What is more is that, it improves the effectiveness of information flow between LSTM cells. Obtaining more competent information from the former cell, frame-wise segmentation accuracy is greatly improved. Based on the segmentation result, an algorithm is proposed to estimate cardiac state. This is the first time that deals with both cardiac time-sequential LV segmentation problems and, robustly, estimates cardiac state. Rather than segmenting each frame separately, utilizing cardiac sequence information is more stable. The proposed method ensures an Intersection over Union (IoU) of 92.13%, which outperforms other classical deep learning algorithms.

Keywords: four-chamber view cardiac, recurrent neural network, image segmentation, left ventricle wall, cardiac state estimation

OPEN ACCESS

Edited by:
Xiaoguang Zhou,
Beijing University of Posts and Telecommunications (BUPT), China

Reviewed by:
Miao Zhang,
Monash University, Australia
Jun Zhang,
Shanghai Normal University, China

***Correspondence:**
Wanjun Zhang
wjz@henu.edu.cn

Specialty section:
This article was submitted to Bionics and Biomimetics, a section of the journal Frontiers in Bioengineering and Biotechnology

Received: *16 April 2021*
Accepted: *21 June 2021*
Published: *06 August 2021*

Citation:
Wang Y and Zhang W (2021) A Dense RNN for Sequential Four-Chamber View Left Ventricle Wall Segmentation and Cardiac State Estimation. Front. Bioeng. Biotechnol. 9:696227. doi: 10.3389/fbioe.2021.696227

1. INTRODUCTION

The sequential segmentation of the left ventricle (LV) wall in a four-chamber view MRI image plays an important role in clinical disease diagnosis and physiological mechanism research works. Compared with a two-chamber view cardiac image, a four-chamber view image has distinctive advantages in cardiac assessment. For example, it is needed to compare the four chambers of cardiac in size and contractility to diagnose congenital heart disease (Copel et al., 1987); an LV sequence image can be used to evaluate the LV wall motion, which has been used to evaluate the risk of heart

failure (Konstam et al., 2011); Many studies have focused on the mechanisms of excitable tissue in cardiac based on the morphological feature of an LV wall (Constantino et al., 2010). Furthermore, a four-chamber view sequence is used to measure the relationship between left ventricular diastolic dysfunction and exercise intolerance in obese heart failure with preserving (Samuel et al., 2021), the cardiac state estimate is critical for the assessment of cardiac function and morphology. Thus, it is desired to propose a method to solve the sequential LV wall segmentation problem in a four-chamber view MRI image.

1.1. Challenges of LV Segmentation

However, the automatic segmentation of LV wall in four-chamber view MRI images is still a challenge, as shown in **Figure 1**, (1) the complex structure of four-chamber view MRI image makes it hard to separate LV wall with other tissues. **Figure 1A** also shows that, compared with the two-chamber view cardiac image, the influence of the right ventricle (RV) and right atrium makes it harder to segment the LV wall. The similarity in intensity and structure feature with RV wall also increased the difficulty of LV wall segmentation. (2) High segmentation accuracy is desired in clinical for wall motion evaluation. **Figure 1B** shows LV wall changes at contraction state and diastole state. The difference between neighbor frames is small, which needs high accuracy on distinguishing contraction state and diastole state. (3) Segmentation error evaluation problem. **Figure 1C** shows that, the error area and IoU of the two error detection illustration examples are the same; however, in sequential image processing progress, their effect on clinical evaluation is different and may lead to misdiagnosis. Thus, a method is needed to be proposed to deal with time-sequential cardiac images and to achieve both frame-wise and sequence-wise accuracy.

1.2. Related Works

1.2.1. Automated Cardiac Segmentation Methods

Unfortunately, there is no successful reported research work focusing on automatic sequential LV wall segmentation due to the challenges mentioned above. Most research studies focus on the assessment of LV sequence parameters (such as LV wall thickness, area, and so on) and the LV wall segmentation of a single frame. Recently, the deep learning method is widely used in medical image processing. An anatomically constrained neural network (ACNN) based cardiac image enhancement and segmentation method is proposed in Oktay et al. (2018). The method works well on MRI images. In most previous segmentation works (Tran, 2016; Oktay et al., 2018; Khened et al., 2019), each frame of the MRI sequence is processed independently. To achieve continuity of segmentation or quantification and take advantage of the sequence information, a correlation between different frame must be established. In the language generative deep learning method, sequence generate adversarial nets (SGAN) proposed in Yu et al. (2017) performs well in sequence processing and achieves a good result; however, this model can-not get a satisfactory result when it comes to sequence image segmentation.

1.2.2. Deep Learning Architectures for Medical Image Segmentation

In the context of medical image segmentation method, convolutional neural networks (CNN)-based works have shown great potential in recent studies (Renard et al., 2020). In methods (Avendi et al., 2016; Ngo et al., 2017; Kasinathan et al., 2019; Ma and Yang, 2020), CNN and traditional methods (such as level set method and deformable models) are combined to achieve good segmentation accuracy. Fully convolutional

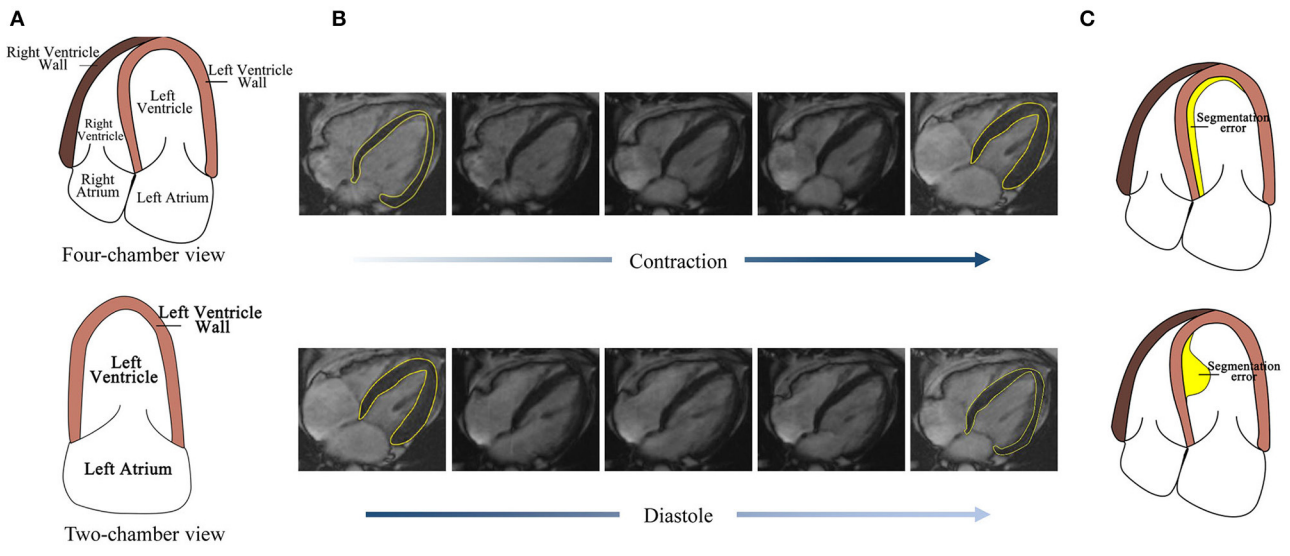

FIGURE 1 | Challenges for four-chamber view MRI image segmentation. **(A)** The structure of the four-chamber view cardiac image is more complex than that of the two-chamber view. **(B)** The LV wall difference between frames caused by cardiac motion is small, thus high accuracy is needed. **(C)** Detection error with the same area but the different effect to its subsequent frames.

networks (FCN) (Long et al., 2015) and U-net (Ronneberger et al., 2015) have achieved remarkable success in the image segmentation problem. Compared with original U-net, attention modules combined U-net (Dong et al., 2018; Schlemper et al., 2019), self-guided attention U-net (Ashish and Jose, 2021) has resulted in enhanced models for pixel-wise segmentation tasks. Based on U-net, a recurrent convolutional neural network (RCNN) is proposed in Alom et al. (2018). The feature accumulation in RCNN ensures better feature representation for segmentation tasks. In Peng et al. (2020), a deep snake method is proposed to segment image by controlling the movement of object boundaries. In Xie et al. (2020), a PolarMask method is proposed and contour of instance in a polar coordinate is predicted. These two methods are good at segment instance with less concave property.

Recurrent Neural Network

Recurrent Neural Network (RNN) (Zaremba et al., 2014) is specialized in processing sequential data. Long short term memory (LSTM) cell (Greff et al., 2015) or gated recurrent unit (GRU) Cho et al. (2014) are combined in RNN to transfer information. Promising results have been achieved by RNN or RNN variants in speech processing (Karita et al., 2019; Li et al., 2019), text generation (Pawade et al., 2018; Yang et al., 2019), classification (Premkumar et al., 2020), and image processing (Yao et al., 2019; Zhou et al., 2020). RNN has been used in Xue et al. (2017) regional wall thicknesses of LV.

Convolutional networks, such as FCN and U-net, focus on the problem of single-frame image processing. Compared with other neural networks, RNN is good at dealing with sequential image processing problems. The cardiac in MRI sequence contracts and diastole continuously. To make the best of information between frames, we choose RNN to achieve the LV wall segmentation goal.

1.3. Contributions

We proposed a dense RNN method to deal with the challenges and overcome the shortage of existing methods mentioned above. The details of highlights are as follows:

(1) It is the first time that an RNN successfully deals with a time-sequential cardiac segmentation problem. Existing methods focus on single frame segmentation or difference slice sequential segmentation. In this article, the time-sequential frames belong to one slice of cardiac, but with different cardiac state, which is able to observe cardiac structure change. Rather than segment a single image, segment sequence takes advantage of the relationship between frames, which makes it better to solve the complex structures and wall motion problems.

(2) A dense RNN is proposed to improve the effectiveness of the information transmitted between LSTM cells and achieve frame-wise accuracy. In RNN, the first frame acquires no hidden information, but its LSTM output is transmitted to the rest of the frames and plays a most important role. The proposed dense RNN contains two RNNs. The first RNN aims at providing dense hidden information for the first LSTM cell in the second RNN. The second RNN receives the hidden information and generates the segmentation result. This not only contributes to improving the accuracy of the first image but also makes the output of the first LSTM cell contain more useful information. It is the same with the subsequent cells. Thus, frame-wise accuracy is improved.

(3) Based on the LV wall segmentation result, an algorithm is proposed to determine the cardiac state. The algorithm uses mean cardiac change difference instead of the difference between frames, which is more robust. As the change of neighbor frames is relatively small, we first calculate the difference between two neighbor frames and then use the mean difference to determine the cardiac state.

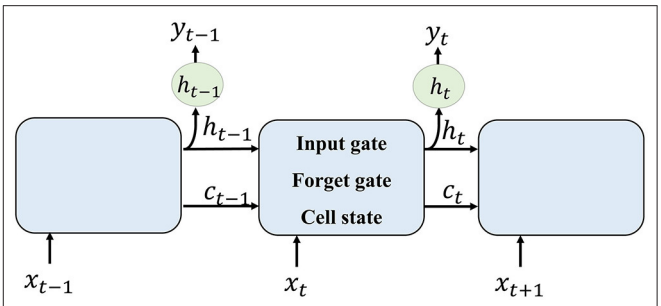

FIGURE 2 | Recurrent neural network (RNN) method illustration.

This article is organized as follows: first, the background of cardiac LV segmentation and the existing method are introduced; second, the proposed method will be illustrated; third, the experimental result will be analyzed.

2. METHOD

The proposed network mainly contains two RNNs. In this section, RNN is first introduced. And then, the proposed dense RNN is described.

2.1. Recurrent Neural Network

Recurrent neural network is good at dealing with sequential information. It consists of several LSTM cells. Each unit receives a hidden layer from the former cell, together with the current input, the output layer is generated.

The method of RNN is shown in **Figure 2**. Each LSTM cell receives information from the previous cell and transmits information to the next one. For an input image sequence $x_1, x_2, \ldots, x_n$, each x_t input into an LSTM cell. In general, an LSTM cell contains an input gate that generates i_t, a forget gate that generates f_t, and a memory vector c_t. The relationship between these gates and the vector of LSTM can be denoted as follows:

$$\begin{aligned} f_t &= sigm(W_f \cdot [h_{t-1}, x_t] + b_f) \\ i_t &= sigm(W_i \cdot [h_{t-1}, x_t] + b_i) \\ \widetilde{c}_t &= tanh(W_o \cdot [h_{t-1}, x_t] + b_o) \end{aligned} \tag{1}$$

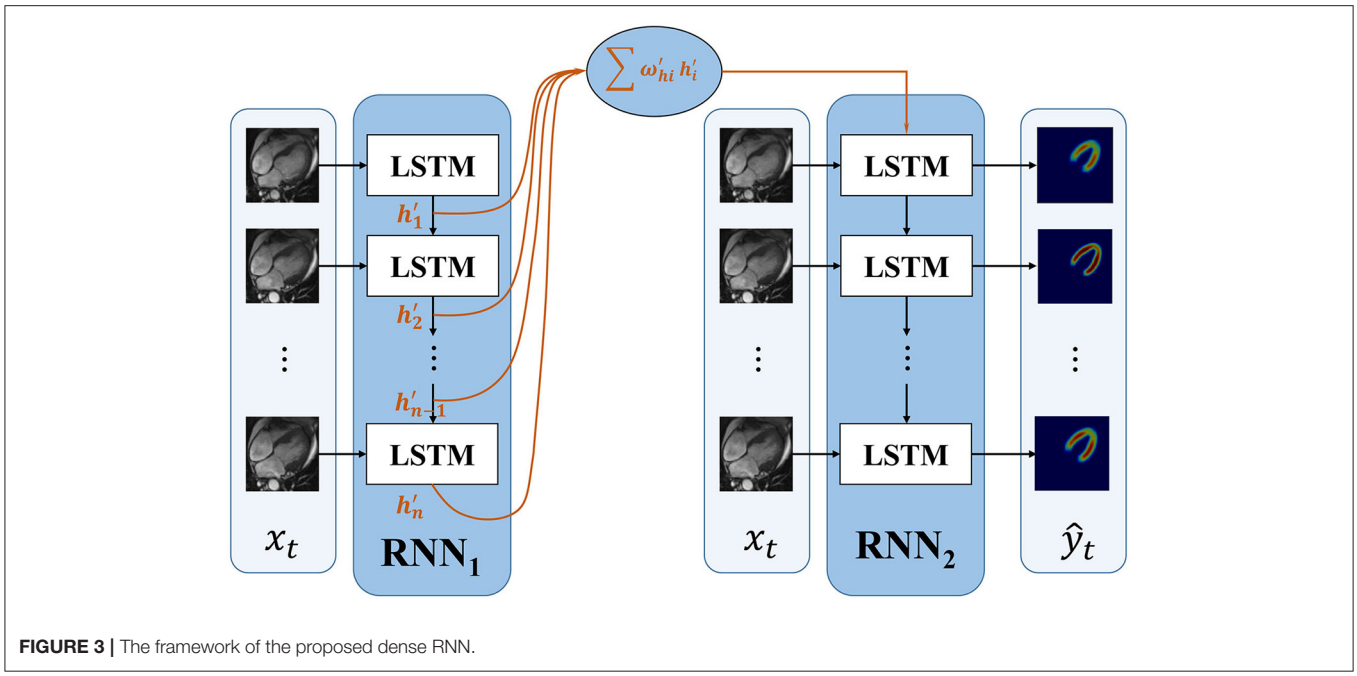

FIGURE 3 | The framework of the proposed dense RNN.

where h_{t-1} is the hidden layer of the former cell and b is the bias factor. Then, the memory cell of LSTM can be calculated as follows:

$$c_t = f_t * c_{t-1} + i_t * \tilde{c}_t \tag{2}$$

where $*$ is convolution transform. The output o_t and the hidden layer to the next LSTM are given by the following :

$$\begin{aligned} o_t &= sigm(W_o \cdot [h_{t-1}, x_t] + b_o) \\ h_t &= o_t \odot tanh(c_t) \end{aligned} \tag{3}$$

To formulate the segmentation result of one input x_t, the current cell receives hidden layer h_{t-1} and memory vector c_{t-1} from former cell. The forget gate selects information that should be abandoned. Combining h_{t-1} and current input x_t, the input gate selects new information that should be kept and generates a new cell state. The output of one cell is generated by the current input and formerly hidden layer.

2.2. Dense RNN

As illustrated in section RNN and shown in **Figure 2**, an LSTM cell L_i receives a hidden layer and memory cell from LSTM cell L_{i-1}, together with input image x_i, its segmentation image is generated. The first image in the sequence receives no information from the former cell. Thus, the accuracy of the first image is lower than the others. The hidden layer information and memory cell it flows to its following frames contain lower effective information.

To improve the accuracy of the first frame and make the information transmitted between frames more efficient, we propose an improved RNN. The proposed dense RNN is constituted by two RNNs. As shown in **Figure 3**, dense generator, main RNN (RNN_2 in **Figure 3**) is used to generate segmentation results, while compensation RNN(RNN_1 in **Figure 3**) provides compensation for the first LSTM cell in main RNN. With this compensation, the first frame acquires more information and makes the information flow in the main RNN more effective.

The first LSTM cell plays an important role in RNN. Its output information transmits to the subsequent LSTM cells; however, the first LSTM receives no hidden information, which means $h_0 = 0$. The only input information it deals is x_1. In this proposed dense RNN, the input hidden layer of the first LSTM cell in RNN_2 can be denoted as follows:

$$h_0 = \sum_{i=1}^{n} \omega'_{hi} h'_n \tag{4}$$

where $h'_1, h'_2, \ldots, h'_n$ denote the output hidden layer of each LSTM in RNN_1. The proposed dense RNN allows the network itself to choose the proper input hidden layer for the main RNN. The weight ω'_{hi} in Equation 4 is trained by the network. With the weighted input hidden layer, the accuracy of the first frame is improved and the output of the first LSTM in the main RNN contains more useful information. In this way, the segmented accuracy of the subsequent frames is also improved.

The loss function is calculated by measuring the difference of ground truth and the output of the second RNN:

$$L = \sum_{t=1}^{T} \left(-y_t \log \hat{y}_t - (1 - y_t) \log(1 - \hat{y}_t)\right) \tag{5}$$

where y_t is the ground truth of frame t and $\hat{y}_t$ is the output of RNN_2.

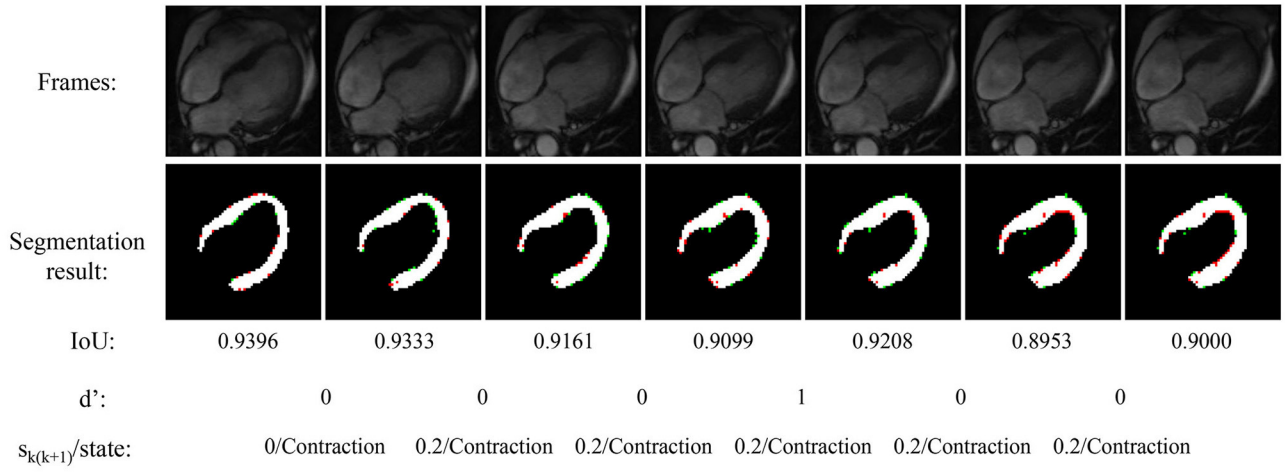

FIGURE 4 | Experimental result of the proposed method during cardiac contraction. Red points in segmentation result: undetected LV pixels. Green points in segmentation result: error-detected pixels.

2.3. Cardiac State Estimation

The LV wall becomes thick during the contraction state and becomes thin during the diastole state. However, the change is not obvious for adjacent frames. In this article, we first calculate the difference between two adjacent frames as a reference. The difference of frame k and frame $k+1$ is defined by comparing the area of LV wall using Equation 6.

$$d'_{k(k+1)} = \begin{cases} 1, & if\ Area(f_k) > Area(s_{k+1}) \\ 0, & else \end{cases} \tag{6}$$

where $Area_{(f_k)}$ is the LV wall segmentation result of the area of the kth frame. Then, the cardiac state is estimated by the following equation:

$$s_{k(k+1)} = \frac{1}{N} \sum_{i=k-N/2}^{k+N/2-1} d'_{i(i+1)} \tag{7}$$

With the result of equation 7, $s_{k(k+1)} < 0.5$ means that the cardiac frame is in a state of diastole, or else it is in a state contraction. By using Equation 7, the incorrect estimation by only two adjacent frames was reduced.

3. EXPERIMENTAL RESULTS AND DISCUSSION

3.1. Dataset and Setting

The proposed method is tested using 137 groups of four-chamber view MRI cardiac images from 137 patients. Each group contains 18 continuous frames of the image, and every group contains frames of contraction and diastole cardiac states. The images are resized to 64×64. The ground truth of the LV wall is manually marked by doctors. We adopt 130 groups of images for training and the other 7 groups for testing. During training process, we use different frames as start frames to improve the robustness of the networks. The proposed network is implemented based on PyCharm and performed on NVIDIA Tesla P100.

3.2. Evaluation Metrics

The proposed method performs better than SeqGAN (Yu et al., 2017) and CNN method. The segmentation result is evaluated using the IoU factor. The IoU factor is obtained by $IoU = \frac{S \cap G}{S \cup G}$, where S is the segmentation result and G is the ground truth. $\cap$ and $\cup$ is the action of intersection and union.

3.3. Generation Performance

Figure 4 shows the experimental result of the proposed method. The frames in this sequence are during a contraction state, and the LV wall changes from thin to thick. The mean IoU of these frames is 91.64%. Though the changes between frames are little, the segmentation result reflex the change of LV wall thickness. **Figure 5** shows the segmentation result during cardiac diastole. It can be seen from **Figures 4** to **5** that the proposed method can obtain accurate diastole and contraction cardiac LV wall.

Figure 4 also illustrated the cardiac state method. All the frames are in a period of contraction. The difference of adjacent frames d' incorrect estimate two frames as diastole with value 1. After the mean value calculated by equation 7, the incorrect estimate is corrected.

Figure 6 shows the IoU of the proposed method and other methods at different training interactions. The proposed method reaches an IoU of 92.13%, while the RNN method without dense net gets a result of 38.92%. We also use Unet (Ronneberger et al., 2015), a classic CNN deep learning method in image segmentation, to segment the LV wall. After 2000 times of interactions, the IoU reaches 61.75%. Compared with the other

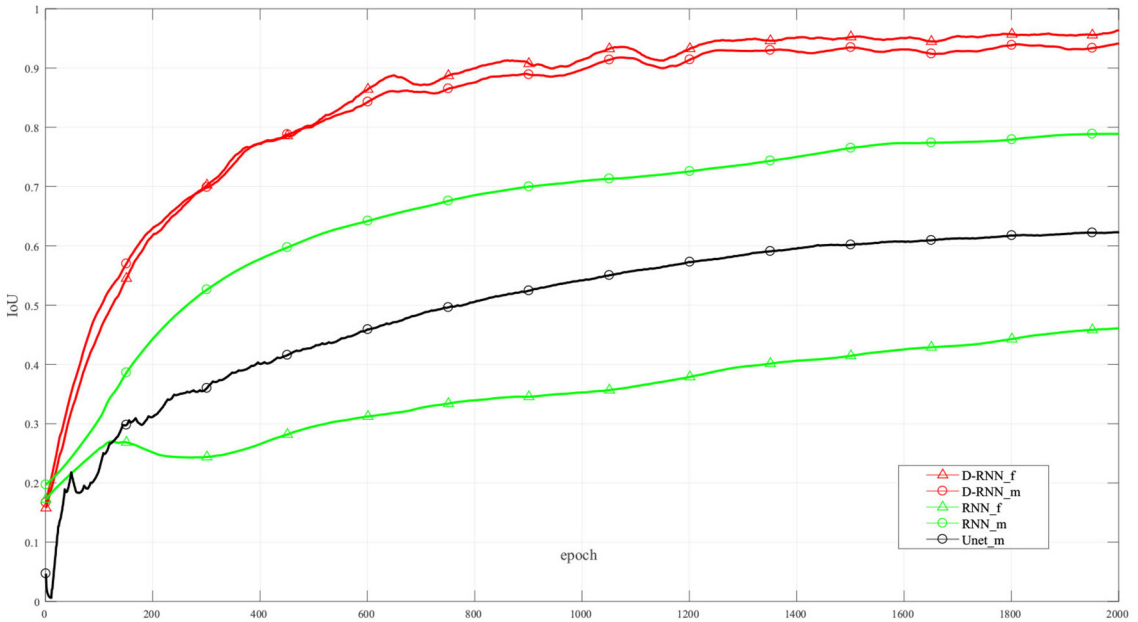

FIGURE 5 | Segmentation result of the proposed method during cardiac diastole.

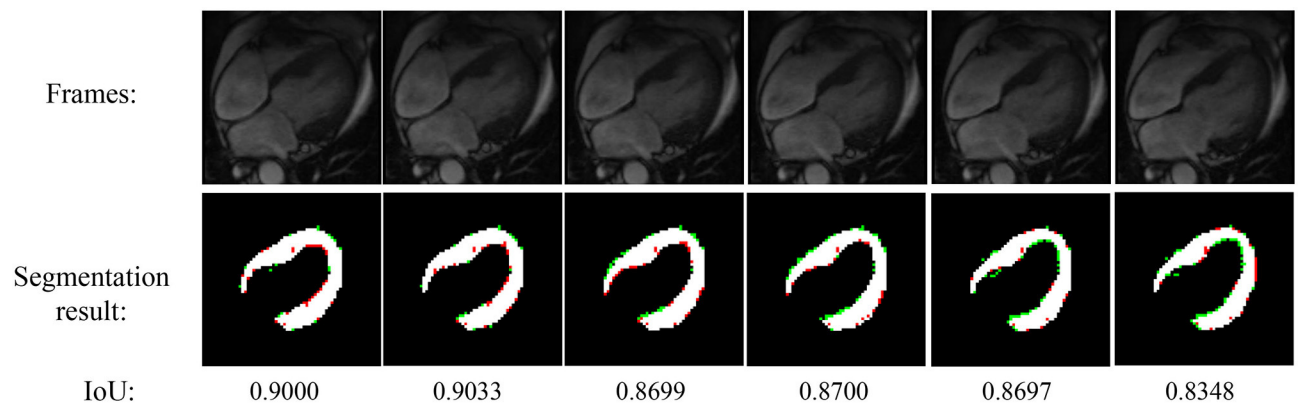

FIGURE 6 | IoU at difference training interactions. _f: IoU of the first frame; _m: mean IoU of the sequence. For illustration propose, the line in this figure is filtered.

method, the proposed method highly improved the mean sequential segmentation accuracy.

The dense compensation for an RNN proposed in this method greatly improved the accuracy of the first frame in the sequence. Thus, the proposed method makes the hidden information flow in different LSTM cells more effectively, and the mean IoU is improved. It can be seen from **Figure 6**, the NoDense curve, that although the mean IoU by NoDense network is increasing with the increasing interaction, the IoU of the first frame remains unsatisfied. Each frame in the image sequence needed to be segmented with a promising result. The proposed dense RNN in DL-GAN works improves the mean accuracy and also ensures the accuracy of each frame. It can be seen from the DL-GAN curve in **Figure 6** that the IoU factor of the first frame increases along with the mean IoU of the sequence. The mean accuracy is increased by 55.21% than the NoDense network.

4. CONCLUSION

In this article, a dense RNN method is proposed to segment the LV wall in a sequential four-chamber view MRI image. With the dense RNN, the segmentation accuracy of each frame in the sequence is guaranteed, and the accuracy of the first frame is greatly improved. The network reaches an IoU of 92.13%, which indicates the proposed method has prospects in cardiac disease diagnosis and cardiac mechanism analysis.

DATA AVAILABILITY STATEMENT

The original contributions presented in the study are included in the article/supplementary material, further inquiries can be directed to the corresponding author/s.

AUTHOR CONTRIBUTIONS

YW contributed to the conception of the study and data analysis. WZ performed the experiment and wrote the manuscript. Both authors contributed to the article and approved the submitted version.

FUNDING

This work was funded by Key R&D and Promotion Projects of Henan Province (No. 212102311014), National Natural Science Foundation of China (No. 62002100), Henan Province Philosophical Social Science Planned Item (No. 2019CTY016), and the Education Department of Henan province of Humanities and Social Science Project (No. 2020-ZDJH-039).

REFERENCES

Alom, M. Z., Hasan, M., Yakopcic, C., Taha, T. M., and Asari, V. K. (2018). Recurrent residual convolutional neural network based on u-net (r2u-net) for medical image segmentation. *arXiv preprint arXiv*:1802.06955. doi: 10.1109/NAECON.2018.8556686

Ashish, S., and Jose, D. (2021). Multi-scale self-guided attention for medical image segmentation. *IEEE J. Biomed. Health Inform*. 25, 121–130. doi: 10.1109/JBHI.2020.2986926

Avendi, M., Kheradvar, A., and Jafarkhani, H. (2016). A combined deep-learning and deformable-model approach to fully automatic segmentation of the left ventricle in cardiac mri. *Med. Image Anal*. 30,108–119. doi: 10.1016/j.media.2016.01.005

Cho, K., van Merriënboer, B., Gulcehre, C., Bougares, F., Schwenk, H., and Bengio, Y. (2014). Learning phrase representations using rnn encoder-decoder for statistical machine translation. *arxiv*. Available online at: https://arxiv.org/abs/1406.1078v3. doi: 10.3115/v1/D14-1179

Constantino, J., Long, Y., Ashihara, T., and Trayanova, N. A. (2010). Tunnel propagation following defibrillation with icd shocks: hidden postshock activations in the left ventricular wall underlie isoelectric window. *Heart Rhythm* 7, 953–961. doi: 10.1016/j.hrthm.2010.03.026

Copel, J. A., Pilu, G., Green, J., Hobbins, J. C., and Kleinman, C. S. (1987). Fetal echocardiographic screening for congenital heart disease: the importance of the four-chamber view. *Am. J. Obstet. Gynecol*. 157, 648–655. doi: 10.1016/S0002-9378(87)80022-4

Dong, N., Yaozong, G., Li, W., and Dinggang, S. (2018). "Asdnet: attention based semi-supervised deep networks for medical image segmentation," in *International Conference on Medical Image Computing and Computer-Assisted Intervention* (Granada: Springer), 370–378.

Greff, K., Srivastava, R., Koutník, J., Steunebrink, B., and Schmidhuber, J. (2015). Lstm: a search space odyssey. *IEEE Trans. Neural Netw. Learn. Syst*. 28, 2222–2232. doi: 10.1109/TNNLS.2016.2582924

Karita, S., Chen, N., Hayashi, T., Hori, T., Inaguma, H., Jiang, Z., et al. (2019). "A comparative study on transformer vs rnn in speech applications," in *2019 IEEE Automatic Speech Recognition and Understanding Workshop (ASRU)* (Sentosa), 449–456.

Kasinathan, G., Jayakumar, S., Gandomi, A. H., Ramachandran, M., Fong, S. J., and Patan, R. (2019). Automated 3-d lung tumor detection and classification by an active contour model and cnn classifier. *Expert. Syst. Appl*. 134, 112–119. doi: 10.1016/j.eswa.2019.05.041

Khened, M., Kollerathu, V. A., and Krishnamurthi, G. (2019). Fully convolutional multi-scale residual densenets for cardiac segmentation and automated cardiac diagnosis using ensemble of classifiers. *Med. Image Anal*. 51, 21–45. doi: 10.1016/j.media.2018.10.004

Konstam, M. A., Kramer, D. G., Patel, A. R., Maron, M. S., and Udelson, J. E. (2011). Left ventricular remodeling in heart failure: current concepts in clinical significance and assessment. *JACC Cardiovasc. Imaging* 4, 98–108. doi: 10.1016/j.jcmg.2010.10.008

Li, J., Zhao, R., Hu, H., and Gong, Y. (2019). "Improving rnn transducer modeling for end-to-end speech recognition," in *2019 IEEE Automatic Speech Recognition and Understanding Workshop (ASRU)* (Singapore: IEEE), 114–121.

Long, J., Shelhamer, E., and Darrell, T. (2015). Fully convolutional networks for semantic segmentation. *IEEE Trans. Pattern Anal. Mach. Intell*. 39, 640–651. doi: 10.1109/CVPR.2015.7298965

Ma, J., and Yang, X. (2020). "Combining cnn and hybrid active contours for head and neck tumor segmentation in ct and pet images," in *3D Head and Neck Tumor Segmentation in PET/CT Challenge* (Springer), 59–64.

Ngo, T. A., Lu, Z., and Carneiro, G. (2017). Combining deep learning and level set for the automated segmentation of the left ventricle of the heart from cardiac cine magnetic resonance. *Med. Image Anal*. 35, 159–171. doi: 10.1016/j.media.2016.05.009

Oktay, O., Ferrante, E., Kamnitsas, K., Heinrich, M., Bai, W., Caballero, J., et al. (2018). Anatomically constrained neural networks (acnns): application to cardiac image enhancement and segmentation. *IEEE Trans. Med. Imaging* 37, 384–395. doi: 10.1109/TMI.2017.2743464

Pawade, D., Sakhapara, A. M., Jain, M., Jain, N., and Gada, K. (2018). Story scrambler-automatic text generation using word level rnn-lstm. *Int. J. Inform. Technol. Comput. Sci*. 10, 44–53. doi: 10.5815/ijitcs.2018.06.05

Peng, S., Jiang, W., Pi, H., Li, X., Bao, H., and Zhou, X. (2020). "Deep snake for real-time instance segmentation," in *Proceedings of the IEEE/CVF Conference on Computer Vision and Pattern Recognition* (Seattle, WA), 8533–8542.

Premkumar, K. A. R., Bharanikumar, R., and Palaniappan, A. (2020). Riboflow: using deep learning to classify riboswitches with ∼99% accuracy. *Front. Bioeng. Biotechnol*. 8:808. doi: 10.3389/fbioe.2020.00808

Renard, F., Guedria, S., De Palma, N., and Vuillerme, N. (2020). Variability and reproducibility in deep learning for medical image segmentation. *Sci. Rep*. 10, 1–16. doi: 10.1038/s41598-020-69920-0

Ronneberger, O., Fischer, P., and Brox, T. (2015). "U-net: Convolutional networks for biomedical image segmentation," in *International Conference on Medical Image Computing and Computer-Assisted Intervention* (Cham: Springer), 234–241.

Samuel, T. J., Kitzman, D., Haykowsky, M., Upadhya, B., Brubaker, P., Nelson, M., et al. (2021). Left ventricular diastolic dysfunction and exercise intolerance in obese heart failure with preserved ejection fraction. *Am. J. Physiol. Heart Circ. Physiol*. 320, H1535– 1542. doi: 10.1152/ajpheart.00610.2020

Schlemper, J., Oktay, O., Schaap, M., Heinrich, M., Kainz, B., Glocker, B., et al. (2019). Attention gated networks: learning to leverage salient regions in medical images. *Med. Image Anal*. 53, 197–207. doi: 10.1016/j.media.2019.01.012

Tran, P. V. (2016). A fully convolutional neural network for cardiac segmentation in short-axis mri. *arXiv preprint arXiv*:1604.00494.

Xie, E., Sun, P., Song, X., Wang, W., Liu, X., Liang, D., et al. (2020). "Polarmask: Single shot instance segmentation with polar representation," in *Proceedings of the IEEE/CVF Conference on Computer Vision and Pattern Recognition* (Seattle, WA), 12193–12202.

Xue, W., Nachum, I. B., Pandey, S., Warrington, J., Leung, S., and Li, S. (2017). "Direct estimation of regional wall thicknesses via residual recurrent neural network," in *Information Processing in Medical Imaging*, eds M. Niethammer, M. Styner, S. Aylward, H. Zhu, I. Oguz, P. -T. Yap, and D. Shen (Boone, NC: Springer International Publishing), 505–516.

Yang, Z., Guo, X., Chen, Z., Huang, Y., and Zhang, Y. (2019). Rnn-stega: Linguistic steganography based on recurrent neural networks. *IEEE*

Trans. Inform. Forensics Secur. 14, 1280–1295. doi: 10.1109/TIFS.2018.2871746

Yao, H., Zhang, X., Zhou, X., and Liu, S. (2019). Parallel structure deep neural network using cnn and rnn with an attention mechanism for breast cancer histology image classification. *Cancers* 11:1901. doi: 10.3390/cancers11121901

Yu, L., Zhang, W., Wang, J., and Yu, Y. (2017). "Seqgan: sequence generative adversarial nets with policy gradient," in *Proceedings of the Thirty-First AAAI Conference on Artificial Intelligence* (San Francisco, CA: AAAI-2017), 2852–2858.

Zaremba, W., Sutskever, I., and Vinyals, O. (2014). Recurrent neural network regularization. *arXiv preprint arXiv*: 1409.2329.

Zhou, X., Li, Y., and Liang, W. (2020). Cnn-rnn based intelligent recommendation for online medical pre-diagnosis support. *IEEE/ACM Trans. Comput. Biol. Bioinform*. 18, 912–921. doi: 10.1109/TCBB.2020.2994780

Conflict of Interest: The authors declare that the research was conducted in the absence of any commercial or financial relationships that could be construed as a potential conflict of interest.

frontiers in Bioengineering and Biotechnology

ORIGINAL RESEARCH
published: 26 August 2021
doi: 10.3389/fbioe.2021.657866

Application of Surgical Decision Model for Patients With Childhood Cataract: A Study Based on Real World Data

Jingjing Chen[1†], Yifan Xiang[1†], Longhui Li[1†], Andi Xu[1], Weiling Hu[1], Zhuoling Lin[1], Fabao Xu[1], Duoru Lin[1], Weirong Chen[1‡] and Haotian Lin[1,2*‡]*

[1] State Key Laboratory of Ophthalmology, Zhongshan Ophthalmic Center, Sun Yat-sen University, Guangzhou, China, [2] Center of Precision Medicine, Sun Yat-sen University, Guangzhou, China

OPEN ACCESS

Edited by:
Jian Yang,
Wuyi University, China

Reviewed by:
Giovanni Badiali,
University of Bologna, Italy
Honghua Yu,
Guangdong Provincial People's Hospital, China

***Correspondence:**
Duoru Lin
lindr3@mail2.sysu.edu.cn
Haotian Lin
linht5@mail.sysu.edu.cn

[†] These authors have contributed equally to this work

[‡] These authors share senior authorship

Specialty section:
This article was submitted to Bionics and Biomimetics, a section of the journal Frontiers in Bioengineering and Biotechnology

Received: 24 January 2021
Accepted: 04 May 2021
Published: 26 August 2021

Citation:
Chen J, Xiang Y, Li L, Xu A, Hu W, Lin Z, Xu F, Lin D, Chen W and Lin H (2021) Application of Surgical Decision Model for Patients With Childhood Cataract: A Study Based on Real World Data. Front. Bioeng. Biotechnol. 9:657866. doi: 10.3389/fbioe.2021.657866

Reliable validated methods are necessary to verify the performance of diagnosis and therapy-assisted models in clinical practice. However, some validated results have research bias and may not reflect the results of real-world application. In addition, the conduct of clinical trials has executive risks for the indeterminate effectiveness of models and it is challenging to finish validated clinical trials of rare diseases. Real world data (RWD) can probably solve this problem. In our study, we collected RWD from 251 patients with a rare disease, childhood cataract (CC) and conducted a retrospective study to validate the CC surgical decision model. The consistency of the real surgical type and recommended surgical type was 94.16%. In the cataract extraction (CE) group, the model recommended the same surgical type for 84.48% of eyes, but the model advised conducting cataract extraction and primary intraocular lens implantation (CE + IOL) surgery in 15.52% of eyes, which was different from the real-world choices. In the CE + IOL group, the model recommended the same surgical type for 100% of eyes. The real-recommended matched rates were 94.22% in the eyes of bilateral patients and 90.38% in the eyes of unilateral patients. Our study is the first to apply RWD to complete a retrospective study evaluating a clinical model, and the results indicate the availability and feasibility of applying RWD in model validation and serve guidance for intelligent model evaluation for rare diseases.

Keywords: childhood cataract, real-world data, surgical type, model validation, rare disease

INTRODUCTION

The application of artificial intelligence (AI) in medicine has achieved significant progress in medical researches (Crea, 2020; Xiang et al., 2020; Mervis, 2021). In most reported studies, medical AI systems perform excellently in both internal and external validations (Lin et al., 2018; Gurovich et al., 2019; Topol, 2019; Yamashita et al., 2021). However, the performances of AI systems in real-world applications are below expectations with much lower accuracies than the reported results (Lin H. et al., 2019; Baylor et al., 2020; Lee et al., 2021). More valid and exact methods are necessary to verify the effectiveness of the real application of medical AI systems to translate AI into clinical practice more safely (Cabitza et al., 2020; Lin and Yu, 2020).

A real-world clinical study (RWCS) was carried out to assess AI performance in clinical practice (Johnston et al., 2019; Nagendran et al., 2020), which is more objective and close to real application. However, the conduct of RWCS has executive risks for the indeterminate effectiveness of AI systems, especially in diagnosis (Sinha et al., 2020; Zhang et al., 2020) and therapy assistance (Schurink et al., 2005; Skrede et al., 2020). In addition, the RWCS probably takes a long time to validate clinical models for rare diseases, as it is not possible to accumulate enough cases in a short term for intelligent system evaluation.

Real-world data (RWD) can probably solve the executive risks of RWCSs. RWD is from patient medical chart reviews and registries rather than conventional randomized controlled trials (Elliott et al., 2016; Goldstein et al., 2019), which has been acknowledged as more favorable and valuable for guiding medical decisions (Goulooze et al., 2020). Published study has achieved a surgical decision model for a rare disease, childhood cataract (CC) (Lin D. et al., 2019). In our study, we collected RWD from 251 patients with CC and conducted a retrospective study to validate the CC surgical decision model. Our study applied RWD to complete a "retrospective RWCS" for model evaluation for the first time, and the results indicate the availability and feasibility of the application of RWD in model validation and serve as a guidance for AI system evaluation for rare diseases.

MATERIALS AND METHODS

A retrospective study was conducted from December 2018 to June 2020 at the Zhongshan Ophthalmic Center (ZOC), Guangdong, China. The RWD was collected from a national project for CC treatment and research, the Childhood Cataract Program of the Chinese Ministry of Health (CCPMOH) (Lin D. et al., 2019). This study followed the tenets of the Declaration of Helsinki and was approved by the Institutional Review Board of the ZOC at Sun Yat-sen University (IRB-ZOC-SYSU).

RWD Collection

Only patients diagnosed with CC and registered in CCPMOH were enrolled. The inclusion criteria were as follows: patients registered at CCPMOH (1) who were under the age of 18 years; (2) who were diagnosed with CC in the first year after birth; (3) who had surgical treatment at ZOC; (4) who had complete medical data before and after surgical treatment; and (5) for whom written informed consent was obtained from the legal guardian. The exclusion criteria were as follows: patients (1) who were diagnosed with CC complicated with other ocular lesions; and (2) who were diagnosed with other ophthalmic diseases.

The RWD included sex, laterality, axial length, anterior photography, surgical age, surgical type, surgical laterality and other examination and therapy information. The surgical plans were all designed and performed by three cataract professors (Yizhi Liu, WC, and HL). The primary surgical types included cataract extraction (CE) and cataract extraction combined with intraocular lens implantation (CE + IOL). Posterior continuous curvilinear capsulorhexis and anterior vitrectomy surgical procedures were also performed in CC patients younger than 6 years old at the time of surgery. All CC patients were regularly followed up at 1 day, 1 week, 1 month, 3 months, and 6 months postoperatively. At each follow-up, the best corrected visual acuity (BCVA), ocular pressure (non-contact tonometer, TX-F, Canon, Tokyo, Japan), and anterior photography were collected. The children unable to cooperate with ocular pressure examination and anterior photography were sedated with 10% chloral hydrate (0.6–0.8 ml per kilogram, oral or clyster) and tested with a Tonopen contact electronic tonometer (Reichert Inc., United States) and a slit-lamp (BX900, HAAG-STRETT, Switzerland) to record the occurrence of postoperative complications.

CC Surgical Type Decision Model

The CC surgical type decision model was established based on the data of 2421 CC patients recruited over 10 years from 1 January 2005 to 31 December 2014 (Lin D. et al., 2019). The original research aimed to provide timings of CE and IOL implantation for CC patients based on large-scale clinical experience, and to serve as a guidance for ophthalmologists to make treatment strategies. The model aimed to help choose the surgical type between CE and CE + IOL for CC patients.

$$\text{Logit}(P) = 7.929 - 0.096 \times \text{age} + 0.612 \times \text{laterality} - 0.317 \times \text{axial length}$$

Notes: Age in months; laterality: 1 for bilateral patients and 0 for unilateral patients; axial length in mm. Logit (P) $\geq$ 0.5 suggested CE; Logit (P) $<$ 0.5 suggested CE + IOL. The model behaved well in the internal validation and obtained an AUC of 0.96 [95% confidence interval (CI): 0.94–0.97] and a Youden index of 0.86.

Model Evaluation

We input the collected RWD into the surgical model to assess the consistency of the real surgical type and model-recommended surgical type. In addition, we compared the endpoint BCVAs, and the rates of complications between the real-recommended matched patients and the unmatched patients.

RESULTS

A total of 398 eyes of 251 patients with CC were enrolled. In total, 139 patients were male, and 112 patients were female. The mean follow-up time was 10.87 months [standard deviation (SD): 6.26 months]. The characteristics of RWD are shown in **Table 1**. There were 100 patients undergoing CE and 151 patients undergoing CE + IOL. The mean ages at surgery were 10.71 and 59.52 months in the two groups, respectively. The average endpoint BCVAs at 3 months after surgery were 0.52 ± 0.29 and 0.30 ± 0.28 for the right eyes of bilateral patients and the diseased eyes of unilateral patients, respectively.

The consistency of the real surgical type and model-recommended surgical type was 94.16% (**Figure 1**). In the CE group, the model recommended the same surgical type for

TABLE 1 | The characteristics of real-world data of enrolled patients with CC.

Characteristics	CE group	CE + IOL
Number	100	151
Male/Female	47/53	92/59
Age (month)	10.71 ± 13.455	59.52 ± 32.325
Bilateral/Unilateral	74/26	73/78
Eyes	174	224
Axial length (mm)	19.04 ± 1.97	22.39 ± 2.04
Endpoint BCVA (snellen)	0.10 ± 0.07	0.45 ± 0.30
Ocular hypertension	6/174	6/224
PCO	5/174	1/224

CE, cataract extraction; CE + IOL, cataract extraction combined with intraocular lens implantation; CC, childhood cataract; BCVA, best corrected visual acuity; PCO, posterior capsule opacification.

84.48% of eyes. In 15.52% of eyes, the model advised conducting CE + IOL surgery, which was different from the real-world choices. In the CE + IOL group, the model recommended the same surgical type for 100% of eyes. The real-recommended matched rates were 94.22% in the eyes of bilateral patients and 90.38% in the eyes of unilateral patients.

There were 27 eyes of 20 patients (17 eyes of 10 bilateral patients and 10 eyes of 10 unilateral patients) in RWD not consistent with the recommended surgical types in the CE group. The mean age was 23.41 ± 17.82 months and the mean axial length was 22.05 ± 1.20 mm in the 27 unmatched eyes. The mean visual acuity was 0.13 at 3 months after surgery and no complications occurred, which was not significantly different from the matched eyes in the CE group.

In our research, the mean axial lengths were 19.04 ± 1.97 mm and 22.39 ± 2.04 mm in CE group and CE + IOL group, respectively, at baseline. The axial lengths of unilateral patients were longer than those of bilateral patients before 7 years of age. The healthy eyes of unilateral patients had longer axial lengths than the diseased eyes before 6 years old, and the axial lengths of the diseased eyes of unilateral patients became close to the healthy eyes after the age of 6 years (**Figure 2**). In the bilateral patients, the axial lengths became longer than those in the unilateral patients after 7 years of age.

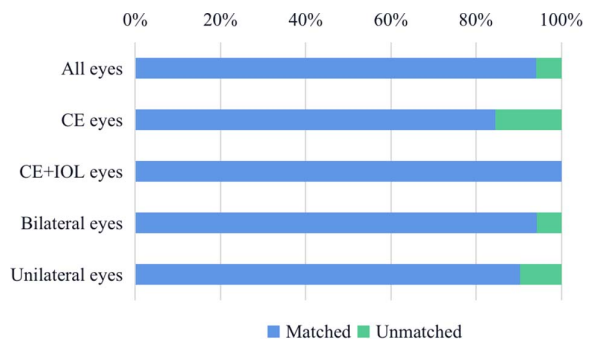

FIGURE 1 | The consistency of the real surgical type and recommended surgical type. In the CE group, the model recommended the same surgical type for 84.48% of eyes; In the CE + IOL group, the model recommended the same surgical type for 100% of eyes; In the eyes of bilateral patients, the model recommended the same surgical type for 94.22% of eyes; In the eyes of unilateral patients, the model recommended the same surgical type for 90.38% of eyes. CE, cataract extraction; CE + IOL, cataract extraction combined with intraocular lens implantation.

DISCUSSION

Our study adopted RWD to validate the performance of real-world applications, which is a more efficient and objective method with lower risks. The consistency of the real surgical type and recommended surgical type was 94.16% in our study, which proved that the CC surgical decision model was reliable but still needed some improvement to obtain higher accuracy in real-world applications.

Childhood cataract is a rare disease with a mean morbidity of 4.24/10000 (Wu et al., 2016), and is a leading cause of childhood blindness (Lenhart et al., 2015). Surgery is the only effective treatment for most CC patients (Lim et al., 2017). However, the ocular structure of CC patients is abnormal and smaller than that of adults (Gopinath et al., 2013; Lin D. et al., 2016; Lin H. et al., 2016); consequently, CC surgery is difficult and challenging. On account of the rarity and exceptionality of CC patients, there is no consensus regarding the surgery time and surgery type for CC, which remain controversial worldwide. CCPMOH is a hospital-based national program with the largest clinical database of CC patients (Lin et al., 2015), based on data of 2421 patients from which, a ZOC team constructed a CC surgical decision model (Lin D. et al., 2019). The model can potentially serve as an objective basis for ophthalmologists to decide on surgical plans after more validations. Our study can further validate the real-world performance of the model, and ensure that it can be safely applied to clinical work.

In our study, we adopted the RWD of 398 eyes of 251 patients with CC. The consistency of the real surgical type and model-recommended surgical type was 94.16%, and the recommended surgical types for 27 eyes of 20 patients were not consistent with the real surgical types in the CE group. The 27 eyes had longer axial lengths at younger ages, and the model might recommend CE + IOL based on the data. However, in clinical work, considering that younger patients will have myopia shift and eye growth (Weakley et al., 2017; Liu et al., 2019) afterward and the high morbidity of postoperative complications (Kumar and Lambert, 2016), ophthalmologists usually choose CE surgery for young patients with long axial lengths. Aphakic patients can wear frame glasses and contact lenses to achieve necessary refractive correction before IOL implantation surgery (Russell et al., 2017). In addition, other ocular parameters, including anterior chamber depth and capsular size, can be included in the model to improve its accuracy and general applicability. As most IOLs are designed for adults and too large for children, severe deformities of the anterior and posterior capsula were observed in 30% of CC patients with IOL, which potentially led to IOL eccentricity and dislocation (Lin D. et al., 2019). The model with capsular-associated parameters may have a higher applied effectiveness.

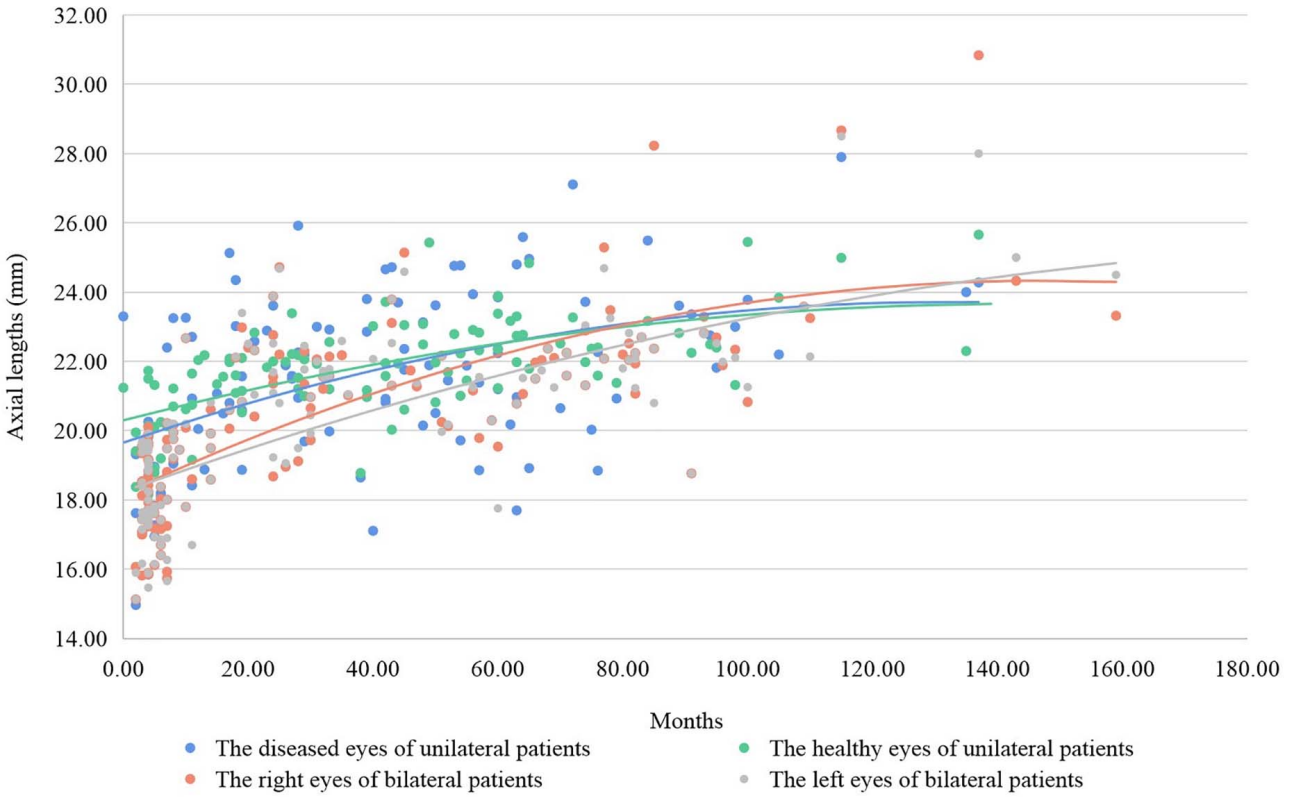

FIGURE 2 | The axial lengths and growing fit lines of patients according to laterality. The axial lengths of unilateral patients were longer than those of bilateral patients before 7 years of age, and the axial lengths of bilateral patients became longer than those of unilateral patients after 7 years of age. The axial lengths of the healthy eyes of unilateral patients were longer than those of the diseased eyes before 6 years of age, and the axial lengths of the diseased eyes of unilateral patients became close to the healthy eyes of unilateral patients after 6 years of age.

In the unilateral patients, the axial lengths of diseased eyes were shorter than those of healthy eyes before 6 years of age and then the axial lengths of both eyes became closer. CC may lead to the developing suppression of the diseased eyes of unilateral patients at a younger age (Lin H. et al., 2016). After that, the diseased eyes may undergo rapid secondary development and approach the healthy eyes. The eyes of bilateral patients had a similar developing pattern to the diseased eyes of unilateral patients. The myopia shift of bilateral patients has a larger span (Liu et al., 2019), and most bilateral patients have longer axial lengths than both eyes of unilateral patients after myopia shift.

Rare diseases have a low morbidity of 0.5–1‰ (Europe, 2005; Haendel et al., 2020). It is usually difficult to conduct clinical control studies on rare diseases (Dong and Wang, 2016). The applications of RWD may solve the validation problems regarding medical models for rare diseases. The retrospective study we conducted achieved close-to-real and reliable test results based on RWD, which proved the feasibility and availability of our method. By collecting the RWD retrospectively from clinical centers, model validations can be efficiently accomplished. Compared to RWCS, our method has fewer executive risks for the indeterminacy of the real-world application of diagnosis and therapy assistance, which is safer and more generally accessible.

LIMITATIONS

Some limitations of our research should be considered. RWD from more clinical centers is necessary to prove the general applicability of the surgical decision model. In addition, longer follow-up would contribute to the assessment of model efficacy. Additionally, the model may include more parameters to make it more precise.

CONCLUSION

Our study has brought up a new method to validate the performance of medical assistant models. This is the first research to apply RWD to retrospectively evaluate a medical model and the results indicate the availability and feasibility of our new method, which may serve guidance for intelligent model evaluation for rare diseases.

DATA AVAILABILITY STATEMENT

The data is available from the corresponding authors upon reasonable request.

ETHICS STATEMENT

The studies involving human participants were reviewed and approved by the Institutional Review Board of the ZOC at Sun Yat-sen University. Written informed consent to participate in this study was provided by the participants' legal guardian/next of kin.

AUTHOR CONTRIBUTIONS

JC, DL, WC, and HL conceived and designed the experiments. JC, YX, LL, ZL, and WH collected the data. YX and AX cleaned the data. YX and DL performed the experiments and analyzed the data. YX wrote the manuscript. JC, FX, DL, and HL revised the manuscript. All authors read and approved the final manuscript.

FUNDING

This study was funded by the Science and Technology Planning Projects of Guangdong Province (2018B010109008) and the National Natural Science Foundation of China (81770967, 81822010, and 82000946). The sponsors of the study played no role in the study protocol design; data collection, analysis, or interpretation; manuscript preparation; or the decision to submit the manuscript for publication.

ACKNOWLEDGMENTS

We are grateful to all participant CC patients for supporting our study.

REFERENCES

Baylor, E., Beede, E., Hersch, F., Iurchenko, A., and Wilcox, L. (2020). "A human-centered evaluation of a deep learning system deployed in clinics for the detection of diabetic retinopathy," in *Proceedings of the 2020 CHI Conference on Human Factors in Computing Systems*, (Honolulu, HI).

Cabitza, F., Campagner, A., and Balsano, C. (2020). Bridging the "last mile" gap between AI implementation and operation: "data awareness" that matters. *Ann. Transl. Med.* 8:501. doi: 10.21037/atm.2020.03.63

Crea, F. (2020). A fresh look at ischaemic heart disease: from artificial intelligence to reappraisal of old drugs. *Eur. Heart J.* 41, 4367–4370. doi: 10.1093/eurheartj/ehaa964

Dong, D., and Wang, Y. (2016). Challenges of rare diseases in China. *Lancet* 387:1906. doi: 10.1016/S0140-6736(16)30418-4

Elliott, L., Fidler, C., Ditchfield, A., and Stissing, T. (2016). Hypoglycemia event rates: a comparison between real-world data and randomized controlled trial populations in insulin-treated diabetes. *Diabetes Ther.* 7, 45–60. doi: 10.1007/s13300-016-0157-z

Europe, E. (2005). *Rare Diseases: Understanding this Public Health Priority*. Available online at: www.eurordis.org

Goldstein, B. A., Phelan, M., Pagidipati, N. J., Holman, R. R., Pencina, M. J., and Stuart, E. A. (2019). An outcome model approach to transporting a randomized controlled trial results to a target population. *J. Am. Med. Inform. Assoc.* 26, 429–437. doi: 10.1093/jamia/ocy188

Gopinath, B., Wang, J. J., Kifley, A., Tan, A. G., Wong, T. Y., and Mitchell, P. (2013). The association between ocular biometry and retinal vascular caliber is comparable from early childhood to adolescence. *Invest. Ophthalmol. Vis. Sci.* 54, 1501–1508. doi: 10.1167/iovs.12-11036

Goulooze, S. C., Zwep, L. B., Vogt, J. E., Krekels, E., Hankemeier, T., van den Anker, J. N., et al. (2020). Beyond the randomized clinical trial: innovative data science to close the pediatric evidence gap. *Clin. Pharmacol. Ther.* 107, 786–795. doi: 10.1002/cpt.1744

Gurovich, Y., Hanani, Y., Bar, O., Nadav, G., Fleischer, N., Gelbman, D., et al. (2019). Identifying facial phenotypes of genetic disorders using deep learning. *Nat. Med.* 25, 60–64. doi: 10.1038/s41591-018-0279-0

Haendel, M., Vasilevsky, N., Unni, D., Bologa, C., Harris, N., Rehm, H., et al. (2020). How many rare diseases are there. *Nat. Rev. Drug. Discov.* 19, 77–78. doi: 10.1038/d41573-019-00180-y

Johnston, S. S., Morton, J. M., Kalsekar, I., Ammann, E. M., Hsiao, C. W., and Reps, J. (2019). Using machine learning applied to real-world healthcare data for predictive analytics: an applied example in bariatric surgery. *Value Health* 22, 580–586. doi: 10.1016/j.jval.2019.01.011

Kumar, P., and Lambert, S. R. (2016). Evaluating the evidence for and against the use of IOLs in infants and young children. *Expert Rev. Med. Devices* 13, 381–389. doi: 10.1586/17434440.2016.1153967

Lee, A. Y., Yanagihara, R. T., Lee, C. S., Blazes, M., Jung, H. C., Chee, Y. E., et al. (2021). Multicenter, Head-to-Head, Real-World validation study of seven automated artificial intelligence diabetic retinopathy screening systems. *Diabetes Care [Online ahead of print]* doi: 10.2337/dc20-1877

Lenhart, P. D., Courtright, P., Wilson, M. E., Lewallen, S., Taylor, D. S., Ventura, M. C., et al. (2015). Global challenges in the management of congenital cataract: proceedings of the 4th International Congenital Cataract Symposium held on March 7, 2014, New York, New York. *J. Am. Assoc. Pediatric Ophthalmol. Strabismus* 19, e1–e8.

Lim, M. E., Buckley, E. G., and Prakalapakorn, S. G. (2017). Update on congenital cataract surgery management. *Curr. Opin. Ophthalmol.* 28, 87–92. doi: 10.1097/ICU.0000000000000324

Lin, D., Chen, J., Lin, Z., Li, X., Wu, X., Long, E., et al. (2015). 10-Year overview of the hospital-based prevalence and treatment of congenital cataracts: the CCPMOH experience. *PLoS One* 10:e0142298. doi: 10.1371/journal.pone.0142298

Lin, D., Chen, J., Liu, Z., Wu, X., Long, E., Luo, L., et al. (2016). Prevalence of corneal astigmatism and anterior segmental biometry characteristics before surgery in chinese congenital cataract patients. *Sci. Rep.* 6:22092.

Lin, D., Liu, Z., Chen, J., Lin, Z., Zhu, Y., Chen, C., et al. (2019). Practical pattern of surgical timing of childhood cataract in China: a cross-sectional database study. *Int. J. Surg.* 62, 56–61. doi: 10.1016/j.ijsu.2019.01.012

Lin, H., Li, R., Liu, Z., Chen, J., Yang, Y., Chen, H., et al. (2019). Diagnostic efficacy and therapeutic decision-making capacity of an artificial intelligence platform for childhood cataracts in eye clinics: a multicentre randomized controlled trial. *EClinicalMedicine* 9, 52–59. doi: 10.1016/j.eclinm.2019.03.001

Lin, H., Lin, D., Chen, J., Luo, L., Lin, Z., Wu, X., et al. (2016). Distribution of axial length before cataract surgery in Chinese pediatric patients. *Sci. Rep.* 6:23862. doi: 10.1038/srep23862

Lin, H., Long, E., Ding, X., Diao, H., Chen, Z., Liu, R., et al. (2018). Prediction of myopia development among Chinese school-aged children using refraction data from electronic medical records: a retrospective, multicentre machine learning study. *PLoS Med.* 15:e1002674. doi: 10.1371/journal.pmed.1002674

Lin, H., and Yu, L. (2020). Medical artificial intelligent research: translating artificial intelligence into clinical practice. *Ann. Transl. Med.* 8, 695–695. doi: 10.21037/atm-2020-mair-21

Liu, Z. Z., Long, E. P., Lin, D. R., Ye, L., Xiang, Y. F., Li, W. T., et al. (2019). Dynamic profile of ocular refraction in pediatric cataract patients after lens surgeries. *Int. J. Ophthalmol.* 12, 1839–1847. doi: 10.18240/ijo.2019.12.04

Mervis, J. (2021). U.S. law sets stage for boost to artificial intelligence research. *Sci.* 371, 112–113. doi: 10.1126/science.371.6525.112

Nagendran, M., Chen, Y., Lovejoy, C. A., Gordon, A. C., Komorowski, M., Harvey, H., et al. (2020). Artificial intelligence versus clinicians: systematic review of design, reporting standards, and claims of deep learning studies. *BMJ* 368:m689. doi: 10.1136/bmj.m689

Russell, B., Dubois, L., Lynn, M., Ward, M. A., Lambert, S. R., and The Infant Aphakia Treatment Study Group (2017). The infant aphakia treatment study contact lens experience to age 5 years. *Eye Contact Lens* 43, 352–357. doi: 10.1097/icl.0000000000000291

Schurink, C. A., Lucas, P. J., Hoepelman, I. M., and Bonten, M. J. (2005). Computer-assisted decision support for the diagnosis and treatment of infectious diseases in intensive care units. *Lancet Infect Dis.* 5, 305–312. doi: 10.1016/S1473-3099(05)70115-8

Sinha, P., Delucchi, K. L., McAuley, D. F., O'Kane, C. M., Matthay, M. A., and Calfee, C. S. (2020). Development and validation of parsimonious algorithms to classify acute respiratory distress syndrome phenotypes: a secondary analysis of randomised controlled trials. *Lancet Respir. Med.* 8, 247–257. doi: 10.1016/S2213-2600(19)30369-8

Skrede, O. J., De Raedt, S., Kleppe, A., Hveem, T. S., Liestøl, K., Maddison, J., et al. (2020). Deep learning for prediction of colorectal cancer outcome: a discovery and validation study. *Lancet* 395, 350–360. doi: 10.1016/S0140-6736(19)32998-8

Topol, E. J. (2019). High-performance medicine: the convergence of human and artificial intelligence. *Nat. Med.* 25, 44–56. doi: 10.1038/s41591-018-0300-7

Weakley, D. R. Jr., Lynn, M. J., Dubois, L., Cotsonis, G., Wilson, M. E., Buckley, E. G., et al. (2017). Myopic shift 5 years after intraocular lens implantation in the infant aphakia treatment study. *Ophthalmology* 124, 822–827. doi: 10.1016/j.ophtha.2016.12.040

Wu, X., Long, E., Lin, H., and Liu, Y. (2016). Prevalence and epidemiological characteristics of congenital cataract: a systematic review and meta-analysis. *Sci. Rep.* 6:28564. doi: 10.1038/srep28564

Xiang, Y., Zhao, L., Liu, Z., Wu, X., Chen, J., Long, E., et al. (2020). Implementation of artificial intelligence in medicine: status analysis and development suggestions. *Artif. Intell. Med.* 102:101780. doi: 10.1016/j.artmed.2019.101780

Yamashita, R., Long, J., Longacre, T., Peng, L., Berry, G., Martin, B., et al. (2021). Deep learning model for the prediction of microsatellite instability in colorectal cancer: a diagnostic study. *Lancet Oncol.* 22, 132–141. doi: 10.1016/S1470-2045(20)30535-0

Zhang, Y., Shi, J., Peng, Y., Zhao, Z., Zheng, Q., Wang, Z., et al. (2020). Artificial intelligence-enabled screening for diabetic retinopathy: a real-world, multicenter and prospective study. *BMJ Open Diabetes Res. Care* 8:e001596. doi: 10.1136/bmjdrc-2020-001596

Conflict of Interest: The authors declare that the research was conducted in the absence of any commercial or financial relationships that could be construed as a potential conflict of interest.

frontiers in Bioengineering and Biotechnology

ORIGINAL RESEARCH
published: 05 November 2021
doi: 10.3389/fbioe.2021.651340

Deep Learning for Detecting Subretinal Fluid and Discerning Macular Status by Fundus Images in Central Serous Chorioretinopathy

Fabao Xu[1†], Shaopeng Liu[2†], Yifan Xiang[1†], Zhenzhe Lin[1], Cong Li[1], Lijun Zhou[1], Yajun Gong[1], Longhui Li[1], Zhongwen Li[1], Chong Guo[1], Chuangxin Huang[1], Kunbei Lai[1], Hongkun Zhao[1], Jiaming Hong[3], Haotian Lin[1,4]* and Chenjin Jin[1]**

[1]State Key Laboratory of Ophthalmology, Zhongshan Ophthalmic Center, Sun Yat-sen University, Guangzhou, China, [2]School of Computer Science, Guangdong Polytechnic Normal University, Guangzhou, China, [3]School of Medical Information Engineering, Guangzhou University of Chinese Medicine, Guangzhou, China, [4]Center of Precision Medicine, Sun Yat-sen University, Guangzhou, China

OPEN ACCESS

Edited by:
Vincenzo Ferrari, University of Pisa, Italy

Reviewed by:
Olivier Ly, Université de Bordeaux, France
Xin Liu, University of California, San Diego, United States

***Correspondence:**
Jiaming Hong
jmhong@outlook.com
Haotian Lin
haot.lin@hotmail.com
Chenjin Jin
jinchj@mail.sysu.edu.cn

†These authors have contributed equally to this work

Specialty section:
This article was submitted to Bionics and Biomimetics, a section of the journal Frontiers in Bioengineering and Biotechnology

Received: *09 January 2021*
Accepted: *11 October 2021*
Published: *05 November 2021*

Citation:
Xu F, Liu S, Xiang Y, Lin Z, Li C, Zhou L, Gong Y, Li L, Li Z, Guo C, Huang C, Lai K, Zhao H, Hong J, Lin H and Jin C (2021) Deep Learning for Detecting Subretinal Fluid and Discerning Macular Status by Fundus Images in Central Serous Chorioretinopathy. Front. Bioeng. Biotechnol. 9:651340. doi: 10.3389/fbioe.2021.651340

Subretinal fluid (SRF) can lead to irreversible visual loss in patients with central serous chorioretinopathy (CSC) if not absorbed in time. Early detection and intervention of SRF can help improve visual prognosis and reduce irreversible damage to the retina. As fundus image is the most commonly used and easily obtained examination for patients with CSC, the purpose of our research is to investigate whether and to what extent SRF depicted on fundus images can be assessed using deep learning technology. In this study, we developed a cascaded deep learning system based on fundus image for automated SRF detection and macula-on/off serous retinal detachment discerning. The performance of our system is reliable, and its accuracy of SRF detection is higher than that of experienced retinal specialists. In addition, the system can automatically indicate whether the SRF progression involves the macula to provide guidance of urgency for patients. The implementation of our deep learning system could effectively reduce the extent of vision impairment resulting from SRF in patients with CSC by providing timely identification and referral.

Keywords: deep learning, central serous chorioretinopathy, subretinal fluid, serous retinal detachment, fundus image

INTRODUCTION

As the fourth most common nonsurgical retinopathy, central serous chorioretinopathy (CSC) is an idiopathic ophthalmopathy in which the neurosensory retina is often detached in the central macular region due to serous leakage from defects of the retinal pigment epithelium, causing a condition where fluid accumulates under the retina and thus causes a visual impairment (Wang et al., 2008; Manayath et al., 2018). In Western countries, such as the United States, a population-based study reported that annual age-adjusted incidences of CSC from 1980 to 2002 were 9.9 and 1.7 per 100,000 in men and women, respectively, in a predominantly Caucasian population (van Rijssen et al., 2019). In Eastern countries, however, pachychoroid diseases, such as CSC and polypoidal choroidal vasculopathy, have been considered to be more prevalent than in Caucasian populations (Wong et al., 2016; van Rijssen et al., 2019). Although CSC often causes irreversible visual disability in its

later stage, the early diagnosis and timely and proper treatment, such as photodynamic therapy and other laser therapies, can improve the rate of complete absorption of subretinal fluid (SRF) and lead to a satisfactory prognosis of CSC (van Rijssen et al., 2019).

However, identifying all the serous retinal detachments (SRDs) at an early stage remains challenging, as a low volume of SRF often exists asymptomatically and leads to atrophy of the outer layers of the retina (Wong et al., 2016; Xu et al., 2020). Fundus fluorescein angiography (FFA) and optical coherence tomography (OCT) are more sensitive examinations for detecting CSC in clinical work. However, these imaging methods are still not widely available and expensive, especially in some less developed countries and regions (Daruich et al., 2015; Manayath et al., 2018; Zhen et al., 2020). In addition, FFA, as an invasive examination, sometimes leads to severe allergic reactions such as nausea and shock caused by fluorescent dye, which is not suitable for routine detection of SRD (Soomro et al., 2018; He et al., 2020). In the past, there have been some efforts on assessing CSC based on FFA and OCT (Narendra Rao et al., 2019; Zhen et al., 2020); however, considering the clinical practicality, a fundus photograph is the best imaging manner to routinely detect status and severity of patients with CSC. Unfortunately, it is not easy, even for experienced ophthalmologists, to reliably identify CSC on fundus photography. If a computer tool is available to automatically assess the status and severity of patients with CSC using a fundus photograph, an ophthalmologist can perform a timely intervention to avoid the possibility of severe poor prognosis. Consequently, it is essential to develop an intelligent screening approach to detect SRF at an early stage of CSC.

In addition to the presence or absence of SRF, the location of SRF is also a major factor affecting prognosis and treatment (Daruich et al., 2015; Manayath et al., 2018). The presence of macula-on SRF is a potential indicator of the urgency of intervention and the central visual prognosis after treatment, indicating that the macula-on SRF patient needs a more urgent intervention than those with macula-off SRF (Mrejen et al., 2019; Yu et al., 2019). Therefore, to assess the patient's condition in more detail, we aimed to develop and evaluate a cascaded artificial intelligence (AI) system for detecting SRF and discerning the macular status in patients with CSC based on the fundus photograph.

MATERIALS AND METHODS

To develop the cascaded AI system, a total of 12,532 fundus photographs were retrospectively obtained from CSC patients presenting for retinopathy examinations or undergoing a routine ophthalmic health evaluation between February 2015 and January 2020 at the Zhongshan Ophthalmic Center (ZOC) using Zerss (FF-450plus), Topcon (TRC–NW8), and Newvision (RetiCam3100) fundus cameras with 30 or 50° fields of view. For each patient with CSC enrolled, we have both fundus photographs and their corresponding OCT images. We used the OCT images to determine the presence or absence of SRF (**Figure 1**). An experienced retinal specialist (Chenjin Jin) was responsible for reviewing OCT examinations. All privacy information was removed, and all images were deidentified before transfer to research investigators. Our ethics committee ruled that written informed consent was not required because of the retrospective nature of our study and all the images were fully anonymized. This study was approved by the Institutional Review Board of ZOC, Sun Yat-sen University, and adhered to the tenets of the Declaration of Helsinki.

Image Classification and the Reference Standard

According to OCT images, all fundus photographs were classified into SRD and non-SRD. Then, we further classified SRD images into macula-on SRD and macula-off SRD according to whether SRF extended to involve the fovea within 300 microns. Image quality was defined as follows: 1) high quality referred to images without any problems; 2) relatively high quality referred to images with slight deficiencies in focus, illumination, or topo-artifacts, but the region of optic disc and macula could still be identified completely; 3) medium quality referred to images with an obscured view of the image (smaller than one-third of the image), but part of the SRD region could still be identified, and the region of the optic disc and the macula could be identified; 4) poor quality referred to images that were insufficient for any interpretation (an obscured area over one-third of the image), or the region of the optic disc and the macula could not be identified. To ensure the accuracy of image classification, all anonymous fundus photographs were classified separately by three board-certified retinal specialists with at least 5 years of clinical experience (Zhongwen Li, Fabao Xu, and Longhui Li). Any disagreement was arbitrated by another senior retinal specialist with more than 30 years of clinical experience (Chenjin Jin). **Figure 2** illustrates the workflow of the study.

Data Preprocessing and Augmentation

The image data were standardized and normalized before deep learning model training. Firstly, all the images were resized to 512 × 512 pixels, where each pixel value was further rescaled to the range of 0–1. Secondly, to build deep learning models adapting different kinds of variations in fundus images, three data augmentation operations were deployed to expand our image datasets artificially, including random rotation (at the angle of 90, 180, and 270°, respectively), cropping (512 × 512 to 320 × 320, and then resize back to 512 × 512), and flipping.

Deep Learning System Development

To effectively detect SRD and discern macular status by fundus images, a cascaded architecture of convolutional neural networks (CNNs) was deployed. To be specific, cascaded systems have two separate CNN models. The model in the first stage focuses on the early identification of SRD by fundus images, whereas the model in the second stage focuses on further classifying SRD images into macula-on SRD or macula-off SRD (shown in **Figure 3**).

Two models were trained separately using a state-of-the-art CNN model, EfficientNet-B0 (Zhao et al., 2020). EfficientNet is a

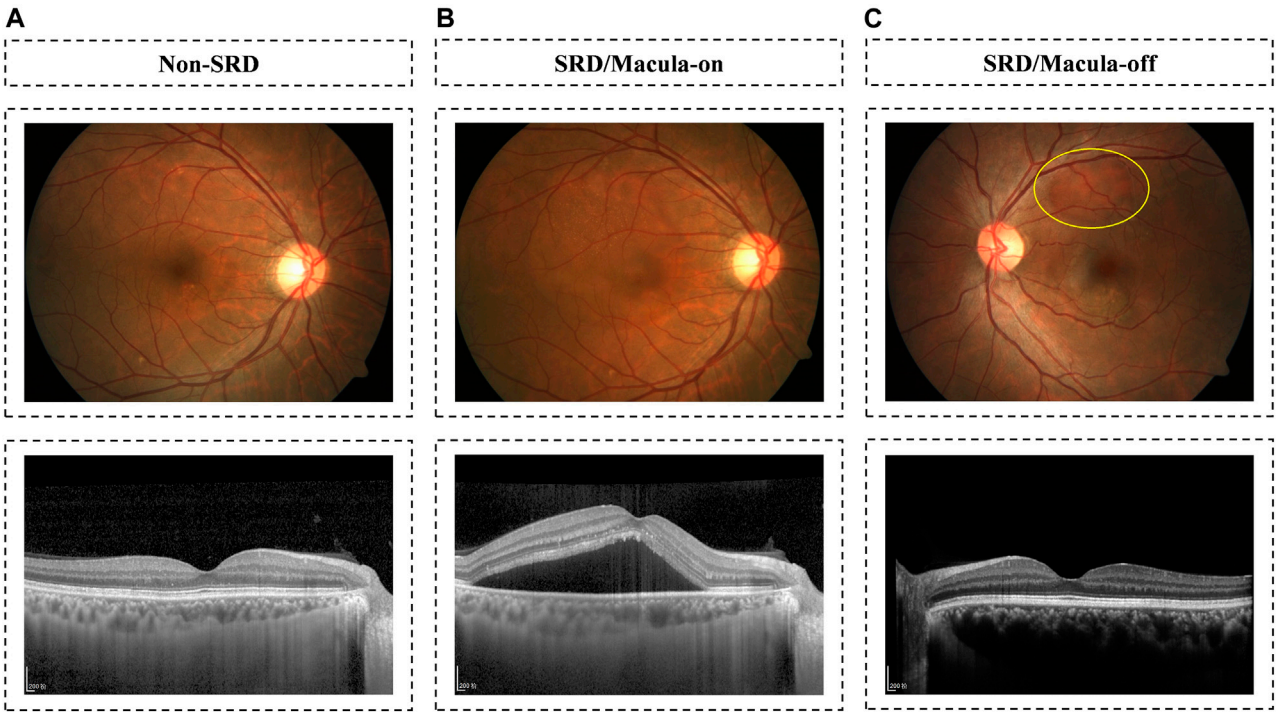

FIGURE 1 | Fundus image examples with OCT-verified CSC. Examples of three CSC states: non-SRD on the panel **(A)**; macula-on SRD on the panel **(B)**; and macula-off SRD in the panel **(C)**.

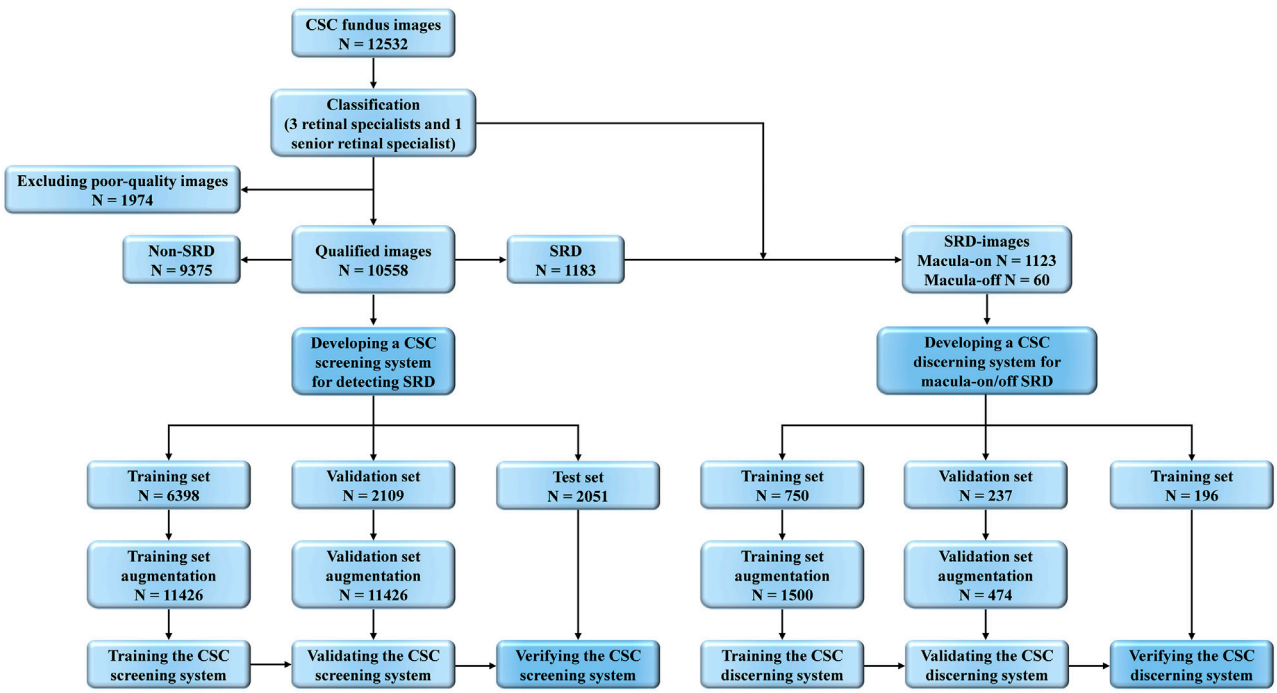

FIGURE 2 | Overall Study Workflow. Workflow of developing deep learning systems for identifying SRD and discerning macula-on/off SRD based on fundus images. SRD, serous retinal detachment; CSC, central serous chorioretinopathy.

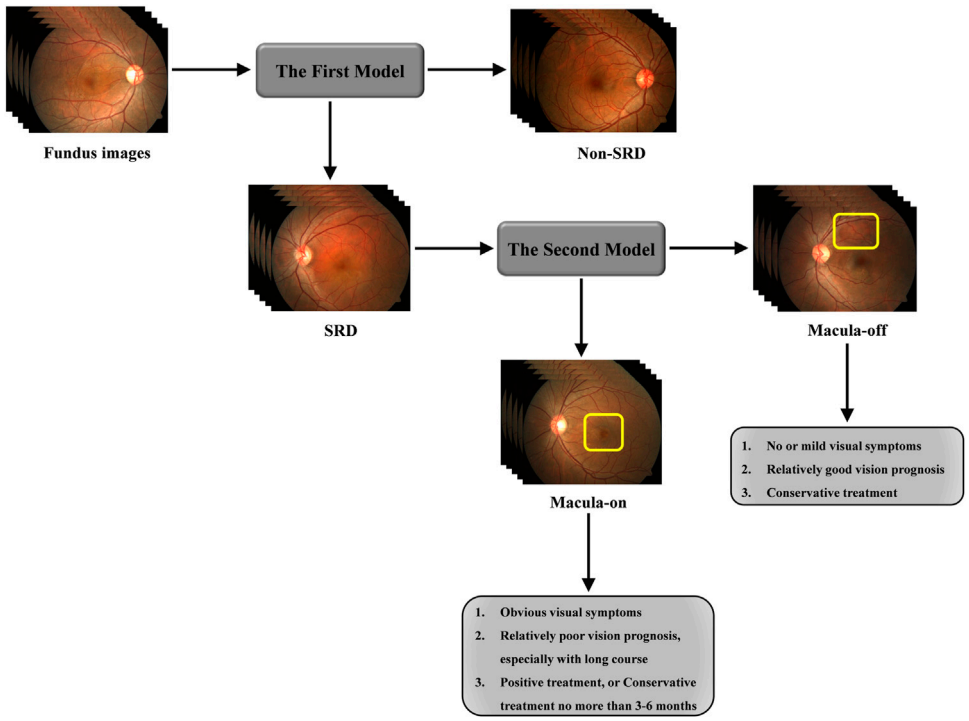

FIGURE 3 | Framework of cascaded deep learning system and its corresponding clinical application. CSC often has a halo-like appearance in macula regions due to SRD. Top left, A fundus image of a normal subject without SRD; Top middle, A fundus image of a patient with SRD at macula; Top right, A fundus image of a patient with SRD away from macula (circled in yellow). SRD, serous retinal detachment; CSC, central serous chorioretinopathy.

powerful CNN model proposed by Google in recent years, which can automatically scale network height, width, and resolution to achieve an efficient classification effect. To train the first model, all the fundus images collected were used with labels of SRD or non-SRD. As for the second model, the SRD images were used with labels of macula-on SRD or macula-off SRD. To make models more reliable, a whole data set was randomly divided into three non-overlapping subsets, namely, training set, validation set, and testing set. The training set was used to produce candidate models; the validation set was used to assess these models and help determine the optimal ones as the final applied models. The final models were then evaluated using the testing set. We performed image standardization before deep feature learning, and data augmentation was applied to increase the diversity of the dataset and thus reduce the chance of overfitting. The implementation and training details of the models are as follows. Firstly, transfer learning from the pretrained EfficientNet-B0 was adopted to improve the training effect. Secondly, we use the focal loss as loss functions of the two EffecientNet models considering that the sample sizes for different classes are unbalanced. As is universally acknowledged, the focal loss function is specially designed for training problems with class imbalance. Therefore, the models can pay more attention to the samples in the minority class in the training process. To be concrete, we set the alpha parameter in the focal loss function to be 0.5 in both models. Lastly, we use Adam as the optimizer in training EfficientNet and set the learning rate to be 0.003, the learning rate decay factor as 0.99, the total number of epochs to be 50, and the batch size to be 16.

Model Evaluation

We evaluated the performance of the developed AI system using the independent testing data set, among which no image was involved in the training set. We accessed nonparametric receiver operating characteristic analysis on the testing data set and calculated the 95% confidence intervals. The sensitivity, specificity, and accuracy of the systems for detecting SRD and discerning the macular status were also computed. We asked three retinal specialists (Cong Li, Hongkun Zhao, and Lijun Zhou) who had 3, 5, and 10 years of experience, respectively, to independently assess CSC status in the testing data. Then, we compared their performance with the deep learning models.

RESULTS

Demographic Characteristics

As shown in **Figure 1**, 12,532 fundus photographs from 568 CSC patients (mean age 45.23 ± 7.45 years; range, 31–72 years) and 4,126 subjects (mean age 46.41 ± 8.84 years; range, 12–78 years) presenting for retinopathy examinations or undergoing a routine ophthalmic health evaluation were labeled for SRD or non-SRD. In the quality control phase, 1,974 poor-quality images of 51 CSC patients and 1,028 normal subjects were deleted due to the

TABLE 1 | Patient demographics.

Characteristic	CSC group	Normal group
Patients (*n*)	568	4,126
Images (SRF label)	4,316 (1,183)	6,242
Age (years)	45.23 ± 7.45	46.41 ± 8.84
Males (%)	482 (84.86)	2,105 (51.02)
Train set (SRF label)	2,566 (685)	3,823
Validation set (SRF label)	906 (271)	1,203
Test set (SRF label)	844 (227)	1,207

CSC, central serous chorioretinopathy.

opacity of the refractive media or artifacts (e.g., images without decipherable optic disc or fovea, arc defects over one-third of the area, dust spots on the optic disc and/or fovea, or images with incorrect focus). The first AI system designed to identify SRD was developed using 10,558 fundus photographs, 1,183 of which were classified as SRD, whereas the remaining 9,375 images were classified as non-SRD. All eligible images were randomly divided into three sets in a patient-level (no overlapping patients), with 60% (6,398 images) as a training set, 20% (2,109 images) as a validation set, and 20% (2051 images) as a test set. Then, the second AI system was developed using 1,183 SRD images to discern macula-off SRD from macula-on SRD, with 60% (750 images) as a training set, 20% (237 images) as a validation set, and 20% (196 images) as a test set. The functions of the two AI systems are shown in **Figure 3**. The numbers of labels and demographic data in the training, validation, and test sets are shown in **Table 1**.

Performance of Deep Learning Models

The performance of the AI models and general ophthalmologists to detect SRD and discern the macular status is shown in **Table 2**. For SRD detection, the retinal specialist 1 with 3 years of experience had a sensitivity of 59.7% and a specificity of 66.7%, the retinal specialist 2 with 5 years of experience had a sensitivity of 63.7% and a specificity of 71.1%, and the retinal specialist 3 with 10 years of experience had a sensitivity of 65.6% and a specificity of 75.6%, whereas the first AI model had a sensitivity of 92.1% and a specificity of 92.0% (**Figures 4A–C**) with an area under the curve (AUC) of 0.961 (**Figure 5A**).

For discerning macula-on SRD from macula-off SRD, the retinal specialist 1 with 3 years of experience had a sensitivity of 74.4% and a specificity of 33.3%, the retinal specialist 2 with 5 years of experience had a sensitivity of 76.0% and a specificity of 42.9%, and the retinal specialist 3 with 10 years of experience had a sensitivity of 77.3% and a specificity of 47.6%, whereas the second AI model had a sensitivity of 92.3% and a specificity of 82.0% (**Figures 4D–F**) with an AUC of 0.910 (**Figure 5B**).

DISCUSSION

In this study, we developed a cascaded deep learning system containing two models based on 11,087 fundus images and verified its feasibility. The first deep learning model was used to identify SRD and showed robust performance (AUC 0.961, a sensitivity of 92.1%, and a specificity of 92.0%). The second model used to discern macula-on SRD from macula-off SRD also exhibited ideal performance (AUC 0.910, a sensitivity of 92.3%, and a specificity of 82.0%). The deep learning models performed better than the retinal specialists in both tasks. These results validate that our deep learning models provide an objective SRD detection with high accuracy and efficiency in patients with CSC, while also precisely determining whether the macula is involved. Overall, the intelligent system achieved a better performance in classification, demonstrating the potential of the deep learning technology in evaluating CSC based on fundus photography.

As shown, the specificities of both deep learning models were higher than those of the retinal specialists (**Table 2**). As high sensitivity and specificity are a prerequisite for a screening tool and can reduce the workload and medical costs by avoiding the need for further examinations of evidently normal eyes. High-dose hormone shock therapy and long-term maintenance dose corticosteroids intake often lead to secondary CSC (Tsai et al., 2014; Daruich et al., 2015; Manayath et al., 2018), so this system can be used to screen CSC as a part of the ophthalmic routine evaluations in common corticosteroids therapy departments, such as endocrinology, gastroenterology, and rheumatology, that were lacking ophthalmologists or be deployed in hospitals with a large number of patients to assist ophthalmologists.

TABLE 2 | Performance of the AI systems *vs.* general ophthalmologists in the test sets.

SRD/non-SRD	Sensitivity (95% CI)	Specificity (95% CI)	Accuracy (95% CI)
AI system	0.921 (0.846, 0.996)	0.920 (0.845, 0.995)	0.920 (0.845, 0.995)
Retinal specialist 1	0.597 (0.549, 0.645)	0.667 (0.621, 0.713)	0.605 (0.557, 0.653)
Retinal specialist 2	0.637 (0.590 0.684)	0.711 (0.667, 0.755)	0.645 (0.598, 0.692)
Retinal specialist 3	0.656 (0.609, 0.703)	0.756 (0.714, 0.798)	0.668 (0.622, 0.714)
Macula on/off			
AI system	0.923 (0.849, 0.997)	0.820 (0.698, 0.916)	0.852 (0.708, 0.930)
Retinal specialist 1	0.744 (0.701, 0.787)	0.333 (0.287, 0.379)	0.725 (0.681, 0.769)
Retinal specialist 2	0.760 (0.718, 0.802)	0.429 (0.380, 0.478)	0.743 (0.700, 0.786)
Retinal specialist 3	0.773 (0.732, 0.814)	0.476 (0.427, 0.525)	0.758 (0.716, 0.800)

AI, artificial intelligence. Ophthalmologist 1 with 3 years of working experience at a physical examination center; ophthalmologist 2 with 5 years of working experience at a physical examination center; ophthalmologist 3 with 10 years of working experience at a physical examination center. CI, confidence interval.

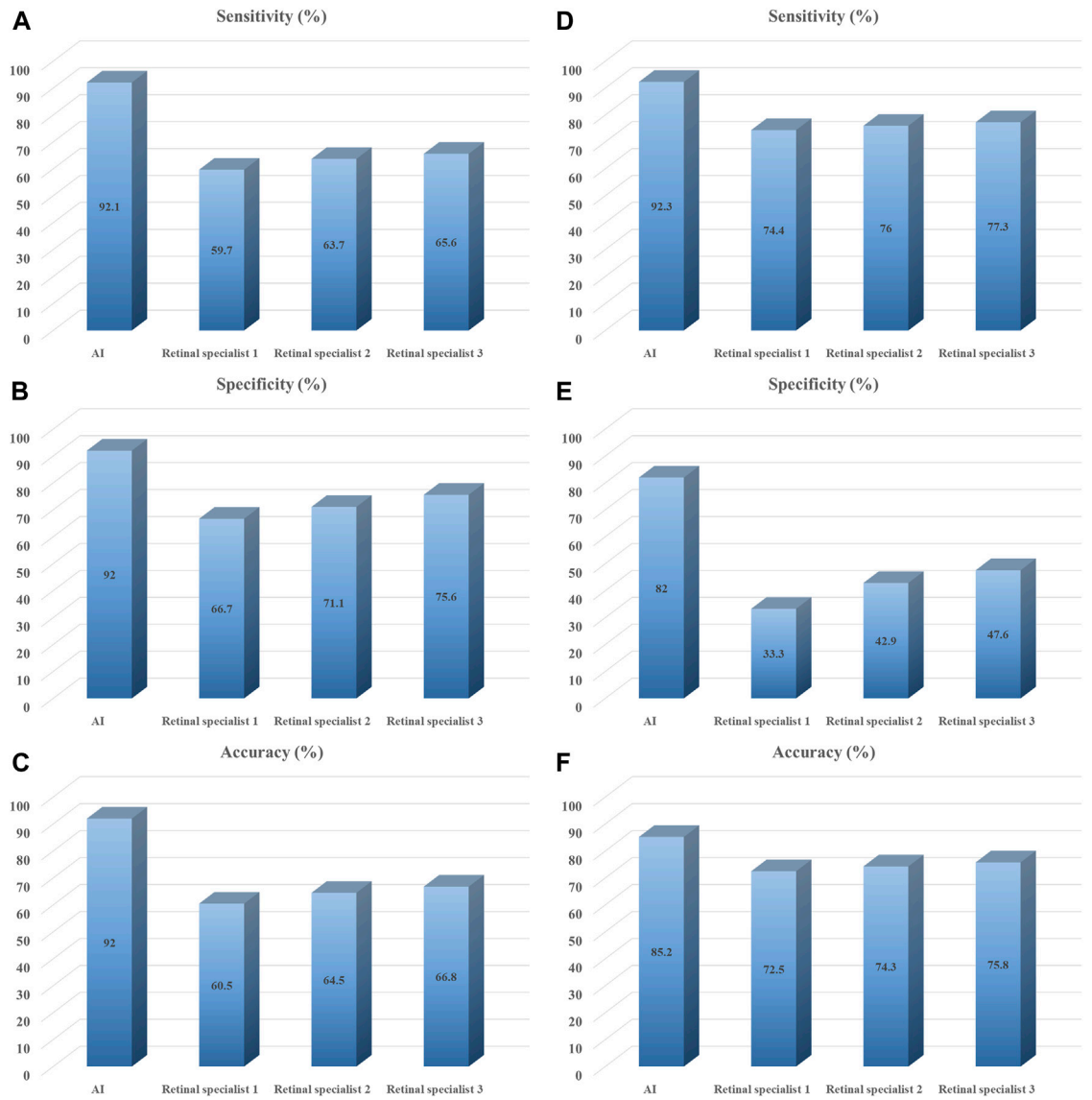

FIGURE 4 | Performance of deep learning models *vs.* retinal specialists in test set. Summary of classification results by deep learning models and three retinal specialists on testing data set. **(A–C)** Identification performance of SRD; **(D–F)** Discern performance of macula-on SRD. Retinal specialist 1 with 3 years of working experience at a physical examination center; retinal specialist 2 with 5 years of working experience at a physical examination center; retinal specialist 3 with 10 years of working experience at a physical examination center.

Advances in OCT have enabled observation of the SRD, but not all hospitals and clinics possess OCT devices, especially in developing countries. If SRDs of patients with CSC could be detected by deep learning models with a fundus image instead of an OCT device, we could detect the status of patients more conveniently at a lower cost. Besides, the models could be used to alert patients to the emergency of SRD.

There have been a number of deep learning architectures developed for fundus disease evaluation, and they can be largely grouped into three different categories based on their objectives, including screening (Gulshan et al., 2016; Voets et al., 2019), prognosis prediction (Poplin et al., 2018), and computer-assisted system for diagnosis and treatment (Khojasteh et al., 2018; Shankaranarayana et al., 2019). AI is playing an increasingly important role in medical activities, such as diabetes screening systems, which has begun to serve ophthalmic health evaluations in physical examination centers or community hospitals lacking ophthalmologists, or be deployed in hospitals with a large number of patients for ophthalmologists' assistance (Ting et al., 2017; Ting et al., 2019). Previously, Narendra Rao et al. (2019) reported a deep learning-based system for automatic detection and segmentation of sub-retinal fluid in CSC by OCT images. However, limited work has been dedicated to identifying CSC using color fundus. Compared with their study, the system developed in our study can detect SRDs based on fundus images and evaluate the emergency of CSC, which is more

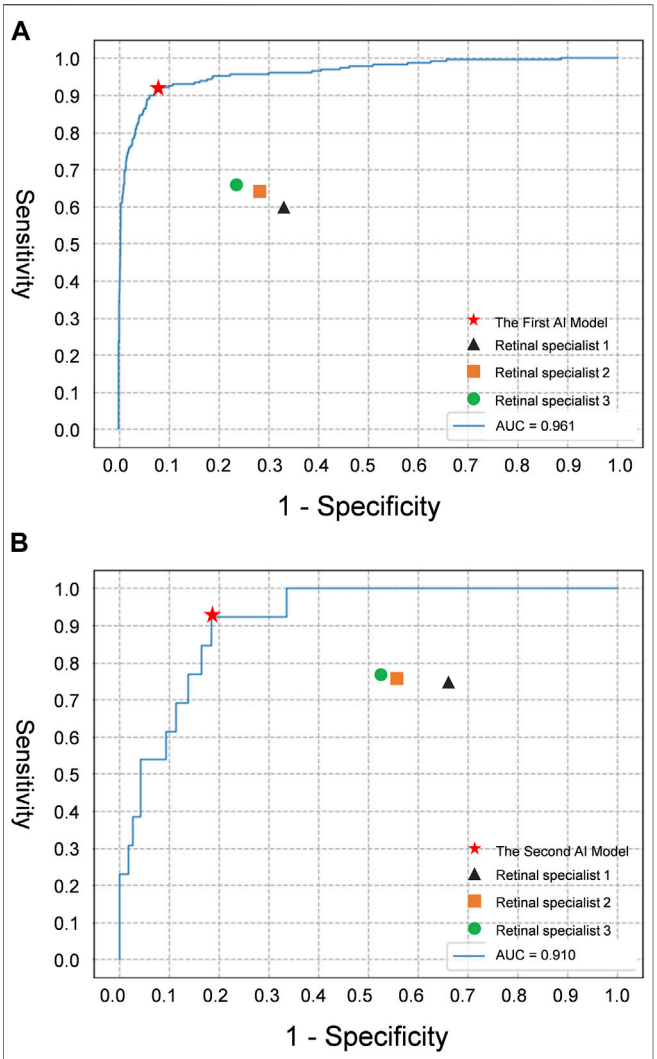

FIGURE 5 | The receiver operating characteristic curve of the deep learning models for evaluating CSC depicted on fundus images, compared with retinal specialists' performance. **(A)** Detection performance of SRD; **(B)** Detection performance of macula-on SRD. AUC area under the receiver operating characteristic curve; Retinal specialist 1, 3 years of working experience; retinal specialist 2, 5 years of working experience; retinal specialist 3, 10 years of working experience.

conformed to clinical application. The availability of such a tool could be helpful to ophthalmologists as a second eye to timely and accurately detect CSC with the wide-applied and noninvasive color fundus photography. In particular, it may reduce unnecessary fluorescein angiography and/or OCT examinations, which may involve adverse effects or additional cost and often not be available in developing areas.

Several limitations exist in this study. First, all follow-up data for a patient at different times were included, the variety and the number of the images were limited, and all these images were acquired from a single institution. We expect that the performance may significantly improve when using a large, diverse data set for training the deep learning network and dedicating additional effort to optimize the training parameters. Second, we did not verify whether, and to what extent, different fundus camera equipment may affect CSC assessment. It is well known that the standardization of train data remains a key point to the development of AI, such as image scope, light exposure, focus, and sharpness. Finally, the training set and test set did not distinguish between acute and chronic CSCs due to a lack of reference standards (Manayath et al., 2018). Despite the importance of defining a recognized classification system for CSC, no consensus has been reached so far. CSC is commonly divided into two categories based on the duration of symptoms (6 months), acute and chronic CSCs (Manayath et al., 2018). However, many of the enrolled patients were followed for more than 6 months, but their imaging findings may not change obviously before or after this demarcation line. Therefore, we did not conduct a subgroup analysis of acute and chronic CSCs in this study.

In conclusion, the present study verifies that our robust cascaded deep learning system can be applied to detect SRF and discern macula status efficiently in patients with CSC. Furthermore, our deep learning system provides a template to patients with fundus diseases, which are characterized by SRF progression. Due to the convenience and versatility of fundus images, a future effort is desirable to make it available to the clinical practice for initial CSC screening in common therapy departments and CSC follow-up departments. Prospective clinical studies to evaluate the cost-effectiveness and the performance of this system in real-world settings are needed.

DATA AVAILABILITY STATEMENT

The data analyzed in this study is subject to the following licenses/restrictions: The data are temporarily not available for privacy reasons but can be obtained for legitimate reasons in consultation with the corresponding author. Requests to access these datasets should be directed to HL, haot.lin@hotmail.com.

ETHICS STATEMENT

Our ethics committee rules that written informed consent was not required because of the retrospective nature of our study, and all the images were fully anonymized. This study was approved by the Institutional Review Board of ZOC, Sun Yat-sen University, and adhered to the tenets of the Declaration of Helsinki.

AUTHOR CONTRIBUTIONS

Conception and design: FX, YX, HL, and CJ. Administrative support: CJ and HL. Provision of study materials or patients: CJ, FX, HL, SL, YX, and JH. Collection and assembly of data: FX, CJ, YX, ZL, LZ, CL, LL, YG, and JH. Data analysis and interpretation: ZL, LS, and JH. Manuscript writing: All authors; Final approval of the manuscript: All authors.

REFERENCES

Daruich, A., Matet, A., Dirani, A., Bousquet, E., Zhao, M., Farman, N., et al. (2015). Central Serous Chorioretinopathy: Recent Findings and New Physiopathology Hypothesis. *Prog. Retin. Eye Res.* 48, 82–118. doi:10.1016/j.preteyeres.2015.05.003

Gulshan, V., Peng, L., Coram, M., Stumpe, M. C., Wu, D., Narayanaswamy, A., et al. (2016). Development and Validation of a Deep Learning Algorithm for Detection of Diabetic Retinopathy in Retinal Fundus Photographs. *JAMA* 316 (22), 2402–2410. doi:10.1001/jama.2016.17216

He, L., Chen, C., Yi, Z., Wang, X., Liu, J., and Zheng, H. (2020). Clinical Application of Multicolor Imaging in Central Serous Chorioretinopathy. *Retina* 40 (4), 743–749. doi:10.1097/iae.0000000000002441

Khojasteh, P., Aliahmad, B., and Kumar, D. K. (2018). Fundus Images Analysis Using Deep Features for Detection of Exudates, Hemorrhages and Microaneurysms. *BMC Ophthalmol.* 18 (1), 288. doi:10.1186/s12886-018-0954-4

Manayath, G. J., Ranjan, R., Karandikar, S. S., Shah, V. S., Saravanan, V. R., and Narendran, V. (2018). Central Serous Chorioretinopathy: Current Update on Management. *Oman J. Ophthalmol.* 11 (3), 200–206. doi:10.4103/ojo.OJO_29_2018

Mrejen, S., Balaratnasingam, C., Kaden, T. R., Bottini, A., Dansingani, K., Bhavsar, K. V., et al. (2019). Long-Term Visual Outcomes and Causes of Vision Loss in Chronic Central Serous Chorioretinopathy. *Ophthalmology* 126 (4), 576–588. doi:10.1016/j.ophtha.2018.12.048

Narendra Rao, T. J., Girish, G. N., Kothari, A. R., and Rajan, J. (2019). Deep Learning Based Sub-Retinal Fluid Segmentation in Central Serous Chorioretinopathy Optical Coherence Tomography Scans. 2019 41st Annual International Conference of the IEEE Engineering in Medicine and Biology Society (EMBC), 978–981. doi:10.1109/EMBC.2019.8857105

Poplin, R., Varadarajan, A. V., Blumer, K., Liu, Y., McConnell, M. V., Corrado, G. S., et al. (2018). Prediction of Cardiovascular Risk Factors from Retinal Fundus Photographs via Deep Learning. *Nat. Biomed. Eng.* 2 (3), 158–164. doi:10.1038/s41551-018-0195-0

Shankaranarayana, S. M., Ram, K., Mitra, K., and Sivaprakasam, M. (2019). Fully Convolutional Networks for Monocular Retinal Depth Estimation and Optic Disc-Cup Segmentation. *IEEE J. Biomed. Health Inform.* 23 (4), 1417–1426. doi:10.1109/jbhi.2019.2899403

Soomro, T., Talks, J., and Medscape (2018). The Use of Optical Coherence Tomography Angiography for Detecting Choroidal Neovascularization, Compared to Standard Multimodal Imaging. *Eye* 32 (4), 661–672. doi:10.1038/eye.2018.2

Ting, D. S. W., Cheung, C. Y.-L., Lim, G., Tan, G. S. W., Quang, N. D., Gan, A., et al. (2017). Development and Validation of a Deep Learning System for Diabetic Retinopathy and Related Eye Diseases Using Retinal Images from Multiethnic Populations with Diabetes. *JAMA* 318 (22), 2211–2223. doi:10.1001/jama.2017.18152

Ting, D. S. W., Peng, L., Varadarajan, A. V., Keane, P. A., Burlina, P. M., Chiang, M. F., et al. (2019). Deep Learning in Ophthalmology: The Technical and Clinical Considerations. *Prog. Retin. Eye Res.* 72, 100759. doi:10.1016/j.preteyeres.2019.04.003

Tsai, D.-C., Chen, S.-J., Huang, C.-C., Chou, P., Chung, C.-M., Chan, W.-L., et al. (2014). Risk of Central Serous Chorioretinopathy in Adults Prescribed Oral Corticosteroids. *Retina* 34 (9), 1867–1874. doi:10.1097/iae.0000000000000159

van Rijssen, T. J., van Dijk, E. H. C., Yzer, S., Ohno-Matsui, K., Keunen, J. E. E., Schlingemann, R. O., et al. (2019). Central Serous Chorioretinopathy: Towards an Evidence-Based Treatment Guideline. *Prog. Retin. Eye Res.* 73, 100770. doi:10.1016/j.preteyeres.2019.07.003

Voets, M., Møllersen, K., and Bongo, L. A. (2019). Reproduction Study Using Public Data of: Development and Validation of a Deep Learning Algorithm for Detection of Diabetic Retinopathy in Retinal Fundus Photographs. *PLoS One* 14 (6), e0217541. doi:10.1371/journal.pone.0217541

Wang, M., Munch, I. C., Hasler, P. W., Prünte, C., and Larsen, M. (2008). Central Serous Chorioretinopathy. *Acta Ophthalmol.* 86 (2), 126–145. doi:10.1111/j.1600-0420.2007.00889.x

Wong, K. H., Lau, K. P., Chhablani, J., Tao, Y., Li, Q., and Wong, I. Y. (2016). Central Serous Chorioretinopathy: What We Have Learnt So Far. *Acta Ophthalmol.* 94 (4), 321–325. doi:10.1111/aos.12779

Xu, F., Zhou, L., Lai, K., Gong, Y., Li, L., Lian, P., et al. (2020). Quantitative Evaluation of Retinal Vessel Density in Central Serous Chorioretinopathy after Half-Dose Photodynamic Therapy. *Curr. Eye Res.* 46, 855–864. doi:10.1080/02713683.2020.1843684

Yu, J., Xu, G., Chang, Q., Ye, X., Li, L., Jiang, C., et al. (2019). Risk Factors for Persistent or Recurrent Central Serous Chorioretinopathy. *J. Ophthalmol.* 2019, 5970659. doi:10.1155/2019/5970659

Zhao, L., Ishag Mahmoud, M. A., Ren, H., and Zhu, M. (2020). A Visual Tracker Offering More Solutions. *Sensors (Basel)* 20 (18), 5374. doi:10.3390/s20185374

Zhen, Y., Chen, H., Zhang, X., Meng, X., Zhang, J., and Pu, J. (2020). Assessment of Central Serous Chorioretinopathy Depicted on Color Fundus Photographs Using Deep Learning. *Retina* 40 (8), 1558–1564. doi:10.1097/iae.0000000000002621

Conflict of Interest: The authors declare that the research was conducted in the absence of any commercial or financial relationships that could be construed as a potential conflict of interest.

Publisher's Note: All claims expressed in this article are solely those of the authors and do not necessarily represent those of their affiliated organizations or those of the publisher, the editors, and the reviewers. Any product that may be evaluated in this article, or claim that may be made by its manufacturer, is not guaranteed or endorsed by the publisher.

Advantages of publishing in Frontiers

OPEN ACCESS
Articles are free to read for greatest visibility and readership

FAST PUBLICATION
Around 90 days from submission to decision

HIGH QUALITY PEER-REVIEW
Rigorous, collaborative, and constructive peer-review

TRANSPARENT PEER-REVIEW
Editors and reviewers acknowledged by name on published articles

Frontiers
Avenue du Tribunal-Fédéral 34
1005 Lausanne | Switzerland

Visit us: www.frontiersin.org
Contact us: frontiersin.org/about/contact

REPRODUCIBILITY OF RESEARCH
Support open data and methods to enhance research reproducibility

DIGITAL PUBLISHING
Articles designed for optimal readership across devices

FOLLOW US
@frontiersin

IMPACT METRICS
Advanced article metrics track visibility across digital media

EXTENSIVE PROMOTION
Marketing and promotion of impactful research

LOOP RESEARCH NETWORK
Our network increases your article's readership